JAEA-Review
2006-005

JP0650345

JAEA-Review

研究炉利用における研究成果集(平成16年度)

Activity Report on the Utilization of Research Reactors
(Japanese Fiscal Year, 2004)

(編) 研究炉利用課

(Ed.) Research Reactor Utilization Section

東海研究開発センター
原子力科学研究所
研究炉加速器管理部

Department of Research Reactor and Tandem Accelerator
Nuclear Science Research Institute
Tokai Research and Development Center

March 2006

Japan Atomic Energy Agency

日本原子力研究開発機構

JAEA-Review 2006-005

研究炉利用における研究成果集（平成１６年度）

日本原子力研究開発機構 東海研究開発センター 原子力科学研究所
研究炉加速器管理部
（編）研究炉利用課

（2006年1月26日受理）

平成16年度、原子力科学研究所においてはJRR-3の7サイクルとJRR-4の41サイクルの共同利用運転を行なった。

研究炉は、中性子散乱、即発ガンマ線分析、中性子ラジオグラフィ、医療照射（ＢＮＣＴ）などの実験利用及び、各種試料の放射化分析、原子炉材料照射試験、RI製造、フィッショントラック年代測定のための照射利用など、先端的研究を含め様々な目的に利用されている。

本報告書は、研究炉の利用者（原子力機構外を含む）から成果の提出235件を受け、中性子散乱（10分野）、中性子ラジオグラフィ、即発ガンマ線分析、放射化分析、RIの製造、その他の分野別に取りまとめたものである。

原子力科学研究所：〒319-1195　茨城県那珂郡東海村白方白根2-4

JAEA-Review 2006-005

Activity Report on the Utilization of Research Reactors (Japanese Fiscal Year, 2004)

(Ed.) Research Reactor Utilization Section

Department of Research Reactors
and Tandem Accelerator
Nuclear Science Research Institute
Tokai Research and Development Center
Japan Atomic Energy Agency
Tokai-mura, Naka-gun, Ibaraki-ken

(Received January 26, 2006)

During the fiscal year 2004, the Nuclear Science Research Institute research reactors carried out 7 cycles of joint use reactor operation at JRR-3 and 41 cycles at JRR-4.
The research reactors are being utilized for various purposes including experimental studies such as neutron scattering, prompt gamma analysis, neutron radiography and medical irradiation (BNCT), and irradiation utilization such as neutron activation analysis of various samples, RI production, Irradiation Test of Reactor Materials and fission track, advanced Science Research.
This volume contains 235 activity reports, which are categorized into the fields of neutron scattering (10 subcategories), neutron radiography, neutron activation analysis, RI Production, prompt gamma analysis, and others, submitted by the users in JAEA and from other organizations.

Keywords: JRR-3, JRR-4, Research Reactor, Neutron Scattering, Neutron Radiography, Neutron Activation Analysis, Neutron Beam, Irradiation

目　次

Contents

はじめに

平成１６年度には、ＪＲＲ－３において７サイクルの共同利用運転、ＪＲＲ－４において４１サイクルの共同利用運転が行なわれ、これに伴いさまざまな利用が行われた。

本報告書は、利用者（原子力機構外利用者を含む）から当該利用の成果の提出を受け、取りまとめたものである。

提出して頂いた成果の件数は、中性子散乱２０９件、中性子ラジオグラフィ７件、即発ガンマ線分析４件、放射化分析１１件、RIの製造１件、その他３件で合計２３５件であった。なお、本報告書の一部は下記報告書の中から転載させて頂いた。

最後に、原稿を提出して頂いた利用者の皆様のご協力に感謝するとともに、今後も研究炉が有効に利用され、種々の研究がさらに進展されることを期待します。

研究炉利用課長
楠　剛

---

1)標　　題　：ACTIVITY REPORT ON NEUTRON SCATTERING RESEARCH issued by ISSP-NSL,University of Tokyo
（東京大学物性研究所発行）
レポート番号：Vol.12（第１２巻）
編　　者　：東京大学物性研究所
発 行 年　：２００５年

2)標　　題　：原研施設利用共同研究成果報告書（平成１６年度）
レポート番号：UTRCN-G-34
編　　者　：東京大学原子力研究総合センター
発 行 年　：２００５年

This is a blank page.

研 究 成 果 一 覧

Research Reports

This is a blank page.

This is a blank page.

1. 中性子散乱 1)構造・励磁

1. Neutron Scattering 1) Structure・Excitation

This is a blank page.

研究テーマ：熱電材料中の低エネルギー励起
表題：冷中性子散乱による **Co-121** および関連したコバルト酸化物の研究

1) Cold neutron inelastic scattering study for Co-121 and related cobaltites

Tsuyoshi Kajitani, Yuzuru Miyazaki, Yasuhiro Ono, Ken-ichi Hamano, Shingo Inayama and Yuh-ki Hasegawa
Department of Applied Physics, Graduate School of Engineering, Tohoku University
6-6-05 Aoba, Aoba-ku , Sendai 980-8579
FAX:+81-22-795-7969, e-mail: kajitani@mail.tains.tohoku.ac.jp

ABSTRACT Cold neutron ,_=4.22_, inelastic scattering experiment was carried out for the thermoelectric oxides Co-121 ,i.e. $[Ca_2CoO_3]_{0.62}[CoO_2]$, and related cobalt oxides by the use of a TOF-type multicounter cold neutron spectrometer, AGNES, in JAERI. Polycrystalline samples were used for the experiment at 12K, 90K and room temperature. Low energy inelastic intensities, being _E < 3meV, are observed in the Co-121 in which _E=1.7±0.2meV peak is observed at room temperature. This peak becomes broad at 90K and 12K, being stronger at 12K. Since the paramagnetic to ferromagnetic phase transition at 27K was previously found with decreasing temperature by the _SR measurement by Sugiyama et al.[1],above low energy excitation could be discussed in terms of the spin ordering of Co^{4+} ions or localized motion of displaced oxygen atoms

1. INTRODUCTION

Strongly correlated $3d^5$ or $3d^6$ electrons of Co^{4+} and Co^{3+} ions, respectively, situated in the triangular CdI_2-type CoO_2 layers has attracted much attentions because of the semiconducting and some times superconducting behaviors below 4.2K[2]. High Seebeck coefficient and low electrical resistivity are reported for Na_xCoO_2 with x=0.7 and Co-121, i.e. $[Ca_2CoO_3]_{0.62}CoO_2$ and identified as Ca349, being typical thermoelectric oxide semiconductors. Sugiyama et al.[1] proposed three phase transition temperatures at about 27K, 100K and 600K or above which correspond, respectively, to the long-range-spin ordered phase(LRO) to the short-range ordered one(SRO), SRO to the metallic paramagnetic phase(PM) and PM to the semiconducting paramagnetic(PM) phase with increasing temperature.

For better understanding of the high thermoelectric performance of the Co-121 and related cobaltites, it has been needed to elucidate temperature dependent behaviors of magnons and phonons of these crystal systems in the low temperature range below and over 27K by the neutron inelastic scattering measurement.

2. RESULTS

Fig.1 shows cold neutron scattering intensity, S(_), of (Cu,Co)-221, Co-121 and Co_3O_4 at room temperature. The horizontal axis corresponds to the energy transfer values of the incidence. The negative side of the spectra corresponds to the kinetic energy loss side, i.e. the Stokes side. The central peaks are the elastic scattering components.

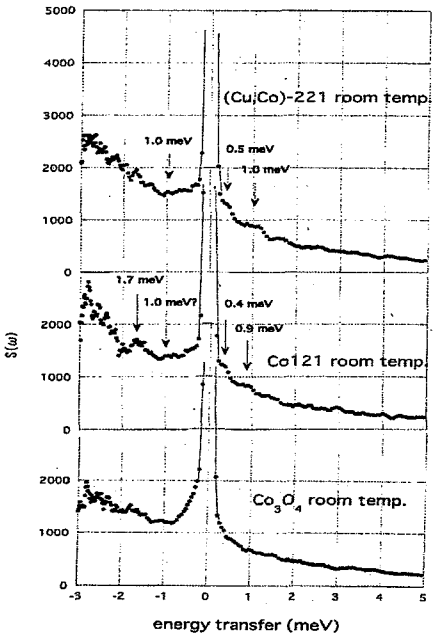

Figure 1 represents observed cold neutron scattering intensities of (Cu,Co)-221, Co-121 and Co_3O_4.

3.REFERENCES

[1].J.Sugiyama, C.Xia and T.Tani:Phys.Rev.B 68(2003) 134423. [2].K.Takada,H.sakkurai,E.Takayama-Muromachi,F.Izumi,R.A.Dilanian and T.Sasaki:Nature 422(2003),53.

使用施設：**JRR-3M**, 装置：**AGNES (C3-1-1)**, 分野：構造・励起

研究テーマ： IRT(MINE)
表題： 中性子反射率法による水素吸蔵金属箔中の水素量分布測定

2) Report on hydrogen content in hydrogen absorbing materials using neutron reflectometry

S. Tasaki[1], T.Ebisawa[2], D.Yamazaki[2], M. Hino[3], Y.Kawabata[3], Y.Yoshino[3]

[1] *Dept. of Eng. Kyoto Univ. Yoshida-honmachi, Sakyou-ku Kyoto, 606-8501*
[2] *Japan Atomic Energy Research Institute, Tokai Ibaraki Pref. 319-1195*
[3] *Res.React. Inst. Kyoto Univ. Kumatori Osaka, 590-0494*

In the cource of developing new method for hydrogen content measurement, we have studied here hydrogen content in thin films of hydrogen absorber, using neutron reflectometry as test experiments.

We have prepared Pd, $LaNi_{4.9}Al_{0.1}$, and $Ti_{30}Cr_{50}V_{20}$ as hydrogen absober, the latter two of which are supplied by T.Ebisawa in Nihon Seikoujo Co.Ltd.

The reflectometry samples are fabricated with vacuum evaporation system at Research Reactor Institute Kyoto University. Each material was stacked over Si wafer with 1mm-thickness and 75mm-diameter. The thickness of the materials was 40nm for Pd, 250nm for $LaNi_{4.9}Al_{0.1}$, and 250nm for $Ti_{30}Cr_{50}V_{20}$.

The measurements were performed using neutron refletometer at C3-1-2-1 (MINE) beam port of JRR-3M reactor in Japan Atomic Energy Research Agency. The arrangement for the measurements is shown in Fig.1. Since neutron transsibity is very high, neutron reflectivity can be measured in hydrogen environment as shown in the figure.

Neutron reflectivity measurements were performed for various hydrogen pressure for each samples. Typical reflectivity result is shown in Fig.2. Here hydrogen pressure is 0.02MPa and the fact that the interference fringes in the reflectivity curve disappear, implies that scattering length density of Pd containing hydrogen becomes very close to that of Si near the Si substrate. The estimated profile of the scattering length density is shown in Fig.3 as black line and H/Pd ratio as gray line.

Interesting thing in the result is that hydrogen content is higher near the substrate, not near the surface, where at a first glance Pd can contain more hydrogen because volume expansion is not so prohibited.

In the same way, hydrogen content in Pd film was estimated for various hydrogen pressure. H/Pd ratio increases as the hydrogen pressure and the tendency that H/Pd ratio is higher near Si surface is the same for all pressure.

For other samples made of hydrogen absorbing alloys, clear hydrogen absorption was not observed. This might be due to the alloy content change during the evaporation process.

In the next steps, we will perform neutron interferometry experiments with multilayer spin splitter using Pd as a gap layer, in order to develop hydrogen content measurement with higher precision.

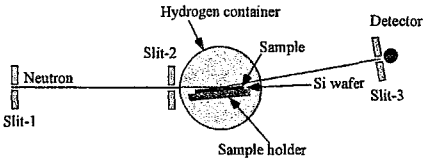

Fig. 1. The arrangement for the neutron reflectivity measurements.

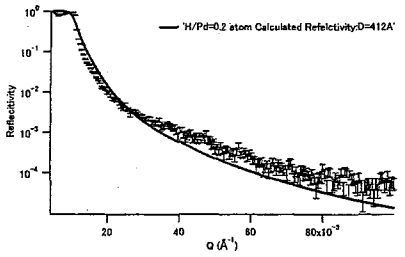

Fig. 2. Neutron reflectivity of Pd film in 0.02MPa hydrogen pressure. Interference fringes disappeared.

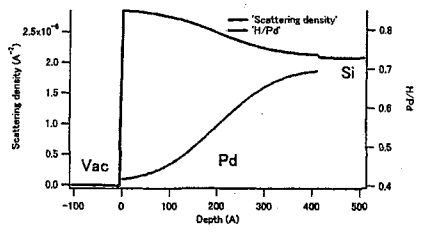

Fig. 3. Neutron scattering length density and H/Pd ratio evaluated from the neutron reflectivity.

使用施設：JRR-3M, 装置： C3-1-2-2 (MINE), 分野： 1.Structures & Excitations.

研究テーマ：孤立水素結合型物質 h-BrHPLN($C_{13}O_2H_7Br$) の水素結合と量子常誘電性の研究
表題： h-BrHPLN における水素結合中水素原子の原子核分布の温度変化

3) Temperature Dependence of the Nuclear Density Distribution of the Hydrogen Atom in the Hydrogen-Bond Region in h-BrHPLN

R. Kiyanagi, H. Kimura [1], M. Watanabe [1], Y. Noda [1], T. Sugawara[2] and T. Mochida[3]
Neutron Science Laboratory, Institute of Materials Structure Science,
Hige Energy Accelerator Research Organization
1-1 Oho Tsukkuba 305-0801
[1] *Institute of Multidisciplinary Research for Advanced Materials, Tohoku University,*
2-1-1 Katahira, Aoba-ku, Sendai 980-8577
[2] *Department of Basic Science, Graduate School of Arts and Science, The University of Tokyo*
3-8-1 komaba, meguro-ku 153-8902
[3] *Department of Chemistry, Faculty of Science, Toho University*
2-2-1 miyama, funabashi 273-8510

The isolated hydrogen-bonded material, 5-bromo-9-hydroxyphenalenon($C_{13}H_7O_2Br$, h-BrHPLN), is a paraelectric material down to 4 K. According to a dielectric measurement, the permittivity of h-BrHPLN increases monotonically without showing any anomalies as the temperature decreases. This behavior is reminiscent of a quantum paraelectric character and thought to be originated in the nature of the hydrogen atom in the hydrogen-bond region. In this study, we carried out neutron structure analyses on h-BrHPLN at several temperature point between 300 K to 10 K in order to elucidate the nature of the hydrogen atom in the hydrogen-bond region.

The experiments were performed with the four circle neutron diffractometer FONDER installed at T2-2 beam port at JRR-3M in JAERI(Tokai). The data collections were carried out at 300 K, 150 K, 100 K, 70 K, 50 K, 30 K and 10 K.

Least-square fitting analyses and Maximum Entropy Method analyses were applied to the collected data to refine the structural parameters and to calculate the nuclear density distribution, respectively. The obtained nuclear density distributions at several temperatures are shown in Fig. 1. As a result, the hydrogen atom in the hydrogen-bond region was found to be disordered occupying two equivalent sites around the center of the hydrogen-bond in whole temperature region. The point is that we can see the clear splitting of the nuclear density distribution even at 10 K. According to the calorimetric measurement[1] and the neutron incoherent inelastic scattering[2], the residual entropy about the hydrogen atom in the hydrogen-bond is zero at 10 K and the hydrogen atom is in a two energy state. Together with these results, it can be concluded that the nuclear density distribution of the hydrogen atom at 10 K means a tunneling state of the hydrogen atom. This is thought to be the origin of the quantum paraelectric character of h-BrHPLN.

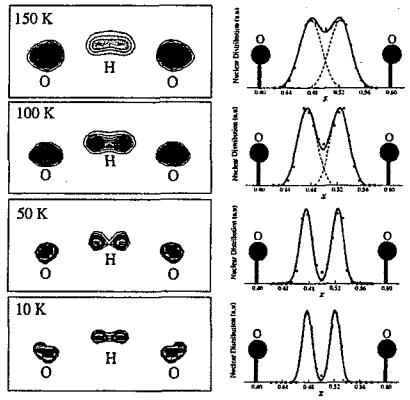

Fig. 1. The nuclear distribution around the hydrogen-bond at each temperature. The right figures show the one-dimensional distribution of the nuclear density distribution along the hydrogen-bond.

References

[1] T. Matsuo *et al* : J. Chem. Phys. **108** (1998) 9809.
[2] Y. Noda *et al.*: *Unpublished Data*

使用施設：JRR-3M，装置： T22: FONDER，分野： 1, Structure and Excitations

研究テーマ：中性子散乱によるウラン化合物の物性研究
表　題：粉末中性子回折による重い電子系超伝導体 $PrOs_4Sb_{12}$ のラットリングの研究

4) Neutron powder diffraction study on rattling of Pr in heavy fermion superconductor $PrOs_4Sb_{12}$

Koji KANEKO[1], Naoto METOKI[1,2], Tatsuma D. MATSUDA[1], and Masafumi KOHGI[3]

[1] *Advanced Science Research Center, Japan Atomic Energy Research Institute, Tokai, Naka, Ibaraki 319-1195*
[2] *Department of Physics, Tohoku University, Sendai 980-8578*
[3] *Department of Physics, Tokyo Metropolitan University, Tokyo 192-0397*

Recently, $PrOs_4Sb_{12}$ was reported to be the first Pr-based heavy fermion superconductor with T_{SC}=1.85 K.[1)] The non-magnetic Γ_1 singlet ground state and the existence of field-induced antiferro-quadrupolar order phase suggest the important role of quadruploar interaction in forming the Cooper pairs.[2,3)] A recent theoretical study also suggests the importance of 'rattling' of Pr, the large localized incoherent thermal vibration under a shallow potential in an over-sized Sb cage.[4,5)] In order to reveal the thermal displacement of Pr, neutron powder diffraction experiments were carried out on HRPD for $PrOs_4Sb_{12}$ down to 7.7 K.

The Rietveld analysis using RIETAN-2000[6)] with the structure with $Im\bar{3}$ where Pr locates at the center of the Sb cage well reproduces the observed powder diffraction patterns with the typical reliable factor R_{wp}=6.82, R_B=3.19 and S =1.56 for 7.7 K. The representative results are summarized in Table 1. In this analysis, the large thermal displacement parameter was obtained for Pr of $U_{Pr} = 0.0344 Å^2$ at 295.1 K, roughly corresponding to mean thermal displacement of 0.18 Å. This value is 5 times larger than those of other constituents, U_{Os} and U_{Sb}. With decreasing temperature, the thermal displacement parameters show gradual decrease as shown in Fig. 1(a). However, U_{Pr} remains large U_{Pr} =0.0062 $Å^2$ even at 7.7 K which is twice as large as those of Os and Sb.

No structural transition was accompanied with this change of U_{Pr}; no additional peak was found to appear down to 7.7 K. The lattice constant a exhibits gradual decrease with decreasing temperature whereas the positional parameters y_{Sb}, z_{Sb} are almost constant, as shown in Fig. 1(b) and (c). Namely, the size of the Sb cage does not show significant change exceeding the thermal variation of the lattice.

The large value of U_{Pr} and its strong temperature dependence indicate the rattling of Pr in $PrOs_4Sb_{12}$ under the shallow potential in the Sb cage. The

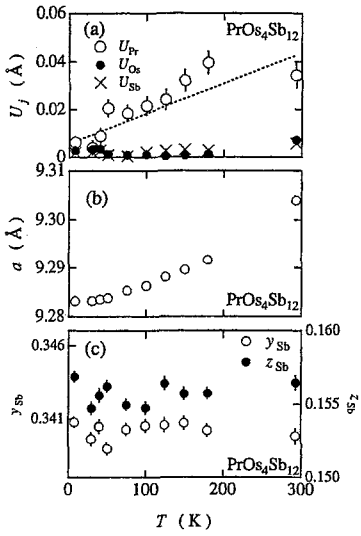

Figure 1: Temperature of dependence of (a) mean square displacement U_j for Pr, Os and Sb, (b) lattice constant a and (c) fractional coordinates y, z of Sb of $PrOs_4Sb_{12}$.

nearest-neighbor distance for Pr, Pr-Sb, of more than 3.47 Å in $PrOs_4Sb_{12}$ which is longer than the *usual* Pr-Sb bond distance and those in P- and As-skutterudites leads to the weak binding of Pr in the cage. The large displacement of Pr at low temperature might be related to the low temperature property in $PrOs_4Sb_{12}$.

References

1) M. B. Maple *et al.*: J. Phys. Soc. Jpn. **71** (2002) Suppl. pp. 23.
2) Y. Aoki *et al.*: J. Phys. Soc. Jpn. **71** (2002) 2098.
3) M. Kohgi *et al.*: J. Phys. Soc. Jpn. **72** (2003) 1002.
4) S. Yotsuhashi *et al.*: J. Phys. Soc. Jpn. **74** (2005) 49.
5) T. Goto *et al.*: Phys. Rev. B **69** (2004) 180511(R).
6) F. Izumi and T. Ikeda: Mater. Sci. Forum **321-324** (2000) 198.

Table 1: Structural parameters, a, y, z and mean square displacement for Pr U_{Pr} of $PrOs_4Sb_{12}$ determined from the Rietveld analysis of neutron powder diffraction data at selected temperatures. Pr atoms are located at 2a (0, 0, 0), Os at 8c ($\frac{1}{4}$, $\frac{1}{4}$, $\frac{1}{4}$) and Sb at 24g (0, y, z), where y, z is a positional parameter. R_{wp}, S, and R_B are conventional reliability factors[6)].

T (K)	a (Å)	y	z	U_{Pr} ($Å^2$)	r_{Pr-Sb} (Å)	R_{wp}	S	R_B
7.7	9.2831(1)	0.3408(1)	0.1569(1)	0.0062(9)	3.482(2)	6.82	1.56	3.19
101.1	9.2864(1)	0.3405(1)	0.1548(2)	0.0216(13)	3.474(0)	8.27	1.34	4.19
151.1	9.2896(1)	0.3407(2)	0.1557(2)	0.0344(18)	3.481(2)	8.99	1.82	5.41

原子炉：JRR-3　　装置：HRPD(1G)　　分野：中性子散乱（構造）

研究テーマ :ブラウンミラライト型酸化物の相転移
表題 新酸化物イオン導電体 $Ba_2In_{2-x}Ga_xO_5$ の構造相転移

5) Structural Phase Transition of New Oxide Ion Conductor, $Ba_2In_{2-x}Ga_xO_5$

T. Hashimoto, T. Furuya, M. Yoshinaga and M. Yashima *

Department of Integrated Sciences in Physics and Biology, College of Humanities and Sciences, Nihon University, 3-25-40 Sakurajousui, Setagaya-ku, Tokyo 156-8550, Japan;
**Department of Materials Science and Engineering, Interdisciplinary Graduate School of Science and Engineering, Tokyo Institute of Technology, 4259 Nagatsuta-cho, Midori-ku, Yokohama 226-8502, Japan*

High temperature phase of $Ba_2In_2O_5$ attracts interest as an oxide ion conductor since it shows higher conductivity than that of yttria stabilized zirconia at temperatures above 900 °C. It has been reported that the crystal structure at temperatures above 900 °C is ideal perovskite with randomly distributed oxide ion vacancies, to which high oxide ion conductivity can be ascribed [1], although definite experimental evidence has not been reported. Recently, we have discovered another phase transition at 1070 °C. Also discovered has been that the phase above 1070 °C is the most promising as an oxide ion conductor. We have also succeeded in decreasing the phase transition temperature by partial Ga substitution for In site [2]. Since we regarded that the precise analysis of crystal structure of newly discovered high temperature phase of $Ba_2In_2O_5$ system should be necessary for elucidation of the origin of high oxide ion conductivity and design of new oxide ion conductor, neutron diffraction analysis was performed by using HERMES, T1-3, JRR-3M in JAERI (TOKAI) equipped with a furnace originally designed by Yashima [3] with 1.8207 Å of incident neutron beam. The crystal structure was refined by Rietveld analysis of diffraction patterns using a program RIETAN-2000 [4].

Fig. 1 shows Rietveld analysis pattern of neutron diffraction data of $Ba_2In_{1.55}Ga_{0.45}O_5$ measured at 1000 °C, at which the phase with the most promising as an oxide ion conductor is observed. The pattern could be successfully analyzed assuming the ideal perovskite-type structure with space group of $Pm\bar{3}m$ (No. 221). As indicated by site occupancy of oxide ion in Table 1, there exists random distribution of oxide ion vacancy in high temperature phase of $Ba_2In_{1.55}Ga_{0.45}O_5$, which can be an origin of high oxide ion conductivity. Diffraction pattern of $Ba_2In_2O_5$ at 1200 °C can also be refined assuming the same space group with random distribution of oxide ion vacancy.

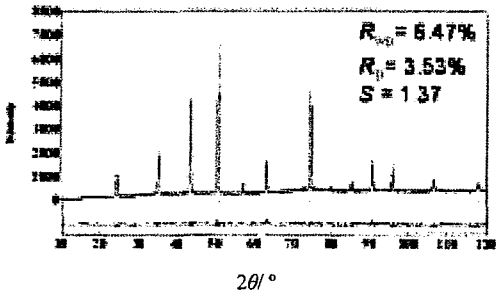

Figure 1: Rietveld analysis pattern of neutron diffraction data of $Ba_2In_{1.55}Ga_{0.45}O_5$ at 1000 °C.

Table 1: Structural parameters of $Ba_2In_{1.55}Ga_{0.45}O_5$ at 1000 °C. space group: $Pm\bar{3}m$, a=4.2427(6) Å

Atom	site	g	x	y	z	U(Å^2)
Ba^{2+}	1b	1.000	0.5	0.5	0.5	0.038(1)
In^{3+}	1a	0.775	0.0	0.0	0.0	0.053(2)
Ga^{3+}	1a	0.225	0.0	0.0	0.0	0.053(2)
O^{2-}	3d	0.833	0.5	0.0	0.0	0.082(2)

References

[1] J. B. Goodenough et al., Solid State Ionics, **52** (1992) 105.
[2] M. Yoshinaga et al., Solid State Ionics, **169** (2004) 9.
[3] M. Yashima, J. Amer. Ceram. Soc., **85** (2002) 2925.
[4] F. Izumi and T. Ikeda, Mater. Sci. Forum, **321-324** (2000) 198.

使用施設 :JRR-3M, 装置 :HERMES(T1-3), 分野 Structures and Excitations

研究テーマ：ペロブスカイト型酸化物プロトン伝導体中の水素占有位置
表　題：粉末中性子回折による $SrZr_{0.95}Sc_{0.05}O_{3-\alpha}$ 中の重水素存在位置の決定

6) The Determination of Deuteron Site in $SrZr_{0.95}Sc_{0.05}O_{3-\alpha}$ by Neutron Powder Diffraction

T. Ito*[1], T. Nagasaki[2], K. Iwasaki[1], M. Yoshino[1], T. Matsui[1,2], N. Igawa[3] and Y. Ishii[3]

[1]*Department of Materials, Physics and Energy Engineering, Graduate School of Engineering, Nagoya University, Aichi 464-8603*
[2] *EcoTopia Science Institute, Nagoya University, Aichi 464-8603*
[3] *Neutron Science Research Center, JAERI, Ibaraki 319-1195*
*[1]E-mail: h042301d@mbox.nagoya-u.ac.jp

Introduction

Acceptor-doped perovskite oxides often show significant proton conductivity in humid atmospheres at high temperature [1]. The proton sites in these samples were estimated from neutron diffraction and electronic structure calculation [2,3]. However, the proton sites are still unclear. In the present study, we try to determine the deuteron sites in $SrZr_{0.95}Sc_{0.05}O_{3-\alpha}$-$D_2O$ by neutron diffraction. These samples were studied by a combined technique including a Rietveld refinement and a maximum-entropy method (MEM)-based pattern fitting of neutron powder diffraction data [4,5].

Experimental

The samples were prepared by solid state reaction of $SrCO_3$ (nominally 99.99 % pure, Ba < 7.4 ppm, Rare Metallic, Japan), ZrO_2 (nominally 99.99 % pure, Hf < 100 ppm, Aldrich) and Sc_2O_3 (nominally 99.99 % pure, Rare Metallic, Japan) powders. These raw materials were mixed and press into pellets, and then the pellets calcined at 1673 K for 24 h in O_2. The obtained materials were ground and press into pellets again. The pellets were finally sintered at 1673 K for 24 h in O_2. The deuteron concentration was determined with a thermobalance. Powdered samples of 10 g were loaded in the thermobalance and heated at 1273 K in dry O_2 flow before the measurement to remove absorbed water. Then oxygen saturated with water vapor (12.8 kPa) was fed into the thermobalance at 673 K. The deuteron concentration was calculated assuming that the change in the sample mass was solely due to the reaction (1) [1].

$$H_2O + V_O^{\cdot\cdot} \leftrightarrow 2H^{\cdot} + O_O^{\times} \qquad (1)$$

The neutron powder diffraction experiments of $SrZr_{0.95}Sc_{0.05}O_{3-\alpha}$-$D_2O$ and $SrZr_{0.95}Sc_{0.05}O_{3-\alpha}$ were carried out in the JRR-3 (JAERI) reactor at 10 K. The wavelength of the incident neutrons was 182.3 pm.

Results and discussion

Rietveld analysis was performed to refine the crystal structure. The crystal structure of these samples was successfully refined assuming perovskite-type structure with the space group *Pnma* at 10 K (Fig. 1). The unit cell volume of $SrZr_{0.95}Sc_{0.05}O_{3-\alpha}$-$D_2O$ is lager than that of $SrZr_{0.95}Sc_{0.05}O_{3-\alpha}$. The MEM calculations were performed using the computer program PRIMA, with 108×156×108 pixels for orthorhombic structures. To reduce the bias imposed by the simple structural model, an iterative procedure named by REMEDY cycle was used after the MEM analysis until no significant improvement was obtained. The calculated profiles agree well with the observed ones. Figure 2 shows the equicontour surface of the nuclear density distribution obtained after REMEDY cycle and provides information on sites of deuteron. The nuclear density is high compared with background in some interstitial sites between two adjacent oxygen atoms. At present we propose this site as a tentative site of the deuteron in $SrZr_{0.95}Sc_{0.05}O_{3-\alpha}$-$D_2O$.

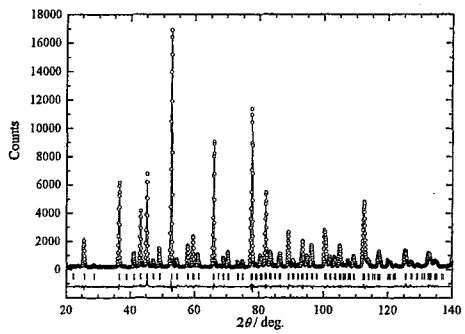

Figure 1: Rietveld refinement of $SrZr_{0.95}Sc_{0.05}O_{3-\alpha}$-$D_2O$ at 10 K. Observed data: dots; calculated profile: full line.

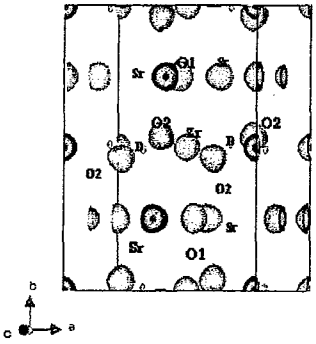

Figure 2: Equicontour surface of scattering amplitude in orthorhombic $SrZr_{0.95}Sc_{0.05}O_{3-\alpha}$-$D_2O$ at 10 K.

References

1) H. Uchida *et al.*: Solid State Ionics 34 (1989) 103.
2) M. Yoshino *et al.*: Solid State Ionics 162-163 (2003) 127.
3) K. S. Knight: Solid State Ionics 127 (2000) 43.
4) F. Izumi *et al.*: Mater. Sci. Forum 321-324 (2000) 198.
5) F. Izumi *et al.*: "Recent Research Developments in Physics" 699-726 (2002) 3.

原子炉：JRR-3　　装置：HRPD (1G)　　分野：中性子散乱 (構造)

研究テーマ：酸化ビスマスの相転移とディスオーダー
表題：酸化ビスマスの格子定数の温度依存性と異方的な熱膨張

7) Temperature Dependence of Lattice Parameters and Anisotropic Thermal Expansion of Bismuth Oxide

Masatomo Yashima, Daiju Ishimura, and Kenji Ohoyama*

*Department of Materials Science and Engineering, Interdisciplinary Graduate School of Science and Engineering, Tokyo Institute of Technology, 4259 Nagatsuta-cho, Midori-ku, Yokohama, 226-8502, Japan; * Institute for Materials Research, Tohoku University, Katahira 2-1-1, Aoba-ku, Sendai, 980-8577, Japan*

The bismuth sesquioxide Bi_2O_3 has polymorphisms of α-, β -, γ- and δ-phases depending on temperature and processing. The electrical conductivity of Bi_2O_3 is increased 3 orders of magnitude by the a-to-d transition at 729°C. To investigate the electrical property-structure correlation, it is important to know the crystal structure of the Bi_2O_3 as functions of temperature. From the temperature dependence of lattice parameters, anisotropic thermal expansion coefficients are obtained, that are important for the design of electrochemical devices. However, little works have been done on the temperature dependence of lattice parameters of Bi_2O_3. The lattice parameters around the transition point (729°C) have not been known yet. The lattice parameters in the literature are not precise. In this work [1], we report the lattice parameters of Bi_2O_3 as functions of temperature using high-temperature neutron powder diffraction data and the Rietveld method.

Commercial bismuth-oxide powders (99.99% purity) were calcined at 400°C for 12 hours to remove the carbonates and then pressed into pellets under the uniaxial pressure of 150 MPa. Neutron powder diffraction experiments were carried out in air with a 150-detector system, HERMES installed at the JRR-3M reactor in Japan Atomic Energy Research Institute. The wavelength of neutron beam was 0.18207 nm. Diffraction data were collected in the 2θ range from 20° to 125° in the step interval of 0.1° from 26° to 778°C. A furnace with $MoSi_2$ heaters [2] was placed on the sample table, and used for neutron-diffraction measurements at high temperatures. The temperature was kept constant within ±1.5°C during each data collection. Lattice and profile parameters were refined by the Rietveld method using a computer program RIETAN-2000.

Between 26° and 187 °C, the neutron-diffraction data were successfully analyzed assuming the coexistence of monoclinic $P2_1/c$ α-Bi_2O_3 and a small amount of orthorhombic $Bi_2(CO_3)O_2$. The $Bi_2(CO_3)O_2$ disappeared between 187° and 350°C. The data obtained at 350° and 511°C were successfully analyzed by a single phase of α-Bi_2O_3. Almost all the peaks at 702° and 721°C were indexed by the a-Bi_2O_3, however the error bars of lattice parameters at 721°C were large due to worse fit. The fit was not improved even assuming either β-, γ-, or δ-Bi_2O_3. The Rietveld analysis did not reproduce well the intensity for some peaks probably due to either some rearrangement of atomic positions, unknown phase or preferred orientation. The diffraction patterns obtained at 740° and 760°C indicated a single phase of δ-Bi_2O_3 [1,3]. Thus, the α-Bi_2O_3 transforms into δ-form between 721° and 740°C. The α-to-δ transition temperature agrees well with the previous works. The crystal structure of δ-Bi_2O_3 was successfully refined assuming the structural model after Harwig ($Fm\bar{3}m$).

Lattice parameters *a*, *b* and *c* increased with an increase of temperature (Fig. 1). The *a* and *c* parameters discontinuously

使用施設：JRR-3M, 装置：HERMES(T1-3), 分野 Structures and Excitations

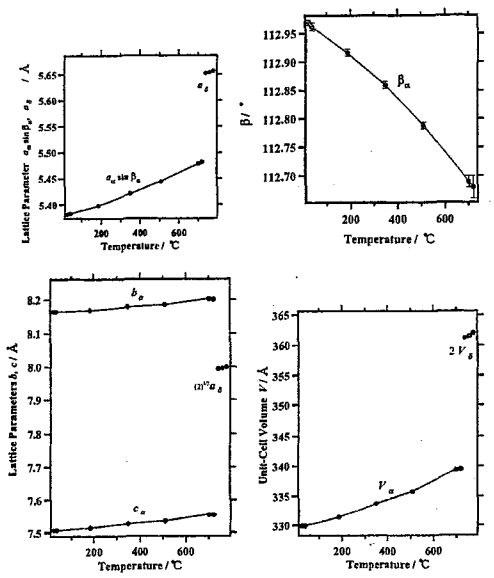

Figure 1: Temperature dependence of unit-cell parameters of bismuth oxide.

increased through the a to d transformation, while the b parameter discontinuously decreased. The β angle of α-Bi_2O_3 decreased with an increase of temperature and then decreased discontinuously to 90° at the α–δ transition point (Fig. 1). The decrease of β angle with temperature indicates that the structural distortion of α-Bi_2O_3 gradually decreases with temperature and that its structure a little approaches that of the δ-phase with increasing temperature. Similar behaviors were observed for the temperature dependence of β angle in monoclinic ZrO_2 and for the compositional dependence of β angle in monoclinic ZrO_2-CeO_2. In contrast to our result, the β angle in the literature increased with an increase of temperature. The unit-cell volume V of α-Bi_2O_3 increased with an increase of temperature and then increased discontinuously at the a-d transition point (Fig. 1). Volume expansion by the α-to-δ transformation was estimated to be 6.8 % using the unit-cell volumes of α and δ phases. The discrete changes in the lattice parameters and unit-cell volume indicate that the α-δ phase transition is of first order. This feature is consistent with the previous works. Gattow and Schroder indicated a discrete change of thermal expansion between α and δ phases. Harwig and Gerards reported a thermal hysteresis and the large transition enthalpy. In the present study we have clearly demonstrated that the α-δ phase transition is of first order using the experimental data of lattice parameters. Temperature dependence of lattice parameters was successfully expressed by straight lines as,

$$a_\alpha^* = 5.3751 + 1.436 \cdot 10^{-4} \cdot T(°C)$$
$$24 \le T \le 721 \quad (°C)$$
$$b_\alpha^* = 5.7713 + 1.910 \cdot 10^{-5} \cdot T(°C)$$
$$24 \le T \le 721 \quad (°C)$$
$$c_\alpha^* = 5.3062 + 4.801 \cdot 10^{-5} \cdot T(°C)$$
$$24 \le T \le 721 \quad (°C)$$
$$\sqrt[3]{V_\alpha^*} = 5.4806 + 7.658 \cdot 10^{-5} \cdot T(°C)$$
$$24 \le T \le 721 \quad (°C)$$
$$a_\delta = \sqrt[3]{V_\alpha} = 5.5656 + 1.173 \cdot 10^{-4} \cdot T(°C)$$
$$740 \le T \le 778 \quad (°C)$$

Then, the thermal expansion coefficients were estimated to be 26.7, 6.6 and 9.0 ($10^6 \times °C^{-1}$) for a_α^*, b_α^* and c_α^* axes, respectively, indicating a large anisotropy in the thermal expansion for the α phase. Orlov *et al.* suggested a notable thermal expansion for a_α. Here we have shown that the a_α^* also has notable thermal expansion comparing with those for b_α^* and c_α^*. The average thermal expansion of α phase ($\left(d(\sqrt[3]{V_\alpha^*})/dT\right)/\sqrt[3]{V_\alpha^*(T=0°C)}$ =14 ($10^{6} \times °C^{-1}$)) agrees with the values obtained in the dilatometric measurements in the literature.

References

[1] M. Yashima, D. Ishimura and K. Ohoyama, J. Am. Ceram. Soc. **88** (2005) in press.
[2] M. Yashima, J. Am. Ceram. Soc. **85** (2002) 2925.
[3] M. Yashima and D. Ishimura, Chem. Phys. Lett. **378** (2003) 395.

研究テーマ：リチウム化合物の電池材料開発への応用
表　題：$La_{1.12}Li_{0.63}Ti_2O_6$ の相転移

8) Phase transition of $La_{1.12}Li_{0.63}Ti_2O_6$

T. Shimoyama, T. Sakuma, H. Takahashi[1], N. Inoue[2], Y. Zou[2], D. Ando[2] and Y. Ishii[3]

Institute of Applied Beam Science, Ibaraki University, Mito 310-8512
[1]*Institute of Applied Beam Science, Ibaraki University, Hitachi 316-8511*
[2]*Department of Physics, Ehime University, Matsuyama, 790-8577*
[3]*Neutron Science Research Center, JAERI, Tokai, Ibaraki 319-1195*

It is known that $La_{1.12}Li_{0.63}Ti_2O_6$ has deficient layered perovskite-type structure and exhibits high ionic conductivity of 10^{-3} S/cm at room temperature. Particularly, $La_{1.12}Li_{0.63}Ti_2O_6$ has the highest Li ion conductivity value among several ionic conductors[1-3]. The ^{7}Li nuclear magnetic resonance revealed a particular behavior of the relaxation time T_1. However, the occurrence of high value of conductivity at high lithium concentration, the 2-D or 3-D conduction mechanism and vacancy positions are still debatable[4,5]. The crystal structure and phase transition mechanism of $La_{1.12}Li_{0.63}Ti_2O_6$ have not been investigated fully. The main objective of this study is to investigate the existence of phase transition in high temperature region and the conducting behavior of Li ions.

The sample was prepared by solid state reactions from stoichiometric amounts of TiO_2, La_2O_3 and Li_2CO_3. The starting materials were mixed and heated for a few hours at 300, 500, 800 and 1150°C. After that the powder was ground, pressed into pellets of 10 mm diameter and 5-6 mm thickness under a pressure of 250 kg/cm^2 and then sintered at 1350°C. During sintering temperature was increased by a rate of 10°C/min form 250 to 1350°C. As the natural Li has large absorption cross section, we used the Li_2CO_3 enriched with ^{7}Li.

The neutron scattering experiments were performed on HRPD in JRR-3 reactor of JAERI. The neutron powder diffraction data of $La_{1.12}Li_{0.63}Ti_2O_6$ were measured at room temperature, 523 K , 673 K and 823 K with the neutron wavelength of 1.8233 Å.

Figure 1 shows the observed intensity from neutron powder diffraction measurement, where (a), (b) and (c) correspond to the intensity at room temperature, 523 K and 823 K, respectively. The split peaks at the scattering angles 46° and 88° (arrow marks) at room temperature had changed to single peak at 823 K. This change might be induced by a tilt of the Ti_2O_6 octahedron. The single peaks at 46° and 88° have been observed around 523 K. From the Rietveld analysis, we would like to clarify the structural change with temperature and the conducting behaviors of Li ions in $La_{1.12}Li_{0.63}Ti_2O_6$.

The observed diffuse scattering intensity is not so large compared to that of α-AgI type superionic conductors[6]. It shows that the disordering of arrangements of atoms and the thermal vibrations of atoms are not so large. However, there are oscillating form in the diffuse scatterng: there are weak peaks around the scattering angle 45 and 90°. These positions correspond to the correlation effects between thermal displacements of atoms from ordered and disordered crystals.

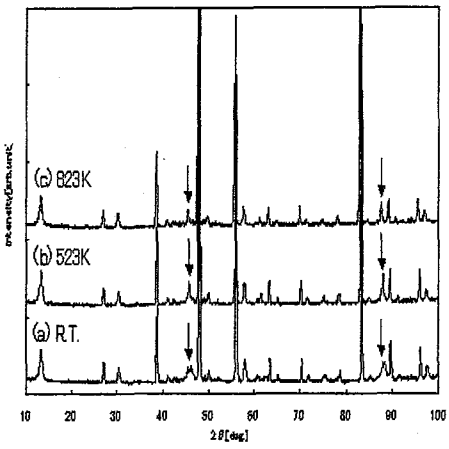

Figure 1: Neutron powder diffraction data from $La_{1.12}Li_{0.63}Ti_2O_6$.

References

1) A. G. Belous, G. N. Novitskaya, S. V. Polyanetskaya and Yu. I. Gornikov, Izv. Kkad: Nauk SSSR. Neorg. Mater. **23** (1987) 470.
2) Y. Inaguma, L. Chen, M. Itoh, T. Nakamura, T. Uchida, H. Ikuta and M. Wakihara: Solid State Commun. **86** (1993) 689.
3) Y. Zou and N. Inoue: IDMSICP (Kyoto, 2003) 14.
4) J. Emery, O. Bohnke, J. L. Fourquet, J. Y. Buzare, P. Florian and D. Massiot: J. Phys. Condens. Matter. **14** (2002) 523.
5) J. L. Fourquet, H. Duroy and M. P. Crosnier-Lopez: Solid State Chem. **127** (1996) 283.
6) R. B. Beeken and T. Sakuma:*Modern Topics in Chemical Physics* (Research Signpost, Trivandrum 2002) 353.

原子炉：JRR-3　　装置：HRPD(1G)　　分野：中性子散乱（構造）

研究テーマ：チタン酸バリウムの強誘電相転移のその場観察
表題：チタン酸バリウムナノ粒子の結晶構造の粒子径依存性

9) Size effect on the crystal structure of barium titanate nanoparticles

Masatomo Yashima, Takuya Hoshina,* Daiju Ishimura, Syuuhei Kobayashi, Wataru Nakamura, Takaaki Tsurumi* and Satoshi Wada *

*Department of Materials Science and Engineering, Interdisciplinary Graduate School of Science and Engineering, Tokyo Institute of Technology, 4259 Nagatsuta-cho, Midori-ku, Yokohama, 226-8502, Japan; *Department of Metallurgy and Ceramics Science, Graduate School of Science and Engineering, Tokyo Institute of Technology, 2-12-1 Ookayama, Meguro-ku, Tokyo 152-8552, Japan*

Phase change in nano-sized $BaTiO_3$ fine particles and the critical size have extensively been studied by many research groups. Some researchers have refined the crystal structure of the $BaTiO_3$ fine particles. However, the $BaTiO_3$ fine particles containing lattice hydroxyl impurities have been utilized in the literature. The purpose of the present study was to investigate the size effect on the crystal structure in the impurity-free $BaTiO_3$ fine particles [1]. The neutron-powder-diffraction technique was utilized to refine the crystal parameters of the $BaTiO_3$ particles. With the help of the relatively large scattering length of oxygen atoms, we could obtain the precise structural parameters and possible structural disorder of oxygen atoms in $BaTiO_3$.

$BaTiO_3$ fine particles were contained in a 10 mm ϕ × 50 mm vanadium can for the data collection from neutron diffraction. Neutron diffraction data for all samples were collected at 299 K on a multi-detector fixed wavelength powder diffractometer (HERMES) installed at the JRR-3M research reactor of the Japan Atomic Energy Research Institute (JAERI), Tokai Research Laboratories by the Institute of Materials Research, Tohoku University. A neutron beam with a 1.8207 Å wavelength was obtained by the (331) plane of a Ge monochromator.

The crystal structure of the $BaTiO_3$ fine particles was refined by Rietveld analysis of the neutron diffraction data. The calculations were performed by a Rietveld analysis program RIETAN-2000. Nuclear-density distribution was obtained by a maximum-entropy method (MEM) using the structure factors obtained in the Rietveld analysis. The calculations were performed by an MEM analysis computer program PRIMA, with 96 × 96 × 96 pixels.

The neutron-diffraction profile showed the tetragonal symmetry. The neutron diffraction profile around 130 deg. in 2θ for 430-nm-sized $BaTiO_3$ particles clearly indicated a splitting into 004_{tet} and 400_{tet} peaks as shown in the enlarged profile in Fig. 1c where hkl_{tet} denotes the *hkl* reflection of tetragonal $BaTiO_3$. The total pattern of the neutron-diffraction profile was successfully analyzed by a single phase of the tetragonal $BaTiO_3$ (Fig. 1c). The neutron-diffraction profile around 130 deg. in 2θ for 140-nm-sized $BaTiO_3$ particles exhibited a shoulder due to the difference in the lengths between the *a* and *c* axes of the tetragonal phase (enlarged profile in Fig. 1b). We refined the crystal parameters assuming a single-phase tetragonal structure in the Rietveld analysis of the neutron-diffraction data of the 140-nm-sized $BaTiO_3$ particles. The observed and calculated profiles agreed well (Fig. 1b). The crystal structures of tetragonal and hexagonal phases of 40-nm-sized sample were refined by Rietveld analysis of the neutron-diffraction data, assuming that the axial ratio *c/a* of the tetragonal $BaTiO_3$ was unity. The calculated profile agreed well with the

使用施設：JRR-3M，装置：HERMES(T1-3)，分野 Structures and Excitations

observed one as shown in Fig. 1a. The weight fractions of the tetragonal and hexagonal phases were estimated to be 0.827 and 0.173, respectively, from the refined parameters. Refined positional parameters of the tetragonal $BaTiO_3$ suggested small displacements of oxygen atoms along the *c* axis. The small displacements of oxygen atoms were also confirmed in the nuclear-density distribution obtained through the maximum-entropy method as shown in Fig. 2. The axial ratio decreased with a decrease in particle size, suggesting a soft-mode mechanism which can explain the reason for the increase in dielectric constant with a decreasing particle size from 430 nm to 140 nm. The nuclear density distribution of the 140-nm-sized particles with a high dielectric constant did not exhibit a large positional disorder, so a structural origin of the high dielectric constant was not observed in the positional disorder. However, the small thermal parameter of the Ba atom for 40-nm-sized particles could be the reason for the small dielectric constant value. Barium titanate particles with a size of 40 nm consist of (1) tetragonal crystals (83 wt%) with a large cell volume and an axial ratio of unity, and of (2) a hexagonal phase (17 wt%) with a large cell volume, leading to a low dielectric constant. A larger unit-cell volume was confirmed with decreasing particle size. The large cell volume would correlate with the decrease in dielectric constant. The large cell volume could be ascribed to (1) the existence of larger sized Ti^{3+} ions, (2) some lattice defects, (3) the surface effect of the fine particles and (4) the metastable state in the chemical reaction from the intermediate amorphous phase to tetragonal $BaTiO_3$ with a large *c/a* ratio. Bond valence sum calculations for the TiO_6 polyhedron suggest the existence of reduced Ti^{3+} ions.

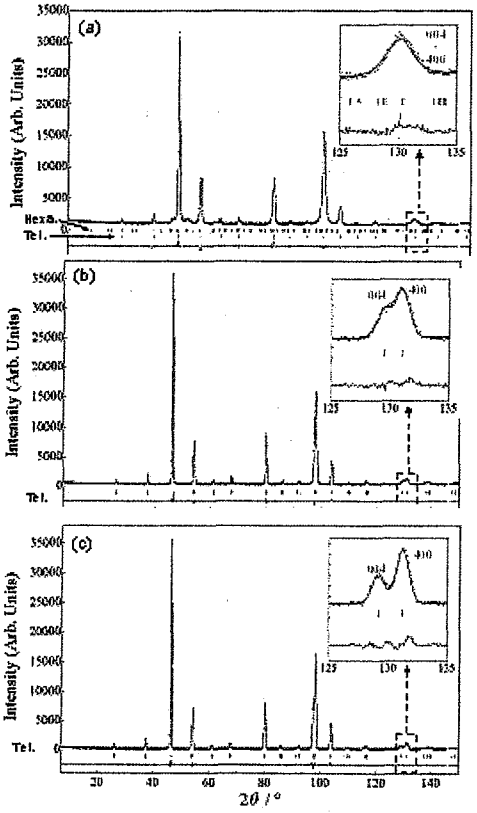

Figure 1: Rietveld patterns of barium titanate nanoparticles. (a) 40nm, (b) 140nm and (c) 430nm.

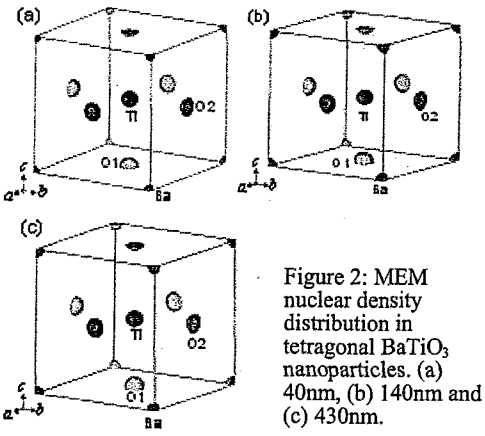

Figure 2: MEM nuclear density distribution in tetragonal $BaTiO_3$ nanoparticles. (a) 40nm, (b) 140nm and (c) 430nm.

Reference

[1] M. Yashima, T. Hoshina, D. Ishimura, S. Kobayashi, W. Nakamura, T. Tsurumi and S. Wada, J. Appl. Phys. **97** (2005) in press.

研究テーマ：包接水和物の動的特性の研究
表　題：メタンハイドレートの動的構造因子からのメタン分子モードの分離

10) A Study of Methane Molecular Mode Separation on Dynamical Structure Factor of Methane Hydrate

T. Kamiyama, S. Ohonuma, N. Seki, Y. Kiyanagi, T. Uchida, T. Ebinuma[1], H. Narita[1], N. Igawa[2] and Y. Ishii[2]

Graduate School of Engineering, Hokkaido University, Sapporo 060-8628
[1]*Institute for Energy Utilization, National Institute of Advanced Industrial Science and Technology, Sapporo 062-8517*
[2]*Neutron Science Research Center, JAERI, Tokai, Ibaraki 319-1195*

Clathrate hydrates are nonstoichiometric inclusion compounds with the host framework composed of water molecules. Methane hydrate consists of two kinds of water cages, two pentagonal dodecahedra and six tetrakaidecahedra, which contain one methane molecular each. It was said that in the cage the methane molecular motion was almost free, and we had made clear its almost free quantum rotation in the cage from the wide Q-E space measurement of dynamical structure factors. On the other hand, it is considered that the translational motion of the methane molecule is strongly hindered with the water cage. In this study we investigate the characteristics of this mode through the wide Q region inelastic scattering spectrum measured by TAS-2 spectrometer.

The methane hydrate sample was prepared by bringing crushed ice around 268 K into contact with the methane gas at 5 MPa. The methane inclusion density was around 80% for CH_4-D_2O and CH_4-H_2O hydrate. The neutron scattering experiments were performed on the TAS-2 at JAERI and MARI spectrometer at ISIS. Measurements were carried around 10 K.

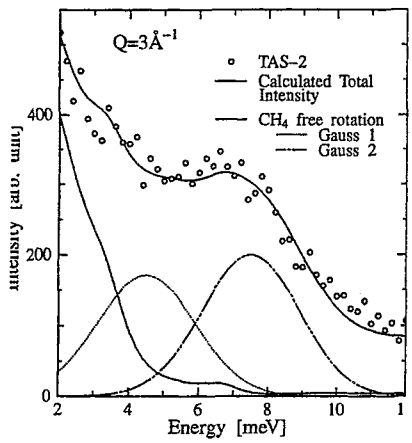

Figure 1: An example of peak analysis of $S(Q,E)$ at 10 K obtained by TAS-2.

In the previous report we have analyzed the methane rotational motion in the water cages.

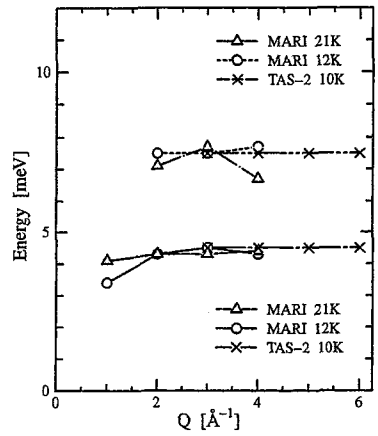

Figure 2: Methane translationsl peak positions on methane hydrate $S(Q,E)$ measured by TAS-2 and MARI.

The obtained dynamical structure factor $S(Q,E)$ of methane hydrate shows characteristic peaks correspond to rotational levels of free methane, but there still remain the excess intensities of the cross-section around 4 meV and over 7 meV. The subtraction of the calculated $S_{rot}(Q,E)$ for methane free rotation from the $S(Q,E)$ measured by TAS-2 leaves the excess peaks on the difference (Figure 1). Figure 2 shows the peak positions appeared on the spectra of TAS-2 and MARI, which show good consistency with each other on tendencies. The peaks are on the almost constant energy around E = 4.5 meV and 7.5 meV. These peaks are at the corresponding positions of methane translational peaks in the cages calculated by MD [1]. It could be said that there exist the translational modes of methane in the water cage in the low E-Q region of $S(Q,E)$. The mean amplitude of the measured methane translational motion is 0.030nm in the large cage and 0.023nm in the small cage, respectively. Now we are trying to analyze the excess peaks more precisely.

References

1) J. S. Tse, C. I. Ratcliffe, B. M. Powell, V. F. Sears and Y. P. Handa : J. Phys. Chem. A **101** (1997) 4491.

原子炉：JRR-3　　装置：TAS-2(T2-4)　　分野：中性子散乱（構造）

研究テーマ：強誘電相転移と磁気相転移が同時に起こる RMn_2O_5(R=希土類)における磁気秩序
表題：RMn_2O_5における磁気相転移と強誘電相転移

11) Simultaneous magnetic and ferroelectric phase transitions in RMn_2O_5

S. Kobayashi, T. Osawa, H. Kimura, Y. Noda, I. Kagomiya[1] and K. Kohn[2]

Institute of Multidisciplinary Research for Advanced Materials, Tohoku University, Sendai 980-8577
[1]Smart Structure Research Center, AIST, Tsukuba 305-8568
[2]Department of Physics, Waseda University, Shinjuku-ku, Tokyo 169-8555

Rare-earth manganese oxides RMn_2O_5 (R= rare-earth,Y,Bi) belong to the orthorhombic space group of *Pbam* and show a paraelectric(PE)-ferroelectric(FE) phase transition at T_{C1} = 32 - 39 K slightly below the Néel temperature of T_{N1}= 39 - 45 K. Recently, we found by neutron diffraction that both $ErMn_2O_5$ [1] and YMn_2O_5(Y:non-magnetic)[2,3] show the sequence of magnetic phase transitions below T_{N1}. With lowering temperature, a two-dimensionally modulated incommensurate magnetic (2D-ICM) phase with the propagation vector $\mathbf{q}_M=(q_x,0,q_z)$ appears at T_{N1} and then two magnetic phase transitions take place in a narrow temperature interval of 1 K around T_{C1}; from 2D-ICM phase to 1D-ICM phase with $\mathbf{q}_M=(q_x,0,1/4)$ and then to a lock-in commensurate magnetic (CM) one with $\mathbf{q}_M=(1/2,0,1/4)$. This implies that the magnetic ordering of Mn moments is correlated with the ferroelectric transition at T_{C1} and it is indispensable to clarify which magnetic ordering (1D-ICM and CM) contributes to the appearance of ferroelectricity at T_{C1}.

We have measured the detailed temperature dependence of $\mathbf{q}_M$ for R = Y, Tb, Tm, Er, and Bi by neutron diffraction, mainly using a four-circle neutron diffractometer (FONDER), installed at guidehall of JRR-3M. Then, small plate-like samples were cut from those used for neutron diffraction measurements and dielectric constant along the *b* axis was measured to compare with $\mathbf{q}_M$.

Figures 1(a)-1(e) show the temperature dependence of the dielectric constant along the *b* axis. With decreasing temperature, the dielectric constant starts to increase around T_{N1} for all samples; the value of T_{N1} is denoted in Fig. 3. This suggests that the dielectric constant along the *b* axis is sensitive to the formation of

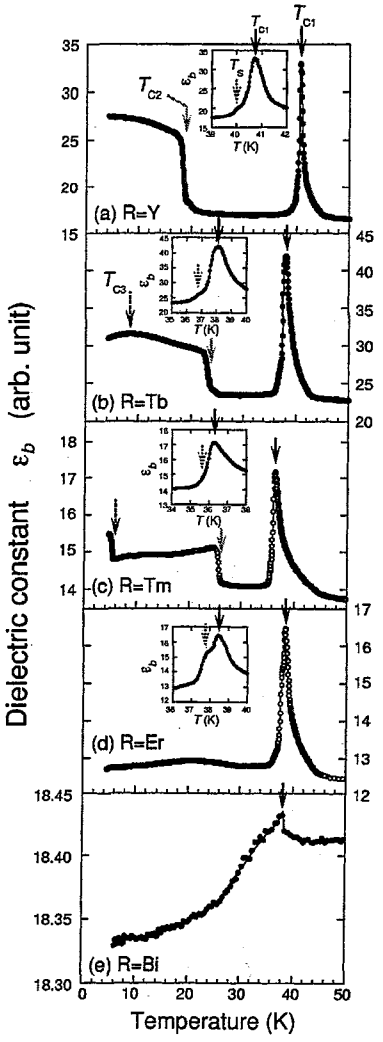

Fig.1 Dielectric constant along the *b* axis as a function of temperature for (a) R=Y, (b) R=Tb, (c) R=Tm, (d) R=Er, and (e) R=Bi. The inset shows enlargements around T_{C1}. The solid, hatched, shaded and dashed arrows represent the position of a dielectric anomaly at T_{C1}, T_S, T_{C2}, and T_{C3}, respectively.

使用施設：JRR-3M，装置：FONDER(T22)，分野：磁気構造

magnetic ordering. On further cooling, YMn_2O_5 shows dielectric anomalies at T_{C1} and T_{C2} as shown in Fig. 1(a), while for R=Tb and Tm, there exists another dielectric anomaly at T_{C3} as shown in Figs. 1(b) and 1(c). On the other hand, for R = Er and Bi, only a sharp peak at T_{C1} appears as shown in Figs. 1(d) and 1(e). In the present measurements, however, we found that a sharp dielectric peak at T_{C1} has a shoulder at T_S slightly below T_{C1} for most R systems except for R = Bi as shown in the inset in Fig. 1.

Now, we discuss the relation between the dielectric anomalies and magnetic phase transitions revealed by neutron diffraction measurements. First, we pay attention to the case for R = Y and Er. As can be seen in the temperature dependence of q_z for R = Y and Er in Figs. 2(a) and 2(b), respectively, both systems show successive magnetic phase transitions around T_{C1} from the 2D-ICM phase with $\mathbf{q_M}$ = $(q_x,0,q_z)$ to the 1D-ICM one with $\mathbf{q_M}$ = $(q_x,0,1/4)$ at T = 40.8 K (R = Y) and 39.1 K (R = Er), and then to the CM phase with $\mathbf{q_M}$ = (1/2,0,1/4) at T = 40.0 K (R = Y) and 37.7 K (R = Er). Since these two temperatures of 2D-ICM-1D-ICM and 1D-ICM-CM phase transitions are very close to T_{C1} and T_S, respectively, the onset of the 1D-ICM ordering can be related to the appearance of the ferroelectricity for R = Y and Er. The formation of such 1D-ICM ordering at T_{C1} was confirmed also for R = Tm, while the CM structure with $\mathbf{q_M}$ = (1/2,0,1/4) and (1/2,0,1/2) was found to appear at T_{C1} for R = Tb [Fig. 2(c)] and Bi, respectively. Taking account that in all the investigated systems q_z is locked at a commensurate value of 1/4 or 1/2 at T_{C1}, we conclude that the commensurability of the magnetic structure along the c axis with the lattice period is important for the appearance of the spontaneous polarization along the b axis at T_{C1} for RMn_2O_5 in general. The relation between ferroelectric and magnetic phase transitions is summarized in Fig. 3.[4]

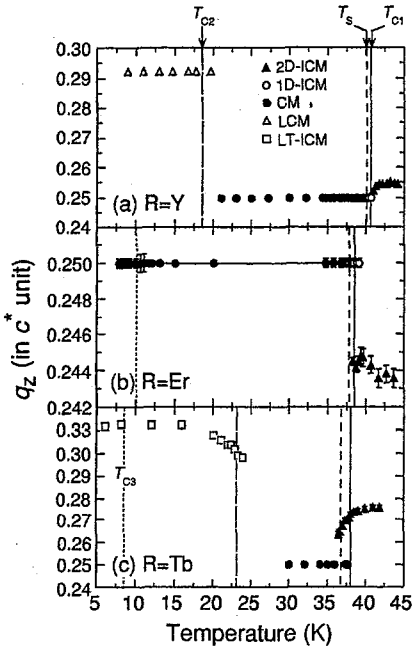

Fig.2 Temperature dependence of q_z for (a) Y, (b) Er, and (c) Tb. T_{C1}, T_S, T_{C2}, T_{C2} show the temperatures of dielectric anomalies.

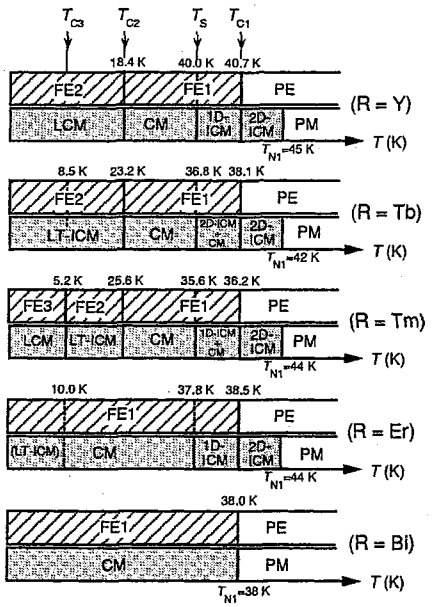

Fig. 3. Relation between ferroelectric and magnetic phase transitions for R = Y, Tb, Tm, Er, and Bi. LT-ICM represents a low-temperature ICM phase with $\mathbf{q_M}$ = $(q_x,0,q_z)$.

References

[1] S. Kobayashi *et al.*: JPSJ **73** (2004) 1031.
[2] I. Kagomiya et al: JPSJ **70**, Suppl. A (2001) 145.
[3] S. Kobayashi *et al.*: JPSJ **73** (2004) 1593.
[4] S. Kobayashi *et al.*: J. Kor. Phys. Soc. **46** (2005) 289.

研究テーマ：中性子散乱による機能材料構造の研究
表　題：中性子回折によるスピネル化合物 $Mg_xCo_{1-x}Cr_xFe_{2-x}O_4$ の構造解析

12) Neutron Diffraction Study of the Spinel Compound $Mg_xCo_{1-x}Cr_xFe_{2-x}O_4$

S. M. Yunus[1,2], H. Yamauchi[2], A. K. M. Zakaria[1], N. Igawa[2], A. Hoshikawa[2] and Y. Ishii[2]

[1]*Bangladesh Atomic Energy Commission, P.O. Box 3787. Dhaka 1000, Bangladesh*
[2]*Neutron Science Research Center, JAERI, Tokai, Ibaraki 319-1195, Japan*

Spinel oxides having the general formula AB_2O_4 are very promising materials for technological applications because of their high magnetic permeability and low magnetic losses[1]. The spinel structure consists of a cubic-close-packed cage of oxygen ions with the metallic ions occupying the tetrahedral (A) and octahedral (B) sites which interact with each other through the superexchange interactions J_{AA}, J_{AB} and J_{BB} (all negative) with $J_{AB} \gg J_{BB} > J_{AA}$. Because of stronger J_{AB}, AA and BB bonds are usually unsatisfied and selective substitution of magnetic and nonmagnetic ions often gives rise to interesting magnetic properties in spinels[2]. Neutron diffraction is especially suitable for characterizing the magnetic structures of such systems since it can provide direct evidence of the presence of long range or short range order[3]. The system $Mg_xCo_{1-x}Cr_xFe_{2-x}O_4$ was selected for neutron diffraction study for its crystallographic and magnetic characterization. The system is diluted and magnetically inhomogeneous due to simultaneous substitution of Mg and Cr and no neutron diffraction study have been reported on this system.

Five compositions of $Mg_xCo_{1-x}Cr_xFe_{2-x}O_4$ (x = 0.0, 0.25, 0.50, 0.75 and 1.0) was synthesized in the ceramic sintering method. Neutron powder diffraction measurements were done on these samples using HRPD at a number of temperatures in the range 10 K – 810 K. Cation distribution and sublattice magnetic moments in the samples were determined from the Rietveld analysis of neutron data.

Table 1 shows that all the cations were distributed in varying proportions over the A and B sites excepting Cr which occupied the B site uniquely. Ferrimagnetic ordering of magnetic moments was revealed from the Rietveld refinement of neutron data. A and B site moments were calculated using the free ion saturation moments of the cations and the determined cation occupancy. Table 2 shows a comparison of the calculated and observed site moments. In case of longitudinal ordering of spins, the calculated moments are usually very close the observed moments. But our deduced site moments appeared considerably smaller than the calculated moments suggesting the presence of non-collinear spins. Figure 1 shows the presence of strong diffuse signal below the (1 1 1) Bragg peak at 10K in the pattern of sample $x = 1.0$. This is a clear indication of the formation of magnetic spin clusters in this sample. The incoherent scattering from this short range clusters gave rise to this diffuse signal. The

Table 1: Cation distribution in spinel $Mg_xCo_{1-x}Cr_xFe_{2-x}O_4$. Bracket ( ) and [ ] represent the A and B sites, respectively

x	cation distribution
0.0	$(Co_{0.15}Fe_{0.85})[Co_{0.85}Fe_{1.15}]$
0.25	$(Mg_{0.05}Co_{0.20}Fe_{0.75})[Mg_{0.20}Co_{0.55}FeCr_{0.25}]$
0.5	$(Mg_{0.14}Co_{0.18}Fe_{0.68})[Mg_{0.36}Co_{0.32}Fe_{0.82}Cr_{0.50}]$
0.75	$(Mg_{0.28}Co_{0.12}Fe_{0.60})[Mg_{0.47}Co_{0.13}Fe_{0.65}Cr_{0.75}]$
1.0	$(Mg_{0.51}Fe_{0.49})[Mg_{0.49}Fe_{0.51}Cr]$

Table 2: Comparison of observed and calculated moments

x	M_A^{cal} (μ_B)	M_A^{obs} (μ_B)	M_B^{cal} (μ_B)	M_B^{obs} (μ_B)
0.0	4.70	4.49(5)	8.30	7.48(6)
0.25	4.35	4.16(4)	7.40	6.63(5)
0.5	3.94	3.59(4)	6.56	5.61(6)
0.75	3.36	3.01(4)	5.89	4.63(6)
1.0	2.45	2.04(6)	5.55	2.89(8)

observed features suggest a perturbed ferrimagnetic structure for the system in the range $x \leq 0.75$ where localized canted transverse spin components coexists with ferrimagnetically ordered longitudinal spins. The composition $x = 1.0$ presents a semi-spin glass like behavior where short range spin clusters are superimposed on ferrimagnetic long range order.

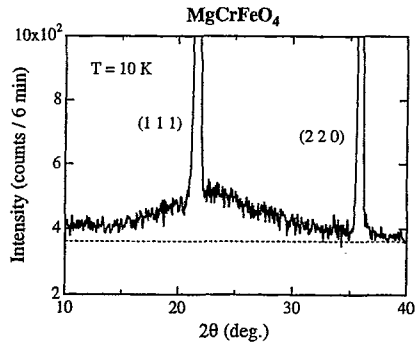

Figure 1: Low-angle diffraction pattern for the sample $x = 1.0$.

References

1) T. Suzuki, T. Tanaka, K. Ikemizu: J. Magn. Magn. Mater. **235** (2001) 159.
2) Kalpesh H. Jani, K. B. Modi, H. H. Joshi, P. D. Babu, S. K. Paranjpe: J. Magn. Magn. Mater. **280** (2004) 334.
3) G. Gavoille, J. Hubsch: J. Magn. Magn. Mater. **36** (1983) 89.

原子炉：JRR-3　　装置：HRPD(1G)　　分野：中性子散乱（構造）

研究テーマ：強誘電体 RMn_2O_5 (R=Tm,Yb,Tb)における希土類イオンの磁性
表題：磁性強誘電体 RMn_2O_5(R=Tm, Tb) の低温磁気相転移

13) Low temperature magnetic phase transitions of multiferroic $TmMn_2O_5$ and $TbMn_2O_5$

S. Kobayashi, H. Kimura, Y. Noda, and K. Kohn *

*Institute of Multidisciplinary Research for Advanced Materials, Tohoku University, Sendai 980-8577; *Department of Physics, Waseda University, Shinjuku-ku, Tokyo 169-8555*

RMn_2O_5(R=rare-earth,Y,Bi) show successive ferroelectric phase transitions at T_{C1} = 32-39 K and T_{C2} ~ 20 K below the Neel temperature of T_{N1} = 39-45 K. When R^{3+} ion is magnetic, there exists another ferroelectric phase transition at T_{C3} ~ 8 K below which ferroelectric properties depend on R^{3+} ion. Previous neutron diffraction measurements down to T = 8 K[1] showed that magnetic phase transitions associated with a change in propagation vector $\mathbf{q}_M=(q_x,0,q_z)$ occur at T_{C1} and T_{C2}, and the magnetic ordering along the c axis due to Mn moments plays a crucial role for the spontaneous polarization along the b axis in RMn_2O_5. However, the magnetic ordering below T_{C3} has been less studied, although the long-range order of R moments is inferred from magnetic structural analysis for R=Er.

We have performed neutron diffraction measurements for R = Tm and Tb down to T = 1.5 K, with a high-Q resolution triple-axis spectrometer (HQR) with a two-axis mode.

Figures 1 and 2 show the temperature dependence of q_x, q_z and integrated intensities for R=Tm and Tb, respectively.[2,3] One can see that in both systems magnetic phase transitions occur simultaneously with the ferroelectric transitions at T_{C1}, T_S, and T_{C2}, being consistent with results of YMn_2O_5 with non-magnetic Y ion.[1] With decreasing temperature below T_{C2}, however, we observed another magnetic phase transition at T_{C3} for R=Tm accompanying with a jump in q_z and integrated intensities. In contrast, for R = Tb no change in $\mathbf{q}_M$ was detected down to 1.5 K as shown in Figs. 2(a) and 2(b), although the integrated intensity steeply increases below T_{C3} due to the magnetic ordering of Tb moments. Considering that the spontaneous polarization along the b axis almost disappears at T_{C3} for R = Tm,[4] we conclude that the reorientation of Mn moments, triggered by Tm moments takes place at T_{C3} in $TmMn_2O_5$. Actually, in $TbMn_2O_5$ where large spontaneous polarization along the b axis remains below T_{C3}, no magnetic structural change was observed at T_{C3}.

References

[1] S. Kobayashi *et al.*: JPSJ **73** (2004) 1593.
[2] S. Kobayashi *et al.*: JPSJ **74** (2005) 468.
[3] S. Kobayashi *et al.*: JPSJ **73** (2004) 3439.
[4] M. Uga *et al.*: Ferroelectrics **219** (1998) 55.

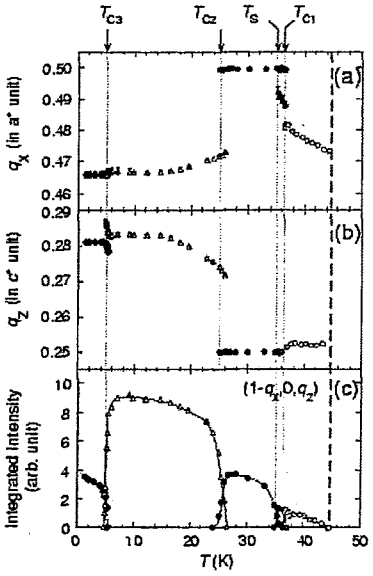

Fig.1 (a) q_x, (b) q_z, and (c) integrated intensities as a function of temperature for R = Tm.

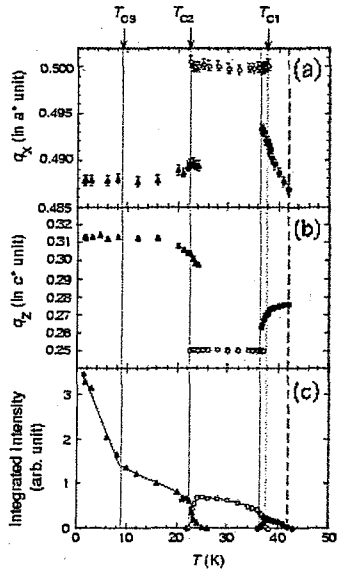

Fig.2 (a) q_x, (b) q_z, and (c) integrated intensities as a function of temperature for R = Tb.

使用施設：JRR-3M, 装置：HQR(T11), 分野：磁気構造

研究テーマ：中性子散乱による機能材料構造の研究
表　題：中性子非弾性散乱によるメタンハイドレートの格子ダイナミクスに関する研究

14) Lattice Dynamics on Methane Hydrate by Inelastic Neutron Scattering

H. Yamauchi, N. Igawa and Y. Ishii
Neutron Science Research Center, JAERI, Tokai, Ibaraki 319-1195

Methane hydrate is a ice-like solid and consists of two types of host water cages (large and small cages) where guest methane molecules are trapped. Methane hydrate especially has attracted much attention as one of the potential future energy resources[1]. It is important to clarify the mechanical and theromodynamical stability of the hydrate system and the formation and dissociation processes for practical supply as an energy source. Understanding the lattice dynamics of the guest-host system can be a key step toward the fundamental comprehension of guest-host interaction, then stability in methane hydrate. For this purpose, inelastic neutron scattering (INS) experiments were carried out on a methane hydrate powder with the triple-axis spectrometer TAS-1.

In order to observe phonon density of states of methane hydrate without incoherent contribution as precise as possible of the vibrational excitations of both the guest methane molecules and the ice-like host lattice, a fully deuterated sample $CD_4 \cdot nD_2O$ ($n \geq 5.75$) was used. A cylindrical Al cell (15 mm in inner diameter) was filled with the powder sample. The scattering measurements were done with a fixed final energy of 13.5 meV separated by the PG(0 0 2) reflection of the analyzer. The horizontal collimation was 40′-40′-sample-40′-40′. The momentum transfer Q in this study was set to 4.0 Å^{-1}.

Figure 1 shows the INS spectra at 10 K (open circles) and 100 K (closed circles). The peak at 6.5 meV could be compared to the INS spectrum of D_2O ice Ih. The INS of ice Ih shows only one well defined peak at 6.8 meV[2]. This excitation is assigned to acoustic modes. Moreover, from previous INS experiments on several gas hydrates it is known that the maximum of the transverse acoustic (TA) modes of the host lattice is found around 7 meV[3,4]. The peak at 6.5 meV is therefore mainly attributed to the TA modes of the host lattice near the zone boundary. The excitation at 10 meV was in good agreement with the peak at about 10 meV shown in the calculated density of states of the host water lattice[4]. It was described in the reference that the maximum of a fold-back of the TA modes towards the zone center due to the open cage structure was located at 10 meV.

In contrast with the excitations of 6.5 meV and 10 meV, the intensity of the small shoulder around 4 meV obviously decreases with increasing temperature. For D_2O ice Ih, no excitation is found below 6.8 meV in INS experiments[2]. It was also reported that for the natural methane hydrate the rotational excitations of methane molecules were observed at 1.08 meV ($J=0 \rightarrow J=1$), 2.2 meV ($J=1 \rightarrow J=2$) and 3.3 meV ($J=0 \rightarrow J=2$)[5]. However, the clear and intense peak was only the rotational excitations of $J=0 \rightarrow J=1$. The apparent peak corresponding to the $J=0 \rightarrow J=1$ excitation at 0.4 meV for $CD_4 \cdot nD_2O$[6] was not found in the case of our experiments. Furthermore, it was predicted from the molecular dynamics calculation[7] that the power spectrum for the translational motion of the CH_4 molecules in methane hydrate showed three peaks at 8.7 meV, 6.4 meV and 4.0 meV. The highest energy peak at 8.7 meV was assigned to the motion of methane molecules in the small cages with the spherical symmetry. The two lower energy vibrations at 6.4 meV and 4.0 meV arose from the motions of methane molecules in the large cages with the ellipsoidal symmetry. It is therefore possible that the small shoulder around 4 meV at 10 K is associated with the motion of methane molecules in the large cages.

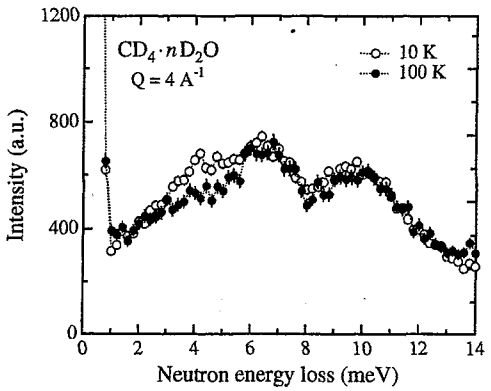

Figure 1: Inelastic neutron scattering spectra for a fully deuterated methane hydrate at 10 K (open circles) and 100 K (closed circles). Dashed lines are guide to eyes.

References

1) E. D. Sloan Jr.: *Clathrate Hydrates of Natural Gases, 2nd ed.*, (Marcel Dekker, New York, 1998).
2) J. Lie: J. Chem. Phys. **105** (1996) 6733.
3) B. Chazallon *et al.*: Phys. Chem. Chem. Phys. **4** (2002) 4809.
4) J. Baumert *et al.*: Phys. Rev. B **68** (2003) 174301.
5) C. Gutt *et al.*: Europhys. Lett. **48** (1999) 269.
6) C. Gutt *et al.*: J. Chem. Phys. **114** (2001) 4160.
7) J. S. Tse *et al.*: J. Chem. Phys. **81** (1984) 6146.

原子炉：JRR-3　　装置：TAS-1(2G)　　分野：中性子散乱（構造）

研究テーマ：亜硝酸ナトリウムの核座標，電荷密度，電気分極
表題：$NaNO_2$ のNの核密度と実効ポテンシャル

15) Nuclear Density and Effective Potential for N of $NaNO_2$

H. Mashiyama, T. Asahi, H. Kasano, Y. Noda* and H. Kimura*

*Faculty of Science, Yamaguchi University, Yamaguchi 753-8512, Japan; * Institute of Multidisciplinary Research for Advanced Materials, Tohoku University, Sendai 980-8577, Japan*

Sodium nitrite ($NaNO_2$) is a ferroelectric crystal which has been considered as a typical order-disorder system. Fourier synthesis of X-ray diffraction data indicates disordered atoms in the paraelectric phase above 438K. But the electron density of the Fourier map is too wide to determine precisely the probability distribution of nuclei. Since neutrons are scattered only from nuclei, neutron scattering study is advantageous in determining the ordering of atoms.

A single crystal of $NaNO_2$ (0.4x0.4x0.38 cm^3 size) was set in a furnace mounted on a four-circle diffractometer (FONDER) installed at JRR-3M reactor in JAERI, Tokai. Diffraction data up to $2\theta<156^\circ$ (neutron wave length 1.2416Å) were collected at seven temperature between 410 ~435K in the ferroelectric phase. Absorption and extinction correction was performed by using RADIEL. Nuclear density was estimated by PRIMA and visualized by VEND supplied by Dr. F. Izumi.[1]

Figure 1 displays the nuclear density images at 410, 427 and 435K. The NO_2 molecules sit at the corner and the body center of the unit cell. With increasing temperature, the occupation probability shows a partially ordered feature gradually.

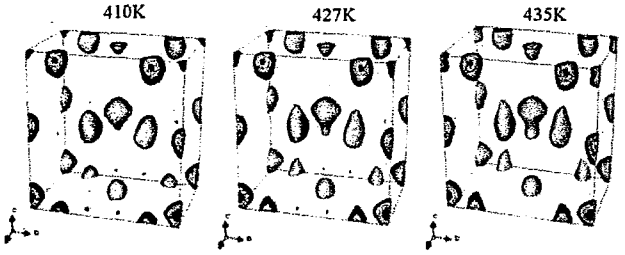

Figure 1:Nuclear density images at 410, 427 and 435K.

It seems as if the atom occupies two-site related by the lost mirror symmetry of the paraelectric phase. However, the density cannot be fitted to a double-peak Gaussian distribution successfully. There appears a residual hump between the two peaks. Figure 2 shows the N nuclear density along the *z*-axis and the curves fitted to a triple-peak Gaussian distribution at 435K.

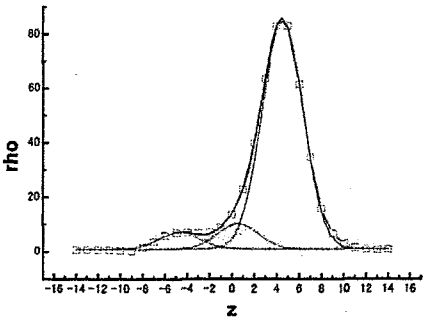

Figure 2: The N nuclear density along the *z*-axis and the curves fitted to a triple-peak Gaussian distribution at 435K.

If we assign a non-equivalent, double-minimum potential for the N atom, the wave function for the nuclear can be calculated from the Schrödinger equation. Then the probability distribution represented from the wave function may have three peaks if the third or higher energy states were occupied thermally at the relevant temperature.

References

[1] F. Iizumi, Japan J. Crsytalography. **44** (2002) 380.

使用施設 JRR-3M，装置 T22:FONDER，分野 101: Structures and Excitations

研究テーマ：中性子散乱による機能材料構造の研究
表　題：重水素化メタンハイドレートの結晶構造

16) Crystal Structure of Deuterated Methane Hydrate

A. Hoshikawa, N. Igawa, H. Yamauchi and Y. Ishii
Neutron Science Research Center, JAERI, Tokai, Ibaraki 319-1195

Methane hydrate (MH) is of great interest as a next generation of resource because a large amount of natural gas hydrate (primarily MH) is deposited on the sea floor. It is known that MH forms structure I in the condition on the sea floor. There are two types of cages (small and large cages) in the structure I. These cage structures (host lattice) can accommodate guest molecules such as methane molecule. The precise crystal structure including the guest molecule was not obvious. Especially, the atomic coordinates of the H atoms of CH_4 were unknown.

In order to discriminate the H atom of CH_4, a sample synthesized from CH_4 and D_2O is used in this study because the coherent neutron scattering lengths between the H atoms and other atoms are opposite in sign.

The neutron diffraction measurements were carried out on the high resolution powder diffractometer (HRPD) installed at JRR-3. Data were collected with constant monitor counts and a step angle of 0.05° over the 2θ range of 2.5–160°. Diffraction patterns were obtained for temperatures of 7, 45, 80, 116, 151, and 185 K. Wavelength of used neutrons was 1.8233 Å.

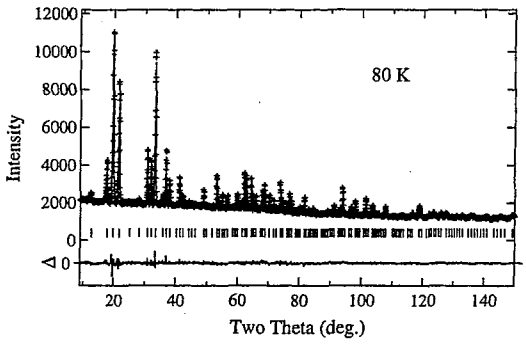

Figure 1: Neutron powder diffraction pattern of deuterated methane hydrate ($CH_4 \cdot nD_2O$, $n \sim 6.7(2)$).

A diffraction pattern of partially deuterated methane hydrate is shown in Fig. 1. In the Rietveld analysis, we used the rigid body model of the CH_4 molecule using RIETAN-2000 [1]. The reliability factors were 4.52 % for R_B , 2.62 % for R_{wp} and 1.10 for S values [2].

Figure 2 shows the results of the Rietveld refinement. There are 48 and 16 sites for H atoms in the small and large cages, respectively. Accordingly, $g(\mathrm{H_{small\ cage}})=\frac{1}{12}g(\mathrm{C_{small\ cage}})$ and $g(\mathrm{H_{large\ cage}})=\frac{1}{4}g(\mathrm{C_{large\ cage}})$, where g is site occupancy. It is indicated that the number of stable positions for H atoms in the small cage is larger than that in the large cage. Consequently, the atomic arrangements of the H atoms in the small cage are similar to a spherical shell. The diffraction patterns for all temperature are in good agreement with this structure model.

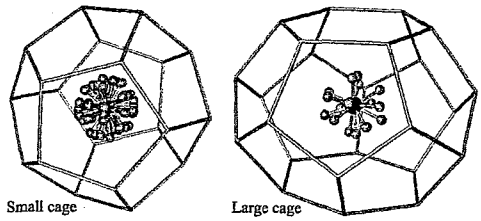

Figure 2: Geometry of the CH_4 molecules in the cages. Large spheres (black)and small spheres (gray) represent the C and H atoms, respectively.

The g values about the C atom are 0.96(5) and 0.83(3) in the small and large cages, respectively. The g values did not change at 7 K and 185 K within analytical error. From these values, the number of the C atom in a unit cell is 6.9(2). If the cages are fully occupied by CH_4, the number of the C atom is 8. Accordingly, 86(3) percent of the cages is occupied by the CH_4 molecule. Then, the composition is $CH_4 \cdot 6.7(2)D_2O$.

The cage occupancy was estimated to be 0.945 and 0.988 in the small and large cages on the synthetic condition (278 K, 7 MPa) by the ideal solution model and the Langmuir constants [3]. As a result, the total cage occupancy is 97.7 %. When the sample was put into the holder, the pressure was dropped. Since the above equilibrium condition was changed, the cage occupancy could decrease. Consequently, our results are considered reasonable. For the first time, the atomic arrangement of the H atoms in the cages was determined by the rigid body model of CH_4 in the Rietveld analysis.

References

1) F. Izumi and T. Ikeda : Mater. Sci. Forum **198** (2000) 321.
2) R.A. Young (ed.): *The Rietveld Method*, (Oxford, New York, 1993) p. 22.
3) J. Munck, S. Skjold-Jorgensen and P. Rasmussen : Chem. Eng. Sci. **43** (1988) 2661.

原子炉：JRR-3　　装置：HRPD(1G)　　分野：中性子散乱（構造）

研究テーマ：ジルコニア固溶体およびイットリア-酸化タンタル化合物における酸化物イオンのディスオーダーと伝導経路
表題：中性子粉末回折法によるイットリウムータンタル酸塩の構造解析

17) Structural Analysis of Yttrium Tantalates though Neutron Powder Diffraction Method

Takayuki Tsuji and Masatomo Yashima

Department of Materials Science and Engineering, Interdisciplinary Graduate School of Science and Engineering, Tokyo Institute of Technology, 4259 Nagatsuta-cho, Midori-ku, Yokohama, 226-8502, Japan

Yttrium tantalates ($Y_{1-x}Ta_xO_{1.5+0.5x}$) exhibit high oxygen-ion conductivity and fluorescence. The Y_2O_3-Ta_2O_5 system has some compounds, but there are few reports on the precise structural analysis. The purpose of the present work is to refine the crystal structure of two compounds of $Y_4TaO_{8.5}$ and Y_3TaO_7 and to investigate the structural disorder in the materials. Neutron powder diffraction technique was utilized to refine the crystal parameters of the $Y_4TaO_{8.5}$ and Y_3TaO_7. With the help of the relatively large scattering length of oxygen atoms, we could obtain the precise structural parameters and possible structural disorder of oxygen atoms in $Y_4TaO_{8.5}$.

$Y_4TaO_{8.5}$ and Y_3TaO_7 were contained in a 10 mm ϕ × 50 mm vanadium can for the data collection from neutron diffraction. Neutron diffraction data for the samples were collected at 299 K on a multi-detector fixed wavelength powder diffractometer (HERMES) installed at the JRR-3M research reactor of the Japan Atomic Energy Research Institute (JAERI), Tokai Research Laboratories by the Institute of Materials Research, Tohoku University. A neutron beam with a 1.8207 Å wavelength was obtained by the (331) plane of a Ge monochromator.

The crystal structure of the $Y_4TaO_{8.5}$ and Y_3TaO_7 was refined by the Rietveld analysis of the neutron diffraction data. The calculations were performed by a Rietveld analysis program RIETAN-2000. Nuclear-density distribution was obtained by a maximum-entropy method (MEM) using the structure factors obtained in the Rietveld analysis. The calculations were performed by an MEM analysis computer program PRIMA, with 64× 64 × 64 pixels.

First the neutron-diffraction data of $Y_4TaO_{8.5}$ was analyzed with an ideal fluorite-type structure. Refined atomic displacement parameter of oxygen atoms in the $Y_4TaO_{8.5}$ was large (B=5.13(4) Å^2). In the nuclear density distribution map of the $Y_4TaO_{8.5}$, the oxygen ions distributed largely along <1 0 0> direction. Thus, we used a split-atom model where the oxygen atoms are put at the 8c (1/4, 1/4, 1/4) and 48i (1/4, 1/4, z) sites. In the Rietveld analysis with the split-atom model, the reliability factor R_{wp} was improved from 5.05% to 4.86%, and atomic displacement parameter of oxygen was decreased to 2.02(2) Å^2. The calculated profile in the Rietveld analysis of $Y_4TaO_{8.5}$ with the split-atom model agreed well with the observed one as shown in Fig. 1. This split-atom model indicates that the oxygen ions in $Y_4TaO_{8.5}$ have a large disorder. The nuclear density distribution of the oxygen atom in $Y_4TaO_{8.5}$ with a high ionic conductivity exhibits a large positional disorder as shown in Fig. 2a.

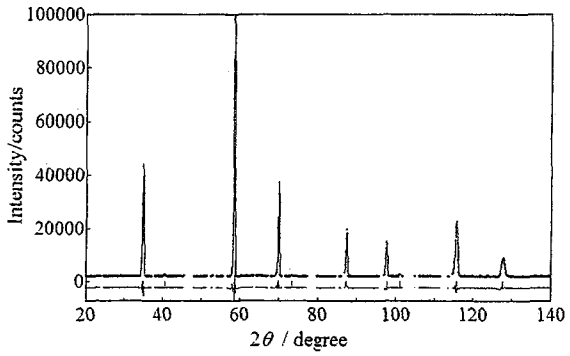

Fig.1 Rietveld analysis pattern of $Y_4TaO_{8.5}$

使用施設：JRR-3M，装置：HERMES(T1-3)，分野 Structures and Excitations

All the peaks of the neutron-diffraction profile of Y_3TaO_7 were indexed by the orthorhombic weberite-type structure. The calculated profile in the Rietveld analysis of Y_3TaO_7 agreed well with the observed one as shown in Fig. 3. The atomic displacement parameters of oxygen atoms in the Y_3TaO_7 were ranged from 1.5 to 2.0 $Å^2$, which are smaller than that 5.13 $Å^2$ for the ideal fluorite-type model in the $Y_4TaO_{8.5}$. This corresponds to the difference of oxygen ion conductivity between the Y_3TaO_7 and $Y_4TaO_{8.5}$. Nuclear density maps of $Y_4TaO_{8.5}$ and Y_3TaO_7 are shown in Fig.2. In contrast to the $Y_4TaO_{8.5}$, oxygen atoms were localized near the stable position in the Y_3TaO_7 (Fig.2b).

The large distribution of oxygen ions has been observed in the fluorite-structured fast-oxide ion conductors such as bismuth oxide [1]. The diffusion path of oxygen ions in Fig. 2a would be along the [001] directions as well as in the bismuth oxide and ceria [1,2].

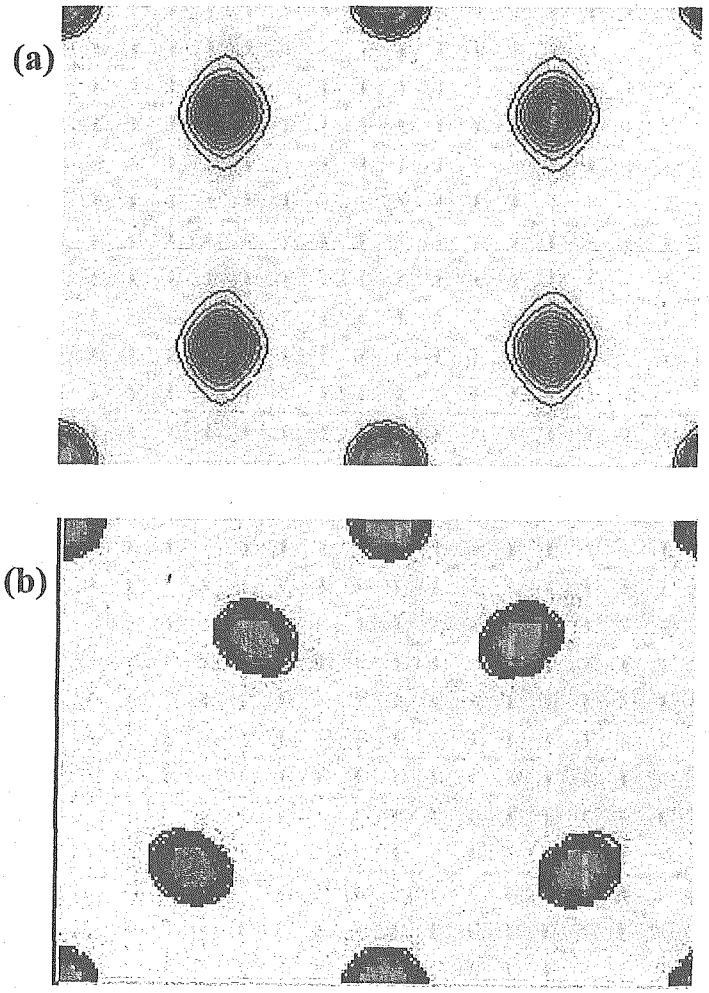

Fig.2 Nuclear density maps of (a) $Y_4TaO_{8.5}$ on the (1 1 0) plane and of (b) Y_3TaO_7 on the (0 0 2) plane.

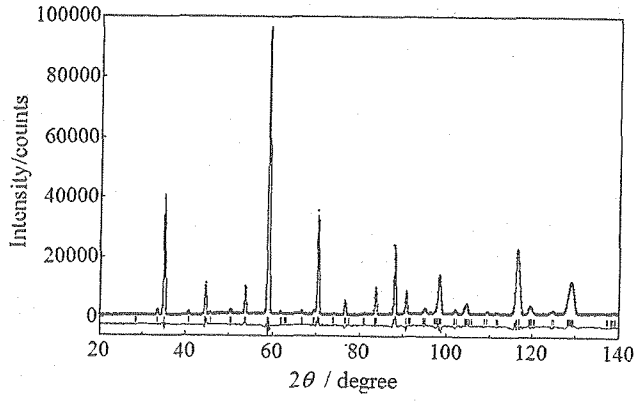

Fig.3 Rietveld analysis pattern of Y_3TaO_7

References

[1] M. Yashima & D. Ishimura, Chem. Phys. Lett., **378**, (2003) 395.

[2] M. Yashima & S. Kobayashi, Appl. Phys. Lett., **84**, (2004) 526.

研究テーマ：中性子散乱による機能材料構造の研究
表　題：マキシマムエントロピー法による重水素化メタンハイドレートの構造解析

18) Structure Analysis of Deuterated Methane Hydrate by Maximum Entropy Method

A. Hoshikawa, N. Igawa, H. Yamauchi and Y. Ishii
Neutron Science Research Center, JAERI, Tokai, Ibaraki 319-1195

In clathrate hydrate, H_2O molecules form a three dimensional hydrogen-bonded network in the space-filling of polyhedral cage-like structures (host lattice) that can accommodate guest molecules. In this study, we investigate the thermal motions of methane molecules in deuterated methane hydrate in terms of crystal structure.

In order to discriminate the hydrogen atom of the methane molecule, a sample synthesized from CH_4 and D_2O is used in this study because the coherent neutron scattering lengths between the H atoms and other atoms are opposite in sign. The neutron diffraction patterns were obtained for temperatures of 7, 45, 80, 116, 151, and 185 K by the high resolution powder diffractometer (HRPD).

The diffraction patterns were analyzed by the Rietveld method using RIETAN-2000 [1]. After Rietveld analysis, the maximum entropy method (MEM) analysis was carried out with PRIMA [2], using 128 × 128 × 128 pixels for a unit cell.

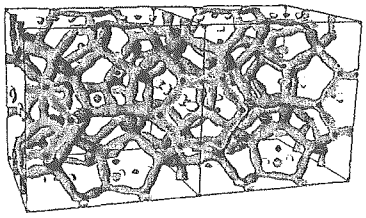

Figure 1: Scattering length density distribution of deuterated methane hydrate. The isosurface level is 1.0 fm/Å^3 as the absolute value.

Figure 1 shows the scattering length density distribution obtained by MEM. The positive and negative scattering length densities are represented by dark and light gray, respectively. Figure 2 shows the temperature dependence of the scattering length density. All figures were drawn with the same isosurface level. Left and right parts represent the small and large cage, respectively. The top, middle, and bottom figures represent the scattering length densities at 7, 45, and 116 K, respectively. There was a positive scattering length density at the center of the small cage regardless of temperature. In the large cage, the scattering length density depended on temperature. At 7 K, the positive and negative scattering length densities corresponding to the C and H atoms were observed at the center of the large cage and near the hexagonal faces

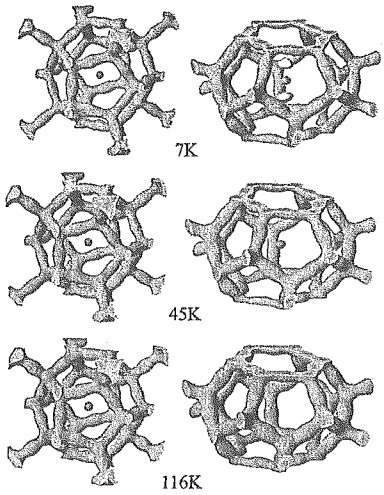

Figure 2: Temperature dependence of scattering length density distribution in deuterated methane hydrate. The isosurface level is 1.0 fm/Å^3 as the absolute value.

of the large cage, respectively. At 45 K, only a positive scattering length density remained at the center of the large cage. At 116 K, even the positive scattering length density disappeared from the center of the cage. It is clear that the temperature dependence of the scattering length density differs between the large and small cages. These differences of the temperature dependence of the scattering length density indicate that the motions of the CH_4 molecule differ between the samll and large cages.

We propose a model of the thermal motion of CH_4 as follows. In the small cage, the CH_4 molecule isotropically rotates at the center of the cage regardless of temperature. In the large cage, the rotational motion is not uniform at 7 K. At 45 K, the rotational motion becomes uniform at the center of the large cage. At 116 K, the CH_4 molecule moves around the center of the large cage in a manner similar to that of an orbital motion in response to the shape of the large cage.

References

1) F. Izumi and T. Ikeda : Mater. Sci. Forum **198** (2000) 321.
2) F. Izumi and R.A. Dilanian : *Recent Research Developments in Physics, Vol. 3, Part II,* (Transworld Research Network, Trivandrum, 2002) p. 699.

原子炉：JRR-3　　装置：HRPD(1G)　　分野：中性子散乱（構造）

研究テーマ： β -Sn における異方的散漫散乱
表題： β-Sn 単結晶の熱散漫散乱分布

19) Measurement of Diffuse Scattering in β- Tin Single Crystal

M. Takahashi[1], K. Ohshima[1] and Y. Noda[2]
[1] *Institute of Materials Science, University of Tsukuba, Tsukuba 305-8573*
[2] *Institute of Multidisciplinary Research for Advanced Materials, Tohoku University, Sendai 980-8577*

β-Sn shows anomalous diffuse scattering distributed over large volumes in reciprocal space with rod-like shape. To study its detailed structure and understand the origin, we have measured three-dimensional intensity distribution of the diffuse scattering by using four-circle single crystal diffractometer FONDER. Figures 1 show intensity contour maps around 1/2 1/2 3 on the scattering plane of *hhl* (upper) and *hk*3 (lower) measured at R.T.. The rod-like diffuse scattering appears along [110] with $l = 3$ on the *hhl* plane, which is the plane of the zone-boundary (z.b.). The diffuse intensity shows maximum at 1/2 1/2 3, which is X-point of the Brillouin zone for β-Sn structure. As seen in the scattering on *hk*3 plane, the maximum is due to the diffuse streaks distributed from 103 and 013 zone centers. Since the diffuse intensities strongly depend on temperature and distributed around the z.b., the origin is considered as temperature diffuse scattering (TDS) with two-phonons process. To confirm it, second-order TDS was calculated using values of elastic constants obtained by Rayne & Chandrasekhar [1].

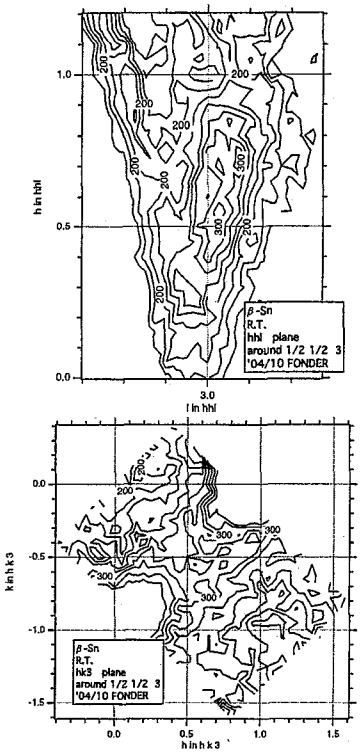

Fig. 1. Intensity contour maps around 1/2 1/2 3 on the scattering planes of *hhl* (upper) and *hk*3 (lower) at R.T..

Figures 2 show calculated intensity distributions on the *hhl* and *hk*3 planes around 1/2 1/2 3. They reproduce the observed diffuse intensities of rod-like distribution with X-points maxima. The results show strong effect of the two-phonons process in β-Sn. In our studies for the structural transition of β to α phase in Sn, appearance of X-point peaks has been observed in the process of the transition. It is thus of interesting to study the relation between the present results and mechanism of β to α structural transition in Sn, which is now on progress.

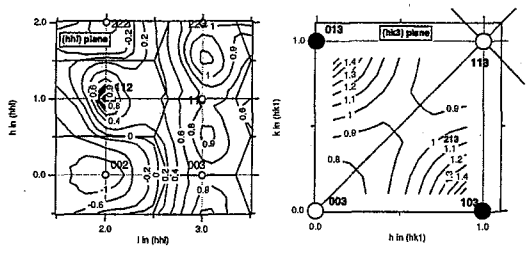

Fig. 2. Calculated intensity distributions of second-order TDS on the *hhl* (left) and *hk*3(right) planes around 1/2 1/2 3.

References

[1] J. A. Rayne and B. S. Chandrasekhar : Phy. Rev. **120** (1960)1658.

使用施設：JRR-3M, 装置： T2-2 , 分野： 101. Structural and Excitations

研究テーマ：中性子散乱による機能材料構造の研究
表　題：マキシマムエントロピー法による完全重水素化メタンハイドレートの結晶構造解析

20) Crystal Structure Analysis of Fully Deuterated Methane Hydrate by Maximum Entropy Method

A. Hoshikawa, N. Igawa, H. Yamauchi and Y. Ishii
Neutron Science Research Center, JAERI, Tokai, Ibaraki 319-1195

We studied crystal structure of partially deuterated methane hydrate (CH_4+D_2O) in terms of thermal motion of CH_4. Although H atoms of CH_4 are emphasized, the H atom has large incoherent neutron scattering length. For the reduction of incoherent neutron scattering from the H atoms, samples were fully deuterated (CD_4+D_2O).

Figure 1 shows a Rietveld refinement pattern of fully deuterated methane hydrate at 7.7 K. The background becomes smaller by deuterating as shown in Fig. 1. After Rietveld analysis with RIETAN-2000 [1], the maximum entropy method (MEM) analysis was carried out with PRIMA [2], using 128 × 128 × 128 pixels for a unit cell.

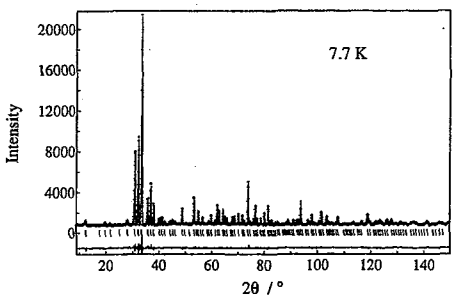

Figure 1: Neutron powder diffraction pattern of fully deuterated methane hydrate.

Figure 2 shows the temperature dependence of the scattering length density obtained by MEM. The positive scattering length density was only observed. All figures were drawn with the same isosurface level. Left and right parts represent the small and large cage, respectively. There was a spherical density distribution at the center of the small cage regardless of temperature. In the large cage, the scattering length density depended on temperature. At 7.7 K, a tetrahedral density distribution were observed at the center of the large cage. In addition, there were 6 slender density distributions around the tetrahedral distribution. Because of the geometry, the tetrahedral distribution corresponds to the C atom. Accordingly, this result indicates the C atom of CD_4 is located at an off-center position of the large cage. At 45 K, the tetrahedral distribution combined with 2 slender distributions and a cylindrical distribution appeared. There were 4 slender distributions around the cylindrical distribution. At 80 K, the 4 slender distributions disappeared. At 116 K, the cylindrical distribution was divided into 2 distributions.

It is clear that the temperature dependence of the scattering length density differs between the large and small cages. These differences of the temperature dependence of the scattering length density indicate that the motions of the CH_4 molecule differ between the large and small cages. These results consistent with the study of partially deuterated methane hydrate.

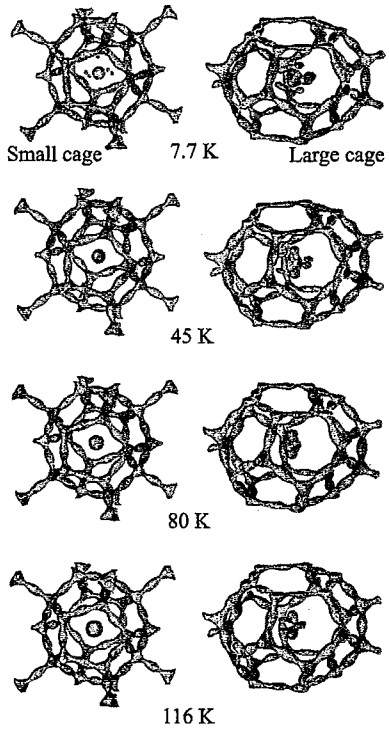

Figure 2: Temperature dependence of scattering length density distribution in deuterated methane hydrate. The isosurface level is 5.0 fm/Å^3 as the absolute value.

References

1) F. Izumi and T. Ikeda : Mater. Sci. Forum **198** (2000) 321.
2) F. Izumi and R.A. Dilanian : *Recent Research Developments in Physics, Vol. 3, Part II*, (Transworld Research Network, Trivandrum, 2002) p. 699.

原子炉：JRR-3　　装置：HRPD(1G)　　分野：中性子散乱（構造）

研究テーマ :高温における$PbTiO_3$のフォノン分散
表題 :立方晶 $PbTiO_3$ の格子ダイナミックス

21) Lattice dynamics of cubic $PbTiO_3$

I. Tomeno, M. Nishi[1], Y. Tsunoda [2], Y. Ishii[3], and K. Oka[4]

Faculty of Education and Human Studies, Akita University, Akita 010-8502, Japan
[1] Institute for Solid State Physics, The University of Tokyo, Tokai 319-1106, Japan
[2]School of Science and Engineering, Waseda University, Tokyo 169-8555, Japan
[3]Neutron Science Research Center, JAERI, Tokai, Ibaraki 319-1195, Japan
[4]Nanoelectrics Research Institute, AIST, Tsukuba, Ibaraki 305-8568 Japan

$PbTiO_3$ occupies an important position in perovskite oxides ABO_3. $PbTiO_3$ is the end member of relaxor ferroelectric $(1-x)Pb(Zn_{1/3}Nb_{2/3})O_3$-$xPbTiO_3$ (PZN-PT). Unlike $BaTiO_3$, $PbTiO_3$ undergoes only a single first-order transition at T_c=520 C from a cubic paraelectric to a tetragonal phase. In the 1970s, Shirane *et al.*[1] have revealed the existence of the well-defined soft mode in cubic $PbTiO_3$. Unfortunately, experimental data are insufficient to confirm the phonon dispersion relations computed from first-principles calculations [2, 3].

The single crystal used in this study was grown by the top seeded solution growth method from a PbO flux [4]. Inelastic neutron scattering measurements were performed using the triple-axis spectrometer T-11 (HQR) at JRR-3M. Figure 1 shows the phonon dispersion relations along the [ζζ0] direction. TA phonon energies measured at 520 C are lower than those at room temperature in the entire q range. The TA-Σ_4 phonon dispersion curve is almost same as the TA-Δ_5 dispersion curve. The zone-boundary TA phonon energies for $PbTiO_3$ are approximately half of those for $BaTiO_3$. A rough estimate suggests that zone-boundary TA phonon energy depends on the A atom mass for $ATiO_3$. The TO-Σ_4 phonon measured at 520C is found to decrease markedly with decreasing q. The softening of TO phonons seems to be limited in a small q region. The TO-Σ_4 phonon dispersion curve is similar to the TO-Δ_5 phonon dispersion curve in the small q region. The isotropic nature of phonon dispersion relations is common to $ATiO_3$ perovskites. It was difficult to determine accurately the zone-center TO phonon energy, because a broad peak exists at ω=0 and q=0. Further experiments are necessary to investigate the TO phonons around the zone center.

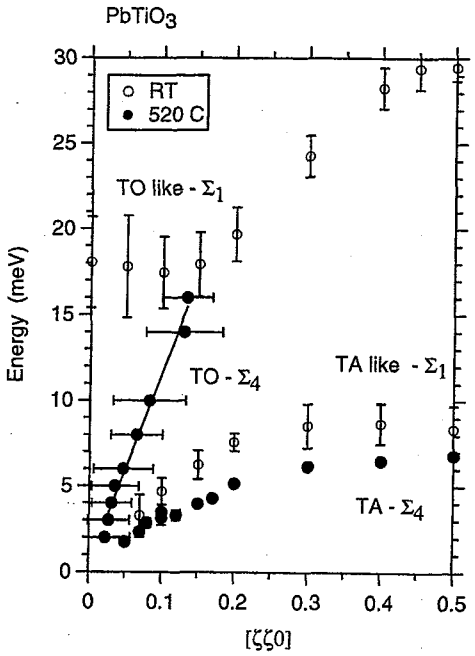

Fig.1 Phonon dispersion relations for $PbTiO_3$

References
[1] G. Shirane et al., Phys. Rev. B **2** (1970) 155.
[2] A. García. and D. Vanderbilt, Phys. Rev. B **54** (1996) 3817.
[3] Ph. Ghosez et al., Phys. Rev. B **60** (1999) 836.
[4] K. Oka et al. J. Crysal Growth **166** (1996) 380.

使用施設 :JRR-3M, 装置 :T11:HTQ, 分野 Structures and Excitations

研究テーマ：物質の静的・動的構造と機能との相関に関する研究
表　題：三元型層状硫化物 $AuCrS_2$ の磁気構造の解析

22) Phase transition and mangetic structure of antiferromagnetic sulfide, $AuCrS_2$

H. Fukuoka[1] K. Yoshii[2], A. Nakamura[3], N. Igawa[4], Y. Shimojo[3], Y. Ishii[4], and Y. Morii[4]

[1]*Department of Applied Chemistry, Hiroshima University, Higashi-Hiroshima, Hiroshima 739-8527,*
[2]*Synchrotron Radiation Research Center, JAERI, Mikazuki, Hyogo 679-5148,*
[3]*Advanced Science Research Center, JAERI, Tokai-mura, Naka-gun, Ibaraki 319-1195,*
[4]*Neutron Science Research Center, JAERI, Tokai-mura, Naka-gun, Ibaraki 319-1195*

Gold is known to have outstanding sulfidation resistance and only a few gold sulfides have been discovered. Several years ago, we studied the ternary system of Au - Cr - S, and prepared a new compound, $AuCrS_2$. It was the second gold sulfide containing a transition metal element. The magnetic susceptibility measurement revealed that $AuCrS_2$ followed the Curie-Weiss law above 150 K, and showed an antiferromagnetic transition at 55 K. In the present study, we have tried to determine the crystal structure and magnetic ordering of $AuCrS_2$ by means of neutron powder diffraction.

Neutron diffraction data have been collected at 2 and 300 K on HRPD of JRR-3. The neutron wavelength was 1.8233 Å. The structure refinement was performed using total pattern fitting program RIETAN-2000[1)].

$AuCrS_2$ crystallized in the trigonal space group $R3m$ with $a = 3.4814(1)$ Å and $c = 21.451(8)$ Å at room temperature. The neutron diffraction analysis at 2 K revealed that $AuCrS_2$ showed an phase transition from $R3m$ to $C2/m$ at a low temperature. The new lattice constants of the low temperature phase were determined to be $a = 5.9869(2)$ Å, $b = 3.4971(1)$ Å, $c = 21.4513(8)$ Å, and $\beta = 89.839°$. The crystal structure was refined using a starting model derived from the fundamental $R3m$ structure. In the 2 θ region higher than 30°, no magnetic peaks were observed. Therefore, magnetic scattering effects were not considered in this analysis. The final refinement converged into $R_{wp} = 8.78\%$, $R_p = 5.87\%$. $R_B = 2.52\%$, $R_F = 1.39\%$, *and* $S = 1.40$. The result is presented in Fig.1, and the refined structure is shown in Fig.2. It was a layered compound composed of CrS_2 layers and Au ions which reside in the interlayer region.

Some magnetic reflections were observed in the lower 2 θ region. The reflections could be indexed on a monoclinic unit cell with dimensions $a = 2 \times a0, b = b0, c = c0$, and $\beta = \beta 0$, where a0, b0, c0, and $\beta 0$ are the lattice constants of the $C2/m$ cell. As no extinction condition is observed, $P2/m$ symmetry can be applied to the ordering of Cr moments. The detailed magnetic structure is now under investigation.

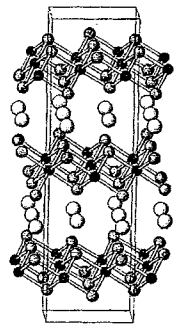

Figure 2: Crystal structure of $C2/m$ $AuCrS_2$. Open, large and small filled circles indicate Au, S, and Cr atoms, respectively.

Reference
1) F. Izumi and T. Ikeda, *Mater.Sci.Forum* **321** (2000) 198.

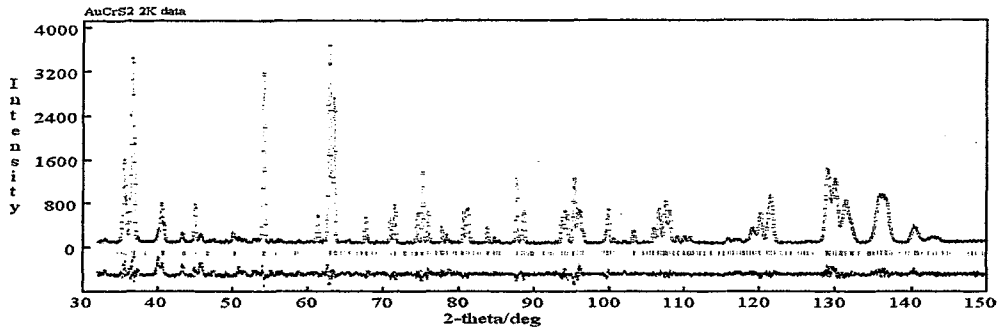

Figure 1: Observed and calculated neutron diffraction profiles of $AuCrS_2$ at 2 K.

原子炉：JRR-3　　装置：HRPD(1G)　　分野：中性子散乱（構造）

研究テーマ： 5G-IRT, C11-IRT
表題：リラクサー $(1\text{-}x)Pb(Mg_{1/3}Nb_{2/3})O_3\text{-}xPbTiO_3$ 系における diffuse scattering の組成依存性

23) Doping dependence of the diffuse scattering in relaxor $(1\text{-}x)Pb(Mg_{1/3}Nb_{2/3})O_3\text{-}xPbTiO_3$ $(x = 0, 0.10)$

M. Matsuura[1], K. Hirota[1], and G. Shirane[2]

[1] *Institute for Solid State Physics, The University of Tokyo, 106-1 Shirakata, Tokai, 319-1106*
[2] *Department of Physics, Brookhaven National Laboratory, Upton, New York 11973-5000*

The relaxor ferroelectrics in the chemical form of $PbBO_3$ gains much attention due to their extreme piezoelectric responses over a wide temperature range [1, 2]. One of the important concepts to understand the mechanism of the high piezoelectricity is polar nanoregion (PNR) with short range correlation of polarization proposed by Burns and Dacol [3]. Such a short range order of polarization was observed in the typical relaxors $PbMg_{1/3}Nd_{2/3}O_3$ (PMN) and $PbZn_{1/3}Nb_{2/3}O_3$ (PZN) as a characteristic diffuse scattering elongated along the [110] and/or [1$\bar{1}$0] directions [4]. One can induce a long ranged polar order in PMN by applying external electrical field or making solid solutions with ferroelectric $PbTiO_3$ (PT). In order to elucidate the evolution of the diffuse scattering as a function of temperature and PT doping, we have performed neutron scattering experiments on PMN and PMN-10%PT single crystals.

PMN and PMN-10%PT single crystals were grown by Zuo-Guang Ye at Simon Fraser University. The neutron scattering experiments were performed on the triple-axis spectrometers PONTA and HER installed at the JRR-3M Reactor of the Japan Atomic Energy Research Institute.

Fig.1 shows contours of diffuse scattering near (110) measured at $T = 300$ K for PMN and PMN-10%PT. The same plot range is adopted to compare data between PMN and PMN-10%PT directly. We confirmed the same diffuse scattering in PMN as previous reports[4]. In PMN-10%PT, although the shape of diffuse scattering remains similar, the intensities of the branches along [110] and [1$\bar{1}$0] directions drastically changes from PMN. This PT doping dependence of the diffuse scattering in PMN contrast with that in PZN showing the same diffuse scattering between PZN and PZN-8%PT. For PMN, as the PT ratio increases, the width of diffuse scattering along [110] and [1$\bar{1}$0]. This indicates larger coherent length, in other words, larger PNR in the PMN-10%PT.

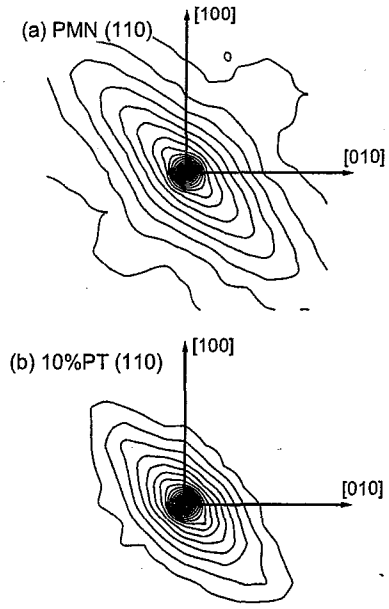

Fig. 1. Logarithmic intensity contours of the diffuse scattering near (1,1,0) for PMN and PMN-10%PT measured at room temperature.

References

[1] S. E. Park and T. R. Shrout: J. Appl. Phys. **82** (1997) 1804.
[2] Z. -G. Ye: Key. Eng. Mater. **155-156** (1997) 8.
[3] G. Burns and F. H. Dacol: Solid State Commun. **48** (1983) 853.
[4] S. B. Vakhrushev *et al.*: Ferroelectrics **90** (1989) 173.

使用施設：JRR-3M, 装置： 5G, C11 , 分野： 101: Structures and Excitations

研究テーマ：中性子散乱による機能材料構造の研究
表　題：D_2O 氷の結晶構造の時間依存性

24) Time Dependence of Crystal Structure of D_2O Ice

A. Hoshikawa, H. Fukazawa[1], N. Igawa, H. Yamauchi and Y. Ishii

Neutron Science Research Center, JAERI, Tokai, Ibaraki 319-1195
[1]Department of Materials Science, JAERI, Tokai, Ibaraki 319-1195

Crystal structure of ordinary ice (Ih) has been studied by X-ray [1,2] and neutron diffraction [3] methods since early in the 20th century. The structure of ice Ih is described by the fixed position of O atom with a hexagonal symmetry (space group: $P6_3/mmc$) and by the equal distribution of H (D) atoms among the two possible sites on each O-O bond. This structure has been known as the hydrogen- (deuterium-) disordered structure proposed by Pauling [4]. An ordered arrangement of hydrogens (deuteriums) is likely to become the thermodynamically stable structure at very low temperatures. However, the change of water molecule orientations is so slow at low temperatures that thermodynamic equilibrium is not attained over laboratory time scales. In this study, we investigated whether the crystal structure of the ordinary ice had the time dependence.

We measured the neutron powder diffraction intensity was measured at 255 K by the high resolution powder diffractometer (HRPD) installed at JRR-3 was used. Data were collected with constant monitor counts and a step angle of 0.05° over the 2θ range of 2.5–160°. Wavelength of used neutrons was 1.8233 Å.

Figure 1 shows the time dependence of neutron powder diffraction pattern. The plus and open circle symbols represent the initial diffraction pattern and the diffraction pattern after 7 days, respectively. The solid line shows the diffraction pattern after 18 days. Since the background levels were same among three diffraction patterns, the measurement was done under the same condition. Each peak position was same. However, the integrated intensity changed. Accordingly, it indicates that an atomic arrangement changes with time in a unit cell although the crystal symmetry does not change.

We analyzed these diffraction patterns by the Rietveld method using RIETAN-2000 [5]. The change of the integrated intensity was not explained by the preferred orientation. When we used the structure model of the previous study [3], the R_B values [6] were 10.31 % for 'Start', 12.85 % for 'After 7 days' and 13.40 % for 'After 18 days', respectively. the R_B value increases with time. Accordingly, it indicates that the crystal structure of D_2O ice becomes misaligned from the structure model for ice Ih with time. We find the time dependence of the crystal structure of D_2O ice. It is necessary to clarify the mechanism for the time dependence of the ordinary ice structure.

References

1) W. H. Barnes : Proc. R. Soc. London Ser. A **125** (1929) 670.
2) P. G. Owston : J. Chem. Phys. (Suppl.) **50** (1953) C-13.
3) S. W. Peterson and H. A. Levy : Acta Crystallogr. **10** (1957) 70.
4) L. Pauling : J. Am. Chem. Soc. **57** (1935) 2680.
5) F. Izumi and T. Ikeda : Mater. Sci. Forum **198** (2000) 321.
6) R.A. Young (ed.): *The Rietveld Method*, (Oxford, New York, 1993) pp. 21–24.

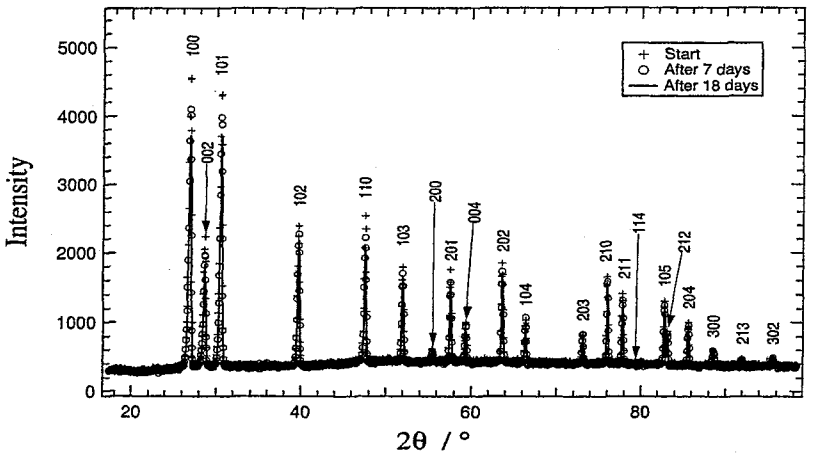

Figure 1: Neutron powder diffraction pattern of D_2O hexagonal ice.

原子炉：JRR-3　　装置：HRPD(1G)　　分野：中性子散乱（構造）

研究テーマ :$(La_{0.9}Sr_{0.1})MO_{3-\delta}$(M=Al,Ga,Sc,In)系ペロブスカイト型酸化物イオン導電体の高温中性子回折
表題 :$(La_{0.9}Sr_{0.1})AlO_{3-\delta}$ペロブスカイトの結晶構造と酸化物イオン伝導経路

25) Crystal structure and oxide-ion conduction path of $(La_{0.9}Sr_{0.1})AlO_{3-\delta}$ perovskite

K. Nomura, N. Takeichi, H. Kageyama, M. Yashima [1], and K. Ohoyama [2]

Research Institute for Ubiquitous Energy Devices, National Institute of Advanced Industrial Science and Technology – Kansai, 1-8-31 Midorigaoka, Ikeda, Osaka 563-8577, Japan
[1]Department of Materials Science and Engineering, Interdisciplinary Graduate School of Science and Engineering, Tokyo Institute of Technology, 4259 Nagatsuta-cho, Midori, Yokohama, Kanagawa, 226-8502, Japan
[2]Institute for Materials Research, Tohoku University, 2-1-1 Katahira, Aoba, Sendai, 980-8577, Japan

Recently, calcium, strontium, and (or) magnesium doped $LaAlO_3$ perovskites have been investigated as the electrolyte materials of solid oxide fuel cells, because of the relatively high oxide-ion conductivity of *ca.* 10^{-2} S/cm at 1000°C [1, 2]. In this study, we measured the high temperature neutron diffraction data and analyzed the nuclear density distributions of 10 mol% Sr doped $LaAlO_3$, $(La_{0.9}Sr_{0.1})AlO_{3-\delta}$ (LSA), to elucidate the crystal structure and oxide-ion conduction path of $LaAlO_3$-based perovskites.

A high purity LSA sintered material was prepared by using a solid-state reaction method. La_2O_3 (4N), $SrCO_3$ (3N), and Al_2O_3 (4N) were used as starting materials. Neutron diffraction data were collected in the temperature range from 29 to 1503°C in air, using an electric furnace with $MoSi_2$ heaters [3] and a diffractometer HERMES installed at JRR-3M in JAERI (Tokai) [4]. The diffraction data obtained were analyzed by the combination technique of Rietveld analysis using a computer program RIETAN-2000 [5] and a maximum-entropy method (MEM)-based pattern fitting. MEM calculation was carried out using a computer program PRIMA [6].

Figure 1 shows the diffraction patterns of LSA from 29 to 1503°C. Between 29 and 543°C, super lattice peaks (which cannot be indexed as a cubic phase $Pm\bar{3}m$) were observed at around 2θ = 47, 63, 77, 90, 104, 118, and 134°. The intensity of these peaks decreased with an increase in temperature, and the peaks disappeared at above 543°C. All the diffraction peaks of LSA could be indexed as rhombohedral symmetry ($R\bar{3}c$) between 29 and 543°C, and cubic one ($Pm\bar{3}m$) between 596 and 1503°C.

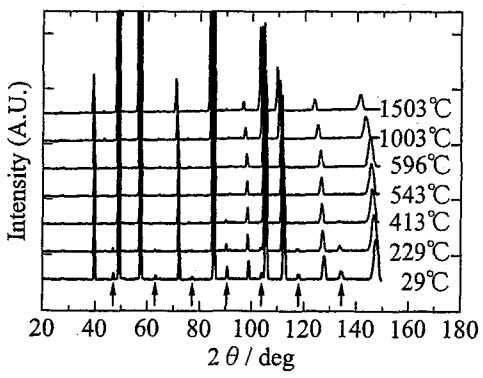

Figure 1: Neutron-diffraction patterns of $(La_{0.9}Sr_{0.1})AlO_{3-\delta}$ from 29 to 1503°C. Arrows show the positions of super lattice peaks.

Figure 2 shows the scattering amplitude distributions on the (100) planes and equicontour surfaces of scattering amplitude (0.05fm/Å) in the cubic ($Pm\bar{3}m$) perovskite LSA at 1503°C. The result showed that oxide-ions have a wide nuclear density distribution perpendicular to Al-O bonds. The conduction path of oxide-ions was speculated to be an arc shape between two stable oxygen positions (O1 and O2) with a constant Al-O bond length. The

使用施設 :JRR3-M, 装置 :HERMES(T1-3), 分野 :構造と励起

conduction path was similar to that of $(La_{0.8}Sr_{0.2})(Ga_{0.8}Mg_{0.15}Co_{0.05})O_{3-\delta}$ [7].

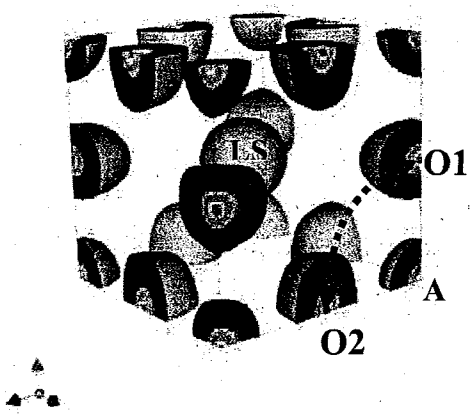

Figure 2: Scattering amplitude distributions on the (100) planes and equicontour surfaces of scattering amplitude (0.06fm/Å) in the cubic perovskite $(La_{0.9}Sr_{0.1})AlO_{3-\delta}$ at 1503°C. LS and A refer to the A-site cation $(La_{0.9}Sr_{0.1})$ and B-site one (Al), respectively. The expected conduction path of oxide-ions between two stable positions (O1, O2) is depicted as a curved dashed arrow.

References

[1] K. Nomura, K. Kakinuma, and H. Yamamura, in: Recent Research Development in Solid State Ionics, Vol. 2(2), Transworld Research Network, Trivandrum, pp.281-316 (2004).

[2] T.L. Nguyen, M. Dokiya, S. Wang, H. Tagawa, and T. Hashimoto, *Solid State Ionics*, **130** (2000) 229.

[3] T. Yashima, *J. Am. Ceram. Soc.*, **85**, 2925 (2002).

[4] K. Ohoyama, T. Kanouchi, K. Nemoto, M. Ohashi, T. Kajitani, and Y. Yamaguchi, *Jpn. J. Appl. Phys.*, **37**, 3319 (1998).

[5] F. Izumi and T. Ikeda, *Mater. Sci. Forum*, **321-324**, 198 (2000).

[6] F. Izumi and R.A. Dilanian, in: Recent Research Developments in Physics, vol.3, Transworld Research Network, Trivandrum, 2002, p.699.

[7] M. Yashima, K. Nomura, H. Kageyama, Y. Miyazaki, N. Chitose, and K. Adachi, *Chem. Phys. Lett.*, **380**, 391 (2003).

研究テーマ：BCC 系水素吸蔵合金の中性子回折による吸放出可能な水素サイトの解析
表　題：BCC 系水素吸蔵合金の中性子回折による吸放出可能な水素サイトの解析

26) Neutron Scattering Analysis of Hydrogen Occupation Site to Absorption/Desorption in BCC MH alloys

T. Shibayama, T. Kamiyama[1], Y. Kiyanagi[1] and N. Igawa[2]

Center for Advanced Research of Energy Conversion Materials, Hokkaido University, Sapporo 060-8628
[1]Graduate School of Engineering, Hokkaido University, Sapporo 060-8628
[2]Neutron Science Research Center, JAERI, Tokai, Ibaraki 319-1195

1 Introduction

Hydrogen absorption alloys are currently being considered for energy storage materials to the advanced energy conversion equipment such as a fuel cell by using hydrogen and air. The hydrogen absorption material would have many advantages as follows; (1) no release of air pollution by chemical combustion products, (2) no limitation of federal or national low to the handling of high pressure gas and (3) non flammable properties in air. Especially, the total amount of absorbed hydrogen in V-Cr-Ti has been reached about 3.7 wt%. However, after several times of hydrogen absorption and desorption cycle, the effective hydrogen absorption capacity would be rapidly degraded. Therefore microstructure analysis were done by SEM, TEM and X-ray, but still not clear the degradation mechanism. Then, we predicted that a change of quantity of this effective hydrogen absorption capacity has a relationship to be close to a hydrogen site in the alloy. In this study, neutron powder diffraction (JRR-3, HRPD) was conducted to clarify a lattice position in the V-Cr-Ti alloy before and after hydrogen absorption and desorption cycle.

2 Experimental procedure

V-Cr-Ti alloy was prepared by arc-melting and annealed at the elevated temperatures for several hours. After several times of hydrogen absorption and desorption cycle, neutron powder diffraction (JRR-3, HRPD) was conducted in low temperature (10K) to reduce heat vibration and diffusion of hydrogen (deuterium) in the alloy. Because Vanadium shows strong non elastic scattering property, overlap method was applied to get the precision diffraction intensity in this study.

3 Results and discussion

In X-ray diffraction analysis, FWHM of each diffraction in a b.c.c. matrices phase was relatively expanded after hydrogen absorption and desorption cycle.

In this study, neutron scattering was mainly caused by hydrides and the other impurities, because Vanadium has strong non elastic scattering property. Several kinds of hydrides (deuterium) in V-Cr-Ti alloys were reported in elsewhere. Therefore we tried to obtain the simulation pattern of expected hydrides in V-Cr-Ti alloy, then to compare them with our experimental results. Back ground intensity did not change before and after hydrogen absorption and desorption cycle. It is suggested that less strain induced in matrices before and after hydrogen absorption and desorption cycle in this alloy. From our preliminary analysis, it was found that D_3V_4 would be candidate hydrides in V-Cr-Ti in this study. However highest intensity peak position does not fit well. We tired to introduce the isotropy distortion to the hydride and tried fitting again several times, but it does not show good agreement with experimental result yet, This result suggests that anisotropy strain introduced to the hydrides after hydrogen absorption and desorption cycle, then after every cycle it would not be easy to relax the introduced strain, finally hydrogen absorption and desorption properties was degraded.

4 Summary

Neutron powder diffraction (JRR-3, HRPD) experiments were done to V-Cr-Ti alloy at low temperature (10K). Our preliminary results may interpret the degradation mechanism of hydrogen absorption and desorption properties after several cycle in this alloy. We are still keeping efforts to this study. We hope to try again it at J-PARC.

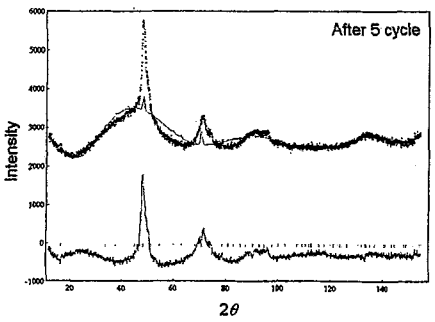

Figure 1: Neutron diffraction pattern of V-Cr-Ti alloy.

原子炉：JRR-3　　装置：HRPD(1G)　　分野：中性子散乱（構造）

表題： 中性子散乱による as-grown $Pb(In_{1/2}Nb_{1/2})O_3$ のフォノン観測

27) Phonon Measurement of as-grown $Pb(In_{1/2}Nb_{1/2})O_3$

K. Ohwada[1], K. Hirota[2], H. Terauchi[3], H. Ohwa[4], N. Yasuda[4]

[1] *Synchrotron Radiation Research Center (SPring-8), J.A.E.R.I., Kohto, Hyogo 679-5148*
[2] *Institute for Solid State Physics, The university of Tokyo, 106-1 Shirakata, Tokai 319-1106*
[3] *School of Science, Kwansei-Gakuin University, Sanda, Hyogo 669-1337*
[4] *School of Engineering, Gifu University, Gifu 501-1193*

Structural properties of *as-grown* $Pb(In_{1/2}Nb_{1/2})O_3$(PIN) single crystals [?] at room temperature (RT) were investigated by x-ray and neutron scattering techniques, taking much account of a difference of penetration depth and spatial resolution. A strong diffuse scattering was observed by x-ray while $h/4$ $k/4$ 0 superlattice reflections were found by neutron, indicating a relaxor state in the outer-layer of the crystal and an antiferroelectric (AFE) state in the bulk.

The phonon dispersion was measured for the first time for the PIN series. As shown in Fig. **1** (a), two transverse optic (TO1 and TO2) modes were clarified near the zone center though neither water-fall behavior nor folding of phonon branches was confirmed. We compare the phonon dispersions with those of the ferroelectric (FE) phase of $PbTiO_3$ (PT) as shown in Fig. 1 (b) [?]. By analogy with PT, the overall character of the two phonon dispersions observed in the as-grown PIN crystal can be understood as that of ferroelectricity, however, it is impossible to specify the direction of polarization vector in the unit cell of the FE PIN at present.

From the above investigation, it seems most reasonable to conclude that a major part of the *as-grown* PIN crystal at RT is FE. This result imply that the *B*-site chemical ordering, i.e. inhomogeneity, which controls the structural properties of PIN, is unevenly distributed throughout the crystal. It is also presumed that small AFE grains coexist with the FE matrix while the outer-layer is in a relaxor state in the *as-grown* PIN.

References

[1] H. Ohwa *et al.*, J. Phys. Soc. of Jpn. **69** (2000) 1533.
[2] G. Shirane *et al.*, Phys. Rev. B **2** (1970) 155.

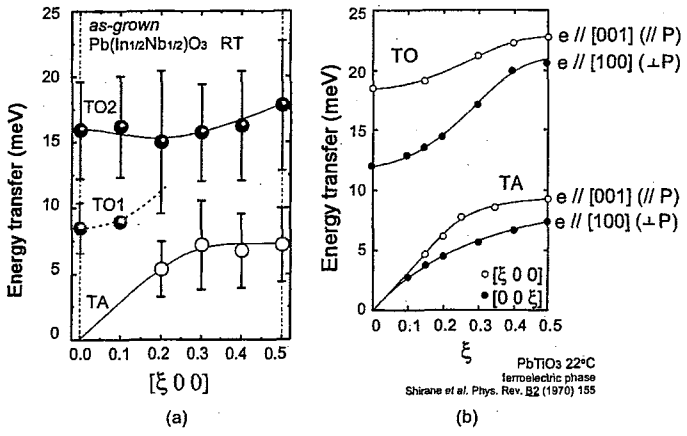

Fig. 1. (a) Determined phonon dispersions of the as-grown PIN crystal at RT. (b) Phonon dispersions of FE phase of $PbTiO_3$ at 22 °C observed by Shirane *et al.* [?]. Since the TO branch was observed at the zone center, the water-fall anomaly is not recognized in the as-grown PIN crystals.

使用施設：JRR-3M，装置： 5G: PONTA，分野： 101: Structures and Excitations

研究テーマ：ヒドリド（ヒドロシリレン）タングステン錯体の構造研究
表　題：ヒドリド（ヒドロシリレン）タングステン錯体の中性子線構造解析

28) Neutron Structure Analysis of a Hydrido(hydrosilylene)tungsten Complex

T. Watanabe, H. Hashimoto, H. Tobita, T. Ohhara,[1] I. Tanaka,[2] and N. Niimura[2]

Department of Chemistry, Graduate School of Science, Tohoku University, Sendai 980-8578
[1]*Neutron Science Research Center, JAERI, Tokai, Ibaraki 319-1195*
[2]*Institute of Science and Engneering, Ibaraki Univ., Hitachi, Ibaraki 316-8511*

Silylene complexes, i.e., transition-metal complexes having a M=Si double bond, have attracted much attention owing to their hypothetically important roles in various catalytic processes. Although many silylene complexes have been isolated, the ones bearing a Si-H bond on the silylene ligand are still rare. This type of complexes are particularly interesting because unprecedented reactivity is expected from the new bonding mode.

We have recently reported the photoreaction of Cp'W(CO)$_3$Me with H$_3$SiC(SiMe$_3$)$_3$ that produces a hydrido(hydrosilylene)tungsten complex Cp'(CO)$_2$(H)W=Si(H)[C(SiMe$_3$)$_3$] (**1a**; Cp' = Cp*, **1b**; Cp' = η^5-C$_5$Me$_4$Et) containing both W-H and Si-H bonds [1]. We suggested that complex 1 takes an unusual interligand interaction between the hydrido and silylene ligands based on its ^{1}H NMR, ^{29}Si NMR , and IR spectra, and the X-ray crystal structure analysis. However, it is generally difficult to determine the precise positions of H atoms bound to a heavy atom by X-ray diffraction study. To confirm this new interaction, we tried the neutron crystal structure analysis, which is the most powerful method to determine the exact positions of the H atoms, of the deuterated derivative of **1b**, (η^5-C$_5$Me$_4$Et)(CO)$_2$(D)W=Si(D)[C(SiMe$_3$)$_3$] (**1b**-d_2). We summarize the results here.

A large crystal of **1b**-d_2 was grown by recrystallization from hexane at room temperature and was sealed in an NMR sample tube under nitrogen atmosphere. Neutron diffraction data were collected at room tempeature at the JRR-3 reactor using the BIX-3M single-crystal diffractometer. All heavy atoms were refined anisotropically and two deuterium atoms were refined isotropically. The final residue $R1$ and the weighted $wR2$ were 0.1275 and 0.2647, respectively, for 3921 reflections with $I > 2\sigma(I)$. The ORTEP drawing of **1b**-d_2 is depicted in Figure 1.

Table 1 shows that the neutron crystal structure of **1b**-d_2 is essentially identical to the X-ray crystal structure of **1b**. A D atom was observed at the position where the D atom bridges the W=Si bond. The W-D(1) and Si(1)-D(1) distances are 1.832(5) Åand 1.720(6) Å, respectively, which are both within the range of distances for bonding interaction. The Si(1), W, D(2), and C(3) atoms are coplanar, and the sum of the valence angles around Si(1) excluding D(1) is 359.5(3) ° , which indicates the complete sp^2-hybridization of the Si atom. These angles as well as the W-D and Si-D distances in **1b**-d_2 unambiguously proved the existence of a significant interligand interaction between the silylene and hydrido ligands. This interaction is understood to be formed by the electron donation from the W-H bond to the empty p orbital on the Si atom of the silylene ligand, according to the DFT calculation [1].

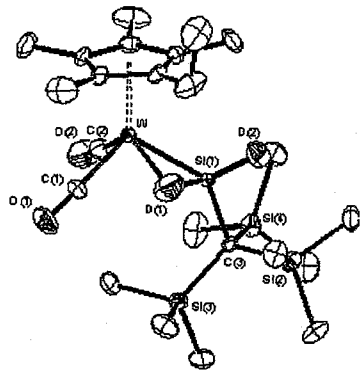

Figure 1: ORTEP drawing of **1b**-d_2.

Table 1: Selected Bond Lengths (Å) and Angles (°) for the X-ray Crystal Structure of **1b**, the Neutron Crystal Structure of **1b**-d_2 and the Energy-Minimized Structure of the Model Complex **1'** (by DFT)

	1b (X-ray)	**1b**-d_2 (Neutron)	**1'** (Calcd)
W-Si(1)	2.3703(11)	2.357(4)	2.377
W-H/D(1)	1.82(7)	1.832(5)	1.85
Si(1)-H/D(1)	1.71(6)	1.720(6)	1.71
Si(1)-H/D(2)	1.54(7)	1.483(6)	1.50
W-C(1)	1.950(5)	1.931(5)	1.97
W-C(2)	1.964(5)	1.958(4)	1.98
Si(1)-W-H/D(1)	46(2)	46.4(2)	46
W-Si(1)-H/D(1)	50(2)	50.5(2)	51
W-Si(1)-H/D(2)	110(3)	114.8(3)	121
W-Si(1)-C(3)	141.4(1)	142.2(2)	135

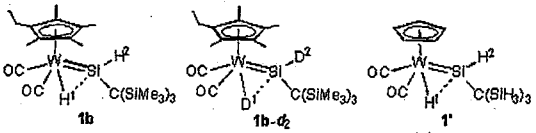

References

1) T. Watanabe, H. Hashimoto, and H. Tobita: Angew. Chem. Int. Ed. **43** (2004) 218-221.

原子炉：JRR-3　　装置：BIX-3M(1GB)　　分野：中性子散乱（構造）

研究テーマ：リチウム二次電池用正極材料斜方晶 $LiMn_{1-x}M_xO_2$ の充放電サイクルに伴う結晶構造変化および熱力学安定性と電池特性
表題：リチウム二次電池正極活物質 $Li_xMn_{1-y}M_yO_2$ (M=Mn, Al, Cu) の結晶構造，熱力学安定性と電極特性の Li 組成依存

29) Li Content Dependence of Crystal Structure, Thermodynamic Stability and Electrode Performance of $Li_xMn_{1-y}M_yO_2$(M=Mn, Al, Cu) as a Cathode Active Material for the Lithium Secondary Battery

Y. Idemoto, Y. Konno, T. Mochizuki, and N. Koura

Faculty of Science and Technology, Tokyo University of Science,

2641 Yamazaki, Noda-shi, Chiba 278-8510, Japan

1. Li content dependence of thermo-dynamic stability and the crystal structure of $Li_xMn_{1-y}M_yO_2$(M=Mn, Al, Cu) as a cathode active material for Li secondary battery

We investigated the relationship between the thermodynamic stability and Li content in the crystal structure of the orthorhombic $LiMn_{1-x}M_xO_2$(M=Mn, Al, Cu). The enthalpy change for mol of atoms for the reaction, ΔH_R, were calculated from the heat of dissolution. ΔH_R increased with the decreasing Li content except for the two-phase region and significantly increased the two-phase region for each sample. For the same Li content, the Li_xMnO_2 sample obtained by reflux heating was more thermodynamically stable than the other samples. Furthermore, the $Li_xMn_{0.95}Al_{0.05}O_2$ sample was unstable, and the $Li_xMn_{0.95}Cu_{0.05}O_2$ sample was more stable than that of Li_xMnO_2, which was obtained by the same method.

The crystal structure of $Li_xMn_{1-y}M_yO_2$ (M=Mn, Al) was analyzed by the neutron powder diffraction method [HERMES, JRR3M in JAERI (Tokai)]. The Madelung energy and bond lengths of each sample were calculated using the Rietveld analysis(Rietan 2000). The Madelung energy of the spinel phase was low, and the spinel phase was more stable than the orthorhombic phase. The distributions of the nuclear density and electron density were calculated by MEM(Prima) in order to determine the bonding state. The nuclear density decreased with the decreasing Li content. In o-$LiMn_{0.95}M_{0.05}O_2$ (M=Al, Cu), the Li localization and strong covalence of (Mn,M)-O were estimated from the distribution of the electron densities. [1]

2. Properties, crystal structure and performance of orthorhombic $LiMnO_2$ as cathode material for Li secondary batteries

Orthorhombic $LiMnO_2$ was prepared as a cathode material for Li secondary batteries by the solid-state, sol-gel, and reflux heating methods. Reflux heating yielded a single phase, whose composition we were able to control. The particle size distribution of this orthorhombic $LiMnO_2$ was uniform. Its discharge capacity at 25^0C was the lowest, its cycle performance, the most stable, among the $LiMnO_2$ produced by the three methods. The discharge capacity increased with cycle number and stabilized at about 30-40 cycles at 25^0C.

We investigated the relationship between the Li^+ diffusion coefficient and the crystal structure during the cycles, The chemical diffusion coefficient of Li^+(D_{Li+}) for $Li_{1-x}MnO_2$ at the stable cycle region is larger than that at the initial cycle and was almost constant during the charge-discharge process at 25^0C. The D_{Li+} at 30, 40 cycles corresponded almost exactly to that of the spinel $Li_{1-x}Mn_2O_4$. Refinement of the samples was performed in 30 cycles by assuming two phases of space group Fd-3m, and the best-fit indicator was obtained

使用施設：JRR-3M，装置：HERMES(T1-3)，分野 Structure & Excitations(101)

using the Rietveld analysis(Rietan 2000). by the neutron powder diffraction method [HERMES, JRR3M in JAERI (Tokai)].

The neutron diffraction intensity profile of o-$LiMnO_2$ was analyzed assuming the space group Pmmn. In particular, the S value(=R_{wp}/R_e) of o-$LiMnO_2$ synthesized by reflux heating was the lowest in all samples. The bond lengths of Mn-O1(O2) in samples synthesized by reflux heating were the shortest. This suggested that the covalent bond of Mn-O in samples synthesized by reflux heating was the strongest in all samples. The bond angles of O1(O2)-Mn-O1(O2) for samples synthe-sized by reflux heating were the largest in all samples. This suggested that the distortion of the MnO_6 octahedron was large. The distortion of o-$LiMnO_2$ synthesized by reflux heating was large in all samples. The distortion of this single-phase o-$LiMnO_2$ sample synthesized by reflux heating, was large due to the presence of a Jahn Teller ion (Mn^{3+}). The B.V.S. of Mn for the samples was about 3. However, the B.V.S. for the samples synthesized by the solid-state and sol-gel methods was slightly less than 3 because these samples contained a second phase, namely Li_2MnO_3. The electron-density images suggest that the covalent bond of Mn-O was stronger for the sample synthesized be reflux heating than those synthesized by the solid-state method.

References

[1] Y. Idemoto et al., Electrochemistry, in printing.

研究テーマ：中性子散乱による機能材料構造の研究
表　題：中性子回折を用いたNi添加スピネル化合物の結晶構造解析

30) Structural Study of the Ni-doped Spinels by Neutron Diffraction Experiments

H. Yamauchi[1], T. Suzuki[2], Y. Ohishi[2] and N. Igawa[1]

[1] *Neutron Science Research Center, JAERI, Tokai, Ibaraki 319-1195*
[2] *Optical Functional Materials Laboratory, Toyota Technological Institute, Nagoya, Aichi 468-8511*

Oxide spinels AB_2O_4, where A and B are cations, have long been a considerable topic of interest in the solid state sciences because of their usefulness as magnetic materials, semiconductors, optical materials and so on. Investigation of cation distribution in oxide spinels are relevant to the many technological application of oxide spinels. Cation site preference in binary spinels are well investigated, but ternary spinels (i.e., spinels with three kinds of cations) are not so well understood. Recently, Ni-doped ternary spinels have drawn attention for a potential as tunable laser source and broadband optical amplification medium[1]. In order to contribute to a better understanding of the Ni-ion preference in oxide spinels, structural investigations of binary and ternary spinels $Ni_xZn_{1-x}Al_2O_4$, $Ni_xZn_{1-x}Ga_2O_4$, $Ni_xMg_{1-x}Al_2O_4$ and $Ni_xMg_{1-x}Ga_2O_4$ ($x=0$ and 0.5) were carried out by neutron diffraction.

Neutron powder diffraction measurements were performed at room temperature on the High Resolution Powder Diffractometer, HRPD, installed at JRR-3. The incident wave length of 1.8233 Å was used. The first collimator with 6′ was chosen. The structural refinement and determination of cation distribution were carried out by the program RIETAN-2000[2].

Figure 1 shows the observed neutron diffraction pattern and the best fit result of Rietveld refinement for $Ni_{0.5}Zn_{0.5}Al_2O_4$. The vertical marks indicate the positions of Bragg reflections. The present Rietveld refinement provided a good result for a cubic close-packed structure (space group: $Fd\bar{3}m$) with the lattice parameters of $a=8.0733(9)$ Å and the oxygen parameter of $u=0.3848(1)$ Å. The reliability factors of this refinement were $R_B=1.34\%$, $R_{wp}=7.24\%$ and $S=0.97$. Table 1 shows the cation distribution in $Ni_{0.5}Zn_{0.5}Al_2O_4$. In the structural refinement for $ZnAl_2O_4$, almost all of Zn^{2+} ions occupied the $8a$ site. We therefore assumed in the Rietveld analysis of $Ni_{0.5}Zn_{0.5}Al_2O_4$ that all the Zn^{2+} ions remained in the $8a$ position. The occupancy of O^{2-} ions in the $32e$ site held almost 1.0. It turns out that Ni^{2+} ions mainly prefer the ochtahedral $16d$ site to the tetrahedral $8a$ site in $ZnAl_2O_4$. The refinement of $Ni_{0.5}Zn_{0.5}Ga_2O_4$ showed the same tendency.

Table 1: Cation distribution in $Ni_{0.5}Zn_{0.5}Al_2O_4$

atom	position	occupation factor
Ni1	$8a$	0.068(4)
Ni2	$16d$	0.216(4)
Zn	$8a$	0.500
Al1	$8a$	0.430(4)
Al2	$16d$	0.785(4)

Further detailed analyses for all samples are now in progress. We intend to investigate the relationship between the site selectivity and emission efficiency of Ni^{2+} ions in the spinel crystals in the future.

References

1) T. Suzuki and Y. Ohishi: Appl. Phys. Lett. **84** (2004) 3804.
2) F. Izumi and T. Ikeda: Mater. Sci. Forum **321–324** (2000) 198.

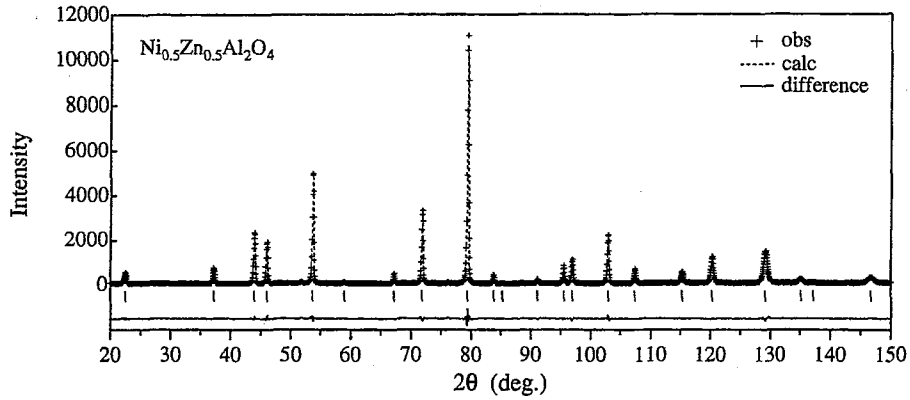

Figure 1: Best result of Rietveld refinement for $Ni_{0.5}Zn_{0.5}Al_2O_4$ at room temperature.

原子炉：JRR-3　　装置：HRPD(1G)　　分野：中性子散乱（構造）

研究テーマ：重水の準・非弾性散乱測定による群定数の構築
表題：AGNES による D_2O 散乱の MIEZE 分光器のための予備測定

31) Preliminary experiments of D2O scattering for MIEZE spectrometer with AGNES

S.Tasaki, Y.Edura, M.Hino*, T. Ebisawa**

Dept. of Nucl. Eng., Kyoto University, Yoshida-Honmachi Sakyo-ku Kyoto, 606-8501 Japan;
** Research Reactor Institute, Kyoto University, Kumatori Osaka,590-0494 Japan;*
***Japan Atomic Energy Research Institute, Shirakata-Shirane Tokai, 319-1195, Japan*

Mieze spectrometer is a modified version of NSE spectrometer, in which echo condition (cancellation of Larmor precession phase) is realized when the distance between the detector and the last $\pi/2$-flipper is adjusted and hence, contrast of NSE signal depends on the distance. Since the sensitivity on the distance is proportional to the energy resolution of the Mieze spectrometer, the thickness of the detector and the size of the sample should be small (less than a few millimeter) for high resolution. Since besides the other NSE spectrometer, no spin analyzer is required between the sample and the detector in Mieze spectrometer, new types of experiments such as inelastic or quasi-elastic scattering with neutron spin flip is measurable with Mieze.

We intend to construct Mieze spectrometer as one of the three NSE spectrometers. In order to reduce the sensitivity on the detector position, the energy resolution of the Mieze spectrometer is confined to that of the conventional inelastic scattering spectrometers. The advantage of the Mieze comparing to the inelastic scattering spectrometer is the compactness of its size and the beam intensity at the sample position.

In order to check the properties of Mieze, it is important to measure standard samples and compare the measured data to that of some conventional spectrometer. For this purpose, we measured the inelastic scattering of D_2O (as the standard sample) using the inelastic scattering spectromter AGNES (as reference spectromter).

D_2O is contained in a Al-cell and the measurements were performed at various temperatures under normal pressure. Two of the results for 4 degree and 70 degree are shown in Fig.1 and 2, respectively. Difference of elastic and inelastic scattering due to the change of the temperature is clearly shown. These data will be used for calibration of Mieze spectrometer.

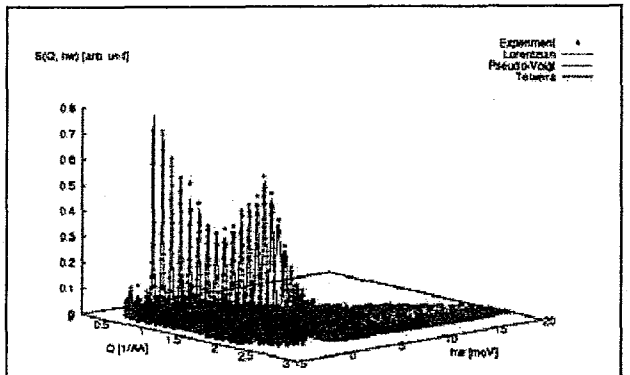

Fig.1 The result of neutron inelastic scattering from D2O at 4 degree.

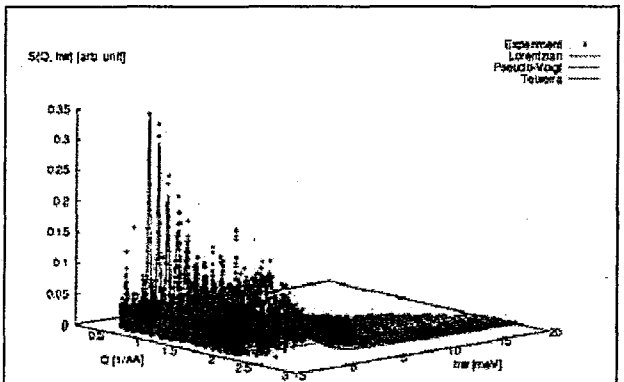

Fig.2 The result of neutron inelastic scattering from

使用施設：JRR-3M，装置：AGNES(C3-1-1)，分野 Structures and Excitations

研究テーマ：ヌクレオチド結晶の高水和状態における水和構造の解析
表　題：中性子回折法によるシチジン 5′-リン酸二ナトリウム水和物の水素結合網の解析

32) Neutron Diffraction Study on Hydrogen-Bonding Networks in Disodium Cytidine 5′-Monophosphate Hydrate

S. Yamamura, A. Mineyama, Y. Sugawara, T. Ohhara[1], I. Tanaka[2] and N. Niimura[3]

School of Science, Kitasato University, 1-15-1 Kitasato, Sagamihara,Kanagawa 228-8555
[1]*Neutron Science Research Center, JAERI, 2-4 Shirakata-shirane, Naka, Tokai, Ibaraki 319-1195*
[2]*Faculty of Engineering, Ibaraki University, 4-12-1 Naka-narusawa-cho, Hitachi, Ibaraki 316-8511*
[3]*Graduate School of Science and Engineering, Ibaraki University, 4-12-1 Naka-narusawa-cho, Hitachi, Ibaraki 316-8511*

Numbers of crystal water molecules of nucleotide hydrates are function of relative humidity, and phase transitions proceed coupled with reconstruction of hydrogen bonding networks. In the case of disodium cytidine 5′-monophosphate (Na_2CMP), the number of crystal water molecules changes from 9 to 1.3, through 8, 6.5 and 3.5 in the relative humidity range 90-0% [1].

Neutron diffraction analysis of Na_2CMP was started with the nonahydrate. An as-grown crystal with approximate dimensions of 2.5 × 1.1 × 1 mm^3 was sealed in a quartz capillary tube, and intensity data were collected at room temperature with the wavelength of 1.51 Å using a BIX-3 diffractometer installed at 1G-A port of JRR-3 in JAERI (Tokai). Crystal data are shown in Table 1. Hydrogen positions were determined by iteration of difference Fourier syntheses and full-matrix least squares refinement cycles starting from the coordinates of non-hydrogen atoms of CMP determined by X-ray analysis. The R value is 0.12 for 6013 observed reflections ($|F_o| > 4\sigma(F_o)$) up to 0.9 Å at the present stage.

The crystal structure is shown in Fig. 1. There are four CMP molecules and 39 water sites of 37 crystal water molecules in an asymmetric unit. All hydrogen atom positions of CMP molecules and 72 hydrogen atom positions of 38 water sites were determined. In the case of 30 water sites, both hydrogen atoms form hydrogen bonds. On the other hand, the rest 8 water molecules form one hydrogen bond each as a hydrogen donor. Nuclear distribution of some crystal water molecules seems to reflect large librational motions, where the hydrogen bonds play the role of an anchor. Similar figures were obtained for inosine 5′-monophosphate hydrates [2].

Table 1: Crystal data

Chemical formula	$4(C_9H_{12}N_3O_8PNa_2)\ 37H_2O$
Space group	$P2_12_12_1$
a/Å	20.726(4)
b/Å	47.791(9)
c/Å	9.0950(4)
Z	4

References

1) Sugawara *et al.*: J. Chem. Phys., **106** (2002) 10363.
2) Sugawara *et al.*: ISSP Activity Report on Neutron Scattering Research, **10** (2003) 86.

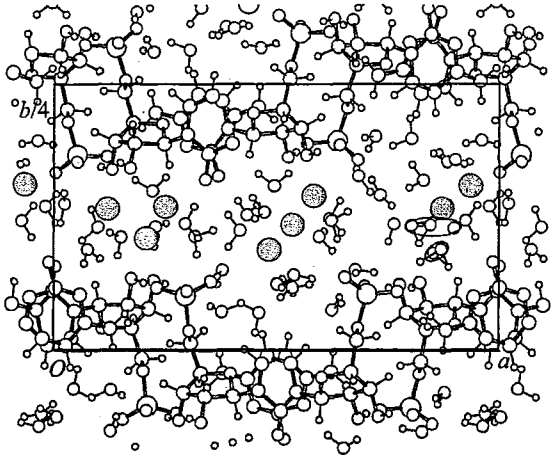

Figure 1: Crystal structure of Na_2CMP nonahydrate. Gray circles indicate sodium ions and disordered water sites are included in ellipses.

原子炉：JRR-3　　装置：BIX-3(1GA)　　分野：中性子散乱（構造）

研究テーマ：欠陥エンジニアリングを利用した蛍光体材料の構造解析
表題：Aサイト欠陥ペロブスカイト型化合物の結晶構造解析

33) Crystal Structure Refinement of A-site defect Perovskite-type compounds

Yutaka Ito, Akira Komeno, Yoshio Aoyama, Kazuyoshi Uematsu*, Kenji Toda, Mineo Sato*

*Graduate School of Science and Technology, Niigata University,8050 Ikarashi 2-nocho, Niigata 950-2181, Japan; *Department of Chemistry and Chemical Engineering, Niigata University,8050 Ikarashi 2-nocho, Niigata 950-2181, Japan*

An ideal perovskite has the general formula ABO_3 and their framework structure is composed of corner shared BO_6 octahedra. The large A-site atom is at the centre of a cube with twelve coordinating O atoms. Transition-metal oxides with the perovskite structure are important materials that can exhibit the ion conductive, superconductive, magnetoresistive, ferroelectric and luminescence properties, depending on the choice and stoichiometry of the A- and B-site cations. In order to maintain electroneutrality of perovskite oxide, the total charge of the cation sites must be 6+. The possible combinations of A and B site charges in a simple ABO_3 phase are A^{+1}/B^{+5}, A^{+2}/B^{+4}, A^{+3}/B^{+3}. As a matrix compound for trivalent ion conductor and phosphor, the A-site highly deficient perovskite compound of YTa_3O_9 is potentially interesting in a view point of large amount of A-site vacancies and highly charged central cations of Ta. We have previous by sufficient evidence of trivalent ion conduction in $Y_x(Ta_{3x}W_{1-3x})O_3$ (YTWO) [1]. In addition, a order-disorder transition of the rare earth ion can affect the luminescence properties in A-site defect perovskites. In this study, we show the crystallographic data on $Y_x(Ta_{3x}W_{1-3x})O_3$ (x=0.06, 0.22) refined from the neutron powder diffraction patterns.

The samples were prepared by a conventional solid state reaction. Starting materials were stoichiometric mixtures of Y_2O_3, Ta_2O_5 and WO_3 powders. The mixture was pressed into a pellet and heated in a platinum boat at 1473 K for 30 min in air.

The completion of the reaction and the phase purity of the samples were confirmed by powder X-ray diffraction methods. We performed neutron powder diffraction experiments on the Kinken powder diffractometer for high efficiency and high resolution measurements, HERMES [2] with λ = 0.18196 nm, of Institute for Materials Research(IMR), Tohoku University, installed at the JRR-3M reactor in Japan Atomic Energy Research Institute (JAERI), Tokai. The fine powder sample was sealed in a vanadium cylinder. Rietveld structure refinement was carried out with the program RIETAN2000 [3].

Crystal structures of $Y_{1/3}TaO_3$, were first reported by Studer *et al.* [4]. They refined two types of structure; one is $Y_{0.06}Ta_{0.18}W_{0.82}O_3$ on the basis of a cubic

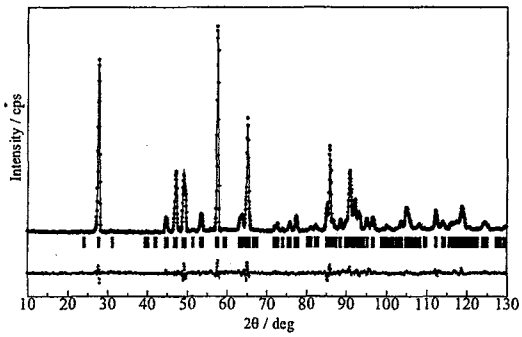

Fig. 1. Powder neutron fitting of $Y_{0.06}Ta_{0.18}W_{0.82}O_3$.

Table1 Structural parameter of $Y_{0.06}Ta_{0.18}W_{0.82}O_3$

Atom	Site	x	y	z	B_{eq}
Y	4c	0.060(4)	1 / 4	-0.006(4)	1.34(4)
Ta	4b	0	0	1 / 2	2.36(5)
W	4b	0	0	1 / 2	2.36(5)
O(1)	4c	0.492(4)	1 / 4	0.064(3)	1.07(4)
O(2)	8d	0.281(2)	0.031(1)	0.717(2)	0.98(3)

Pnma (62), a = 0.5373(3)nm, b = 0.7547(5)nm, c = 0.5297(3) nm, R_{wp} = 6.51 %, R_p = 5.08 %, R_I = 2.50 %, R_F =1.52 %

使用施設：JRR-3M, 装置：HERMES(T1-3), 分野 Structure and Excitations

system with space group $Pm\bar{3}m$ (a = 0.3833 nm) and the other is $Y_{0.24}Ta_{0.72}W_{0.28}O_3$ on the basis of a orthorhombic system with in the space group *Cmmm* (a = 0.5298, b = 0.5377 and c = 0.3774 nm). However, since these structures were deduced only from the electron and powder X-ray diffractions, the information on light elements, especially for oxygen atom, was quite poor. To investigate the occupancy at the A-site and possible tilting of $(Ta,W)O_6$, the powder neutron diffraction data were collected from the single phase samples with x = 0.06 and 0.22.

Figure 1 and Table 1 shows the powder neutron diffraction pattern fitting and structural parameters for the $Y_{0.06}Ta_{0.18}W_{0.82}O_3$. All of the diffraction peaks were well indexed on orthorhombic system *Pnma*. A good fitting profile were obtained with R_{wp} = 6.51 %. The orthorhombic Pnma structure is a distorted form of ideal cubic perovskite. The distortion mechanism is a tilting of essentially rigid $(Ta,W)O_6$ octahedra. It occurs when the A-site cation is too small for its 12 coordinate cavity in the cubic perovskite structure. This distortion is the predominant for perovskites with tolerance factors smaller than 0.98. In the A-site deficient perovskites $Y_x(Ta_{3x}W_{1-3x})O_3$, the tolerance factor is 0.91 and the coordination number of the yttrium ion is effectively lowered from 12 to 8. In addition, neutron diffraction pattern analysis confirmed the disorder arrangement of A-site cations. The yttrium ions are statistically distributed only over 6 % of a single 4c site with 94 % vacancy in the space group *Pnma*.

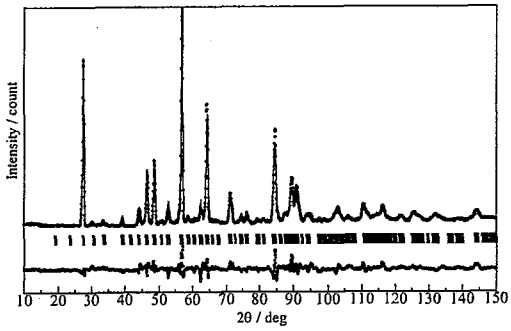

Fig.2 Powder neutron fitting of $Y_{0.22}Ta_{0.66}W_{0.34}O_3$.

Table2 Structural parameter of $Y_{0.22}Ta_{0.66}W_{0.34}O_3$

Atom	Site	g	x	y	z	B_{iso}
Y(1)	4e	0.25(3)	0	-0.025	0.25	0.1(1)
Y(2)	4e	0.13(2)	0	0.5	0.25	0.0(2)
Ta(1)	4c	0.66(9)	0.25	0.25	0	0.35(9)
W(1)	4c	0.29(7)	0.25	0.25	0	0.35(9)
Ta(2)	4d	0.675(7	0.25	0.25	0.5	1.2(5)
W(2)	4d	0.322(8	0.25	0.25	0.5	1.2(5)
O(1)	8f	1.0	0.220(1)	-0.006(3	-0.017(1)	3.7(5)
O(2)	8f	1.0	-0.001(1	0.285(1)	-0.032(1)	0.4(4)
O(3)	8f	1.0	0.203(1)	0.237(1)	0.239(1)	0.6(3)

C2/c (15), a = 0.764(1)nm, b = 0.764(1)nm, c = 0.763(1)nm, β= 90.36(1)°R_{wp} = 9.40 %, R_p = 7.14 %, R_I = 4.48 %, R_F = 2.27 %, R_E=4.27 %, S= 2.20

Figure 2 and Table 2 shows the powder neutron diffraction pattern fitting and structural parameters for the $Y_{0.22}Ta_{0.66}W_{0.34}O_3$. All of the diffraction peaks were well indexed on monoclinic space group *C2/c*. A good fitting profile were obtained with R_{wp} = 9.40 %. The refined occupancies of the B-sites are listed in Table2 together with other crystallographic data. The total occupancy ratios of tantalum and tungsten were 0.66(9): 0.29(7) for site 1 of B-site and 0.675(7): 0.322(8) for site2 of B-site, in good agreement with nominal composition ratio. This fact indicates that there is no long-range ordering in the B-site cation of Ta and W cations. On the other hand, the refinement data showed clear evidence of A-site ordering (Table2). The occupancy factors refined for yttrium are 0.25(3) for Y(1) and 0.13(2) for Y(2) indicating an order state with the ratio of 2: 1 for A-site.

References

[1] N. Sakai *et al.*, *Electrochemistry*, **6** (2000), 504.
[2] K. Ohoyama *et al.*, *Jpn. J. Appl. Phys.*, **37** (1998), 3319.
[3] F. Izumi *et al.*, *Mater. Sci. Forum.*, **321-324** (2000), 198.
[4] F. Studer *et al.*, *J. Solid State Chem.*, **7** (1973), 269.

研究テーマ：中性子散乱による機能材料構造の研究
表　題：KOD を含有した氷の重水素秩序化: 粉末中性子回折研究

34) Deuteron Ordering in KOD-doped Ice: A Powder Neutron-Diffraction Study

H. Fukazawa, A. Hoshikawa[1], H. Yamauchi[1], Y. Yamaguchi[2], N. Igawa[1] and Y. Ishii[1]

Department of Materials Science, Japan Atomic Energy Research Institute, Tokai-mura, Ibaraki 319-1195, Japan
[1]*Neutron Science Research Center, Japan Atomic Energy Research Institute, Tokai-mura, Ibaraki 319-1195, Japan*
[2]*Institute for Materials Research, Tohoku University, Sendai 980-8577, Japan*

The arrangement of hydrogen atoms in ice Ih (ordinary ice) is disordered at temperatures from 273 K down to about 0 K. In ice Ih, the oxygen atoms are arranged in the space group $P6_3/mmc$ but the hydrogen atoms (or deuterium atoms for D_2O ice) are disordered in the sense that they are equally distributed among the two possible sites on each O-O bond according to the ice rules [1].

The structure with an ordered arrangement of hydrogen atoms, which must have a lower energy than the disordered structure, is likely to become a thermodynamically stable structure at very low temperatures. But the thermodynamic equilibrium state is not attained in a limited period of time because the mobility of the hydrogen atoms in ice is very low at low temperatures. Therefore, ice Ih has the disordered arrangement of hydrogen atoms even at very low temperatures.

However, doping with KOH speeds the transition from the hydrogen-disordered structure to a hydrogen-ordered structure because the impurity introduces defects that increase the mobility of the hydrogen atoms. Leadbetter *et al.* [2] measured neutron diffraction profiles of 0.11-M KOD doped D_2O ice that was annealed at 65 K, and proposed under the analyses with a reliable factor R of 24% that the arrangement of oxygen atoms in ice XI is the same as that in ice Ih, whereas the deuterium atoms in ice XI (or hydrogen for H_2O ice) partially occupy ordered positions in the space group $Cmc2_1$.

To obtain more direct evidence of the occurrence and formation of deuterium-ordered ice XI, we measured the neutron diffraction of 0.1M KOD-doped ice, which made carefully under several conditions of temperature and annealing time, using a powder diffractometer HRPD. Then, we carry out the Rietveld analysis with smaller reliable factors of less than 5% for all diffraction profiles to obtain the mass fraction f, the ratio of mass of ice XI to that of the doped ice, as a function of time and temperature.

The structural analysis provided direct evidence for the existence of ice XI at 68 K. On the basis of the Rietveld analysis, we determined the mass fraction of ice XI as a function of time and temperature. The temporal dependence of the mass fraction was consistent with random nucleation events. The results showed that the nucleation of ice XI, which can be detected using the neutron diffraction, began just after warming up to 68 K. Then ice XI grew for several days in the KOD-doped ice. This work is the first study to report structural observations of formation and growth of the deuterium-ordered structure [3].

These results strongly suggest the existence of the hydrogen ordering in pure ice crystal as low-temperature equilibrium structure, which has been kept for a long period of time. Natural ice on satellite of the outer planets and comets may have the hydrogen-ordered arrangements. This implies the existence of the electricity produced by the ordered ice on the surface of the planets, because ice XI is ferroelectric.

Future studies to find out why the growth of ice XI is so slow and whether or not f reaches 1.0 at $t = \infty$ are important for understanding the nature of the hydrogen bond and occurrence of ice in the universe. According to our analyses, the mass fraction cannot exceed a small value (about 50%) at $t = \infty$. This is because growth process of ice XI nuclei is not clear. Long-term measurements of the size of ice XI nuclei may be required to investigate other processes. To solve the growth mechanism precisely, more difficult structural analyses of the two phases using a partial deuterium-ordered model as ice XI and high-quality neutron measurements that needed by the analyses might be useful. Thus, structural studies on neutron diffraction from doped ice under various conditions (such as temperature variation and impurity effects) should be done.

References

1) L. Pauling: J. Am. Chem. Soc. **57** (1935) 2680.
2) A. J. Leadbetter, R. C. Ward, J. W. Clark, P. A. Tucker, T. Matsuo, H. Suga: J. Chem. Phys. **82** (1985) 424.
3) H. Fukazawa, A. Hoshikawa, H. Yamauchi, Y. Yamaguchi, Y. Ishii: J. Crystal Growth (in press).

原子炉：JRR-3　　装置：HRPD(1G)　　分野：中性子散乱（構造）

研究テーマ： 希土類6硼化物 RB_6 におけるフォノン異常
表題： 希土類6硼化物 RB_6 におけるフォノン異常の研究

35) Study of Phonon Anomalies of Rare Earth Hexaborides RB_6

M. Kohgi[1], K. Kuwahara[1], M. Udagawa[2], and F. Iga[3]
[1]*Department of Physics, Tokyo Metropolitan University, Tokyo 192-0397*
[2]*Fac. of Int. Arts and Sciences, Hiroshima Univ., Higashihiroshima 739-8521*
[3]*Grad. School of Advanced Sciences of Matter, Hiroshima Univ., Higashihiroshima 739-8530*

Rare earth hexaborides, RB_6, have attracted attention due to their unusual thermal and magnetic properties including $4f$ electron multipole-order phenomena as well as dense-Kondo behaviors in CeB_6 and Kondo-semiconductor properties in SmB_6. These phenomena are principally attributed to the $4f$ electron degrees of freedom. However, there are evidences of contributions of lattice degrees of freedom to some of anomalies found in RB_6 due to the peculiar crystal structure in which rare earth atoms are confined rather loosely in cages formed by B atom network [1]. Concerning this problem, Ogita et al. reported that a couple of unusual Raman peaks, which cannot be attributed to the one-phonon or crystal field excitations, were observed for trivalent rare earth hexaborides such as CeB_6, PrB_6, GdB_6 or DyB_6 [2]. These peaks are observed clearly at room temperature and their intensities decrease rapidly with decreasing temperature. Similar but broader peaks are also observed for divalent rare earth hexaborides, which are semiconductors, such as YbB_6, however, their intensities are very weak and show little temperature dependence. Ogita et al. attributed the anomalous peaks to the two-phonon scattering process involving the acoustic phonons which show almost flat dispersions except around the zone center reflecting rather weak coupling of R atoms with B cages. They claimed that the difference of phenomena between trivalent and divalent RB_6 is due to the effect with or without conduction electrons on the R-ion motion. The purpose of the present work is to get direct information by neutron inelastic scattering on the phonons in both types of hexaborides in connection with the above argument on the unusual Raman peaks.

Neutron scattering experiments were carried out on the triple axis spectrometer 4G (GPTAS) installed at JRR-3 with a fixed final neutron energy of 14.7 meV. An assembly of two single crystals of PrB_6 (the size of each crystal is $\sim$ 4 mm in diameter and $\sim$ 6 cm in length) and a single crystal of YbB_6 ($\sim$ 6 mm in diameter and 2.4 cm in length) were prepared as the samples representing trivalent and divalent rare earth hexaborides, respectively. The sample were set in the cryostat equipped with a ^{4}He closed cycle refrigerator with the $[1\bar{1}0]$ axis vertical. Due to limited beam time, measurements of phonon excitations were restricted only at the zone boundaries and midpoints (only for YbB_6) along the [0 0 1], [1 1 0] and [1 1 1] axes.

Fig. 1 depicts the observed temperature dependences of the phonon excitation energies at the zone boundaries X-point, $(0, 0, 0.5)$, M-point, $(0.5, 0.5, 0)$, and R-point, $(0.5, 0.5, 0.5)$, for PrB_6 and YbB_6. Labels

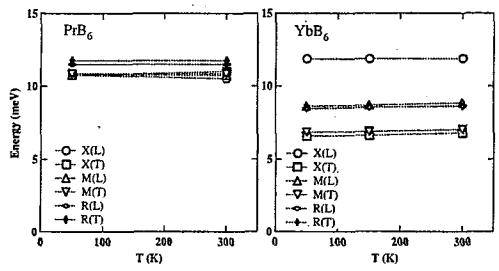

Fig. 1. Temperature dependencse of phonon energies of PrB_6 and YbB_6 at the zone boundaries.

"L" and "T" are used in Fig. 1 (and Fig. 2 below) to indicate the longitudinal and transverse modes, respectively. Note that the excitation energies of PrB_6 at the zone boundaries almost degenerate at the energies around 11 meV. This situation is quite similar to the case of LaB_6 and indicates the existence of non-interacting vibration of the

使用施設：JRR-3M, 装置： 4G (GPTAS), 分野： 101: Structures and Excitations

rare earth ions [3]. In contrast, the excitation energies of YbB_6 at the zone boundaries are distributed in rather wide energy range from about 6 to 12 meV, indicating an anisotropy of the interaction of Yb ions with the B cages.

Fig. 2 shows the relative temperature dependences of the integrated intensities of the phonon peaks of PrB_6 and YbB_6 which are normalized to those at 50 K and corrected for the temperature factor, $n(E) + 1$, where E is the phonon energy and $n(E)$ is the Bose-Einstein distribution function. The vertical

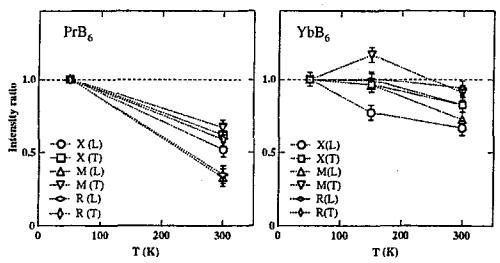

Fig. 2. Temperature dependencse of relative intensities of phonon excitations of PrB_6 and YbB_6 at the zone boundaries.

axis of Fig. 2 is thus proportional to the temperature dependence of the square of dynamical structure factor for each phonon scattering process. It is clearly seen that the temperature dependences of the intensities of PrB_6 is quite stronger than those of YbB_6. Since the temperature dependence of the phonon dynamical structure factor is primarily governed by the Debye-Waller factors of rare earth atoms in the present case, this fact demonstrate that the amplitudes of thermal vibration of Pr atoms in PrB_6 at high temperatures are quite large compare to those of Yb atoms in YbB_6.

The observation of almost degenerate phonon energies at the zone boundaries for PrB_6 indicates that the phonon density of state of this compound has a single strong peak at the energy around 11 meV. The flattened dispersion relations expected for this compound as observed for LaB_6 enhance this peak more. Therefore, this feature will give a prominent peak in the two-phonon Raman scattering process for PrB_6. Actually, the energy of the dominant anomalous peak of PrB_6 is just at twice the energy. In contrast, the phonon density of state of YbB_6 will show weaker peak structure because the phonon energies at the zone boundaries are distributed around at least three blocks in the energy range from about 6 to 12 meV, giving more moderate peaks in the two-phonon Raman scattering for YbB_6.

It is also pointed out that the strong temperature dependence of the Debye-Waller factor of Pr atoms in PrB_6 as shown in Fig. 2 will give rise to an additional enhancement of the two-phonon Raman scattering process at high temperatures compared to the rather normal case of YbB_6 because the intensity of Raman scattering is proportional to the square of the amplitude of thermal vibration of the atoms.

In summary, the present neutron scattering work gives strong support to the scenario of two-phonon scattering process as the origin of the anomalous Raman peak observed for trivalent rare earth hexaborides. The physical meaning of the result is that rare earth atoms in trivalent hexaborides are confined rather loosely in the cages of boron atoms and vibrate almost isotropically with a large amplitude. It is reasonable to ascribe this feature to the existence of conduction electrons because such feature is less prominent in the divalent rare earth hexaborides which are semiconductive [2]. Therefore, the effects of coupling of the motion of rare earth atoms, such as rattling, with conduction electrons as well as the lattice instability due to the existence of off-center potential minima for rare earth atom potition [1] cannot be ruled out to fully understand the variety of the physical properties of rare earth hexaborides.

References

[1] T. Kasuya: J. Phys. Soc. Jpn. **66** (1997) 2950.

[2] N. Ogita *et al.*: Phys. Rev. B **68** (2003) 224605.

[3] H. G. Smith *et al.*: Solid state Commun. **53** (1985) 15.

研究テーマ：アミド類からラクタム環の形成における水素移動反応の機構解明
表　題：単結晶中性子回折による4-シアノブチルコバロキシムの結晶相光異性化反応における重水素移動の直接観察

36) Direct Observation of Deuterium Transfer in Crystalline-State Photoisomerization of 4-Cyanobutyl Cobaloxime Complex by Neutron Diffraction Analysis

T. Hosoya, H. Uekusa, Y. Ohashi, T. Ohhara[1], R. Kuroki[1]

Department of Chemistry and Materials Science, Tokyo Institute of Technology, Meguro, Tokyo 158-8551
[1]Neutron Science Reserch Center, JAERI, Tokai, Ibaraki 319-1195

Cyanoalkyl cobaloxime complex,[1)] is known to be isomerized by photoirradiation with retention of the single crystal form. For example, 3-(2)-1 isomerization of 3-cyanopropyl group has been reported[2)], and the intermediate 2-cyanopropyl group has been indicated by direct observation of deuterium transfer from $-CH_2CH_2CD_2CN$ to $-C(CN)DC(H_{1/2}D_{1/2})_2CH_3$ using neutron diffraction analysis.[3)]

For 4-cyanobutyl cobaloxime, 4-3 isomerization has been recently observed in the crystalline state, and X-ray diffraction analysis after irradiation showed the initial 4- and 3-cyanobutyl group corresponding to the reactant and product, respectively.[4)] For further successive isomerization to 2- or 1-cyanobutyl group, two 4-cyanobutyl cobaloximes with a bulky diphenylboron group placed into the bis(diemthylglyoximato) ligand, **1a** and **1b**, have been prepared. Photoirradiation to the single crystals of **1a** and **1b** has resulted in different behaviors, the former has showed expected "alkyl slide" 4-3-1 isomerization and the latter 4-1 isomerization, in which 3- and 2-cyanobutyl groups were not observed by X-ray and IR. In order to elucidate the reaction process of **1b**, we tried to analyze hydrogen transfers during the reaction. Successive hydrogen transfers to the neighboring carbon atoms will be observed if the reaction proceeds via conventional "alkyl slide" 4-(3)-(2)-1 isomerization, while different hydrogen transfers will be expected in direct 4-1 isomerization. Two hydrogen atoms bonded to C^{α} atom of 4-cyanobutyl group were replaced with deuterium atoms, **1c**. This study was carried out to clarify the mechanism of the isomerization of **1c** by direct observation of deuterium transfer using neutron diffraction analysis.

(4-cyanobutyl-α,α-d_2)[3,4-lutidine](diphenylboron-dimethylglyoximato)(dimethylglyoximato)cobalt(III), **1c**, was synthesized from 5-iodovaleronitrile-*2,2*-d_2, dimethylglyoxime, diphenylboronic anhydride, 3,4-lutidine and cobalt(II) chloride hexahydrate, and recrystallized from methanol and acetonitrile. Then, UV/Vis reflectance spectrum of the crystals was recorded to optimize the irradiation condition. Three peaks around the wavelength of 400, 500 and 700 nm were observed and assigned to LMCT, singlet and triplet d-d transition of the cobalt atom, respectively. To keep the single-crystalline nature during the photoreaction, target band of the irradiation was focused on wavelengths that are weekly absorbed by the triplet excitation. Furthermore, alkyl radical produced by the triplet excitation has long lifetime and the reaction proceeds more efficiently. Then, the crystals were irradiated (680 nm~) by Xe lamp at 0 °C for 2 days and the photoreaction of KBr pellet of **1c** was monitored using FT-IR measurements. Only a band was located at 2244 cm^{-1} corresponding to the stretching vibrations of the C≡N bond in 4-cyanobutyl group before irradiation. Photolysis causes a decrease in the intensity of the band of 4-cyanobutyl group, while the band corresponding to 1-cyanobutyl group appeared at 2193 cm^{-1} and increased. Any other peak did not appear around the band. This result suggested that 4-cyanobutyl group of **1c** was isomerized by the direct path 4 to 1.

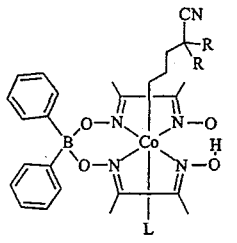

1

a. L = pyridine R = H
b. L = 3,4-lutidine R = H
c. L = 3,4-lutidine R = D

Neutron diffraction measurement of the photoirradiated crystal of **1c** (4.5×1.5×1.4 mm) was carried out with BIX-3. The neutron diffraction data were collected for 7 days at 293 K, and the data reduction was carried out with *Denzo & Scalepack*. The structure was refined with *SHELXL*-97 using the structure of non-hydrogen atoms determined by X-rays as a starting model. The experimental details are summarized in Table 1. Figure 1-(a) shows disordered structure of 4- and 1-cyanobutyl groups by X-rays. Only the cyano group moves during the isomerization. Figure 1-(b) shows the structure analyzed by neutron diffraction. One deuterium atom is located at methyne position (D/H ~100/0), another is located at the terminal methyl group, in which the two hydrogen atoms and one deuterium atom were disordered by rotation.

Figure 2 shows the three possible reaction paths adopted to **1c**, "alkyl slide", "cyano rearrangement" and "alkyl turn" isomerization.

(a) For "alkyl slide", which is a successive isomerization previously observed in isomerization of cyanoalkyl cobaloximes, *i.e.*, 4-3-2-1 isomerization for

原子炉：JRR-3　装置：BIX-3M(1GB)　分野：中性子散乱（構造）

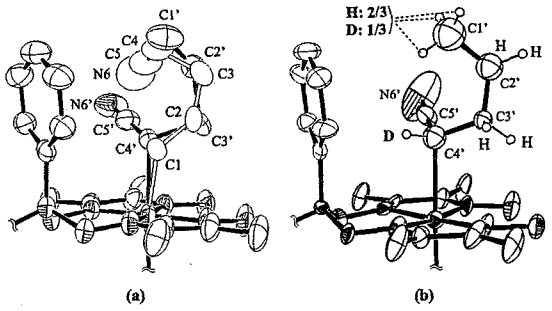

Figure 1: Molecular structures of the photoirradiated crystal of **1c** around the alkyl group. Thermal ellipsoids are drawn in 30% probability level. (a) X-rays: 4- and 1-cyanobutyl groups are disordered (white and black bond, respectively). (b) Neutron diffraction analysis: only 1-cyanobutyl group produced is shown for clarity.

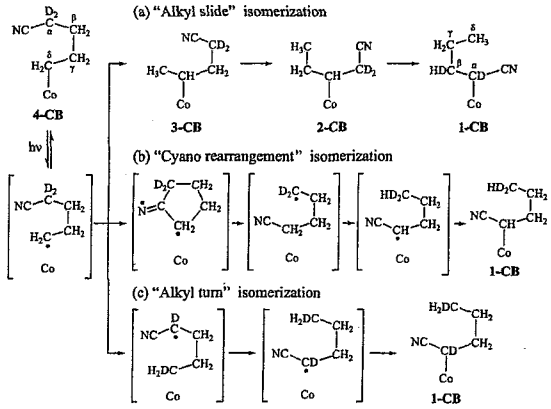

Figure 2: Three possible reaction mechanisms for the isomerization, where CB is cyanobutyl cobaloxime.

4-cyanobutyl cobaloxime. From the result of X-ray diffraction and IR analysis, 3- and 2-cyanobutyl cobaloximes were not observed, therefore, these cyanobutyl cobaloximes are assumed to be unstable intermediates. Each step of the isomerization involves hydrogen or deuterium transfer. Two deuterium atoms in the anticipated product will be located at the C^{α} and C^{β} atoms, which are different from that observed with the neutron diffraction study.

(b) For "cyano rearrangement", which is a direct rearrangement of a cyano group via 5-membered ring, which is occurred in organic reactions. This 4-1 isomerization involves no deuterium transfers and does not go through 3- and 2-cyanobutyl cobaloximes, which is agree with the analyses of X-ray diffraction and IR. The distance between C1 bound to the cobalt atom and the carbon atom of cyano group was 3.41 Å which is slight longer than the sum of van der Waals radii of carbon atoms. However, two deuterium atoms in the anticipated product will be located at the terminal methyl group, which is different from the result of neutron diffraction analysis.

(c) For "alkyl turn", this 4-1 isomerization includes a deuterium transfer from C^{α} to C^{δ}. This process does not go through 3- and 2-cyanobutyl cobaloximes, which is consistent with the result of X-ray diffraction and FT-IR that no 3- or 2-cyanobutyl cobaloximes were observed. To explain it in order, C^{α} atom of photoproduced 4-cyanobutyl radical abstracts a deuterium atom bonded to C^{δ}, and then the 4-cyanobutyl radical is turned upside down. Finally, a bond formation between the cobalt atom and C^{α} atom is followed. The distance between C^{α} atom and the deuterium atom abstracted, D4 (*see*, Fig. 1-(b)), was 2.84 Åwhich was shorter than the sum of van der Waals radii of a carbon and a deuterium atoms. Two deuterium atoms in the anticipated product will be located at the C^{α} and C^{δ} atoms, which is completely agree with that observed with neutron diffraction study. Since D4' atom bound to C4' atom occupied 100%, the stage of alkyl turn is assumed to be irreversible.

Table 1: Crystal data and experimental details

Empirical Formula	$C_{30}H_{34}BCoD_2N_6O_4$
Crystal system, space group	Monoclinic, $P2_1/c$
a /Å	11.4714(5)
b /Å	14.567(1)
c /Å	19.8202(9)
β /°	92.839(3)
V /Å^3	3308.1(3)
Z, D_x /Mg m^{-3}	4, 1.238
Radiation type, λ /Å	Thermal neutron, 1.51000
θ range /°	3.69-48.86
μ /mm^{-1}	0.47
Temperature /K	293(2)
Crystal size /mm	$2.0 \times 1.8 \times 0.8$
Diffractometer	BIX-III
Data collection method	ω scan
Absorption correction	Numerical (ABSG)
T_{max}, T_{min}	0.7052, 0.4537
No. of measured, unique, observed ($I > 2\sigma(I)$) refls.	5666, 2425, 2424
R_{int}	0.0503
Range of h, k, l	-11∼11, -14∼13, -19∼18
No. of parameters	500
$R_1(F^2 > 2\sigma(F^2))$, wR_2, S	0.1586, 0.3273, 1.241
$\Delta\rho_{max}$, $\Delta\rho_{min}$ /e Å^{-3}	0.13, -0.13

From the single crystal neutron diffraction analysis of the photoirradiated crystal of **1c**, the following mechanism has been established; (i) the photoisomerization of the 4-cyanobutyl group occurs by the cyanobutyl turn, *i.e.*, a novel direct 4-1 isomerization process, (ii) the stage of the cyanobutyl turn is irreversible.

References

1) Cobaloxime complex is abbrevited as R-Co^{III}(dmgH)$_2$-L, where R and L are axial alkyl and base ligand, respectively.
2) A. Sekine, M. Yoshiike, K. Ishida, Y. Arai and Y. Ohgo: Mol. Cryst. Liq. Cryst. **313** (1998) 321.
3) T. Ohhara, J. Harada, Y. Ohashi, I. Tanaka, S. Kumazawa and N. Niimura: Acta Crystallogr. **B56** (2000) 245.
4) C. Vithana, H. Uekusa and Y. Ohashi: Bull. Chem. Soc. Jpn. **74** (2001) 287.

研究テーマ：ヌクレオチド水和物結晶の低温における水素結合網の秩序化の解析
表題：中性子回折法によるイノシン 5′-リン酸二ナトリウム水和物の低温での水素結合網の秩序化の解析

37) Neutron Diffraction Analysis of Ordering of Hydrogen Bonding Networks of Disodium Inosine 5′-Monophosphate Hydrate at Low Temperature

S. Yamamura, T. Hiramatsu, Y. Sugawara, H. Kimura*, and Y. Noda*

*School of Science, Kitasato University, 1-15-1 Kitasato, Sagamihara, Kanagawa 228-8555, Japan; *Institute of Multidisciplinary Research for Advanced Materials, Tohoku University, 2-1-1 Katahira, Aoba-ku, Sendai 980-8577, Japan*

Disodium inosine 5′-monophosphate (Na_2IMP) crystallizes as octahydrate (wet form), and changes to heptahemihydrate (dry form) below 60% relative humidity. Neutron diffraction analysis of the wet form [1] and the dry form [2] revealed that part of crystal water molecules and sodium ions are in 'local' or 'long-ranged' disorder. Recently, we found that the wet form undergoes a phase transition around 200 K. To clarify a quench process of the disordered hydrogen-bonding networks, neutron diffraction analysis of the wet form was performed at 123K.

An as-grown crystal with approximate dimensions of $8 \times 5 \times 1.2$ mm^3 was sealed in a quartz capillary tube. Neutron diffraction experiment was carried out with the neutron wavelength of 1.24 Å by a four-circle diffractometer, FONDER installed at T2-2 port of JRR-3 in JAERI (Tokai). Neutron intensity data of 1401 fundamental reflections up to 1.2 Å and 477 super-lattice reflections up to 1.8 Å were collected at 123 K. Crystal data are shown in Table 1. Hydrogen positions were determined by iteration of difference Fourier syntheses starting from the coordinates of non-hydrogen atoms of the IMP molecules determined by X-ray analysis. At the present stage, R value is 0.13 for 1094 observed reflections ($|F_o| > 4\sigma(F_o)$).

Table 1: Crystal data

Chemical formula	$Na_2C_{10}H_{11}N_4O_8P.8H_2O$
Crystal system	monoclinic
Space group	$P2_1$
a/Å	8.727(7)
b/Å	22.296(17)
c/Å	23.088(18)
β/°	90.994(6)
Z	8

The crystal structure is shown in Fig. 1. An asymmetric unit of the low temperature phase (LTP) is two times that of the room temperature phase (HTP). Total 42 hydrogen positions of four symmetrically independent IMP molecules and 46 hydrogen sites of 33 crystal water molecules were determined. The disordered water sites and sodium ions in HTP are classified into two interaction schemes. The hydrogen positions in LTP are consistent with the interpretation that two overlapped networks in HTP separate into two regions in LTP.

References

[1] Yamamura et al., ISSP Activity Report on Neutron Scattering Research, **11** (2004) 65.
[2] Sugawara et al., ISSP Activity Report on Neutron Scattering Research, **10** (2003) 86-87.

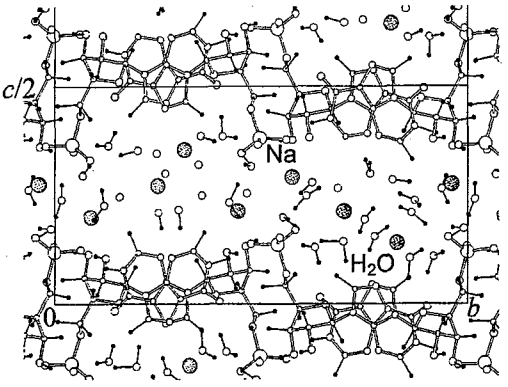

Figure 1: Crystal water region of the wet form of Na_2IMP at 123 K.

使用施設：JRR-3，装置：FONDER(T2-2)，分野：Structures & Excitations

研究テーマ：六方晶系M型フェライトの席占有率と磁気構造の研究
表　題：中性子粉末回折法による $BaTiCoFe_{10}O_{19}$ の磁気構造と席占有率に関する研究

38) Magnetic and Site Preference Study on $BaTiCoFe_{10}O_{19}$ by Neutron Powder Diffraction

T. Toyoda, T. Nakamichi, N. Igawa[1] and Y. Ishii[1]

Industrial Research Institute of Ishikawa, Kanazawa, Ishikawa, 920-8203
[1]Neutron Science Research Center, JAERI, Tokai, Ibaraki 319-1195

Hexagonal barium ferrites have been traditionally used as permanent magnets and microwave devices because of their high coercivity and large uniaxial anisotropy [1]. It is recognized that the magnetic anisotropy can be optimized by Fe^{3+} ion for several magnetic and non-magnetic ions, which makes M-type ferrites suitable for microwave absorber in 1 - 75 GHz range [2]. In this study to use high resolution neutron powder diffraction, site preference and magnetic structure of iron sites on $BaTiCoFe_{10}O_{19}$ are examined by crystal structure analysis.

Neutron diffraction experiments have been made at High Resolution Powder Diffractometer (HRPD) installed at JRR-3 research reactor in JAERI. Diffraction intensity measurement on synthetic Ba M-type ferrite were made at 8 K, 573 K and 723 K with a neutron incident wavelength $\lambda = 1.82301$ Å. Site preference and magnetic structure were refined by the Rietveld method using the RIETAN-2000 program [3].

Figure 1 shows the result of the Rietveld analysis at 8 K and 723 K, below and above T_c, respectively. Intensity profiles can be explained by the basis of space group $P6_3/mmc$. The difference of the magnetic scattering between 8 K and 723 K was Cleary observed, showing ferrimagnetic spin arrangement along with c-axis. Since the result of the magnetic structure analysis using diffraction profile with lower angle range at 8 K, the site preference model, which Ti and Co ions substitute for $2b$, $4f_2$, $12k$ and $4f_1$, $12k$, $2a$, respectively, gives a good agreement with experimental data. The crystal structure and magnetic structure are illustrated in Figure 2.

References

1) O. Kubo, T. Ido and H.Yokoyama: IEEE Trans. Magn. Mag. **18** (1982) 1200.
2) S. Sugimoto, K. Okayama, S. Kondo, H. Ota, M. Kimura, Y. Yoshida, H. Nakamura, D. Book, T. Kagotani and M. Honma: Mater. Trans. JIM **39** (1998) 1080.
3) F. Izumi and T. Ikeda: Mater. Sci. Forum **321** (2000) 198.

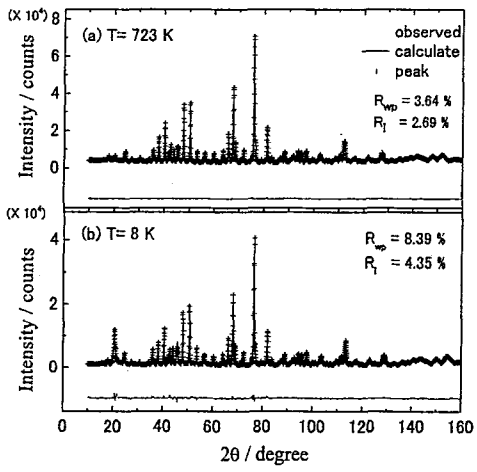

Figure 1: Diffraction patterns of for $BaTiCoFe_{10}O_{19}$ at 8 and 723 K. (a) T=723 K, (b) T= 8 K.

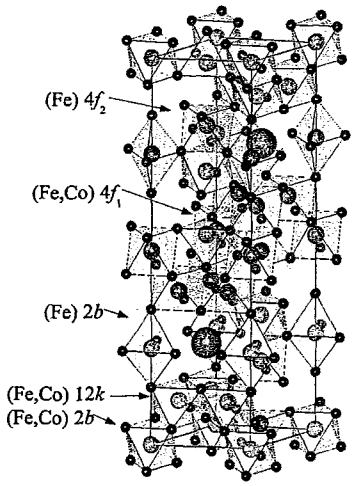

Figure 2: The magnetic structure of $BaTiCoFe_{10}O_{19}$.

原子炉：JRR-3　　装置：HRPD(1G)　　分野：中性子散乱（構造）

研究テーマ：準結晶フォノンダイナミクスの研究
表題：Zn-Mg-Sc 準結晶および Zn-Sc 近似結晶の格子振動

39) Phonon Dynamics in the $Zn_{80}Mg_5Sc_{15}$ Icosahedral Quasicrystalline phase and in the $Zn_{17}Sc_3$ 1/1 Cubic Approximant

S. Francoual*,**, M. de Boissieu**, K. Shibata*** and T. Sato****

*Institut Laue-Langevin (ILL), BP 156, F-38042 Grenoble Cedex 9, France
**LTPCM/ENSEEG, UMR CNRS 5614, INPG, BP 75, 38402 St Martin d'Hères Cedex, France
***Neutron Science Research Center, JAERI, Tokai, Ibaraki 319-1195
****Institute for Solid State Physics, The University of Tokyo, 106-1 Shirakata, Tokai 319-1106

Introduction : The phonon dynamics has been investigated in several icosahedral (i-) quasicrystalline (QC) phases as in i-AlPdMn [1,2], i-ZnMgY [3] using Inelastic Neutron Scattering (INS) and, more recently, in i-$Cd_{5.7}Yb$ using Inelastic X-ray Scattering (IXS) [4]. Those 3 phases are representative of the 3 different families in which i-QCs can be classified depending on their local atomic arrangements : Mackay-type, Bergman-type and new-type, respectively. In all phases, the overall dynamical response is found very similar. In the low-frequency region, there is a well-defined acoustic regime with resolution-limited acoustic excitations originating from strong Bragg peaks while for higher frequencies, the dynamical response is made of several broad (4 meV) dispersion-less optic bands. The crossover between both regimes is always accompanied by an abrupt broadening of the transverse acoustic TA mode. The dynamics in QCs remains however to be explained in terms of a microscopical model of atomic vibrations. In that sense, the recent discovery of the i-$Cd_{5.7}Yb$ and i-$Zn_{80}Mg_5Sc_{15}$ QC phases, for which a 1/1 real cubic approximant can be easily grown, is of main importance. Indeed, QCs and approximants can be described as a compact packing of the same icosahedral atomic clusters. While those units are arranged quasiperiodically in QCs, they are arranged periodically in approximant phases. Comparing the dynamics in both systems should thus allow to understand further how far the local structure influences the dynamical response compared to the longrange order. We have recently initiated such a comparative work using IXS in i-$Cd_{5.7}Yb$ and in its 1/1 Cd_6Yb approximant [5]. Using INS, in the present experiment, we investigate the dynamical response in the 1/1 cubic $Zn_{17}Sc_3$ approximant phase of the i-$Zn_{80}Mg_5Sc_{15}$-QC phase. $Zn_{17}Sc_3$ contains 160 [*] atoms in the unitcell. Its space group is Im3 with lattice parameter a=13.85 A. It can be described as a bcc packing of i-clusters of the same type as the ones found in the 1/1 approximant of the i-$Cd_{5.7}Yb$ QC. The 1st shell is adodecahedron of 20 Zn atoms, the 2nd shell a 12 Sc icosahedron and the 3rd shell a Zn icosidodecahedron.

Experimental details : We have investigated the dispersion of TA modes on the PONTA-5G three-axis spectrometer at JRR3M in JAERI(Tokai) on a 0.5 cm^3 Brigmann-grown single-grain sample. We worked in a constant-k_F mode with k_F=2.662 A^{-1}. The energy of incoming (outgoing) neutrons was selected using a PG002 monochromator (analyzer). We used a sapphire filter after the monochromator and a graphite filter after the sample in order to reduce fast neutron background and contamination by higher order harmonics, respectively. We used 60'x40'x40'x80' apertures for the collimations. With such a set-up, we could probe low energy acoustic excitations from 2 to 5 meV with a ΔE_{fwhm} = 0.93 meV energy resolution and a $\Delta Q/Q = 0.65\ 10^{-2}$ spatial accuracy. For higher energy transfers, counting rates increasing, we opened to 80'x80' the collimations before and after the sample so that we increase by 2.2 the intensity at the expense of less resolution :

使用施設：JRR-3M，装置：PONTA(5G)，分野：Structures and Excitations

ΔE_{fwhm} = 1.25 meV and $\Delta Q/Q = 1.3\ 10^{-2}$. The sample was placed in an Al-vacuum box and orientated so that the (1,0,0) and (0,1,0) reflections define the scattering plane. The sample quality was checked performing large elastic A3 scans in and outside the scattering plane. Within constant-k_F constant-Q E-scans, we measured TA modes originating from the (10,0,0) and (3,5,0) strong Bragg peaks, with a q wave vector lying along the (0,-1,0) and (1,-1,0) directions, dispersing up to 8 and 4 meV, respectively.

Experimental Results: The most important result is the measured anisotropy of the sound velocity with the direction of the q wavevector. The transverse sound velocity for modes propagating along (0,-1,0) is 2705 +/- 30 $m.s^{-1}$ along (0,-1,0) whereas it is 2870 +/- 50 $m.s^{-1}$ along (1,-1,0). We can estimate A, the anisotropy factor, from the relation $A = (v_{TA,110}/v_{TA,100})^2$. It gives A = 1.125 +/- 0.06. This value will have certainly to be revisited using most precise techniques [**]. If it can be confirmed, this anisotropy factor would be the strongest ever measured for a 1/1 cubic approximant of a QC phase [***]. It would mark, moreover, a new difference with the $Cd_{5.7}Yb$ approximant which one exhibits lowest TA sound velocities due to the larger atomic mass of Cd atoms and for which no elastic anisotropy could be measured [4]. Other noticeable results concern excitations propagating along (0,-1,0). As shown in Fig.1, the dispersion relation is almost linear up to the 1st Brillouin Zone (ZB). Almost no curvature is observed when approaching the BZ and no low-lying flat optic branch is observed up to 9 meV. Moreover, TA modes are found resolution limited up to q=0.3 A^{-1} as this is usually observed in QCs. For higher q values, a broadening seems to occur but the exact way it takes place must be estimated from a fitting procedure taking into account the convolution of the phonon response function with the 4D instrumental resolution. Such data treatment is underway.

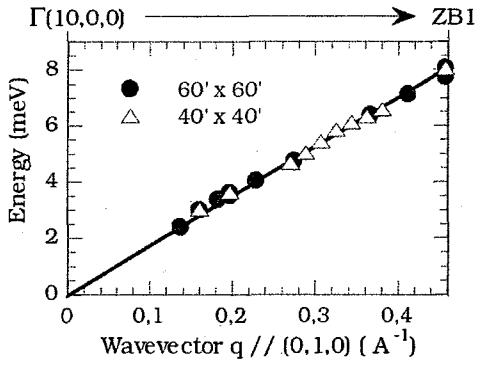

Figure 1: Dispersion curve for the Transverse Acoustic mode propagating along the (0,1,0) direction. Different symbols indicate measurements with different configurations of the collimations. Slope is found at 17.80 meV.A.

References

[1] M. de Boissieu *et al.*, J. Phys.: Condens. Matter 5 (1993)4945-4966

[2] M. Boudard *et al.*, J. Phys.: Condens. Matter 7 (1995)7299-7308

[3] K. Shibata *et al.*, J. Phys.: Condens. Matter 14 (2002)1847-1863

[4] M. de Boissieu *et al.*, J. of Non-Cryst. Solids 334-335(2004)303-307

[5] S. Francoual *et al.* (2004), *Proceedings of the Aperiodic 2003 conference*, Ferroelectrics 305, p. 235

[*] In the Cd_6Yb 1/1 approximant of the i-CdYb QC phase, the unit cell contains 168 atoms, the core of the icluster consisting of a disordered 4 Cd tetrahedron. Whether this position is occupied or empty in the $Zn_{17}Sc_3$ crystal is still matter of debate. Within recent X-ray structure refinements, Lin *et al.* ((2004), Inorg. Chem. 43, 1912-1919) have given the composition at Zn_6Sc as for Cd_6Yb while former admitted composition was found $Zn_{17}Sc_3$ by Andrusiak *et al.* ((1989), Sov. Phys. Crystallogr., 34, 600)

[**] No anisotropy could be evidenced from measurements performed on the same sample on the TAS-1 instrument. Since we work with 40'x40' collimations before and after the sample, modes can be probed with a better energy resolution and on top of all for lowest q values so that we can be confident in the estimation of that factor in the present experiment. On TAS-1, only 2 points are measured up to 0.3 A^{-1} along (1,1,0) !. In any case, we must be careful with the value of A estimated in the present experiment. This value should be measured again and 1.06 should be preferred to 1.12 !

[***] Because QCs and approximants have very similar local structure, a nearly isotropic elastic behavior is expected for cubic approximants as it is observed in isotropic QCs. Such structural argument was verified, for instance, in the R-phase of the AlCuLi QC where the A anisotropy factor is found equal to 0.9895 +/- 0.0014 by P.S. Spoor *et al.* ((1995), Phys. Rev. Lett. 75(19), p. 3462-3465).

研究テーマ：中性子小角散乱によるナノヘテロ構造を有する実用金属材料の微細構造の解明
表　題：中性子小角散乱による Al-Mg-Si 合金 の中断熱処理による微細組織変化

40) Effect of Interrupted Aging on Microstructures of Al-Mg-Si Alloys Studied by SANS

M. Ohnuma, J. Suzuki[1], and J. Buha[2]

National Institute for Materials Science, Tsukuba, Ibaraki 305-0047
[1] Advanced Science Research Center, JAERI, Tokai, Ibaraki 319-1195
[2] University of New South Wales, Sydney, NSW 2052, Australia

The aluminium alloys are one of the key materials for reduction of the energy consumption because of their high strength-weight ratio. The precipitation hardening is the major mechanism for the enhancement of strength by ageing in these alloys. In the case of Al-Mg-Si alloys, the following sequence of precipitates are widely accepted [1,2],
discrete clusters of Mg and Si → co-clusters containing Mg and Si → GP zones → β" → β' → β(Mg_2Si)
Because both zones and precipitates are intermediate phases of β(Mg_2Si), their crystalline structure and chemical composition are quite similar. Therefore, the major differences are shape and size and the mechanical properties are strongly depend on them. For optimizing the morphology and shape, the heat treatment condition has been extensively studied. Recently, new heat treatment which is called "interrupted ageing" has been proposed for getting higher strength and fracture toughness than those of the alloys aged continuously [3,4]. The refinement of microstructures of the alloys prepared by new heat treatment were reported by means of transmission electron microscopy. However, because of the low contrast between matrix and precipitates due to the similar crystalline structures and electron densities between Al, Mg and Si, qualitative analysis of average scale of the precipitates is very difficult. To understand the mechanism of the increment in both strength and fracture toughness, it is needed to evaluate average scale of the precipitates in different annealing condition in high accuracy. For this purpose, small-angle neutron scattering is the best tool which can distinguish Al, Mg and Si with detectable contrast. The comercial alloy AA6061 (Al-0.59wt%Si-0.99wt%Mg-0.25wt%Cu-0.16wt%Fe-0.112wt%Cr-0.002wt%Zn-0.13wt%Mn-0.012wt%Ti) was used for this study. The following heat treatments were applied to the samples;
as solution treated: 560°C for 2h→quenched in cold water→storage in LN_2
T6 heat treatment: 560°C for 2h→quenched in cold water→aged at 177°C for different times.
T6I6/177 heat treatment: 560°C for 2h→quenched in cold water→aged at 177°C for 20 min.→quenced into petroleum ether→aged at 65°C for 14 days→aged at 177°C for different times.
T6I6/150 heat treatment: 560°C for 2h→quenched in cold water→aged at 177°C for 20 min.→quenced into petroleum ether→aged at 65°C for 14 days→aged at 150°C for different times.
In every heat treatments, the Vickers hardness reaches maximum value for around 15h[4]. Further annnealing cause over ageing, i.e., degrading hardness due to coarsening of the precipitates. For understanding the effect of heat treatment, 15 and 160 hours were selected as the optimum and overaged conditions, respectively. Corresponding phase for peak aged condition is mainly β", while β' phase also forms in addition to β" for over aged conditionref-4. The mechanical properties of these samples are listed in Table 1. Dimension of the samples for SANS measurements are 1.5cm × 1.5cm × 0.8cm.

Figure 1 shows SANS profiles of T6I6/150°C and as-solution treated sample. All the profiles show the contribution from large particles which were formed during solidification. These large particles are thought to be unchanged by aging at 177 and 150°C. Therefore, the difference between profiles of as-solution treated and aged samples were used for further analysis of the size of the precipitates except T6I6/177 for 160h. Only in the profile of T6I6/177°C for 160h, the contribution from a large particles still

Table 1: Mechanical properties of alloy 6061 in the T6 and T6I6 heat treatments

		T6	T6I6/177°C	T6I6/150°C
Vikerse hardness	15h	135	145	144
	160h	123	110	130
0.2% Proof stress (MPa)	15h	311	335	302
Ultimated tensile strength (MPa)	15h	352	368	369
Elongation (%)	15h	8.2	7.3	11.6
Fracture toughness ($MPa\sqrt{m}$)	15h	30.5	37.0	41.6

原子炉：JRR-3　　装置：SANS-J(C3-2)　　分野：中性子散乱（構造）

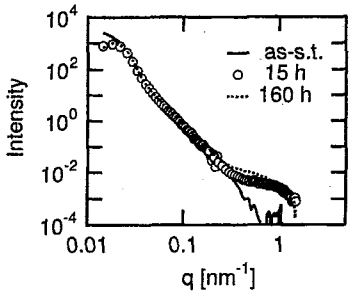

Figure 1: SANS profiles of T6I6/150°C and as-solution treated sample.

remains as the intensity proportional to q^{-4} in the region below $0.1nm^{-1}$ which is shown in Fig.2. In this case, q^{-4} contribution is subtracted again from the differential profile of T6I6/177°C-160h. Figure 3 shows differential SANS profiles of different aging conditions. All the profiles show extra scattering corresponding to the particle with nm scale compare to as-solution treated sample. Based on the TEM observations[4], profile fitting has been performed assuming randomly oriented cylindrical particles. Poly-disperse cross section radius with normal distribution (FWHM=0.15nm) was assumed mainly for suppressing oscillation effect in high-q region. The fitted curve are plotted together with obeserved profiles in Fig.3. Fitting results are summarized in Table 2. For 15 hours ageing, the smallest

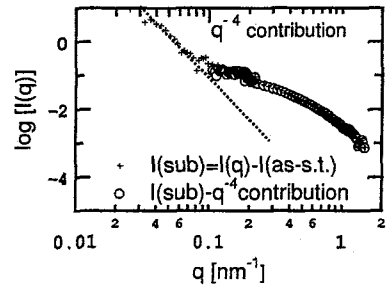

Figure 2: Differential SANS profiles for the alloy aged by T6I6/1770°C-160h. Circles are subtracted profiles by q^{-4} contribution from the differential profile.

characteristic lengths (cross-section radius in cylinder/radius in sphere) are more or less same in all the heat treatments. In contrast, the degree of anisotropy in shape depends on the process. The length of the cylinder is shorter in T6I6/177°C-15h than that

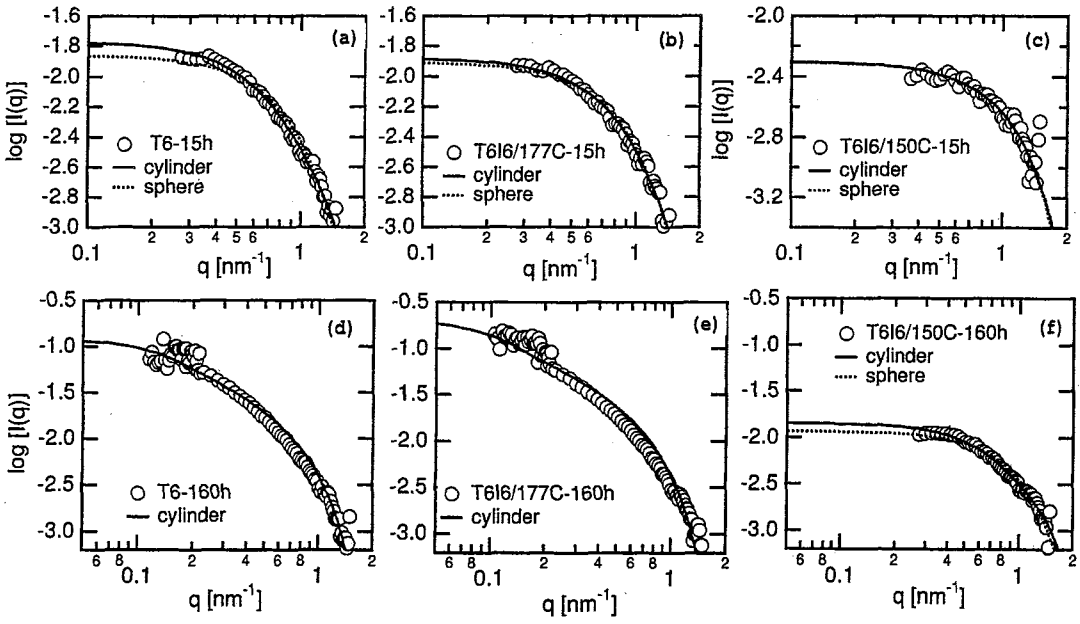

Figure 3: Differential SANS profiles of different aging conditions. (a) T6-15h, (b)T6I6/177°C-15h, (c)T6I6/150°C-15h, (d) T6-160h, (e)T6I6/177°C-160h, (f)T6I6/150°C-160h. Solid curves are fitted curve by randomly oriented poly-disperse cylindrical particles. For (a)-(c) and (d), the profiles are also fitted using poly-disperse spherical particle. FWHM for cross section of cylinder is fixed at 0.15nm, while that for radius of sphere is as a fitting parameter. Fitting results are listed in Table 2.

of T6-15h as shown in Table 2 and Fig.4(a). This tendency become more visible in T6I6/150°C-15h; L and 2R become too close to be separated by the fitting of the cylinder. In fact, the fitting using spherical shape gives better results. Over aging cause increment of the size in both L and R in T6 and T6I6/177°C. The level of the coarsening is higher in T6I6/177°C than that of T6. This results explain the reason why the hardness in T6I6/177°C-160h decrease steeper than that of T6-160h by over aging as shown in Fig.4(b). In the alloy aged by T6I6/150°C, the spherical shape for 15h becomes anisotropic by over ageing. However, the length of the cylinder in T6I6/150°C-160h is the same level of T6-15h, and hence, the hardness keeps the same level with that of T6-15h. All the results explains the relation between the size and the hardness well, which were observed by TEM. In addition, the quantitative analysis of average length of cylinder evaluated by SANS reveals another important fact about relation between the shape and mechanical properties, i.e. the reason of increment of a fracture toughness. The SANS results shows that interrupted ageing can suppress the anisotropy in shape. Although the fine particles give positive effect for increasing harness as the obstacles against dislocation motion, they can give a negative effect for fracture because of a stress concentration. The stress concentration is seems to be more prominent in the anisotropic particles. Therefore, the interrupted aging increase both the strngth (hardness) and fracture toughness which are normally in incompatible relationship, due to suppressing anisotropy in addition to refinement of the particles.

References

1) I. Dutta and S. M. Allen: J. Mater. Sci. Lett. **10** (1991) 323.
2) G. A. Edwards, K. Stiller, G. L. Dunlop and M. J. Couper: Acta Mater. **46** (1998) 3898.
3) R. N. Lumley, I. J. Polmear and A. J. Morton: International Patent Application PCT/AU00/01601 (2000).
4) J. Buha, R. N. Lumley, P. R. Munroe and A. G. Crosky: Proceedings of ICAAG (2004).

Table 2: Size of the precipitates for different annealing conditions. The bracket means that the fitting can be converged but chi-square gives worse value than the other

			T6	T6I6/177°C	T6I6/150°C
aged for 15h	cylinder	R [nm]	1.6±0.1	1.6±0.1	(1.5 fixed)
		L [nm]	7.5±0.6	6.0±0.3	(3.6±0.2)
aged for 15h	sphere	R [nm]	(1.7±0.4)	(1.7±0.3)	1.9±0.4
		FWHM [nm]	(0.6±0.2)	(0.6±0.2)	0.1±0.8
aged for 160h	cylinder	R [nm]	2.0±0.1	2.2±0.1	1.5±0.1
		L [nm]	≈30(29±7)	≥30(40±17)	7.5±0.4
aged for 160h	spherer	R	-	-	(1.6±0.4)
		FWHM	-	-	(0.6±0.2)

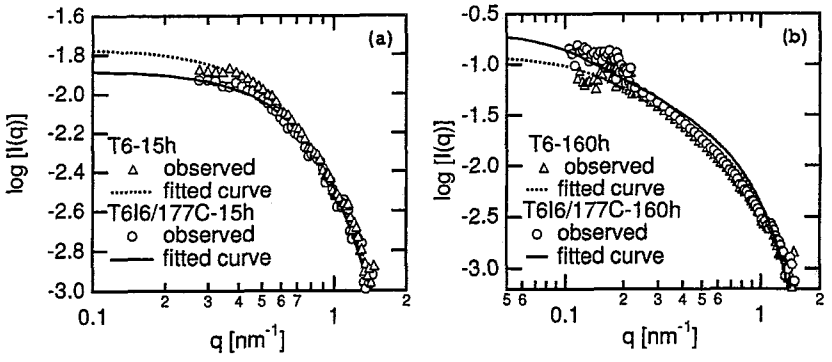

Figure 4: Differential SANS profiles of T6-15h and T6I6/177°C, (a) for 15h, (b) for 160h. Fitted curves are calculated by randomly oriented cylinder.

研究テーマ:還元六方晶チタン酸バリウムの高圧誘起絶縁体・金属転移
表題:六方晶チタン酸バリウムの分散関係

41) Phonon Dispersions in Hexagonal Barium Titanate

H. Shigematsu, and Y. Akishige

Department of Physics, Faculty of Education, Shimane University, Matsue 690-8504, Japan

Barium titanate has two structural polymorphic forms: one is the well known and extensively investigated ferroelectrics (cubic-$BaTiO_3$) and the other is the hexagonal modification (hexagonal -$BaTiO_3$). Hexagonal-$BaTiO_3$ undergoes a structural phase transition from the hexagonal phase (space group $P6_3/mmc$) to the orthorhombic phase ($C222_1$) at $T_0 = 222$ K [1]. This phase transition is believed to be caused by freezing of a soft E_{2u} silent mode at the zone center [2, 3]. Below T_0, the E_{2u} mode becomes two Raman-active soft optical mode, ω_1 and ω_2 [2]. With further decreasing temperature, it undergoes a ferroelectric phase transition related to a c_{66} soft acoustic mode at $T_C = 74$ K [4]. Recently, it has been revealed that both of the cubic and hexagonal $BaTiO_{3-\delta}$ exhibit metallic conduction down to 4.2 K by applying hydrostatic pressure [5].

We have started investigations on the phonon-dispersion curve in order to clarify mechanism of the metal-insulator transition and the influence of oxygen vacancy in hexagonal $BaTiO_{3-\delta}$. As the first step, we performed inelastic neutron scattering experiments on the hexagonal $BaTiO_3$ by using the triple-axis spectrometers (4G and T1-1) at JRR-3M in JAERI (Tokai). Single crystals were grown from the molten $BaTiO_3$. A crystal with the dimensions of 5 × 5 × 6 mm was used for the neutron experiment. The data collections were carried out in the (a^*, c^*) scattering plane at 250, 300 and 450 K. The measurements of phonon dispersion were performed along the lines 202 – 203, 006 – 106 and so on.

Figure 1 shows the phonon dispersion curves at 300 K in the major symmetry directions M-Γ-A. The phonon dispersion curves agree each other in the temperature range of 250-450 K. The presence of E_{2u} soft mode has not been clearly confirmed in phase I, because the mode becomes so broad and so week above room temperature.

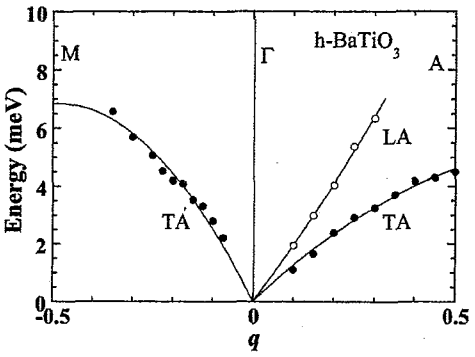

Figure 1: Phonon dispersion curves at 300 K in the major symmetry directions M-Γ-A. Peak positions of the clearly observed peaks are plotted.

In the present experiment, soft E_{2u} silent mode was not observed around the zone center. However, the phonon-dispersion curves of the E_{2u}, ω_1 and ω_2 modes will be observed by another experiment using plural samples together in near future.

References

[1] E. Sawaguchi *et al.*, J. Phys. Soc. Jpn. **54** (1985) 480.
[2] Y. Yamaguchi *et al.*, J. Phys. Soc. Jpn. **56** (1987) 589.
[3] K. Inoue *et al.*, Phys. Rev. B**38** (1988) 6352.
[4] Y. Yamaguchi *et al.*, Phys. Rev. Lett. **74** (1995) 2126.
[5] Y. Akishige *et al.*, J. Korean Phys. Soc. **32** (1998) S386.

使用施設:JRR-3M, 装置:GPTAS(4G) and HQR(T1-1), 分野 Structures and Excitations

This is a blank page.

1. 中性子散乱 2) 磁　性

1. Neutron Scattering　2) Magnetism

This is a blank page.

1) Magnetic structure of $YbMn_2Ge_2$ under high pressure

Tetsuya Fujiwara[1], Naofumi Aso[2], Masakazu Nishi[2], Yoshiya Uwatoko[1] and Kazuma Hirota[2]
[1] *Institute for Solid State Physics, The University of Tokyo, Kashiwa, Chiba, 277-8581*
[2] *Neutron Sci. Lab., ISSP, Univ. of Tokyo, Tokai, Ibaraki, 319-1106,*

In the last decade, the family of the intermetallic compounds RMn_2Ge_2 with $ThCr_2Si_2$ type body centered tetragonal structure have attracted a great deal of attention. Among them, mixed valence system $YbMn_2Ge_2$ shows a quite unique magnetism; there exists two kinds of antiferromagnetic states[1], AFM I at $T_{N1} \approx 405$ K and AFM II at $T \leq T_{N2} = 163$ K and the Néel temperatures, T_{N1} and T_{N2}, simultaneously exhibit a minimum and maximum at $\sim$ 1.25 GPa, respectively, as is shown in P - T phase diagram (Fig.1)[2]. This suggests that a magnetic phase transition accompanied with magnetic structural change occurs at $P_C \sim 1.25$ GPa and AFM I state competes with AFM II state. In addition, it was clarified from X-ray absorption measurements near the Yb L_{III} threshold under high pressures that this phase transition originates in a drastic change of Yb ionic valence near 1.25 GPa[3]. These reveal that the instability of Yb $4f$ electron states much affect on the Mn $3d$ - Mn $3d$ dominant magnetic interactions in RMn_2Ge_2 systems.

To elucidate that how the valence transition of Yb ion does correlate with the exchange interactions between Mn magnetic moments, neutron scattering experiments for single-crystal $YbMn_2Ge_2$ were performed under both ambient and high pressures using a triple-axis spectrometers (HQR and PONTA) at JRR-3M reactor of JAERI. Hydrostatic pressures were generated by a clamping-type high pressure cell, which can sustain up to $\sim$ 2 GPa. The pressure cell primarily made of hardened Cu-Be alloy[4].

Fig.2 shows integrated intensities of (002), (110) and (111) bragg peaks as a function of temperature in $YbMn_2Ge_2$. At $P \sim 1.7$ GPa, a magnetic superlattice reflection indexed as (111) on the basis of chemical unit cell appears. This indicates that a ferromagnetic

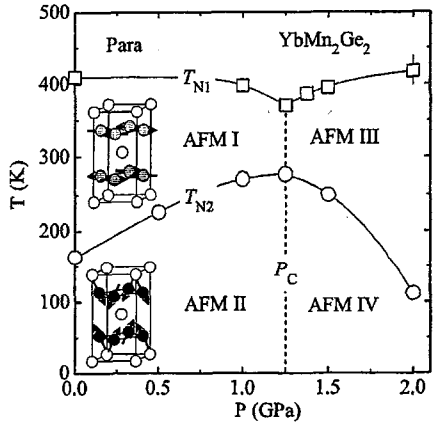

Fig. 1. P-T phase diagram of $YbMn_2Ge_2$. Magnetic structures at AFM I and II phases identified by Hofmann et al.[1] are also schematically drawn.

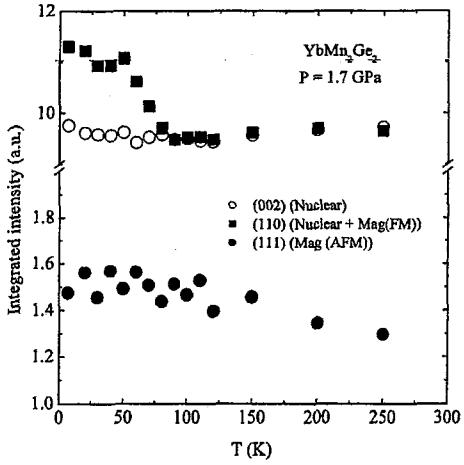

Fig. 2. Integrated intensities of (002), (110) and (111) reflections as a function of temperature in $YbMn_2Ge_2$.

(00l) Mn planes are coupled antiferromagnetically along the [001] direction, namely, Fig.3 (a) is expected to be stabilized at AFM III state. With decreasing temperature, thermal evolution of (110) is observed below $\sim$ 70 K,

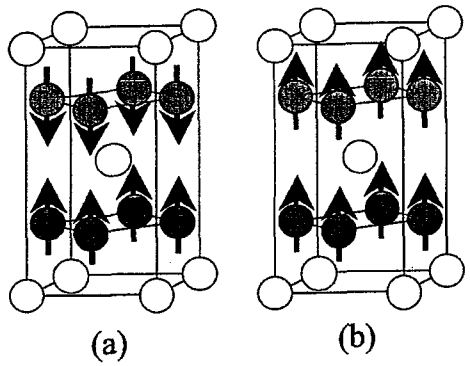

Fig. 3. Identified magnetic structures of $YbMn_2Ge_2$ under $P \sim 1.7$ GPa.

while an intensity of (002) is independent of temperature. Therefore, it may be said that the system ferromagnetically orders below $\sim$ 70 K and the ferromagnetic components are parallel to the [001] direction as shown in Fig.3(b). However, (111) reflection is simultaneously observed below $\sim$ 70 K. This simultaneous appearance of (111) and (110) magnetic reflections is puzzling. Because, this suggests that the antiferromagnetic ordering coexists with the ferromagnetic one at AFM IV state. Furthermore, strangely enough, the peak intensity of (111) is insensitive to temperature. That is to say, although partial Mn moments contribute to the antiferromagnetic ordering at T_{N1}, remaining ones does not order magnetically yet. And, beyond T_{N2} by cooling, those orders ferromagnetically without breaking existing antiferromagnetic coupling. At present, we are not sure that why this system does show such an unconventional magnetic ordering accompanied with strong frustration.

References

[1] M.Hofmann *et al.*: J. Alloys Comp, **311** (2000)137.

[2] T. Fujiwara *et al.*: Acta Physica Pol. B, **34** (2003)1541.

[3] T. Fujiwara *et al.*: J. Magn. Magn. Mat., **272-276** (2004)599.

[4] N. Aso *et al.* : in this activity report

研究テーマ：$ZnCr_2O_4$の中性子散乱
表題：$ZnCr_2O_4$単結晶の磁気中性子散乱における電場磁場冷却効果 V

2) Field Cooling Effect on Magnetic Neutron Scattering of $ZnCr_2O_4$ Crystal V

I. Kagomiya, A. Hatanaka[A], H. Yanagihara[A], K. Kohn, K. Nakajima[B], E. Kita[A], K. Nishi[C], K.Kakurai[B] and K. Siratori

Adv. Res. Inst. for Sci. and Eng., Waseda University, 3 Shinjyuku-ku, Tokyo 169-8555, Japan;
[A]Institute of Applied Physics, Tsukuba University, Tsukuba, Ibaraki 305-8573, Japan;
[B]Advanced Science Research Center, JAERI, Tokai, Ibaraki 319-1195, Japan
[C]Institute for Solid State Physics, University of Tokyo, Kashiwa, Chiba 277-8581, Japan

A normal spinel $ZnCr_2O_4$ is considered as a typical example of a geometrically frustrated system. In fact, however, this crystal undergoes antiferromagnetic transition at T_N =12(±1) K.

The goal of this study is to determine the magnetic structure of the antiferromagnetic phase. Our previous studies have revealed the following results; (1) the magnetic unit cell is composed of four chemical cells (2 × 2 × 2). (2) The antiferromagnetic transition accompanies a lattice deformation of tetragonal or orthorhombic. (3) The intensities of the magnetic reflections depend on uniaxial pressure along the *c* axis. (4) Magnetic cooling effect along the <111> axes is remarkable for the intensity of magnetic reflections. These facts indicate that the magnetic symmetry on the ordered phase is in a monoclinic or lower symmetry state. Therefore, the symmetry possesses 12 kinds of magnetic domains at least.

In the present study, we tried to make the crystal in a single-domain state in the ordered phase and then investigated the magnetic neutron reflections. The sample applied uniaxial pressure along the [001] was set in a rotating sample folder. The rotating axis was parallel to the [110] direction. (Fig. 1) A vertical magnetic field of 5 T was applied along the [1 $\bar{1}$ 1] axis during the cooling through T_N=12 K. Diffraction data was collected at 2.5 K using the PONTA diffractometer installed at JRR-3M in JAERI with the incident wave length λ=1.637 Å. Totally 82 reflections were collected within the (001), (1-10), (1-11), and (1-1-1).

Figure 2 shows one of magnetic reflections cooled with the pressure and the magnetic field (FC). It is compared with that of no applied cooling (NFC). The differences between the two intensities were obviously observed. For the future work, it is necessary to collect more reflections to determine the magnetic structure.

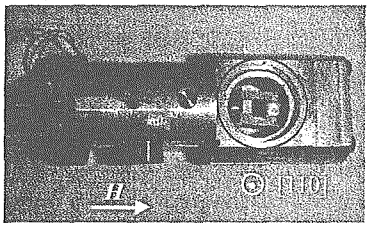

Fig.1. Rotating sample folder

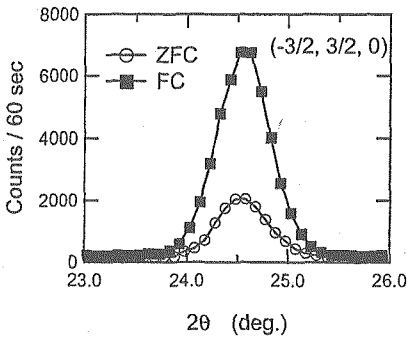

Fig.2. Examples of the observed magnetic reflections with the FC and the NFC

References

[1] I. Kagomiya *et al.*, this report **11** (2004) 80.

使用施設：JRR-3M，装置：PONTA(5G)，分野 Magnetism

Bi_2Te_3系熱電材料のフォノンの中性子散乱による研究

Bi_2Te_3の格子振動

3) Lattice vibrations in Bi_2Te_3

S. Tomiyoshi[1], T. Ochi[1], K. Satou[1], O. Yamashita[1] and M. Nishi[2]

[1] *Faculty Engineering, Ehime University, Matsuyama 790-8577, Japan*

[2] *Institute for Solid State Physics, The University of Tokyo, Tokai 319-1106, Japan*

Bismuth telluride (Bi_2Te_3) is one of the best material for thermoelectric refrigeration at ordinary temperature. In order to improve the thermoelectric property it is necessary to reduce the heat conductivity which is the sum of phonon and electron parts, and in the case of Bi_2Te_3 the former contribution is larger, so the control of the phonon conduction is most important, for that we need detailed information about the anisotropy of lattice vibrations.

In the present work we studied phonon dispersion relation of Bi_2Te_3 by neutron inelastic scattering. The crystal structure of Bi_2Te_3 has rhombohedral symmetry of space group $R\bar{3}m$ (D^5_{3d}) with atoms arranged in planes perpendicular to the trigonal axis forming layers of five planes in the sequence Te_1-Bi-Te_2-Bi-Te_1, where the binding between Te_1-Te_1 is believed to be weak due to Van der Waals character in contrast to the largely covalent Bi-Te bonds. This structure can be taken as a hexagonal cell with lattice constants a=4.369Å and c=30.422Å. In the present measurements a single crystal sample grown by Bridgeman method was used, which includes several grains with different c-plane orientations deviating in few degrees. Phonon dispersion relations were measured at room temperature in the a-c plane of the hexagonal lattice using 4G 'triple axis neutron spectrometer with a neutron beam of k_F=2.66Å^{-1} with collimations of 40'-40'-80'-80'. Figure 1 shows the branches of the normal mode of Bi_2Te_3, propagating along the a-axis for a transversal polarization. A low frequency branch rises quickly in low q and becomes almost flat at frequency of 1THz, which is considered to be an acoustic branch with a slope comparable to the sound velocity and at 3THz an optical branch was observed. At higher frequencies more optical branches are expected, but because of the incident neutron energy the observed ones are limited. Data analysis to derive force constants and density of states is now in progress.

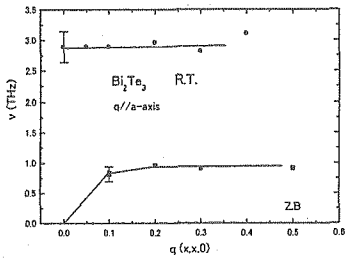

Fig.1 Transversal acoustic and optical phonon modes along the a-axis in Bi_2Te_3.

使用施設：JRR-3M、装置 GPTAS、分野 1.

研究テーマ：YbB_6の結晶・磁気構造解析
表題：CrB_2の磁気構造解析

4) Magnetic Structure in CrB_2

Y. Kousaka[1], H. Ichikawa[1], H. Kimura[2], Y. Noda[2] and J. Akimitsu[1]

[1]*Department of Physics and Mathematics, Aoyama-Gakuin Univ., 5-10-1 Fuchinobe, Sagamihara 229-8558;* [2]*IMRAM, Tohoku Univ., 2-1-1 Katahira, Aoba-ku, Sendai 980-8577*

CrB_2, which shows an itinerant antiferromagnetism below 88 K, has a hexagonal AlB_2-type structure with a space group of $P6/mmm$. We have two important unsolved problems in this material. The first one is whether magnetic behavior of CrB_2 can be described by the itinerant picture or localized one. The second one is that the magnetic structure has not yet been determined. Funahashi *et al.* performed neutron diffraction experiment using single crystal without enriching ^{11}B [1]. They concluded the helical spin structure in the $[110]^*$-c^* plane with the propagation vector $\tau = 0.285\tau_{110}$. However, we don't think that the magnetic structure has been conclusively determined, because the observed intensities are not so accurate due to the large absorption of ^{10}B and collected magnetic reflection data is not enough to conclude the magnetic structure uniquely.

We performed neutron diffraction experiment at T1-1 (HQR), T1-2 (KSD) and 6G (TOPAN), JRR-3M reactor in JAERI (Tokai), using powder and single crystal with enriching ^{11}B. Powder neutron diffraction experiment showed temperature-independent reflection, being equivalent to [0 0 1/6], which indicates that our crystal structure may be different from that of AlB_2-type structure. Therefore, we reexamined not only magnetic structure, but also crystal structure at the 4-circle diffractometer T2-2 (FONDER), JRR-3M reactor in JAERI (Tokai).

The data were taken at room temperature and 10 K. First, we searched the reflection equivalent to [0 0 1/6], however no significant scattering intensity was observed. Second, we observed nuclear scattering and magnetic scattering at 10 K in order to determine the magnetic structure. The propagation vector is confirmed to be $0.283\tau_{110}$. The nuclear scattering intensities were severely affected by a extinction effect. However this effect was negligible for the magnetic scattering because the magnetic scattering intensities were too weak to be affected by the extinction effect.

We compared our magnetic structure factor with Funahashi model. [Fig.1] It is plotted as a function of κ_{110}^2 which is the direction cosine of the scattering vector with respect to the reciprocal $[110]^*$ direction. The solid line in Fig.1 represents calculated structure factor of the helical structure in the $[110]^*$-c^* plane. The observed structure factor is significantly different from the calculated one. Therefore, the magnetic structure is different from that of Funahashi model.

In order to determine the magnetic structure in detail, we are now analyzing the experimental results.

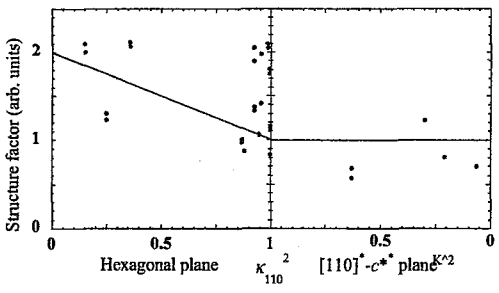

Fig.1 The observed magnetic structure factor. The open circles denote our result. The solid line denote Funahashi model which is the helical structure in the $[110]^*$-c^* plane

References

[1] Funahashi et al.: Solid State Comm. **23** (1977) 859.

使用施設：JRR-3M，装置：FONDER(T2-2)，分野 Magnetism

研究テーマ：$Lu_2Cr_2O_7$の軌道秩序の観測
表題：CeB_6の磁気形状因子の観測

5) Magnetic Form Factor in CeB_6

Y. Kousaka[1], H. Ichikawa[1], K. Hirota[2], M. Nishi[2], K. Kakurai[3], Y. Noda[4] and J. Akimitsu[1]

[1]Department of Physics and Mathematics, Aoyama-Gakuin Univ., 5-10-1 Fuchinobe, Sagamihara 229-8558; [2]Institute for Solid State Physics, The Univ. of Tokyo, 106-1 Shirakata, Tokai 319-1106; [3]Japan Atomic Energy Research Institute (JAERI), 2-4 Shirakata, Tokai 319-1195; [4]IMRAM, Tohoku Univ., 2-1-1 Katahira, Aoba-ku, Sendai 980-8577

A typical dense Kondo compound CeB_6 has a cubic CsCl-type structure with a space group of $Pm\bar{3}m$. It shows mysterious magnetic phase transitions at low temperature: paramagnetic state, antiferro-quadrupolar ordering and antiferro-magnetic ordering, which are denoted as phase I, II and III, respectively.

In 2002, we have reported the spin density distribution in CeB_6 using polarized neutron diffraction technique, and analyzed by maximum entropy method (MEM). We concluded that the magnetic moment exists not only on the Ce site, but also in-between the B sites [1]. On the other hand, Givord *et al.* pointed out that our result was distorted by an extinction effect, and the magnetic moment was localized only on the Ce site after correcting the extinction effect [2]. However, they ignored the (114), (441) and (116) reflections in the MEM analysis because these nuclear scattering intensities are very weak and are easily distorted by multiple scattering. We reexamined the multiple scattering for the weak nuclear reflections and also corrected the extinction effect for the strong nuclear reflections.

The single crystal was grown by the floating zone method using enriched ^{11}B to avoid the large neutron absorption due to ^{10}B. The polarized neutron diffraction experiment was performed at PONTA (5G), JRR-3M reactor in JAERI (Tokai). The experimental condition was 1.6 K under an applied magnetic field of 5.9 T parallel to the <110>-axis (phase II). Only (116) was heavily distorted by multiple scattering. Therefore, we did not employ the (116) reflection to magnetic form factor analysis, but did the (114) and (441) reflections.

In order to estimate how the extinction effect affects the observed intensities, we measured nuclear scattering intensities at 10K (phase I), and determined an extinction parameter g by solving Zachariasen's differential equations [3].

After correcting the extinction effect by using the extinction parameter, we obtained the extinction free magnetic form factor. Assuming the extinction parameter to be 1900 (120), the magnetic form factor quantitatively reproduces the dipole approximation, being consistent with magnetization data. [Fig.1]

In order to reexamine the spin density distribution in CeB_6, MEM analysis is now in progress.

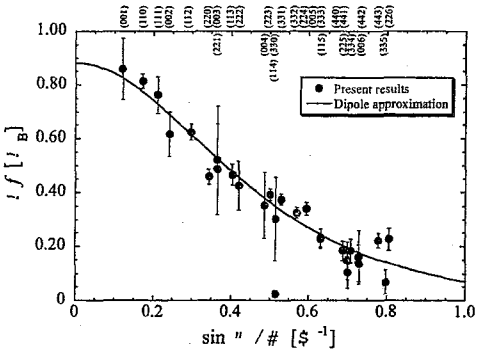

Fig.1 The observed magnetic form factor.

References

[1] M. Saitoh et al.: J. Phys. Soc. Jpn. **71** (2002) 2369.

[2] F. Givord et al.: J. Phys.: Condens. Matter **15** (2003) 3095.

[3] P. J. Becker and P. Coppense: Acta. Cryst. **A30** (1979) 129.

使用施設：JRR-3M，装置：PONTA(5G)，分野 Magnetism

研究テーマ：高分解能中性子散乱装置（HQR）
表題：二次元スピン系化合物 Nd_2BaZnO_5 の磁気構造

6) Magnetic Structure of the 2D Spin System Nd_2BaZnO_5

M. Nishi[1], K. Taniyama[1], H. Kageyama[2] and Y. Ueda[1]

[1] *ISSP, University of Tokyo, Kashiwa 277-8581, Japan*
[2] *Dept. Chemistry, Kyoto University, Kyoto 606-8502, Japan*

Two-dimensional quantum spin system with orthogonal dimer $SrCu_2(BO_3)_2$ has been studied with many experimental and theoretical efforts because the spin network of $SrCu_2(BO_3)_2$ is topologically equivalent to the Shastry-Sutherland model. The crystal structure of Nd_2BaZnO_5 is also orthogonal dimer system with Nd spin J=9/2 in the space group *I*4/mcm. Neutron diffraction of Nd_2BaZnO_5 powder sample was performed using ISSP-HQR spectrometer installed at the T1 guide of JRR-3M reactor at JAERI in Tokai using the fixed incident energy E_i = 13.54 meV. In the results of the experiments the Neel temperature is obtained as 1.7K and the magnetic Bragg peak intensities were obtained by subtracting from the data of 1.4K to that of 3.0K. All magnetic Miller indices are represented by (h+1/2, k+1/2, l). Antiferromagnetic (AF) structure supposed by the Shastry-Sutherland model is that with AF nearest neighbor interaction of simple square lattice, and then the magnetic structure should be same as nuclear unit cell included four Nd atoms in *ab* plane. 8 Nd spins in *ab* plane and two planes in magnetic unit cell are considered in analyzing the neutron diffraction data as another AF structure. As the model satisfied extinction rule the magnetic moments must be noncollinear. In the result of final analysis intra-dimer interaction is ferromagnetic and spin direction of neighbor dimer is orthogonal. As shown in Fig.1 spin direction between two dimers inter plane is also orthogonal. This complicated magnetic structure is caused by the geometrical arrangement of orthogonal dimer system. This result shows also the evidence of the frustration effect at higher spin (J=9/2) system

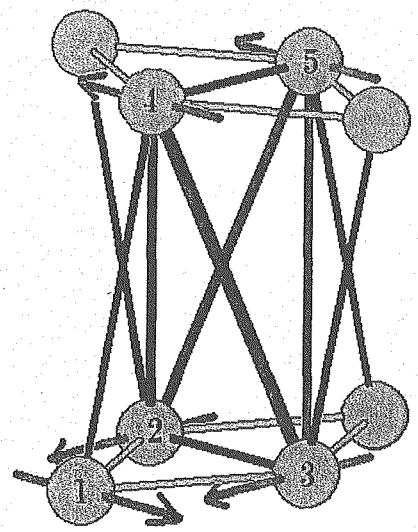

Fig.1. Arrows show the spin direction of Nd atoms. Intra-dimer spins (2 & 3) are parallel and neighbor dimer spin (1 & 3) is orthogonal. The dimer spin direction inter plane (3 & 4) is also orthogonal.

使用施設：JRR-3M，装置：HQR(T1-1)，分野 Magnetism

研究テーマ：二次元パーコレーション反強磁性体における磁気フラクトンの観測
表題：二次元ハイゼンベルグ型パーコレーション反強磁性体の磁気フラクトンの分散関係

7) Dispersion Relation of Magnetic Fractons in Percolating Two-Dimensional Heisenberg Antiferromagnet, $Rb_2Mn_{0.598}Mg_{0.402}F_4$

S. Itoh, R. Kajimoto[1], N. Aso[2] and H. Yoshizawa[2]

High Energy Accelerator Research Organization, Tsukuba 305-0801; [1]Japan Atomic Energy Research Institute, Tokai 319-1195; [2]The University of Tokyo, Tokai 319-1106

Magnetic fractons in $Rb_2Mn_{0.598}Mg_{0.402}F_4$, the near-perolating two-dimensional (2D) Heisenberg antiferromagnet, were studied by means of inelastic neutron scattering experiments on triple-axis spectrometers, HER (C1-1) and GPTAS (4G) at JRR3M in JAERI (Tokai), in the energy range up to 20 meV. The magnetic concentration of this system is very close to the percolation concentration for a square lattice (c_p = 0.598). The experiments were performed with G-open-Be(PG)-S-80'-A-80' and k_f = 1.56 Å^{-1} on HER, and with 40'-40'-S-PG-40'-40' and k_f = 2.67 Å^{-1} on GPTAS. The Néel temperature of this system was determined to be T_N = 4 K by measuring the temperature dependence of the intensity of the magnetic (100) reflection. The inelastic spectra were measured with the fixed k_f and at T = 1.5 K below T_N.

The observed inelastic spectra in the magnetic zone consisted of some non-dispersive peaks and a dispersive peak. Since these signals disappeared in the nuclear zone, these are of magnetic origin. The nondispersive peaks were able to be assigned as spin cluster excitations such as dimmers as well as Ising cluster excitations. The peak positions of the dispersive peaks are plotted as a function of the wavenumber (q) from the (100) magnetic zone center in Fig. 1. In theory of magnetic fractons, the dispersion relation of the magnetic fractons is described as $E(q) \sim q^z$ with $z = D_f$, where D_f is the fractal dimension of the system [1]. The solid line in Fig. 1 is q^z with z = 1.896, where the value of this exponent, z, is the fractal dimension of a 2D system. The observed dispersion relation was well described by the theory.

It was previously reported the exponent in the dispersion relation smaller than D_f, where the excitations were measured at the energy transfers up to 8 meV with conventional resolutions on GPTAS and PRISMA (the crystal analyzer spectrometer at ISIS) at T = 4 K just at T_N [2]. At present, we newly found magnetic excitations in higher energies, and observed magnetic spectra in a wide dynamic energy range in combination with GPTAS and HER. Since magnetic fractons exist only at low temperatures [2], the present experiments at T = 1.5 K give us clearer spectra of magnetic fractons. As the result, we demonstrated that $E(q) \sim q^z$ with $z = D_f$ in the 2D system at the first time.

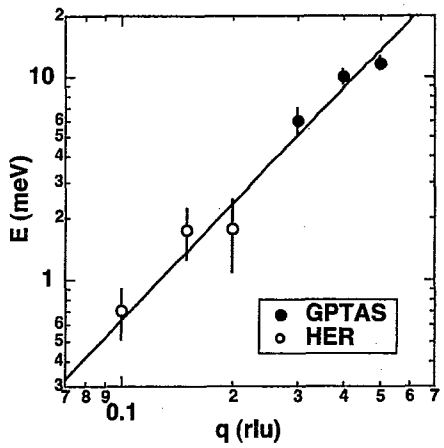

Figure 1: Dispersion relation of magnetic fractons in the 2D percolating Heisenberg antiferromagnet, $Rb_2Mn_{0.598}Mg_{0.402}F_4$.

References

[1] K. Yakubo et al., J. Phys. Soc. Jpn. **62** (93) 2196.
[2] S. Itoh et al., J. Phys. Soc. Jpn. **67** (98) 3610.

使用施設：JRR-3M，装置：GPTAS(4G)、HER(C1-1)，分野 102:Magnetism

研究テーマ：Na_2RuO_4の磁性と結晶構造
表題：Na-Ru-O 系化合物の磁気構造の解明

8) Magnetic and Structural Properties of Na_2RuO_4

M. Shikano, H. Kobayashi, and M. Tabuchi

Research Institute for Ubiquitous Energy Devices, National Institute of Advanced Industrial Science and Technology (AIST), 1-8-31 Midorigaoka, Ikeda, 563-8577 Osaka, Japan

In ternary Na-Ru-O system, as shown in Fig. 1, many phases exist because of various oxidation state of ruthenium [1-7]. Here, chemical formulae with double quotation marks such as "Ru_2O_3" and "Ru_2O_5" mean virtual substances. Recently, a novel sodium ruthenate Na_2RuO_4 was discovered [1]. Oxidation state of the ruthenium for Na_2RuO_4 only exceeds +5 in ternary Na-Ru-O system.

The crystal structure of Na_2RuO_4 is determined by x-ray diffraction using single crystals at the room temperature [1]. Figure 2 shows a schematic representation of the arrangement of Ru and oxide ions. The crystal structure of Na_2RuO_4 is built up of trans corners sharing [RuO_5] trigonal bipyramids along the $c_{hex.}$ axis. There are

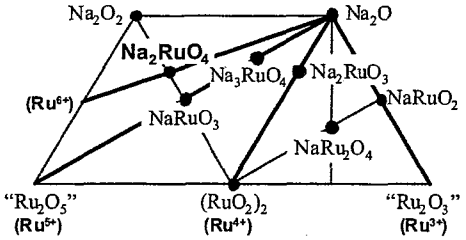

Figure 1: Phase diagram of ternary Na-Ru-O.

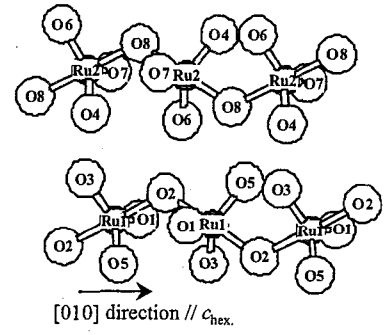

Figure 2: Tilting of the corner sharing RuO_5 bipyramids [1].

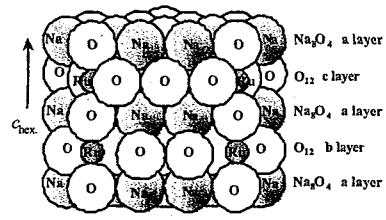

Figure 3: Ideal stacking of the Na_8O_4 (**a**) and O_{12} (**b** and **c**) layers corresponding to the structure of Na_2RuO_4. [1].

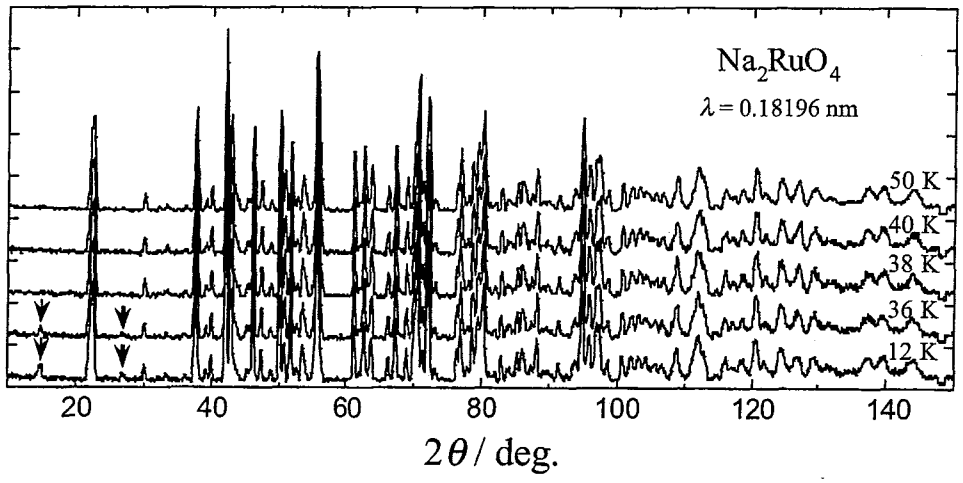

Figure 4: Powder neutron diffraction profiles of Na_2RuO_4 at T = 12, 36, 38, 40 and 50 K. Below 36 K, ordered peaks are observed around 14.8° and 26.9°.

使用施設：JRR-3M，装置：HERMES(T1-3)，分野 Magnetism

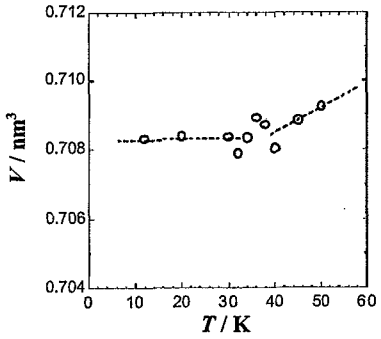

Figure 5: Temperature dependence of cell volume for Na_2RuO_4.

two independent chains (Ru1 and Ru2) in the unit cell, which are geometrically very similar. As shown in Fig. 3, one can conclude that the structure of Na_2RuO_4 can simply be described by a closed stacking of two types of closed packed layers of composition Na_8O_4 and O_{12} respectively.

The temperature T dependence of the molar magnetic susceptibility χ_M for Na_2RuO_4 shows three-dimensional feature below 37 K as well as one-dimensional feature above 37 K [1]. Around 37 K, an anomaly of the curve is observed, which has been confirmed by heat capacity measurement to be due to long range anti-ferromagnetic ordering [1]. Then, the magnetic structure of Na_2RuO_4 below 37 K is very attractive.

The powder neutron diffraction measurements were carried out between 12 and 50 K with a wavelength of 0.18196 nm. Measurements were performed on the Kinken powder diffractometer for high efficiency and high resolution measurements (HERMES) at the Institute for Materials Research (IMR), Tohoku University, installed at the JRR-3M in JAERI (Tokai). Lattice parameters are determined by Le Bail method using Jana2000 system [8].

Figure 4 shows powder neutron diffraction profiles of Na_2RuO_4. Above 38 K, all diffraction peaks are indexed as a space group $P2_1/n$ [1]. On the other hand, below 36 K, two extra peaks are observed around 14.8° and 26.9° originated from the magnetic reflections. These peaks are indexed as 010 and 012 of the monoclinic cell for Na_2RuO_4, respectively. The magnetic propagation vector $\boldsymbol{k}$ = [010] is parallel to $c_{hex.}$ axis (Fig. 2), showing that an antiferromagnetic Ru sublattice is present below 36 K. Figure 5 shows the thermal variation of cell volumes V for Na_2RuO_4. Around 36 K, an anomaly in V-T curve was observed, that may be concerned with the magnetic transition. The interaction between -Ru-O-Ru- chains should be considered carefully because crystallographically different Ru sites (Ru1 and Ru2) exist. To understand the detail of the magnetic structure, the Rietveld refinement is needed.

References

[1] M. Shikano et al., Inorg. Chem. **43** (2004), 5.
[2] M. Shikano et al., Inorg. Chem. **43** (2004) 1214.
[3] J. Darriet and A. Vidal, Comptes Rendus de l' Academie des Sciences Serie IIc: Chemie **277** (1973) 1235.
[4] J. Darriet and J. Galy, Bull. Soc. Franç. Minér. Crist. **97** (1974) 3.
[5] J. Darriet, Acta Crystallogr. B **30** (1974) 1459.
[6] J. Darriet and A. Vidal, Bull. Soc. Franç. Minér. Crist. **98** (1975) 374.
[7] K. M. Mogare et al., Z. anorg. allg. Chem. **630** (2004) 547.
[8] V. Petricek et al., *Jana2000. The crystallographic computing system.* Institute of Physics, Praha, Czech Republic (2000).

研究テーマ：斜方晶 $CeCu_2$ 及びε-TiNiSi 型 YbPdGe 化合物の磁気構造
表題：YbPdGe 化合物の中性子回折

9) Neutron Diffraction Study on YbPdGe Compound

G. Nakamoto, D.T.K. Anh, M. Kurisu, Y. Andoh[1], T. Tsutaoka[2], and S. Kawano[3]

Japan Advanced Institute of Science and Technology, Ishikawa 923-1292, Japan
[1]Faculty of Regional Science, Tottori University, Tottori 680-8551, Japan
[2]Graduate School of Education, Hiroshima University, Hiroshima 739-8524, Japan
[3]Research Reactor Institute, Kyoto University, Osaka 590-0494, Japan

YbPdGe has been known as one of ferromagnetic Yb-based compounds [1]. It has been also reported that YbPdGe compound crystallizes in the $CeCu_2$-type orthorhombic structure [2]. Magnetic measurements have strongly indicated that at least two magnetic ordered phases exist below T_C=11.9 K and T_1=8.3 K. The magnetization curve below T_1 shows metamagnetic-like transition at low field, suggesting antiferromagnetic spin arrangement in the low temperature phase. The saturation magnetic moment at 1.8 K is 1.4 μ_B at 7 T. Electrical resistivity exhibits a Kondo maximum around 100 K. In the present study, powder neutron diffraction experiments have been performed on YbPdGe compound to determine the magnetic structure.

Poly-crystalline sample of YbPdGe were prepared by arc-melting the constituent elements. Subsequent annealing was done at 873 K for 7 days. The main phase of the sample was confirmed to be the $CeCu_2$-type orthorhombic structure by the Rietveld analysis of the powder X-ray diffraction pattern. Neutron diffraction measurements were carried out by using the HQR spectrometer installed at JRR-3M of JAERI at Tokai in the temperature range between 1.4 K and 300 K.

Figure 1 shows powder neutron diffraction patterns at 1.8 K and 30 K. All the reflection peaks except at 52 deg. in the paramagnetic state can be indexed by assuming the $CeCu_2$-type orthorhombic structure. Small enhancement of the peak intensity is observed only at the nuclear positions at 1.8 K as displayed in the inset of Fig. 1. The peak intensity of (002) reflection decreases with increasing temperature as shown in Fig. 2. These facts imply ferromagnetic spin configuration at 1.8 K. The detailed analysis of the magnetic structure is now in progress.

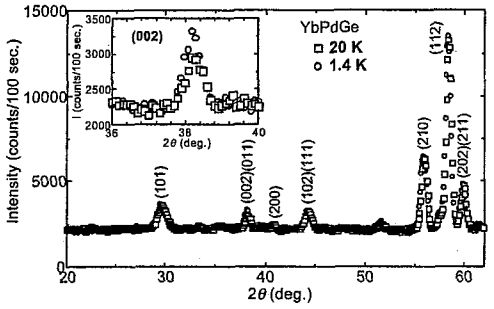

Figure 1: Powder neutron diffraction patterns of YbPdGe at 1.4 K and 30 K.

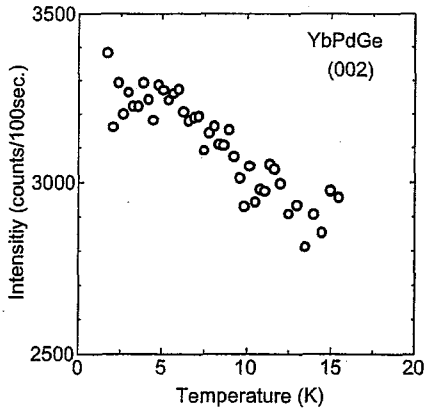

Figure 2: The peak intensity of (002) reflection as a function of temperature.

References

[1] V. N. Nikiforov *et al.*, Phys. Solid State **36** (1994) 259.
[2] Yu. D. Seropegin *et al.*, J. Alloys Compounds **216** (1994) 259.

使用施設：JRR-3M, 装置：HQR(T1-1), 分野 Magnetism

研究テーマ： CoO のパラマグノンの測定によるフラストレーションの検証
表題： CoO のパラマグノン

10) Paramagnon of CoO

K. Tomiyasu
Neutron Science Laboratory, Institute of Materials Structure Science, High Energy Accelerator Research Organization, 1-1 Oho, Tsukuba, Ibaraki, 305-0801

CoO has a cubic NaCl structure in a paramagnetic phase, and simultaneously exhibits a crystallographic distortion and type-II-fcc magnetic order with a propagation vector $\boldsymbol{Q}_{\mathrm{II}} = (\frac{1}{2}, \frac{1}{2}, \frac{1}{2})$ below T_{N}=289 K. In the magnetic order, ferromagnetic sheets of (111) planes are antiferromagnetically stacked along the [111] direction. On the other hand, the strong magnetic diffuse elastic scattering described by the same $\boldsymbol{Q}_{\mathrm{II}}$ is observed even at 340 K ($>T_{\mathrm{N}}$).[1] The problem has been untouched for more than 30 years. Thus, I studied origin of the diffuse scattering by inelastic neutron scattering on a single crystal of CoO.

A single crystal of CoO about 6 × 6 × 4 mm^3 was used. Neutron scattering experiments were performed on the PONTA triple axis spectrometers installed at JRR-3M, Tokai, Japan. The energy of the final neutrons was fixed at 30.5 meV. A pyrolytic graphite filter efficiently eliminated the higher order contamination.

Figure 1 shows the temperature dependence of energy spectra at the magnetic reciprocal point $\frac{1}{2}\frac{1}{2}\frac{3}{2}$ above T_{N}. Although the lattice is cubic in the paramagnetic phase, a gap energy of ~10 meV is observed. Figure 2 shows the temperature dependence of integrated intensity of elastic scattering around the magnetic reciprocal point. As the temperature increases from below T_{N}, the slope changes at T_{N} and gradually decreases to around 340 K.

In the present experiments, it was revealed that the strong diffuse elastic scattering is caused by the skirt of the paramagnon. However, the gap of paramagnon is still unsolved and is under calculation.

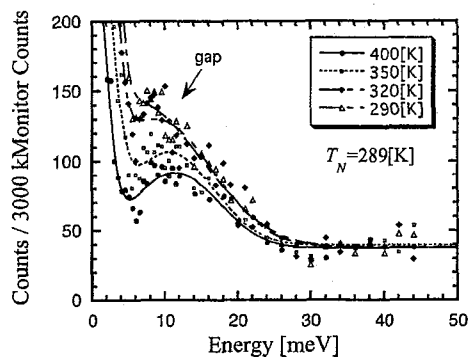

Fig. 1. The temperature dependence of energy spectra at the magnetic reciprocal point $\frac{1}{2}\frac{1}{2}\frac{3}{2}$ above T_{N}.

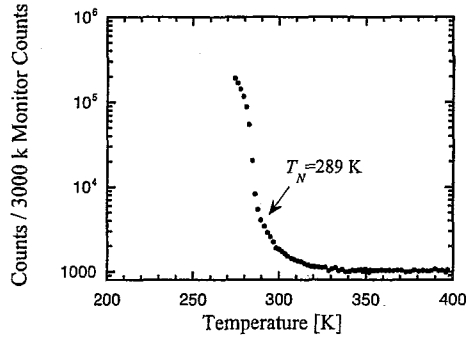

Fig. 2. The temperature dependence of of integrated intensity of elastic scattering around the magnetic reciprocal point $\frac{1}{2}\frac{1}{2}\frac{3}{2}$.

References

[1] M. D. Rechtin and B. L. Averbach: Phys. Rev B **5** (1972)2693.

使用施設：JRR-3M, 装置： 5G (PONTA) , 分野： 102. Magnetism

研究テーマ： 弱い磁気幾何学的フラストレーション系 $MnCr_2O_4$ のスピン構造とスピンダイナミクス
表題： 磁気幾何学的弱フラストレーション系 $MnCr_2O_4$ の磁気短距離秩序

11) Magnetic short-range order of magnetic geometrical weak frustration system $MnCr_2O_4$

K. Tomiyasu[1] and H. Suzuki[2]

[1] *Neutron Science Laboratory, Institute of Materials Structure Science, High Energy Accelerator Research Organization, 1-1 Oho, Tsukuba, Ibaraki, 305-0801*

[2] *Department of Applied Physics, School of Science and Engineering, Waseda University, 3-4-1 Ohkubo, Shinjuku, Tokyo, 169-8555*

The magnetic geometrical frustration has attracted much interest of researchers. In usual magnetic geometrical frustration systems, magnetic moments are located on only one regular triangular or tetrahedral lattice (B sites). On the other hand, we proposed the concept of magnetic geometrical *weak* frustration. The concept means that the effect of magnetic geometrical frustration still survives in systems that magnetic moments occupy both B sites and the other sites (A sites), if exchange interactions between A sites and B sites J_{AB} is smaller than that among the B-sites J_{BB} (; $|J_{AB}|<|J_{BB}|$).[1] In magnetic geometrical weak frustration systems, magnetic short-range order must be observed even in lowest temperature phase.

$CoCr_2O_4$ and $MnCr_2O_4$ are cubic normal spinel ferrimagnets ($T_C \simeq 93$ and 51 K), in which magnetic Co^{2+} and Mn^{2+} ions occupy A site and magnetic Cr^{3+} ions occupy B sites. Therefore, we can expect them as the magnetic geometrical weak frustration systems.

Magnetic moments in $CoCr_2O_4$ and $MnCr_2O_4$ are classified into a ferrimagnetic component and a spiral component, corresponding to fundamental reflections and satellite reflections, respectively. As the temperature decreases, the former component shows long-range order below T_C. Menyuk *et al.* and Hastings *et al.* reported that the latter component also forms long-range order below $T_S \simeq 31$ and 18 K.[2, 3] However, we found that the satellite reflection of $CoCr_2O_4$ is diffusive even at lowest temperature, which is the sign of magnetic geometrical weak frustration, in our neutron scattering experiments until the year before last.[1] The correlation length of the spiral component is estimated to 3.1 nm. In the present paper, we report the similar data of $MnCr_2O_4$ taken in the last year to examine the concept of magnetic geometrical weak frustration.

Figure 1(a) shows the line profile of the 220 fundamental reflections at 60 K ($T>T_C$) and 4 K. At both temperatures, the 220 fundamental reflections are coherent Bragg reflections, indicating that the ferrimagnetic component exhibits long-range order (>50 nm, a resolution limit in the present experiments) at 4 K. Figure 1(b) shows scan data around the 1.38 1.38 0 reciprocal lattice point at 30 K ($T>T_S$) and 4 K. The satellite reflection at 4 K is diffusive, meaning that the spiral component exhibits short-range order at 4 K. The diffusive line profile is well fitted by a Lorentzian, with a half width at half maximum κ value of 0.014 ($2\pi/a$ unit) after correction of the Cooper and Nathans' resolution function. The correlation length of the spiral component ξ is estimated to 9.9 nm by taking the inverse of κ.

The diffusive satellite reflections of $CoCr_2O_4$ and $MnCr_2O_4$ indicate that the magnetic geometrical weak frustration is valid for those materials at least. The simultaneous formation of ferrimagnetic long-range order and spiral short-range order characterizes the magnetic geometrical weak frustration. We would also like to emphasize that the concept can be applied not only to the chromite spinel systems but also to many other systems including a pyrochlore lattice or a triangular lattice. For further information, please see Ref.[1].

References

[1] K. Tomiyasu, J. Fukunaga and H. Suzuki : Phys. Rev B **70** (2004)214434.

使用施設：JRR-3M, 装置： T1-1 (HQR) , 分野： 102: Magnetism

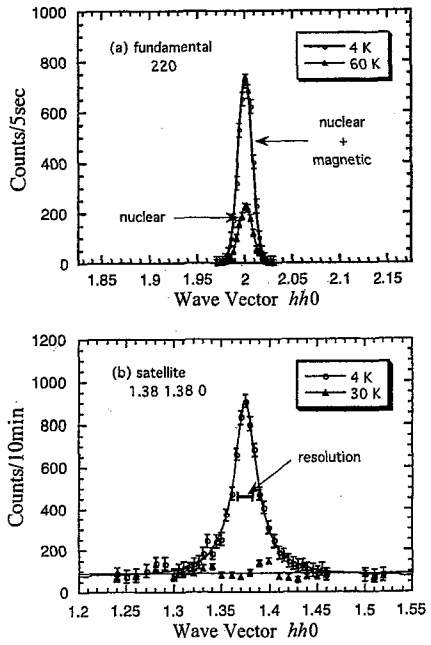

Fig. 1. Neutron scattering data of $MnCr_2O_4$ obtained by scanning along the [110] direction around the 220 reciprocal lattice point at 60 K ($T>T_C$) and 4 K (a) and around the 1.38 1.38 0 reciprocal lattice point at 30 K ($T>T_S$) and 4 K (b). In Figure (b), the solid line is drawn by fitting the experimental data at 4 K with a Lorentzian.

[2] N. Menyuk, K.Dwight and A. Wold : J. Phys. (Paris) **25** (1964)528.
[3] J. M. Hastings and L. M. Corliss : Phys. Rev. **126** (1962)556.

研究テーマ： NiAS 型 $CrTe_{1-x}Sb_x$ の異常ホール効果と磁気構造
表題： $CrTe_{1-x}Sb_x$ の磁気構造と異常ホール効果

12) Magnetic Structure and Anomalous Hall Effect in $CrTe_{1-x}Sb_x$

H. Harashina

Department of Physics, School of Liberal Arts and Science, Daido Institute of Technology, 10-3 Takiharu-cho, Minamik-ku, Nagoya 457-8530, Japan

Unusual behaviors of the anomalous Hall resistivity ρ_H have been often observed in ferromagnetic systems with a non-trivial spin structure [1,2]. Although detailed studies have been performed for various systems, the origin of the behaviors has not been understood sufficiently. In previous studies, complicated magnetic structure and/or crystal structure of the intriguing system may make it difficult.

$CrTe_{1-x}Sb_x$ has the simple hexagonal NiAs-type crystal structure in the whole x-region ($0 \le x \le 1$) and its detailed magnetic phase diagram has been reported [3]. CrTe is a ferromagnet with the Curie temperature $T_C \sim$ 340 K and CrSb is an antiferromagnet with the Neel temperature $T_N \sim 700$ K. For $0.2 \le x \le 0.7$, $CrTe_{1-x}Sb_x$ exhibits the magnetic phase transition to the canted state from the collinear ferromagnetic or antiferromagnetic state with decreasing T. Around the temperature T_m where the spin canting occur, the Hall resistivity ρ_H of $CrTe_{1-x}Sb_x$ exhibits unusual temperature (T) dependence as shown in Fig. 1. A purpose of this study is to elucidate how the change of the magnetic structure affects the behavior of ρ_H by comparing experimental results of ρ_H and calculated ones with using detailed T-dependence of the magnetic structure. In order to obtain detailed information of the magnetic structure of $Cr_{1-x}Sb_x$, neutron diffraction studies were performed for powder samples of $x = 0.3$ and 0.4

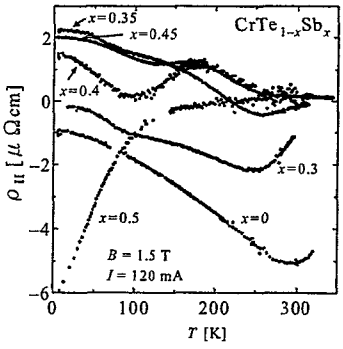

Figure 1: Temperature dependence of the Hall resistivity of $CrTe_{1-x}Sb_x$

Neutron measurements have been carried out with using the HQR spectrometer at JRR-3M of JAERI in Tokai. The double axis condition was adopted.

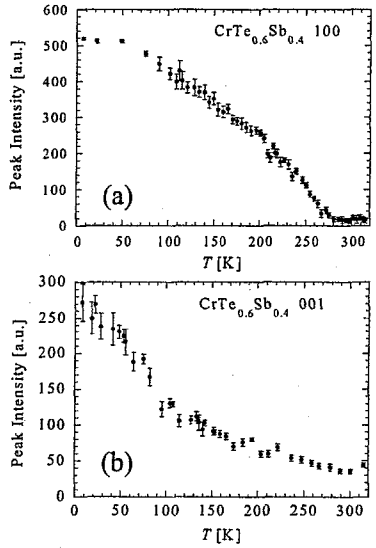

Figure 2: Peak intensities of (a) 100 and (b) 001 reflections of $Cr_{0.6}Te_{0.4}$ are plotted against T.

Figure 2 shows temperature dependence of peak intensities of 100 and 001 reflections for $CrTe_{0.6}Sb_{0.4}$. The 100 reflection appears with a ferromagnetic order along the c-axis and the 001 reflection appears when the ordered moments have a component perpendicular to the c-axis. In this sample T_C is about 280 K and T_m is about 100 K. The obtained magnetic structure at low temperatures is consistent with the previous studies [4].

The unusual behavior of ρ_H observed around 100 K for $CrTe_{0.6}Sb_{0.4}$ is considered to related to the occurrence of the spin canting. It is, however, difficult to be considered that the behavior of ρ_H is caused by change of the uniform magnetization M because the T-dependence of ferromagnetic component of the ordered moments hardly changes around T_m.

As the detailed T-dependences of the ordered moment and of the cant angle have been obtained, calculations of the Hall resistivity will be performed as the next step.

References

[1] Y. Yoshii et al., J. Phys. Soc. Jpn. **69** (2000) 3777.
[2] K. Oda et al., J. Phys. Soc. Jpn. **70** (2001) 2999.
[3] N. Suzuki et al., J. Alloys and Compounds **290** (1999) 25.
[4] W. J. Takei et al., Phys. Rev. **129** (1963) 2008.

使用施設：JRR-3M，装置：HQR(T1-1)，分野 Magnetism

研究テーマ：二本脚梯子系におけるスピン・ダイナミックス
表題：二本脚梯子系 $Sr_{0.33}V_2O_5$におけるスピン・ギャップの観測 II

13) Observation of Spin-Gap in the Two-Leg Ladder System $Sr_{0.33}V_2O_5$ II

M. Nishi[1], M. Isobe[2] and Y. Ueda[2]

[1]*Neutron Science Laboratory, ISSP, University of Tokyo, Tokai 319-1106, Japan*
[2]*Material Design and Characterization Laboratory, ISSP, University of Tokyo, Kashiwa 277-8581, Japan*

One-dimensional quantum spin system with spin gap has been studied also with many experimental and theoretical efforts since discover of two-leg ladder compound $SrCu_2O_3$. The crystal structure of vanadium oxide bronze $Sr_{0.33}V_2O_5$ was considered to be isostructural with $Na_{0.33}V_2O_5$ in the space group *C*2/m. From the structural point of view, $Sr_{0.33}V_2O_5$ can be regarded as a two-leg spin ladder system. The characteristic broad peak of magnetic susceptibility was observed around 50K indicating clearly one-dimensionality and exponential decrease related to spin-gap was observed also below 40K. Inelastic neutron scattering of $Sr_{0.33}V_2O_5$ powder sample were performed using ISSP-PONTA spectrometer installed in JRR-3M reactor at JAERI in Tokai using the fixed incident energy E_i = 30.5 meV. In the results of the experiments the spin gap energy is obtained as 6.1 meV and is almost constant at several Q positions. Q dependence of the scattering intensities at E = 6 meV was shown in Fig. 1 by subtracting from the data of 3.7K to that of 51K. Broken line shows the Q dependence of squared V^{4+} magnetic-formfactor. Solid line shows the fitting line of isolated dimer model with parameter of intra-dimer distance 5.44 A^{-1}.

In the first approximation spin-gap is proportional to the exchange interaction $J_\perp$ along rung at two-leg ladder and also the temperature at maximum peak of magnetic susceptibility is related to the ratio of exchange interactions along the chain and in the rungs. In the data analysis on $Sr_{0.33}V_2O_5$ the ratio of $J_\perp$ / $J_{//}$ becomes 6 corresponding to very week interaction of inter dimer and the ratio of first two leg ladder compound $SrCu_2O_3$ was 0.5 contrarily.

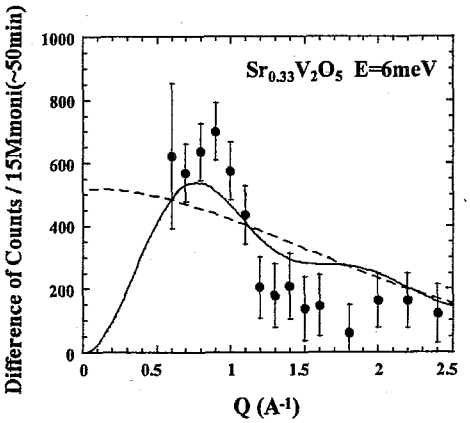

Fig. 1. Difference of the Q-dependent intensities between the scattering profile at 3.7K and that at 51K at E = 6 meV. Broken line shows the Q dependence of V^{4+} magnetic formfactor. Solid line shows the fitting line of isolated dimer model.

使用施設：JRR-3M，装置：PONTA(5 G)，分野 Magnetism

研究テーマ：先端偏極中性子散乱によるスピン－格子物性の研究
表　題：中性子と放射光散乱による $LuFe_2O_4$ における磁気・電荷秩序相関の研究

14) Neutron and Synchrotron Scattering Investigation on Correlation of Magnetic and Charge Ordering in $LuFe_2O_4$

K. Kakurai, N. Ikeda[1], S. Nagai[2], M. Matsuda, Y. Ishii[3], T. Inami[4], K. Ohwada[4], Y. Murakami[5], H. Kito[6] and Y. Yamada[7]

Advanced Science Research Center, Japan Atomic Energy Research Institute, 2-4 Shirakata Shirane, Tokai, Ibaraki, 319-1195 Japan
[1]Japan Synchrotron Radiation Research Institute, SPring-8, Hyogo 679-5198, Japan
[2]Neutron Science Laboratory, ISSP, Univ. of Tokyo, Tokai, Ibaraki 319-1106 Japan
[3]Neutron Science Research Center, Japan Atomic Energy Research Insitute, 2-4 Shirakata Shirane, Tokai, Ibaraki, 319-1195 Japan
[4]Synchrotron Radiation Research Center, SPing-8, Japan Atomic Energy Research Institute, Hyogo 679-5148, Japan
[5]Department of Physics, Tohoku University, Sendai 980-8578, Japan
[6]National Institute of Advanced Industrial Science and Technology, Tsukuba 305-8561, Japan
[7]ARCSE, Waseda University, Tokyo 169-0072, Japan

$LuFe_2O_4$ belongs to a class of materials expressed by RFe_2O_4, R being rare-earth metals. The crystals of these materials belong to the rhombohedral system. The Fe ions are arranged to form the hexagonal double layers and stack in the sequence of (AB), (CA), (BC),... along the rhombohedral unique axis. The average valence of the Fe ions is expected to be $Fe^{+2.5}$ in these materials and hence a mixed valence state of Fe^{2+} and Fe^{3+} ions occupying the equivalent Fe sites on the hexagonal plane with equal probability is expected. Recently a more stoichiometric sample became available and 3-D charge and magnetic ordering in the new sample has been vividly investigated by means of both x-ray and neutron scattering. Y. Yamada *et al.* reported the sequential charge ordering observed by means of X-ray scattering in a $LuFe_2O_4$ single crystal grown by H. Kito[1]. The charge ordering is characterized by an 3-D incommensurate charge-density wave state in the lowest temperature phase for T<320K. The neutron scattering experiments on the same crystal showed the onset of the 3-D magnetic ordering at T_N=242K, but at the same time the temperature dependence of (1/3,1/3,1) and (1/3,1/3,2) indicates the existence of the second characteristic temperature T_f=177K[2]. On one hand, the temperature variation of the spontaneous electric polarization strongly indicated the existence of the magnetic – ferroelectric correlation, as shown in Fig. 1[3]. At the magnetic transition temperature, 242K, a shoulder appears in the spontaneous electric polarization. This sudden decrease of electric polarization clearly indicates the coupling of magnetization with electric polarization.

To investigate the magnetic – ferroelectric correlation we performed resonant X-ray scattering

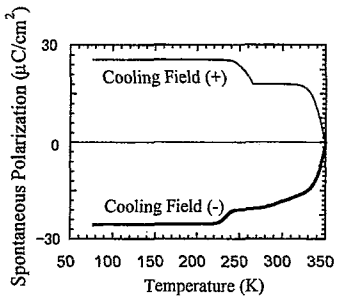

Figure 1: Temperature variation of the electric polarization in $LuFe_2O_4$.

(RXS) experiments using synchrotron radiation around the two magnetic characteristic temperatures T_N and T_f. The resonant spectra at T=250K>T_N, at T_N>T=200K>T_f and at T_f>T=160K are shown in Figure 2. As can be seen in the figures no significant difference was detected in RXS spectra at these temperatures. This result indicates that the charge ordering pattern is not modified at the magnetic transition temperatures.

On the other hand the detailed investigation of the line widths of the charge order peak in the x-ray scattering and of the magnetic peak in the neutron scattering revealed a striking correlation of the competing character. Figure 3 depicts the temperature dependence of the FWHM of the charge ordering superlattice peak at Q=(1/3,1/3,5.5) in [0k0] direction. A change in the in-plane correlation of the charge ordering can be recognized at T_N and T_f. Figure 4 indicates the linewidth of the magnetic peak in c* direction around T_f. In contrast to the increase of the in-plane correlation length in the

原子炉：JRR-3　　装置：TAS-1（2G），TAS-2（T2-4）　　分野：中性子散乱（磁性）

charge ordering, a decrease of the inter-plane correlation in the magnetic ordering is observed at T_f, thus indicating a competition between in-plane charge correlation and inter-plane magnetic correlation. The coherence length of the charge ordered region seems to be intimately related to the development of exchange coupling of iron spins.

References

1) Y. Yamada *et al.*: Phys. Rev. B 62 (2000) 12167.
2) K. Kakurai *et al.* Progress Report on Neutron Scattering Research JAERI-Review 2004-005 (2004) 82.
3) N. Ikeda *et al.*: J. Phys. Soc. Jpn 69 (2000) 1526.

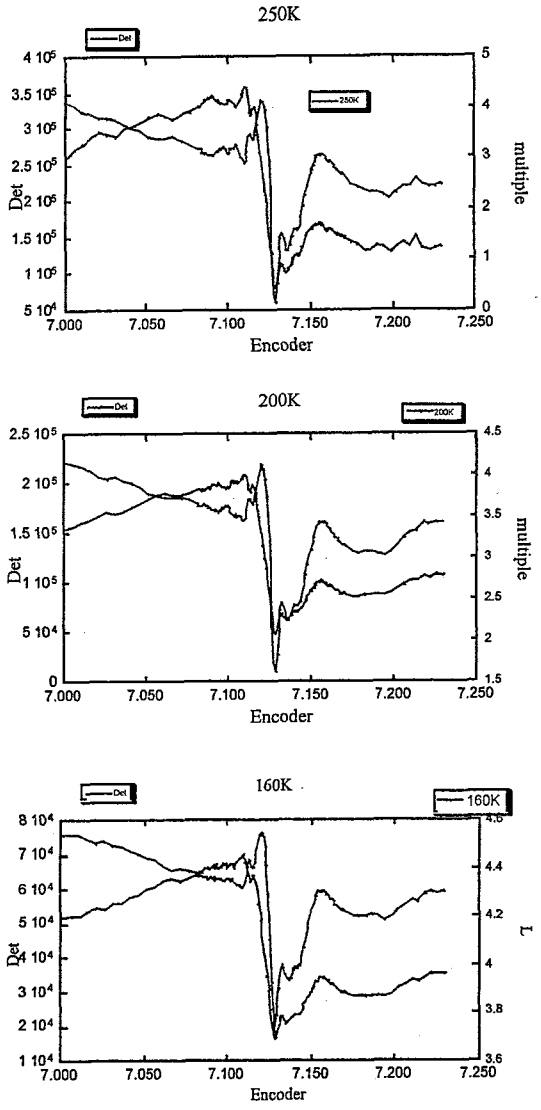

Figure 2: RXS spectra of $LuFe_2O_4$ at 250, 200 and 160K for Q = (1/3 1/3 5.5). Blue line is the raw data. The data corrected for absorption effect is drawn with red line.

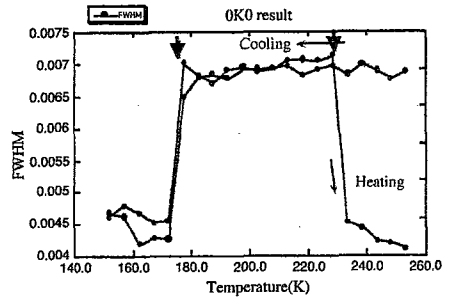

Figure 3: Line width (FWHM) of the superlattice peak at Q=(1/3,1/3,5.5) in X-ray scattering versus temperature.

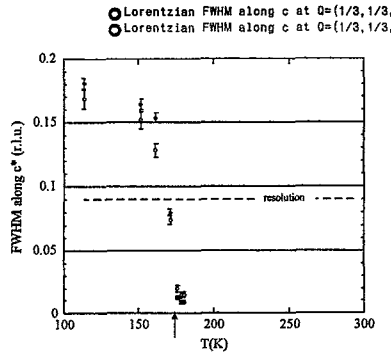

Figure 4: The line width (FWHM) of the magnetic peak at Q=(1/3,1/3, 3) and (1/3, 1/3, 4) versus temperature.

研究テーマ： 歪んだ三角格子イジングスピン系 $TlCoCl_3$ の格子歪みと磁気変調構造
表題： 歪んだ三角格子イジングスピン反強磁性体 $TlCoCl_3$ の構造相転移と磁気相転移

15) Structural and Magnetic Phase Transitions of Distorted-Triangular-Lattice Ising-like Antiferromagnet $TlCoCl_3$

Y. Nishiwaki, T. Kato[A], Y. Oohara[B] and K. Iio

Department of Physics (Cond.Mat.Phys.), Graduate School of Science and Engineering, Tokyo Institute of Technology, 2-12-1 Oh-okayama, Meguro-ku, Tokyo 152-8551
[A]Faculty of Education, Chiba University, 1-33 Yayoi-cho, Inage-ku, Chiba 263-8522
[B]Neutron Scattering Laboratory, Institute for Solid State Physics, The University of Tokyo, Shirakata 106-1, Tokai, Ibaraki 319-1106

The $CsNiCl_3$-family crystals with a prototypic structure of space group symmetry $P6_3/mmc$ exhibit the spin frustration originating from the antiferromagnetic interactions on the basal-plane triangular lattice(TL).[1] $TlCoCl_3$ is distorted from this structure through successive structural phase transitions at T_{st2} =165K, T_{st3} =75K and T_{st4} =68K,[2] and the lowest-temperature ($T < T_{st4}$) structure is identified to the orthorhombic *Pbca* model. The magnetic interaction on the TL is modified to the zigzag-row type.[3] From the previous experiment using the HQR spectrometer installed at JRR-3M guide hall, we obtained the data indicating that the Ising spins are arranged in an up-up-down-down manner below T_N = 29.5K.

In the present study, we found that both nuclear peaks of structural phase III ($T_{st3} < T < T_{st2}$) and V($T < T_{st4}$) appeared in the intermediate phase IV($T_{st4} < T < T_{st3}$). The profile around the characteristic nuclear peaks $(\frac{1}{3}\frac{1}{3}2)$ and $(\frac{1}{4}\frac{1}{4}2)$ is shown in Fig.1. The $(\frac{1}{3}\frac{1}{3}2)$ peak, which is prominent at 90K, is disappeared at 50K, and instead the $(\frac{1}{4}\frac{1}{4}2)$ peak is appeared. At 70K, both peaks coexisted. We performed additional measurements of such profiles at several temperatures between 66K and 84K, but only the change of intensities of these peaks was observed.

Moreover, just above T_N, a satellite peak is found to appear on the shoulder of magnetic peak $(\frac{3}{8}\frac{3}{8}1)$, as shown in Fig.2. The satellite was observed at only the temperatures from ~30.0K to 29.5K(=T_N), with its intensity and the center position gradually changed with the temperature variation.

We can propose a possible mechanism of this satellite peak using the Axial Next-Nearest-Neighbor Ising (ANNNI) model which arise with the magnetic ordering.

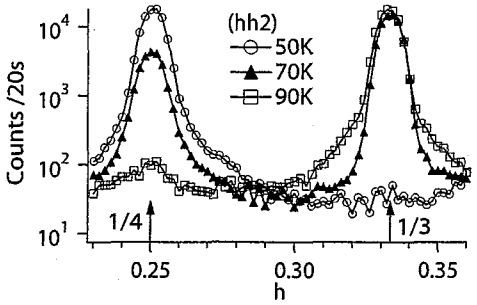

Fig. 1. The $(hh2)$ profiles around $(\frac{1}{4}\frac{1}{4}2)$ and $(\frac{1}{3}\frac{1}{3}2)$ at 90K (phase III), 70K (IV) and 50K (V).

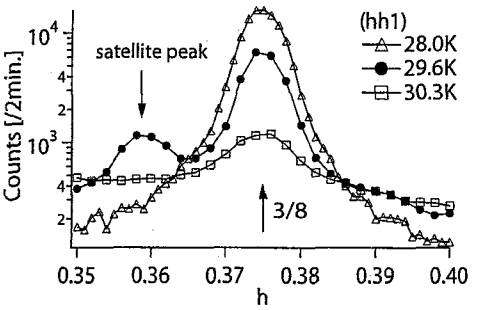

Fig. 2. The $(hh1)$ profiles around $(\frac{3}{8}\frac{3}{8}1)$ at some temperatures around T_N(=29.5K).

References

[1] M.F.Collins and O.A.Petrenko :Can. J. Phys. **75** (1997) 605.
[2] Y. Nishiwaki, T. Mitsui and K. Iio: J. Phys. Soc. Jpn. **72** (2003) 2608.
[3] T. Kato: J. Phys. Soc. Jpn. **71** (2002) 300.

使用施設：JRR-3M, 装置： T1-1 HQR)，分野： 2. Magnetism

研究テーマ：先端偏極中性子散乱によるスピン一格子物性の研究
表　題：偏極中性子ポラリメトリーによる幾何学的フラストレートした反強磁性体 $CdCr_2O_4$ の非整合スピン秩序の研究

16) Investigation of the Incommensurate Spin Order in a Geometrically Frustrated Antiferromagnet $CdCr_2O_4$ by Means of Polarized Neutron Polarimetry

K. Kakurai, M. Takeda, M. Nakamura, A. Oosawa, M. Matsuda, Y Shimojo,
S.-H. Lee[1] and E. Lelivre-Berna[2]

Advanced Science Research Center, Japan Atomic Energy Research Institute, 2-4 Shirakata Shirane, Tokai, Ibaraki, 319-1195 Japan
[1] Department of Physics, University of Virginia, charlottesville, Virginia 22904, USA
[2] Institut Laue-Langevin, 6 rue Jules Horowitz BP 156 - 38042 Grenoble Cedex 9, France

The ground states of the Cr-based spinel compounds ACr_2O_4 (A=Zn, Cd) are attracting much attention because of its strong magnetic frustration with the simplest spin Hamiltonian with isotropic antiferromagnetic nearest neighbour interaction among the magnetic Cr^{3+} ions forming a network of corner-sharing tetrahedra. It has been shown theoretically that the spins on such a pyrochlore lattice cannot order even at zero temperature. Consequently ACr_2O_4 remains paramagnetic to temperatures far below the Curie-Weiss temperature 390 K and 88 K for A=Zn and Cd, respectively. The real system, however, undergoes a first order spin Peierls-like phase transition from a cubic paramagnetic phase to a tetragonal Néel state upon further cooling. $CdCr_2O_4$ elongates along the c-axis and undergoes an incommensurate Néel order at T_N=7.8 K. The high Q resolution data indicate that the incommensurate magnetic structure has a single characteristic wave vector of Q_M=(0, δ, 1) with the incommensurability δ~0.09 perpendicular to the unique c-axis. To investigate the nature of the ground state we performed polarized neutron polarimetry experiment using the newly installed CRYOPAD on TAS-1.

Figure 1 indicates schematically the incommensurate magnetic peak positions in the (100) (010) zone of $CdCr_2O_4$ in the cubic notation stemming from the three tetragonal domains with c-axis lying in the scattering plane and perpendicular to it. One recognizes that the different domains contribute to the different magnetic peak groups.

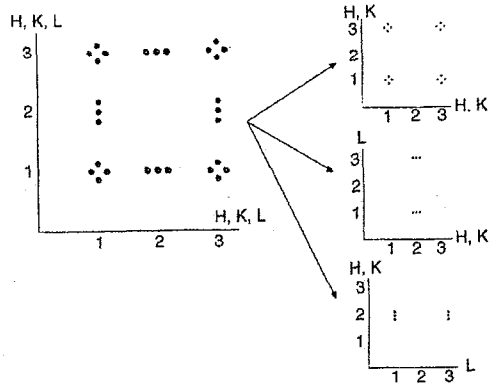

Figure 1: Schematic drawing of the incommensurate magnetic peak positions in the (100) (010) zone of $CdCr_2O_4$ in the cubic notation consisting out of the incommensurate magnetic peak positions from the three tetragonal domains with c-axis lying in the scattering plane and perpendicular to it.

Figure 2 shows the summary of the polarized neutron polarimetry results on selected magnetic peaks. The incident polarization is chosen in three orthogonal directions x, y and z, where x is defined to be along the scattering vector, y is defined to be in the scattering plane perpendicular to x direction and z is defined to be perpendicular to the scattering plane. The polarization of the scattered beam is also analyzed in these three direction, thus giving nine P_{ij}; i,j=x,y,z as the results for one given peak.

Even before the detailed analysis of these results, characteristic features of the polarization can be recognized.

1) P_{xx} is always almost close to the negative instrumental beam polarization, i.e. ~-0.9

原子炉：JRR-3　　装置：TAS-1（2G）　　分野：中性子散乱（磁性）

indicating the magnetic nature of the observed peaks.

2) The y or z polarized incident beam is almost depolarized, i.e. $P_{yy} \sim P_{zz} \sim 0$ when the scattering vector Q is almost parallel to the incommensurability vector, see *e.g.* at Q=(1,2.09,0) or (1,1.91,0), while at Q=(3,1.09,0) or (3,-0.91,0), when Q is almost perpendicular to the incommensurability vector, y polarized incident neutrons are almost flipped, i.e. $P_{yy} \sim -0.9$, and z polarized incident neutrons are almost not flipped, i.e. $P_{zz} \sim +0.9$.

These features indicate directly that we have a spiral spin structure with the spins lying on the plane that is perpendicular to the incommensurability direction.

The triangles in Fig.2 indicate the results of the best fit with such a spiral structure. The excellent fit is obtained if one assumes an elliptical spiral with an elongated axis in c-direction. One should note that even finite chiral term in P_{yx} and P_{zx} due to a small unbalance in the chirality domains are well reproduced.

To summarize, the details of the magnetic spiral ground state of the magnetically frustrated spinel compound $CdCr_2O_4$ could be determined by means of the newly developed polarized neutron polarimetry experiment. The results indicate the strong spin-lattice correlation resulting in the unusual elliptical spiral ground state in this system.

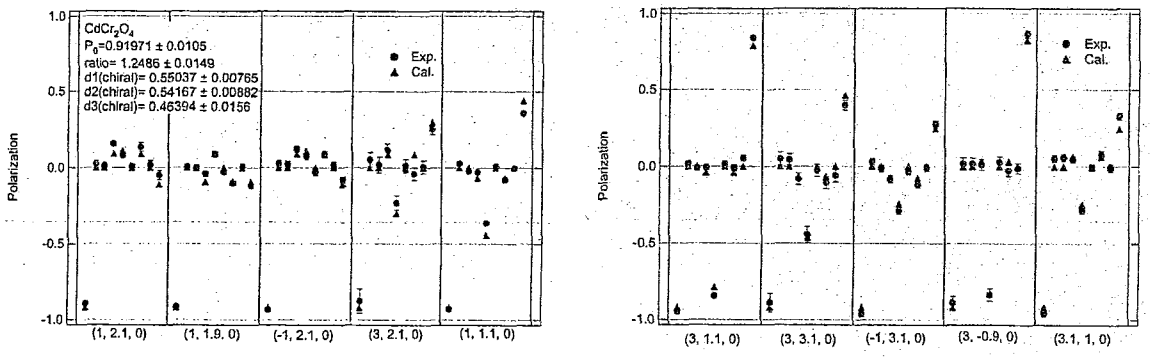

Figure 2: Summary of the polarized neutron polarimetry results of the geometrically frustrated antiferromagnet $CdCr_2O_4$. The data points indicate the measured nine polarizations Pxx, Pxy, Pxz, Pyx, Pyy, Pyz, Pzx, Pzy, Pzz (see text) in this order for each satellite position. Triangles are the results of the best fit with an elliptical spiral model (see text).

研究テーマ：三元系 Ni_2In 型金属間化合物の磁性
表題：Ni_2In 型 $(Mn_{1-x}Fe_x)_{65}Sn_{35}$ 合金の中性子回折実験および磁気的研究

17) Magnetic and Neutron Diffraction Study on Ni_2In type $(Mn_{1-x}Fe_x)_{65}Sn_{35}$

H.Shiraishi, T.Hori, N.Ohokubo[1] and K.Ohoyama[2]

Shibaura Institute of Technology, Fukasaku 307, Saitama 337-8570, Japan;
The Physical Sscience Labolatory, Nihon university, Chiba 274-850 Japan[1];
Institute Materials Research, Tohoku University 980-8577, Japan[2]

The hexagonal Ni_2In type ($P6_3/mmc$) $(Mn_{1-x}Fe_x)_{65}Sn_{35}$ compound shows a single phase in the range of $0 \leq x \leq 0.4$ showing glass-like phase at lower temperature range. The sample with nearly x=0 shows a ferrimagnetism[1]. The pressure effect of this system is already reported[2]. The χ^{-1}-T curve is shown in Fig.1. The χ^{-1}-T curve with smaller x is bent remarkably and this is one of the features of ferrimagnetic substances. The χ^{-1}-T curve with larger x such as x =0.3, 0.4 is nearly on the straight line reflecting the ferromagnetic nature. Neutron diffraction(ND) experiment was done at T1-3 in JRR-3M. Fig.2(a) shows the observed ND intensity versus Bragg angle 2θ at T=295K for x=0.25, refined ND intensity and the difference between observed and refined ones. The data were analyzed by the Rietveld refinement methods. Fig.2(b) shows the observed ND intensity at T=10K for x=0.25, refined ND intensity (magnetic+ lattice), and the difference between observed and refined ones. No extra magnetic peak is observed and only increased intensity of some reflections are observed. Fig.2(c) shows the contribution from magnetic and lattice part to the ND intensity. From these experiments and analysis, the x=0.25 sample is collinear ferromagnet with magnetic moment 1.2 μ_B/magnetic atom in 2(a) site and 0.7 μ_B/magnetic atom in 2(d) site and these are aligned parallel to the c axis. Fig.2(c) shows the contribution from magnetic and lattice part to the ND intensity. From these experiments and analysis the x= 0.25 sample is collinear ferromagnet with magnetic moment 1.2 μ_B/magnetic atom in 2(a) site and 0.7 μ_B/magnetic atom in 2(d) site and these are aligned parallel to the c axis. The sample at T=10K is the temperature range of the glass-like phase, but the long range ferromagnetic order could be observed. It is suggested for this reason that the glass-like phase consists of large magnetic clusters and the neutron diffraction will observe the inside of the cluster.

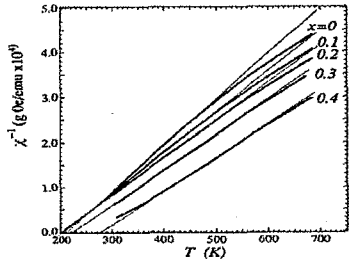

Figure 1: The temperature dependence of inverse magnetic susceptibility χ^{-1}-T for x =0 to 0.4.

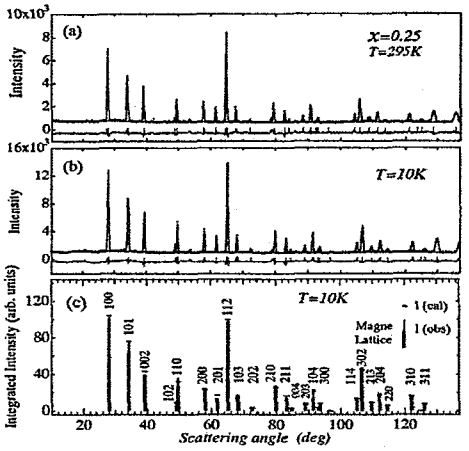

Figure 2: The observed and calculated neutron diffraction intensity at (a) T=295K and (b) T=10K for x=0.25. (c)The observed neutron diffraction integrated intensity and calculated nuclear and magnetic intensity at T=10K for x=0.25.

References

[1] N.S.Satya Murthy et al., Phys. Lett. **15** (1965) 225.
[2] S. Anzai et al., High Pressure Sci. Technol. **7**, (1998) 547.

使用施設：JRR-3M, 装置：T1-3, 分野：Magnetism

研究テーマ：先端偏極中性子散乱によるスピン－格子物性の研究
表　題：擬一次元イジング型反強磁性体 $TlCoCl_3$ の磁気励起

18) Magnetic Excitations in the Quasi-1D Ising-like Antiferromagnet $TlCoCl_3$

A. Oosawa, Y. Nishiwaki[1], T. Kato[2] and K. Kakurai

Advanced Science Research Center, JAERI, Tokai, Ibaraki 319-1195
[1]*Department of Physics, Tokyo Institute of Technology, Oh-okayama, Meguro-ku, Tokyo, 152-8551*
[2]*Faculty of Education, Chiba University, Yayoi-cho, Inage-ku, Chiba 273-8522*

$TlCoCl_3$ is the ABX_3-type Ising-like antiferromagnet, in which the magnetic Co ions with large Ising anistropy form the chains along the c-axis and these chains make the triangular lattice in the c-plane. This system undergoes the successive structural phase transitions from the hexagonal crystal structure to orthorombic one [1]. At T_N=29.5 K, the magnetic phase transition occurs, and the up-up-down-down-type magnetic structure have been observed below T_N [2]. In order to investigate the magnetic excitations in this system, we performed the neutron inelastic scattering experiments on TAS-2.

Figure 1 shows the profiles of the constant-$\boldsymbol{Q}$ energy scans in $TlCoCl_3$ for $\boldsymbol{Q}$ along $(\frac{3}{8}, \frac{3}{8}, l)$ at $T = 10$ K, which is below T_N. As shown in Fig. 1, two magnetic excitations were observed at $E \sim 3$ meV and 13 meV. The higher magnetic excitation is a little dispersive and asymmetric, while lower one is less dispersive. Previously, the magnetic excitations have been theoretically studied in the 1D Ising-like antiferromagnet with the following Hamiltonian (1) by Ishimura and Shiba (IS) [3].

$$\mathcal{H} = 2J \sum_j \left[S_j^z S_{j+1}^z + \epsilon \left(S_j^x S_{j+1}^x + S_j^y S_{j+1}^y \right) \right] \quad (1)$$

In this theory, two magnetic excitations were found. One is the spin-wave excitation continuum corresoponding to the domain-wall pair excitation. This excitation is a little dispersive and have the asymmetrical spectrum due to the continuum. Another is the central mode corresponding to the motion of thermally activated domain walls firstly predicted by Villain [4]. These features correspond to the observed two magnetic excitations, therefore we conclude that the magnetic excitations of $TlCoCl_3$ can be well interpreted as the domain-wall excitation in the 1D Ising-like antiferromagnet system. These excitations have been also observed in the quasi-1D Ising-like antiferromagnet $CsCoCl_3$ [5].

In the IS theory, it was found that the peak position of the spin wave excitation continuum can be expressed as

$$\omega_q = 2J(1 - 8\epsilon^2 \cos^2 \pi l) \quad (2)$$

and the boundaries of the continuum extending from ω_q^- to ω_q^+ are given by

$$\omega_q^{\pm} = 2J(1 \pm 2\epsilon \cos \pi l) \quad (3)$$

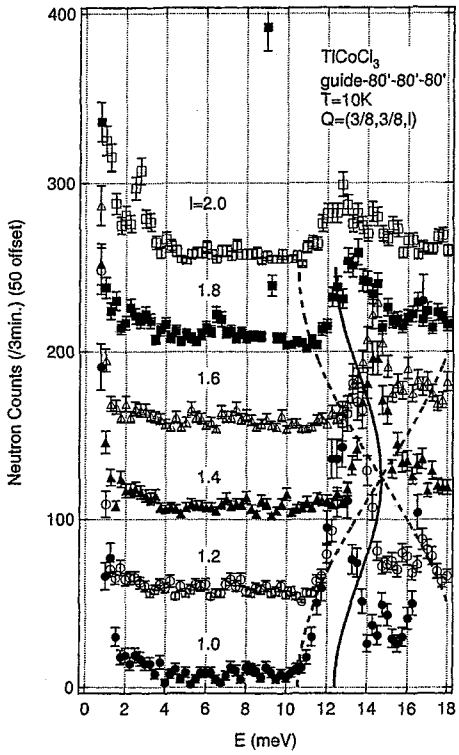

Figure 1: Profiles of the constant-$\boldsymbol{Q}$ energy scans in $TlCoCl_3$ for $\boldsymbol{Q}$ along $(\frac{3}{8}, \frac{3}{8}, l)$ at $T = 10$ K. The solid and dotted lines denote the fitting results of the $\boldsymbol{Q}$-dependence of the peak position (eq. (2)) and the boundaries of the continuum (eq. (3)) derived from the IS theory, respectively.

by means of the perturbation theory from the pure Ising limit. We fit the obtained profiles by these equations, and then the exchange constant $2J$ and the anistropy ϵ was obtained as 14.7 meV and 0.14, respectively, as shown in Fig. 1.

References

1) Y. Nishiwaki *et al.*: see in this JAERI-Review.
2) Y. Nishiwaki *et al.*: in preparation.
3) N. Ishimura and H. Shiba: Progr. Theor. Phys. **63** (1980) 743.
4) J. Villain: Physica B **79** (1975) 1.
5) H. Yoshizawa, H. Hirakawa, S. K. Satija and G. Shirane: Phys. Rev. B **23** (1981) 2298.

原子炉：JRR-3　　装置：TAS-2(T2-4)　　分野：中性子散乱（磁性）

研究テーマ： p 型 ZnMgRE(RE: 希土類元素) 準結晶の磁性
表題： p 型 Zn-Mg-RE 準結晶の単準結晶実験

19) Single-grain experiments on the p-type icosahedral Zn-Mg-RE quasicrystals

T. J. Sato[1,3] and A. P. Tsai[2,3,4]

[1] *NSL, ISSP, University of Tokyo, Tokai, Ibaraki 319-1106, Japan*
[2] *IMRAM, Tohoku University, Sendai 980-8577, Japan*
[3] *SORST-JST, Kawaguchi Saitama 332-0012, Japan*
[4] *MEL, NIMS, Sengen, Tsukuba, 305-0047, Japan*

Quasicrystals are characterized by sharp Bragg reflections with a point symmetry that is forbidden in a periodic lattice, such as the five-fold symmetry. Magnetism of quasicrystals has been a fundamental issue of study since its discovery. To date, the face-centered-icosahedral Zn-Mg-RE (RE: rare-earth) quasicrystals have been well investigated, whereas knowledge on other lattice types is lacking. Last year, first neutron scattering experiment on the primitive-icosahedral Zn-Mg-RE quasicrystals was performed using powder samples by the present authors. This year, we have succeeded in growing a large single-grained samples of the p-Zn-Mg-Ho quasicrystal, and performed neutron scattering experiments on the single-grained samples.

We used two triple-axis spectrometers 4G-GPTAS and C11-HER; only 4G results are shown here. Single grains of the p-Zn-Mg-Ho quasicrystals were grown by the Bridgman method. Two single grains are co-aligned with their two-fold (2f) planes coinciding the scattering plane.

Shown in Fig. 1 is magnetic scattering intensity along the 2f axis at the lowest temperature $T = 1.5$ K; the magnetic component was estimated by the temperature difference between 1.5 K and the paramagnetic temperature 20 K. The development of the short-range magnetic correlations is clear from the significant diffuse scattering peaks appearing at $Q \simeq 0.55, 1.15$, and 2.2 Å^{-1} We have also mapped whole scattering intensity in the 2f plane (Fig. 2). From the line and map scans, we found that the magnetic diffuse scattering patterns are almost identical to those of the f-Zn-Mg-RE quasicrystals [1].

Implication of the above identity between two different lattice types is very intriguing;

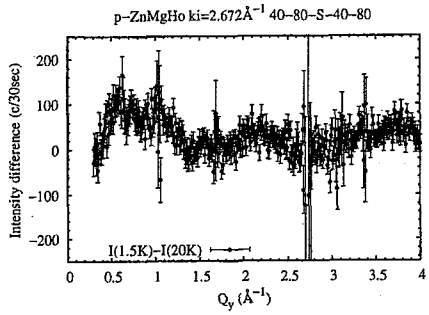

Fig. 1. Temperature difference ($I(1.5\text{ K}) - I(20\text{ K})$) of the scans along the 2f axis.

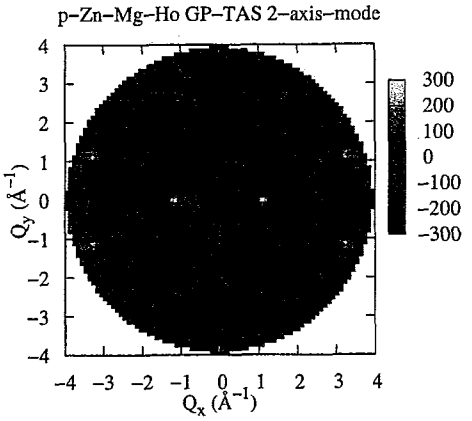

Fig. 2. Magnetic diffuse scattering intensity map in the 2f plane, obtained by the difference between $T = 1.5$ K and $T = 20$ K.

this suggests that the long-range quasiperiodicity is not intrinsic to the observed magnetic diffuse scattering patterns, but they should rather be related to local atomic structure, *i.e.*, atom clusters.

References

[1] T. J. Sato *et al.*: Phys. Rev. Lett. **81** (1998) 2364; T. J. Sato *et al.*: Phys. Rev. B **61** (2000) 476; T. J. Sato *et al.*: Acta. Crystallogr. Sec. A **61** (2005) 39.

使用施設：JRR-3M, 装置： 4G (GPTAS), C11 (HER) , 分野： 2. Magnetism

研究テーマ：先端偏極中性子散乱によるスピン－格子物性の研究
表　題：偏極中性子非弾性散乱による擬一次元イジング型反強磁性体 $TlCoCl_3$ の磁気揺らぎの研究

20) Polarized Neutron Inelastic Scattering Study of Magnetic Fluctuations in the Quasi-1D Ising-like Antiferromagnet $TlCoCl_3$

A. Oosawa, Y. Nishiwaki[1], T. Kato[2] and K. Kakurai

Advanced Science Research Center, JAERI, Tokai, Ibaraki 319-1195
[1]*Department of Physics, Tokyo Institute of Technology, Oh-okayama, Meguro-ku, Tokyo, 152-8551*
[2]*Faculty of Education, Chiba University, Yayoi-cho, Inage-ku, Chiba 273-8522*

Magnetic excitations of $TlCoCl_3$ can be interpreted as the domain-wall excitation in the 1D Ising-like antiferromagnet system with the following Hamiltonian [1)]

$$\mathcal{H} = 2J \sum_j \left[S_j^z S_{j+1}^z + \epsilon \left(S_j^x S_{j+1}^x + S_j^y S_{j+1}^y \right) \right]. \quad (1)$$

In the Ishimura-Shiba (IS) theory [2)], the anistropy of the dynamical correlation functions $S_{xx}(Q,\omega)$ and $S_{zz}(Q,\omega)$, which correspond to the transverse and longitudinal magnetic fluctuations respectively, have been also discussed. Main features of them are shown in Table 1. The peak position of the $S_{xx}(Q,\omega)$ with *asymmetrical* spectral shape is *dependent* on Q, while that of the $S_{zz}(Q,\omega)$ with *symmetrical* spectral shape is *independent* on Q. The intensity of the $S_{zz}(Q,\omega)$ is a hundredth as large as that of the $S_{xx}(Q,\omega)$. In order to investigate the anistropy of the magnetic fluctuations in $TlCoCl_3$, we carried out the polarized neutron inelastic scattering experiments.

Polarized neutron inelastic scattering experiments using the uniaxial polarized neutron scattering technique [3)], were performed on TAS-1. The sample was mounted in the cryostat with its $[h,h,0]$- and $[0,0,l]$-axes in the scattering plane. In the present experiments, the guide field was applied perpendicular to the scattering (h,h,l) plane, *i.e.* , vertical field (VF) configuration. In this configuration, the inelastic scattering intensity of the spin-flip (SF) scattering is proportional to dynamical correlation function perpendicular to the scattering vector $\boldsymbol{Q}$ in the scattering (h,h,l) plane, while that of the non-spin-flip (NSF) scattering is proportional to the dynamical correlation function perpendicular to both the scattering vector $\boldsymbol{Q}$ and the scattering (h,h,l) plane, namely,

$$I_{\mathrm{NSF}} = C \cdot S_{xx}(Q,\omega) \quad (2)$$

$$I_{\mathrm{SF}} = C \left(\sin^2\theta \cdot S_{xx}(Q,\omega) + \cos^2\theta \cdot S_{zz}(Q,\omega) \right) \quad (3)$$

where C is a constant and θ is the angle between the scattering vector $\boldsymbol{Q}$ and $[h,h,0]$-axis.

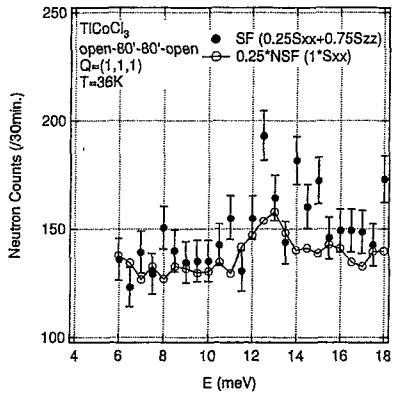

Figure 1: Profiles of the constant-$\boldsymbol{Q}$ energy scans in $TlCoCl_3$ at $\boldsymbol{Q} = (1,1,1)$ for $T \simeq 36$ K.

Figure 1 shows the profiles of the constant-$\boldsymbol{Q}$ energy scans in $TlCoCl_3$ at $\boldsymbol{Q} = (1,1,1)$ for $T = 36$ K, which is above $T_N = 29.5$ K. Because the angle θ is estimated as 30° at $\boldsymbol{Q} = (1,1,1)$, the intensity corresponding to the $0.25S_{xx}(Q,\omega) + 0.75S_{zz}(Q,\omega)$ should be observed in SF scattering. The intensity of the $S_{xx}(Q,\omega)$ can be estimated using the NSF scattering, as indicated in eq. (2). We plot the NSF scattering intensity multiplied by 0.25 in Fig. 1. As shown in Fig. 1, the difference of intensity between the SF scattering and the NSF scattering intensity multiplied by 0.25 can be seen at $E \sim 14.5$ meV corresponding to $2J$ estimated in the unpolarized neutron scattering experiments [1)]. Because this result is consistent with the IS prediction, this difference infers the existence of the longitudinal magnetic fluctuation $S_{zz}(Q,\omega)$.

References

1) A. Oosawa *et al.*: see in this JAERI-Review.
2) N. Ishimura and H. Shiba: Progr.Theor.Phys. **63**(1980)743.
3) R. M. Moon, T. Riste and W. C. Koehler: Phys. Rev. **181** (1969) 920.

Table 1: Comparison of main features between the dynamical correlation functions $S_{xx}(Q,\omega)$ and $S_{zz}(Q,\omega)$ [2)]

	Spectral shape	Peak position	Intensity
S_{xx}	asymmetric	Q-dependent	
S_{zz}	symmetric	$\omega = 2J$	$\propto \epsilon^2$ ($\sim$ a hundredth as large as S_{xx} in $TlCoCl_3$) [1)]

原子炉：JRR-3　　装置：TAS-1(2G)　　分野：中性子散乱（磁性）

研究テーマ：6H ペロブスカイト型酸化物 $Ba_3LnRu_2O_9$ の磁気構造
表題：2 次元反強磁性体 Na_2TbO_3 の磁気構造

21) Magnetic structure of the two-dimensional antiferromagnet Na_2TbO_3

Y. Doi, K. Ninomiya, Y. Hinatsu, and K. Ohoyama*

*Division of Chemistry, Graduate School of Science, Hokkaido University, Sapporo 060-0810, Japan; * Institute for Materials Research, Tohoku University, Sendai 980-8577, Japan*

Crystal structure and magnetic properties of ternary oxide Na_2TbO_3 were investigated. The crystal structure is illustrated in Fig. 1(a). This compound is monoclinic with space group $C2/c$; cations form two kinds of layers, one of which is composed of Na and O atoms, and the other is consisted of Na, Tb, and O atoms. The powder x-ray diffraction measurement shows that a partially disordered arrangement has been found between Na and Tb sites (~20 %). Thus, the Tb ions form a diluted two-dimensional triangular lattice.

This compound shows a broad peak of the magnetic susceptibility against temperature at ~60 K, which is due to a two-dimensional characteristic of the magnetic order of Tb ions. At lower temperatures, an antiferromagnetic transition is found (T_N = 38.3 K).

The neutron diffraction measurements were performed at 2.6, 50, and 290 K using the high efficiency and resolution powder diffractometer, HERMES, of Institute for Materials Research, Tohoku University, installed at the JRR-3M Reactor in JAERI (Tokai). The wavelength of a neutron incident is 1.8035 Å. The data were analyzed by the Rietveld technique.

In the diffraction profile at 2.6 K, some additional reflection peaks were found at lower angles, which were not observed at 290 K. All the magnetic peaks can be indexed in the crystallographic unit cell. The data at 50 K show a broad background peak around $2\theta \sim 22°$, which indicates that the onset the magnetic ordering occurs above T_N.

In order to determine the magnetic structure, we assumed that the ordered magnetic moments of Tb ions at the three sets of 4*e* sites have the same size and adopt a collinear structure. The determined magnetic structure is shown in Fig. 1(b). In this magnetic structure, the magnetic moments of Tb ions order antiferromagnetically in each 4*e* site, i.e., antiparallel between atomic positions with z = 1/4 and 3/4. The moments of the Tb^{4+} in the Tb1 and Tb2 sites are antiparallel to those in the Tb3 site in the xy layer. The direction of magnetic moments is parallel to the c axis. The ordered magnetic moment of Tb^{4+} is 6.04(7) μ_B, which is slightly smaller than 7 μ_B expected from the $4f^7$ electronic configuration. This may be due to the influence of the cation disorder.

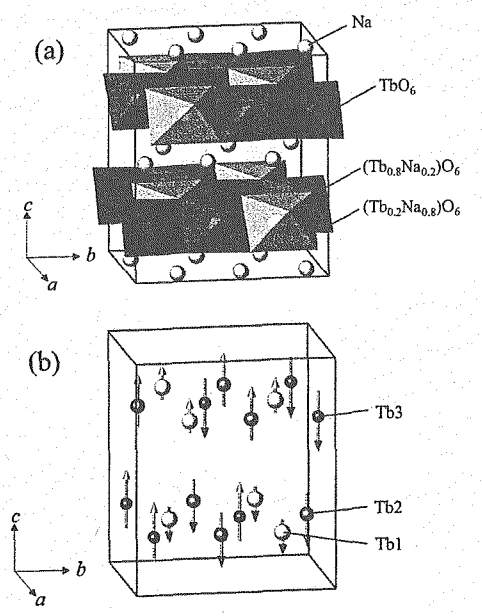

Figure 1: Crystal (a) and magnetic (b) structures of Na_2TbO_3.

使用施設：JRR-3M，装置：HERMES(T1-3)，分野 Magnetism

研究テーマ：先端偏極中性子散乱によるスピン－格子物性の研究
表　題：$S=\frac{1}{2}$ 擬二次元三角格子反強磁性体 Cs_2CuBr_4 における短距離相関

22) Short Range Correlations in the $S=\frac{1}{2}$ Quasi-2D Triangular Antiferromagnet Cs_2CuBr_4

A. Oosawa, T. Ono[1], K. Kakurai and H. Tanaka[2]

Advanced Science Research Center, JAERI, Tokai, Ibaraki 319-1195
[1]*Department of Physics, Tokyo Institute of Technology, Oh-okayama, Meguro-ku, Tokyo, 152-8551*
[2]*Research Center for Low Temperature Physics, Tokyo Institute of Technology, Oh-okayama, Meguro-ku, Tokyo 152-8551*

Recently, both quantum fluctuations and frustration effects have been energetically investigated in the $S=\frac{1}{2}$ triangular antiferromagnet together with the title compound Cs_2CuBr_4. Figure 1 shows the arrangement of the $CuBr_4{}^{2-}$ tetrahedras in the $b-c$ plane for Cs_2CuBr_4. The linked $CuBr_4{}^{2-}$ tetrahedras form a chain along the b-axis. The chains are separated by Cs^+ ions, which are omitted in Fig. 1. From this arrangement, Cs_2CuBr_4 can be described as the $S=\frac{1}{2}$ quasi-2D distorted triangular antiferromagnet [1]. This system undergoes the three-dimensional magnetic ordering with the incommensurate helical spin structure $\boldsymbol{Q}=(0,0.575,0)$ at $T_N=1.4$ K [2]. The notable feature of magnetic properties of this system is the magnetization plateaus at one-third and two-thirds of the saturation magnetization observed for the magnetic field $\boldsymbol{H}$ parallel to the b and c-axis, not the a-axis, in the ordered phase [1,2].

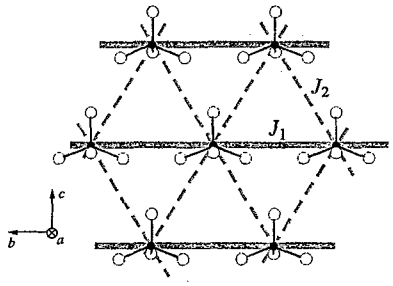

Figure 1: Arrangement of the $CuBr_4{}^{2-}$ tetrahedras in the $b-c$ plane for Cs_2CuBr_4. J_1 and J_2 are the exchange interactions in the distorted triangular lattice.

Recently, by means of specific heat measurments on this system, it has been found that the short range order begins to develop below $T=20$ K, consequently, the ninety percents of the entropy are consumed just above T_N [3]. This infer that the short range correlations already develop well on the two-dimensional triangular lattice in $b-c$ plane far above T_N and then the three-dimensional long range ordering occurs with the help of the inter-layer exchange interaction at T_N. Such short range order should be observed as "Bragg rods", namely magnetic Bragg reflections are resolution limited along the b and c-axis, while are broadened along a-axis. In order to investigate the short range correlations of Cs_2CuBr_4, we carried out the neutron elastic scattering experiments.

The neutron elastic scattering experiments were performed using the TAS-2 spectrometer. Collimations were set as 14'-40'-40'-80'. The sample was mounted in an ILL-type orange cryostat with its a^*- and b^*-axes in the scattering plane.

Figure 2 shows the elastic scan profiles along $\boldsymbol{Q}=(0,k,0)$ in Cs_2CuBr_4 at T=1.4, 1.8 and 4.2 K. At $T=4.2$ K, which is far above T_N, no distinct peak can be seen. With decreasing temperature to $T=1.4$ K, magnetic Bragg reflection indicative of the three-dimensional magnetic ordering clearly appears. At $T=1.8$ K, which is just above T_N, the intensity suddenly vanishes, and no remarkable difference can be seen between the profile at $T=1.8$ K and 4.2 K. Besides, no remarkable difference was not observed between the profile at $T=1.4$ K and 4.2 K for $\boldsymbol{Q}=(h,k\pm0.575,0)$ with various integers h and k, same as $\boldsymbol{Q}=(0,0.575,0)$. Measurements at $\boldsymbol{Q}=(h,k,l)$ with other h, k and l may be needed, namely the Bragg rods indicative of the two-dimensional short range ordering may emerge at $\boldsymbol{Q}$, which are different from $\boldsymbol{Q}=(h,k\pm0.575,l)$ with integer h, k and l indicative of the three-dimensional long range ordering.

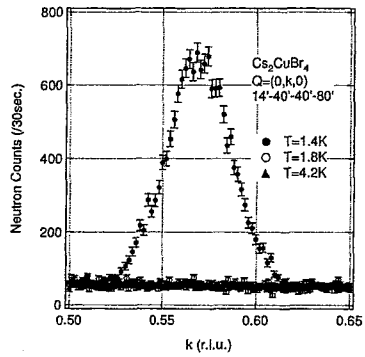

Figure 2: Elastic scan profiles along $\boldsymbol{Q}=(0,k,0)$ in Cs_2CuBr_4 at T=1.4, 1.8 and 4.2 K.

References

1) T. Ono *et al.*: Phys. Rev. B **67** (2003) 104431.
2) T. Ono *et al.*: J. Phys. Condens. Matter **16** (2004) S773.
3) T. Ono *et al.*: Meeting Abstracts of the Phys. Soc. Jpn. **59** Issue 1 (2004) 429.

原子炉：JRR-3　　装置：TAS-2(T2-4)　　分野：中性子散乱（磁性）

研究テーマ：二次元正方格子磁性体の非弾性中性子散乱
表題：正方格子上で実現したスピン液体状態：$(CuCl)LaNb_2O_7$の非弾性中性子散乱

23) Spin Liquid State in the Two-Dimensional $S = 1/2$ Frustrated Square Lattice System $(CuCl)LaNb_2O_7$

H. Kageyama, N. Oba, T. Kitano, J. Yasuda, Y. Baba, Y. Ajiro, K. Yoshimura, M. Nishi* and K. Hirota*

*Department of Chemistry, Graduate School of Science, Kyoto University, Kyoto 606-8502 Japan; * Institute for Solid State Physics, The University of Tokyo, 106-1 Shirakata, Tokai 319-1106*

In recent years, much attention has been given to low-dimensional antiferromagnetic (AFM) quantum spin systems that have a ground state with no long-range magnetic order and an energy gap in the magnetic excitation spectrum. Among them, the S = 1/2 frustrated square lattice AFM system (J_1-J_2 model) is of special importance in light of Anderson's resonating valence bond (RVB) concept to explain high-T_c superconductivity in doped layered cuprates.

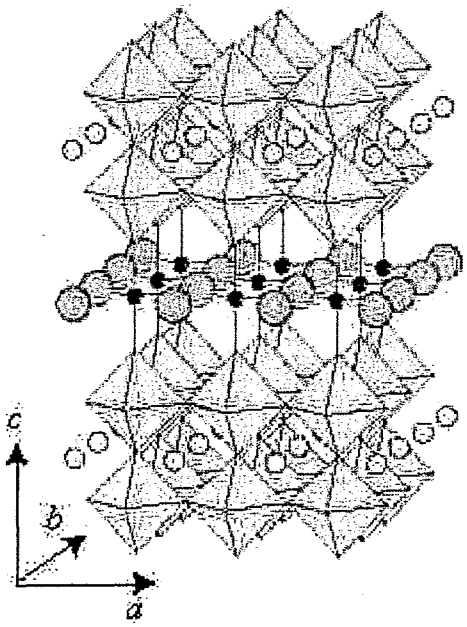

Figure 1: The schematic respresentation of the crystal structure of $(CuCl)LaNb_2O_7$.

Low-temperature topotactic strategies such as intercalation/deintercalation offer effective routes for the design and construction of new two-dimensional (2D) magnetic materials. As shown below, our magnetic susceptibility and inelastic neutron scattering experiments have revealed that a double-layered Dion-Jacobson phase $(CuCl)LaNb_2O_7$, prepared from topochemical ion exchange, provides a new class of 2D Heisenberg spin systems, where a spin-singlet ground state with a finite energy gap is achieved in the S = 1/2 frustrated square lattice. The lattice is tetragonal (space group $P4/mmm$), the room-temperature cell constants being a = 3.879 Å and c = 11.728 Å. As shown in Fig. 1, the structure consists of magnetic CuCl planes widely separated by nonmagnetic double perovskite slabs.

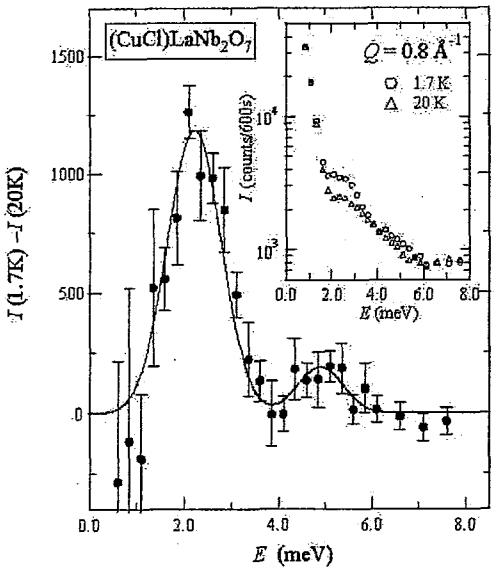

Figure 2: Inset: Constant Q-scan at Q=0.8 A^{-1} and T =1.7 K (circles) and 20 K (triangles). The cicles in the main panel are the difference, I(1.7K)- I(20K).

使用施設：JRR-3M，装置：PONTA(5G)，HER (C1-1)分野 magnetism

Inelastic neutron scattering experiments were carried out on the ISSP-PONTA triple-axis spectrometer installed at a 5G beam port of JRR-3M at the Japan Atomic Energy Research Institute. A powder sample of 12.6 g was put into an aluminum cylinder. Most of the data were collected using a fixed final energy E_f of 14.7 meV (k_f = 2.67 Å^{-1}) and a horizontal collimation of open-40'-S-80'-80' in combination with a pyrolytic graphite (PG) filter placed after the sample to eliminate higher-order beam contaminations. We also performed inelastic neutron scattering study at HER (C1-1), but we will not demonstrate the results since space is limited.

Typical constant-Q scans collected at T = 1.7 K and 20 K are shown in the inset of Fig. 3. There are two symmetric inelastic peaks indicating magnetic scattering from the spin-singlet ground state, which we call transitions I and II.

In order to gain an insight into the dynamical properties of the one-triplet mode, a number of constant-Q scans were performed for 0.4 Å^{-1} < Q < 3.2 Å^{-1}. Our results for (CuCl)$LaNb_2O_7$ obviously exhibit different behavior from conventional 2D systems; the most prominent features of the inelastic scattering are that the spectrum shapes in constant-Q scans for transition I are completely symmetric (Fig. 2) and that it is almost independent of Q (ΔE is 0.2 meV at most) (Fig. 3(a)). We believe that in (CuCl)$LaNb_2O_7$, the geometrical frustration should play a crucial role in making the one-triplet excitation extremely localized, thus giving rise to the flat dispersion.

In Fig. 3(b), we demonstrate the Q dependence of the scattering intensity, I(1.7K)–I(20 K), measured at the center of the first energy gap, where an oscillating behavior is clearly seen. From the qualitative point of view, not only does the intensity decrease, as expected for $F^2(Q)$, but the modulation due to the interference term is reproduced well by the isolated dimer model. The surprise came from the quantitative analysis; we obtained an extraordinarily long intradimer distance of R = 8.8 Å, corresponding to the 4NN bond (8.674 Å).

We strongly hope that our experiments will trigger intensive theoretical investigations on the (generalized) J_1-J_2 model with FM J_1 for greater understanding of the nature of the spin-liquid phase in (CuCl)$LaNb_2O_7$.

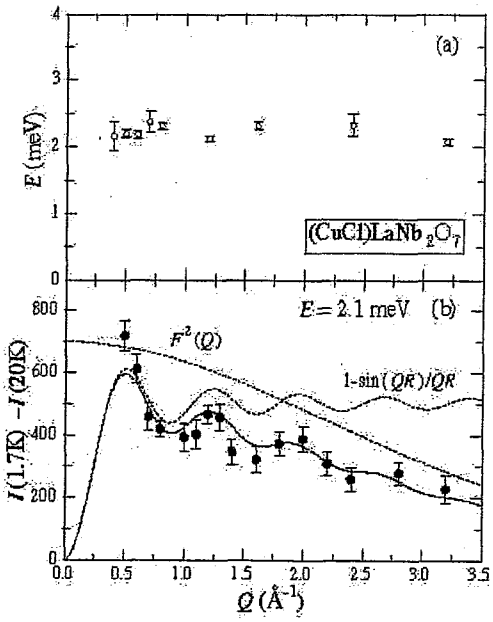

Figure 3: ϕ dependence of $R(Q)$, with shifts following to show in the legend for better visualization.

References

[1] H.Kageyama al., J. Phys. Soc. Jpn **74** (2005) 1702.

[2] H. Kageyama et al., Phys. Rev. Lett **84** (2000) 5876.

研究テーマ：中性子散乱によるウラン化合物の物性研究
表　題：S=1 異方的反強磁性交替鎖 NTENP の磁場中スピン励起

24) Spin Excitations under Magnetic Fields in an Anisotropic Bond-Alternating S=1 Chain NTENP

M. Hagiwara, L. P. Regnault[1], A. Zheludev[2], A. Stunault[3], N. Metoki[4], Y. Koike[4] and K. Kakurai[4]

KYOKUGEN, Osaka University, Toyonaka, Osaka 560-8531
[1]*CEA-Grenoble, DRFMC-SPSMS-MDN, 17 rue des Martyrs, 38054 Grenoble Cedex 9, France*
[2]*Condensed Matter Science Division, Oak Ridge National Laboratory, Oak Ridge, Tennessee 37831-6393, USA*
[3]*Institut Laue Langevin, 6 rue J. Horowitz, 38042 Grenoble Cedex 9, France*
[4]*Advanced Science Research Center, JAERI, Tokai, Ibaraki 319-1195*

Field induced phenomena in quantum spin systems with an excitation spin gap have attracted much attention. Antiferromagnetic chains with spin (S) one are well known as gapped quantum magnets with an exotic spin-liquid ground state (Haldane state). In the case of bond alternation, spin chains can have a fundamentally different ground state, namely the singlet-dimer one. The difference of features between these ground states is believed to be subtle and both ground states enter the same magnetized phase above a critical field H_c at which the enegy gap closes. At a first grance, one can expect the magnetic excitation at zero field and in a magnetic field to be similar for the Haldane and dimerized spin chains.

A recently discovered nickel chain compound $Ni(C_9H_{24}N_4)(NO_2)ClO_4$, alias NTENP, is an ideal material [1] for an experimental approach to the above problem, because it is regarded as the S=1 quasi-one-dimensional bond-alternating antiferromagnet in the gapped dimerized phase. NTENP crystalizes in the triclinic system and the Ni chain runs along the a axis with two different Ni bond distances. The singlet-dimer ground state below H_c was confirmed by some experiments [2] below H_c. From the specific heat experiments, it was reported that the long range order takes place above H_c at low temperatures [3].

We report the results of inelastic neutron scattering experiments on single crystals of deuterated NTENP under magnetic fields below and above H_c [4]. The scattering plane was the (a^*,c^*) plane and the external field was applied to the b aixs. We observed three excited modes below 4 T. These three modes corresponding to a triplet split by single-ion anisotropy. The field dependence of the excited triplet modes below H_c are nearly that of the Haldane material NDMAP for H perpendicular to the chain [5], but the highest mode is unusually small and smears out with increasing field as indicated by an arrow in Figure 1. This behavior is qualitatively different from previously studied Haldane systems such as NENP and NDMAP. Above H_c, we find only one intermediate excited mode and the lowest mode does not reappear after bumping into the ground state at H_c, in stark contrast with three gapped excitations previously observed in the structurally similar Haldane-gap material NDMAP [5].

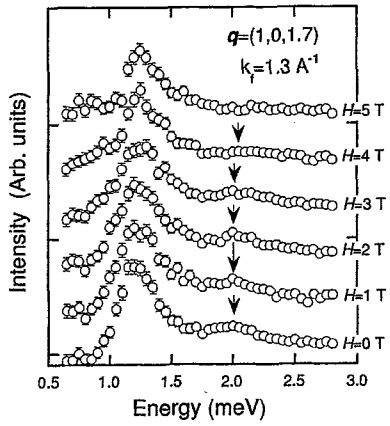

Figure 1: Inelastic energy scans near q=(1,0,1.7) around 0.1 K at H=0, 1, 2, 3, 4, 5 T.

It is important that a low-lying two-magnon continuum is around $q = \pi$ due to the violation of translational symmetry in a dimerized chain. When the anisotropy is present, this allows the highest mode moves into this low-lying continuum and can decay. The mode moves deeper into the continuum due to the Zeeman effect, resulting in weakening and broadening. Numerical calculations [6] show that the lower bound of the continuum in S^{zz} is beneath the lowest state above H_c. In a magnetic field along the b axis, the highest and the lowest modes have mixed polarization in the (y,z) plane. They become weakening and decay into multi-particle states. Therefore, only the intermediate mode with a polarization along the x axis was observed.

References

1) A. Escuer *et al.*: J. Chem. Soc. Dalton Trans. (1997) 531 .
2) Y. Narumi, M. Hagiwara, M. Kohno and K. Kindo: Phys. Rev. Lett. **86** (2001) 324.
3) N. Tateiwa, M. Hagiwara, H. A. Katori and T. C. Kobayashi: Physica B **329-333** (2003) 1209.
4) M. Hagiwara *et al.*: Phys. Rev. Lett. **94** (2005) 177202.
5) A. Zheludev *et al.*: Phys. Rev. B **68** (2003) 134438.
6) T. Suzuki and S. Suga: Phys. Rev. B (2005) in press; cond-mat/0505196.

原子炉：JRR-3　　装置：LTAS(C2-1),TAS-2(T2-4)　　分野：中性子散乱（磁性）

研究テーマ :強磁性と反強磁性相互作用が競合する系の磁性
表題 :中性子非弾性散乱実験による PtFe 合金の magnon の測定

25) Magnon dispersion relation in PtFe alloy

S. Akiyama and Y. Tsunoda

School of Science and Engineering, Waseda University,
3-4-1, Ohkubo, Shinjuku-ku, Tokyo 169-8555, Japan

An $L1_0$(CuAu)-type PtFe alloy has rather high Curie temperature (T_c~750K) and is considered to show ferromagnetism. Since the PtFe ordered alloy has a large magnetic anisotropy energy (7×10^7 erg/cm^3) and saturation magnetization (1150 emu/cm^3), it is expected to apply to a high density perpendicular magnetic recording media. Many data for the application have been accumulated in last few years. However, the microscopic magnetic property is hardly known. Thus we tried to study the magnon dispersion relation curve in PtFe alloy and determine the exchange coupling constants between spins.

Neutron inelastic scattering measurements were carried out at T1-1 triple axis spectrometer in the guide hole of JRR-3M in JAERI (Tokai). Most of the data were taken at room temperature. We scanned around the point 0 0 1 in a reciprocal space along the direction of [001], [010], and [110] by the constant-E mode. Typical line profiles of the [001]-scan are given in Fig.1.

We fitted the data to the theoretical formula of magnon dispersion relation in a ferrimagnet which is based on the Holstein-Primakoff approximation (Fig.2). The magnetic moments of Fe and Pt atoms are fixed at 3.01μ_B and 0.38μ_B, respectively, which were determined from the band calculation. From the least square fitting to the obtained dispersion curve, the unknown parameters of magnon dispersion relations were determined. The sign of the exchange constant between Pt and Fe atoms, one of the unknown parameters, showed that Fe moments couple with Pt moments anti-parallel. However the determined another parameter, the effective magnetic field around Pt atoms, is unexpectedly large. Thus, we suspect that the calculated value of Pt moment would be too small. Now we are trying to decide the magnetic moments of Pt atoms experimentally.

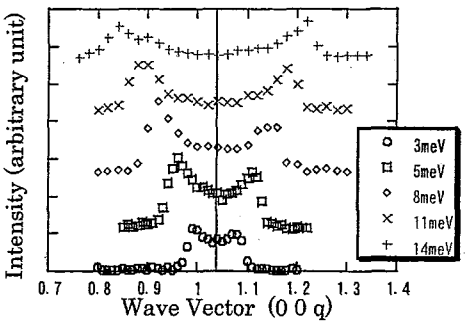

Fig.1 Line profiles of [001]-scan

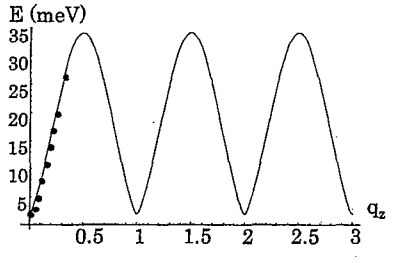

Fig.2 The least square fitting

使用施設 :JRR-3M, 装置 :HQR(T1-1), 分野 Magnetism

研究テーマ：$(Pr_{1-y}R_y)_{1-x}Ca_xCoO_3$ (R=稀土類元素) の金属－絶縁体転移
表　題：$(Pr_{1-y}R_y)_{1-x}Ca_xCoO_3$ (R=稀土類元素) のスピン状態転移

26) Spin State Transition of $(Pr_{1-y}R_y)_{1-x}Ca_xCoO_3$ (R=rare earth elements)

T. Fujita, S. Kawabata, Y. Yasui, M. Sato, Y. Shimojo[1], N. Igawa[1], Y. Ishii[1] and K. Kakurai[1]

Department of Physics, Division of Material Science, Nagoya University, Furo-cho, Chikusa-ku, Nagoya 464-8602, Japan

[1]*Japan Atomic Energy Research Institute, Tokai, Ibaraki, 319-1195, Japan*

Co^{3+} ions in various Co oxides such as $RCoO_3$ (R=rare earth elements) often exhibit a spin state change from the low spin (LS; spin s=0; t_{2g}^6) ground state to the intermediate spin (IS; s=1; $t_{2g}^5e_g^1$) or the high spin (HS; s=2; $t_{2g}^4e_g^2$) state with increasing temperature T, indicating that the difference of the electronic energies (δE) between these states is rather small. We can control the physical properties of Co oxides by controlling the value of δE by various methods. For example, by changing the ionic radius r_R of R^{3+}, the value of δE can be changed, because the crystal field splitting Δ_c depend on r_R. The Co-Co transfer energy t also depends on r_R through the changes of Co-O-Co bond angle α. In $R_{1-x}A_xCoO_3$ (A= Ba, Sr and Ca), effects of the hole doping should also be considered besides the effects stated above.

For $Pr_{1-x}Ca_xCoO_3$, a transition from the high temperature conducting phase to the low temperature less conducting (insulating) one has been reported by Tsubouchi *et al.*[1] in the very narrow region of $x \sim 0.5$. We have independently found a similar transition in the wide x region under the condition of external pressure $p > 5$ kbar.[2] At the transition temperature T_s, the abrupt decrease of the magnetic susceptibility χ is observed with decreasing T. In order to clarify the mechanism of this electronic-state change, we have carried out by various kinds of means, transport and magnetic measurements as well as ^{59}Co-NMR studies, and found that the transition is accompanied by the IS→LS spin state change of Co^{3+} ions with decreasing T. Then, to further understand the mechanism of this structural transition (the spin state change), we have carried out neutron diffraction studies at the high resolution powder diffractometer (HRPD) of JRR-3M of JAERI in Tokai and the Rietveld structure analysis is applied by using Rietan 2000.

The T-dependences of the unit cell volumes V_u, the volume of CoO_6 octahedra V_o and Co-O-Co bond angles α of $Pr_{1-x}Ca_xCoO_3$ with x=0.3 and 0.5 are shown in Fig.1 together with those of $(La_{0.2}Nd_{0.8})_{0.5}Ca_{0.5}CoO_3$. From the figure, it can be found that the transition of $Pr_{0.5}Ca_{0.5}CoO_3$ is primarily due to an abrupt decrease of α or an abrupt increase of the tilting angle of the CoO_6 octahedra at T_s, which is accompanied by the release of the volume contraction of the octahedra. This tilting stabilizes the LS state through the reduction of the Co-Co transfer energy t.

The large suppression of the transition has been observed by the $(La_{0.2}Nd_{0.8})$-substitution for Pr, even though the average ionic radius of $La_{0.2}Nd_{0.8}$ is equal to that of Pr^{3+}. Then, there remains a question why the transition takes place only in Pr-based systems. On this point, we note that recent studies[3] of the charge density distribution by the maximum entropy method (MEM) using powder X-ray diffraction evidenced the Pr-O hybridization below T_s, suggesting that the same mechanism of the hole trapping as that observed in the $PrBa_2Cu_3O_7$ is also working in the present Co oxide system.

References

1) S. Tsubouchi *et al.*: Phys. Rev. **B 66** (2002) 052418.
2) T. Fujita *et al.*: J. Phys. Soc. Jpn. **73** (2004) 1987.
3) E. Nishibori *et al.*: in preparation.

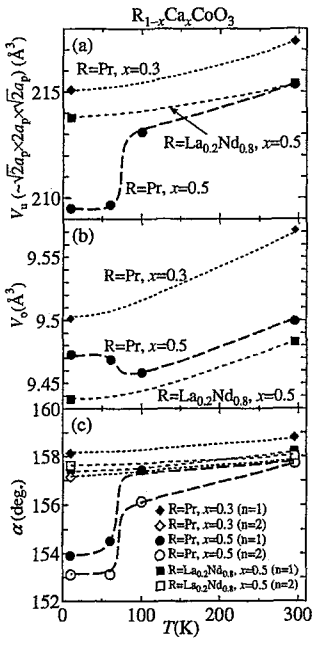

Figure 1: Unit cell volumes V_u (a), volumes of CoO_6 octahedra V_o (b) and Co-O-Co bond angles α (c) of $Pr_{1-x}Ca_xCoO_3$ and $(La_{0.2}Nd_{0.8})_{0.5}Ca_{0.5}CoO_3$ are shown against T in (a), (b) and (c), respectively. In (c), data for two crystallographycally distinct sites (n=1 and 2) are shown.

原子炉：JRR-3　　装置：HRPD(1G)　　分野：中性子散乱（磁性）

研究テーマ:強磁性と反強磁性スピン相関が競合する系の磁性
表題:$L1_0$(CuAu)-型 MnPt 合金の磁気異方性

27) Magnetic Anisotropy in MnPt $L1_0$-type Ordered Alloy

R. Motomura and Y. Tsunoda

Department of Applied Physics, Waseda University, 3-4-1, Ohkubo, Sinjuku-ku, Tokyo 169-8555 Japan

MnPt alloy shows an $L1_0$ (CuAu) type atomic ordering and tetragonal (c/a<1) lattice structure. Due to very high Neel temperature (T_N=930 K) and strong magnetic anisotropy energy, antiferromagnetic MnPt alloy is one of important materials for recently developed spintronics (GMR devices). Mn magnetic moments couple antiferromagnetically on the c-plane. At room temperature, Mn moments are parallel to the c-axis. However, as temperature increasing, the spin axis turns angle 90 degree from parallel to perpendicular to the c-axis. This spin flip transition takes place gradually and starts at 570 K and finishes at 730 K. Accompanying with this transition, drastic lattice contraction of the c-axis was reported. In order to investigate the origin of the gradual change of the spin axis at the phase transition, local magnetic anisotropy energy was studied through neutron inelastic scattering measurements.

A single crystal of PtMn alloy was grown by a furnace with carbon electrodes. Inelastic neutron scattering measurements were performed at T1-1 triple axis spectrometer. To study the local anisotropy energy, magnon gap energy was measured at the 1 0 0 reciprocal lattice point (Γ-point) as a function of temperature. The data obtained at various temperatures are given in Fig. 1. Magnon gap energy is almost constant at around 4.5 meV for all temperature range of the measurements. However, another peak was observed below the gap energy at 453 K as indicated by the arrow. As increasing temperature, the new peak gradually shifts towards low energy side and merges into elastic incoherent peak at around 600 K which corresponds to the starting temperature of the spin flip transition. To study the extension of the new peak in the Q-space, the constant-E mode scan at dE=2.8 meV was performed at 500 K. The new peak is localized at the Γ-point, indicating that Mn moments uniformly fluctuate with frequency lower than the gap energy. This is a new magnetic excitation mode and it has strongly connected with the gradual spin flip transition in PtMn alloy. Further measurements on the temperature variation and different Γ-points are now on progress.

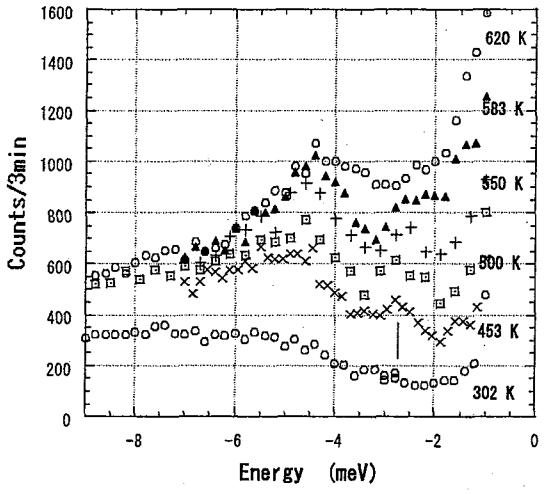

Fig. 1

使用施設:JRR-3M, **装置:**HQR(T1-1), **分野:**Magnetism

研究テーマ：新超伝導物質 $Na_xCoO_2 \cdot yD_2O$ の磁気励起スペクトル
表　題：$Na_{0.5}CoO_2$ における磁気転移

28) Magnetic Transitions of $Na_{0.5}CoO_2$

T. Moyoshi, M. Soda, Y. Yasui, M. Sato and K. Kakurai[1]

Department of Physics, Nagoya University, Chikusa-ku, Nagoya 464-8602
[1]*Advanced Science Research Center, JAERI, Tokai, Ibaraki 319-1195*

Na_xCoO_2 with triangular lattice of Co atoms is known as the mother system of the superconducting $Na_xCoO_2 \cdot yH_2O$.[1)] At $x = 0.5$, two phase transitions accompanied with magnetic anomalies have been found at the temperatures $T_{c1} \sim 87$ K and $T_{c2} \sim 53$ K.[2)] In the latter transition, the system goes to the insulating phase with decreasing temperature T.

In the present work, neutron diffraction studies have been carried out on a single crystal of $Na_{0.5}CoO_2$ to investigate what kinds of electronic and magnetic states are realized below these transition temperatures and then, to extract information on the mechanism of the superconductivity of $Na_xCoO_2 \cdot yH_2O$.

Neutron measurements were carried out between 8 K and 120 K by using the spectrometer TAS-2 installed at the thermal guide of JRR-3 of JAERI in Tokai. The double axis-condition was used and crystal orientations with the [100] and [001] axes and [110] and [001] axes in the scattering plane were used. The effective collimations were 17'-40'-80'.

Integrated intensities of the Bragg reflections have been measured at various reciprocal points in the temperature (T) range of 8-120 K. Superlattice peaks, which are due to the magnetic ordering, appears at $T_{c1} \sim 87$ K at (h, 0, l) or (h, h, l) (h:half integer, l:odd) with decreasing T. We observed another set of T-independent superlattice peaks in the studied T range (8 K $< T <$ 120 K) at $Q = (h, 0, l)$ or (h, h, l) (h:zero or half integer, l:integer). They are considered to be due to the Na ordering.

The magnetic structure is analyzed at 8 K by using the neutron data as well as those of NMR/NQR studies carried out by our own group.[3)] Figures 1(a) and 1(b) shows the structures which can reproduce the collected data within the experimental accuracy, where μ_1 is within the ab plane and μ_2 is perpendicular to the plane. We used an approximate relation $\mu_1/\mu_2 = 3$. $\mu_1 = 0.34 \pm 0.03\ \mu_B$ for both patterns shown in Figs. 1(a) and 1(b). We cannot distinguish which one of these two patterns is more realistic. It is because the superlattice intensities, which provide information to distinguish these patterns, cannot be obtained precisely for the reasons that μ_2 is small and that contributions from the Na ordering are superposed on the reflections.

The close relationship between the ordering patterns of the Co moments with that of the Na atoms indicates that for the determination of the electronic structures and the magnetic moments of Co atoms, Na atoms seem to have an important role: Chains $Co^{3.5+\delta}$ and $Co^{3.5-\delta}$ exist alternatingly within the CoO_2 plane and one of the crystallographically distinct sites of Na ions (Na1) is located above or below the center of gravity of the Co triangles formed $Co^{3.5+\delta}$ and $Co^{3.5-\delta}$. Another one of the sites (Na2) is located above or below the Co sites of the $Co^{3.5-\delta}$ chain in an alternating way (see Fig. 1(c)).

Results of neutron scattering studies on $Na_{0.82}CoO_2$[4)] and $Na_{0.75}CoO_2$[5,6)] have pointed out followings. The in-plane and inter plane spin correlation is ferromagnetic and antiferromagnetic, respectively, and the spins are along the c-axis. The inter plane exchange interaction of the samples with $x > 0.7$ is comparable with that of in-plane one, resulting in the three dimensional nature of the spins system. The origin of this three dimensional nature has been argued by considering the inter plane Co-Co interaction via Na sites (the sp^2 hybridized orbit).[7)] We expect that for $Co^{3.5+\delta}$ sites, which do not have Na ions above or below their sites, the exchange interaction is two dimensional-like. On the other hand, spins at $Co^{3.5-\delta}$ sites, which have Na ions above or below their sites, it is three dimensional-like.

The present results present important information on the electronic nature of Na_xCoO_2 and provide detailed clues to understand what things are occurring in the system and hydrated superconductor.

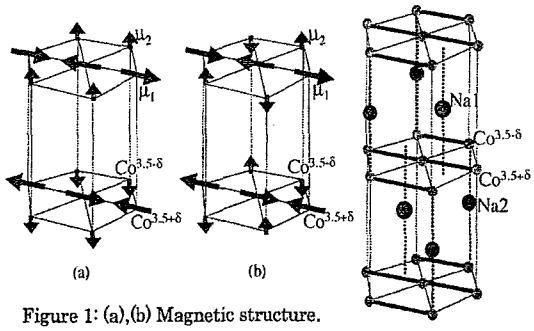

Figure 1: (a),(b) Magnetic structure.
(c) Crystallographic structure.

References

1) M. L. Foo *et al.*: Phys. Rev. Lett. **92** (2004) 247001.
2) K. Takada *et al.*: Nature **422** (2003) 53.
3) M. Yokoi *et al.*: cond-mat/0506220.
4) S. P. Bayrakci *et al.*: Phys. Rev. Lett. **94** (2005) 157205.
5) A. T. Boothroyd *et al.*: Phys. Rev. Lett. **92** (2004) 197201.
6) L. M. Helme *et al.*: Phys. Rev. Lett. **94** (2005) 157206.
7) M. D. Johannes *et al.*: cond-mat/0412663.

原子炉：JRR-3　　装置：TAS-2(T2-4)　　分野：中性子散乱（磁性）

研究テーマ $ZnMn_2O_4$ の中性子回折
表題 $ZnMn_2O_4$ の中性子回折

29) Neutron Scattering Study on $ZnMn_2O_4$

T. Arai, K. Kamazawa, and Y. Tsunoda

Dept. of Appl. Phys., School of Science and Enginnering, Waseda Univ, 3-4-1 Ohkubo, Shinjuku-ku, Tokyo 169-8555, Japan

$ZnMn_2O_4$ has a normal spinel structure. The magnetic Mn^{3+} ions in the B-sites form the network of corner sharing tetrahedra. Although $ZnMn_2O_4$ has considered to be an antiferromagnetic material from the magnetic susceptibility date, details have not been clarified. The Néel temperature of $ZnMn_2O_4$ reported by previous authors is conflicting. [1], [2], [3] Thus, the magnetic behavior of $ZnMn_2O_4$ is still not well known.

To clarify the magnetic behavior of $ZnMn_2O_4$ and the Néel temperature, neutron scattering and magnetic susceptibility measurements were done using the powder sample.

Fig.1 shows the temperature dependences of the susceptibility studied for zero-field-cooled and field-cooled samples. In lowering temperature, an anomalous point was observed at 55K. In the heating process, an anomalous point was observed at 65K. In addition, another anomaly was observed at 21K.

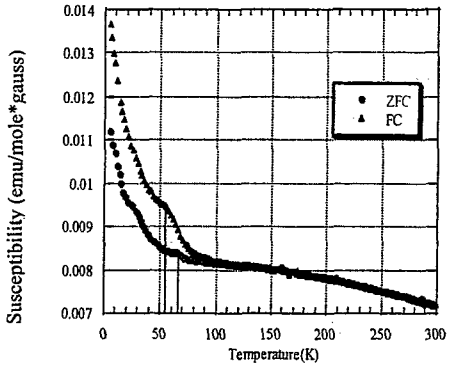

Fig.1: magnetic susceptibility for powder $ZnMn_2O_4$

The neutron diffraction experiment was carried out at 4K and 81K, and magnetic long range order peaks were observed in 4K data. However, peak positions are incommensurate with the lattice periodicity, indicating that the magnetic structure of $ZnMn_2O_4$ is modulated structure. This is consistent with the previous report that $ZnMn_2O_4$ is an antiferromagnetic material.

Fig.2 shows the temperature variation of the magnetic peak. When the temperature is increased, the magnetic peak disappears at around 80K, but the temperature is decreased, the peak appears at around 65K, indicating that the magnetic phase transition is of the first order.

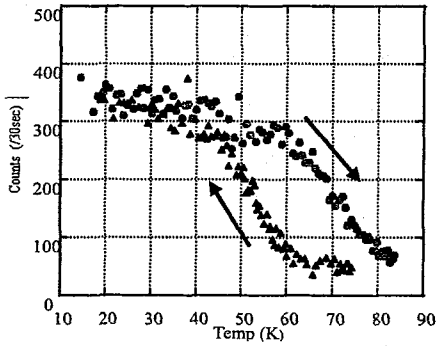

Fig.2 Temperature dependency at $2\theta = 28.26°$

References

[1] Y.Aiyama, J. Phys. Soc. Jpn. 21, 1684(1966)

[2] K.CHHOR, J.F.BOCQUET, C.POMMIER, J. Chem. The 18, 1856(1986)

[3] A.Asbrink, Phys. Rev. B 60, 18(1999)

使用施設 JRR-3M, 装置 HQR(T1-1), 分野 Magnetism

研究テーマ：新超伝導物質 $Na_xCoO_2 \cdot yD_2O$ の磁気励起スペクトル
表　題：中性子非弾性散乱による Na_xCoO_2 における磁気ゆらぎの研究

30) Search for Magnetic Fluctuations in Na_xCoO_2 by Neutron Inelastic Scattering

T. Moyoshi, M. Soda, Y. Yasui, M. Sato and K. Kakurai[1]

Department of Physics, Nagoya University, Chikusa-ku, Nagoya 464-8602
[1]*Advanced Science Research Center, JAERI, Tokai, Ibaraki 319-1195*

In order to investigate the origin of the superconductivity found in $Na_xCoO_2 \cdot yH_2O$(x~0.3, y ~1.3) with triangular lattice of Co atoms,[1] we have been searching for the magnetic excitations of its mother system Na_xCoO_2 by neutron inelastic scattering.

Up to now, we have used three samples of aligned crystals with x = 0.7, 0.6 and 0.3, where the x values were estimated by using the lattice parameter c.[2] Measurements were carried out by using the spectrometer TAS-1 with the triple axis-condition. The [100] and [110] axes of the crystals were set in the scattering plane for x =0.7 and 0.6. For x =0.3, the [100] and [001] axes were oriented in the scattering plane.

In the measurements carried out at 10 K, 30 K and 150 K for $Na_{0.7}CoO_2$, we have not observed magnetic excitation spectra in the l = 0 plane of the reciprocal space. It is because the magnetic correlation is three-dimensional-like and antiferromagnetic between the neighboring CoO_2 planes, as has been experimentally shown for the region of large x.[3-5] The origin of this three dimensional nature has been argued by considering the inter plane Co-Co interaction via the sp^2 hybridized orbit of Na ions.[6]

For $Na_{0.6}CoO_2$, the measurements were also carried out at 6 K, 30 K and 200 K in the l = 0 plane. The results are similar to those of $Na_{0.7}CoO_2$.

For $Na_{0.3}CoO_2$, the measurements were carried out at 1.4 K, 10 K, 100 K and 250 K. The peaks of the inelastic scattering intensity were found at (1,0,l) by the scans along (h,0,l). The examples of the spectra are shown at Fig. 1. We think that the peaks arise from the phonons contribution for following reasons: The intensities of these peaks increase with increasing temperature. Peaks were not obtained at the equivalent point (0,0,l). At this moment, we have not found any clear evidence for magnetic fluctuations. Further experiments are necessary to clarify where in the reciprocal space and how the system exhibits the magnetic fluctuations. The x- and T- dependence of the magnetic susceptibility, NMR Knight shift and NMR relaxation rate studied by our group[7] provide useful information to choose the proper window of the search work.

References

1) K. Takada *et al.*: Nature **422** (2003) 53.
2) M. L. Foo *et al.*: Phys. Rev. Lett. **92** (2004) 247001.
3) S. P. Bayrakci *et al.*: Phys. Rev. Lett. **94** (2005) 157205.
4) A. T. Boothroyd *et al.*: Phys. Rev. Lett. **92** (2004) 197201.
5) L. M. Helme *et al.*: Phys. Rev. Lett. **94** (2005) 157206.
6) M. D. Johannes *et al.*: cond-mat/0412663.
7) M. Yokoi *et al.*: cond-mat/0506220.

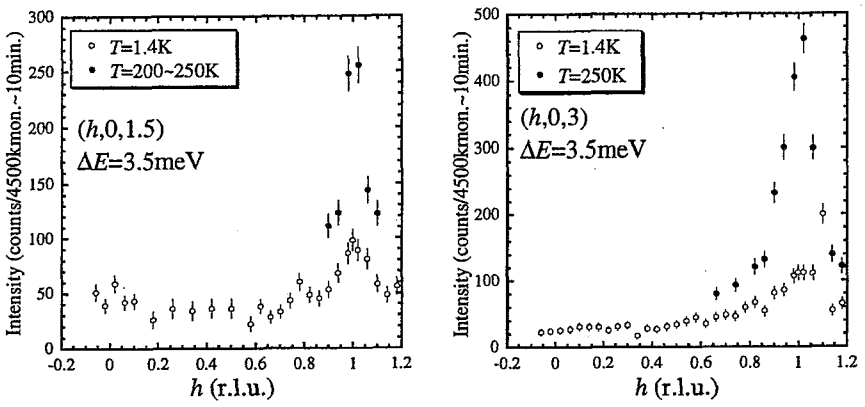

Figure 1: Inelastic scattering intensities measured along (h,0,1.5) and (h,0,3) for $Na_{0.3}CoO_2$.

原子炉：JRR-3　　装置：TAS-1(2G)　　分野：中性子散乱（磁性）

研究テーマ：スピネル型硫化物の特異な異常ホール効果と磁気構造
表題：$Sr_2MnO_{3.5}$の磁気構造

31) Magnetic Structure of $Sr_2MnO_{3.5}$

C. Kato, S. Iikubo, M. Soda, Y. Yasui, M. Sato, K. Kakurai [1] and S. Yoshii[2]

Department of Physics, Division of Material Science, Nagoya University, Furo-cho, Chikusa-ku Nagoya 464-8602, Japan; [1]Advanced Science Research Center, JAERI, Tokai, Ibaraki, 319-1195, Japan; [2]KYOKUGEN, Osaka University, Machikaneyama, Toyonaka, Osaka 560-8531, Japan

$Sr_2MnO_{3.5}$ has the two-dimensional linkage of corner-sharing MnO_5 pyramids derived by regularly reducing the oxygen atoms from the MnO_2 layers of Sr_2MnO_4, which has the well-known layered perovskite structure.[1,2] The oxygen shared by two neighboring pyramids belongs, in one case, to the basal planes of both pyramids, or in another case, to the basal plane of one pyramid and the apex of another one. Due to the existence of these two kinds of the bridging oxygens, it may provide a quite characteristic example of moment systems with two different exchange couplings. Here, magnetic behavior of $Sr_2MnO_{3.5}$ has been studied by measuring the magnetic susceptibility χ, high-field magnetization and specific heat C.[2] The magnetic structure has also been determined by the powder neutron diffraction study, where the data were collected by the triple axis spectrometer T1-1 installed at the guide hall of JRR-3M of JAERI in Tokai.

The obtained magnetic structure is shown at 10 K in Fig. 1, where the arrows indicate the directions of Mn^{3+} moments. (The Neel temperature T_N is 126 K.) It is characterized, as is expected, by the four spin clusters aligned ferromagnetically along the b axis, which are coupled antiferromagnetically to neighboring clusters. The signs of these exchange couplings among the spins are consistent with those obtained by the high temperature expansion of χ (J_1=18.7 K(F) and J_2=–50.9 K(AF)). The inter layer exchange coupling

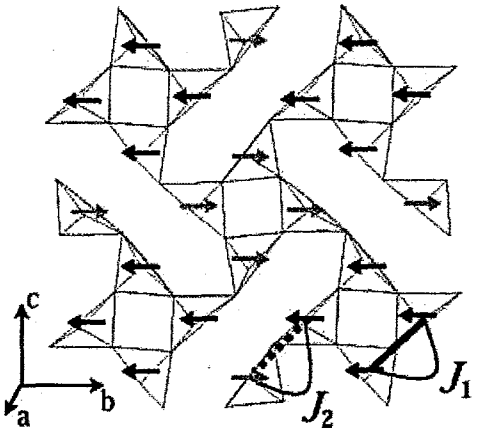

Figure 1: Magnetic structure of $Sr_2MnO_{3.5}$ determined at 10 K. Only one plane is drawn and the arrows indicate the directions of Mn^{3+} moments. The Mn moment at the site shifted by the unit lattice vector a is antiparallel to that at the original site. Thick solid and thick broken lines indicate the two kinds of the exchange interaction between neighboring Mn^{3+} moments, J_1 and J_2, respectively.

is antiferromagnetic so that the unit cell of the magnetic structure at $T<T_N$ is doubled along the a axis. The value of the Mn magnetic moments is estimated to be 3.13 μ_B (±0.05)/Mn. The signs of J_1 and J_2 can be understood by considering the detailed processes of the superexchange interactions between the moments of Mn^{3+} with the 3d electronic configuration of $t_{2g}^3e_g^1$. The magnetic structure is consistent with the picture of interacting clusters, though the ferromagnetic interaction is weaker than the antiferromagnetic one.

References

[1] L. J. Gillie *et al.*: J. Solid State Chem. **167** (2002) 145.
[2] C. Kato *et al.*: J. Phys Soc. Jpn. **74** (2005) 1026.

使用施設：JRR-3M，装置：HQR(T1-1)，分野：磁性

研究テーマ：強磁場中性子回折実験による YbSb での四極子秩序の証明
表　題：YbSb での強磁場中性子回折実験

32) Neutron diffraction under high magnetic fields of YbSb

K. Ohoyama, A. Oyamada[1], K. Kuwahara[2], S. Katano[3], and M. Kohgi[2]

Institute for Materials Research, Tohoku University, Sendai 980-8577
[1] *Graduated School of Human and Environmental Studies, Kyoto University, Kyoto 606-8501*
[2] *Department of Physics, Tokyo Metropolitan University, Tokyo 192-0397*
[3] *Advanced Science Research Center, JAERI, Tokai, Ibaraki 319-1195*

Yb monopnictides, which have the NaCl-type structure, are characterised by the Kondo-like specific heat, large γ value, and suppressed magnetic moments in the antifferomagnetic ordered states [1-3]. Similar characteristics are observed in typical heavy fermion compounds as well; however, it is disputed whether the anomalies in Yb monopnictides are caused by the mixing effect between $4f$ electrons and conduction electrons because Yb monopnictides are semimetals with a carrier concentration of only a few %.

To understand magnetism in Yb monopnictides, we pay notice to antiferroquadrupolar (AFQ) interactions because the first excited quartet in this system shows unexpected splitting which can not be understood under the cubic symmetry. Although the ground state doublet has no degree of freedom on quadrupolar moments, Oyamada *et al.* have theoretically pointed out the possibility of the AFQ ordering in this system. [4]

Thus, aiming at finding evidence of AFQ ordering in Yb monopnictides, we performed neutron diffraction experiments under high magnetic fields to observe quadrupolar moments through the observation of induced magnetic moments. We measured powder patterns of a powder sample of YbSb on the triple axis spectrometer TAS-2 at JRR-3, using the liquid helium free 10T magnet. The data were obtained under the condition of Ei=Ef=14.7meV and the collimation of Guide-40'-S-40'-Open. The powder sample was set in a vanadium cell with a diameter of 10 mm.

In the experiments, we obtained no evidence of AFQ ordering because no additional reflection was observed. We think that the induced magnetic moments are so small even under 10 T that we could not observe it; single crystal samples are indispensable.

However, we observed characteristic field dependence in this experiments. Figure 1 shows the magnetic field dependence of the peak height of the nuclear 200 reflection at 4.2 K. The peak height is constant up to 8 T and increases with increasing magnetic field above 8 T; the magnetic field dependence shows obvious hysteresis. On the other hand, the background level shows different dependence. Figure 2 shows the magnetic field dependence of background at 2θ=18.4° at T=4.1 K. The background decreases rapidly above H=1 T, and decreases slowly above 2 T. Since we have confirmed that the field dependence of the nuclear reflection and background level is reproducible, we can deny the possibility that the field dependence was due to just rotation of particles of the powder sample.

The origin of the field dependence is still an open question. However, since the background level of YbSb was anomalously high though the incoherent scattering cross section of YbSb is not particularly larger than those of the other elements, some kind of distortion which is affected by magnetic field might exist in this sample.

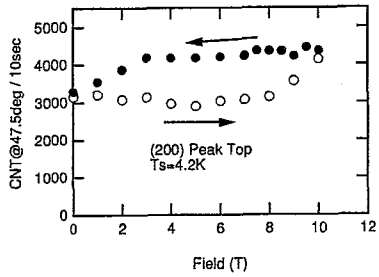

Figure 1: Magnetic field dependence of peak height of the nuclear 200 reflection at 4.2 K up to 10 T. Open and closed circles indicate field increase and decrease processes, respectively.

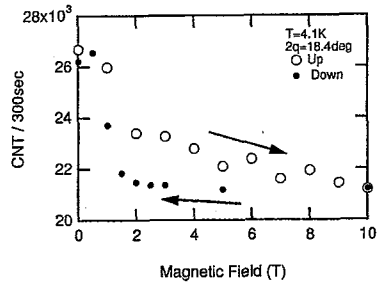

Figure 2: Magnetic field dependence of the back ground level at 2θ=18.4° at 4.1 K.

References

1) A. Oyamada *et al.*: J. Magn. Magn. Matter. 90-91 (1990) 443.
2) T. Sakon *et al.*: J. Phys. Soc. Japan 61 (1992)2209.
3) A. Donni *et al.*: J. Magn. Magn. Matter. 90-91 (1990) 143.
4) A. Oyamada *et al.*: J. Phys. Soc. Japan 73 (2004) 1953.

原子炉：JRR-3　　装置：TAS-2(T2-4)　　分野：中性子散乱（磁性）

研究テーマ：スピネル型硫化物の特異な異常ホール効果と磁気構造
表題：$PrBaCo_2O_5$の磁気・電荷秩序転移

33) Magnetic and Charge-Ordering Transitions of $PrBaCo_2O_5$

M. Soda, Y. Yasui, M. Sato, and K. Kakurai *

*Department of Physics, Division of Material Science, Nagoya University, Furo-cho, Chikusa-ku Nagoya 464-8602, Japan; *Advanced Science Research Center, JAERI, Tokai, Ibaraki, 319-1195, Japan*

For oxygen deficient perovskites $RBaCo_2O_{5+\delta}$ (R=Y and rare earth elements), various kinds of magnetic and charge-ordering transitions have been reported.[1-5] In the ordered states, the value of spin S of Co ions sensitively depends on the ionic radius of R^{3+} and/or the local oxygen arrangement around their sites.[3-5] These results can be understood by considering the crystal field strength at the Co sites.

In the present work, neutron measurements on a single crystal of $PrBaCo_2O_5$, which has the linkage of CoO_5 pyramids, have been carried out by using the triple axis spectrometer T1-1 installed at JRR-3M of JAERI. In this system, transitions to an antiferromagnetic state and to a charge ordered one have been found at T_N~360 K and T_{CO}~255 K, respectively. The magnetic structures have been analyzed at T=300 K and 15 K.

We have observed several superlattice reflections as well as the fundamental ones for the unit cell size of $\sim a_p \times a_p \times 2a_p$, where a_p is the lattice parameter of the pseudo cubic perovskite cell. Because the sample has the $\boldsymbol{a}^*$- and $\boldsymbol{b}^*$-domains, the indices hkl may be khl. The superlattice reflections at $\boldsymbol{Q}=(h/2,h/2,l)$ with odd h, which correspond to the antiferromagnetic order, appear at T_N~360 K with decreasing T. With further decreasing T, another set of peaks at $\boldsymbol{Q}=(h/2,0,l)$ or $(0,h/2,l)$ with odd h appears at T_{CO}~255 K. As is shown later, the latter peaks indicate the existence of two distinct Co sites with different magnetic moments, implying that the charge ordering takes place at T_{CO}.

At 300 K, the chemical unit cell with the size of $\sim a_p \times a_p \times 2a_p$ (space group; P*mmm*) is used in the analysis, where the G-type antiferromagnetic structure is found to be realized. (At this temperature, the white and gray pyramids in Fig. 1 are crystallographically equivalent.) The Co moment μ is within the ab plane and μ=2.28±0.05 μ_B for each $Co^{2.5+}$. Because the lattice parameters a and b are very close to each other, we cannot determine its direction within the ab plane due to the domain distribution.

At 15 K, we use the space group P*mma*, where the chemical unit cell is doubled along a, as shown in Fig. 1 by the white and gray pyramids. Because the magnetic reflections, which appear at T_N with decreasing T, do not exhibit any anomalies at T_{CO}, we consider that the G-type magnetic structure is basically preserved below T_{CO}, though the magnitudes of μ at the distinct sites may not be equal.

If the magnitudes μ of the Co moments in the white and gray pyramids in Fig. 1 are equal, the h/200 and 0h/20 magnetic reflections with odd h are forbidden for the G-type magnetic structure. Even if the moments at these distinct sites are not equal, the magnetic reflections do not exist, if the moment-directions are along b. It is also noted that the h/200 and 0h/20 nuclear reflections with odd h are forbidden for P*mma*. In the actual experiments, we have observed the 1/200 (01/20) and 3/200 (03/20) reflections below T_{CO}, which indicates that the moments are not along the b-axis within the present model. If there exist the μ components along a which are different between two distinct Co sites, we

使用施設：JRR-3M，装置：HQR(T1-1)，分野：磁性

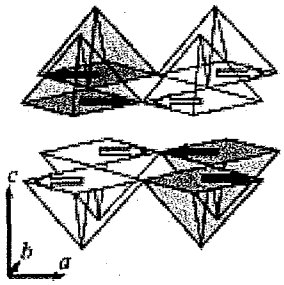

Figure 1: Magnetic structure of $PrBaCo_2O_5$ at 15 K. The Co moments indicated by the white and black arrows have different magnitudes. It is obtained with the assumption that the directions of the Co moments are parallel or anti-parallel to [100]. See the text for details.

have the uniform(ferromagnetic) component parallel to *a* within an *ac* plane, whose direction is reversed in the alternating way along the *b* direction. Then, the 0*h*/20 reflections with odd *h* are expected.

The fitting has been carried out first by using the G-type magnetic structure with the Co moments parallel or anti-parallel to the *a*-axis and with the μ values at the two distinct sites as the fitting parameters. The crystal structure has also been optimized simultaneously. In Table I, the observed and the calculated values of the intensities are compared, where the agreement is reasonably well, indicating that the present model used in the fitting is appropriate. We have found in the present fittings that the white and gray pyramids expand and contract, respectively, when *T* is lowered through T_{CO}. It indicates that the charge ordering really exists at low temperatures.

It is not easy to determine the angle between μ and the *a*-axis, because the fitting is equally well, if only the angle is between 0 and ~50°. There exists a correlation of the angle with the difference of the moment values between two distinct Co sites. If μ is parallel or anti-parallel to [100], the magnitudes μ of two distinct sites are 2.87±0.03 μ_B and 2.65±0.02 μ_B, respectively, while for μ parallel or anti-parallel to [110], they are 2.99±0.05 μ_B and 2.65±0.04 μ_B, respectively. Similar results were reported for $NdBaCo_2O_5$.[4] These values found here are larger than the corresponding values for $NdBaCo_2O_5$. The difference between these aligned moments is significantly smaller than the difference expected between those of Co^{3+} and Co^{2+}. Then, the time- or spatially-averaged valences of Co ions at the distinct sites cannot be considered to be +3 and +2. The small difference of the moments observed here between the distinct sites indicates that the real charge difference between the sites may not be unity. This result does not change even when the moment direction is varied in the region between [100] and [110]. The μ values suggest that Co ions are almost in the HS state (S=2 for ideal Co^{3+} ions; S=3/2 for ideal Co^{2+} ions), because the magnetic moments of the intermediate spin state are expected to be smaller than the observed values. It is consistent with the consideration of the crystal field strength at the Co ion sites.

Table I: The observed integrated intensities of the superlattice reflections are compared with the calculated values for the spin structure shown in Fig. 1.

T = 15 K

h k l	I_{obs}	I_{cal}*
1/2 1/2 1	14952±7936	16151
1/2 1/2 2	85±42	178
1/2 1/2 3	7544±1792	6546
1/2 1/2 4	217±58	218
3/2 3/2 1	2504±392	2277
1/2 0 0 / 0 1/2 0	37±14	44 (0+44)
3/2 0 0 / 0 3/2 0	11±8	18 (0+18)
1/2 0 1 / 0 1/2 1	118±32	101 (40+61)
1/2 0 2 / 0 1/2 2	246±90	136 (98+38)
1/2 0 3 / 0 1/2 3	107±34	176 (38+138)
3/2 0 1 / 0 3/2 1	103±16	51 (34+17)
3/2 0 2 / 0 3/2 2	167±30	230 (206+24)
3/2 0 3 / 0 3/2 3	66±14	71 (1+70)

**hkl* ($h \neq 0$): Reflection are magnetic.
**h0l* or 0*kl*: The total (nuclear + magnetic) intensities are shown.

References

[1] A. Maignan *et al.*: J. Solid State Chem. **142** (1999) 247.
[2] D. Akahoshi and Y. Ueda: J. Solid State Chem. **156** (2001) 355.
[3] M. Soda *et al.*: J. Phys. Soc. Jpn. **72** (2003) 1729.
[4] M. Soda *et al.*: J. Phys. Soc. Jpn. **73** (2004) 464.
[5] M. Soda *et al.*: J. Phys. Soc. Jpn. **73** (2004) 2857.

研究テーマ：高磁場中性子回折実験による希土類化合物 RB_2C_2 での四極子秩序の観測
表　題：反強四極子秩序化合物 DyB_2C_2 の磁場下での磁気構造

34) Magnetic Structures under magnetic fields of the antiferroquadrupolar ordering compound DyB_2C_2

K. Ohoyama, A. Tobo[1], H. Onodera[1], S. Katano[2]

Institute for Materials Research, Tohoku University, Sendai 980-8577
[2] *Fac. of Science, Tohoku University, Sendai 980-8578*
[2]*Advanced Science Research Center, JAERI, Tokai, Ibaraki 319-1195*

The RB_2C_2 (R=rare earth) compounds, which have the tetragonal LaB_2C_2 type structure [1,2], show diversified magnetic properties caused by coexistence of antiferroquadrupolar (AFQ) and antiferromagnetic (AFM) interactions. In particular, DyB_2C_2 is the first tetragonal rare earth compound in which an AFQ ordering is realised [3]. Since the exact ground state by crystalline field under tetragonal symmetry has no degree of freedom on electric quadrupolar moments, it was thought that no AFQ ordering can be realised in the tetragonal rare earth compounds before the finding of the AFQ ordering in DyB_2C_2. Thus, to understand necessary conditions of AFQ orderings in rare earth compounds, it is indispensable to clarify characters of the AFQ ordering in DyB_2C_2.

DyB_2C_2 undergoes an AFQ ordering at T_Q=24.7 K and an AFM ordering at T_N=15.3 K [3,4]. Under magnetic fields along the [110] direction, three field induced transitions occur at H~2.2 T, 3.2 T, and 13 T at T=5 K; each phase has been named phase III, III', and II' in ref. 4. The magnetic structure in phase III is a characteristic 90° structure in which the adjacent magnetic moments along the c-axis are nearly perpendicular; this structure requires four propagation vectors: k_1=(1,0,0), k_2=(0,1,1/2), k_3=(0,0,0), and k_4=(0,0,1/2) [3,5]. This 90° structure can not be understood by the simple exchange interaction.

To understand characters of AFQ orderings in each phase of DyB_2C_2, it is dispensable to clarify the magnetic structures because the magnetic structure strongly reflects the alignment of quadrupolar moments through the strong L-S coupling. Therefore, we performed neutron diffraction experiments on a single crystalline sample of DyB_2C_2 under high magnetic fields in phase III' and II' on the triple axis spectrometer, TAS-2, with a 10T liquid-He free superconductivity magnet, installed at JRR-3M in Japan Atomic Energy Research Institute, Tokai.

We observed the magnetic reflections at (0,0,1/2) and (0,0,1/4) under several magnetic fields along the [1$\bar{1}$0] direction at T=5.4 K. The magnetic field dependence of the integrated intensity of the two reflections are plotted in Fig.1. Applying magnetic field , we observed decrescence of the (0,0,1/2) reflection in the phase III' (2.25 T$\leq H \leq$3.25 T), while the (0,0,1/4) reflection develops only in phase III'. This result indicates that the magnetic unit cell of phase III' and phase II' are $a \times a \times 4c$ and $a \times a \times 2c$, respectively, where a and c are the lattice constants.

Base on the present results and magnetisation measurements, we discuss change of the magnetic structures. Under magnetic field along the [110] direction, in phase III ($H \leq$2.25 T), two of the four magnetic moments at the face centre position of the c-plane in a region of $a \times a \times 4c$ has an antiparallel component against the magnetic field (see fig 4 of ref. 5), which are not advantageous to the Zeeman effect. In phase III' (2.25 T$\leq H \leq$3.25 T), only one of the two magnetic moments which have antiparallel components flips by the Zeeman effect, while the other one of the two still holds the antiparallel component; consequently this flip makes the magnetic unit cell $a \times a \times 4c$ in Phase III' from $a \times a \times 2c$ in phase III. In phase II' ($H \geq$ 2.35 T), the other magnetic moment flips by the Zeeman effect as well; the magnetic unit cell becomes $a \times a \times 2c$. Note that the characteristic 90° relation along the c-axis observed under zero magnetic field still remains even in phase III' and phase II' in this model. This model well represents the change of the magnetisation at the boundaries of the phases.

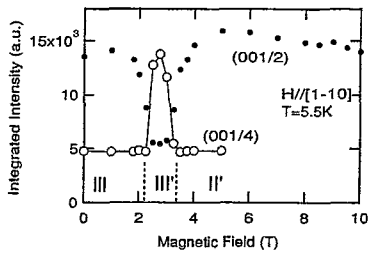

Figure 1: Magnetic field dependence of the integrated intensity of the (0,0,1/2) (closed circles) and (0,0,1/4) (open circles) magnetic reflections. at T=5.4 K~5.5 K. III, III and II' are the name of each phase in ref. 4.

References

1) T. Onimaru *et al.*, J. Phys. Soc. Jpn. **68** (1999) 2287.
2) K. Kaneko *et al.*,J. Phys. Soc. Jpn. **69** (2000) 3762.
3) H. Yamauchi *et al.*, J. Phys. Soc. Jpn. **68** (1999) 2057.
4) K. Indoh *et al.*, J. Phys. Soc. Jpn. **73** (2004) 669.
5) K. Ohoyama *et al.*, J. Phys. Soc. Jpn. **69** (2000) 3401.

原子炉：JRR-3　　装置：TAS-2(T2-4)　　分野：中性子散乱（磁性）

研究テーマ Z 型六方晶フェライトの磁気構造解析
表題 :希土類置換型 Co_2Z 型フェライト電磁波吸収特性と磁気構造との相関の調査

35) Improvement of permeability of Co_2Z-type hexaferrite by addition of rare earth –Magnetic structure analyses by neutron diffraction–

Y. Takada, T. Nakagawa, Y. Fukuta, T. A. Yamamoto, *T. Tachibana and **S. Kawano

*Department of Nuclear Engineering, Osaka University, 2-1 Yamadaoka, Suita, Osaka 565-0871, Japan; *Sumitomo Special Metals Co., Ltd., 2-15-17 Egawa, Shimamoto-cho, Mishima-gun, Osaka 618-0013, Japan; **Kyoto University Research Reactor Institute, Noda, Kumatori-cho, Sennan-gun, Osaka 590-0494, Japan*

Co_2Z-type ferrite $Ba_3Co_2Fe_{24}O_{41}$ belongs to the family called "*ferroxplana*", in which the easy magnetization direction lies in the basal plane (*c*-plane) of the hexagonal structure. Therefore this material maintains a high permeability even in the UHF region (from 300 MHz to 3 GHz), and is regarded as a promising candidate material for shielding electromagnetic noise in this region.

Traditionally, the formation of Co_2Z-type ferrite involves in high temperature up to 1573 K due to its complicated structure [1]. In an attempt to promote the formation of Co_2Z-type ferrite at a low temperature, we tried to incorporate Cu^{2+}, an effective constituent for lowering the sintering temperature. We substituted Cu^{2+} not for Co^{2+} but for Fe^{3+} because the Z-type structure has an easy magnetization direction parallel to the *c*-plane only when Me = Co in $Ba_3Me_2Fe_{24}O_{41}$ (Co_2Z-type). Furthermore, we substituted Nd^{3+} (magnetic ion) for Ba^{2+} (non-magnetic ion) for the charge compensation of the substitution of Cu^{2+} for Fe^{3+} and the enhancement of saturation magnetization.

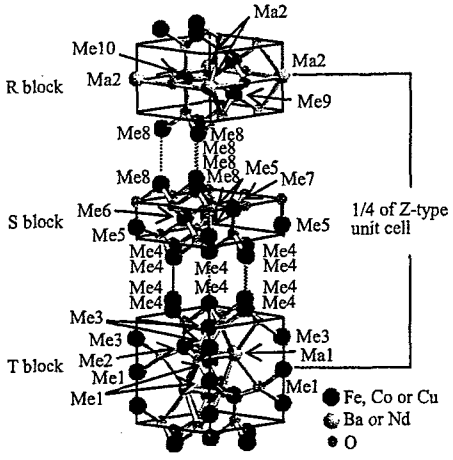

Figure 1. Metal Sites in the Co_2Z-type Ferrite.

The permeability of Z-type hexaferrite is represented as $I_S/3H_p$, where I_S saturation magnetization and H_p anisotropic field in the direction parallel to *c*-plane [2]. Therefore enhancement of M_S in $Ba_{3-x}Nd_xCo_2Fe_{24-x}Cu_xO_{41}$ may lead to improvement of permeability.

To understand the correlation between the permeability and the crystal and magnetic structures particularly in terms of magnetic ions, and to acquire a guideline for designing a further advanced material, we investigated the distributions of magnetic ions in the present Co_2Z-type ferrite crystal as shown in Figure 1 and the orientations of magnetic moments by applying the neutron diffraction technique and the Rietveld analyses.

The powder samples of $Ba_{3-x}Nd_xCo_2Fe_{24-x}Cu_xO_{41}$ (x = 0.1, 0.2, 0.4) were prepared by conventional solid-state reaction method with high-purity $BaCO_3$, Nd_2O_3, Co_2O_3, Fe_2O_3 and CuO powders as starting materials. The mixtures were sintered at 1523 K for 16 hours in air.

We performed neutron diffraction experiments on HERMES (T1-3), of IMR, Tohoku University, installed at the JRR-3M reactor in JAERI, Tokai [3]. Neutrons with a wavelength 1.820 Å were obtained by the 331 reflection of the Ge monochrometer

使用施設 JRR-3M, 装置 HERMES(T1-3), 分野 Magnetism

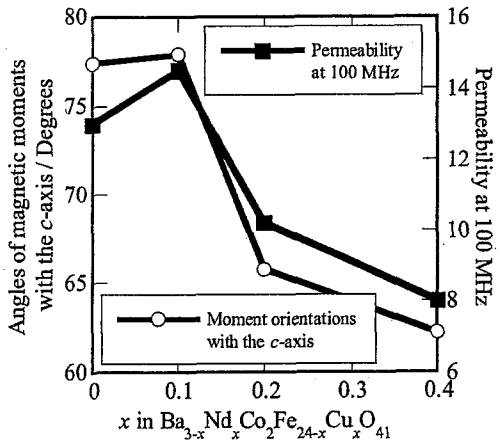

Figure 2. Dependence of Permeabilities at 100 MHz and Orientation of Magnetic Moments with The *c*-axis on *x*.

and 12'-blank-sample-22' collimation. The powder samples were sealed in a vanadium cylinder of 10 mm diameter. The diffraction angle 2θ was swept in a range 3–153° at an interval of 0.1°.

Table 1 shows site distributions of metal ions in the present Co_2Z-type ferrites. Co and Cu atoms were located on particular 5 sites, Me2, 4, 5, 8 and 10. Nd atoms occupied only in Ma1 site in the material with the composition of $x = 0.1$, and both Ma1 and 2 sites in the material with the composition of $x = 0.2$ and 0.4. Calculated saturation magnetizations from the magnetic structure obtained from the present neutron diffraction analyses were consistent with the measured ones. The material of $x = 0.1$ shows the lowest value of maturation magnetization, but the highest value of permeability. Therefore the behavior of permeability is not responsible for that of saturation magnetization.

Figure 2 shows the dependence of the permeabilities at 100 MHz and the orientation of magnetic moments with the *c*-axis on *x*. Higher angles of magnetic moments with the *c*-axis result in lower anisotropic field in the direction parallel to *c*-plane. These results indicate that the behavior of permeability is responsible for the moment orientation.

References

[1] T. Tachibana et al., J. Magn. & Magn. Mater. **262** (2003) 248.

[2] J. Smit and H. P. J. Wijn: *Ferrites*, Phlips Technical Library, Eindhoven (1959) p. 257.

[3] K. Ohyama et al., Jpn. J. Appl. Phys. **37** (1998) 3319.

Table 1. Occupation Number of Metal Ions in Each Crystal of $Ba_{3-x}Nd_xCo_2Fe_{24-x}Cu_xO_{41}$

Sites	W.L.	$x = 0$			$x = 0.1$			$x = 0.2$			$x = 0.4$		
		Fe	Co	Cu	Fe	Co	Cu	Fe	Co	Cu	Fe	Co	Cu
Me1	2*a*	0.69	0.31	0	1	0	0	1	0	0	1	0	0
Me2	4*f*	2	0	0	1.93	0.06	0.01	1.76	0.23	0.01	1.77	0.21	0.02
Me3	4*e*	2	0	0	2	0	0	2	0	0	2	0	0
Me4	12*k*	5.05	0.95	0	4.95	1.02	0.03	5.28	0.65	0.07	4.90	0.91	0.19
Me5	4*e*	1.76	0.24	0	1.88	0.11	0.01	1.92	0.07	0.01	1.64	0.26	0.10
Me6	4*f*	2	0	0	2	0	0	2	0	0	2	0	0
Me7	4*f*	2	0	0	2	0	0	2	0	0	2	0	0
Me8	12*k*	5.72	0.28	0	5.43	0.54	0.03	5.07	0.83	0.10	5.61	0.32	0.07
Me9	4*f*	2	0	0	2	0	0	2	0	0	2	0	0
Me10	2*d*	0.78	0.22	0	0.72	0.27	0.01	0.77	0.22	0.01	0.69	0.29	0.02
		Ba	Nd		Ba	Nd		Ba	Nd		Ba	Nd	
Ma1	4*f*	2	0		1.9	0.1		1.92	0.08		1.88	0.12	
Ma2	2*d*	1	0		1	0		0.88	0.12		0.72	0.28	

研究テーマ：中性子回折によるZ型Baフェライトの磁気構造とその温度依存性の研究
表　題：高温中性子回折によって評価したCo_2Z型六方晶フェライト$(Ba,Sr)_3Co_2Fe_{24}O_{41}$の磁気モーメント方位の温度依存性

36) **Temperature dependence of magnetic moment orientation in Co_2Z-type hexaferrite $(Ba,Sr)_3Co_2Fe_{24}O_{41}$ estimated by high-temperature neutron diffraction**

Y. Takada, T. Nakagawa, Y. Fukuta, M. Tokunaga, T. Tanaka, T. A. Yamamoto, T. Tachibana[1], S. Kawano[2], Y. Ishii[3] and N. Igawa[3]

Graduate School of Engineering, Osaka University, 2-1 Yamadaoka, Suita, Osaka 565-0871
[1]*NEOMAX Co. Ltd., 2-15-17 Egawa, Shimamoto-cho, Mishima-gun, Osaka 618-0003*
[2]*Kyoto University Research Reactor Institute, Noda, Kumatori-cho, Sennan-gun, Osaka 590-0494*
[3]*Neutron Science Research Center, JAERI, Tokai, Ibaraki 319-1195*

1 1. Introduction

Co_2Z-type ferrite $Ba_3Co_2Fe_{24}O_{41}$ with hexagonal structure belongs to a family called *ferroxplana*, in which the easy magnetization direction lies in the basal plane (c-plane) of the hexagonal structure[1]. Therefore this material maintains a high permeability even in the UHF (from 300 MHz to 3 GHz) region and is regarded as a candidate for electromagnetic noise absorbent material in this region. We previously found that, when the temperature was risen from 523 to 573 K, the magnetic moments in $Ba_3Co_{1.8}Fe_{24.2}O_{41}$ turned to the c-axis from a direction parallel to the c-plane[2]. In our present work, the temperature dependence of magnetic moment orientations in $Ba_3Co_2Fe_{24}O_{41}$ (Ba_3Z), $Ba_{1.5}Sr_{1.5}Co_2Fe_{24}O_{41}$ ($Ba_{1.5}Sr_{1.5}Z$) and $Sr_3Co_2Fe_{24}O_{41}$ (Sr_3Z) and the effect of substitution of Sr for Ba on magnetic structure were investigated by high-temperature neutron diffraction.

2 Experimental

Powder samples of Ba_3Z, $Ba_{1.5}Sr_{1.5}Z$ and Sr_3Z were prepared by the conventional ceramic method. Sintering conditions were as follows; [Ba_3Z: T = 1573 K and P_{O2} = 61.3 kPa], [$Ba_{1.5}Sr_{1.5}Z$: T = 1523 K and P_{O2} = 101.3 kPa] and [Sr_3Z: T = 1483 K and P_{O2} = 21.3 kPa].

High-temperature neutron diffraction patterns of the samples were obtained using HRPD installed at JRR-3 in JAERI. Neutron wavelength was 1.823 Å, monochromized by the Ge(331) reflection. The powder samples were cast in a vanadium folder with 15 mm in diameter. Diffraction patterns in the range of 2θ = 2.5 - 162.5° were measured at different temperatures lower than 773 K in high vacuum. Angle step was 0.05° and the duration time at each step was 390 sec.

3 Results and Discussion

Figure 1 shows the temperature dependence of angles of magnetic moments against c-axis of Ba_3Z, $Ba_{1.5}Sr_{1.5}Z$ and Sr_3Z determined from the Rietveld analyses for the present neutron diffraction patterns. The magnetic moments in Ba_3Z and $Ba_{1.5}Sr_{1.5}Z$ mostly lie in the c-plane at room temperature and turn significantly from the direction parallel to the c-plane to the c-axis in the temperature region from 523 to 573 K. On the other hand, the magnetic moments in Sr_3Z deviate from the c-plane at room temperature and turns in the region from 473 to 523 K. These results indicate that the substitution of Sr for all of Ba in $Ba_3Co_2Fe_{24}O_{41}$ induces drastic change in magnetic anisotropy. And these changes in average orientation of the magnetic moments must be induced by the disappearance of the contribution of cobalt to magnetism in each temperature range.

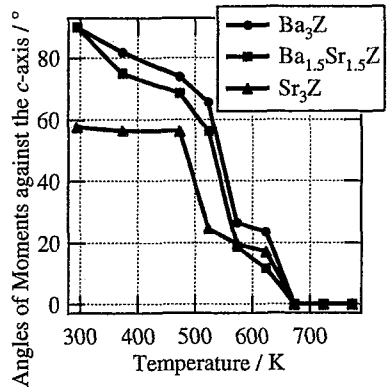

Figure 1: Temperature dependence of angles of magnetic moments against c-axis of Ba_3Z, $Ba_{1.5}Sr_{1.5}Z$ and Sr_3Z.

References

1) J. Smit and H. P. J. Wijn: *Ferrites*, ed. N. V. Philips (Phlips Technical Library, Eindhoven, 1959) p. 257.
2) Y. Takada, T. Nakagawa, Y. Fukuta, M. Tokunaga, T. A. Yamamoto, T. Tachibana, S. Kawano, N. Igawa and Y. Ishii: Jpn. J. Appl. Phys. Vol. 44 No. 5A (2005) 3151.

原子炉：JRR-3　　装置：HRPD(1G)　　分野：中性子散乱（磁性）

研究テーマ:強磁性と反強磁性スピン相関が競合する系の磁性
表題:MnCu スピングラス合金の中性子散乱

37) Spin-Glass Like Behavior of the MnCu Alloy

M. Yanagida and Y. Tsunoda

School of science and engineering, Waseda University,
Okubo 3-4-1, Shinjuku-ku, Tokyo 169-8555, Japan

The ordered Mn_3Pt alloy has an $L1_2$-type (Cu_3Au) structure, in which the corner and the face center are occupied by Pt and Mn, respectively. Then, Mn atoms at the face center positions construct an octahedral structure, which is composed of eight equilateral triangles. Thus, Mn_3Pt alloy is a geometrical spin frustration system. Recent neutron scattering data show that the introduction of the randomness to Mn_3Pt alloy induces the spin-glass like behavior.

MnCu alloy with low Mn concentration is well known as a typical spin-glass alloy which is stabilized through the RKKY interaction. In Mn-rich MnCu alloy, however, T_N rapidly decreases as Cu concentration increases. We supposed that this is induced by the geometrical spin frustration due to the octahedral anti-ferromagnet identical with Mn_3Pt alloy.

To investigate the spin-glass like behavior of MnCu alloy, we carried out the neutron scattering experiments on a single crystal specimen of MnCu alloy with Mn concentration of 75at.% at the T1-1 triple axis spectrometer, JRR-3M in JAERI (Tokai).

Fig. 1 shows the intensity contour map of elastic scattering on the (001) scattering plane obtained at room temperature. The peaks at 1 0.5 0 and 1 1 0 RLPs are the same ones as observed with Mn concentration of 50at.% and above 85at.%, respectively, indicating the inhomogeneous distribution of Mn concentration within the specimen. However, the diffuse scattering extends along the first brillouin zone boundary of fcc structure. These data suggest the spin frustration of MnCu alloy.

Fig. 2 shows the energy spectrum obtained at 1 0 0 RLP at room temperature. It shows that the strong inelasticity remains at high energy region together with the quasi-elastic scattering. The result is similar to that of Mn_3Pt alloy with randomness. Therefore it would be argued that causes of the spin-glass of MnCu alloy come from the frustration in the octahedral anti-ferromagnet and the randomness of the atomic arrangement.

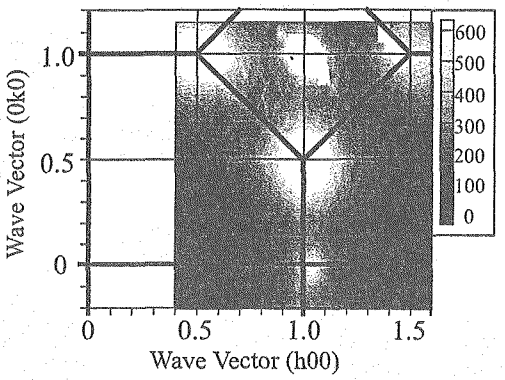

Figure 1: Intensity contour map of elastic scattering on the (001) scattering plane obtained at room temperature. Solid lines represent the first brillouin zone boundary of fcc structure.

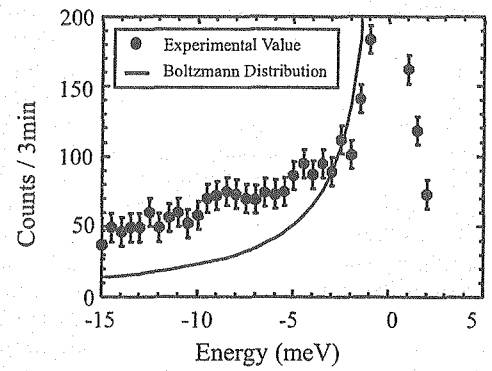

Figure 2: Energy spectrum obtained at 1 0 0 RLP at room temperature. Solid line represents the Boltzmann distribution normalized at -3meV.

使用施設:JRR-3M, 装置:HQR (T1-1), 分野 Magnetism

研究テーマ：高圧・低温における Ce 化合物強相関伝導系における特異な磁気相
表　題：重い電子系 $Ce_3Ir_4Sn_{13}$ の磁気秩序

38) Magnetic Order of the Heavy-Fermion System $Ce_3Ir_4Sn_{13}$

M. Kohgi, C. Nagoshi, T. Osakabe[1] and N. Metoki[1]

Department of Physics, Tokyo Metropolitan University, Tokyo 192-0397
[1]*Advanced Science Research Center, JAERI, Tokai, Ibaraki 319-1195*

$R_3T_4X_{13}$ (R=rare earthes, T=Rh, Ir, Pt, X=Sn, In) has a cubic structure with the space group of $Pm\bar{3}n$[1], in which nearest neighbor R atoms form one-dimensional straight chains along x, y, and z directions. On the other hand, second nearest neighbor R atoms form equilateral triangles which connect the three orthogonal chains. Therefore, this system potentially involves one-dimensionality as well as frustration with respect to the magnetic interaction. Due to these features, possible magnetic structures in the commpounds are such ones that are composed of three interpenetrating sub-structures formed by R atoms in the chains with same directions (along x, y, and z directions, respectively). The sub-structures are magnetically identical and independent together due to the unique crystal structure. So far, magnetic structures were determined only for $Eu_3Ir_4Sn_{13}$ and $Gd_3Ir_4Sn_{13}$ by our neutron diffraction experiments.[2] The magnetic structures are determined as the ones with three sub-structures in which the magnetic moments of the R atoms in a chain couple together antiferromagnetically and couple antiferromagnetically or ferromagnetically with those in the nearest parallel chains for $Eu_3Ir_4Sn_{13}$ and $Gd_3Ir_4Sn_{13}$, respectively. This fact clearly indicates the importance of the one-dimensionality and the frustrated interactions in the compounds. The long range orders result from the finite inter-chain interaction though the distance between chains is around 9.7 Å.

Among many $R_3T_4X_{13}$ compounds, $Ce_3Ir_4Sn_{13}$[3,4] and $Ce_3Pt_4In_{13}$[5] are especially interesting because they were reported to show heavy-fermion behaviors in their transport and thermal properties; for example, they show large T-liner specific heat coefficients of ~1000 and 670 mJ/K^2/mol, respectively. They show also evidences for antiferromagnetic ordering at low temperatures below 1 K and 0.6 K with rather small entropies of 0.3Rln2 and 0.2Rln2 at the ordering temperatures, respectively. Since, one-dimensionality as well as frustration in the magnetic interactions as mentioned above may give similar thermal properties at low temperatures as those caused by the Kondo effect, careful studies from the microscopic point of view are necessary to clarify the origin of the heavy-fermion properties of these compounds. In the present work, we synthesized single crystals of $Ce_3Ir_4Sn_{13}$, and tried to get information on the magnetic order of this compound below about 0.6 K.

A neutron diffraction experiment was carried out on the TAS-2 spectrometer installed at JRR-3. A single crystal sample of $Ce_3Ir_4Sn_{13}$ with the size of $2.5\times3\times3$ mm^3 was set in the cryostat equipped with a ^{3}He-^{4}He dilution refrigerator with the [1 $\bar{1}$ 0] axis vertical. We searched for magnetic peaks at 0.02 K around reciprocal lattice points such as (0 0 1). (1 1 0) or (1 1 1). However, no trace of magnetic Bragg scattering was observed for q-vectors along the axes [0 0 1], [1 1 0], [1 1 1] and [1 1 2] within experimental errors. For examples, the scans around (1/2,1/2,1) and (1,1,1) reciprocal lattice points are shown in Fig. 1. The absence of magnetic peak indicates that the ordered moment value of $Ce_3Ir_4Sn_{13}$, if exists, is below the sensitivity of the present experiment. From the counting statistics of the data shown in Fig. 1, the upper limit of the moment value is well below 0.3 μ_B in the case of the magnetic structure which is same as either of those of $Eu_3Ir_4Sn_{13}$ and $Gd_3Ir_4Sn_{13}$ which are the most probable ones due to the unique crystal structure. Since $Ce_3Ir_4Sn_{13}$ shows well-defined crystal field excitations[2], the present result indicates that the ordered moment is strongly reduced due to some reasons. The Kondo effect may be a candidate, however, the effect of the one-dimensionality as well as the frustrated interactions cannot be ruled out.

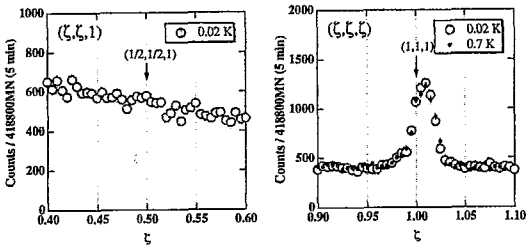

Figure 1: Scans around (1/2,1/2,1) and (1,1,1) where magnetic peaks are observed in the ordered states of $Eu_3Ir_4Sn_{13}$ and $Gd_3Ir_4Sn_{13}$, respectively.

References

1) J. L. Hondeau *et al.*, Solid State Commun 42 (1982) 97.
2) unpublished.
3) H. Sato *et al.*, Physica B 186-188 (1993) 630-632.
4) S. Takayanagi *et al.*, Physica B 199-200 (1994) 49-51.
5) M. F. Hundley *et al.*, Phys. Rev. B, 65 (2001) 024401.

原子炉：JRR-3　　装置：TAS-2(T2-4)　　分野：中性子散乱（磁性）

研究テーマ：金属間化合物 R_7Ni_3 (R = Pr, Nd)の磁気構造
表題：Nd_7Ni_3 の中性子回折

39) Neutron Diffraction Studies on Nd_7Ni_3

T. Tsutaoka, Y. Andoh[1], S. Kawano[2], G. Nakamoto[3], Do Thi Kim Anh[3], and M. Kurisu[3]

Graduate School of Education, Hiroshima University, Hiroshima 739-8524, Japan
[1]*Faculty of Regional Sciences, Tottori University, Tottori 680-8551, Japan*
[2]*Research Reactor Institute, Kyoto University, Osaka 590-0494, Japan*
[3]*Japan Advanced Institute of Science and Technology, Ishikawa 923-1292, Japan*

The rare earth compound Nd_7Ni_3 crystallizes in the hexagonal Th_7Fe_3-type structure with three different crystallographic sites of Nd. The magnetic and specific heat measurements indicate the four magnetically ordered states: (1) antiferromagnetic (A.F.I phase) below T_N =29 K, (2) A.F.II phase below T_t =25 K, (3) ferrimagnetic (Ferri.I) phase below T_C = 11 K and (4) Ferri.II phase below T_R = 7.8 K [1,2]. In the powder and single crystal neutron diffraction measurements, a magnetic satellite with large intensity has been observed at low diffraction angle; the magnetic propagation vector is $\mathbf{Q}_2$ = (0 0 1/3) below T_R and its Q_Z has a drop at T_R and decreases with temperature [3]. Since the intensity of this magnetic satellite has disappeared at T_t, the magnetic structure of the A.F.I phase has not been clear. In this study, we performed precise neutron diffraction measurements using a large Nd_7Ni_3 single crystal to reveal the magnetic structure of the antiferromagnetic phase between T_t and T_N. The neutron diffraction measurements were made using the HQR spectrometer of JRR-3M of JAERI at Tokai.

Figure 1 shows the contour maps of the diffraction intensity in the a^* - c^* reciprocal plane at 23, 26 and 32 K, respectively. We found a small new magnetic reflection which is characterized by $\mathbf{Q}_1$ = (0 0 0.12) at low temperature. The intensity of this reflection is about one tenth as large as that of $\mathbf{Q}_2$ and exists up to T_N as shown in Fig.2. The Q_Z of the magnetic reflection of $\mathbf{Q}_2$ is almost constant up to T_N. This new magnetic reflection indicates that a long period magnetic structure along the c-axis exists in Nd_7Ni_3.

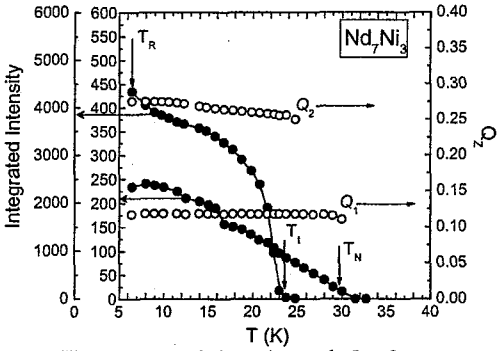

Fig.2 Integrated intensity and Q_Z for two magnetic reflections $\mathbf{Q}_1$ and $\mathbf{Q}_2$ of Nd_7Ni_3 as a function of temperature.

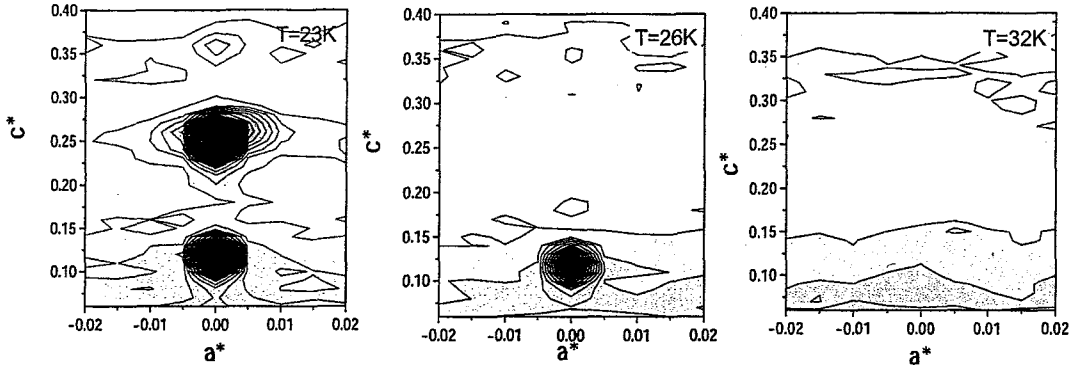

Fig.1 Contour map of the intensity of magnetic reflections in the a^* - c^* plane of Nd_7Ni_3 at T = 23, 26 and 32 K.

References

[1] T. Tsutaoka et al., *J. Magn. Magn. Mat.* **167** (1997) 249.

[2] T. Tsutaoka et al., *J. Phys. Soc. Jpn.* **69** (2001) 1850.

[3] X. Xun et al., *Physica B* **241-243** (1998) 742.

使用施設：JRR-3M，装置：HQR(T1-1)，分野 Magnetism

研究テーマ：集光型偏極中性子小角散乱法による遷移金属ナノ粒子内部の磁気構造の研究
表　題：遷移金属ナノ粒子の集光型偏極中性子小角散乱測定

40) Small-angle polarized neutron scattering experiment of transition metal nano particles in focusing geometry

T. Shinohara, T. Oku[1], J. Suzuki[1], Y. Oba[2], T. Sato[2]

Image Information Research Unit, RIKEN, Wako, Saitama 351-0198
[1]*Advanced Science Research Center, JAERI, Tokai, Ibaraki 319-1195*
[2]*Department of Applied Physics and Physico-Informatics, Keio University, Yokohama, Kanagawa 223-8522*

Magnetic properties of transition metal nano particles are very sensitive to its surface condition, because the electronic structure at the surface of metallic nano particle changes from one in the particle core. For example, 4*d* transition metal Pd shows ferromagnetism in the size of nano particle [1]. This ferromagnetic ordering appears only in the particle surface and rest of particle is paramagnetic. However the detailed magnetic structure inside the Pd nano particle has not been clarified. To study the intraparticle magnetic structure of nano particle, small-angle polarized neutron scattering experiment is most suitable.

Small angle neutron scattering (SANS) measurements were performed in focusing geometry using highly polarized cold neutron beam and superconducting sextupole electromagnet as a magnetic focusing device [2] at C3-1-2-1 (NOP). As the nano particle sample, we selected Ni (average diameter of 20 nm) and Pd (average diameter of 12 nm) nano particle samples. A two-dimensional (2D) neutron detector, consisted of a plate of ZnS(Ag)/^{6}LiF scintillator and a position-sensitive photo multiplier tube [3], was used for neutron detection. Neutron beam was focused on the detector surface plane, and the distance between sample and detector was set to 486 mm. Magnetic field of 0.6 T was applied vertically on the particle sample using electromagnet, which was enough to saturate the sample magnetization. A spin-flipper was followed the neutron focusing device, and the neutron scattering intensity I^- (magnetic field parallel to neutron spin) and I^+ (magnetic field antiparallel to neutron spin) were obtained with spin-flipper on and off.

The 2D neutron scattering images of the difference signal $(I^- - I^+)$ and the sum signal $(I^- + I^+)/2$ are shown in Fig. 1 for Ni nano particles. $(I^- - I^+)$ image clearly demonstrates an anisotropic scattering perpendicular to the direction of applied magnetic field H. This indicates the existence of magnetic scattering. From $Q \perp H$ and $Q \parallel H$ scattering components, we obtained the magnetic-nuclear cross term, $(I^-_{Q\perp H} - I^+_{Q\perp H}) = 2P(1+\epsilon)F_N F_M = B(Q)$, and the nuclear term, $(I^-_{Q\parallel H} + I^+_{Q\parallel H})/2 = F_N^2$. Here P is the polarization of incident neutron beam, ϵ is the efficiency of spin flipper, F_N and F_M are the form factors of nuclear and magnetic scattering [4]. The q dependences of $B(Q)$ and F_N^2 are shown in Fig. 2. And the ratio F_M/F_N was evaluated by $B(Q)$ and F_N^2 (inset of Fig. 2). Assuming that F_M/F_N is constant against the change in q, the magnetic moment per Ni atom is estimated to be 0.38 μ_B. This value is slightly smaller than that of bulk, but is consistent of the results from magnetization measurements. When a nano particle has an intraparticle magnetic structure, such as core-shell structure, F_N and F_M show different q dependence. Therefore, q dependent F_M/F_N should be studied more precisely.

For Pd nano particles, the scattering pattern of $(I^- - I^+)$ demonstrates no anisotropic scattering. The ferromagnetism of Pd nano particle may be disappeared due to gas adsorption.

References

1) T. Shinohara *et al.*: Phys. Rev. Lett. **91** (2003) 197201.
2) A. Tokai *et al.*: J. Phys. Soc. Jpn. **67** (1998) 2000.
3) K. Hirota *et al.*: Phys. Chem. Chem. Phys. **7** (2005) 1836.
4) A. Wiedenmann: J. Appl. Cryst. **33** (2000) 428.

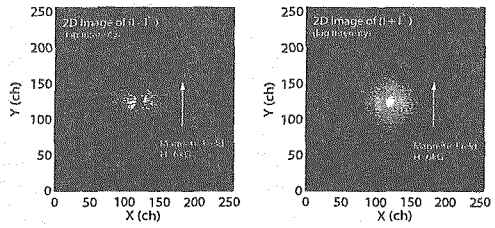

Figure 1: 2D SANS images of Ni nano particles. Left image is difference signal $(I^- - I^+)$ and right is sum signal $(I^- + I^+)/2$.

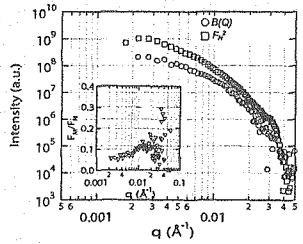

Figure 2: q dependent $B(Q)$ and F_N^2. Inset is q dependent F_M/F_N.

原子炉：JRR-3　　装置：NOP(C3-1-2-1)　　分野：中性子散乱（磁性）

研究テーマ:RPdSn (R = Tb, Dy, Ho, Er)**の磁気構造**
表題: DyPdSn **の中性子回折**

41) Neutron Diffraction Studies on DyPdSn

Y. Andoh, M. Kurisu[1], G. Nakamoto[1], T. Tsutaoka[2] and S. Kawano[3]

Faculty of Regional Sciences, Tottori University, Tottori 680-8551, Japan
[1]Japan Advanced Institute of Science and Technology, Ishikawa 923-1292, Japan
[2]Graduate School of Education, Hiroshima University, Hiroshima 739-8524, Japan
[3]Research Reactor Institute, Kyoto University, Osaka 590-0494, Japan

Ternary equiatomic rare-earth compounds, *R*PdSn (*R* = Tb, Dy and Ho), crystallize in the orthorhombic (*Pnma*) TiNiSi-type structure. TbPdSn and HoPdSn exhibit a multi-step metamagnetic transition at low temperatures, when the magnetic field is applied along the easy magnetization direction of the *b*-axis [1]. Neutron diffraction measurements have shown that TbPdSn and HoPdSn have two kinds of magnetic reflections with propagation vectors $\boldsymbol{Q}_1$ = (1 0 0.45) and $\boldsymbol{Q}_2$ = (0 ~0.4 1) at 1.8 K, respectively [2]. While for DyPdSn, the bulk magnetic and specific heat measurements have revealed that there are two magnetic transition at T_N = 7.0 K and T_t = 4.8 K. Our recent powder neutron diffraction measurements on DyPdSn have indicated that there are three strong magnetic reflections at 1.6 K indexed with the magnetic propagation vector $\boldsymbol{Q}_M$ = (0.21 0 0.66). In the present work, we have carried out the neutron diffraction studies on single crystal of DyPdSn as part of continuous studies of the magnetic properties of *R*PdSn compounds. The single crystal of DyPdSn was grown by the Czochralski method using a tri-arc furnace. A piece of single crystal with 200 mg was cut out from the grown ingot for the neutron diffraction measurement. The HQR spectrometer installed at JRR-3M of JAERI at Tokai was used to collect the reflections in the reciprocal *a**-*c** plane at temperature range between 1.6 and 12.0 K.

Figure 1 shows the neutron-diffraction pattern for DyPdSn single crystal at 1.7 K scanning to the (0 0 *l*) direction. The magnetic reflection is not found at (0.21 0 0.66), (0.79 0 0.34) and (1.21 0 0.34) positions that were observed in the previous powder neutron diffraction.

A single crystal with larger size is now under preparation and more detailed neutron diffraction studies in other reciprocal plane are now in progress.

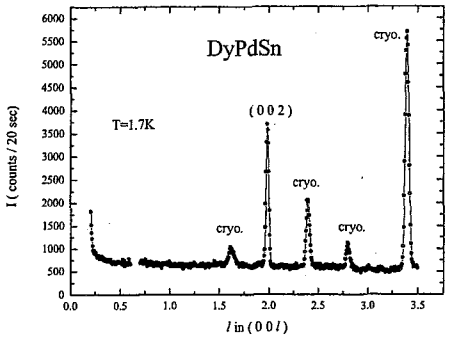

Fig. 1 The neutron-diffraction pattern for DyPdSn single crystal at 1.7 K scanning to the (0 0 *l*) direction.

REFERENCES

[1] Y. Andoh et al., Meeting Abstract of Phys. Soc. Jpn. **54** Part 3 (1999) 365.

[2] Y. Andoh et al., Activity Report On Neutron Scattering Research, Vol. 7 (2000) 104.

使用施設:JRR-3M, **装置:**HQR(T1-1), **分野** Magnetism

研究テーマ：量子スピン系 $TlCuCl_3$ 及び関連物質の素励起と相転移
表　題：S=1/2 量子反強磁性体 $Cu_2Cl_4{\cdot}H_8C_4SO_2$ の励起の観察

42) Excitation in S=1/2 Quantum Antiferromagnet $Cu_2Cl_4{\cdot}H_8C_4SO_2$

M. Fujisawa, A. Oosawa[1], H. Tanaka and K. Kakurai[1]

Department of Physics, Tokyo Institute of Technology, Meguro, Tokyo 152-8551
[1] *Advanced Science Research Center, JAERI, Tokai, Ibaraki 319-1195*

We have investigated the magnetic properties of an $S = 1/2$ quasi-one dimensional quantum antiferromagnet $Cu_2Cl_4{\cdot}H_8C_4SO_2$, which has a small spin gap of $\Delta/k_B \approx 5.8$ K. From the crystal structure, it can be deduced that $Cu_2Cl_4{\cdot}H_8C_4SO_2$ has double spin chains, in which the exchange interactions along the leg (c-axis) are strong and weakly alternate, while the exchange interactions between the legs are weak. We analyzed magnetic susceptibilities with numerical calculation, which Johnston *et al.* provided for $S = 1/2$ Heisenberg antiferromagnetic alternating chain systems.[1)] From this analysis, we estimated the alternation parameter $\alpha(= J'/J) = 0.98$ and the exchange interaction $J/k_B = 104.6$ K.[2)]

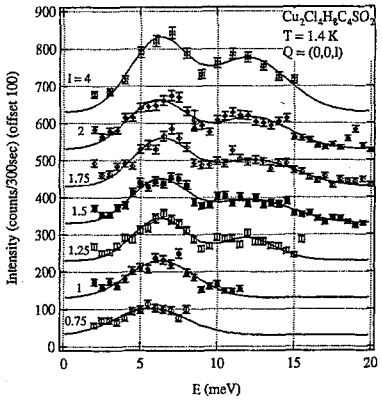

Figure 1: Profiles of the constant-Q energy scans in $Cu_2Cl_4{\cdot}H_8C_4SO_2$ for $Q = (0,0,l)$ with $0 \leq h \leq 4$ at $T = 1.4$ K. Solid lines are fits with two Gaussian functions.

In order to investigate the magnetic excitations in $Cu_2Cl_4{\cdot}H_8C_4SO_2$, we carried out neutron inelastic scattering experiments. Neutron inelastic scattering was performed using the TAS-1 triple axis spectrometer installed at JRR-3, JAERI Tokai. A single crystal sample with a volume of approximately 0.5 cm^3 was used. The sample was mounted in an orange cryostat with a^*- and c^*-axes in the scattering plane. The crystallographic parameters were determined as a^*= 0.798 /Å, c^* =0.981/Å and $\beta^* = 77.7°$ at $T = 1.4$ K. The constant-k_f mode was taken with a fixed final neutron energy E_f of 14.2 meV. Collimations were set as open - sapphire filter - 80' - sample - pyrolitic graphite filter - 80' -analyzer - 80' - detector. In order to obtain the dispersion relation $\omega(Q)$, we collected scan profiles for selected reciprocal lattice points at $T = 1.4$ K. Scan profiles were measured along $Q = (0,0,l)$ for $0.75 \leq l \leq 4$, $(h,0,0)$ for $1 \leq h \leq 1.75$ and $(h,0,1.25)$ for $0 \leq h \leq 2$.

Figure 1 shows scan profiles for $Q = (0,0,l)$. Two peaks are observed at $E = 6.2 \pm 0.1$ and 11.5 ± 0.2 meV for $1.25 \leq l \leq 4$. The peak positions do not change with varying l, while the peak intensities change. If the magnetic interactions are strong along the c-axis, the magnetic excitations will be dispersive along the c-axis. We investigated scan profiles along $Q = (h,0,0)$ for $1 \leq h \leq 1.75$ and $Q = (h,0,1.25)$ for $0 \leq h \leq 2$. These scan profiles have also two peaks, the positions of which are almost the same as those for $Q = (0,0,l)$. These results suggest two possibilities. One possibility is that excitations for different direction has large dispersion, for example b^*-axis, which is not accessible with the present settings. Another possibility is that the excitations observed in the present experiments are not magnetic but phonon excitations. In order to confirm the latter, we investigate the inelastic measurement for $Q = (0,0,2)$ at $T = 100$ K, at which magnetic excitations should be negligible. The result is shown in Fig. 2. At $T = 100$ K, there are two excitations. This result indicates that the origin of excitations observed at 1.4 K is phonon excitations.

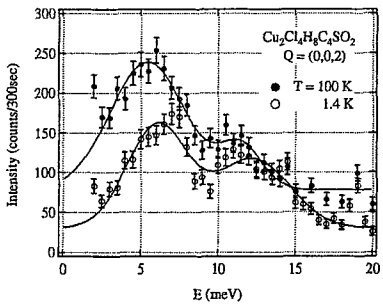

Figure 2: Profiles of the constant-Q energy scans in $Cu_2Cl_4{\cdot}H_8C_4SO_2$ for $Q = (0,0,2)$ at $T = 1.4$ and 100 K. Solid lines are fits with two Gaussian functions.

References

1) D. C. Johnston *et al.*: Phys. Rev. B **61** (2000) 9558.
2) M. Fujisawa *et al.*: J. Phys. Soc. Jpn. **72** (2003) 694.

原子炉：JRR-3　　装置：TAS-1(2G)　　分野：中性子散乱（磁性）

研究テーマ： 三角格子反強磁性体 $CuFeO_2$ の擬 Ising 性と磁気励起
表題：三角格子反強磁性体 $CuFe_{1-x}Al_xO_2$ の非弾性中性子散乱

43) Inelastic neutron scattering study of the triangular lattice antiferromagnet $CuFe_{1-x}Al_xO_2$

N. Terada[1] and S. Mitsuda[1]
[1]*Department of Physics, Faculty of science, Tokyo University of Science, 1-3 kagurazaka, shinjuku-ku, Tokyo, 162-0825*

$CuFeO_2$ has been extensively investigated as one of ABO_2-type triangular lattice antiferromagnet model materials. Although the Heisenberg spin character is expected from the electronic configuration of the magnetic Fe^{3+} (S=$\frac{5}{2}$, L=0), the 4-sublattice magnetic ordering ($\uparrow\uparrow\downarrow\downarrow$) with quasi-Ising character is stabilized as the ground state of $CuFeO_2$.[1] Also, the spin-wave dispersion relation has an energy gap, and the bottom positions do not correspond to the magnetic Bragg point.[2]

We have also studied non-magnetic impurity effect on the magnetic orderings and the magnetic excitations of $CuFe_{1-x}Al_xO_2$.[3, 2] The 4-sublattice state disappears only for the $x \sim 0.014$ non-magnetic Al impurity. And instead, the magnetic ordering that consists of the two magnetic modulations, PD-modulation and LT-modulation, with the slightly different wave numbers, is realized as orthogonal double sinusoidal (ODS) structure in the low-temperature (LT) phase for $0.014 \leq x \leq 0.030$, where the polarization axes of the two modulations are orthogonalized to each other.[4] (The polarization axes of the PD-modulation and the LT-modulation are almost parallel and perpendicular to the c axis, respectively.) Although the spin-wave dispersion relation at the lowest temperature for the LT phase was obtained from the measurements on the x=0.0208 sample with HER and GPTAS last year (ISSP Activity Report, **11** (2004) 102.), we did not identified to which spin-wave branches (higher branch and lower branch shown in Fig. 1(a)) the two magnetic modulations of the ODS structure correspond. This time, we measured the temperature dependence of the spin-wave dispersion relations by the inelastic neutron scattering measurements on the x=0.0155 sample using HER.

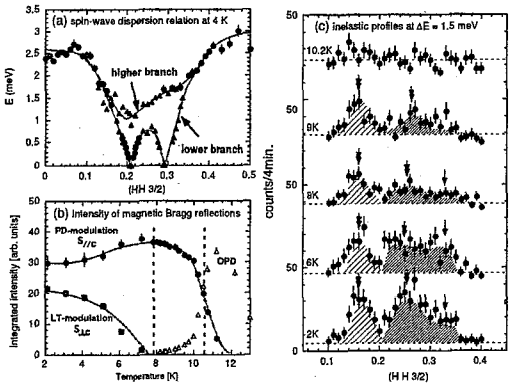

Fig. 1. (a) Spin-wave dispersion relation for the LT state of the x=0.0155 sample. (b) Temperature dependence of the integrated intensity of the magnetic Bragg reflections corresponding to the PD-modulation and the LT-modulation in the x=0.0155 sample. (c) Typical inelastic scattering profiles along the (h h $\frac{3}{2}$) line at ΔE=1.5 meV for several temperatures.

As shown in Fig. 1(c), the magnetic inelastic signals corresponding to both the higher branch and the lower branch were observed at 2 K. With increasing temperature, while the inelastic signal corresponding to the lower branch first disappears above 8 K as shown by the single arrows in Fig. 1(c), that corresponding to the higher branch remains up to 9 K as shown by the double arrows. Comparing the temperature dependence of the inelastic signals with that of the Bragg intensity shown in Fig. 1(b), we can conclude that the PD-modulation and the LT-modulation correspond to the higher branch and the lower branch, respectively.

References

[1] S. Mitsuda et al, JPSJ **67**, 4026 (1998).
[2] N. Terada et al, J. Magn. and Magn. Mater. **272-276S**, E997 (2004).
[3] N. Terada et al, JPSJ **73**, 1442 (2004).
[4] N. Terada et al, submitted to PRB.

使用施設：JRR-3M, 装置： HER (c1-1) , 分野： 2. Magnetism

研究テーマ：先端偏極中性子散乱によるスピン－格子物性の研究
表　題：TAS-1 の偏極中性子高強度化

42) Status of the Polarized Neutron Triple-axis Spectrometer TAS-1

M. Takeda, M. Nakamura[1], Y. Shimojo, and K. Kakurai

Advanced Science Research Center, JAERI, Tokai, Ibaraki 319-1195
[1]Neutron Science Research Center, JAERI, Tokai, Ibaraki 319-1195

Three years ago we started an program to upgrade the polarized neutron analysis option of TAS-1. The main part of the strategy is replacement of previous polarizing monochromator and analyzer. The new monochromator had been already installed and used for two years[1)]. The installation of the new analyzer was finished in this fiscal year. Finally we succeeded in a remarkable improvement of data collection rate of polarized neutron experiments including the spherical polarization analysis using CRYOgenic Polarization Analysis Device (CRYOPAD) [2)]. In this brief report the feature of the achievement is described.

The new polarized neutron analyzer is a doubly focusing one and is very similar to the monochromator. The analyzer consists of 35 pieces of Cu_2MnAl crystals and has a reflection plane of the area of 140 mm wide and 100 mm high (Fig. 1). The Cu Heusler crystals were synthesized in ILL and have polarizing efficiency higher than at least 90 %. 5 pieces of crystals were glued on one Boron Nitride (BN) plate so as to make composite curvature for the fixed vertical focusing optimized for 30.5 meV neutrons. 7 columns of the BN plates were inserted in a gap of the magnetic circuit. Except the centered plate they can pivot around the vertical axis to enable variable horizontal focusing by two stepping motors.

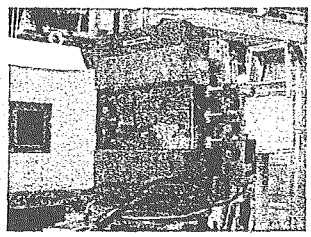

Figure 1: Picture of the doubly focusing polarized neutron analyzer newly installed on TAS-1.

Figure 2 shows the incoherent magnetic scattering from a Vanadium sample using three different combinations of the monochromators and analyzers: 1. the old monochromator and the old analyzer, 2. the new monochromator and the old analyzer, and 3. the new monochromator and the new analyzer. This figure shows that the gain factor of 31 was finally achieved by replacement of both old monochromator and analyzer for 14.7 meV neutrons. The analyzer bent angle dependence of the detected intensities is plotted in the inset of Fig. 2. By the horizontal focusing of the analyzer the intensity increases by 50 % under the condition that the horizontal bent angle of the monochromator is also optimized.

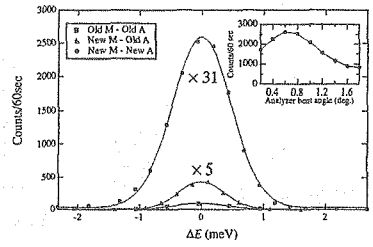

Figure 2: Intensities of the spin-flip neutron incoherent scattering from Vanadium sample using three combination of monochrometers and analyzers. Inset is the analyzer bent angle dependence of detected intensities. A PG filter was used to remove the higher order contamination of the incident beam.

The energy resolution becomes slightly worse by the horizontal focusing . At the optimum bent angles for 14.7 meV neutrons it increases from 0.94 to 1.12 meV (FWHM) in comparison with the data obtained by using the combination of old flat monochromator and analyzer. The polarizing efficiencies, however, remain excellent. Figure 3 displays a crystal angle dependence of spin-flip and non-spin-flip intensities from the nuclear diffraction peak of PG(004). This figure clearly shows that the flipping ratio is 30 even under the optimum condition of horizontal bent angles.

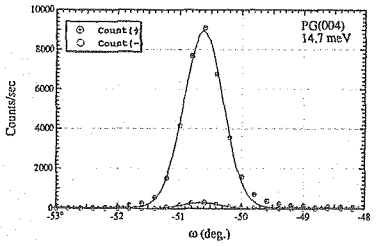

Figure 3: Intensities of spin-flip and non-spin-flip diffractions from PG(004) reflection. The flipping ratio reaches 30. The beam collimation is Open-Open-Open-Open, and a PG filter was used to remove the higher order contamination of the incident beam.

References

1) M. Nakamura, M. Takeda, Y. Shimojo and K. Kakurai, JAERI-Review **2004-005** (2004) 140.
2) M. Takeda, M. Nakamura, K. Kakurai, E. Lelièvre-Berna, F. Tasset, and L. -P. Regnault, Physica B **356** (2005) 136.

原子炉：JRR-3　　装置：TAS-1(2G)　　分野：中性子散乱（磁性）

研究テーマ： $PrPb_3$ の反強四重極秩序
表題： $PrPb_3$ における変調四重極構造

45) Modulated Quadrupole structures in $PrPb_3$

T. Onimaru[1], T. Sakakibara[1], N. Aso[2], H. Yoshizawa[2], H.S. Suzuki[3], T. Takeuchi[4]
[1] *Institute for Solid State Physics, University of Tokyo, 5-1-5 Kashiwanoha, Kashiwa, 277-8581*
[2] *Institute for Solid State Physics, University of Tokyo, 106-1 Shirakata, Tokai, 319-1106*
[3] *National Institute for Materials Science, Tsukuba 305-0047*
[4] *Low Temperature Center, Osaka University, Toyonaka 560-0043*

We concentrate our attention on the intermetallic compound $PrPb_3$ with $AuCu_3$-type cubic structure. The crystalline field ground state of $PrPb_3$ is a Γ_3 non-Kramers doublet, with a magnetic Γ_4 triplet lying 15∼19 K above the ground state.[2, 3, 4] Since the Γ_3 doublet carries quadrupolar moments $O_2^0=(3J_z^2-J^2)/2$ and $O_2^2=\sqrt{3}(J_x^2-J_y^2)/2$, $PrPb_3$ is a good candidate for the quadrupole transition. This compound actually exhibits a second-order transition at 0.4 K with a lambda-type anomaly in the specific heat.[5, 6] Absence of a magnetic superlattice reflection nor a lattice distortion in the neutron diffraction measurement performed in zero magnetic field[2] suggests the phase transition to be of antiferroquadrupolar ordering.

We performed neutron diffraction measurements on the cubic compound $PrPb_3$in a [001] magnetic field to examine the quarupolar ordering.[1] Fig. 1 shows the results of $\boldsymbol{Q}$−scans along the $(h\frac{1}{2}0)$ line carried out in a field of H=4 T at various temperatures ranging from 0.125 K to 0.8 K. The inset of Fig. 1 shows the $(hk0)$ reciprocal plane ($\perp H$) investigated, where open and closed circles represent the nuclear and the magnetic reflections, respectively, observed in a field of H=4 T at T=0.125 K. On cooling below the transition temperature T_Q=0.65 K, superlattice reflections with $\boldsymbol{q}=(\frac{1}{2}\pm\delta\frac{1}{2}\ 0)$, $(\frac{1}{2}\frac{1}{2}\pm\delta\ 0)$, $(\delta\sim\frac{1}{8})$ are observed. These reflections show that quadrupoles are ordering with a sinusoidal modulated structure. The intensity of these reflections vary linear to H and vanish at zero field, providing the first evidence for a modulated quadrupolar phase. For H<1 T, a non-square modulated state persists to below 100 mK suggesting quadrupole moments associated with a Γ_3 doublet ground state to be partially quenched by hybridizations with conduction electrons. On further cooling below T_t=0.45 K, the third-order harmonics $(\frac{1}{2}\pm3\delta\frac{1}{2}\ 0)$ and $(\frac{1}{2}\frac{1}{2}\pm3\delta\ 0)$ with much weaker intensity is found to develop. This state undergoes a first-order transition to an antiphase structure.

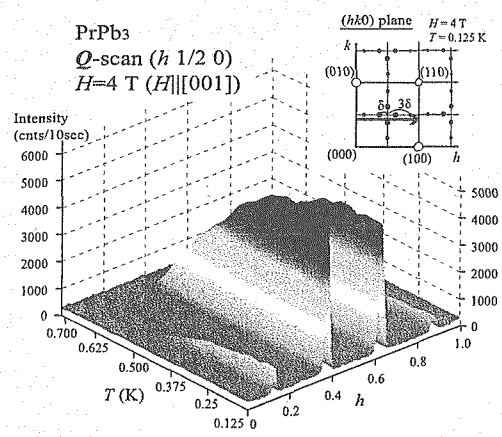

Fig. 1. Evolution of the magnetic scattering in H=4 T applied along the [001] direction, at 0.125 K<T<0.81 K. The $\boldsymbol{Q}$−scans were performed along the line $(h\frac{1}{2}0)$, as indicated by a arrow in the $(hk0)$ reciprocal plane (inset) where open and closed circles represent the nuclear and the magnetic reflections, respectively, observed at T=0.125 K.

References

[1] T. Onimaru *et al.*, Phys. Rev. Lett. **94**, 197201 (2005).
[2] M. Niksch *et al.*, Helv. Phys. Acta **55**, 688 (1982).
[3] W. Gross *et al.*, Z. Phys. B **37** 123(1980).
[4] T. Tayama *et al.*, J. Phys. Soc. Jpn. **70** 248 (2001).
[5] E. Bucher *et al.*, J. Low Temp. **2** 322 (1972).
[6] D. Aoki *et al.*, J. Phys. Soc. Jpn. **66** 3988 (1997).

使用施設：JRR-3M, 装置： 4G (GPTAS) , 分野： 102: Magnetism

研究テーマ：中性子散乱によるウラン化合物の物性研究
表　題：$NpNiGa_5$ の磁気構造と低モーメント－高モーメント間の相転移

46) Magnetic structure and the metamagnetic transition between the low-moment and high-moment states in $NpNiGa_5$

F. Honda[1], N. Metoki[1,2], K. Kaneko[1], S. Jonen[1], D. Aoki[3], Y. Homma[3], E. Yamamoto[1], Y. Shiokawa[1,3] and Y. Ōnuki[1,4]

[1]*Advanced Science Research Center, JAERI, Tokai, Ibaraki, 319-1195, Japan*
[2]*Department of Physics, Tohoku University, Sendai 980-8578, Japan*
[3]*Institute for Materials Research, Tohoku University, Oarai, Ibaraki 311-1313, Japan*
[4]*Graduate School of Science, Osaka University, Toyonaka, Osaka 560-0043, Japan*

After the discovery of the superconductivity in $PuCoGa_5$ [1] with quite high critical temperature, $T_c \sim 18K$, actinide based '115' compounds have received increasing attention. With this as a trigger, high quality single crystalline samples of $NpTGa_5$ (T: transition metal) have been grown and studied intensively [2,5,8]. Among the existing $NpTGa_5$ compounds, $NpNiGa_5$ exhibits rather intriguing magnetic properties such as successive two magnetic phase transitions at 30 and 18 K and a metamagnetic transition below 18 K [2]. In order to elucidate the magnetic structures and the metamagnetic transition, we carried out systematic neutron diffraction experiments.

Neutron scattering experiments were carried out on TAS-1, TAS-2 and LTAS installed at the research reactor JRR-3 in JAERI. Neutron spin polarization analysis was performed on TAS-1 in order to clarify wether the magnetic moment exists on transition metal site or not.

The line scan profiles along (h h 0) and (h h $\frac{1}{2}$) at different temperatures are shown in Fig.1. We have observed a ferromagnetic (FM) scattering below T_C = 30 K (hatched region) at (1 1 0). We have also observed a ($\frac{1}{2}$ $\frac{1}{2}$ $\frac{1}{2}$) superlattice peak below T_N = 18 K, indicating the antiferromagnetic (AFM) component coexisting with FM. Neutron spin polarization analysis revealed practically no spin polarization on Ni site below 30 K. That is to say, only Np carries a magnetic moment in both FM and AFM states in this compound. From results of the careful analysis of FM and AFM reflection intensities, we have revealed that the magnetic structures of $NpNiGa_5$ are simple ferromagnetic order along the c-axis for $T_N < T < T_C$, while a canted structure with the AFM component along [1 1 0] coexisting with FM one along the c-axis for $T < T_N$. The magnetic form factor can be described with a dominant orbital contribution μ_L/μ = 3.1, which differs from that of Np^{3+} free ionic state ($\sim$ 2.33). The smaller $|\mu_L/\mu_S|$ = 1.48 in comparison with localized Np system ($\sim$ 1.75) indicates the partially quenching of the orbital moment. The determined magnetic structures are schematically drawn in Fig.2.

The remarkable feature in this compound is the unusual transition between the FM and the canted AFM

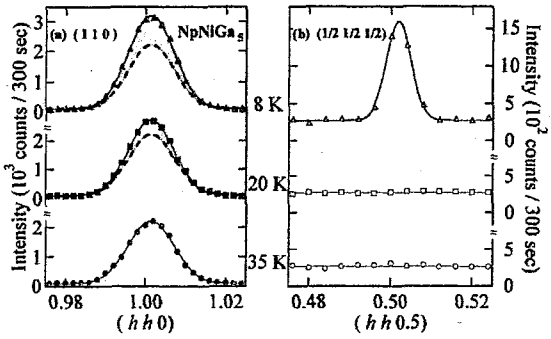

Figure 1: Line scan along the (a) (1 1 0) and (b) ($\frac{1}{2}$ $\frac{1}{2}$ $\frac{1}{2}$) at different temperatures.

structure. Figure 3 shows the total Np magnetic moment and the angle between adjacent Np moments as a function of temperature derived from the temperature dependence of magnetic scattering intensities of (1 1 0) and ($\frac{1}{2}$ $\frac{1}{2}$ $\frac{1}{2}$). As can be seen, a considerable increase, roughly 50 %, of Np moment has been observed below T_N, when the Np moment tilts from the c-axis in the canted structure. It means that the non-collinear structure in AFM state cannot be explained by the simple reorientation of Np moment from the c-axis in FM state. The large difference of Np moment in each magnetic ordered states indicates the $5f$ electronic transition between the low- and high-moment states.

The magnetic phase diagram of $NpNiGa_5$ shown in Fig.2 has been constructed by our neutron diffraction experiments under high magnetic fields up to 10 T applied along the [1 -1 0]. We have clarified that the metamagnetic transition is accompanied by the sudden disappearance of the AFM component and surprisingly, the reduction of the FM moment with application of magnetic field. As a consequence, the total Np moment discontinuously decreases down to 0.5 μ_B/Np from 0.78 μ_B/Np at the metamagnetic transition. In other words, the low-moment states recovered after the metamagnetic transition.

The key issue is that the high-moment state ac-

原子炉：JRR-3　　装置：LTAS(C2-1)　　分野：中性子散乱（磁性）

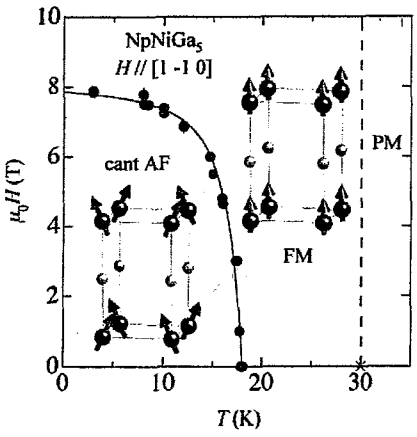

Figure 2: The $H-T$ magnetic phase diagram of $NpNiGa_5$. The derived magnetic structures of each phase are shown schematically in the inset.

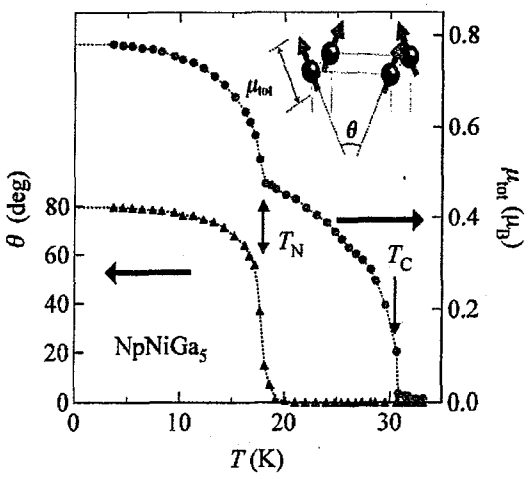

Figure 3: The temperature dependence of the size of the Np moment, μ_{tot}, and θ which denotes the angle between the adjancent magnetic moments of Np, shown by close circles and triangles, respectively.

companies in-plane magnetic moment perpendicular to the quantization axis, c-axis. A very similar successive magnetic order associated with $5f$ electronic transition has been reported in $NpRhGa_5$, in which the high-moment state appears with the reorientation of the moment direction from the c-axis to [1 1 0] in the basal plane [3].

The successive ordering with the transition of the $5f$ electronic state can be qualitatively understood based on a localized $5f$ model. The $\boldsymbol{J}$ multiplet of Np^{3+} ion splits into doublet and singlet states under tetragonal crystalline electric field (CEF). The doublet yields only J_z due to its symmetry of the wave function. The mixing of singlets and/or doublets is necessary to yield the in-plane AFM component J_x and J_y realized in the canted structure.

The CEF level scheme of $NpNiGa_5$ has not been clarified yet, but the doublet ground state and the singlet first excited states separated by the energy 87 K has been proposed in $NpCoGa_5$ from the susceptibility data [4]. If $NpNiGa_5$ exhibits a similar level scheme with much lower excitation energy, the competing magnetic and/or multipolar interactions plays significant role for the magnetic properties. The small splitting is reasonable because of the small magnetic anisotropy in $NpNiGa_5$ [2] compared to the strong uniaxial anisotropy in $NpCoGa_5$ [5].

On the other hand, however, the obtained magnetic form factor in $NpNiGa_5$ is consistent with the itinerant character of $5f$ electrons. Actually the cylindrical Fermi surface topology of $NpCoGa_5$ [6] and $NpRhGa_5$ [7] belonging to the same family can be well understood in terms of the band structure calculation based on a model with itinerant $5f$ electrons. Thus the unification of the pictures based on localized and itinerant models is the most essential part of the underlying physics in strongly correlated $5f$ electron systems, where the unusual magnetic properties in $NpTGa_5$ shed some lights on this issue. Detailed results and further discussions will be published elsewhere [8].

References

1) J.L. Sarrao *et al.*, Nature (London) **420** (2002) 297.
2) D. Aoki *et al.*, J. Phys. Soc. Jpn. *in press.*
3) S. Jonen *et al.*, presented at this progress report.
4) D. Aoki *et al.*, J. Phys. Soc. Jpn. **73** (2004) 1665.
5) N. Metoki *et al.*, Phys. Rev. B *in press.*
6) D. Aoki *et al.*, J. Phys. Soc. Jpn. **73** (2004) 2608.
7) D. Aoki *et al.*, J. Phys.: Condens. Matter **17** (2005) L169.
8) F. Honda *et al.*, Phys. Rev. B *to be submitted.*

研究テーマ：ドープしたNiOのスピンダイナミクス
表題： NiOにおける$1.18T_N$での常磁性スピン相関

47) Paramagntic Spin Correlation in NiO at $1.18\,T_N$

Y. Todate[1] and K. Kohn[2]

[1] *Department of Physics, Ochanomizu University, 2-1-1 Otsuka, Bunkyo-ku, Tokyo, 112-8610*
[2] *Waseda Univ., 3-4-1 Okubo, Shinjyuku-ku, Tokyo, 169-8555*

Dynamics of magnetic moments in the paramagnetic state would be the key information for complete understanding of the finite-temperature properties of the transition-metal oxides. We have reported an interesting feature of the neutron paramagnetic scattering from prototypical antiferromagnetic (AF) monoxide NiO [1, 2] measured at T=1.06T_N: the scattering intensities are observed in a narrow q-region around the AF zone-centers while the energy spectrum is extending over 30meV. Since measurements at higher temperatures are highly desirable, experiments at $1.18\,T_N$ (640K) have been carried out with the use of the 5G-triple axis spectrometer at JRR-3M with the same single crystal sample used before.

The experimental data (Fig. 1) have been analyzed by the double-Lorentzian scattering function based on the spin-diffusion model. The parameter for energy width of the scattering function is $\Gamma(q)=\Gamma_0+\Lambda q^2$, where Λ is the diffusion constant for the three-dimensional spin-diffusion. A set of parameters (Γ_0=25meV, Λ=787meVÅ^2 and κ=0.366Å^{-1}) has been obtained by fitting the resolution-convoluted model function to the experimental data. According to the conventional theory, Λ is given by $r_c^2/(6\tau_c)$ and obtained large Λ corresponds to either the short correlation time τ_c or the large mean square distance r_c^2 in which the moments are correlated within an elemental time scale τ_c. If we assume that, based on the Heisenberg spin model at high temperatures, the correlation time is given by $\tau_c^{-1}=(J_2\hbar)[zS(S+1)]^{1/2}\sim 7.9\times 10^{12}$Hz, then the dynamically correlated distance becomes $r_c^2\sim 204$Å^2, which value is 11.7 times larger than a_0^2, i.e., the distance between Ni ions connected by the magnetic interaction J_2. (Conversely if we put r_c^2=a_0^2 then τ_c is a tenth of the estimation based on the Heisenberg model.) Note that, for the typical Heisenberg antiferromagnet $RbMnF_3$, the difference (ratio) between experimentally determined (10meVÅ^2 at $1.2\,T_N$ [3]) and calculated diffusion constant (6.35meVÅ^2) is only 1.6. Therefore this may be another distinct deviation from the simple Heisenberg model found for NiO. At the present time there is no adequate microscopic description for this dynamical paramagnetic spin correlation. Anomalous transport in NiO could have some relation to this unique dynamical spin correlation. It is also interesting to investigate the remarkable similarity between the paramagnetic dynamics of moments in NiO and the dynamics of spin density in some AF-alloys.

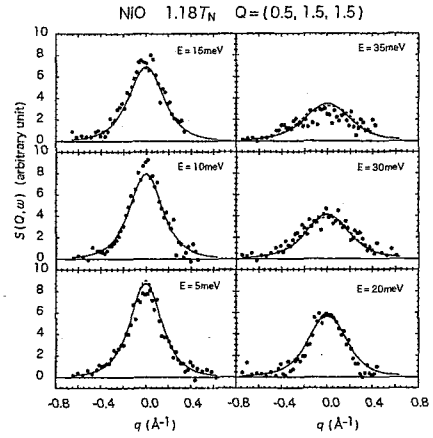

Fig. 1. Observed and fitted paramagnetic scattering intensities at a higher temperature.

References

[1] Y.Todate: J. Phys. Soc. Jpn., **70** (2001) Suppl. A97.
[2] Y.Todate *et al.*: Act. Rep. on Neutron Scatter. Res., vol 9 (2002) 181.
[3] A. Yazaki *et al.*: J. Phys. Soc. Jpn., **63** (1994) 784.

使用施設：JRR-3M，装置：5G (PONTA)，分野：102 :Magnetism

研究テーマ：先端偏極中性子散乱によるスピン－格子物性の研究
表　題：中性子回折による α-Gd_2S_3 の磁気構造の研究

48) Neutron Diffraction Study of α-Gd_2S_3

M. Matsuda, A. Kikkawa[1], K. Katsumata[1], S. Ebisu[2] and S. Nagata[2]

Advanced Science Research Center, Japan Atomic Energy Research Institute, Tokai, Ibaraki 319-1195
[1]*RIKEN Harima Institute, Mikazuki, Sayo, Hyogo 679-5148*
[2]*Department of Materials Science and Engineering, Muroran Institute of Technology, 27-1 Mizumoto-cho, Muroran, Hokkaido 050-8585*

α-Gd_2S_3 consists of a stacking of square lattice Gd1 and triangular Gd2 planes. Recently, the observation of a novel phase transition in α-Gd_2S_3, which was interpreted as being due to geometrical frustration, was reported.[1] This compound has the orthorhombic crystal structure (space group *Pnma*) with the lattice constants a = 7.34431 Å, b = 3.93157 Å and c = 15.2886 Å[2]. The temperature, T, dependence of the magnetic susceptibility, χ, of a single crystal of α-Gd_2S_3 was first measured by Ebisu *et al.*[2] The χ along the b-axis begins to decrease at about 10 K, while that perpendicular to the b-axis steadily increases with decreasing T. Ebisu *et al.* interpreted this anisotropic behavior in the T dependence of χ on the basis of a coupled two-leg spin ladder model[2]. Subsequently, Kikkawa *et al.*[1] have made magnetic susceptibility, magnetization and heat capacity measurements on a single-crystal sample of α-Gd_2S_3. From heat capacity measurements, they found an anomaly at T_N = 9.8 K indicating the occurrence of a long-range magnetic order. Unlike a conventional second-order phase transition, a large amount of heat capacity remains below the transition temperature.

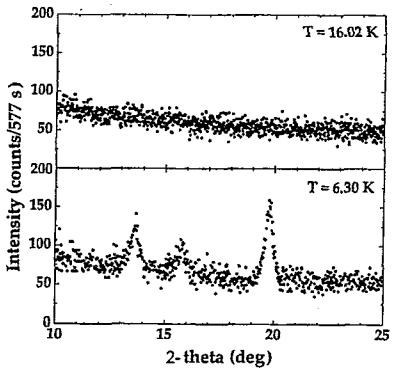

Figure 1: The neutron powder diffraction patterns of α-$^{160}Gd_2S_3$ obtained at T = 16.02 K ($> T_N$) and at T = 6.30 K ($< T_N$).

Neutron diffraction measurements on a powder sample of α-$^{160}Gd_2S_3$ are performed. [3] Figure 1 shows the results obtained with the HRPD. We see clear magnetic peaks at T = 6.30 K. The magnetic unit cell is found to be the same as the chemical unit cell. We performed a magnetic structural analysis and determined the magnetic structure of α-Gd_2S_3 as shown in Fig. 2. The magnetic moments order parallel with each other along the b-axis. The magnetic structure in the ac plane is such that a Gd1 moment is ordered antiparallel to the nearest neighboring Gd1 moments and is coupled parallel to the next-nearest neighboring Gd1 moments. The Gd2 moment is coupled antiparallel to the nearest neighboring Gd1 moment. The temperature dependence of the order parameter is extracted (not shown) and is found to be explained rather well by the result of an $S = \frac{7}{2}$ molecular field approximation. The collinear structure of the magnetic moments in the triangular lattice and the absence of large magnetic fluctuations around the magnetic transition temperature suggest that the geometrical frustration is not so distinct in α-Gd_2S_3.

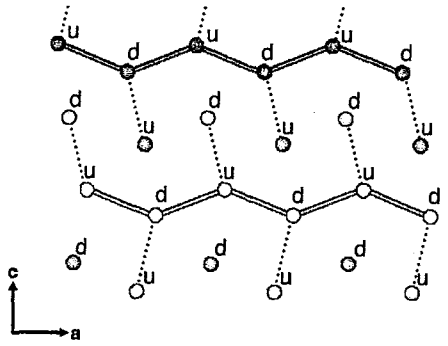

Figure 2: The proposed magnetic structure of α-Gd_2S_3 projected onto the ac plane. Only Gd atoms are shown, for clarity. There are two crystallographically inequivalent sites for Gd labeled Gd1 and Gd2. Dark circles: Gd1 at y=0, gray circles: Gd2 at y=0, tint circles: Gd2 at y=1/2 and open circles: Gd1 at y=1/2. Here, u and d mean the magnetic moments directed parallel and antiparallel to the b-axis, respectively.

References

1) A. Kikkawa, K. Katsumata, S. Ebisu and S. Nagata: J. Phys. Soc. Japan **73** (2004) 2955.
2) S. Ebisu, Y. Iijima, T. Iwasa and S. Nagata: J. Phys. Chem. Solids **65** (2004) 1113.
3) M. Matsuda, A. Kikkawa, K. Katsumata, S. Ebisu and S. Nagata: J. Phys. Soc. Japan **74** (2005) 1412.

原子炉：JRR-3　　装置：HRPD(1G)　　分野：中性子散乱（磁性）

研究テーマ： 三角格子反強磁性体 $CuFeO_2$ の微量希釈による磁気構造変化
表題：三角格子反強磁性体 $CuFe_{1-x}Al_xO_2$ の磁気構造解析

49) Magnetic structure analysis of the triangular lattice antiferromagnet $CuFe_{1-x}Al_xO_2$

N. Terada[1], T. Fujii[1], S. Mitsuda[1] and Y. Noda[2]
[1]*Department of Physics, Faculty of science, Tokyo University of Science, 1-3 kagurazaka, shinjuku-ku, Tokyo, 162-0825*
[2]*Institute of Multidisciplinary Research for Advanced Materials, Tohoku University, Sendai 980-8577*

Delafossite compound $CuFeO_2$ has been extensively investigated as one of ABO_2-type materials for triangular lattice antiferromagnet. In recent years, we have studied nonmagnetic impurity effects on the magnetic properties, using $CuFe_{1-x}Al_xO_2$ sample up to $x \sim 0.05$.[1, 2, 3] As for the magnetic structures in the thermally induced phases, using FONDER, we found that the oblique partially disordered (OPD) state is realized in $T_{N2}^{high} \leq T \leq T_{N1}$ in the x=0.0208 sample, instead of the PD state seen in the x=0.0000 sample.[2] In the case of the x=0.0208 sample, however, we cannot provide access to the temperature region of $T_{N2}^{low} \leq T \leq T_{N2}^{high}$, using FONDER. This time, in order to determine the magnetic structure in the magnetic phase that lies in $T_{N2}^{low} \leq T \leq T_{N2}^{high}$, we first prepared the x=0.0155 single-crystal sample ($T_{N2}^{low} \sim 8$ K and $T_{N2}^{high} \sim 10.2$ K (see Fig. 1(a))), and subsequently, we performed neutron diffraction measurements at 9 K with FONDER.

The magnetic structure analysis method used here is the same as that used in the previous study[2]. We first performed crystal structure analysis to obtain the extinction parameter and the scale factor. As a result, the reliable factor was $R(F) = 6.89\%$. Subsequently, we performed the magnetic structure analysis. Although the integrated intensities of the equivalent reflections reflecting the hexagonal three-fold symmetry are considered to be equal each other, the intensities observed in this measurement were different from each other. Specifically, the ratios of the domain population are (28.8 ± 3.1, 29.8 ± 2.8 and 41.4± 3.2%). Therefore, we performed the analysis individually for the three domains. As shown in Fig. 1(b) and Table 1, in the PD phase of the x=0.0155 sample, the sinusoidal structure with the magnetic moments canted by about 10 degrees from the c axis toward the $\langle 1\bar{1}0 \rangle$ direction, which is shown in the inset of Fig. 1(b), is realized. This structure is almost the same as that observed in the previous magnetic structure analysis for the PD phase in the x=0.0000 sample[2]. We thus found that the PD phase seen in the x=0.0000 sample extends to the finite x region.

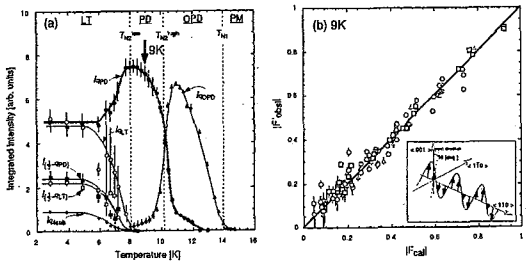

Fig. 1. (a) Temperature dependence of the magnetic Bragg intensities in the x=0.0155 sample, which is taken from ref. [3]. (b) The relationships between the structure factors observed ($|F'_{obs}|$) and the calculated ($|F_{cal}|$). Circle, triangle and square symbols correspond to the data observed in the three different magnetic domains.

Table 1. Results of the magnetic structure analysis at 9 K for the x=0.0155 sample. θ, ϕ, μ and R(F) were defined in a previous paper.[2] This table is taken from ref. [3]

domain	θ (deg)	ϕ (deg)	$\mu(\mu_B)$	R(F)
domain-1	13±12	-1±40	2.07±0.20	7.54%
domain-2	11±8	7±38	2.07±0.13	4.60%
domain-3	14±11	-3±23	2.07±0.15	4.78%

References

[1] N. Terada *et al.*, JPSJ **73**, 1442 (2004).
[2] N. Terada *et al.*, JPSJ **74**, 1561 (2005).
[3] N. Terada *et al.*, submitted to JPSJ.

使用施設：JRR-3M, 装置： FONDER(T2-2) , 分野： 2. Magnetism

研究テーマ：ランタノイドと白金族元素を含む複合ペロブスカイト酸化物の結晶構造および磁気構造
表　題：6H-ペロブスカイト $Ba_3Fe_2ReO_9$ における反強磁性

50) Antiferromagnetic Structure of 6H-Perovskite $Ba_3Fe_2ReO_9$

M. Wakeshima, K. Yamamura, Y. Hinatsu, N. Igawa[1], and Y. Ishii[1]

Division of Chemistry, Graduate School of Science, Hokkaido University, Sapporo 060-0810
[1]NSRC, JAERI, Tokai, Ibaraki 319-1195

The crystal structure and magnetic properties of the triple-perovskite type compound $Ba_3Fe_2ReO_9$ were investigated. Through magnetic susceptibility measurements, this compound showed complicated magnetic behavior below 450 K. The Mössbauer spectrum measurements indicated that a half of the Fe ions showed the magnetic ordering below 450 K and the other half of Fe ions did below 320 K. In order to elucidate these behaviors, powder neutron measurements were performed at 10 K and 300 K with a High Resolution Powder Diffractometer (HRPD) in the JRR-3 reactor with a neutron incident wave length (λ = 1.82268 Å).

Neutron diffraction profile measured at 300 K shows that $Ba_3Fe_2ReO_9$ crystalizes in the hexagonal type structure (stacking sequence hcchcc) with space group $P6_3/mmc$. Figure 1(a) is illustrated the crystal structure of $Ba_3Fe_2ReO_9$. The structure consists of dimers of face-sharing octahedra separated by single corner sharing octahedra. By the Rietveld analysis, it was revealed that the Fe ions occupy the single corner site, and that the Re and Fe ions occupy the dimer sites randomly in the ratio of 1:1.

In the data collected at 10 K (Fig. 2), no additional peaks are observed and the clear enhancement of peak intensities is recognized. This result means that the magnetic unit cell is equal to the nuclear unit cell. The magnetic structure of $Ba_3Fe_2ReO_9$ was determined by the Rietveld analysis. The two octahedral transition metal sites (single corner and dimer sites) were allowed to have different magnetic moments.

The magnetic structure at 10 K is illustrated in Fig. 1(b). In this figure, only the magnetic moment of the Fe^{3+} ion is extracted. In the dimer sites, the magnetic moments of Fe^{3+} are coupled antiferromagnetically. The magnetic coupling between the single corner and dimer sites is also antiferromagnetic. The direction of the magnetic moments is along the c axis. The ordered magnetic moments are listed in Table 1. These magnetic ordered moments are considerably smaller than theoretical one ($gS = 5\mu_B$) of the Fe^{3+} ions. From this result, it is suggested that the randomness of the Fe and Re ions in the dimer sites leads to the frustrations between the magnetic couplings such as a spin-glass.

Table 1: Ordered magnetic moments (μ_B) of $Ba_3Fe_2ReO_9$

	dimer	corner
10 K	2.88(4)	2.67(7)
300 K	2.82(5)	2.53(8)

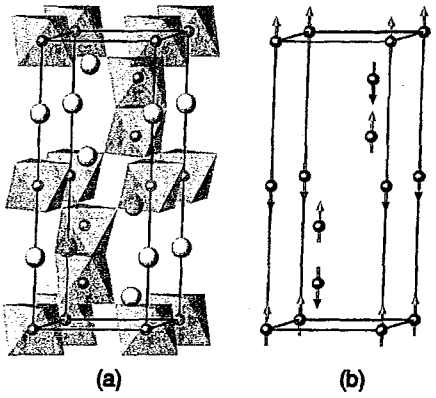

Figure 1: (a) Crystal structure of $Ba_3Fe_2ReO_9$; (b) Magnetic structure of $Ba_3Fe_2ReO_9$ at 10 K.

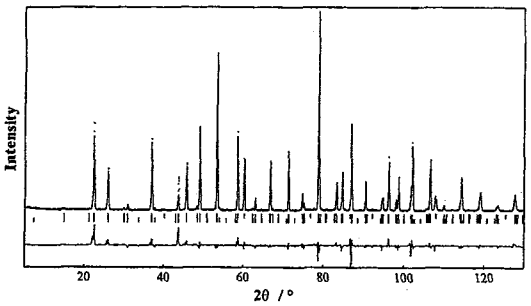

Figure 2: Neutron diffraction profile at 10 K of $Ba_3Fe_2ReO_9$.

原子炉：JRR-3　　装置：HRPD(1G)　　分野：中性子散乱（磁性）

研究テーマ：三角格子反強磁性体 $CuFeO_2$ の微量希釈による磁気構造変化
表題：三角格子反強磁性体 $CuFe_{1-x}Al_xO_2$ の x-T 磁気相図

51) Magnetic phase diagram of the triangular lattice antiferromagnet $CuFe_{1-x}Al_xO_2$

N. Terada[1], T. Fujii[1], K. Kitagawa[1] and S. Mitsuda[1]
[1]*Department of Physics, Faculty of science, Tokyo University of Science, 1-3 kagurazaka, shinjuku-ku, Tokyo, 162-0825*

As one of the model materials of the triangular lattice antiferromagnet (TLA), $CuFeO_2$ has been extensively investigated. In spite of the orbital singlet ^6S state of the electronic configuration in the magnetic Fe^{3+} (S=$\frac{5}{2}$, L=0), $CuFeO_2$ shows *quasi-Ising* character. Moreover, the non-magnetic impurity strongly affects the magnetic properties of $CuFe_{1-x}Al_xO_2$ by disturbing the delicate balance of the competing exchange interactions.[1] In particular, we have intensively investigated the x=0.0208 sample; the successive magnetic phase transitions are entirely modified by the substitution of the small amount of the non-magnetic impurity, suggesting that the quasi-Iisng character disappears and the original Heisenberg character is retrieved. However, we had not investigated how the magnetically ordered phases, which were observed in the x=0.0000 and the x=0.0208 samples, extend to the (x, T) region. This time, in order to investigate how the successive magnetic phase transitions are modified by the non-magnetic impurity, we performed the neutron diffraction measurements on the x=0.0097 and the x=0.0126 samples where the complex successive magnetic phase transitions were observed in magnetic susceptibility measurements, using HQR.

We obtained the x-T magnetic phase diagram shown in Fig. 1(a). $CuFeO_2$ shows the successive magnetic phase transitions (PM $\Rightarrow$ PD $\Rightarrow$ 4-sublattice) characterized by the quasi-Ising character. With increasing x, the 4-sublattice state first disappears for $x_c \sim$ 0.014; however, the PD state survives up to $x \sim 0.030$. Above $x \sim 0.030$, the single magnetic phase transition from the PM phase to the OPD phase that reflects the original Heisenberg spin character of the orbital singlet Fe^{3+} simply occurs. In addition, we found that the LT phase lies for $0.014 < x < 0.030$. Observing that these various magnetically ordered phases compete with each other on the x-T magnetic phase diagram and that the non-magnetic impurity strongly affects the magnetic orderings in this system, we confirmed that the quasi-Ising orderings are stabilized in $CuFeO_2$ with the delicate balance of competing interactions.

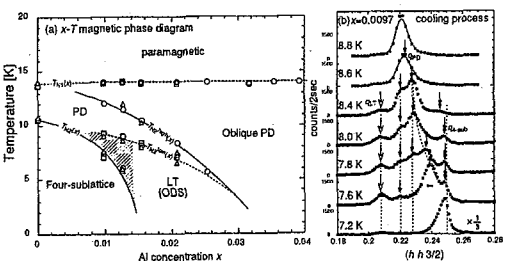

Fig. 1. (a) Al-concentration, x, vs temperature magnetic phase diagram of $CuFe_{1-x}Al_xO_2$. Anomalies found in the neutron diffraction, the magnetic susceptibility and the specific heat are depicted by triangle, circle and square symbols, respectively. (b) Typical diffraction profiles in the *tip region* of the LT phase for cooling process.

In addition, we newly defined the temperature region of $T_{N2} \leq T \leq T_{N2}^{low}$, which is shown by the hatched area in Fig. 1(a), as the *tip region* of the LT phase. As shown in Fig. 1(b), when the system enters the *tip region* from the PD phase, the single magnetic Bragg reflection reflecting the PD state, q_{PD}-reflection, bifurcates into several reflections with different wave numbers, shown by the single arrows. The bifurcation indicates that the magnetic orderings characterized by slightly different wave numbers must be spatially distributed. Moreover, the *tip region* does not appear for a heating process. These significant thermal hysteresis has been mentioned in our recent paper in detail.[2]

References

[1] N. Terada et al, JPSJ **73**, 1442 (2004).
[2] N. Terada et al, submitted to JPSJ.

使用施設：JRR-3M, 装置： HQR(T1-1) , 分野： 2. Magnetism

研究テーマ：$LaCoO_3$中間スピン状態の軌道揺らぎに伴うフォノン異常
表題：$LaCoO_3$フォノン分散と磁気励起

52) Phonon Dispersion and Magnetic Excitations in $LaCoO_3$

K. Asai, M. Suzuki, Y. Kobayashi, T. S. Naing, M. Akimitsu, K. Yamada*[1], J. Akimitsu*[2], P. Manuel*[3], J. M. Tranquada*[4], and G. Shirane*[4]

Dept. Appl. Phys. and Chem., The University of Electro-Commun., Tokyo 182-8585, Japan;
[1]IM R, Tohoku University, Sendai, 980-8577, Japan;
[2]Dept. of Phys. & Mathematics, Aoyama Gakuin University, Sagamihara 229-8551, Japan;
[3]ISIS, RAL, Didcot OX110QX, UK; [4]BNL, New York 11973 USA

The magnetic anomaly of $LaCoO_3$ around 100 K has been ascribed to a broad spin-state transition from the nonmagnetic low spin (LS) to an intermediate spin state (IS; S=1) [1]. However, the nature of the "Jahn-Teller active" IS state, especially its orbitals, has not been clarified. We have investigated the phonon and the magnetic excitations by inelastic neutron scattering with TOPAN at JRR-3M in JAERI (Tokai) using a pseudo-cubic crystal consisting of four rhombohedral twins.

Figure 1 shows the phonon dispersion along the principal axes of the pseudo-cubic reciprocal space containing one chemical formula of $LaCoO_3$. The acoustic phonon dispersions show some characteristic features of the folded Brillouin zone (BZ) due to the doubling of the unit cell for the rhombohedrally distorted perovskite structure. We observed two transverse optical (TO) phonon branches along (δ, δ, δ), consistent with the previously reported Raman active E_g modes which show remarkable softening associated with the spin-state transition [2]. We found that the softening takes place in the TO modes over the whole BZ. In contrast, the acoustic phonons show no anomalous softening associated with the spin-state transition.

We investigated paramagnetic scattering at (1.04, 0.04, 0.04) (not shown). At 8 K, the paramagnetic scattering is weak at low energy and starts to increase at around 15 meV. The scattering is ascribable to the magnetic excitation of Co^{3+} from LS to IS states. The energy scale is comparable to the energy gap between the LS and IS states obtained from other type of measurements [3].

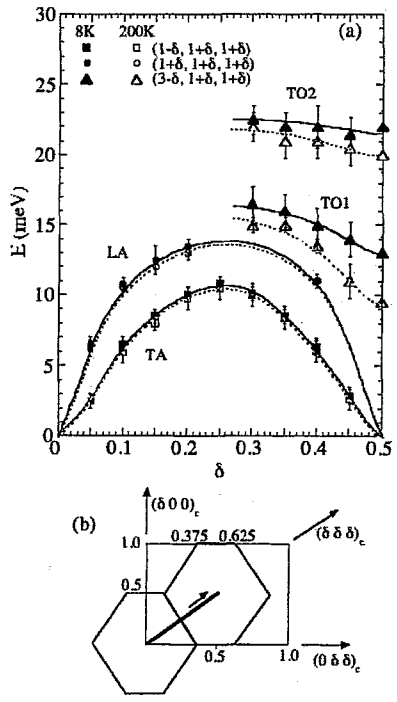

Figure 1: The phonon dispersion curves of $LaCoO_3$. Inset in (c) shows the trajectories for the scans. The hexagon and the rectangle are the $(011)_C$ section of the BZ for the rhombohedral and pseudo-cubic unit cells, respectively.

References

[1] For example, K. Asai et al., J. Phys. Soc. Jpn. **67** (1989) 290.
[2] A. Ishikawa et al., Phys. Rev. Lett. **93** (2004) 136401.
[3] Y. Kobayashi et al., Phys. Rev. B **62** (2000) 410.

使用施設：JRR-3M，装置：TOPAN(6G)，分野：強相関電子系

研究テーマ :界面効果を利用したCr薄膜のスピン構造制御 −スピン密度波の温度依存位相スリップの検証−
表題 :Cr(001)/非磁性金属単原子層人工格子におけるCrスピン構造の非磁性元素依存性

53) Spin Structures of Cr in Cr(001)-Based Multilayers with Periodically Inserted Nonmagnetic Monatomic Layers

K. Mibu, N. Jiko*, Y. Otsuka, and M. Takeda**

*Research Center for Low Temperature and Materials Sciences, Kyoto University, Uji, Kyoto 611-0011, Japan; *Institute for Chemical Research, Kyoto University, Uji, Kyoto 611-0011, Japan; **Advanced Science Research Center, JAERI, Tokai, Ibaraki 319-1195, Japan*

Magnetic structures of epitaxial Cr(001)/X multilayers, where monatomic layers of X (X = V, or Au) are periodically embedded in Cr, were studied by neutron diffraction measurements using a triple-axis spectrometer, TOPAN, at JRR-3M. The scans were carried out through the Cr(100) and Cr(010) reciprocal points, around which magnetic peaks due to antiferromagnetic structures are expected to appear. For Cr(001)/Sn multilayers, it has already been reported that spin-density-wave (SDW) antiferromagnetic structures with the modulation along the perpendicular direction to the film plane are stabilized at low temperatures when the Cr layer thickness is larger than 8 nm [1, 2].

The observed temperature dependence of neutron diffraction patterns for [Cr(16.0 nm)/Au(0.2 nm)] and [Cr(16.0 nm)/V(0.2 nm)] multilayers around the Cr(010) point along the [001] direction (i.e., (01*L*) scan profiles) is shown in Figs. 1 (a) and (b). In the Cr/Au multilayer, a commensurate antiferromagnetic structure is stabilized at room temperature and an incommensurate SDW structure with the wave vector parallel to the film normal and with antinodes pinned at the interfaces appears at low temperatures, as in [Cr(16.0 nm)/Sn(0.2 nm)] multilayer. In the Cr/V multilayer, on the other hand, the magnetic structure at room temperature is not simply commensurate-antiferromagnetic, but modulated by the artificial periodicity due to a quenching of magnetic moments at the interface regions. At low temperatures, an incommensurate SDW phase with a node at each Cr/V interface and four nodes at the inner part of the Cr layer appears. In this way, it is clearly shown that the spin structure of Cr is quite different dependent on the sort of nonmagnetic element even when the Cr layer thickness is the same. The results are interpreted as a consequence of a competition between the nesting effect, which stabilizes the incommensurate SDW structure, and the interface effect, which enhances or quenches the magnetic moment of Cr at the interface regions.

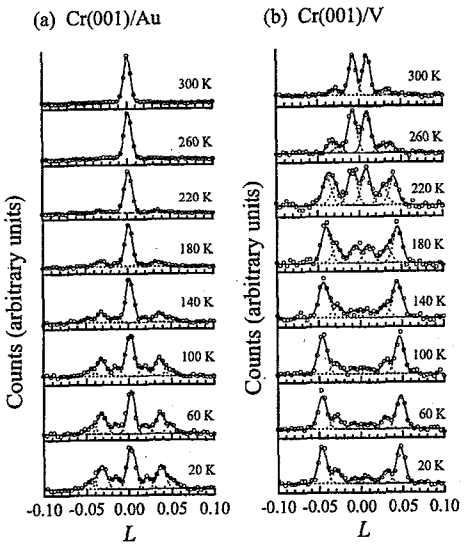

Figure 1: Temperature dependence of neutron diffraction patterns for (a) [Cr(16.0 nm)/Au(0.2 nm)] and (b) [Cr(16.0 nm)/V(0.2 nm)] multilayers around the Cr(010) point along the [001] direction. The abscissa is expressed by the reciprocal lattice units of $2\pi/a_{001}$.

References

[1] K. Mibu *et al.*, Phys. Rev. Lett. **89** (2002) 287202.
[2] M. Takeda *et al.*, Phys. Rev. B **70** (2004) 104408.

使用施設 :JRR-3M, 装置 :TOPAN(6G), 分野 Magnetism

1. 中性子散乱 3)超伝導現象

1. Neutron Scattering 3) Superconductivity

This is a blank page.

研究テーマ：$La_{1.875}Ba_{0.125-x}Sr_xCuO_4$高温超伝導体における電荷ストライプ秩序と低エネルギーフォノン

表題： $La_{1.875}Ba_{0.125}CuO_4$のソフトフォノンと構造相転移

1) Soft phonons and structural phase transitions in $La_{1.875}Ba_{0.125}CuO_4$

H. Kimura[1], H. Goka[2], M. Fujita[3], Y. Noda[1], K. Yamada[3], and G. Shirane[4]

[1] *IMRAM, Tohoku University, Sendai 980-8577, Japan*

[2] *Department of Physics, Kyoto University, Kyoto 606-8502, Japan*

[3] *IMR, Tohoku University, Sendai 980-8577, Japan*

[4] *Brookhaven National Laboratory, Upton, New York 11973-5000, U. S. A.*

It is well known that high-T_c cuprates of $La_{2-x}Ba_xCuO_4$ shows a structural phase transition from the high-temperature tetragonal (HTT) to the low-temperature orthorhombic (LTO). In addition, around the Ba concentration of $x = 0.125$, further phase transition from the LTO to the low-temperature tetragonal (LTT) follows the HTT – LTO transition on cooling temperature. Previous neutron scattering study have shown that the HTT – LTO transition is caused by the softening of the zone-boundary TO phonon[1]. Although the LTO – LTT transition is also understood as the displacive phase transition with the condensation of the soft phonon, there have been no systematic study about the soft phonon associated with the LTO – LTT phase transition.

In the present study, the soft phonon of $La_{1.875}Ba_{0.125}CuO_4$, of which superconductivity is almost suppressed by a charge stripe order, was measured for a wide temperature range involving HTT – LTO – LTT structural phase transitions. We clarified that the LTO – LTT transition is a first order and thus the LTO and LTT phase coexist in the vicinity of phase transition temperature. The dispersion relation of phonons along a-axis suddenly changes at the LTO – LTT transition, while that along c-axis is temperature independent, which is not seen in the HTT – LTO transitions.

The single crystal of $La_{1.875}Ba_{0.125}CuO_4$ was grown by TSFZ method. Inelastic neutron scattering measurements for soft phonons were performed at triple-axis spectrometers TOPAN and HER, where the final energy of neutrons was fixed at 13.5 meV and 4 meV, respectively. The energy resolutions in TOPAN and HER experiments are 0.9 meV and 0.2 meV, respectively.

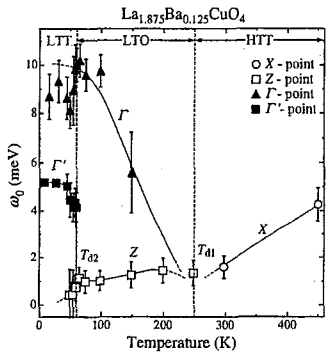

Fig. 1. The soft phonon energies for several modes as a function of temperature.

Figure 1 shows the summary of soft phonon behaviors as a function of temperature. The phonon at degenerate X-point (open circles) in the HTT phase goes soft with decreasing temperature and splits into two modes in the LTO phase, which correspond to zone-boundary phonon at Z-point and zone-center one at Γ-point. On further cooling temperature, the Z-point phonon (open squares) remains soft and start decreases again in energy while the Γ-point phonon (filled triangles) keeps on hardening with decreasing temperature. Below $T \sim 60$ K, Z-point phonon discontinuously hardens and its energy becomes almost temperature independent (filled squares), showing that the first-order LTO-LTT phase transition occurs and the LTT phase becomes robust rapidly.

Details of this study were published elsewhere[2].

References

[1] T. R. Thurston *et al.*:Phys. Rev. B **39** (1989) 4327 and references therein.

[2] H. Kimura *et al.*: J. Phys. Soc. Jpn **74** (2005) 445.

使用施設：JRR-3M, 装置： 6G (TOPAN), C1-1 (HER) , 分野： 3. Strongly Correlated Electron Systems

研究テーマ：強相関電子系酸化物の結晶・磁気構造同時解析
表題： 単結晶磁気構造解析による Nd_2CuO_4 のスピン密度分布の可視化

2) Imaging of spin density distribution by single crystal magnetic structure analysis in Nd_2CuO_4

H. Kimura[1], K. Kadoshita[1], Y. Noda[1],and K. Yamada[2]
[1] *IMRAM, Tohoku University, Sendai 980-8577, Japan*
[2] *IMR, Tohoku University, Sendai 980-8577, Japan*

Imaging of spin density distribution has been tried to understand the 3*d*-electron orbital state which contributes to a large variety of physics in strongly correlated electron systems. A polarized neutron diffraction has been used for this trial and clarified the orbital order in ferromagnetic $YTiO_3$[1]. In the present study, we performed crystal- and magnetic structure analyses by using four-circle diffractometer with unpolarized neutron to visualize the spin density distribution on 3*d*-electron orbital. In this method, we can obtain the absolute value of magnetic structure factors in a wide Q-region, of which inverse Fourier transform corresponds to the spin density. The target material of this study is Nd_2CuO_4 (NCO). NCO is an antiferromagnet with $3d^9$ configuration for Cu^{2+} ion and thus $S = 1/2$ spin localizes on $d_{x^2-y^2}$ orbital.

The single crystal of NCO was grown by TSFZ method and cut and shaped into 5 mm sphere to minimize the corrections of absorption and extinction effect. The measurements were performed using the four-circle diffractometer FONDER installed at T_{2-2} thermal guide in JRR-3M. The wavelength of neutron was 1.243 Å. The maximum values of $\sin\theta/\lambda$ for nuclear and magnetic Bragg reflections were about 0.79 and 0.6 $Å^{-1}$, respectively.

Crystal structure analysis was firstly performed to obtain the exact scale factor, which was well solved with a reliability factor $R = 5$ %. The magnetic structure with an assumption of $< j_0 >$ magnetic form factor was solved with $R_M = 8$ %, which is consistent with the previous result[2]. Somewhat poor accuracy of R_M indicates that the magnetic form factor becomes anisotropic due to a $d_{x^2-y^2}$ orbital. We performed Fourier synthesis of observed magnetic form factor

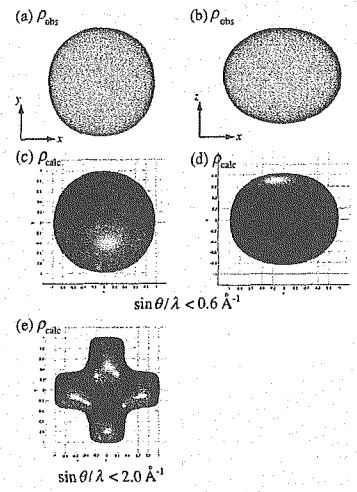

Fig. 1. Comparison of the (a),(b); observed spin density and (c)-(e); calculated one projected into xy-plane (left side) and zx-plane (right side).

f_{obs} within $\sin\theta/\lambda < 0.6$ Å, which corresponds to the $S = 1/2$ spin density ρ_{obs}. Figures 1(a) and (b) shows ρ_{obs} projected into xy- and zx-plane, respectively, indicates 2-dimensional distribution of $S = 1/2$ electron along xy-plane. For comparison, the calculated spin density ρ_{calc} based on a $d_{x^2-y^2}$ orbital is displayed in Figs. 1(c) and (d), which quite well reproduces ρ_{obs}. Both the ρ_{obs} and ρ_{calc} are almost isotropic in xy-plane, which is due to a narrow Q-range with $\sin\theta/\lambda < 0.6$ Å. In fact, when a $\sin\theta/\lambda$ is extended to 2 Å, ρ_{calc} well describes a $d_{x^2-y^2}$ orbital (See Fig. 1(e)). The present study have shown that our method using four-circle diffractometer is useful to obtain the spin density distribution.

References

[1] H. Ichikawa *et al.*: Physica B **281&282** (2000) 482.
[2] M. Matsuda *et al.*: Phys. Rev. B **42** (1990) 16.

使用施設：JRR-3M, 装置： T2-2 (FONDER), 分野： 3. Strongly Correlated Electron Systems

研究テーマ： 強磁性超伝導体の自発的渦糸構造の観測
表題： YNi_2B_2C の磁束格子に関する研究

3) *H-T* Phase Diagram of Flux Line Lattice Structure in YNi_2B_2C

H. Kawano-Furukawa[1], H. Tsukagoshi[1], F. Yano[1], T. Nagata[1], N. Sakiyama[2], H. Yoshizawa[2], M. Yethiraj[3], H. Takeya[4], J. Suzuki[5]

[1] *Department of Physics, Ochanomizu Univ., Tokyo 112-8610, Japan*
[2] *Neutron Science Laboratory, I.S.S.P., The University of Tokyo, Ibaraki 319-1106, Japan*
[3] *Center for Neutron Scattering, Oak Ridge National Laboratory, TN 37831-6393, USA*
[4] *National Institute for Materials Science, Ibaraki 305-0047, Japan*
[5] *Advanced Science Research Center, J.A.E.R.I., Ibaraki 319-1195, Japan*

Recently, Nakai *et al.* proposed a theoretical *H-T* phase diagram of the FLL structure [1] for a system with fourfold anisotropies in Fermi velocity and superconducting gap. Both anisotropies stabilize a square FLL. Here $\square_v$ and $\square_g$ denote FLL structures reflecting each anisotropy. $RENi_2B_2C$ system has both anisotropies and orientations of FLL structures stabilized by such anisotropies seem to be 45° off. Therefore, successive FLL transitions from a triangular ($\triangle$) → a square ($\square_v$) → a triangular ($\triangle$) → another square ($\square_g$) may appear with increasing a magnetic field. To check their prediction, we have performed small angle neutron scattering (SANS) experiments.

A single crystal of $YNi_2^{11}B_2C$ was grown by the floating zone method. In order to reduce neutron absorption by ^{10}B, ^{11}B isotope was used. A superconducting transition temperature and an extrapolated upper critical magnetic field of our sample are $T_c(0) = 14.2$ K and $H_{c2}(0) \sim 6.5$ T, respectively. Small angle neutron scattering (SANS) measurements were performed at SANS-J and SANS-U installed in the guide hall of the JRR-3 reactor. An incident neutron beam with $\lambda = 6.5 \sim 11$ Å was set to be parallel to a magnetic field and the crystal *c*-axis. All measurements were performed in a field cooled process, and an oscillating field (maximum amplitude 0.15 T) was applied at each measuring temperature to bring a FLL alignment to the equilibrium state [2]. In addition, above 0.5 T, the sample was rotated to satisfy a Bragg condition.

We studied the FLL structure under various magnetic fields up to $H = 5$T, $H/H_{c2} \sim 0.77$. In Fig. 1 the resultant *H-T* phase diagram of the FLL structure in $YNi_2^{11}B_2C$ is depicted. The present results revealed that the $\triangle$ lattice appears only in a low magnetic field region near H_{c1}, and the $\square_v$ lattice occupies almost entire region of the $H-T$ phase diagram. Furthermore, in the latter case, the orientation of the nearest neighbor FLL is along the [110] direction, where the Fermi velocity has the minimum value, indicating the square lattice is of $\square_v$ type. There is no sign of a transition either towards the $\square_g$ lattice or to the $\triangle$ lattice in higher magnetic fields region.

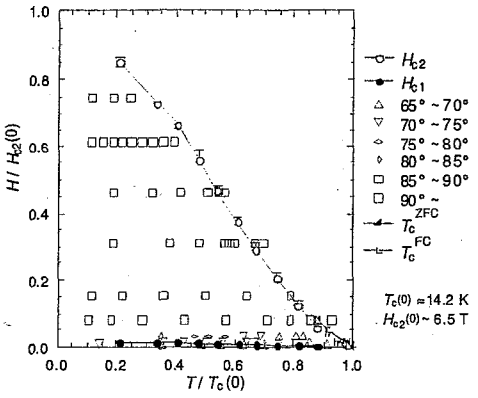

Fig. 1. *H-T* phase diagram of FLL in YNi_2B_2C. Temperature and magnetic field is normalized by $T_c(0)$ and $H_{c2}(0)$, respectively.

References

[1] N. Nakai et al., *Phys. Rev. Lett*, **89**, 237004 (2002).
[2] S. J. Levett et al., *Phys. Rev. B*, **66**, 014515 (2001).

使用施設：JRR-3M, 装置： C1-2, C3-2 , 分野： 103. Strongly Correlated Election Systems

研究テーマ： UGe_2 における強磁性と超伝導の共存状態の研究
表題： 強磁性超伝導体 UGe_2 におけるストーナーギャップ

4) Stoner Gap in the Superconducting Ferromagnet UGe_2

Naofumi Aso, Gaku Motoyama[A], Yoshiya Uwatoko, Seiko Ban[B], Yoshiya Homma[C], Yoshinobu Shiokawa[C], Kazuma Hirota, and Noriaki K. Sato[B]

ISSP U. Tokyo, [A] Hyogo Pref. U., [B] Dept. Phys., Nagoya U., [C] IMR Tohoku U.

Saxena et al. discovered the ferromagnetic superconductor UGe_2 in which superconductivity occurs at high pressures [1]. In the ferromagnetic phase, there seems to be another phase transition or crossover at T_x ($\simeq$ 32 K at ambient pressure). This characteristic temperature T_x also decreases with increasing pressure and becomes suppressed to zero at another critical pressure P_x ($\simeq$ 1.2 GPa). Superconductivity appears in the pressure range between $\sim$1.0 and $\sim$1.5 GPa. Since a maximum superconducting transition temperature ($T_{SC} \sim$ 0.7 K) appears at around P_x [1], we speculate that the critical point P_x can be related to the onset of the superconductivity, as was theoretically argued by Watanabe and Miyake [2] and Sandeman et al. [3]. However, it remains unclear what happens at P_x. In this work, we present the temperature dependence of magnetic Bragg peak intensities under pressure by the neutron diffraction technique to reveal the nature of the transition at P_x.

A single crystal was grown by Czochralsky pulling method with a tetra-arc furnace. [4] The pressure was generated by a beryllium-copper based piston-cylinder clamp device using Fluorinert FC-75 as a pressure transmitting medium and was estimated by determining the change in lattice parameter of the NaCl. Elastic neutron scattering experiments has been performed on the triple-axis spectrometers HER (C1-1) and PONTA (5G).

In fig. 1 we show the pressure dependence of magnetic Bragg peak intensities $I_B(T)$ at Q = (0,0,1) as a function of temperature. All data were accumulated at $k_i = 1.555$ Å^{-1} in the process of increasing temperature. While there is no apparent anomaly at 0.28 GPa, we clearly observed at 1.1 GPa a steep increase below $T_x \sim$ 10 K. (In the present study, we define T_x as a maximum temperature appearing in the second derivative of the $I_B(T)$ curve with respect to T.) We note that the overall feature of the present result is consistent with the Bragg peak intensity and static magnetization data previously reported in Refs. [5, 6, 4]. At 1.23 GPa, such an anomalous behavior was not observed in accordance with $P_x \sim$ 1.2 GPa.

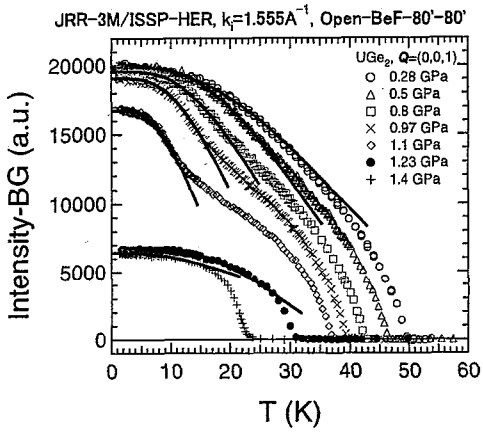

Fig. 1. Temperature dependence of the ferromagnetic Bragg peak intensities at Q = (0,0,1) against the temperature T measured at various pressures. The solid lines are calculated results on the basis of the Stoner model described in the text.

we calculate the magnetic Bragg peak intensities in terms of a conventional Stoner model, which is expressed as follows (see, for example, [7]);

$$M = M_0\{1 - \alpha \cdot T^{\frac{3}{2}} \cdot \exp(-\Delta/T)\}, \quad (1)$$

$$\alpha = \frac{3}{4}\sqrt{\pi}\{\frac{1}{E_F}\}^{\frac{3}{2}}, \Delta = 2E_F\{\frac{\Theta'}{E_F} - 2^{-\frac{1}{3}}\}, \quad (2)$$

where M_0 indicates the magnetization at zero temperature, Δ a so-called Stoner gap, E_F a Fermi energy, and Θ' is a molecular field coefficient. The results are shown in fig. 1 by the solid lines. Interestingly, we find remarkably good accordance between the experiment and the calculation. This suggests

使用施設：JRR-3M，装置： C1-1 (HER), 5G (PONTA)，分野： 103: Strongly Correlated Electron Systems

that the decrease of the magnetization at very low temperatures is mainly caused by the electron-hole excitation in quasiparticle bands.

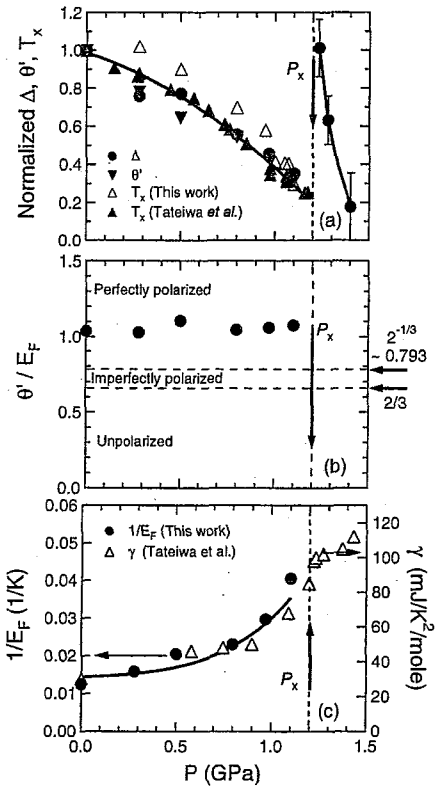

Fig. 2. Pressure dependence of the obtained parameters from the Stoner model. The solid lines are guides to the eye. (a) Δ, Θ', and T_x (b) Ratio of Θ'/E_F (c) Inverse Fermi energy $1/E_F$ are plotted against P below P_x.

From the least square fitting, we estimate a set of parameters α and Δ in eq. (1), which further enables us to evaluate E_F and Θ' using eq. (2). In Fig. 2 (a) we show Δ and Θ' together with T_x, each of which is normalized to a respective value at ambient pressure. It is interesting to note that these quantities seem to lie on a single line, suggesting that the characteristic temperature of the unknown origin, T_x , is related to the Stoner gap Δ (equivalently Θ') in the quasiparticle band. In Fig. 2 (b) we plot a ratio of Θ'/E_F against P. According to the Stoner model, if the ratio is greater than $2^{-\frac{1}{3}}(\sim 0.793)$, then the system is in a perfectly polarized ferromagnetic state, where only a majority spin band is occupied. When the ratio lies between 2/3 and $2^{-\frac{1}{3}}$, an imperfectly polarized ferromagnetic state occurs, where a minority spin band becomes to be partially occupied by quasiparticles. Further in the case that the ratio is smaller than 2/3, the system is paramagnetic. As seen in the figure, our analysis indicates that the perfectly polarized state is realized below P_x in UGe_2. Actually, band structure calculations indicate that Fermi surfaces have a predominantly majority spin character [8, 9], providing a supporting evidence for our model. We plot $1/E_F$ vs. P in Fig. 2 (c). Assuming that $E_F D(E_F)$ is a constant value independent of the pressure, where $D(E_F)$ denotes a density of states at E_F, then $1/E_F$ is proportional to $D(E_F)$, and hence to an electronic specific heat coefficient γ. As clearly seen in Fig. 2 (c), we find that $1/E_F = c\gamma$, where c is a constant independent of P and γ is an observed value reported by Tateiwa et al. [10]. This coincidence between $1/E_F$ and γ strongly supports the applicability of the present model to UGe_2.

References

[1] S.S. Saxena et al., Nature (London) **406** (2000) 587.

[2] S. Watanabe and K. Miyake, J. Phys. Soc. Jpn. **71** (2002) 2489.

[3] K.G. Sandeman et al., Phys. Rev. Lett. **90** (2003) 167005.

[4] G. Motoyama et al., Phys. Rev. **B 65** (2002) 020510.

[5] A. Huxley et al., Phys. Rev. **B 63** (2001) 144519.

[6] N. Tateiwa et al., J. Phys. Soc. Jpn. **70** (2001) 2876.

[7] E.C. Stoner, Proc. Roy. Soc. **A 165** (1938) 372.

[8] H. Yamagami, J. Phys. Cond. Matt. **15** (2003) S2271.

[9] A.B. Shick and W.E. Picket , Phys. Rev. Lett. **63** (2001) 300.

[10] N. Tateiwa et al., J. Phys. Cond. Matter **13** (2001) L17.

[11] N. Tateiwa et al., Physica **B 312-313** (2002) 109.

研究テーマ： UGe_2 の磁気揺動
表題： UGe_2 の磁気揺動

5) Magnetic fluctuations in UGe_2

H. Sagayama[1], K. Kuwahara[2], M. Kohgi[2], M. Nishi[3],
Y. Haga[4], T.D. Matsuda[4], E. Yamamoto[4] and Y. Ōnuki[4,5]

[1] *Photon Factory, IMSS, High Energy Accelerator Research Organization, Tsukuba 305-0801*
[2] *Department of Physics, Tokyo Metropolitan University, Tokyo 192-0397*
[3] *ISSP, University of Tokyo, Chiba 277-8581*
[4] *ASRC, Japan Atomic Energy Research Institute, Ibaraki 319-1195*
[5] *Department of Physics, Graduate School of Science, Osaka University, Osaka 560-8531*

The discovery of the pressure-induced superconductivity of the Ising ferromagnet UGe_2 with an easy magnetization axis a and a Cure temperature T_C = 52 K at ambient pressure has been attracting much interest [1]. As increasing pressure, T_C deceases and vanishes at ~1.6 GPa. The superconductivity appears in a limited pressure range between 1.0 GPa and 1.6 GPa below the superconducting transition temperature T_{SC} ~0.8 K. Other than the characteristic energy scales T_C and T_{SC}, this system has a characteristic energy scale T^* (~35 K at ambient pressure), where the macroscopic anomalies have been observed in some measurements. As increasing pressure, the characteristic temperature T^* also decreases and vanishes around P^* = ~1.2 GPa. It has been discussed that T^* is related to the superconductivity because T_{SC} is a maximum in the vicinity of P^*. In order to investigate the relation between the magnetic fluctuation and the T^* anomaly, therefore, we performed the inelastic neutron stcattering experiment on UGe_2.

Cylindrical UGe_2 single crystals with approximate 3.5 mm diameter by 3~5 cmm long were grown in a tetra-arc furnace using the Czochralski pulling method. They had the a-axis along the cylinder axis. The four single crystals were assembled in an aluminum holder. The assembly was set in the 4 K cryostat. The inelastic neutron scattering experiment was performed on the three-axis spectrometer PONTA (5G) at the JRR-3M reactor. Energy scans at constant Q in the $(h0l)$ plane were done with the fixed final neutron energy 14.7 meV and with collimation open-80'-80'-80'.

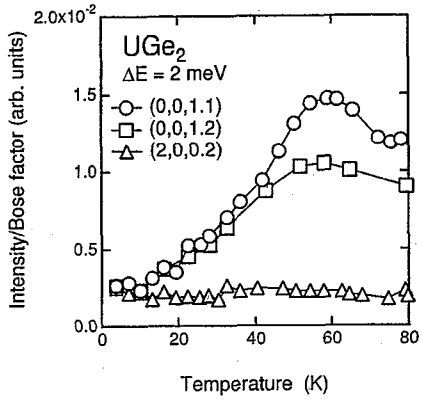

Fig. 1. Temperature dependence of the intensities at transfer energy 2 meV with Q = (0,0,1.1), (0,0,1.2) and (2,0,0.2).

Figure 1 shows the temperature dependence of the intensities at transfer energy 2 meV with the different Q vectors. The intensties for Q = (0,0,1.1) and (0,0,1.2) show the strong temperature depemdence and have a peak at T_C, while the intensity for Q = (2,0,0.2) are almost background level. This longitudinal magnetic fluctuations along the a-axis are consistent with the uniaxial magnetic anisotropy of UGe_2. It is obscure whether the intensities for Q = (0,0,1.1) and (0,0,1.2) change around T^*. Further inelastic neutron scattering study with higher resolution and counting statics may be needed.

References

[1] S.S. Saxena *et al.*, Nature 406 (2000) 587.

使用施設：JRR-3M, 装置： 5G(PONTA), 分野： 3. Strongly Correlated Electron Systems

研究テーマ：高温超伝導体 $La_{2-x}Sr_xCuO_4$ における低エネルギー磁気励起と静的磁気相関の磁性・非磁性不純物置換効果

表題：ZnおよびNiを置換した $La_{1.85}Sr_{0.15}CuO_4$ におけるスピン揺動の q-ω 構造の質的な相違

6) Qualitative differences of q-ω structure of spin excitations between Zn and Ni-doped $La_{1.85}Sr_{0.15}CuO_4$

M. Kofu[1,2], H. Kimura[3], M. Matsuura[2], and K. Hirota[2]

[1] *Department of Physics, Tohoku University, Sendai 980-8578*

[2] *Institute for Solid State Physics, The University of Tokyo, 106-1 Shirakata, Tokai 319-1106*

[3] *Institute of Multidisciplinary Research for Advanced Materials, Tohoku University, Sendai 980-8577*

In high-T_c cuprates, impurity substitution for the Cu site dramatically suppresses the superconductivity. In particular, nonmagnetic ion Zn^{2+} ($3d^{10}$, $S = 0$) is a strong high-T_c killer and reduces T_c more than magnetic ion Ni^{2+} ($3d^8$, $S = 1$). These behaviors are different from those for BCS superconductors and imply a close relation between the magnetism and the superconductivity. We systematically investigated how impurities affect the low-energy spin excitations, particularly paying attention to the difference between the effects of Zn and those of Ni.

Neutron scattering experiments were performed with the triple-axis spectrometer TOPAN installed at 6G beam port. We selected the final energy of 13.5 meV with the horizontal collimator sequence of 40′-30′-30′-80′. Single crystals of Zn and Ni doped $La_{1.85}Sr_{0.15}CuO_4$ were grown by a traveling solvent floating zone method. Impurity-free $La_{1.85}Sr_{0.15}CuO_4$ exhibits T_c of 36.8 K, and the reduction rates of T_c are 12.5 K/% for Zn and 8.7 K/% for Ni.

Figure 1 shows the q-ω sturucture of spin excitations for impurty-free ($y = 0$), Zn-doped (Zn:$y = 0.017$) and Ni-doped (Zn:$y = 0.029$) sample. In $y = 0$, a well defined energy gap in the spin excitation spectrum was observed at low temperature, and the gap is called "spin gap" [?]. In Zn:$y = 0.017$ and Ni:$y = 0.029$, low-energy excitations below the spin gap energy ($\omega \sim 4$ meV) appear. However, we observed obvious differences of q-ω sturucture between the Zn and Ni-doped samples. In Zn:$y = 0.017$, the peak positions and widths are independent of the excitation energy and almost coincide with those of $y = 0$. While in Ni:$y = 0.029$, as the excitation energy ω increases, the peak width broadens and the peak position shifts toward the magnetic zone center. These results suggest that the effects on spin excitations by non-magnetic Zn are qualitatively different from those by magnetic Ni.

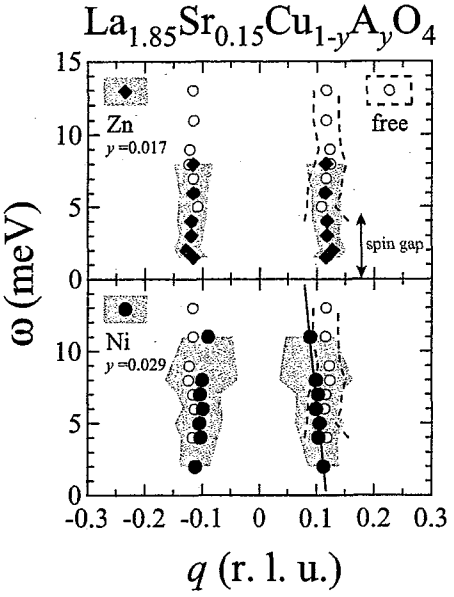

Fig. 1. Spin excitations for $y = 0$, $La_{1.85}Sr_{0.15}Cu_{1-y}Zn_yO_4$ (Zn:$y = 0.017$) and $La_{1.85}Sr_{0.15}Cu_{1-y}Ni_yO_4$ (Ni:$y = 0.029$) at low temperature. q denotes the propagation vector of spin correlation; $q = 0$ means the magnetic zone center Q =(0.5, 0.5, 0). Closed (open) circles and shaded (dashed) regions represent the peak position and FWHM of incommensurate magnetic signals estimated from curve-fitting for impurity-doped (free) samples. A solid line indicates a guide to the eye of dispersion for Ni:$y = 0.029$.

References

[1] K. Yamada *et al.*: Phys. Rev. Lett. **75**, 1626 (1995).

使用施設：JRR-3M，装置：6G (TOPAN)，分野：3. Strongly Correlated Electron Systems (c)

研究テーマ：強磁性モット絶縁体 $Y_{1-x}Ca_xTiO_3$（x＜0.15）の軌道秩序
表題：偏極中性子回折法による強磁性モット絶縁体 $Y_{1-x}Ca_xTiO_3$ の軌道秩序観測

7) Determination of Orbital Ordering in $Y_{1-x}Ca_xTiO_3$ ($x < 0.15$) Ferromagnet by using Polarized Neutron Diffraction Technique

F. Iga[1], M. Tsubota[1], T. Matsumura[2], K. Hirota[2,3], K. Nakajima[3], T. Nakano[1], H. Ichikawa[4], and J. Akimitsu[4]

1 *AdSM, Hiroshima University, Higashi-Hiroshima 739-8530*
2 *Department of Physics, Tohoku University, Aoba, Sendai 980-8578*
3 *Institute for Solid State Physics, University of Tokyo, Shirakata, Tokai 319-11006*
4 *Department of Physics, Aoyama-gakuin University, Fuchinobe, Sagamihara 229-8558*

In transition-metal oxides, an interplay among the spin, charge, and orbital orderings has attracted much attention [1]. The orbital ordering, *i.e.*, ordering of the polarization of occupation among degenerate 3*d* orbits of transition-metal ions, affects the physical properties such as transport, magnetic, and thermal properties. $YTiO_3$ is a d^1-system, which is well known as a Mott-Hubbarad insulator with a Coulomb repulsion energy $U \sim 1$ eV. The ferromagnetic state with a Curie temperature $T_C \sim 30$ K is archetypal for a Mott insulator because most of Mott insulators are antiferromagnetic as seen in $LaTiO_3$ and V_2O_3. $YTiO_3$ crystallize in an orthorhombic perovskite (so-called $GdFeO_3$-type) structure. The axes of TiO_6 octahedra in a $GdFeO_3$-type structure tilt from the principal crystal axes. The distorted bond angle of Ti-O-Ti is ~ 140 deg. For orbital polarizations, the order parameters are represented in terms of a component of quadrupole or higher multipole moments or a superposition of the degenerate atomic orbits.

Polarized neutron diffraction (PND) technique is a powerful method to observe the orbital ordering in a ferromagnet [2]. The advantage of this technique is that it can directly determine the accurate wave func-tions for the orbital ordered state. The disadvantage is that it is useful only below T_C. To determine the wave function, we compare the magnetic form factor μf experimentally observed with that calculated for some supposed wave functions.

For the PND measurements, we measured the forbidden magnetic diffractions which satisfy the condition of $h+k=2n+1$, where h and k are the Miller indices and n is the integer. These diffractions originate from the aspherical contribution of the spin density distribution.

In order to obtain μf, we measured some pairs of the reflection for both parallel spin (spin flipper off) and anti-parallel (on) to the direction of applied magnetic field B which saturates the magnetization (~ 0.8 μ_B). From the observed reflection intensities at the flipper off and on, we obtain the ideal intensities of $I+$ and $I-$, where the subscripts "off" and "on" stand for the switching arrangement of a spin flipper equipment, and + and – denote that the neutron spin is parallel and anti-parallel for the direction of B, respectively. In the analysis of PND, the observed polarization ratio R, which is the ratio of the intensities $I+$ and $I-$, was related to $\gamma_0 = F_M/F_N$ after instrumental corrections as below,

$$R = \frac{I_+}{I_-} = \left(\frac{F_N + F_M}{F_N - F_M}\right)^2 = \left(\frac{1+\gamma_0}{1-\gamma_0}\right)^2,$$

where F_M and F_N are the magnetic structure factor and the nuclear structure factor, respectively.

The PND experiments were done for single crystals of $Y_{1-x}Ca_xTiO_3$ (x = 0.05, 0.10 and 0.15) with the typical sample size

of about $3\times3\times6$ mm^3. We used the triple-axis spectrometer, TOPAN, installed at the beam port 6G. The data was collected at 1.6 K under a magnetic field B = 1 T applied parallel to the easy magnetization axis of c-axis with the incident neutron energy of 32.4 meV(wave length λ = 1.59 Å).

The final analyzed results of μf are shown in Fig. 1 with open circles. The bars indicate the statistical uncertainties. Note that these magnetic reflections are "forbidden" ones in the usual magnetic structure factor calculation. It means that these magnetic reflections should newly appear with the existence of the "antiferro" orbital ordering. These reflections can be observed from the aspherical contribution of the spin density distribution. Therefore, we emphasize that the presence of the magnetic reflections at these forbidden reciprocal points is a strong evidence for the existence of the antiferro orbital ordering in $Y_{1-x}Ca_xTiO_3$ ($x \leqq 0.15$).

Theoretical calculations by means of un-restricted Hartree-Fock approximation by Mizokawa-Fujimori predict orbital ordering in $YTiO_3$ as expressed by the following:

$$|\Psi_1\rangle = c_1|z_1x_1\rangle - c_2|x_1y_1\rangle$$
$$|\Psi_2\rangle = c_1|y_2z_2\rangle - c_2|x_2y_2\rangle$$
$$|\Psi_3\rangle = c_1|z_3x_3\rangle - c_2|x_3y_3\rangle$$
$$|\Psi_4\rangle = c_1|y_4z_4\rangle + c_2|x_4y_4\rangle$$

where $|z_nx_n\rangle$, $|y_nz_n\rangle$ and $|x_ny_n\rangle$ denote the wave function of irreducible representation in the t_{2g} and c_1/c_2 denote the ratio of the wave function with the normalization condition as $c_1^2 + c_2^2 = 1-x$. Here, it is noted that the bond lengths TiO_x and TiO_y are the longest in the TiO_6 octahedron due to the Jahn-Teller distortion for each site n = *odd* and *even*, respectively.

We determined the best-fitted parameters which give the smallest S = 1.1, 1.3 and 0.5 for x = 0.05, 0.1 and 0.15, respectively. The parameters which give the smallest S are listed in the table.

The coefficient c_1^2 of 0.5 = $(0.71)^2$ for x = 0.05 is almost the same value of 0.6 = $(0.77)^2$ for x = 0. This means the orbital ordering is stable for small diluting Ti^{3+} with Ti^{4+}.

However c_1^2 becomes 0 above x = 0.1 in analysis. But this value is uncertain due to the largeness of possible range of c_1^2 within the analytical error. Then, we could not determine the unique wave functions for $0.1<x<0.15$, but it is found that the strong evidence of orbital ordering is obtained by the polarized neutron diffraction $x>x_{FP}$=0.2.

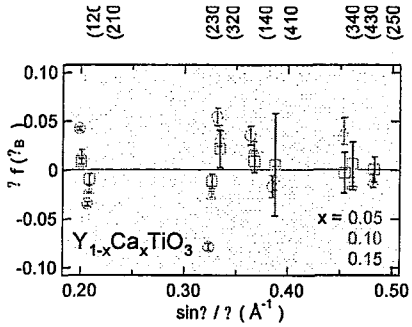

Figure 1: The magnetic form factors indicated by open circles (○), triangle(△) and aquares (□) for x =0.05, 0.10 and 0.15, respectively, with error bars.

x	c_1^2	$\mu(\mu_B)$	
		μ_H	μ_{5T}
0.0	0.6	0.72	0.84
0.05	0.5	0.62	0.78
0.1	0	0.14	0.69
0.15	0	0.07	0.51

Table 1: The fitting parameters c_1^2 and μ_H for comparison between the observed magnetic form factors and calculated ones in $Y_{1-x}Ca_xTiO_3$ (x = 0.05, 0.1 and 0.15). μ_{5T} is estimated from the measurements of the magnetization at 2 K.

References

[1]M. Imada etal., Rev. Mod. Phys. **70** (1998) 1039.
[2]J. Akimitsu etal., J. Phys. Soc. Jpn. **70** (2001) 3475.

研究テーマ： La214系のアンダードープ領域における低エネルギー磁気揺らぎと結晶構造の相関

表題： 平坦CuO_2面を有するアンダードープLa-214系高温超伝導体の磁気励起

8) Spin fluctuations in underdoped high-T_c superconductor with flat CuO_2 planes

M. Fujita[1], H. Goka[2], and K. Yamada[1]

[1] *Institute for Materials Research, Tohoku University, Sendai 980-8577, Japan*

[2] *Department of Physics, Kyoto University, Kyoto 606-8502, Japan*

Since the discovery of spin-density-wave (SDW) and charge-density-wave (CDW) orders in a lamellar copper-oxide [2], much interest has been focused on the role of stripe correlations for high-T_c superconductivity. Recent neutron scattering experiments on a 1/8-hole doped $La_{1.875}Ba_{0.125-x}Sr_xCuO_4$ system [3, 4] clearly demonstrate a distinct structural effect on SDW and CDW orders; the CDW order is stabilized in the LTT (low-temperature-tetragonal) phases and dramatically degraded towards the LTO (low-temperature-orthorhombic) phase, while peak-intensity from the SDW order remains even in the LTO phase.

On the other hand, optimal-doped $La_{2-x}Sr_xCuO_4$ (LSCO) shows an energy gap in the spin excitations below T_c[5], while no evidence of the spin gap is observed in the SC state of underdoped samples where the evidences for existence of static stripe order were observed. Since the underdoped LSCO has LTO structure at low temperature, it would be possible that the spin gap is hidden by the low-energy stripe fluctuations enhanced by a corrugation of CuO_2 planes. Thus, it is important to study spin fluctuations in an idel system which is free from the effects of crystal structure. We therefore investigated low-energy spin fluctuations in Ce-doped $La_{1.76}Sr_{0.24}CuO_4$ whose crystal structure remains to be high-temperature-tetragonal with flat CuO_2 planes.

In Fig. 1, the energy(ω)-dependence of the magnetic peak intensity is shown for $La_{1.64}Ce_{0.12}Sr_{0.24}CuO_4$. Intensity is evaluated from measured q-spectra after subtracting background. Below $\omega\sim$8 meV, the peak-intensity increases with increasing energy. This behavior is quite different from the result for stripe ordered phase of $La_{1.875}Ba_{0.125}CuO_4$, in which the intensity is almost independent of ω. Therefore, component of low-energy stripe fluctuations are reduced in the system with flat CuO_2 plane, compared with the case of LTT phase of $La_{1.875}Ba_{0.125}CuO_4$, although the hole concentration for two system is comparable. Furthermore, in the present sample, no magnetic order was observed. Thus, our experimental result suggests the existence of gap-like structure in the spin excitation spectrum of the underdoped region. In order to conclude the existence of spin gap, further systematic study is required.

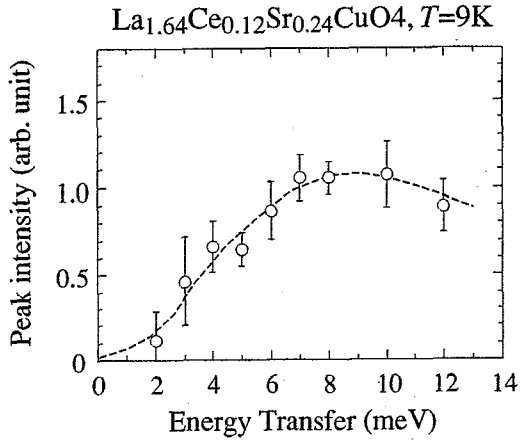

Fig. 1. Energy-dependence of intensity at the incommensurate magnetic peak position for $La_{1.64}Ce_{0.12}Ba_{0.24}CuO_4$. Dashed lines are guides to the eye.

References

[1] J.M. Tranquada*et al.*: Nature (London) **375** (1995) 561.

[2] V. J. Emery*et al.*: Phys. Rev. B **56** (1997) 6120.

[3] M. Fujita*et al.*:Phys. Rev. Lett. **88** (2002) 167008.

[4] M. Fujita*et al.*:Phys. Rev. B **66** (2002) 184503.

[5] C.H. Lee*et al.*:J. Phys. Soc. Jpn. **69** (2000) 1170.

使用施設：JRR-3M，装置： 6G, C1-1 (TOPAN, HER)，分野： 103: Strongly Correlated Electron Systems

研究テーマ： 電子ドープ型高温超伝導体の磁気揺らぎに対する不純物効果
表題： 電子ドープ高温超伝導体の磁気相関に対する不純物置換効果

9) Impurity-effect on spin correlations in electron-doped superconductor

M. Fujita, A. Hino and K. Yamada
Institute for Materials Research, Tohoku University, Sendai 980-8577, Japan

Antiferromagnetic (AF) spin correlations are believed to play a crucial role in the superconducting (SC) mechanism of lamellar copper oxides . In order to reveal the universal nature of spin correlations on underlying CuO_2 planes, impurity effects have been extensively studied for the high-T_c superconductors. Many neutron-scattering experiments on hole-doped (p-type) $La_{2-x}Sr_xCu_{1-y}Zn_yO_4$ showed an experimental evidence for the enhancement of low-energy spin fluctuations in the local AF regions near doped Zn[1] and a microscopic phase separation into superconducting and Fermi liquid regions.[2]

To understand such a novel magnetism revealed by impurity-substitution in carrier-doped Mott insulators and its relevance to the high-T_c superconductivity, comparative studies betweeen hole-doped and electron-doped (n-type) systems are indispensable. However, there are quite few investigations of spin correlations in the n-type system[3], possibly due to difficulties in preparing high quality samples through adequate heat treatments. We recently overcome such experimental difficulties and showed a magnetic and superconducting phase diagram of the n-type $Pr_{1-x}LaCe_xCuO_4$ (PLCCO). [4] We hence performed neutron-scattering experiment to investigate impurity-effect on the spin correlations in the n-type system.

In Figs. 1(a) and (b), inelastic magnetic signal measured at ω=10 meV are shown for Zn-free (T_c=26 K) and Zn-doped (T_c=14 K) $Pr_{0.89}LaCe_{0.11}CuO_4$, respectively. Well-defined commensurte peak was observed in the Zn-free sample, while in the Zn-doped sample the sintensity is rather broadly distributed around (100) position. Broad commensurate peak in the Zn-doped sample comparaed to that in Zn-free sample suggests a degradation of spin correlations by Zn-doping. Furthermore, no clear enhancement

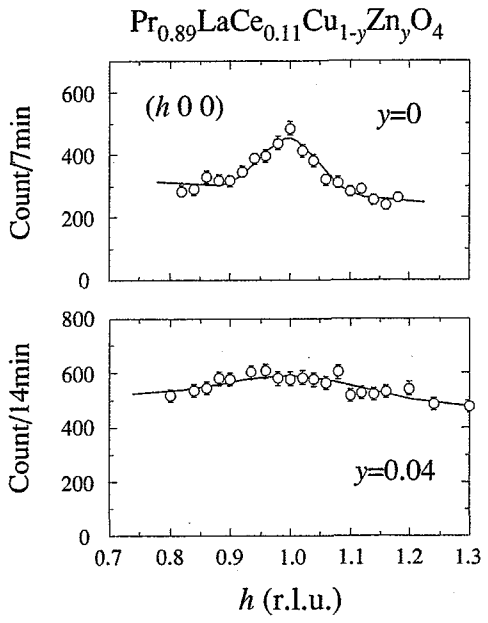

Fig. 1. Constant-ω spectra for (a) $Pr_{0.89}LaCe_{0.11}CuO_4$ and (b) $Pr_{0.89}LaCe_{0.11}Cu_{0.96}Zn_{0.04}O_4$. Scnas were done along the longitudinal direction through (100) in the orthorhombic notation, which correponds to (π, π, 0) reciprocal position.

or inducement of static antiferromagnetic order were observe even though the superconductivity is suppressed by Zn substitution. These resluts suggest a distinct impurity-effect on the spin correlations from those in p-type LSCO system and the effect of substituted non-magnetic Zn ion in the p-type system would correspond to dilution of Cu spin lattice rather than the pinning of stripe correlations.

References

[1] H. Kimura*et al.*:Phys. Rev. Lett. **91** (2003) 067002.
[2] S. Wakimoto*et al.*:cond/mat-053534.
[3] K. Yamada*et al.*:Phys. Rev. Lett. **90** (2003) 137004.
[4] M. Fujita*et al.*:Phys. Rev. B **67** (2003) 014514.

使用施設：JRR-3M，装置： 6G, C1-1 (TOPAN, HER)，分野： 103: Strongly Correlated Electron Systems

研究テーマ： 金属－絶縁体転移系 $PrRu_4P_{12}$ における磁気異常の原因
表題： $PrRu_4P_{12}$ の金属－非金属転移における p-f 混成効果

10) p-f Hybridization Effect in the Metal-Nonmetal Transition of $PrRu_4P_{12}$

K. Iwasa[1], L. Hao[1], T. Hasegawa[1], K. Horiuchi[1], Y. Mori[1], Y. Murakami[1], K. Kuwahara[2], M. Kohgi[2], H. Sugawara[3], S. R. Saha[4], Y. Aoki[2], and H. Sato[2]

[1] *Dep. of Physics, Tohoku Univ., Sendai 980-8578*
[2] *Dep. of Physics, Tokyo Metropolitan University, Hachioji, tokyo 192-0397*
[3] *Dep.of Math. and Natural Sciences, The University of Tokushima, Tokushima 770-8502*
[4] *Dep. of Physics and Astronomy, Faculty of Science, McMaster University, Canada*

$PrRu_4P_{12}$ exhibits a metal-insulator transition at $T_{M-I} = 63$ K [1]. X-ray diffraction studies revealed the structural transformation from bcc ($Im\bar{3}$) to a simple cubic ($Pm\bar{3}$) characterized by the wave vector $\mathbf{q_0} = (1\,0\,0)$ below T_{M-I} [2]. The band calculation study proposed the Fermi-surface nesting condition with $\mathbf{q_0}$, so that this phase transition has been considered as a formation of charge density wave (CDW) [3]. However, the electrical resistivity has a shoulder-like anomaly around 40 K and stays at a finite value below 1 K. Large negative magnetoresistance was also observed under magnetic field less than only 0.5 T at 0.45 K [4]. These facts indicate that the nonmetallic phase below T_{M-I} is different from the expected simple CDW formation. Since $LaRu_4P_{12}$ does not undergo a transition to nonmetallic phase in spite of the same Fermi surface nesting condition as that of $PrRu_4P_{12}$ [3, 5], it is naturally expected that the Pr-ion 4f electrons play an important role in the metal-nonmetal transition. We have carried out inelastic neutron scattering experiments [6]. Above T_{M-I}, we observed overdamped crystal-field (CF) excitations that are attributed to strong hybridization between $4f$ and conduction electrons, and the ground state was assigned to a nonmagnetic singlet Γ_1. With decreasing temperature below T_{M-I}, the excitation peaks shift by a few meV and become sharper, indicating that the $4f$-electron state becomes localized with lowering temperature. We have concluded that the hybridization effect enhances the density of states at the Fermi level and causes the metal-nonmetal transition of $PrRu_4P_{12}$. It should be noted that the Pr-ion sites split into two inequivalent CF-level schemes below T_{M-I}. One of them (Pr1) has a ground state Γ_1 and the other (Pr2) switches to a magnetic triplet $\Gamma_4^{(2)}$ at the lowest temperature. The purpose of the present study is to clarify a mechanism of the metal-nonmetal transition by determining the mutual arrangement between the atomic displacements and the CF schemes below T_{M-I} and by comparing the experimental result with the recent theoretical proposition for p-f hybridization effect in the Pr-filled skutterudite compounds [7]. To accomplish this purpose, we have performed neutron diffraction experiments. This study will be published elsewhere [8].

The experiments were performed at the thermal neutron spectrometers PONTA installed at the beam hole 5G and TOPAN at 6G of JRR-3M reactor. A powder sample and a single crystal sample were set in a cryomagnet, and magnetic fields up to 4 T were applied vertically along the crystalline axis [0 0 1] in the case of the single crystal measurement.

In the diffraction experiment for the powder sample, clear antiferromagnetic reflections induced by the applied magnetic field were observed, which is characterized by the same wave vector $\mathbf{q_0} = (1\ 0\ 0)$. This result indicates the two inequivalent induced magnetic moments at the unit-cell corner and center Pr ion sites. In order to determine the mutual configuration between the magnetic moment distribution and the atomic displacements, we carried out a polarized neutron diffraction measurement. Circles in Fig. 1 shows the flipping ratio $I_+/I_- \cong |F_N(\mathbf{Q}) + F_M(\mathbf{Q})|^2/|F_N(\mathbf{Q}) - F_M(\mathbf{Q})|^2$ at 2.2 K and at 4 T for various $\mathbf{Q}$ positions not only for the superlattice but also for the fundamental reflections. It is obvious that the

使用施設：JRR-3M; 装置： 5G (PONTA), 6G (TOPAN) , 分野： 103. **Strongly Correlated Electron Systems**

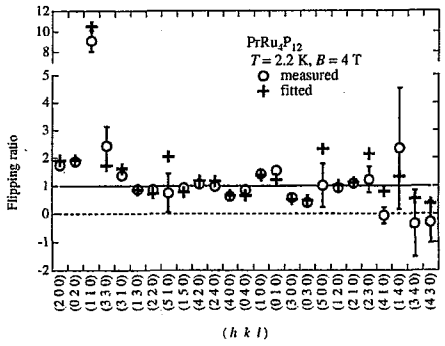

Fig. 1. Circles indicates flipping ratios I_+/I_- for various reflection points measured at 2.2 K and at 4 T. Crosses indicates fitted results.

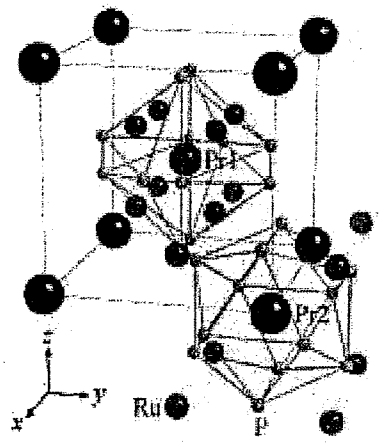

Fig. 2. Schematic drawing of the superlattice in the nonmetallic phase of $PrRu_4P_{12}$. Pr1 and Pr2 indicate the Pr ions with the ground states Γ_1 and $\Gamma_4^{(2)}$, respectively. Atomic displacements of Ru and P are enlarged by a hundred times.

many flipping ratios deviates from unity, indicating an interference between the reflection amplitudes of the nuclear structure factor $F_N(\mathbf{Q})$ and the magnetic one $F_M(\mathbf{Q})$. This result for the superlattice peaks also supports the antiferromagnetic component with $\mathbf{q_0} = (1\ 0\ 0)$. We have carried out a least-squares refinement of I_+/I_- using the two induced magnetic-moment magnitudes μ_a and μ_b at the unit-cell center and the corner, respectively, as free parameters. The atomic coordinates were fixed to the values at 7 K determined by the X-ray diffraction study [2]. The fitted result depicted by cross symbols in Fig. 1 agrees quite well with the observation. The resultant induced magnetic moments are $\mu_a = (1.7 \pm 0.1)\mu_B$ and $\mu_b = (0 \pm 0.1)\mu_B$, which are consistent with those calculated by the CF schemes of Pr2 and Pr1, respectively. Pr1 with Γ_1 ground state giving the smaller magnetic moment μ_b is located at the unit-cell center to which the Ru ions move closer, and Pr2 with $\Gamma_4^{(2)}$ ground state giving μ_a is at the corner site from which the Ru ions move further. The resultant superlattice structure is depicted schematically in Fig. 2.

Recent theoretical study of the $4f$-electron state of the Pr-filled skutterudite compounds, p-f hybridization is responsible for the crystal-field splitting of $4f^2$ state of Pr^{3+}. The p-f hybridization effect by an intermediate state of $4f^3$ with creation of a carrier at the Fermi level lowers the $\Gamma_4^{(2)}$ level, and that by $4f^1$ intermediate state with creation of an electron works in an opposite way. Based on this theory and the present experimental result, the $4f^3$ and $4f^1$ processes are dominant at Pr2 and Pr1 sites, respectively. Therefore, the p-f hybridization effect gives rise to the charge modulation due to the Fermi surface nesting condition combined with the superlattice formation of $4f$-electron CF state.

References

[1] C. Sekine *et al.*: Phys. Rev. Lett. **79** (1997) 3218.

[2] C. H. Lee *et al.*: J. Magn. Magn. Mater. **272-276** (2004) 426, L. Hao *et al.*, J. Magn. Magn. Mater. **272-276** (2004) e271.

[3] H. Harima and K. Takegahara: Physica B **312-313** (2002) 843.

[4] S. R. Saha *et al.*: J. Phys.: Condens. Matter **15** (2003) S2163.

[5] S. R. Saha *et al.*: Phys. Rev. B. **71** (2005) 132502.

[6] K. Iwasa *et al.*: Physica B **359-361** (2005) 833, K. Iwasa *et al.*, to appear in Phys. Rev. B.

[7] J. Otsuki *et al.*: J. Phys. Soc. Jpn. **74** (2005) 200.

[8] K. Iwasa *et al.*, to appear in J. Phys. Soc. Jpn. **74** (2005).

研究テーマ：充填スクッテルダイト $PrOs_4Sb_{12}$ のフォノン（ラットリング）
表題：$PrOs_4Sb_{12}$ における音響フォノンの大きなソフト化

11) Large Softening of Acoustic Phonons of $PrOs_4Sb_{12}$

K. Iwasa[1], M. Kohgi[2], H. Sugawara[3], and H. Sato[2]
[1] *Dep. of Physics, Tohoku Univ., Sendai 980-8578*
[2] *Dep. of Physics, Tokyo Metropolitan University, Hachioji, tokyo 192-0397*
[3] *Dep.of Math. and Natural Sciences, The University of Tokushima, Tokushima 770-8502*

$PrOs_4Sb_{12}$, which crystallizes in the cubic $Im\bar{3}$ structure, has been focused because of the heavy-electron superconductivity [1]. Recently, rattling motion (local anharmonic atomic vibrations with large amplitudes) and off-center displacement of the filled Pr ions inside the cage of Sb have been inferred from the results of ultrasonic [2] and XAFS [3] experiments. Inelastic neutron scattering studies of polycrystalline samples of other skutterudites $LaFe_4Sb_{12}$ [4] and $Tl_x(Fe, Co)_4Sb_{12}$ [5] reported the rattling motion of the filled ions with excitation energy of $5-15$ meV. The rattling motion has been an interest subject because of playing roles in low-temperature electronic states [6] as well as in reduction of thermal conductivity of thermoelectric devices [7]. In the present study, phonon properties of a single crystal of $PrOs_4Sb_{12}$ are investigated by inelastic thermal neutron scattering.

The experiments for a single-crystal sample to observe phonons were carried out by the triple-axis thermal neutron spectrometer TOPAN (6G). A He-gas closed-cycle refrigerator was adopted to cool down the sample.

Figure 1 shows temperature variation of energy spectra measured at the scattering vector $\mathbf{Q} = (6, -0.4, -0.4)$ in units of the reciprocal lattice. Clear inelastic peaks located around 3 meV are originated from excitations of transverse acoustic (TA) phonons with the propagating vector $\mathbf{q} = (0, 0.4, 0.4)$. It is notable that this peak shifts by 30% from 3.4 meV at 300 K to 2.4 meV at 10 K, contrary to the usual behavior of phonons. The longitudinal acoustic mode with $\mathbf{q} = (0.2, 0, 0)$ also softens by 10%. The phonon intensity is described by the Debye-Waller factor of atoms as well as the dynamical structure factor and the Bose factor. The temperature variation of the measured integrated intensities due to the softening TA phonon is closer to that based on the Debye-Waller factor of Pr than those based on Os and Sb, which were determined by X-ray diffraction measurements. Thus, the large softening of the TA phonon dominated by the Pr-ion vibration can be a characteristic behavior of the crystal lattice of $PrOs_4Sb_{12}$.

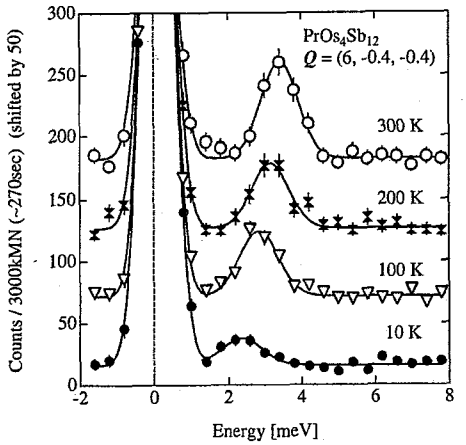

Fig. 1. Marks indicate measured inelastic neutron scattering spectra at $\mathbf{Q} = (6, -0.4, -0.4)$. Lines are fitted Gaussian functions. Higher-temperature data are shifted by every 50 counts along the ordinate.

References

[1] E. D. Bauer *et al.*: Phys. Rev. B **65** (2002) 100506.
[2] T. Goto *et al.*: Phys. Rev. B **69** (2004) 180511.
[3] D. Cao *et al.*: Phys. Rev. B **67** (2003) 180511.
[4] V. Keppens *et al.*: Nature **395** (1998) 876.
[5] R. P. Hermann *et al.*: Phys. Rev. Lett. **90** (2003) 135505.
[6] S. Yotsuhashi *et al.*: J. Phys. Soc. Jpn. **74** (2005) 49.
[7] B. C. Sales *et al.*: Phys. Rev. B **56** (1997) 15081.

使用施設：JRR-3M，装置：6G (TOPAN)，分野：101. Structures and Excitations

研究テーマ： $PrFe_4P_{12}$ における重い電子系－四重極秩序相転移と軌道励起
表題： $PrFe_4P_{12}$ における反強四極子秩序

12) Antiferro-Quadrupolar Ordering of $PrFe_4P_{12}$

K. Iwasa[1], L. Hao[1], K. Kuwahara[2], M. Kohgi[2],
H. Sugawara[3], Y. Aoki[2], H. Sato[2], T. D. Matsuda[4], and M. Nishi[5]

[1] *Dep. of Physics, Tohoku Univ., Sendai 980-8578*
[2] *Dep. of Physics, Tokyo Metropolitan University, Hachioji, Tokyo 192-0397*
[3] *Dep.of Math. and Natural Sciences, The University of Tokushima, Tokushima 770-8502*
[4] *ASRC, Japan Atomic Energy Research Institute, Tokai, Ibaraki 319-119*
[5] *ISSP, University of Tokyo, Kashiwa 277-8581*

$PrFe_4P_{12}$ crystallizing in a bcc structure ($Im\bar{3}$, T_h^5) has recently attracted much attentions because of the heavy electron behavior that is novel for Pr-based compounds [1, 2]. Sharp anomalies of specific heat, electrical resistivity and magnetic susceptibility at T_A = 6.5 K indicate a clear phase transition [2, 3], but no magnetic ordering was observed by the powder neutron diffraction measurement [4]. X-ray superlattice reflections characterized by the wave vector $\mathbf{q}$ = (1 0 0) were observed below T_A and the scattering pattern is explained by the formation of crystal structure modulation mainly with Fe-ion displacements [5]. In our previous unpolarized neutron diffraction study, antiferromagnetic (AFM) reflections induced by magnetic fields were observed below T_A, demonstrating that the $4f$ electrons of Pr ions undergo antiferro-quadrupolar (AFQ) ordering [6]. The superlattice reflection pattern under the magnetic fields along the [1 $\bar{1}$ 0] and [0 0 1] axes observed by the previous unpolarized neutron diffraction measurement is explained well as the sum of the reflections due to the induced AFM moments along the field directions and Fe-ion displacement. Considering the crystal-structure symmetry of T_h, the quadrupoles O_2^0 and O_2^2 are possible order parameters in the AFQ ordered state. The order parameter can be investigated by determining the mutual relation between the induced moment distribution and the atomic displacement. Therefore, we carried out polarized neutron diffraction experiments under magnetic fields applied along the [1 $\bar{1}$ 0] direction.

Single-crystal samples were prepared by the tin-flux method. Polarized neutron diffraction experiments were carried out on the thermal-neutron spectrometer PONTA (5G). Magnetic field was applied along the [1 $\bar{1}$ 0] direction by a superconducting magnet and the temperatures were controlled at 1.6 K.

Figure 1 shows the obtained $|F_N + F_M|^2$ and $|F_N - F_M|^2$ at various superlattice (AFM) points at 1.6 K and 4.2 T in the AFQ ordered phase, where F_N and F_M are structure factors for nuclear and magnetic scattering, respectively. If $O_2^0 = (3J_z^2 - J(J+1))/2$ is the

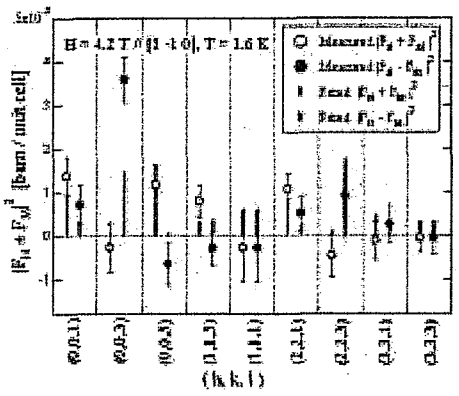

Fig. 1. Open and closed circles represent $|F_N + F_M|^2$ and $|F_N - F_M|^2$, respectively, at various reflections, which were obtained by measurements with flipping incident-neutron spin polarization. Bars are calculated results.

dominant AFQ order parameter under magnetic field along the [1 $\bar{1}$ 0] axis, the Fe-ion displacement is naturally expressed as the atomic coordinate (1/4, 1/4, 1/4)+(δ, δ, δ'), and the two different magnetic moments μ_1 and μ_2 are induced along the [1 $\bar{1}$ 0] direction at the corner and the body center Pr-ion sites in the unit cell, respectively. Taking

使用施設：JRR-3M, 装置： 5G (PONTA) , 分野： 103. Strongly Correlated Electron Systems

into account these atomic and magnetic superlattice structures, we carried out a least-squares fitting procedure of the calculated structure factors to the present data. The best fit results shown by bars in Fig. 1 reproduces well the observed values of $|F_N + F_M|^2$ and $|F_N - F_M|^2$. The obtained parameters are $\delta = 6 \times 10^{-5}$ that is close to that obtained by the previous X-ray diffraction measurement [5], and $(\mu_2 - \mu_1)/2 = 0.09\ \mu_B$ that is close to that obtained by the previous unpolarized neutron diffraction experiments. On contrary, if we assume that the AFQ order parameter is $O_2^2 = \sqrt{3}(J_x^2 - J_y^2)/2$ with atomic displacement described as $(\delta, -\delta, \delta')$, no satisfactorily fit with the data is obtained, because the very small magnitudes of F_N at the measured reflection points and no significant difference between $|F_N + F_M|^2$ and $|F_N - F_M|^2$. Therefore, we conclude that the dominant order parameter of $PrFe_4P_{12}$ can be O_2^0 under magnetic field applied along the $[1\ \bar{1}\ 0]$.

References

[1] H. Sugawara *et al.*: Phys. Rev. B **66** (2002) 134411.

[2] H. Sato *et al.*: Phys. Rev. B **62** (2000) 15125.

[3] Y. Aoki *et al.*: Phys. Rev. B **65** (2002) 064446.

[4] L. Keller *et al.*: J. Alloys and Compounds **323-324** (2001) 516.

[5] K. Iwasa *et al.*: Physica B **312-313** (2002) 834.

[6] L. Hao *et al.*: Acta Physica Polonica B **34** (2003) 1113.

研究テーマ： $PrFe_4P_{12}$ における重い電子系－四重極秩序相転移と軌道励起
表題： $PrFe_4P_{12}$ の重い電子相における磁気励起

13) Magnetic excitations in the heavy-electron phase of $PrFe_4P_{12}$

K. Iwasa[1], L. Hao[1], K. Kuwahara[2], M. Kohgi[2],
H. Sugawara[3], Y. Aoki[2], H. Sato[2], and T. D. Matsuda[4]
[1] *Dep. of Physics, Tohoku Univ., Sendai 980-8578*
[2] *Dep. of Physics, Tokyo Metropolitan University, Hachioji, Tokyo 192-0397*
[3] *Dep.of Math. and Natural Sciences, The University of Tokushima, Tokushima 770-8502*
[4] *ASRC, Japan Atomic Energy Research Institute, Tokai, Ibaraki 319-119*

$PrFe_4P_{12}$ has recently attracted much attentions because of the heavy electron behavior that is novel for Pr-based compounds [1, 2]. It undergoes a nonmagnetic phase transition at $T_A = 6.5$ K [2, 3, 4]. X-ray superlattice reflections characterized by the wave vector $\mathbf{q} = (1\ 0\ 0)$ were observed below T_A [5]. Our neutron diffraction study revealed antiferromagnetic reflections induced by magnetic fields below T_A. These phenomena indicate antiferro-quadrupolar (AFQ) ordering of the $4f$ electrons of Pr ions [6]. In the heavy electron phase, magnetic excitation spectra from the polycrystalline sample are heavily overdamped and quasielastic [7]. This fact indicates that the $4f^2$ electrons of Pr^{3+} ion hybridize strongly with carriers. In order to investigate magnetic fluctuation responsible for the heavy electron state of $PrFe_4P_{12}$, we performed inelastic neutron scattering measurements for single crystal samples.

Single-crystal samples were prepared by the tin-flux method. Inelastic neutron scattering experiments were carried out on the cold- and thermal-neutron spectrometers HER (C1-1) and TOPAN (6G), respectively.

Figure 1 shows energy spectra at $\mathbf{Q} = (1.9, 0, 0)$ near the Brillouin zone center and at $\mathbf{Q} = (1.2, 0, 0)$ near the boundary, measured at HER. The inelastic response at $\mathbf{Q} = (1.9, 0, 0)$ is larger than that at $\mathbf{Q} = (1.2, 0, 0)$ and shows stronger temperature dependence around T_A. One can expect a dominant ferromagnetic fluctuation, which is consistent with the bulk magnetization with the positive Weiss temperature. The ferromagnetic fluctuation of $PrFe_4P_{12}$ is in contrast to the typical Ce-based heavy electron systems that often exhibit antiferromagnetic fluctuation. Such characteristic magnetic fluctuation is a key to understand the heavy electron state and the AFQ ordering in $PrFe_4P_{12}$.

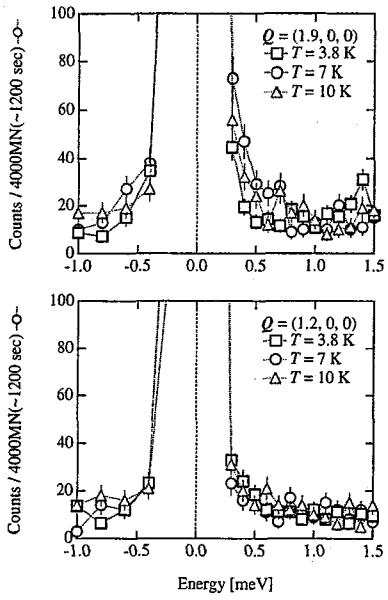

Fig. 1. Magnetic excitation spectra at $\mathbf{Q} = (1.9, 0, 0)$ and $\mathbf{Q} = (1.2, 0, 0)$ measured at HER.

References

[1] H. Sugawara *et al.*: Phys. Rev. B **66** (2002) 134411.
[2] H. Sato *et al.*: Phys. Rev. B **62** (2000) 15125.
[3] Y. Aoki *et al.*: Phys. Rev. B **65** (2002) 064446.
[4] L. Keller *et al.*: J. Alloys and Compounds **323-324** (2001) 516.
[5] K. Iwasa *et al.*: Physica B **312-313** (2002) 834.
[6] L. Hao *et al.*: Acta Physica Polonica B **34** (2003) 1113.
[7] K. Iwasa *et al.*: Acta Physica Polonica B **34** (2003) 1117.

使用施設：JRR-3M，装置： C1-1 (HER), 6G (TOPAN)，分野： 103. Strongly Correlated Electron Systems

研究テーマ：高温超伝導体における電荷ストライプ揺らぎと超伝導の相関
表題：中性子散乱による高温超伝導体のストライプ揺らぎの研究

14) Neutron-scattering study of stripe fluctuations in high-T_c superconductor

M. Fujita[1], H. Goka[2], T. Adachi[3], Y. Koike[3] and K. Yamada[1]

[1] *Institute for Materials Research, Tohoku University, Sendai 980-8577, Japan*
[2] *Department of Physics, Kyoto University, Kyoto 606-8502, Japan*
[3] *Department of Applied Physics, Graduate School of Engineering, Tohoku University, Sendai 980-8579, Japan*

Since the discovery of spatially modulated spin- and charge-density-wave orders in the $La_{2-x}Nd_{0.4}Sr_xCuO_4$ system at x~1/8[1], much interest has been focused on the relationship between the stripe correlations and the high-T_c superconductivity. Systematic study on the 1/8-doped $La_{1.875}Ba_{0.125-x}Sr_xCuO_4$ system revealed the competitive relation between the charge stripe order and the suppression of superconductivity. [2] However, the charge-density-wave order (CDW) is not observed in the $La_{2-x}Sr_xCuO_4$ system.[3] Thus, the universality of stripe correlations in the entire supreconducting phase is still controversial.

To address this issue through the stability of stripe correlations against doping and temperature, we performed neutron scattering measurements on single crystals of $La_{2-x}Ba_xCuO_4$ (LBCO) with x=0.10 and 0.125. The former sample shows bulk supercoductivity with T_c(onset) of 24 K, while in the later sample the fractional superconductivity appears with much lower Tc of 5K. Both samples undergo a structural phase transition between low-temperautre tetragonal and low-temperature orthorhombic (LTO) phases at T_{d2} of 50 K (x=0.10) and 60 K (x=0.125).

Figure 1 shows the temperature dependences of the incommensurability (δ) and resolution-corrected peak-width (κ) for two samples. In both samples, temperature dependences of the δ and κ are steep just below T_{d2} and rather gradual in the LTO phase, which causes an anomalous kink at T_{d2}. Thus, spin correlations are closely related to the crystal structure as expected from the stripe model. In the whole temperature range, κ in the x=0.125 sample is smaller than that in the x=0.10 sample. This

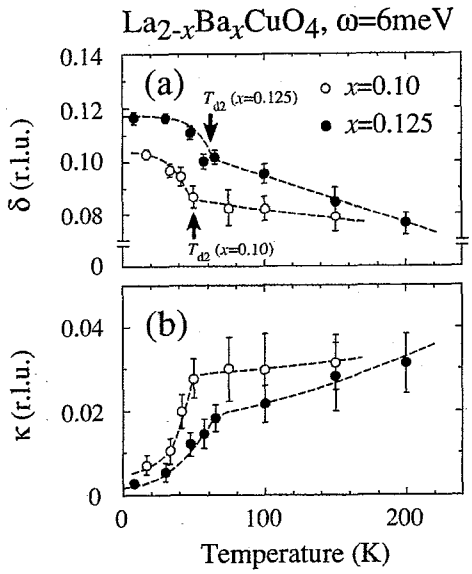

Fig. 1. Temperature dependences of (a) the incommensurability δ and (b) the peak-width (the half-width at the half-maximum) κ at the energy transfers of 6 meV in $La_{1.90}Ba_{0.10}CuO_4$ (open circles) and $La_{1.875}Ba_{0.125}CuO_4$ (closed circles). T_{d2} represents the structural transition temperature between LTT and LTO phases. Dashed lines are guides to the eye.

difference in κ indicates the robustness of spin correlations in the former sample. In other words, the stiffness of stripe correlations seen in the low-energy IC spin fluctuations depends on doping and the deviation from the 1/8 doping more easily loses the coherence of stripe correlations.

temperature.

References

[1] J.M. Tranquada*et al.*: Nature (London) **375** (1995) 561.
[2] M. Fujita*et al.*:Phys. Rev. Lett. **88** (2002) 167008.
[3] H. Kimura*et al.*:Phys. Rev. B **61** (2000) 14366.

使用施設：JRR-3M，装置： 6G, C1-1 (TOPAN, HER)，分野： 103: Strongly Correlated Electron Systems

研究テーマ： URu_2Si_2 における隠れた秩序と反強磁性秩序の競合
表題： $U(Ru_{1-x}Rh_x)_2Si_2$ ($x \leq 0.03$) の隠れた秩序および反強磁性相における磁気励起

15) Magnetic excitations in hidden order and antiferromagnetic phases of $U(Ru_{1-x}Rh_x)_2Si_2$ ($x \leq 0.03$)

H. Amitsuka[1], M. Yokoyama[2], A. Gawase[1], K. Tenya[1], N. Aso[3] and H. Yoshizawa[3]
[1] *Graduate School of Science, Hokkaido University, Sapporo 060-0810*
[2] *Faculty of Science, Ibaraki University, Mito 310-8512*
[3] *Institute for Solid State Physics, The University of Tokyo, Tokai 319-1106*

The nature of the ordered state below T_o = 17.5 K in URu_2Si_2 (the $ThCr_2Si_2$ type, body-centered tetragonal structure) [1] has been attracting renewed interest since the finding of the unusual evolution of the type-I antiferromagnetic (AF) phase under pressure P [2, 3]. Recent ^{29}Si-NMR [4] and μSR [5] experiments under P revealed that the evolution of the inhomogeneous AF phase is due to an effect of volume fraction, and indicates that the majority of the system is occupied by the "hidden order" (HO) at ambient pressure below T_o.

Quite recently, the elastic neutron scattering experiments performed on the Rh substitution system $U(Ru_{1-x}Rh_x)_2Si_2$ revealed that the 2% substitution of Rh for Ru can also enhance the AF phase without applying P [6, 7]. Except the suppression of both the phases at $x \sim 0.04$, the overall features are quite similar to that obtained from the pressure effect for the pure URu_2Si_2 . Because of no restriction of a pressure cell, the Rh dope system is expected to be suitable for the detailed microscopic investigation on the unusual two-phase competition. We have thus performed inelastic neutron scattering experiments on $U(Ru_{1-x}Rh_x)_2Si_2$ ($x \leq 0.03$), for the first time, in order to study the low-energy magnetic excitations in this unusual mixed phase [8].

Single crystals of $U(Ru_{1-x}Rh_x)_2Si_2$ with x = 0, 0.015, 0.02 and 0.03 were grown by the Czochralski method in a tetra-arc furnace, and vacuum-annealed at 1000°C for 5 days. The samples with the volume of $\sim$ 150 mm^3 were cut out of the ingots by means of the spark erosion, mounted in aluminum cans filled with ^{4}He gas so that the scattering plane becomes (hk0), and then cooled to 1.4 K in a ^{4}He refrigerator. The inelastic neutron scattering measurements were performed on the triple-axis spectrometers GPTAS (4G) and HER (C11). We made the constant-Q scans at Q = (1,0,0) and (1,0.4,0) with the fixed final momentum k_f = 2.65 Å^{-1} for GPTAS and 1.32 Å^{-1} for HER.

Figure 1 shows the magnetic-excitation spectra at 1.4 K for Q_a = (1,0,0) and Q_b = (1,0.4,0), obtained using the GPTAS spectrometer. The contributions of instrumental background and incoherent scattering were carefully subtracted by scanning at the corresponding $|Q|$-invariant positions (0.707,0.707,0) and (0.762,0.762,0), where we observed neither magnon nor phonon scattering. The inelastic-scattering intensity at each x is normalized by the integrated intensities of the nuclear Bragg scattering at (110). The sharp peak at the energy transfer $\hbar\omega \sim 0$ in the spectra at Q_a arises mainly from the higher-order nuclear Bragg reflections and the AF Bragg reflections. For pure URu_2Si_2 , clear peaks are observed at $\sim$ 2.4 meV (Q_a) and at $\sim$ 4.6 meV (Q_b), which are in good agreement with the previous results [3, 9]. By substituting 1.5% of Rh for Ru, the position of the inelastic peak at Q_a shifts to $\sim$ 1.2 meV. Interestingly, the peak at Q_a suddenly disappears at x = 0.02 and 0.03, where the AF phase with nearly full volume fraction replaces the HO phase [6]. Such reduction is also seen in the x variations of the spectra at Q_b, but a heavily dumped peak is still observed at x = 0.02 and 0.03 [7].

The reduction of the inelastic peaks in the AF-rich phase is also observed in the temperature scans. In fig. 2, we plot the temperature variations of the magnetic-excitation spectrum at Q_a obtained using the HER spectrometer. We found a broad peak anomaly at Q_a, with a peak position with

使用施設：JRR-3M, 装置： 4G, C11 , 分野： 103: Strongly Correlated Election Systems

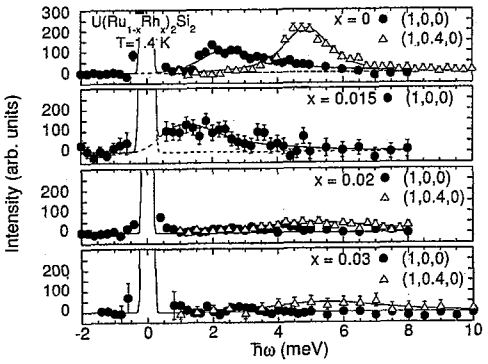

Fig. 1. The inelastic neutron scattering spectra at 1.4 K for $U(Ru_{1-x}Rh_x)_2Si_2$ ($x \leq 0.03$), obtained from the constant-Q scans at $Q = (1,0,0)$ and (1,0.4,0). Incoherent scattering and instrumental background are subtracted. The lines are guides to the eye.

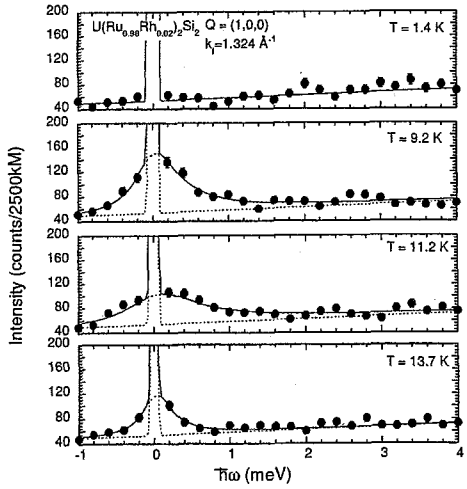

Fig. 2. Temperature variations of the constant-Q scans at $Q = (1,0,0)$ in $U(Ru_{0.98}Rh_{0.02})_2Si_2$. The lines are guides to the eye.

$\hbar\omega \sim 0$, i.e. at clearly lower energy than in pure URu_2Si_2 . It appears below $\sim$ 13.5 K and grows with decreasing temperature. The width (FWHM) of the peak is estimated to be $\sim$ 1 meV, which is significantly larger than the experimental resolution (0.13 meV). On the other hand, the intensity of the inelastic peak is reduced below 8 K. By using the GPTAS spectromenter, we found no significant anomaly in the whole energy range of $\hbar\omega \leq 8$ meV (see Fig. 1). In our study using elastic neutron scattering and specific heat, T_o and the onset temperature T_M of the large AF Bragg reflection are estimated to be $\sim$ 13.7 K and $\sim$ 8.3 K. The magnetic excitation at Q_a seen in the HO phase is thus considered to vanish in the AF phase. In contrast to the strong variations of the spectra at Q_a, the magnitude of the heavily dumped peak observed at Q_b is insensitive to the temperature. It still exists above T_o with almost the same magnitude, suggesting that this magnetic fluctuation is not directly coupled to the two types of order.

The disappearance of the magnetic excitations in the AF phase indicates that the matrix elements on the U 5f magnetic moment between the ground state and the low-energy excited states become zero in the AF order. This feature is consistent with the results for the pure URu_2Si_2 under P [3, 7]. A possible candidate for the HO parameters is the quadrupoles $\psi = J_x^2 - J_y^2$ or $J_xJ_y + J_yJ_x$ originating in the non-Kramers doublet, since ψ is orthogonal to the dipole moment $m = J_z$ bringing the AF order, and does not interact with the spin of neutrons [3, 10].

References

[1] T.T.M. Palstra *et al.*, Phys. Rev. Lett. **55** (1985) 2727.

[2] H. Amitsuka *et al.*, Phys. Rev. Lett. **83** (1999) 5114.

[3] H. Amitsuka *et al.*, J. Phys. Soc. Jpn. **69** (2000) Suppl. A 5.

[4] K. Matsuda *et al.*, Phys. Rev. Lett. **87** (2001) 087203.

[5] H. Amitsuka *et al.*, Physica B **326** (2003) 418.

[6] M. Yokoyama *et al.*, J. Phys. Soc. Jpn. **73** (2004) 545.

[7] F. Bourdarot *et al.*, Physica B **350** (2004) e179.

[8] M. Yokoyama *et al.*, Physica B **359-361** (2005) 1129.

[9] C. Broholm *et al.*, Phys. Rev. B **43** (1991) 12809.

[10] F.J. Ohkawa and H. Shimizu, J. Phys. Condens. Matter **11** (1999) L519.

研究テーマ：f電子系化合物における価数揺動状態
表題：TmTeの高圧下金属相における磁気励起

16) Magnetic Exitation of TmTe in the Anomalous Metallic Phase under High Pressure

T. Matsumura H. Ishida and M. Nishi*

*Department of Physics, Graduate School of Science, Tohoku University, Sendai 980-8578, Japan; * Institute for Solid State Physics, The University of Tokyo, 106-1 Shirakata, Tokai 319-1106, Japan*

TmTe is a magnetic semiconductor with an energy gap ~0.35 eV between the $4f^{13}$ level and the bottom of the 5d conduction band. At ambient pressure, TmTe exhibits characteristic properties of localized f electrons. Application of pressure ~2 GPa closes the gap, and an anomalous metallic state appears. Ferromagnetism appears with Tc=15 K, which decreases with increasing pressure[1]. In addition, the resistivity is reminiscent of the Kondo effect[2].

The purpose of the present study is to examine magnetic excitations near the insulator-metal-transition (IMT). Last year, we performed an experiment at 2.3 GPa where the ferromagnetism was not observed. Although the obtained excitation spectrum seemed to reflect unstable 4f state than at P=0, the basic feature did not change[3].

In this experiment, the pressure was increased to 2.6 GPa. When the sample was cooled down to low temperature, clear signal of ferromagnetic order was observed as shown in Fig. 1. Then, the pressure of this work is just after the IMT.

Neutron scattering experiment was performed with the TOPAN 3-axis spectrometer at the 6G port of JRR-3M in JAERI(Tokai). The pressure was applied using a McWhan-type cell.

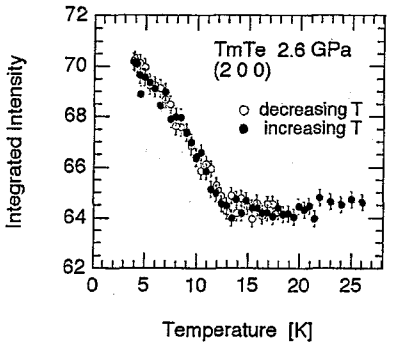

Figure 1: Ferromagnetic order observed at 2.6 GPa.

Figure 2 shows the T-dependence of the magnetic excitation spectrum for the (1 0 0) reflection. At the lowest temperature of 4 K, we can clearly observe the inelastic peak at 10 meV. The peak remains up to well above Tc, and is not ascribed to the spin-wave excitation. With increasing temperature, the spectral weight gradually shifts to lower energy, and at 300 K, it becomes completely quasielastic. These features are the same as in TmSe at ambient pressure. It is intriguing that the valence of TmTe(~+2) and TmSe(~+2.7) are much different.

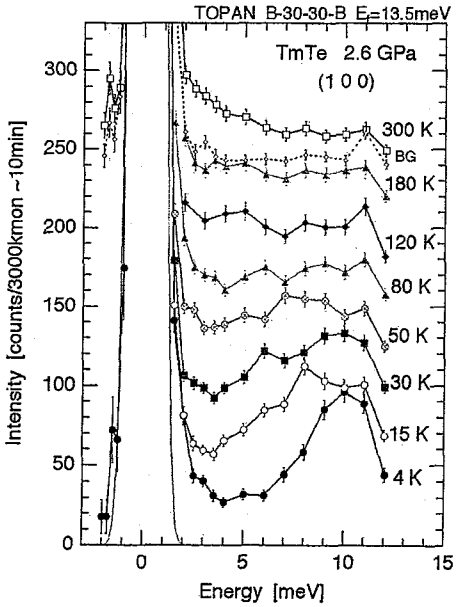

Figure 2: Temperature dependence of the magnetic excitation spectrum for (1 0 0).

References

[1] P. Link et al., Phys. Rev. Lett. **80** (1998) 173.
[2] T. Matsumura et al., Phys. Rev. Lett. **78** (1998) 1138.
[3] Activity Report, **11** (2004) 147.

使用施設：JRR-3M，装置：TOPAN(6G)，分野 Strongly Correlated Electron Systems

研究テーマ：中性子散乱によるウラン化合物の物性研究
表　題：$UCoGa_5$ のフォノン

17) Phonons in $UCoGa_5$

N. Metoki, K. Kaneko, S. Raymond[1], J. P. Sanchez[1], K. Parlinski[2], P. Piekarz[2], A. M. Oleś[3], S. Ikeda, T. D. Matsuda, Y. Haga, Y. Ōnuki[4], G. H. Lander[5]

ASRC-JAERI, Tokai, Naka, Ibaraki 319-1195
[1]*DRFMC-CEA, 38054 Grenoble, France*
[2]*Institute of Nuclear Physics, Polish Academy of Sciences, Radzikowskiego 152, 31-342 Kraków, Poland*
[3]*Max-Planck-Institut für Festkörperforschung, Heisenbergstrasse 1, D-70569 Stuttgart, Germany*
[4]*Grad. School of Science, Osaka University, Toyonaka, Osaka 560-0043, Japan*
[5]*EC-JRC, ITU, Postfach 2340, D-76125 Karlsruhe, Germany*

High temperature heavy fermion superconductivity in $PuCoGa_5$ is one of the most interesting discoveries in the field of actinide science and strongly correlated electron systems. A common superconducting mechanism for Ce and Pu-115 compounds (magnetic fluctuation mediated) has been suggested from the scaling of T_c with c/a ratio. However, the high superconducting transition temperature reminds us that the phonons may play an important role in the mechanism for superconductivity. Unusual coupling of phonons with superconductivity has been reported in many exotic superconductors such as RNi_2B_2C (R=rare earth) and/or high-T_c superconductors. We have studied the low energy phonons in $UCoGa_5$ by means of neutron inelastic scattering as a reference for the $PuCoGa_5$, which will be studied by X-ray inelastic scattering. Neutron scattering experiments have been carried out on triple axis spectrometers, TAS-1 and TAS-2 at research reactor JRR-3 in JAERI.

We observed very distinct LA, TA, TO, and LO phonons in $UCoGa_5$. The observed phonon excitation energies along high symmetry directions agree very well with the *ab initio* calculation, see Fig. 1. From the Γ to M point the observed TA phonon splits into two branches. The lower branch is the TA phonon and the higher one switches to TO phonon. The observed TA phonon was slightly lower than the calculation. The TA phonon with the lowest energy at M point could not be observed due to weak intensity. At low temperatures the observed TA phonon becomes slightly harder of about 9 meV. Thus the agreement with the calculation becomes better at low temperatures. The observed phonon branches in $UCoGa_5$ were well reproduced by the ab-initio calculation. The calculation indicates that the phonons in $UCoGa_5$ are very similar to those for $PuCoGa_5$.

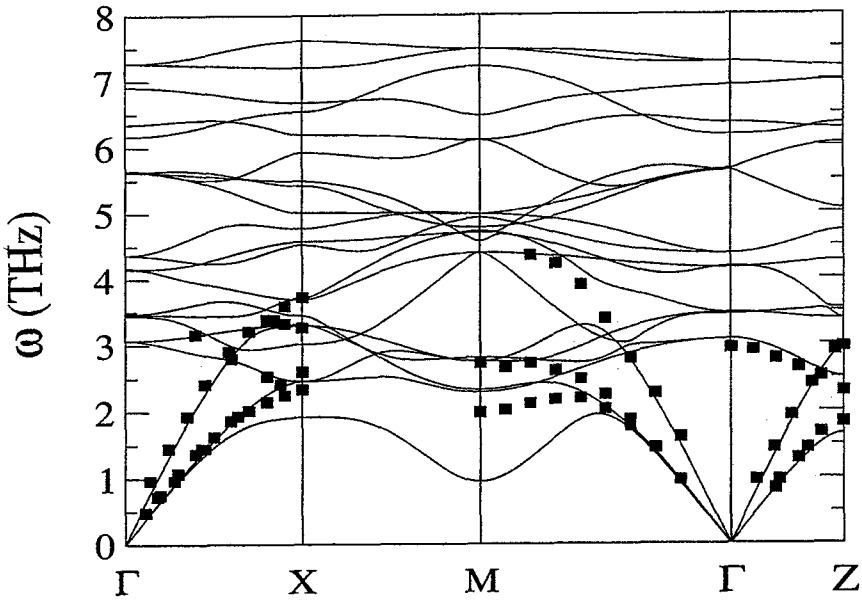

Figure 1: Phonon dispersion relation in $UCoGa_5$.

原子炉：JRR-3　　装置：TAS-2(T2-4)　　分野：中性子散乱（超伝導）

研究テーマ： ペロブスカイト型 Mn 酸化物 RBaMn$_2$O$_6$(R=Pr,Nd,Tb,Y) の A サイトランダムネス効果
表題： PrBaMn$_2$O$_6$ における磁気相分離、磁気抵抗、A サイトランダムネスの相関

18) Correlation among magnetic phase separation, magnetoresistance and A-site randomness in PrBaMn$_2$O$_6$

T. Nakajima and Y. Ueda
Materials Design and Characterization Laboratory, Institute for Solid State Physics, The University of Tokyo, 5-1-5 Kashiwanoha, Kashiwa, Chiba, 277-8581

The A-site randomness effect has been investigated in PrBaMn$_2$O$_6$ with various degrees of Pr/Ba randomness at the A-sites [1, 2]. Ceramic compounds, (PrBa)Mn$_2$O$_6$, were synthesized by a solid state reaction. The A-site randomness suppresses both ferromagnetic and A-type antiferromagnetic transitions, and influences to form a magnetic phase separation (MPS) state and a magnetoresistance (MR) effect. It is important to study the correlation between the MPS and the MR for understanding a role of A-site randomness to MR effect in perovskite manganites. The magnetic structures and MPS state were studied by neutron powder diffraction using HERMES installed at T1-3 port of JRR-3M in JAERI (Tokai).

Figure 1 shows (a) the intensity of magnetic bragg peaks for 001 (I_{A001}) and 110 (I_{F110}) corresponding to the A-type antiferromagntic and the ferromagnetic structures, respectively, and (b) the magnetoresistance effect at 9 T and the magnetic bragg peaks ratio (I_{F110}/I_{A001}) as a function of degree of the A-site order. The A-site order stabilizes A-type antiferromagnetic long-range ordered phase. The magnetic peak intensity I_{A001} strongly decreases with the increase of the A-site randomness inspite of slight change of I_{F110}. The effect of large cation size difference between Pr and Ba is simultaneously enhanced by the A-site disorder and finally results in magnetic glassy state; both I_{A001} and I_{F110} are very small, on the other hand, the MR effect significantly increases with the increasing A-site randomness. This suggests that A-site randomness could change the insulative A-type antiferromagnetic long-range order into short-range ordered micro-domains and it coexists with the metallic ferromagnetic micro-domains. As a results, the MPS state caused by A-site randomness produces the large MR effect. The further experiments are now in progress.

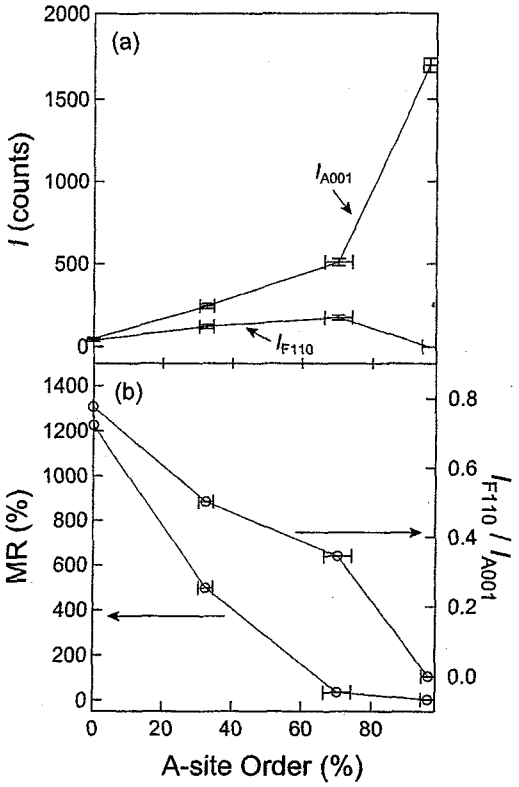

Fig. 1. (a) the intensity of magnetic bragg peaks for 001 (I_{A001}) and 110 (I_{F110}) corresponding to the A-type antiferromagntic and the ferromagnetic structures, respectively, and (b) the magnetoresistance effect (%) at 9 T and the magnetic bragg peaks ratio (I_{F110}/I_{A001}) as a function of degree of the A-site order.

References

[1] T. Nakajima, H. Kageyama and Y. Ueda: J. Mag. Mag. Mat. **272-276** (2004) 405.
[2] T. Nakajima, H. Yoshizawa and Y. Ueda: J. Phys. Soc. Jpn. **73** (2004) 2283.

使用施設：JRR-3M, 装置： T1-3 (HERMES) , 分野： 3. Strongly Correlated Electron Systems

研究テーマ：スピングラス相近傍の $La_{2-x}Sr_xCuO_4$ 超伝導体におけるスピン密度波への磁場効果
表　題：ホールドープ $La_{2-x}Sr_xCuO_4$ の反強磁性秩序に対する Ni 不純物効果

19) Ni Impurity Effect on Antiferromagnetic Order in Hole-doped $La_{2-x}Sr_xCuO_4$

H. Hiraka, T. Machi[1], N. Watanabe[1], Y. Itoh[2], M. Matsuda[3] and K. Yamada

Institute for Materials Research, Tohoku University, Sendai 980-8577
[1] *Superconductivity Research Laboratory, International Superconductivity Technology Center, Tokyo 135-0062*
[2] *Department of Chemistry, Graduate School of Science, Kyoto University, Kyoto 606-8502*
[3] *Advanced Science Research Center, Japan Atomic Energy Research Institute, Tokai, Ibaraki 319-1195*

Carrier doping into the insulating antiferromagnetic (AF) state of cuprates breaks down the three-dimensional (3D) AF order, makes the charge carriers mobile and eventually creates the novel high-Tc superconductivity. Impurity doping into CuO_2 planes can give insight on the 3D AF order in cuprates. The Néel ordered state in the lightly doped LSCO is of particular interest due to its physical properties. [1] In such the lightly-doped AF phase of LSCO, the hole mobility is quite suppressed when the Cu site is replaced. [2,3] Surprisingly, the Néel ordered state which is determined by susceptibility measurements is then stabilized and the Néel temperature (T_N) increases by $\sim$ 100 K, particularly by Ni substitution. [3] This is unusual for conventional magnets, where chemical impurities make the magnetic system disordered and unstable. Hence, it is important to confirm the increase of T_N in the lightly hole-doped LSCO upon Ni doping to verify that close coupling of mobile carriers and the magnetism is one characteristic of hole-doped cuprates.

We explore the microscopic magnetic structure of a hole-and-impurity co-doped system $La_{2-x}Sr_xCu_{1-y}Ni_yO_4$ with $x = 0.01$ and $0.01 \leq y \leq 0.1$. The doped Ni ions function as magnetic impurities of $S = 1$, if the Ni^{2+} valence state is assumed. In addition, the substitution with Ni can introduce a different type of magnetic anisotropy in the CuO_2 plane. Magnetic-neutron-diffraction measurements were carried out on the thermal-neutron triple-axis spectrometer TAS-2 installed in the guide hall of JRR-3 at the Japan Atomic Energy Research Institute.

Figure 1 shows typical thermal-evolution data of two AF Bragg reflections for $y = 0.02$ and 0.05. The Néel ordered state persists above $\sim$ 300 K for both compounds. This temperature is much higher than T_N of Ni-free LSCO ($x = 0.01$) [4] and close to that of non-doped La_2CuO_4. The recovery of the T_N in Ni-substituted LSCO suggests that the doped holes are extremely localized by Ni substitution. Dilute Ni-doping between $y = 0.02$ and 0.05 dramatically changes the Q-dependence of the AF Bragg intensity, corresponding to a switch of spin structure from the La_2CuO_4 type (Cu type) to the La_2NiO_4 type (Ni type) triggered by a spin rotation in CuO_2 planes. More interestingly, between the Cu- and the Ni-type

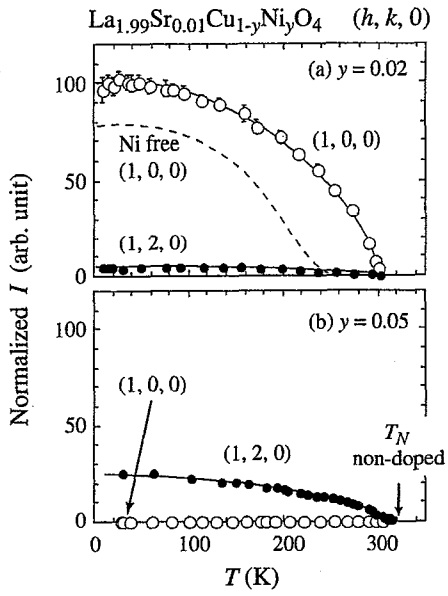

Figure 1: Temperature dependence of AF Bragg reflections (1,0,0) and (1,2,0) in $La_{1.99}Sr_{0.01}Cu_{1-y}Ni_yO_4$ for (a) $y = 0.02$ with $E_i = 13.5$ meV and (b) $y = 0.05$ with $E_i = 14.7$ meV. The vertical scale of (1,0,0) reflection of Ni-free LSCO ($x = 0.01$, broken line) [4] is set using S ratio determined experimentally. T_N of La_2CuO_4 is shown for reference.

structures there exists an intermediate region where the spin direction is in between those of Cu and Ni type (not shown). In this region, we found an unusual temperature dependence of magnetic intensities which suggests the temperature dependence of the spin direction. These unusual behavior must be related to the doped-carrier itinerancy.

References

1) A.N. Lavrov, S. Komiya, and Y. Ando: Nature **418** (2002) 385.
2) M. Hücker, V. Kataev, J. Pommer, J. Harras, A. Hosni, C. Pflitsch, R. Gross, and B. Büchner: Phys. Rev. B **59** (1999) R725.
3) N. Watanabe, T. Masui, Y. Itoh, T. Machi, I. Kato, N. Koshizuka, and M. Murakami: Physica *C* **388-389** (2003) 241.
4) M. Matsuda, M. Fujita, K. Yamada, R.J. Birgeneau, Y. Endoh, and G. Shirane: Phys. Rev. B **65** (2002) 134515.

原子炉：JRR-3　　装置：TAS-2(T2-4)　　分野：中性子散乱（超伝導）

研究テーマ：金属酸化物熱電材料 Na_xCoO_2 の最適組成に関する研究
表題：熱電変換材料 Na_xCoO_2 の最適組成に関する研究

20) Study on the most suitable formation in thermoelectric materials Na_xCoO_2

H. Nakatsugawa and K. Nagasawa

Division of Materials Science and Engineering, Graduate School of Engineering, Yokohama National University
79-5 Tokiwadai, Hodogaya, Yokohama 240-8501 Japan

The electron density distributions of γ -Na_xCoO_2 have been obtained by the maximum entropy method and the Rietveld analysis using powder x-ray diffraction data at room temperature. In the Rietveld refinement, the deviation of (008) and (108) peaks is very large relative to that of other reflections, and the change in x-ray diffraction data is clearer than that in neutron diffraction data at 10K and room temperature. This indicates that electron density distributions in γ -Na_xCoO_2 are slightly modulated with increasing x. In fact, there found to be the obvious overlapping of the charge density between O − O network and Co ions, but no significant overlapping with increasing x. This is the direct observation of decrease of covalency between O *2p* and Co t_{2g} in the CoO_2 layer with increasing the sodium content

We performed powder ND experiments at 10 and 300K on the Kinken powder diffractometer for high efficiency and high resolution measurements, HERMES, of Institute for Materials Research (IMR), Tohoku University, installed at the JRR-3M reactor in Japan Atomic Energy Research Institute (JAERI), Tokai Establishment.[1]

The resulting powder sample was characterized by x-ray diffraction (XRD), neutron diffraction (ND) and inductively coupled plasma atomic-emission spectrometry (ICP-AES) analysis. The XRD and ND patterns showed good identification of the samples as the γ phase, and there was no indication of the presence of other prototypes or residual raw materials.

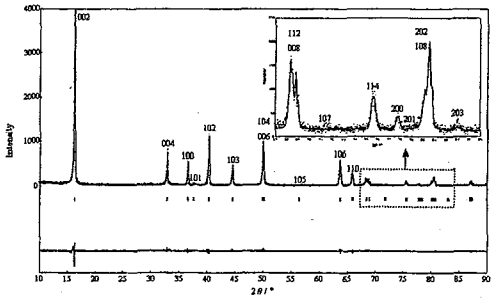

Fig.1 The XRD data for x=0.77 at 300K.

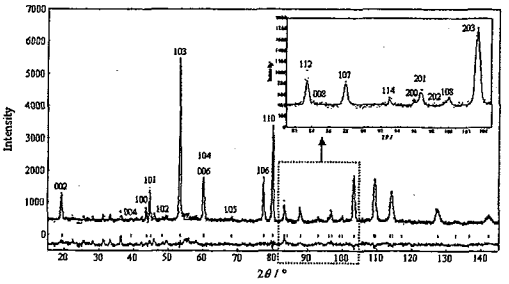

Fig.2 The ND data for x=0.77 at 10K.

In the Rietveld refinement, there are good agreement between x=0.77 and x=0.79, except for (008) and (108) peaks. The deviation of the two reflections is very large relative to that of other reflections, and the change in XRD data is clearer than that in ND data. This means that electron density distributions in γ -Na_xCoO_2 are slightly modulated with increasing x. In fact, there found to be the obvious overlapping of the charge density between O − O network and Co ions for x=0.77, but no significant overlapping for x=0.79. This is the direct observation of decrease of the Co −O hybridization in the CoO_2 layer with increasing the sodium content.

Reference

[1] K.Ohoyama *et al.* Jpn.J Appl.Phys. **37** (1998) 3319-3326.

使用施設：JRR-3M，装置：HERMES (T1-3)，分野 Strongly Correlated Electron Systems

研究テーマ：先端偏極中性子散乱によるスピン－格子物性の研究
表　題：$La_{2-x}Sr_xCuO_4$ の斜め非整合スピン相関に対して電荷不均質性が与える効果

21) Effect of charge inhomogeneity on the diagonal incommensurate spin correlations in $La_{2-x}Sr_xCuO_4$

M. Matsuda, M. Fujita[1] and K. Yamada[1]

Advanced Science Research Center, Japan Atomic Energy Research Institute, Tokai, Ibaraki 319-1195
[1]*Institute for Materials Research, Tohoku University, Katahira, Sendai 980-8577*

One of the interesting aspects of the study in the high-T_c superconductivity is to clarify the relation between transport properties and magnetism at the boundary of the metal-to-insulator transition. Extensive neutron-scattering studies on lightly-doped $La_{2-x}Sr_xCuO_4$ have revealed that a diagonal spin modulation, which is a one-dimensional modulation rotated away by 45° from that in the superconducting phase, occurs universally across the spin-glass phase in $La_{2-x}Sr_xCuO_4$ ($0<x\leq0.055$). It is now established that the static magnetic spin modulation changes from being diagonal to parallel at $x = 0.055\pm0.005$, coincident with the insulator-to-superconductor transition.

One possibility to explain the diagonal incommensurate spin correlations is the stripe model. The stripe phase is experimentally observed in $La_{2-x-y}Nd_ySr_xCuO_4$, $La_{2-x}Ba_xCuO_4$ ($x\sim\frac{1}{8}$), and $La_{2-x}Sr_xNiO_4$. The parallel stripe phase in $La_{2-x-y}Nd_ySr_xCuO_4$ and $La_{2-x}Ba_xCuO_4$ is stabilized by the structural distortion, namely, the low temperature tetragonal (LTT) phase, which is strongly coupled to the charge ordering. It is suggested that the diagonal stripe in $La_{2-x}Sr_xNiO_4$ possibly originates from the orbital ordering. In lightly-doped $La_{2-x}Sr_xCuO_4$, which has no LTT phase and no orbital degree of freedom, there has been no evidence that the stripe phase is realized. Most importantly, no structural distortion, originating from the charge ordering, has been observed although it can be due to disorder in periodicity and direction of the stripe.

Recently, Hasselman *et al.* reported that the diagonal incommensurate spin correlations in lightly-doped $La_{2-x}Sr_xCuO_4$ are explained using the spiral model, originating from magnetic frustration caused by the localized hole spins. [1)] In this model the incommensurate magnetic peaks are purely magnetic in origin and have nothing to do with charge ordering, in contrast to the stripe model. They also suggested neutron-scattering experiments to distinguish if the incommensurate magnetic peaks originate from the stripe or the spiral phase. According to them, co-doped sample $La_{2-x}Sr_xCu_{1-z}Zn_zO_4$ gives important information on this. Since Zn impurity is expected to reduce frustration caused by the hole spin, the magnetic correlation length should increase and the incommensurability should decrease by a factor of 1-γz with $\gamma\sim2$.

In order to clarify the origin of the diagonal incommensurate magnetic peaks, we perform neutron-scattering experiments on the Zn doped $La_{2-x}Sr_xCuO_4$. Ni doped $La_{2-x}Sr_xCuO_4$ is also measured to study the impurity dependence. It is found that Zn doping reduces the incommensurability and enhances the correlation length just slightly. This behavior is explained by both the stripe and the spiral models. On the other hand, Ni doping introduces a considerable change in magnetism. (Fig. 1) This is probably because Ni is doped as Ni^{3+} with $S=\frac{1}{2}$ so that the hole number is reduced with Ni doping. Although it is expected that Ni doping does not disturb the magnetic interactions so much, the magnetic correlations are disordered considerably. This suggests that the charge inhomogeneity, caused by the random Ni^{3+} distribution, disturbs the stripe formation and the magnetic correlations become disordered. This result supports the diagonal stripe state and probably rules out the spiral state.

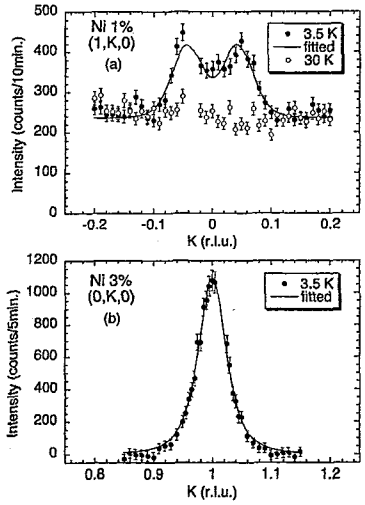

Figure 1: Elastic scans along $(1,K,0)$ in $La_{1.95}Sr_{0.05}Cu_{0.99}Ni_{0.01}O_4$ (a) and along $(0,K,0)$ in $La_{1.95}Sr_{0.05}Cu_{0.97}Ni_{0.03}O_4$ (b). Background intensities measured at a high temperature have been subtracted in (b).

References

1) N. Hasselmann, A. H. Castro Neto and C. M. Smith: Phys. Rev. B **69** (2004) 014424.

原子炉：JRR-3　　装置：LTAS(C2-1)　　分野：中性子散乱（超伝導）

研究テーマ： 一軸応力による重い電子系反強磁性体の物性制御
表題： $CePd_2Si_2$ の反強磁性状態に対する一軸応力効果

22) Uniaxial-stress effect on the antiferromagnetic state in $CePd_2Si_2$

M. Yokoyama[1], A. Gawase[2], H. Amitsuka[2], K. Tenya[2] and H. Yoshizawa[3]
[1] *Faculty of Science, Ibaraki University, Mito 310-8512*
[2] *Graduate School of Science, Hokkaido University, Sapporo 060-0810*
[3] *Institute for Solid State Physics, The University of Tokyo, Tokai 319-1106*

The ternary tetragonal compound $CePd_2Si_2$ shows an antiferromagnetic (AF) order with the Néel temperature of $T_N \sim 8$ K and the ordered moment of $\mu_o \sim 0.6\ \mu_B$ [1, 2]. It is found that the application of hydrostatic pressure P markedly suppresses the AF state, and then induces the superconducting state around the critical pressure $P_c \sim 2.4$ GPa, where T_N approaches to zero [3]. In addition, recent transport measurement under P [4] suggests that the strains other than the volume compression are coupled with the suppression of the AF state. To verify this, we have performed the elastic neutron scattering measurements under the uniaxial stress, for the first time.

The uniaxial stress σ was applied along the $[1\bar{1}0]$ and [001] directions up to 0.8 GPa. The elastic neutron scattering experiments were performed using a triple-axis spectrometer GPTAS located at the JRR-3M reactor of JAERI. We chose the neutron momentum of $k = 2.67$ Å^{-1}, and used a combination of 40'-40'-40'-80' collimators and two pyrolytic graphite filters. The scans were performed in the (hhl) scattering plane for $\sigma \parallel [1\bar{1}0]$, and the $(hk0)$ plane for $\sigma \parallel [001]$.

Since $CePd_2Si_2$ has the AF structure with the modulation of $q = (1/2, 1/2, 0)$ and μ_o polarized along the [110] direction, we expect that there are two domains: $q_+ = (1/2, 1/2, 0)$ with $\mu_o \parallel [110]$ and $q_- = (1/2, 1/2, 0)$ with $\mu_o \parallel [1\bar{1}0]$ [1]. We first estimated μ_o^2 value multiplied by the volume fraction V/V_o for each domain, from the integrated intensities of the magnetic Bragg peaks normarized by the intensities of the (110) nuclear Bragg peaks, and then calculated the total AF moment μ_o. Figure 1 shows the σ variations of $\mu_o/\mu_o(\sigma = 0)$ and $T_N/T_N(\sigma = 0)$, where $\mu_o(\sigma = 0)$ and $T_N(\sigma = 0)$ are estimated to be $0.54(2)\ \mu_B$/Ce and 8.5 K. For $\sigma \parallel [1\bar{1}0]$, we have found that μ_o decreases with increasing σ, whose rate $\partial \ln \mu_o/\partial\sigma$ is estimated to be ~ 0.15 GPa^{-1}. On the other hand, it is nearly independent of σ for $\sigma \parallel [001]$. Similar anisotropy is also observed in the σ dependence of T_N. T_N is found to decrease with increasing σ for $\sigma \parallel [1\bar{1}0]$, while it increases for $\sigma \parallel [001]$. The rates of change $\partial \ln T_N/\partial\sigma$ are roughly estimated to be $\sim -6.3 \times 10^{-2}$ GPa^{-1} and $\sim 5.4 \times 10^{-2}$ GPa^{-1} for $\sigma \parallel [1\bar{1}0]$ and [001], respectively. This anisotropy is qualitatively consistent with that expected from the thermal expansion measurements [1]. These experimental results suggest that the axial strain is also coupled with the suppression of the AF order.

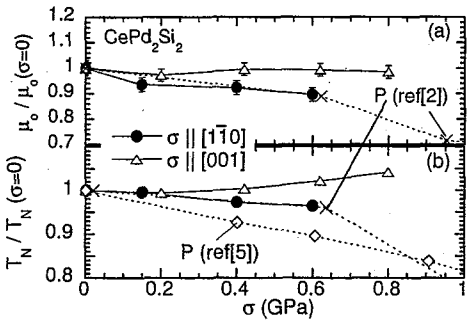

Fig. 1. σ variations of (a) the staggered moment μ_o and (b) the Néel temperature T_N for $CePd_2Si_2$. P variations of these values [2, 5] are also shown.

References

[1] N.H. van Dijk *et al.*, Phys. Rev. B 61 (2000) 8922.
[2] N. Kernavanois *et al.*, Phys. Rev. B 71 (2005) 064404.
[3] N.D. Mathur *et al.*, Nature 394 (1998) 39.
[4] A. Demuer *et al.*, J. Phys. Condens. Matter 14 (2002) L529.
[5] A. Demuer *et al.*, J. Magn. Magn. Mater. 226-230 (2001) 17.

使用施設：JRR-3M，装置： 4G，分野： 103: Strongly Correlated Election Systems

研究テーマ：YNi_2B_2C の磁束格子に関する研究
表　題：YNi_2B_2C の磁束格子構造に関する磁場-温度相図の研究

23) H-T Phase Diagram of Flux Line Lattice Structure in YNi_2B_2C

H. Kawano-Furukawa[1], H. Tsukagoshi[1], F. Yano[1], T. Nagata[1], N. Sakiyama[2], H. Yoshizawa[2], M. Yethiraj[3], H. Takeya[4], J. Suzuki[5]

[1] *Department of Physics, Ochanomizu Univ., Tokyo 112-8610, Japan*
[2] *Neutron Science Laboratory, I.S.S.P., The University of Tokyo, Ibaraki 319-1106, Japan*
[3] *Center for Neutron Scattering, Oak Ridge National Laboratory, TN 37831-6393, USA*
[4] *National Institute for Materials Science, Ibaraki 305-0047, Japan*
[5] *Advanced Science Research Center, J.A.E.R.I., Ibaraki 319-1195, Japan*

The flux line lattice (FLL) in $RENi_2B_2C$ attracts great attentions, because the structural phase transition from triangular to square FLL driven by the magnetic field is observed in the materials with RE = Er, Y, Lu, and Tm. In this experiment, we focused on the FLL structure in YNi_2B_2C which is positioning itself as a nonmagnetic type II superconductor bearing a relatively high superconducting transition temperature T_c ~15 K and a Ginzburg-Landau parameter κ ~20 [1]. Though this material has an s-wave order parameter, extensive studies have indicated its superconducting gap has a point node along the a- and b- axes [2]in addition to a fourfold anisotropic Fermi velocity distribution [3], reflecting its underlying crystalline symmetry.

Recently, Nakai *et al.* proposed a theoretical H-T phase diagram of the FLL structure [4] for a system with fourfold anisotropies in Fermi velocity and superconducting gap. Both anisotropies stabilize a square FLL. Here $\square_v$ and $\square_g$ denote FLL structures reflecting each anisotropy. $RENi_2B_2C$ system has both anisotropies and orientations of FLL structures stabilized by such anisotropies seem to be 45° off. Therefore, successive FLL transitions from a triangular ($\triangle$) → a square ($\square_v$) → a triangular ($\triangle$) → another square ($\square_g$) may appear with increasing a magnetic field. To check their prediction, we have performed small angle neutron scattering (SANS) experiments.

A single crystal of $YNi_2^{11}B_2C$ was grown by the floating zone method. In order to reduce neutron absorption by ^{10}B, ^{11}B isotope was used. A superconducting transition temperature and an extrapolated upper critical magnetic field of our sample are $T_c(0)$ = 14.2 K and $H_{c2}(0)$ ~ 6.5 T, respectively. SANS measurements were performed at SANS-J and SANS-U installed in the guide hall of the JRR-3 reactor. An incident neutron beam with $\lambda = 6.5 \sim 11$ Å was set to be parallel to a magnetic field and the crystal c-axis. All measurements were performed in a field cooled process, and an oscillating field (maximum amplitude 0.15 T) was applied at each measuring temperature to bring a FLL alignment to the equilibrium state [5]. In addition, above 0.5 T, the sample was rotated to satisfy a Bragg condition.

We studied the FLL structure under various magnetic fields up to H = 5T, H/H_{c2} ~ 0.77. In Fig. 1 the resultant H-T phase diagram of the FLL structure in $YNi_2^{11}B_2C$ is depicted. The present results revealed that the $\triangle$ lattice appears only in a low magnetic field region near H_{c1}, and the square lattice occupies almost entire region of the $H-T$ phase diagram. Furthermore, in the latter case, the orientation of the nearest neighbor FLL is along the [110] direction, where the Fermi velocity has the minimum value, indicating the square lattice is of $\square_v$ type. There is no sign of a transition either towards the $\square_g$ lattice or to the $\triangle$ lattice in higher magnetic fields region.

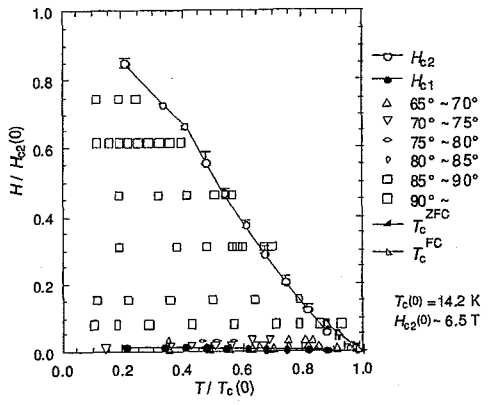

Figure 1: H-T phase diagram of FLL in YNi_2B_2C. Temperature and magnetic field are normalized by $T_c(0)$ and $H_{c2}(0)$, respectively.

References

1) K. Ghosh *et al.*: *Physica B* **223&224** (1996) 109.
2) K. Izawa *et al.*: *Phys. Rev. Lett* **89** (2002) 137006.
3) S. B. Dugdale *et al.*: *Phys. Rev. Lett* **83** (1999) 4824.
4) N. Nakai *et al.*: *Phys. Rev. Lett* **89** (2002) 237004.
5) S. J. Levett *et al.*: *Phys. Rev. B* **66** (2001) 014515.

原子炉：JRR-3　　装置：SANS-J(C3-2)　　分野：中性子散乱（超伝導）

研究テーマ： $Sr(Ru_{1-x}Mn_x)O_3$ の金属絶縁体転移と磁性
表題： $SrRu_{1-x}Mn_xO_3$ $(0.4 \leq x \leq 0.6)$ の絶縁体相に誘起される反強磁性秩序

24) Antiferromagnetic Order in Insulating Phase of $SrRu_{1-x}Mn_xO_3$ $(0.4 \leq x \leq 0.6)$

M. Yokoyama[1], C. Satoh[1], A. Saitou[1], H. Kawanaka[2], H. Bando[2],
K. Ohoyama[3] and Y. Nishihara[1]

[1]*Faculty of Science, Ibaraki University, Mito 310-8512*
[2]*National Institute of Advanced Industrial Science and Technology, Tsukuba, Ibaraki 305-8568*
[3]*Institute for Materials Research, Tohoku University, Sendai 980-8577*

The distorted perovskite compound $SrRuO_3$ is known to be a ferromagnet with the Curie temperature of $\sim$ 160 K and the ordered moment of $\sim$ 1.1 μ_B.[1, 2] Recent macroscopic investigations on the mixed compounds $SrRu_{1-x}Mn_xO_3$ $(0 \leq x \leq 0.6)$ [3] revealed that the substitution of Mn for Ru suppresses the itinerant ferromagnetic phase, and then induces a new insulating phase above the critical point $x_c = 0.39$. For $x \geq x_c$, a clear cusp like anomaly is observed in the temperature variations of the magnetic susceptibility, strongly suggesting the appearance of the antiferromagnetic order in the insulating phase. In $SrRuO_3$, the carrier mean free path is comparable to the lattice constant, and therefore, it is expected that even a small disorder will modify its physical properties quite appreciably. It is thus interesting to investigate the magnetic properties in the insulating phase microscopically. In the present study, we have performed the powder neutron diffraction measurements on $SrRu_{1-x}Mn_xO_3$ $(0.4 \leq x \leq 0.6)$.[4]

The polycrystalline samples of $SrRu_{1-x}Mn_xO_3$ with $x = 0.4$, 0.5 and 0.6 were prepared by the solid-state method. X-ray powder diffraction measurements at room temperature revealed that they form the tetragonal crystal structure, in contrast to the orthorhombic one for $x \sim 0$. The tetragonal crystal structure observed in our samples basically coincides with the first report,[5] but differs from the recent ones,[3, 6] where the orthorhombic structure observed in pure $SrRuO_3$ is kept up to $x = 0.6$. However, magnetic susceptibility and the electrical resistivity on our sample are quite similar to those reported by Cao *et al.*[3], suggesting that the electronic states in the samples with the tetragonal structure are nearly identical to those with the orthorhombic ones.

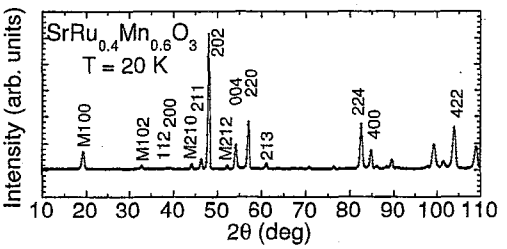

Fig. 1. Neutron powder diffraction profiles of $SrRu_{0.4}Mn_{0.6}O_3$ at $T = 20$ K. The mirror indices of several Bragg peaks in the tetragonal $I4/mcm$ symmetry are also shown.

The neutron diffraction measurements for the powdered samples with $x = 0.4$, 0.5 and 0.6 were performed in the temperature range between 20 K and 290 K, using the HERMES spectrometer located at the research reactor JRR-3M of JAERI. Figure 1 shows the powder neutron diffraction profile for $x = 0.6$ at 20 K.We have found new Bragg reflections at positions corresponding to (hkl) with $h+k = odd$ and $l = even$. The peak intensities in the high scattering angle are smaller than those in the low scattering angle, strongly suggesting that these peaks originate in the magnetic order. We have not observed the other additional reflection due to a ferromagnetic or AF order within the experimental resolution. These results indicate that the system has an AF order with a modulation of $q = (1, 0, 0)$, called the C-type structure in the perovskite compounds. The same magnetic structure can be also derived from the powder patterns for $x = 0.4$ and 0.5 at 20 K.

Figure 2 shows the x dependence of the AF moment μ_o, the unit-cell volume V and the c/a ratio at 20 K. The temperature vari-

使用施設：JRR-3M, 装置： T13 , 分野： 103: Strongly Correlated Election Systems

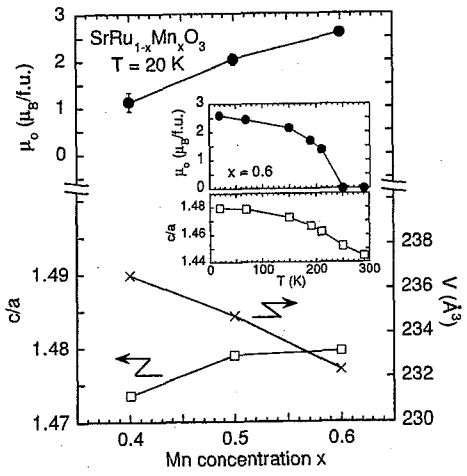

Fig. 2. x variations of the AF moment μ_o, the unit-cell volume V and the c/a ratio at $T = 20$ K for $SrRu_{1-x}Mn_xO_3$. The temperature variations of μ_o and c/a ratio for $x = 0.6$ are also plotted in the insets.

ations of μ_o and c/a for $x = 0.6$ are also plotted in the insets of Fig. 2. The magnitude of μ_o at 20 K for $x = 0.4$ is estimated to be 1.1(2) μ_B. Interestingly, this value is found to be much smaller than μ_{eff} (3.70(18) μ_B). The ratio μ_o/μ_{eff} is estimated to be ~ 0.34, which is close to the value observed in pure $SrRuO_3$ (~ 0.4). By further doping Mn, μ_o increases, and reaches 2.6(1) μ_B at $x = 0.6$. At the same time, μ_o/μ_{eff} is also enhanced to ~ 0.63 at $x = 0.6$, suggesting that the localized characteristic of d electrons becomes strong with increasing x. In the temperature scans for $x = 0.6$, on the other hand, we have observed that μ_o starts increasing at $T_N \sim 220$ K, and shows a tendency to saturate for $T/T_N < 0.6$. T_N estimated from $\mu_o(T)$ corresponds to the temperature at which we observed the cusp like anomaly in the magnetic susceptibility.

We have found a new AF state with the C-type structure in intermediate Mn concentrations, which is completely different from the insulating AF phase with the G-type magnetic structure in pure $SrMnO_3$[7] as well as the itinerant ferromagnetic phase in pure $SrRuO_3$.[1, 2] Furthermore, we have observed that the ratio μ_o/μ_{eff} is enhanced with increasing x from $x = 0$ to 0.6. This enhancement may be ascribed to the itinerant to localized electron transition due to the electron correlation effect, that is, the system is in the crossover region from $W/U > 1$ to $W/U \ll 1$, where W and U are the d-band width and the on-site Coulomb potential, respectively. Under the latter condition, we expect the occurrence of AF order due to the superexchange interaction, as is argued in the Mott-type insulators. In the superexchange mechanism, the positions of the Ru/Mn and O ions play a key role in the stability of the AF order. We have observed in the present study that the Ru/Mn-O bond length in the tetragonal c plane is significantly reduced in the AF phase. We thus expect that the Mn doping makes the hybridization between the d electrons in Ru/Mn ions and the p electrons in O ions strong through the compression in the c plane, and then enhances the superexchange interaction between nearest neighbor Ru/Mn ions, bringing the C-type AF order.

Finaly, we wish to stress that the valence and spin states in Ru and Mn ions are also connected with the magnetic structure. The appearance of the simple C-type AF order in the intermediate Mn concentrations strongly suggests that the dissimilarity of the spin states between Ru and Mn ions is reduced by doping Mn.

References

[1] A. Callaghan *et al.*, Inorg. Chem. **5** (1966) 1572.

[2] A. Kanbayasi, J. Phys. Soc. Jpn. **41** (1976) 1876.

[3] G. Cao *et al.*, Phys. Rev. B **71** (2005) 035104.

[4] M. Yokoyama *et al.*, J. Phys. Soc. Jpn. **74** (2005) 1706.

[5] Y. Xu, X. Chen and Y. Chen: unpublished (JCPDS 52-428).

[6] R. K. Sahu *et al.*, Phys. Rev. B **66** (2002) 144415.

[7] T. Takeda and S. Ōhara: J. Phys. Soc. Jpn. **37** (1974) 275.

研究テーマ：中性子散乱によるウラン化合物の物性研究
表　題：重い電子系超伝導体 $PrOs_4Sb_{12}$ における磁場誘起反強四極子秩序

25) Field-induced antiferroquadrupolar order in heavy fermion superconductor $PrOs_4Sb_{12}$

K. Kaneko[1], N. Metoki[1,2], T. D. Matsuda[1], K. Kuwahara[3], M. Kohgi[3], R. Shiina[3], J. -M. Mignot[4], A. Gukasov[4] and N. Bernhoeft[5]

[1]*ASRC, Japan Atomic Energy Research Institute, Ibaraki 319-1195, Japan*
[2]*Department of Physics, Tohoku University, Sendai 980-8578, Japan*
[3]*Deptartment of Physics, Tokyo Metropolitan University, Hachioji, Tokyo 192-0397, Japan*
[4]*Laboratoire Léon Brillouin, CEA/Saclay, 91191 Gif sur Yvette, France*
[5]*DRFMC-CEA, 38054 Grenoble, France*

The first Pr-based heavy fermion superconductor $PrOs_4Sb_{12}$ attracts considerable interest because of its unusual superconducting properties.[1] The non-magnetic Γ_1 ground state, the field-induced antiferroquadrupolar (AFQ) order phase for $\boldsymbol{H}\|[0\,0\,1]$ and the neutron inelastic scattering intensity indicate the dominant role of AFQ interaction in $PrOs_4Sb_{12}$.[2-4] The field-induced ordered phase (FIOP) exists for $\boldsymbol{H}\|[1\,1\,0]$ and $[1\,1\,1]$ as well.[5] In case for $[1\,1\,0]$, the mean field calculation suggests that the O_{xy} symmetry elements would be the primary order parameter but the energy difference for another one is very small.[6] Besides, the magnetization measurements report the additional phase boundary in FIOP for $\boldsymbol{H}\|[1\,1\,0]$.[5] In order to clarify the origin of FIOP for $\boldsymbol{H}\|[1\,1\,0]$, neutron diffraction experiments were carried out.

Neutron diffraction experimets for the large single crystalline $PrOs_4Sb_{12}$ with ~6 g were carried out on LTAS installed at JRR-3 of JAERI. For the investigation of FIOP, He-free 10 T superconducting magnet and ^{3}He-^{4}He dilution refrigerator both developed by JAERI were used. The scattering plane was set to $(h\,\bar{h}\,l)$ which is perpendicular to the vertical field applied parallel to the $[1\,1\,0]$ direction.

Figure 1 shows the 0 0 1 neutron diffraction profile measured at 0.27 K. The appearance of a weak but clear superlattice reflection was observed under 8 T while no trace was found at 0 T. The field-induced superlattice peaks were observed at the same positions as $H\|[0\,0\,1]$, namely, the propagation vector is $\boldsymbol{q}$=(1 0 0). In order to determine the magnetic structure in FIOP for $\boldsymbol{H}\|[1\,1\,0]$, the integrated intensity of superlattice peaks has been measured. The intensity analysis revealed that the angle factor for the reflections in the $(h\,\bar{h}\,l)$ scattering plane is almost isotropic within the experimental accuracy. In other words, the induced antiferromagnetic moment orients parallel to the applied fields. In addition, the relatively large ferromagnetic moment is also induced parallel to the field. The sum of these two component results in the ferromagnetic structure where the magnetic moment at the corner of the unit cell is larger than that at the center or vice versa, as shown in Fig. 2.

The induced antiferromagnetic component J_x+J_y, parallel to the applied field, cannot be explained by magnetic interactions which favors the magnetic moment perpendicular to the field. This result directly evidences the underlying AFQ order in FIOP for $\boldsymbol{H}\|[1\,1\,0]$ with O_{xy} symmetry of the primary order parameter.[6] In case for $\boldsymbol{H}\|[0\,0\,1]$, the antiferromagnetic component of J_y which couples to the quadrupole O_{yz} is induced in FIOP.[3] In this case, the comparison between experimental results and mean-field calculation clarifies the dominant role of quadrupolar interaction.[3] These facts strongly indicate the dominant role of O_{xy}-type quadrupolar interaction in $PrOs_4Sb_{12}$.

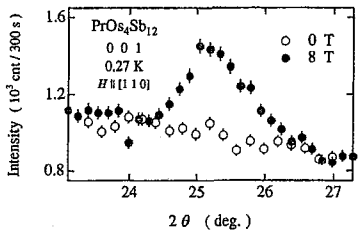

Figure 1: Feld dependence of 0 0 1 diffraction profile at 0.27 K.

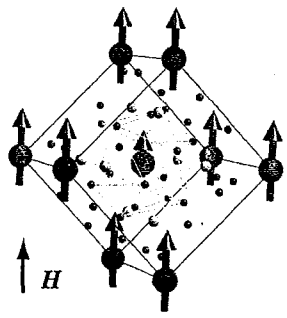

Figure 2: Schematic view of determined magnetic structure of $PrOs_4Sb_{12}$ at 8 T for $\boldsymbol{H}\|[1\,1\,0]$.

References

1) M. B. Maple *et al.*, J. Phys. Soc. Jpn. **71** (2002) Suppl. 23.
2) Y. Aoki, *et al.*, J. Phys. Soc. Jpn. **71**, 2098 (2002).
3) M. Kohgi *et al.*, J. Phys. Soc. Jpn. **72**, 1002 (2003).
4) K. Kuwahara *et al.*, J. Phys. Soc. Jpn. **73**, 1438 (2004).
5) T. Tayama *et al.*, J. Phys. Soc. Jpn. **72**, 1516 (2003).
6) R. Shiina, J. Phys. Soc. Jpn. **73**, 2257 (2004).

原子炉：JRR-3　　装置：LTAS(C2-1)　　分野：中性子散乱（超伝導）

研究テーマ：高温超伝導体の磁気励起
表題：高温超伝導体の高エネルギーまでの磁気励起スペクトルについて

26) On the Magnetic Excitation Spectra of High-T_c Cu Oxides at Energies Up to the Region Far above the Resonance Energy

Satoshi Iikubo, Masafumi Ito, Akito Kobayashi, Masatoshi Sato and Kazuhisa Kakurai*

Department of Physics, Division of Material Science, Nagoya University,Furo-cho, Chikusa-ku, Nagoya 464-8602
*Advanced Science Research Center, JAERI, Tokai, Ibaraki 319-1195

The magnetic excitation spectra $\chi''(q,\omega)$ of $YBa_2Cu_3O_y$ (YBCO or $YBCO_y$) and La214 systems have been studied. For aligned crystals of $La_{1.88}Sr_{0.12}CuO_4$, $\chi''(q,\omega)$ has been measured up to ~30 meV. Existing data of these two kinds of system have been analyzed at energies up to the values far above ω_r, around which $\chi''(q,\omega)$ exhibits the commensurate peak. The expression $\chi(q,\omega) = \chi_0(q,\omega) /\{1+J(q)\chi_0(q,\omega)\}$ is used in the analyses, where $\chi_0(q,\omega)$ is the susceptibility of the electrons without the exchange coupling $J(q)$ among them. It has been already reported by the authors' group [1] that the expression can explain the characteristics of the q- and ω-dependences of the spectra of $YBa_2Cu_3O_y$ (YBCO or $YBCO_y$) in the energy region $\omega \leq \omega_r$. Here, we have also found [2] that the expression can reproduce the rotation of the four incommensurate peaks of $\chi''(q,\omega)$ within the a^*-b^* plane about $(\pi/a, \pi/a)$ point by 45°, which was experimentally shown by Hayden *et al.* [3] to take place as ω goes to the region far above ω_r from an energy below ω_r. (Figure 1 shows the results of the model calculations.) This indicates that for the rotation, "stripe" correlation is not required.

For La214, the observed and calculated results of $\chi''(q,\omega)$ are also studied comparatively up to the region above ω_r.

Results of these studies indicate that for YBCO, the characteristics of $\chi''(q,\omega)$ can be explained qualitatively without considering "stripes" throughout the whole ω region studied, while in La214 systems,

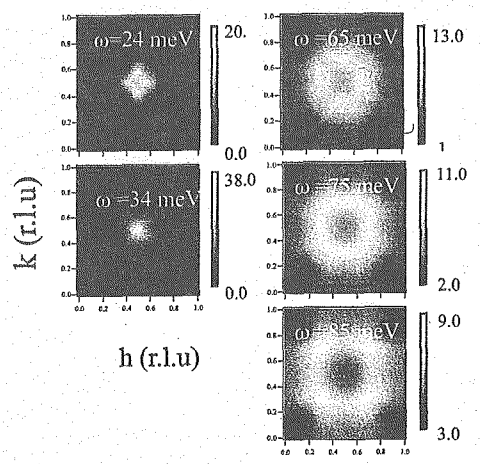

Fig. 1: Magnetic excitation spectra in the q_x-q_y plane calculated by using the parameters for $YBCO_{6.6}$. Experimentally observed characteristics of $\chi''(q,\omega)$ are well reproduced.

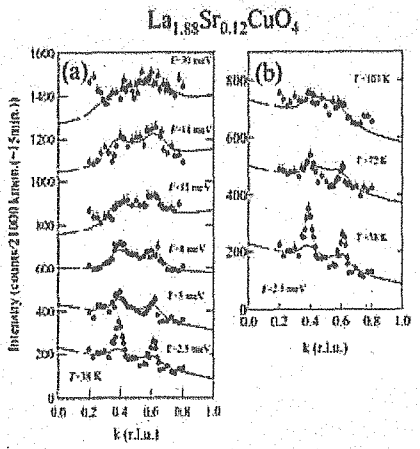

Fig. 2: The magnetic excitation spectra observed for $La_{1.88}Sr_{0.12}CuO_4$ are fitted by the expression shown in the text, at T=38 K (a) and at 2.5 meV(b).

[1] M. Sato et al., J. Phys. Soc. Jpn. 70 (2001) 1342; M. Ito et al. ibid, 71 (2002) 265.
[2] S.M. Hayden et al., Nature 429(2004) 531.
[3] S. Iikubo et al., J. Phys. Soc. Jpn. 74 (2005) 275.

使用施設：JRR-3M，装置：５G，分野：超伝導・磁性

研究テーマ：中性子散乱によるウラン化合物の物性研究
表　題：反転対称を持たない重い電子系超伝導体 $CePt_3Si$ における磁場中中性子回折

27) Neutron diffraction study on non-centrosymmetric heavy fermion superconductor $CePt_3Si$

K. Kaneko[1], N. Metoki[1,2], N. Bernhoeft[3], T. D. Matsuda[1], Y. Haga[1], S. Hashimoto[4], T. Ueda[4], R. Settai[4] and Y. Ōnuki[1,4]

[1]*ASRC, Japan Atomic Energy Research Institute, Ibaraki 319-1195, Japan*
[2]*Department of Physics, Tohoku University, Sendai 980-8578, Japan*
[3]*DRFMC-CEA, 38054 Grenoble, France*
[4]*Graduate School of Science, Osaka University, Toyonaka 560-0043, Japan*

$CePt_3Si$ is a heavy fermion superconductor with non-centrosymmetric structure (space group $P4mm$)[1]. This compound exhibits antiferromagnetic order at $T_N = 2.2$ K and enters into a heavy fermion superconducting state at $T_{SC} \approx 0.75$ K. Initial neutron scattering studies have clarified that the antiferromagnetic structure is characterized with an ordering wave vector $\boldsymbol{q}$=(0 0 1/2); reduced magnetic moments of 0.17 μ_B lying in ferromagnetic sheets in the c plane stacks in antiferromagnetic order along the c-axis.[2] The long range antiferromagnetic order clearly coexists with the superconductivity in $CePt_3Si$. Additional inelastic scattering experiments on a polycrystalline sample revealed an excited state of about 1 meV suggesting that the first crystal field level is close to the ground state and that the pseudo-quartet ground state would be responsible for the physical properties.[2] The magnetization, resistivity and magneto-striction measurements revealed the magnetic phase diagram and reported the existence of additional phase boundary under magnetic fields.[3]

In order to study the magnetic phase diagram, neutron diffraction experiments under fields were carried out.

Neutron diffraction experiments were carried out on TAS-2 and LTAS spectrometer both installed at the guide hall of JRR-3. Magnetic fields up to 5 T for $\boldsymbol{H}\|[1\,0\,0]$ and [0 0 1] were applied by using the vertical and horizontal superconducting magnet, respectively.

With decreasing temperature, no significant anomaly has been found in either the Bragg profile or intensity of magnetic reflection on passing through T_{sc} within our experimental accuracy as shown in Fig. 1. Under magnetic fields of 5 T, the antiferromagnetic reflections with $\boldsymbol{q}$=(0 0 1/2) were clearly observed for fields both $\boldsymbol{H}$ parallel to [1 0 0] and [0 0 1] directions. Figure 2 shows the field dependence of 0 0 1/2 antiferromagnetic peak intensity for $\boldsymbol{H}\|[1\,0\,0]$ at 1.51 K. The antiferromagnetic intensity starts increasing around 2 T at temperatures below T_N. This inflection field is almost independent from both temperature and applied field directions. In addition, T_N is almost constant up to 5 T for both field directions. The observed inflection field and the field independent T_N are consistent with the result of magnetization, resistivity and magnetostriction measurements.[3]

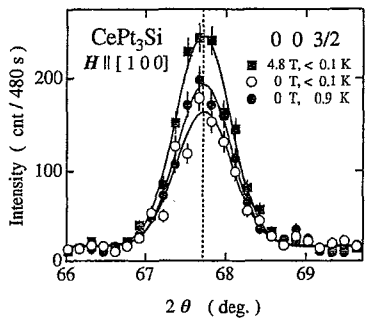

Figure 1: 0 0 3/2 antiferromagnetic reflection profiles measured below and above T_{sc} and under magnetic field for $\boldsymbol{H}\|[1\,0\,0]$.

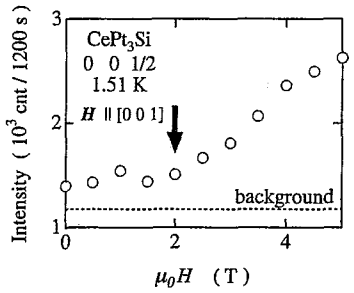

Figure 2: Field dependence of 0 0 1/2 antiferromagnetic peak intensity for $\boldsymbol{H}\|[0\,0\,1]$ at 1.51 K.

The increase of antiferromagnetic intensity is prominent for $\boldsymbol{H}\|[1\,0\,0]$. The antiferromagnetic reflection at 5 T becomes ~5 times stronger than that at zero field, indicating that antiferromagnetic moment increases more than twice as large by applying magnetic fields of 5 T in $CePt_3Si$. These results indicate that the antiferromagnetic state with $\boldsymbol{q}$=(0 0 1/2) in $CePt_3Si$ is quite stable even in the field-induced ordered state. The degenerated excited state associated with quadrupolar degree of freedom may play an important role for the field-induced state in $CePt_3Si$.

References

1) E. Bauer *et al.*: Phys. Rev. Lett. **92** (2004) 027003.
2) N. Metoki *et al.*: J. Phys.: Condens. Matter **16** (2004) L207.
3) T. Takeuchi *et al.*: J. Phys.: Condens. Matter **16** (2004) L333.

原子炉：JRR-3　　装置：LTAS(C2-1)　　分野：中性子散乱（超伝導）

研究テーマ： PONTA-IRT
表題：不純物 Ni,Zn をドープした高温超伝導体 $La_{1.85}Sr_{0.15}CuO_4$ における磁気励起エネルギースケールと T_C の相関

28) Renormalization in energy scale of spin excitations in Ni doped $La_{1.85}Sr_{0.15}CuO_4$

M. Matsuura, M. Kofu, K. Hirota
Institute for Solid State Physics, The University of Tokyo, 106-1 Shirakata, Tokai, 319-1106

The interplay between antiferromagnetic (AF) spin fluctuations and superconductivity is the central issue in the physics of high-T_c superconductivity. From recent inelastic neutron scattering experiments using TOF technique, very similar spectrum of magnetic excitations have been reported in $YBa_2Ca_3O_{6.6}$ (YBCO)[1] and $La_{1.875}Ba_{0.125}CuO_4$ (LBCO)[2], which include incommensurate spin fluctuations at low energy, dispersion toward (π,π) with increasing energy, and outwards dispersion at high energy. These features may be universal in the high-T_c superconductors. We explored impurity (Ni and Zn) doped $La_{2-x}Sr_xCuO_4$ with optimal hole concentration ($x = 0.15$) to elucidate how AF spin fluctuation changes when superconductivity is suppressed by the impurity. Single crystals of $La_{1.85}Sr_{0.15}Cu_{1-y}A_yO_4$ with A=Ni, $y = 0.029$ (Ni:2.9%) and A=Zn, $y = 0.017$ (Zn:1.7%) were grown using travelling-solvent-floating-zone method[3]. T_c's are suppressed to 12 and 16 K from 36.8 K by Ni:2.9% and Zn:1.7% doping, respectively. Neutron scattering experiments were performed on the triple-axis spectrometer PONTA installed at the JRR-3M Reactor of the JAERI. Figure 1 shows constant energy scans of Ni:2.9% and Zn:1.7% along the [100] direction around (π,π) measured at $T = 10$ K ($< T_c$). To obtain a good signal while avoiding spurious peaks, the intensities are averaged for a few of ($h0l$) scans with fixed l's where the major axis of the resolution ellipsoid is nearly parallel to the magnetic rod, i.e, the focusing condition is satisfied. For Ni:2.9%, as the energy increases, the incommensurability δ decreases and goes zero around 21meV (saddle point). This energy dependence of the AF peaks is remarkably similar to those observed in LBCO and YBCO. We confirmed the single broad peak is magnetic in origin from its Q-dependence. In addition, the

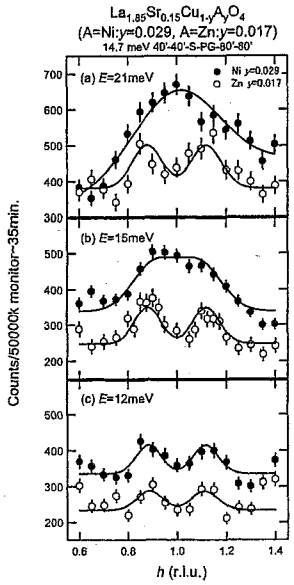

Fig. 1. Constant energy scans of Ni:2.9% and Zn:1.7% along the [100]-direction around (10l) measured at $T = 10$ K. The solid lines show fits assuming equivalent Gaussian peaks at ($1 \pm \delta$ 0 l)

Zn:1.7% data shows no dispersion nor peak-broadening up to 21meV. This indicates that the broadening at high energies is not due to instrumental resolution, but intrinsic to the Ni doping. From the dispersion of incommensurate spin-excitation of impurity-free and optimally-doped $La_{1.86}Sr_{0.14}CuO_4$ measured by Christensen *et al.*, the saddle point was estimated about 40meV, which is twice as large energy as that of Ni:2.9%. Since T_c in Ni:2.9% is suppressed by a factor of three, we speculate that Ni-doping reduces the exchange interaction J resulting in suppression of the saddle-point energy.

References

[1] J. M. Tranquada *et al.*: Nature **429** (2004) 534.
[2] S. M. Hayden *et al.*: Nature **429** (2004) 531.
[3] M. Kofu *et al.*: Phys. Rev. B (to be published, cond-mat/0409747).

使用施設：JRR-3M，装置： 5G，分野： 103: Strongly Correlated Election Systems

研究テーマ：超伝導セラミックスにおけるカイラルグラス相の偏極中性子による探索
表　題：セラミックス超伝導体におけるカイラルグラス相転移の偏極中性子による探索

29) Search for evidence of chiral-grass ordering in seramics-superconductor by means of polaraized neutron scattering

S. Kawarazaki, K. Kakurai[1] and M. Hagiwara[2]

Department of Earth and Space Science, Osaka University, Toyonaka, Osaka 560-0043
[1]Advanced Science Research Center, JAERI, Tokai, Ibaraki 319-1195
[2]Faculty of Engineering and Design, Kyoto Institute of Technology, Matsugasaki, Sakyo-ku, Kyoto, 606-8585

Cuprate high-Tc superconductors have an anisotropic d-wave pairing symmetry, and hence, the coupling constant of the Josephson junction may have two values, $\pm J$, where $-J$ leads to the π-junction across which the order parameter changes the phase by π. Then, for instance, if three superconducting grains form a network of three π-junctions, the phase of the three grains must frustrate each other as is the case for the three Heisenberg spins on a triangular praquet with an antiferromagnetic interaction.

A ceramic high-Tc superconductor is regarded as a random Josephson network, and it is expected that the $\pm J$ of junctions are randomly distributed over the network. Kawamura and Li have proposed that, in this situation, the chirality, that is, the direction of the local loop-supercurrent over grains must undergoes a chiral glass phase transition [1,2]. This novel thermodynamic phase should realize in zero external field and is characterized by a spontaneously broken time-reversal symmetry.

Specifically, with decreasing temperature, all the grains of the sample first undergoes the superconducting phase transition at $Tc1$,and then at certain temperature $Tc2$ below $Tc1$, the chirality starts freezing, that is, the local loop-supercurrent starts flowing with random directions. In zero-external field, in the temperature region between $Tc1$ and $Tc2$, there is no magnetic flux in and around the sample at all, but below Tc2 certain magnitude of flux should appear spontaneously and randomly in and around the surface of the sample.

Up to the present, several experiments have been made in order to prove the existence of this novel thermodynamic phase: The electrical resistivity measurement [3] and the magnetic susceptibility measurement [4] have revealed the existence of a possible $Tc2$ where some anomaly in the non-linear term of the respective quantity were observed. However the result of the μ-SR measurement, which is a microscopic method to detect directly, without external magnetic field, the appearance of the magnetic flux in the sample, was not clear enough to give a definitive conclusion.

The purpose of the present study is to detect the magnetic flux in a sample by means of polarized neutron scattering, which works also without external field. One can observe the internal magnetic field by measuring the rotation or flip of the spin direction of a polarized neutron. The method of the spin depolarization measurement was successfully applied to the cluster-type spin-glass sample. In the present case, the magnitude of the neutron spin depolarization due to the randomly distributed internal field with magnitude of order of magnetic quantum must be too small to be observed. However, the magnitude of the spin-flip coherent cross section due to the possible internal structure of the magnetic flux may give some intensity to the small-angle scattering. The CRYOPAD is quite suitable to this type of experiment because it provides a field-free space around the sample.

We have carried out a depolarization measurement using the CRYOPAD on the TAS-1 thermal neutron spectrometer to test the measuring system and the quality of the sample. A ceramic $YBa_2Cu_4O_8$ sample was prepaired by assembling several discs of the material with about 20 mm diameter and 1.5 mm thickness. The Tc1 of the sample is 50 K. We have found that the measuring system were quite nicely tuned and the sample had good quality. No depolarization was detected in this measurement as was reasonable expected. The next stage is search for the spin-flip component in the small angle scattering of polarized neutrons by using the CRYOPAD on the SANS-J spectrometer.

References

1) H. Kawamura and M. H. Li: Phys. Rev. B **54** (199) 619.
2) H. Kawamura and M. H. Li: Phys. Rev. Letters **78** (1997) 1556.
3) Y. Yamao *et al.*: J. Mag. Mag. Mater. **177-181** (1998) 179.
4) M. Matsuura *et al.*: J. Phys. Soc. Jpn. **64** (1995) 4540.

原子炉：JRR-3　　装置：TAS-1(2G)　　分野：中性子散乱（超伝導）

研究テーマ： 四極子秩序物質RB2C2でのスピン格子ダイナミクス
表題： 希土類四極子秩序化合物HoB2C2での磁気励起

30) Magnetic Excitations in Rare Earth Antiferroquadrupolar Ordeing Compound HoB_2C_2

K. Ohoyama[1], A. Tobo[2], and H. Onodera[2]
[1] *Institute for Materials Research, Tohoku University, Sendai 980-8577*
[2] *Fac. of Science, Tohoku University, Sendai 980-8578*

The RB_2C_2 (R=rare earth) compounds, which have the tetragonal LaB_2C_2 type structure with $P4/mbm$ symmetry show diversified magnetic properties caused by coexistence of antiferroquadrupolar (AFQ) and antiferromagnetic (AFM) interactions. In particular, DyB_2C_2 is the first tetragonal rare earth compound in which an AFQ ordering is realised [1]. Since the exact ground state by crystalline electric field under tetragonal symmetry has no degree of freedom on electric quadrupolar moments, it was thought that no AFQ ordering can be realised in the tetragonal rare earth compounds before the finding of the AFQ ordering in DyB_2C_2. Thus, to understand necessary conditions of AFQ orderings in rare earth compounds, it is indispensable to clarify characters of the AFQ ordering in DyB_2C_2

Of the RB_2C_2 system, HoB_2C_2 is particularly unique; (i) the AFQ ordering in HoB_2C_2 is realised at T_Q=4.5 K below the magnetic ordering temperature, T_N=5.9 K [2], (ii) anomalous magnetic diffuse scattering is observed above T_Q up to $\sim 2T_N$.

We expect that the AFQ orderings in RB_2C_2 probably yield anomalies of dynamic properties because the lattice and spin systems in RB_2C_2 must be coupled by the AFQ orderings through the strong LS coupling. In particular, in HoB_2C_2, characteristic diffuse scattering is observed around the transition temperatures, implying some kind of spin fluctuation. Therefore, to observe magnetic excitations in HoB_2C_2, we performed inelastic scattering experiments on a single crystalline sample of $Ho^{11}B_2C_2$ on the triple axis spectrometer HER at the C1-1 beam hole of JRR3-M of JAERI(Tokai). The experimental conditions were as follows; collimation was g-open-filter-S-80'-80', k_f=1.550 Å^{-1}.

Fig.1 shows inelastic scattering intensity with ϵ=0.3 meV at (1,0,l) through the (1,0,0) position at 5.35 K, where the anomalous diffuse scattering is observed, and 15 K. We observed magnetic scattering around the (1,0,0) positions, and it still remains at 15 K; since no magnetic Bragg peak exists in this temperature region, this component is due to quasi-elastic scattering. This result indicates that the anomalous diffuse scattering observed just above T_Q is due to the quasi-elastic scattering. Thus, as the origin of the magnetic diffuse scattering, spin fluctuation with a characteristic energy of a few K must be important.

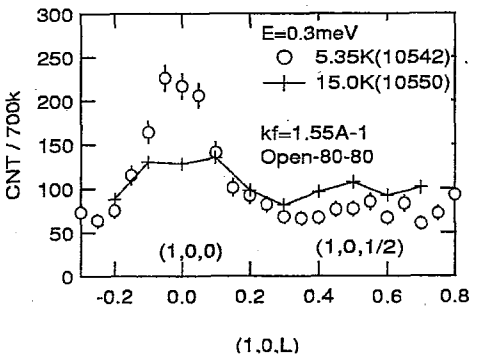

Fig. 1. Magnetic scattering at (1,0,l) through the (1,0,0) position with ϵ=0.3meV at 5.35 K (open circles), where the anomalous diffuse scattering is observed, and 15 K(crosses).

References

[1] H. Yamauchi *et al.*: J. Phys. Soc. Jpn. **68** (1999) 2057.
[2] H. Onodera *et al.*: J. Phys. Soc. Jpn. **68** (1999) 2526.
[3] K. Kaneko *et al.*: Phys. Rev. B. **68** (2003) 012401.

使用施設：JRR-3M, 装置： C1-1 (HER),6G(TOPAN) , 分野： 103: Strongly Correlated Election Syste

1. 中性子散乱 4)非晶質・液体

1. Neutron Scattering 4) Amorphous・Liquid

This is a blank page.

研究テーマ：制限空間内における流体の構造とイダナミクス
表題：ナノ空間における２成分溶液の相挙動と成分分子のダイナミクス

1) Phase Properties and Dynamics of Binary Solutions Confined in Nanospace

S. Kittaka, S. Takahara, Y. Kuroda, * T. Mori, * and T. Yamaguchi **

*Faculty of Science, Okayama University of Science, 1-1 Ridaicho, Okayama 700-0005, Japan; * Graduate School of Natural Science, Okayama University, 3-1-1 Tsushima, Okayama 700-8530, Japan; ** Faculty of Science, Fukuoka University, 8-19-1 Nanakuma, Jonanku, Fukuoka 810-0080, Japan*

Acetonitrile (CH_3CN) and water are completely miscible at ambient temperatures but this system is a non-ideal solution and gives specific interactions between component molecules at around 30 mol percent of CH_3CN [1]. Furthermore, the solution system is separated into two liquid phases at low temperatures, as shown in Fig. 1. And the mixed solution is widely

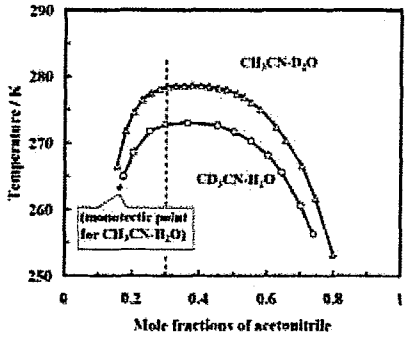

Fig. 1 Phase diagram of acetonitrile-water mixtures

used as solvent for both inorganic and organic chemical reactions. The solutions are passed through the porous beds for liquid chromatography in the chemical analyses. Thus, property of the solution in confined geometry is of special interest. MCM-41 is a most promising material to study the condensed phase in confinement, because of its exceptionally well-defined pore structure [2].

Present work aims to study the effect of confinement of solutions in the mesopores of MCM-41 C14 (d=2.8 nm) on the dynamic properties of component molecules. Two kinds of mixtures were prepared to analyze separately the CH_3CN and water by exchanging deuterium with protons of component molecules: CH_3CN-D_2O (H-D) and CD_3CN-H_2O (D-H) for each of which the former component was adjusted at 30 mol %. Dynamics was studied by quasi-elastic neutron scattering (QENS) using the spectrometer AGNES at the temperature range 263-298 K which was controlled with thermostat equipped with Pertier elements. Liquid mixture was put in a coaxial aluminum cylinder cell. The sample solution was introduced into MCM-41 from vapor phase by an amount corresponding to the capillary condensation.

Results

Fig. 2 shows the QENS spectra for the systems, bulk solution of D-H, and D-H confined in the mesopores and vanadium as

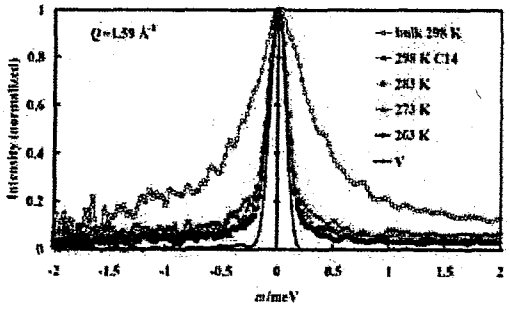

Fig. 2. QENS spectra for CD_3CN-H_2O solution in MCM-41

resolution function. Here, dynamics of water molecules were examined. Similar relations of spectra were observed for the system H-D. It is clear that dynamics of water molecules is strongly decreased by confinement. The spectra are composed of strong sharp part and a broad sleeve. It will be reasonable to consider that rotational

使用施設：JRR-3M, 装置：AGNES(C3-1-1), 分野 Glasses and liquids

motion is included in addition to the translational motion. However, due to poor quality of the spectrum it was not possible to divide into two parts as done before for pure water in MCM-41 [3]. Thus, allowing for the inhomogeneity of the dynamics, stretched exponential analysis was employed for the present experiment.

$$S(Q,\omega)=\frac{A(Q)}{\pi}\int_0^\infty dt\ \cos\omega t \exp[-\left(\frac{t}{\tau}\right)^\beta], \qquad (1)$$

where $A(Q)$ is a Debye-Waller factor, ω energy transfer, τ time fitting parameter, β stretched exponent describing the inhomogeneity of dynamics of molecules. The two fitting parameters present the average relaxation time of dynamic motion of molecules, leading to average energy transfer (2).

$$\Gamma_{av}=\frac{1}{\tau_{av}}=\frac{\tau}{\beta}\Gamma\left(\frac{1}{\beta}\right), \qquad (2)$$

where Γ is a gamma function of $1/\beta$. Fig. 3 shows the average energy transfer of water molecules for bulk solution D-H. The Γ_{av} increases almost linearly with Q^2, and the slope becomes larger with temperature increase. The former fact indicates that translational diffusion of water is significant compared with the rotational motion that should present constant values against Q^2. Similar plots for CH_3CN mixed with heavy water presented a little bit larger values than for water in Fig. 3, which corresponds to the low miscibility of the solution presented in Fig. 1.

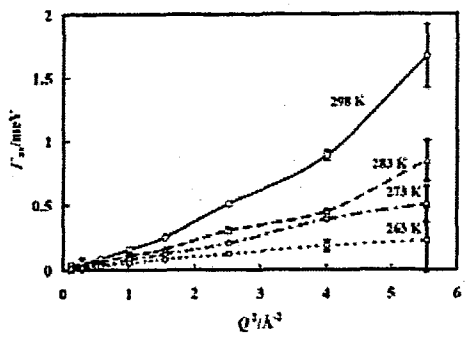

Fig. 3. Γ_{av} of CD_3CN-water solution against Q^2.

When the binary solutions are introduced in the mesopores of MCM-41, the molecules are strongly limited their motions. Stretched exponential analysis was also conducted on the spectra. The Γ_{av} values are shown in Fig. 4 for H-D. Spectral analysis for D-H was not successful due to too small spectral broadening stemming from low dynamics. The analyzed Γ_{av} values for H-D are much smaller than the resolution function (0.08 meV for AGNES). Thus detailed discussion is not possible. However, the fact that Γ_{av} values become finite values as Q increases suggests that CH_3CN molecules are qualitatively understood to migrate obeying jump diffusion model. This fact signifies that a size of clusters formed between CH_3CN and water should decrease by confinement and diffusion of CH_3CN occurs from cluster to cluster by repeating formation and decomposition of clusters [4].

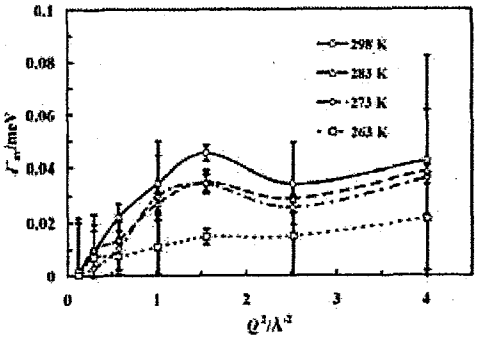

Fig. 4 Γ_{av} of CH_3CN-D_2O solution against Q^2.

References

[1] Jerzy Szydłowski, and Marek Szykuła,*Fluid Phase Equilibria* **154**, 79-87 (1999).

[2] T. Mori *et al.*, *Langmuir*, **18**, 1595 (2002).

[3] S. Takahara *et al.*, *J. Phys. Chem.* B.,**103**, 5814 (2001).

[4] T. Takamuku *et al.*, *J. Phys. Chem.* B.,**105**, 6236 (2001).

研究テーマ :アルコール一水混合系におけるナノスケールゆらぎとダイナミクス
表題 *tert*-ブチルアルコール一水混合系における濃度ゆらぎとスローダイナミクス

2) Concentration Fluctuations and Cluster Dynamics of *tert*-Butyl Alcohol -Water Mixtures

K.Yoshida, T. Yamaguchi, M. Nagao*, and M. Shibayama*

*Department of Chemistry, Faculty of Science, Fukuoka University, 8-19-1 Nanakuma, Jonan-ku, 814-0180 Fukuoka, Japan; *Institute for Solid State Physics, The University of Tokyo, 106-1 Shirakata, Tokai 319-1106, Japan*

Ii is well-known that the formation of molecular aggregates or microinhomogeneities occur in various alcohol-water mixtures from various physico-chemical measurements. All the results have been discussed in connection with the anomalies in various physico-chemical properties of the alcohol-water mixtures in a water-rich region. Recently, concentration fluctuations and cluster dynamics have been measured in butoxyethanol(BE)-water(D_2O) mixture that has a lower critical solution temperature (~38 °C) [1]. However, cluster dynamics in alcohol-water mixtures where phase separation does not occur, such as *tert*-butyl alcohol(TBA)-water, have not been investigated. On a microscopic scale, it has recently been found from the reference interaction site model (RISM) integral equation theory on TBA-water mixture [2] that TBA molecules form clusters with the hydrophobic methyl group as an inside core in dilute aqueous solution. To explain the macroscopic properties in various alcohol-water mixtures in terms of molecular interaction, mesoscopic structural information, such as cluster size and cluster dynamics, is highly needed. In this study, we have measured small-angle neutron scattering (SANS) and neutron spin echo (NSE) in TBA-D_2O mixtures at various mole fractions and temperatures. TBA with the hydroxyl proton substituted with D was used since it can exchange with deuteron of D_2O.

The SANS in TBA-D_2O mixture of 0.05 ~ 0.25 TBA mole fraction was measured at 15 ~ 55 °C. A sample was kept in a quartz cell of 2-mm path length. The cell was inserted into a temperature-controlled chamber. The temperature in the chamber was controlled within ±0.1 °C with a Pertier device. The distances between the sample and detector were 2 and 8 m, corresponding to Q of 0.007 – 0.14 Å^{-1}. Measurements were also made for background, an empty cell, and lupolen used for intensity normalization.

The NSE signals in TBA-D_2O mixtures of 0.10 ~ 0.15 TBA mole fraction were measured at 15, 25, and 45 °C. A sample was kept in a quartz cell of 2-mm path length. The scattering vector Q covered was 0.01 ~ 0.1 Å^{-1}. The Fourier time was varied from 0.15 to 15 ns. The temperature of sample was controlled within ±0.3 °C with circulated water.

For SANS data, the Ornstein-Zernike plots were made according to

$$I(Q)^{-1} = I(0)^{-1}\left(1+\xi^2 Q^2\right) \qquad (1)$$

where ξ is the Ornstein-Zernike (OZ) correlation length, and $I(0)$ is the intensity at Q = 0 Å^{-1} As shown in Fig. 1, the values of ξ have a maximum at x_{TBA} = ~0.13 and increase with rising temperature at the same mole fractions. These results are in good agreement with those obtained from small-angle X-ray scatterings [3]. The temperature dependency of them in TBA-water mixture is smaller than those in BE-water mixture [1].

The intermediate scattering function, $I(Q, t)$, obtained from the NSE signals was fitted

使用施設 :JRR-3M, 装置 :SANS-U(C1-2), iNSE(C2-3-1), 分野 Glass and Liquids

to the following equation on basis of the Brownian motion,

$$I(Q,t)/I(Q,0) = \exp(-\Gamma t) \qquad (2)$$

where Γ is the relaxation rate. The fits of the 0.13 mole fraction TBA-water mixture at 45 °C are shown as an example in Figure 2. Figure 3 shows the Q^2-dependence of the relaxation rates for TBA-water mixtures (x_{TBA} = 0.13) at different temperatures. The diffusion coefficient D was obtained by using a least-square fitting procedure over $0 < Q^2 < 0.01$ Å^{-2} using the following equation.

$$\Gamma = DQ^2 \qquad (3)$$

The values of D collected in Table 1 are considerably smaller than those of a monomer TBA obtained from NMR measurements. (e.g. 3.41×10^{-10} m^{2}s^{-1} at 25 °C [4]) However, those in TBA-water mixture are larger than those in BE-water mixture at the same temperature. From these findings, it is concluded that smaller cluster generates in TBA-water mixture than in BE-water one.

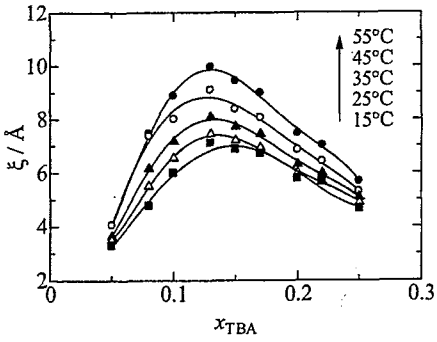

Figure 1. Correlation lengths, ξ, of the TBA-water mixtures at various TBA concentrations and temperatures.

Table 1. The diffusion coefficients, D, (10^{-11} / m^{2}s^{-1}) in the TBA-water mixtures at various temperatures by NSE

χ_{BE}	15°C	25°C	45°C
0.10	5.97±0.12	8.57±0.11	17.79±0.12
0.13	5.34±0.07	8.25±0.07	16.49±0.06
0.15	5.24±0.15	7.76±0.07	15.06±0.08

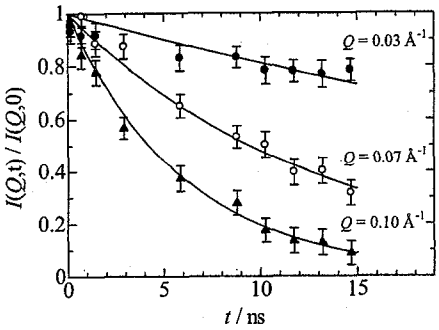

Figure 2. Fourier time dependence of the NSE signal amplitude in the TBA-water mixtures of 0.13 mole fraction of TBA at 45 °C.

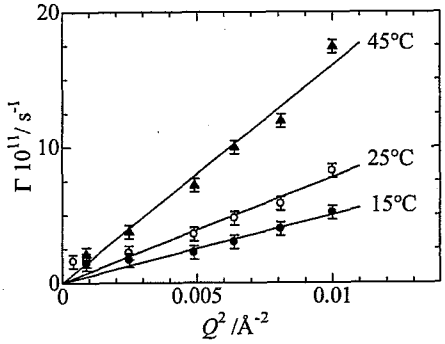

Figure 3. Q dependence of the relaxation rates, $\Gamma(Q)$, in the TBA-water mixtures of 0.15 mole fractions of TBA.

references

[1] K. Yoshida, et al., J. Mol. Liquids, **119** (2005) 125.

[2] K. Yoshida et al., J. Phys. Chem. B **106** (2002) 5042.

[3] K. Nishikawa, et al., J. Phys. Chem. **91** (1987) 3694; J. Phys. Chem. **93** (1989) 6559.

[4] P. K. Kipkemboi et al., Bull. Chem. Soc. Jpn. **67** (1994) 2956.

研究テーマ：中性子小角散乱法によるアミド溶媒の混合状態に関する研究
表題：中性子小角散乱法による DMF-FA および DMF-水二成分溶液の混合状態

3) Small-Angle Neutron Scattering Investigation on Mixing State of DMF-FA and DMF-Water Binary Solutions

T. Takamuku,[a] K. Fujii,[b] Y. Umebayashi,[b] and S. Ishiguro[b]

[a]Department of Chemistry and Applied Chemistry, Faculty of Science and Engineering, Saga University, Honjo-machi, Saga 840-8502, Japan; [b]Department of Chemistry, Faculty of Science, Kyushu University, Hakozaki, Higashi-ku, Fukuoka 812-8581, Japan

Aprotic *N,N*-dimethylformamide (DMF) behaves as a proton acceptor at the carbonyl (C=O) oxygen atom. On the other hand, protic formamide (FA) behaves as not only proton acceptor at the carbonyl oxygen atom, but also proton donors at the amino (NH_2) protons to form cyclic dimers and chain-like clusters in the liquid state. Also, protic water forms tetrahedral-like pentamer. In the present work, to reveal microscopic liquid structure of protic-aprotic solvent mixtures at the molecular level, we carried out small-angle neutron scattering (SANS) experiments in the binary DMF-FA and DMF-water systems.

DMF-FA mixtures at various DMF mole fractions x_{DMF} were prepared by mixing deuterated DMF-d_7 and undeuterated formamide, and similarly, DMF-water mixtures by mixing undeuterated DMF and heavy water (D_2O). The use of deuterated species is essential to obtain higher contrast of the species relative to undeuterated ones. SANS intensities of sample solutions at 25 °C in the Q-range of 0.02-0.15 $Å^{-1}$ were measured using SANS-U spectrometer with the camera length of 2 m. The SANS intensities thus obtained were normalized using the standard material Lupolen, and the incoherent scattering intensities were subtracted from the normalized ones.

Figure 1 (a) shows the normalized SANS spectra for the DMF-d_7-FA mixtures of varying x_{DMF}. No significant SANS intensities are seen for the mixtures over the entire range of mole fraction investigated. In Figure 1 (b), the normalized SANS spectra for the DMF-D_2O mixtures are depicted as a function of x_{DMF}. Also, no significant SANS intensities are seen over the range. These results indicate that no sizable cluster among solvent molecules is formed, and we thus suppose that DMF molecules are homogeneously mixed with FA as well as water. The same has also been found for the mixtures of DMF and *N*-methylformamide (NMF) [1]. Like FA, NMF forms chain-like clusters in the liquid state through hydrogen bonding between the carbonyl oxygen atom and the imino (NH) proton. However, according to SANS spectra for DMF-NMF mixtures, the solvents are homogeneously mixed each other. It is thus concluded that despite that protic FA, NMF and water form hydrogen bonded structure of different bonding types and strength, aprotic DMF is not excluded, but accommodated in these protic solvents, probably due to its strong proton accepting ability.

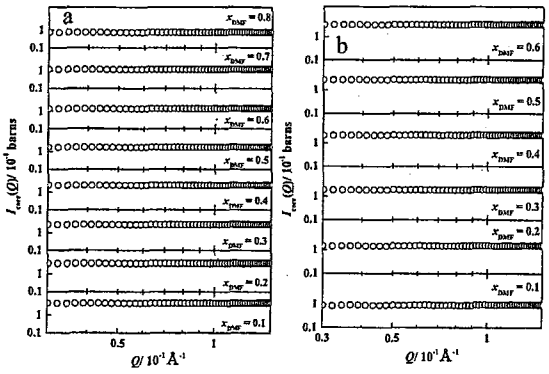

Figure 1: SANS spectra for (a) DMF-d_7-FA and (b) DMF-D_2O binary solutions at various x_{DMF}.

References

[1] T. Takamuku et al., *Activity Report on Neutron Scattering Research*, **11**, 161 (2004).

JRR-3M, SANS-U(C12), Glasses and Liquids

研究テーマ:超臨界水-アルコール系の中性子小角散乱
表題:超臨界水ーアルコール混合物の中性子小角散乱

4) Small-Angle Neutron Scattering of Supercritical Water-Alcohol Mixtures

Toshio Yamaguchi, Nobutaka Yamamoto, and Koji Yoshida

Department of Chemistry, Faculty of Science, Fukuoka University, Fukuoka 814-0180, Japan

Introduction

Supercritical water has novel properties not available under ambient conditions and is used as medium in solvent extraction and chemical reactions. In recent years, supercritical water has been proved to decompose hazardous compounds, such as PCB, dioxin, etc. into environmentally friendly carbon dioxide, mineral acid, and water. It has also been found that addition of alcohols moderates experimental conditions of supercritical water reactions, the so-called co-solvent effect, and that the poorer the co-solvent affects the longer the hydrophobic group of the alcohols. In order to understand the co-solvent effect and further develop the supercritical water technology, it is essential to investigate the structure of supercritical alcohols-water mixture from the microscopic to mesoscopic scale.

So far, we have elucidated the structure of information, such as interatomic distance, coordination number, a change in the hydrogen bond, etc. of moderate-density water [1], methanol [2], and methanol-water mixture in sub critical region by X-ray diffraction, and Raman scattering methods. It has been found from these studies that chemical reactions in supercritical water take place very effectively near the critical point. It will thus be of interest to investigate density fluctuations of supercritical alcohols-water mixture around the critical point and relate them to various properties and chemical reactions in supercritical water.

In this work, we have measured small-angle neutron scattering of supercritical methanol and methanol-water mixtures and obtained the mesoscopic structure information, such as density and concentration fluctuations, as a function of temperature and pressure (density).

Experiment

Small-angle neutron scattering (SANS) measurements were performed on the SANS-U spectrometer of the Institute for Solid State Physics, the University of Tokyo, installed at the beamline of a cold source in JRR-3M. We used a high-pressure high temperature SANS cell (Toyo Koatsu). The high-temperature high-pressure system is shown in Fig. 1. A sample solution was injected into a cell with a syringe *in vacuo*. The pressure was controlled with a high-pressure pump using water as a pressure medium in a high-pressure pump to a separator. The sample to detector distance was 2 m, where the Q-range obtained was from 0.008 to 0.15 $Å^{-1}$. Samples measured were pure CD_3OD, C_2D_5OD, CD_3OD-D_2O (alcohol mole fraction x_a = 0.3), CH_3OD-D_2O (0.3), C_2D_5OD-D_2O (0.2), and C_2H_5OD-D_2O (0.2). Measurements were also made for background, luporen used for normalization, an empty cell. The isotopically substituted samples were used to contrast alcohol clusters with water ones. Thermodynamic states (reduced temperature T_r and reduced pressure P_r) measured were 1.02~1.11 and 1.02~1.98, respectively, for the above samples.

Result and Discussion

To estimate density and/or concentration fluctuations of the samples, we made the Ornstain-Zernike plot given by

使用施設:JRR-3M, 装置:SANS-U, 分野 4 Glass & Liquid

$$\frac{1}{I(Q)} = \frac{\xi^2}{I(0)} \cdot Q^2 + \frac{1}{I(0)}$$

where $I(Q)$ and $I(0)$ are the scattering intensities of a sample at Q and Q=0, respectively. Q is the scattering vector (=$4\pi/\lambda\sin\theta$, λ the wavelength, θ the Bragg angle), and ξ is the correlation length.

The correlation lengths thus obtained were plotted against Tr and Pr for CD_3OD, C_2D_5OD, and 2-C_2D_7OD in Fig. 1.

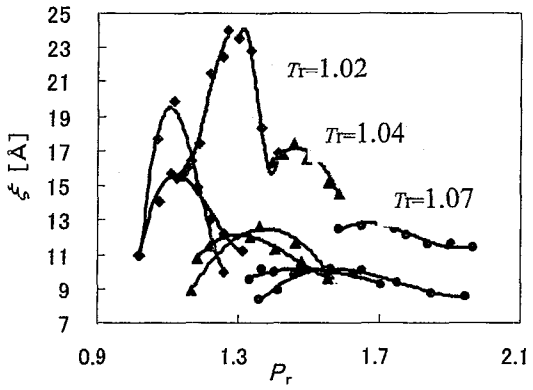

Fig. 1. The correlation length ξ of CD_3OD (black), C_2D_5OD (grey), and 2-C_2D_7OD (thick black) as a function of Tr and Pr.

We can see the size of clusters size does not depend on the size of individual molecule, but certain characteristics of the molecule, such as hydrogen bonding.

Figure 2 shows the plot of ξ_{max} as functions of T_r and P_r. Interestingly, the values of ξ_{max} in the supercritical regime fall on the line extended from the liquid-vapor equilibrium line almost independent of the samples. This finding suggests that some trace of the L.-V. behavior still remains in the supercritical state. This behavior of the supercritical fluids might correlate with the physicochemical properties of the fluids and reactivity of chemical processes in the supercritical fluid technology.

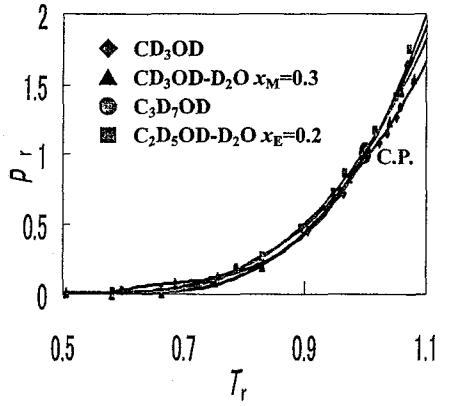

Fig.2. Contour of ξ_{max} in T_r-P_r map.

Figure 3 shows the correlation lengths of isotopically contrasted ethanol-water mixture of alcohol mole fraction 0.2. Apparently, the ξ values are larger for the contrasted sample than for the less contrasted one. This result indicates that concentration fluctuations are still of significance even in the supercritical state.

Further detailed analysis is in progress.

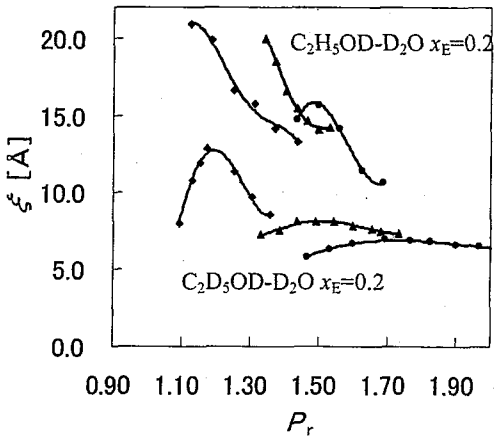

Fig. 3. Correlation length ξ of C_2H_5OD-D_2O x_E=0.2 (black) and C_2D_5OD-D_2O x_E=0.2 as a function of Tr and Pr.

References

[1] T. Yamaguchi, *J. Mol. Liq.*, **78**, 43 (1998).

[2] T. Yamaguchi, et al. *J. Chem. Phys.*, **112**, 8976 (2000).

研究テーマ：イオン液体のダイナミクス
表題：常温イオン液体 bmimCl の中性子準弾性散乱

5) Quesielastic Neutron Scattering Study of Ionic Liquid bmimCl

Y. Inamura, O. Yamamuro, S. Hayashi* and H. Hamaguchi*

*Institute for Solid State Physics, The University of 5-1-5, Tokyo,Kashiwanoha, Kashiwa, Chiba 277-8581 , Japan; *Graduate School of Sciences, University of Tokyo, 7-3-1 Hongo, Bunkyo-ku, Tokyo 113-8656, Japan*

Room temperature ionic liquids are interesting materials as green solvents owing to their non-volatility, non-combustibility and so on. However, there are few basic scientific studies for these materials. We have measured quasielastic and inelastic neutron scattering from 1-butyl-3-methylimidazolium chloride bmimCl, witch is known as a prototype material, to investigate its dynamic properties from a microscopic point of view. These measurements were performed on the AGNES spectrometer installed at the cold neutron guide (C3-1-1) of JRR-3M in JAERI(Tokai). Our previous heat capacity studies for bmimCl have shown that a glass transition occurs at 255 K with large heat capacity gap and indicated that bmimCl is quite disordered and fragile as glass-forming molecular liquids[1].

The temperature scan for the elastic neutron scattering showed that the mean square displacement of glassy bmimCl increases anomalously above the glass transition temperature, T_g(Fig.1). This result may indicate that glassy bmimCl has a fast beta relaxation appearing around T_g as observed in molecular and polymer glasses. The quasielastic neutron scattering data of liquid bmimCl showed that the motion of bmim ions is like simple diffusion as shown in Fig. 2. The activation energy calculated from the temperature dependence of self-diffusion coefficient is 11 kJmol^{-1}, which is smaller than that of the intramolecular rotation of butyl-group, 13-15 kJmol^{-1}. The present results indicate that bmim ion is very flexible in the ionic liquid phase and this fact may be related to the origin of the low melting temperature that is the most important question for room temperature ionic liquids.

Reference

[1] Y.Yamamuro et al., J. Chem. Phys., submitted.

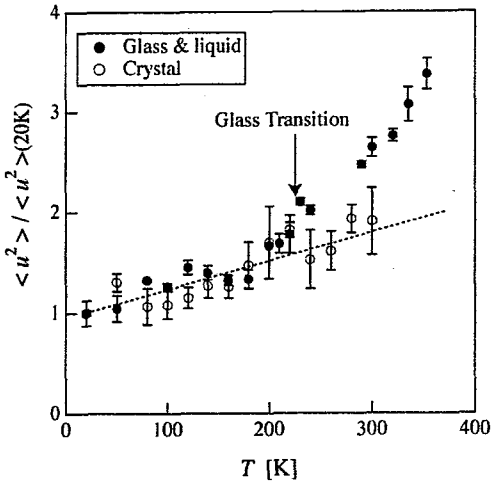

Figure 1: Temperature dependence of mean square displacement of glassy bmimCl.

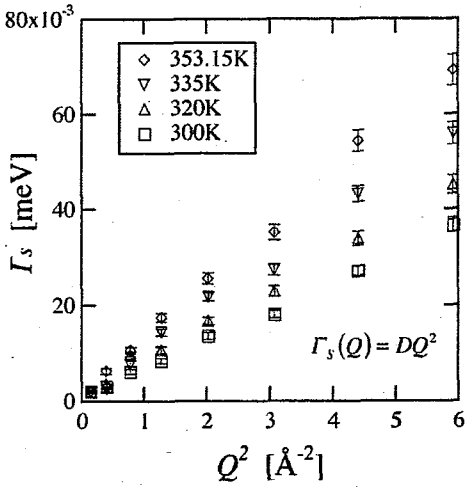

Figure 2: Q^2 dependence of HWHM of quasielastic neutron scattering peak of liquid bmimCl at several temperatures.

使用施設：JRR-3M，装置：AGNES(C3-1-1)，分野 104: Glasses and Liquids

1. 中性子散乱 5) 高分子

1. Neutron Scattering 5) Polymer

This is a blank page.

研究テーマ：界面活性剤 DTAB 水溶液の球状－棒状ミセル転移のダイナミクス
表題：中性子準弾性散乱による DTAB/NaSal 水溶液の球状－棒状ミセル転移

1) Quasi-elastic Neutron Scattering Study on Spherical and Rod-like Micelles of DTAB in Aqueous Sodium Salicylate Solutions

N. Onoda-Yamamuroa, O. Yamamuro[1], and H. Nomura

Department of Natural Sciences, College of Science and Engineering, Tokyo Denki Univ., Hiki-gun, Saitama 350-0394, Japan; [1]ISSP, The Univ. of Tokyo, Tokai, Naka-gun, Ibaraki 319-1106, Japan

Surfactants in aqueous solutions associate to form spherical micelles above a certain critical micellar concentrations, CMC. Some ionic surfactants are known to form rod-like (or thread-like) micelles in the presence of salts. The threshold concentration of organic salt to form rod-like micelles is much lower than that of inorganic salt. As for DTAB(Dodecyl Trimethyl Ammonium Bromide) / NaSal (Sodium Salicylate) / Water system, the spherical micelles transform to rod-like ones around the molar ratio R (= C_{NaSal}/C_{DTAB}) = 0.5 with drastic increase of the solution viscosity. To clarify the dynamical change due to the micellar transformation, we have carried out the quasi-elastic neutron scattering (QENS) measurement of DTAB/NaSal/water system at several R values between 0 and 1.2.

Neutron scattering data in a momentum transfer range ($0.26 < Q < 2.70$ Å^{-1}) were collected with a high-resolution neutron spectrometer, AGNES, installed at C3-1 port of JRR-3M in JAERI (Tokai). D_2O was used as a solvent to extract the dynamics of micellar molecules with ^1H atoms.

The dynamic structure factor, $S(Q,E)$, of miceller molecules was extracted from total QENS spectrum by subtracting the contribution of D_2O (ca. 40 %); the contribution of NaSal is negligible. The obtained $S(Q,E)$ showed an apparent Q-dependent broadening, as shown in Fig. 1, which can be fitted to the Lorentzian function. Taking the Q range (0.26—2.70 Å^{-1}) and energy resolution (0.1 meV) of AGNES into consideration, the broadening is not due to the motion of the micelle itself but due to some local relaxational motion in DTAB molecules forming micelles. Figure 2 shows the self-diffusion coefficient D which was obtained from the Q-dependence of HWHM of Lorentzian function. The slope of D vs. R curve changes at the transition ratio from spherical to rod-like micelles, reflecting dynamic slowing down of the local relaxational motion of the micellar molecules.

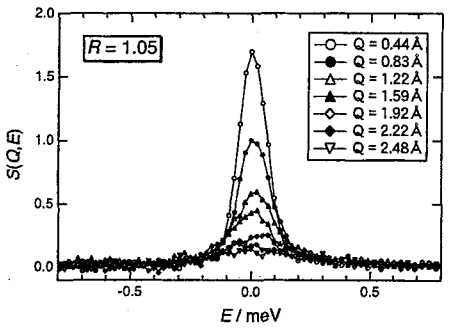

Figure 1: Dynamic structure factor $S(Q,E)$ of the miceller molecules after subtracting the contribution of D_2O

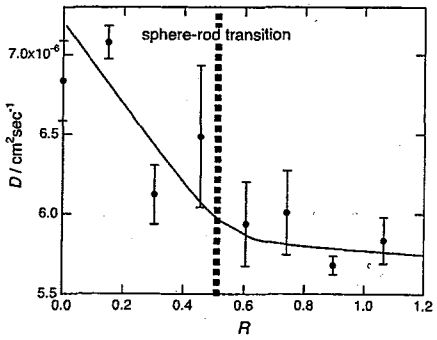

Figure 2: Self-diffusion coefficient D plotted as a function of molar ratio R obtained from QENS spectra by using simple diffusion model.

使用施設：JRR-3M，装置：SANS-U(C1-2)，分野 Softmatter

研究テーマ 新規相溶性ポリマーブレンドの相互作用パラメータの評価
表題 小角中性子散乱によるポリ4-トリメチルシリルスチレン)/ポリイソプレン ブレンドの相挙動解析

2) Analysis on Phase Behavior of Poly(4-trimethylsilylstyrene)/Polyisoprene Blends by Small-Angle Neutron Scattering

M. Harada,[†] T. Suzuki,[‡] M. Ohya, D. Kawaguchi, A. Takano, and Y. Matsushita

Department of Applied Chemistry, Nagoya University, Nagoya, Aichi 464-8603, Japan
[†] *Toyota Central R&D Labs, Inc., Nagakute, Aichi 480-1192, Japan*
[‡] *JSR, Co., Yokkaichi, Mie, 510-8552, Japan*

We found with serendipity that poly(4-trimethylsilylstyrene) (PTMSS) and polyisoprene (PI) dominantly composed of 1,2- and 3,4-microstructure, although no attractive interaction between PTMSS and PI was expected. To elucidate that PTMSS and PI are miscible at the molecular level, the phase behavior of the blends is investigated by small-angle neutron scattering (SANS).

Poly(4-trimethylsilylstyrene) (PTMSS) and the deuterated counterpart (*d*-PTMSS) were synthesized by anionic polymerization in THF at -78 °C, which is initiated with *sec*-butyllithium and quenched with isopropanol, in sealed glass reactors with break seals under high vacuum. Polyisoprene (PI) was also synthesized in almost the same manner using cumyl potassium as an initiator. The molecular characteristics are shown in Table 1.

Table 1. Molecular characteristics

polymer	M_w [a] (g/mol)	M_w/M_n [b]	ρ [c] (g/cm^3)
PTMSS	68,000	1.01	0.963
d-PTMSS	70,000	1.03	1.006
PI	25,000	1.05	0.926

[a] Weight-average molecular weights determined by multi-angle laser light scattering. [b] Polydispersity indices estimated with gel permeation chromatography. [c] Densities measured with gas displacement technique.

Figure 1 gives the phase diagram of a PTMSS/PI blend, which is determined by optical microscopy. The open circles show the phase separation temperature for each blend with different volume fractions and the line is drawn as a guide for eyes. This figure clearly points that this blend has a typical phase diagram of lower critical solution temperature (LCST) type. The critical point is obtained at around 0.4 in terms of PTMSS volume fraction and at around 172 °C in temperature.

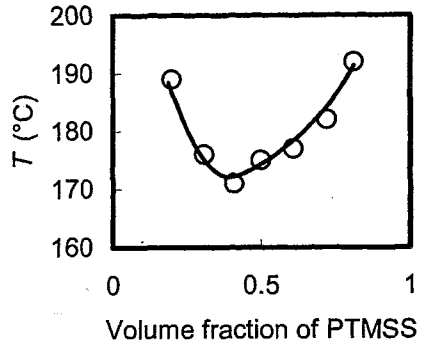

Figure 1. Phase diagram of a PTMSS/PI blend determined by optical microscopy. The line is drawn as a guide for eyes

Figure 2 shows the SANS profiles of the *d*-PTMSS/PI blends, which are measured at three different temperatures with SANS-U at JRR3M in JAERI (Tokai). *d*-PTMSS instead of PTMSS is employed to earn the contrast against PI, providing negligible effects of deuterium-labeling. The intensities in low q regime increase slightly as the blends are heated, indicating the growth of the concentration fluctuation induced by the repulsive interaction between component polymers.

The SANS data are analyzed by the random phase approximation (RPA) for miscible blends according to equation 1.

$$\frac{d\Sigma}{d\Omega} = \frac{\left(\frac{a_A}{v_A} - \frac{a_B}{v_B}\right)^2}{\frac{1}{\phi_A N_A v_A P_A(q)} + \frac{1}{\phi_B N_B v_B P_B(q)} - 2\frac{\chi}{v_0}}, \quad (1)$$

使用施設 JRR-3M, 装置 SANSU (C12), 分野 Soft Matters (106)

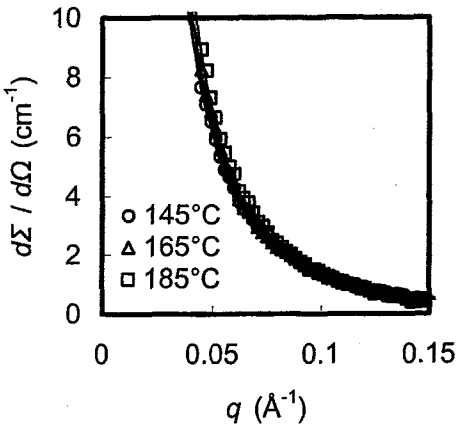

Figure 2. SANS profiles for PTMSS/PI blends. The volume fraction of PTMSS is 0.48. The lines are the fitting results.

where a_i is the scattering length per monomer, v_i is the volume per monomer, ϕ_i is the volume fraction, N_i is the polymerization index, $P_i(q)$ is the particle scattering function of the polymer component i (= A or B), and χ is the Flory-Huggins parameter of the segmental interaction. $P_i(q)$ is expressed by the Debye function with $R_{g,i}$ as the radius of gyration of the component i. The reference volume v_0 is defined as $(v_A v_B)^{1/2}$ and is estimated to be 0.193 nm^3. a_i, v_i, ϕ_i and N_i are calculated with the scattering lengths of the component atoms, bulk densities, weight fractions and molecular weights, and $R_{g,i}$ is evaluated by other experiments. The parameters are shown in Table 2.

Table 2. Parameters of polymers

polymer	a [a] (fm)	v [b] (nm^3)	ϕ [c]	N [d]	R_g [e] (Å)
d-PTMSS	111	0.305	0.479	380	58.3
PI	3.33	0.122	0.521	363	46.7

[a] Scattering lengths per monomer. [b] Volumes per monomer. [c] Volume fractions in blends. [d] Degrees of polymerization. [e] Radii of gyration of polymers.

The interaction parameter χ was evaluated by the least-square fittings of equation 1 to the SANS data as shown in Figure 2, where a baseline factor was introduced to adjust insufficient data correction for absolute coherent scattering cross section.

In Figure 3, the evaluated interaction parameter values are plotted against the inverse of temperature, $1/T$. The plots are on a straight line fairly well, and it is evidenced that the data follows the standard form: $\chi = 0.027\text{-}9.5/T$. Since the χ value decreases as temperature-decreases, the change of χ is consistent with the LCST-type phase behavior.

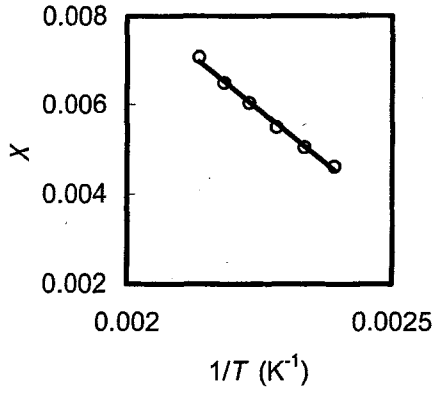

Figure 3. Temperature dependence for χ parameter of PTMSS/PI blends. The line is a least-square linear fitting result.

From the mean field theory, ϕ_A and χ at critical point are deduced as

$$\phi_A = \sqrt{v_B N_B} \Big/ \left(\sqrt{v_A N_A} + \sqrt{v_B N_B}\right) , \qquad (2)$$

$$\chi = \frac{v_0}{2}\left(\frac{1}{\sqrt{v_A N_A}} + \frac{1}{\sqrt{v_B N_B}}\right)^2 . \qquad (3)$$

In the case of the PTMSS/PI blend with the polymerization index in Table 2, ϕ_A and χ are calculated as 0.38 and 0.0057, when the temperature is 173 °C. Thus, the observed results by SANS agrees well with the prediction from the mean field theory and explains the observation of optical microscopy.

研究テーマ：環状ポリスチレンの溶液中およびバルク中における拡がりの分子量依存性
表題：環状高分子の溶液中におけるコンフォーメーション

3) Conformation of Cyclic Polystyrenes in a Good and a Theta Solvent

Atsushi TAKANO, Keisuke MASUOKA, Yutaka OHTA,
Donghyun CHO, and Yushu MATSUSHITA

Department of Applied Chemistry, Nagoya University
Furo-cho, Chikusa-ku, Nagoya, 464-8603 Japan

INTRODUCTION

Study on cyclic polymers has been a quite interesting subject in polymer science for many years, since they are expected to have quite different properties from those of the corresponding linear ones. Although a lot of reports exist for synthesis of cyclic polymers so far, purity of ring molecule in samples has not been investigated quantitatively in most cases. In this study, we have synthesized four cyclic polystyrenes with molecular weights ranging from 20k to 600k, and the purities of the samples were quantitatively checked using a HPLC techniques, that is, liquid chromatography at the critical condition (LCCC). Radii of gyration (R_gs) of the cyclic polymers were measured by small-angle neutron scattering (SANS) for relatively low molecular weight samples ($M_w \leqq 120$k) and light scattering (LS) for a high molecular weight sample ($M_w \geqq 120$k) in both good and theta solvents, and those of the linear counterparts were also measured. Furthermore molecular weight dependence of R_gs of cyclic polymers were investigated and compared with those of the linear ones.

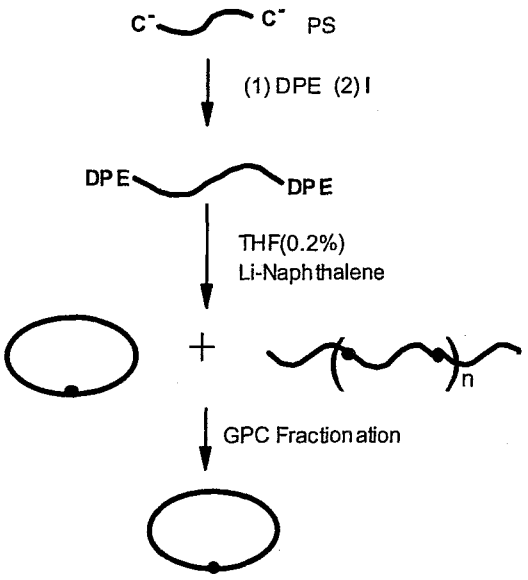

Fig.1 Synthetic scheme for cyclic polystyrene.

EXPERIMENTAL SECTION

Synthesis and isolation of cyclic polystyrene was briefly illustrated in Figure 1. In order to prepare linear telechelic polystyrenes, styrene was anionically polymerized with lithium naphthalenide as an initiator in THF at -78 ℃, and end-capped by 1,1-diphenylethylene (DPE), followed by termination with 1-[3-(3-chloropropyl)phenyl]-1-phenyl-ethylene (**I**). The polymer obtained was purified by precipitation in methanol to remove the residual DPE and **I**. The cyclization reactions in between two end-vinyl groups within telechelic polymers were carried out by adding lithium naphthalenide into the dilute THF solution of the telechelic polymers (less than 0.2 w/v%) at 25℃, and stirred for 1 days. Cyclic polymers were isolated by GPC fractionation to remove high molecular weight polycondensation products. Weight-average molecular weights, M_ws, of all samples were measured by LS in THF at 35℃. Molecular weight heterogeneities, M_w/M_n, were determined by GPC.

HPLC experiments were carried out on a typical isocratic HPLC system equipped

使用施設：JRR-3M，装置：SANS-U(C1-2)，分野 Softmatter

with a C18 bonded silica gel column (Hypersil, 100Å pore, 150 × 4.6 mm, 3 μm particle size). The mobile phase was a mixture of CH_2Cl_2 and CH_3CN (Kishida Chemical, HPLC grade, 57/43 in volume), and the flow rate was 0.5 mL/min. The column temperature was adjusted at 36.5°C.

SANS measurements were performed by using SANS-U spectrometer (λ=0.70nm) equipped with a 4.0 mm thick quartz cell. Adopted measuring temperature for solutions of benzene-d_6 as a good solvent was 25℃, while those of cyclohexane-d_{12} as a theta solvent was 40.0℃ for linear polymers, and 35.0℃ for cyclic polymers.

Tab.1 Molecular characteristics of samples.

Sample	$10^{-4}M_w$ [1)]	M_w/M_n [2)]	P [3)]
1L	2.07	1.05	----
1C	1.74	1.02	0.99
2L	4.42	1.02	----
2C	4.17	1.02	0.97
3L	11.5	1.04	----
3C	10.9	1.03	0.96
4L	63.5	1.01	----
4C	57.3	1.02	0.96

1) Determined by LS in THF at 35℃.
2) Determined by GPC.
3) Purity of cyclic molecules by HPLC.

RESULTS AND DISCUSSION

Molecular characteristics of linear and cyclic polymers were listed in Table 1. Absolute molecular weights (M_ws) of each pair of samples are almost equal, and molecular weight distributions are relatively narrow. Furthermore, purities of cyclic molecules in fractionated samples determined by HPLC were over 95%. The apparent radii of gyration (R_g) of linear and cyclic polymers at several finite concentrations were evaluated by Guinier plots of the measured coherent intensities. The R_gs of all samples were obtained by extrapolation of the apparent R_g values to infinite dilution in good and theta solvent conditions, respectively.

Relationship between R_g and M_w for linear and cyclic polymers are plotted in Figure 2. It was found that R_g of cyclic polymer can be scaled with M_w as $R_g \propto M_w^{0.6}$ in benzene-d_6 and as $R_g \propto M_w^{0.5}$ in cyclohexane-d_{12}, which were the same molecular weight dependence as linear polymers'. The ratio of the R_g for ring molecule to that for linear one, i.e. R_g(Ring) /R_g(Linear), has been theoretically predicted to be $1/\sqrt{2} \fallingdotseq 0.707$ for polymer solution in a theta solvent,[1] and also to be $\sqrt{0.516} \fallingdotseq 0.718$ in a good solvent by renormalized two-parameter theory.[2] Both experimental ratios 0.85 in cyclohexane and 0.81 in benzene are bigger than the theoretically predicted values, 0.707 and 0.718, respectively.

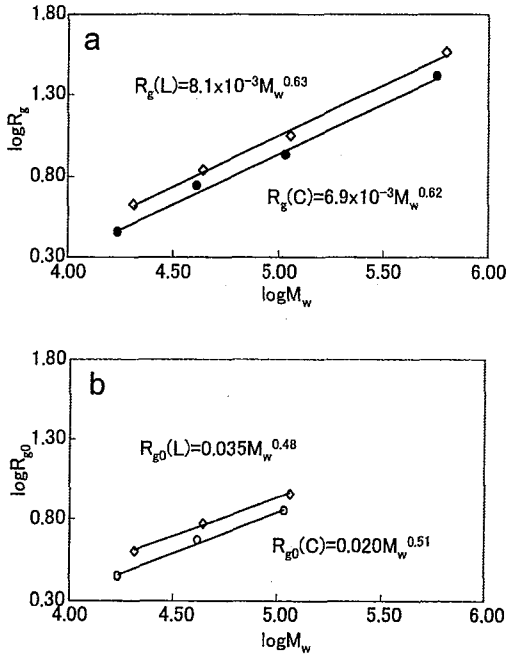

Fig.2 Relationships between R_g and M_w in (a) benzene-d_6 and in (b) cyclohexane-d_{12}.

References

1. Zimm, B.H, Stockmayer, W.H., *J.Chem. Phys.* **1949**, *17*,1301
2. 2.Douglas, J.F.; Freed, K.F. *Macromolecules* **1984**, *17*, 2344

研究テーマ： リン脂質水溶液に見られる膨潤ゲル相の形成要因
表題： 人工リン脂質の単層膜ベシクル形成における浸透圧の効果

4) Effects of Osmotic Pressure on the Formation of Large Uni-lamellar Vesicles.

H. Seto[1], N. L. Yamada[2], and M. Hishida [1]
[1] *Department of Physics, Kyoto University, Sakyo, Kyoto, 606-8502*
[2] *High Energy Accelerator Research Organization, Tsukuba, 305-0801*

Phospholipid, which is the main constituent of cell membrane, forms spontaneously micelles or vesicles in water due to its amphiphilic property. Amongst them, the large unilamellar vesicles (LUV) ranging from 1 to 100 μm size is actively investigated as a model system of living cell. Various method to form LUV's are developed for practical reasons, however, physical background to form LUV's is not yet clear. Recent experimental studies by Tsumoto [1] suggested that the inter-membrane osmotic pressure by sugar or salt could be a trigger to form LUVs. Thus the purpose of the present study is to clarify the effect of osmotic pressure in the structural formation of phospholipid.

To see the effect of osmotic pressure, two types of aqueous solutions of dioleoylphosphatidyl- choline (DOPC) were prepared; (i) NaI in film. NaI was mixed with DOPC, and dissolved in water. (ii) NaI in water. NaI was mixed in water and the lipid is dissolved in the brine. In principle, NaI molecules have no effect in the lamellar stacking structure of DOPC. Comparing these two types of samples, only the osmotic pressure in the process of hydration is different. The osmotic pressure between lipid membranes were changed by changing the NaI concentration.

FIrst, several small angle X-ray scattering (SAXS) experiments were carried out at the BL40B2 beam port in SPring-8 to investigate the effect of osmotic pressure. The multi-lamellar structure was destabilized only when much amount of NaI existed in the "NaI in film" sample, i. e., osmotic pressure between DOPC membranes is strong enough. (See Fig. 1.)

In order to verify the SAXS results, some SANS experiments were done at SANS-U. Four samples of the "NaI in film" were prepared; molar ratios of NaI against DOPC were 0, 1, 2, and 3. Figure 2 indicates the SANS profiles observed for these samples. It is clear that no Bragg peak was observed in the samples including enough NaI. These profiles were analyzed with the form factor of lipid bilayers and verified that bilayer membranes exist in water without correlations between them.

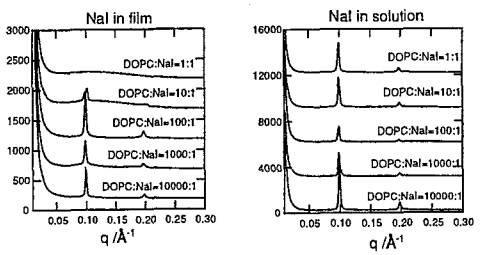

Fig. 1. NaI concentration dependence of SAXS profiles of two types of samples. In the case of "NaI in film", a Bragg peak due to the regular stacking of lipid membranes disappeared in case of enough amount of NaI. On the other hand, no effect of NaI was observed in the case of "NaI in solution".

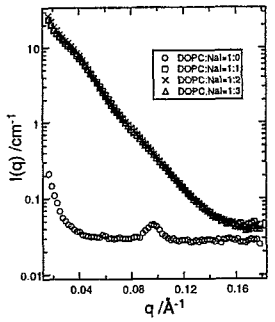

Fig. 2. SANS profiles of the "NaI in film" samples. When the molar ratio of NaI against DOPC is more than 1, a characteristic scattering profile of a single bilayer was observed.

References

[1] K. Tsumoto: private communication.

使用施設：JRR-3M, 装置： C1-2 (SANS-U), 分野： 6. Softmatter

研究テーマ：弱荷電高分子ゲル粒子のミクロ相分離挙動へのゲルサイズ依存
表題：弱荷電高分子ゲルの熱誘起型ミクロ相分離挙動のゲルサイズ依存性

5) Gel-Size Dependence of Temperature-Induced Microphase Separation in Weakly-Charged Polymer Gels

F. IKKAI[1] and M. SHIBAYAMA[2]

[1]Advanced Research Center, NIHON L'ORÉAL K.K., KSP R&D-D637, 3-2-1 Sakado, Takatsu-ku, Kawasaki, Kanagawa 213-0012, Japan; [2]The Institute for Solid State Physics, The University of Tokyo, 5-1-5 Kashiwanoha, Kashiwa, Chiba 277-8581, Japan

INTRODUCTION

We have been investigated the gel-size dependence of microphase separation in weakly-charged gels of N-isopropyl acrylamide (NIPAm; CH_2=CHCONHCH(CH_3)$_2$) and 1-vinylimidazole (VI; CH_2=CH(NC_3H_3N)) copolymers. It is known that weakly-charged polymer gels in a poor solvent show a microphase separation with a characteristic Bragg spacing, Λ, depending on the degree of ionization, f.[1] Since NIPAm polymer is temperature-sensitive, the poor condition is achieved above a critical temperature, T_c, i.e., ca. 34 °C. In many cases, Λ is estimated to be a few hundreds Å by small-angle neutron scattering (SANS). That is, SANS profiles of weakly charged gels have a broad peak at a scattering vector, q, corresponding to Λ. Here, if the gel size is equal to Λ, does the microphase separation take place above the T_c? In the previous report[2], we found that the SANS profiles of bulk gels showed a broad peak at higher temperature, T, but the gel particles with nm-order size, i.e., nanogels, was reproduced only by isolated-particle scattering function. This fact indicated absence of microphase separation was interpreted as the meaning that bulk gel has space large enough to produce microphase separated structure with the size of a few hundreds Å, but nanogels do not.

In this report, we went further the structural analyses of micropahse separated nanogels and bulk gels by using some theoretical function fittings.

SAMPLES

NIPAm/VI (360mM/40mM) nanogels were prepared by heat-induced copolymerization using N,N'-methylene bisacrylamide (BIS; crosslinker), ammonium persulfate (APS; initiator), and sodium dodecylbenzene sulfonate (SDS; surfactant).[3] The nanogel size was tuned with the SDS concentration and the stirring rate. For SANS (with SANS-U at JRR3M in JAERI (Tokai)), the nanogels were dried and then immersed in pure D_2O and pD-controlled D_2O. The bulk gels were prepared in an 8mmϕ test tube with the same composition without SDS, and swollen with D_2O until their equilibrium state after drying.

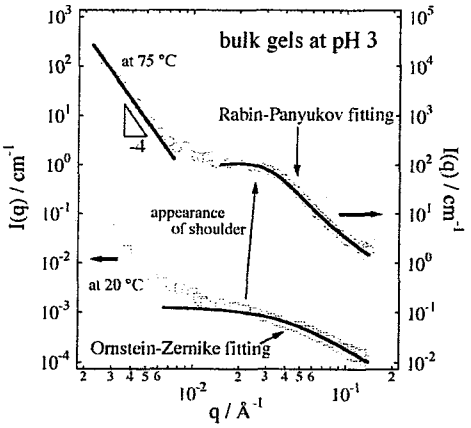

Fig 1 Curve fitting results for bulk gels at 20°C and 75 °C. Open circles and squares show data points at 20 °C and 75 °C, respectively. Thick solid lines are theoretical fitting curves.

RESULTS & DISCUSSION

Figure 1 shows SANS profiles of the bulk gels at 20 °C and 75 °C. At 20 °C, the $I(q)$ of the bulk gel at higher q range was well fitted by the so-called Ornstein-Zernike (OZ) function, i.e.,

$$I(q) = \frac{I(0)}{1+\xi^2 q^2} \qquad (1)$$

使用施設：JRR-3M，装置：SANS-U(C1-2)，分野 Softmatter

where ξ denotes a correlation length of the solution-like concentration fluctuation in the bulk gel. In this case, ξ was estimated to be 24 Å. The steep increase of the $I(q)$ at lower q range probably results from a large-scale structural inhomogeneities.

On the other hand, at 75 °C, a clear shoulder (or broad peak) appeared at $q \approx 0.02$ Å^{-1}, which was not expressed by the OZ equation. In order to do a theoretical fitting to such a broad shoulder, we used the Rabin-Panyukov (RP) theory, assuming that the shoulder is organized from weakly- charged-induced microphase separation in a poor solvent. The theoretical structural factor, $S(q)$, is defined by two contributions, i.e., static inhomogeneities, $C(q)$, and thermal concentration fluctuations, $G(q)$, which are given by

$$S(q) = G(q) + C(q) \tag{2}$$

$$G(q) = \frac{\phi N g(q)}{1 + w(q)g(q)} \tag{3}$$

$$C(q) = \frac{\phi N}{[1 + w(q)g(q)]^2 (1 + Q^2)^2} \times \left[6 + \frac{9}{w_0(q) - 1 + (1/2)Q^2 (\phi_0/\phi)^{2/3} \phi_0^{-1/4}} \right] \tag{4}$$

where a, N, and Q ($=aN^{1/2}q$) indicate the segment length, the average degree of polymerization between cross-links, and dimensionless wave vector, respectively. It should be noted that $G(q)$ and $C(q)$ as well as $w(q)$ and $g(q)$ are expressed with two sets of parameters, i.e., those at sample preparation, ϕ_0 (the polymer fraction), f_0 (the degree of ionization), and χ_0 (the Flory interaction parameter), in addition to those at observation, ϕ, f, and χ. The fitting result in this case was $\chi = 0.89$ and $N = 51$ with $\phi = \phi_0 = 0.04$, and $f = f_0 = 0.090$. Therefore, we chalked up the origin of the broad peak at high T to a temperature-induced microphase separation. Figure 2 shows the SANS profiles of the nanogels at 20 °C and 75 °C. As described in the previous activity report (2003), the $I(q)$ at 75 °C was fitted only by

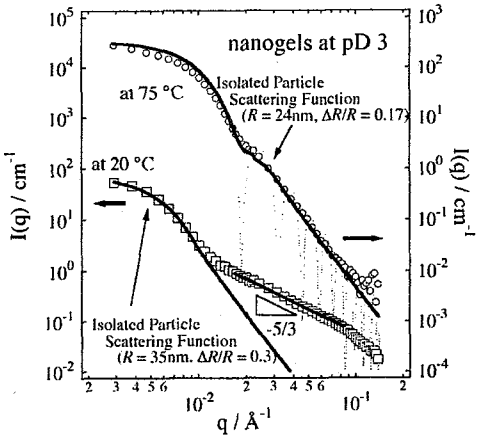

Fig 2 Curve fitting results for nanogels at 20°C and 75 °C. Open circles and squares show data points at 20 °C and 75 °C, respectively. Thick solid lines are theoretical fitting curves.

an isolated-particle-scattering equation;

$$\frac{d\Sigma}{d\Omega}(q) = \frac{w}{d_p}(\rho_{b,p} - \rho_{b,s})^2 \times \frac{\int\int W_R(R) W_\lambda(\lambda) V(R) \Phi^2(qR) dR d\lambda}{\int\int W_R(R) W_\lambda(\lambda) V(R) dR d\lambda} \tag{5}$$

where w, d_p, $\rho_{b,p}$, and $r_{b,s}$ are the polymer weight ratio, the polymer density, the scattering densities of polymer and solvent, respectively. Besides, $W_R(R)$, $W_\lambda(\lambda)$, and $\Phi(qR)$ are the distribution of the particle radius, that of the neutron wavelength, and the isolated particle scattering factor ($3[sin(qR) - qR\cos(qR)]/(qR)^3$), respectively. This fact indicates the absence of microphase separation in the case of nanogels. The I(q) at lower q range at 20 °C was also fitted by eq. (5). As the result, the particle radius, R, changed from 35 nm at 20 °C to 24 nm at 75 °C. The value of R at 20 °C is nearly one-quarter of hydrodynamic radius, R_h, obtained by dynamic light scattering. This is probably due to the fact that nanogels have a considerable size of corona region and R_h is sensitive to the envelope of the corona.

The detailed analyses are still in progress.[4]

References

[1] M. Shibayama, et al. *J.Chem. Phys.* **1992**, 97, 6842.
[2] F. Ikkai, et al. *activity report on NSL* **2004**, vol. 11.
[3] S. Ito, et al. *Langmuir* **1999**, 15, 4289.
[4] F. Ikkai and M. Shibayama, **in preparation**.

研究テーマ：水ーエタノール混合状態の高分子ゲルへの転写
表題：水/エタノール混合溶液中で作製したアクリル酸ゲルの微視的構造解析

6) Microstructure of Poly (Acrylic Acid) Gel Prepared in Water/Ethanol Mixed Solution

F. IKKAI[1], T. KARINO[2], and M. SHIBAYAMA[2]

[1]Advanced Research Center, NIHON L'ORÉAL K.K., KSP R&D-D637, 3-2-1 Sakado, Takatsu-ku, Kawasaki, Kanagawa 213-0012, Japan; [2]The Institute for Solid State Physics, The University of Tokyo, 5-1-5 Kashiwanoha, Kashiwa, Chiba 277-8581, Japan

INTRODUCTION

It is well known that microstructure of polymer gels strongly depends on conditions in gel preparation and in observation. In this study, we prepared poly (acrylic acid) (AAc; CH_2=CHCOOH) gels in water/ethanol (W/E) mixed solutions with various mixing ratio, and investigated how the condition in preparation reflects to gel microstructure in observation from a microscopic viewpoint by means of small-angle neutron scattering (SANS). The advantages of the use of AAc/water/ethanol system are (1) AAc has high solubility against both water and ethanol, and (2) AAc gels are nicely synthesized in W/E mixed solutions with arbitrary mixing ratio by heat-induced radical reaction. Therefore, this system enables us to observe the difference of gel microstructure, which reflects only the difference of the mixing ratio in preparation. The important difference between the AAc gels observed in water (AAc_W) and those in ethanol (AAc_E) is that the former gels are in weakly-charged state for AAc and the later one in non-charged state. Figure 1 shows volume fraction, ϕ, in water and ethanol for AAc gels prepared in different W/E mixing ratios. From the figure, it is found that (1) the AAc_E gels are in swollen state more than the AAc_W gels, as compared with two AAc gels prepared in the same W/E mixing ratio, and (2) the ϕ of both AAc_W and AAc_E gels gradually decreases with increasing ethanol fraction at preparation. The former means that ethanol is a good solvent for AAc gels more than water. The latter indicates that the higher the ethanol fraction at preparation, the more homogeneous the gel network structure.

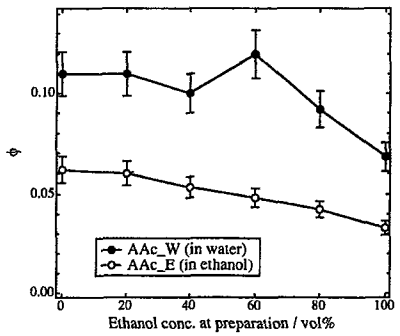

Fig 1 Polymer volume fraction, ϕ, for AAc_W and AAc_E gels prepared in different ethanol fractions.

SAMPLES

The AAc gels were prepared in water/ethanol mixed solutions with different mixing ratio by temperature-induced radical polymerization of a 10 mL of W/E mixed solution containing 5 M of AAc, 50 mM of N,N'-methylene bisacrylamide (BIS; crosslinker), and 2.4 mM of 2,2-azobis isobutyronitrile (AIBN; accelerator) in a 10 mL sample tubing for 24 h at 60 °C. After the gel preparation, each of AAc gels was broken into parts through 500-μm sieves and immersed for washing in the W/E solutions with the same mixing ratio as that in the gel preparation. Then, the AAc gels were freeze-dried and swollen until the equilibrium swelling state by deuterium oxide (D2O) (AAc_W gels) or Ethanol-d_6, Anhydrous (DET) (AAc_E gels). SANS measurements (with SANS-U (C1-2) spectrometer at JRR-3M in JAERI (Tokai), at $\lambda = 7$ Å, at room temperature) were carried out for 0.5 h and 2 h for 2 and 8 m sample-to-detector distance conditions, respectively.

RESULTS & DISCUSSION

使用施設：JRR-3M，装置：SANS-U(C1-2)，分野 Softmatter

Figure 2 shows SANS profiles of AAc_W gels (a) and AAc_E gels (b). In the figure, for examples, "I_W040" means "the SANS intensity for AAc_W gel prepared at 40 % ethanol solution." For AAc_W gels (Figure 2a), the scattered intensity, I(q), at $q \leq$ ca. 0.06 $Å^{-1}$ increased with the ethanol fraction at preparation. For AAc_E gels (Figure 2b), on the other hand, the I(q) hardly depended on the ethanol fraction except I_E100. This means that the ionization of AAc in water enhanced the inhomogeneities of gel microstructure produced in gel preparation stage. To analyze the gel microstructure quantitatively, we tried to make a fitting to the SANS profiles. The fitting function used was combination of a so-called Ornstein-Zernike (OZ) function and an exponential equation, as given by

$$I(q) = aq^{-3.6} + \frac{b}{1+\xi^2 q^2} + c \qquad (1)$$

where a, b, and c are fitting parameters.

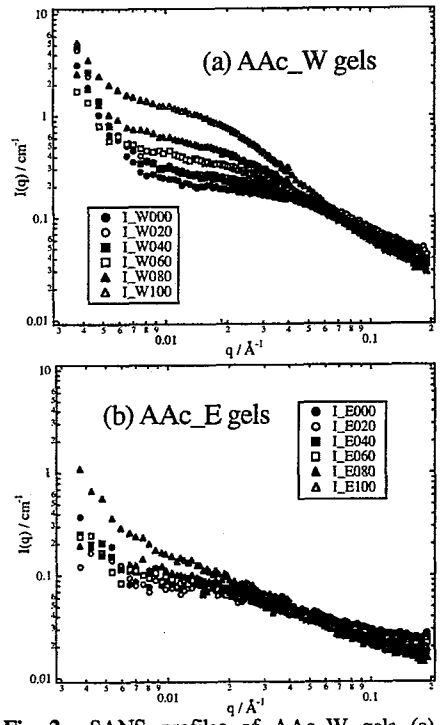

Fig 2 SANS profiles of AAc_W gels (a) and AAc_W gels. The scattered intensities were corrected for cell scattering, fast neutrons, transmission, and gel volume fraction, and then scaled to the absolute intensity.

ξ denotes a correlation length of the solution-like concentration fluctuation in the AAc gel. The power law with the slope of -3.6 was also observed by the other research group for AAc gels[1], but the accurate meaning is still an open question. The SANS profiles were well fitted. Figure 3 shows examples of the curve fitting for I_W080 and I_E080 by using Eq. (1).

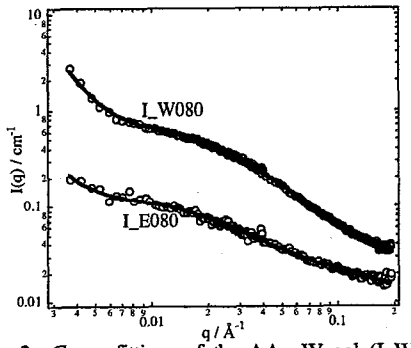

Fig 3 Curve fittings of the AAc_W gel (I_W080) and AAc_E gels (I_E080) by using Eq. (1).

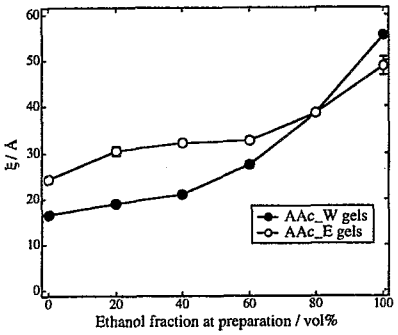

Fig 4 The change in ξ against ethanol volume fraction at gel preparation.

Figure 4 shows the change in ξ against the ethanol fraction at gel preparation. Both of ξ for the AAc_W and AAc_E gels increase with the ethanol fraction at preparation. These results indicate that AAc gels prepared in higher ethanol fraction swell more and become more homogeneous in either AAc_E or AAc_W gels. In water, though the AAc gels are in weakly-charged state, the effect does not contribute to the homogeneous gel swelling but inhomogeneous gel structure (decrease in ξ and power law at lower q). The detailed analyses are in progress.

References

[1] F. Horkay, et al., J. Chem. Phys. 2002, 117, 9103.

表題：非イオン性界面活性剤2元系における圧力誘起相転移

7) Pressure- induced phase transition in a binary system of non-ionic surfactant and water

Y. Kawabata[1], Takehiro Kato[1], M. Nagao[2], Tadashi Kato[1], H. Seto[3], N. L. Yamada[4], T. Takeda[3]

[1] *Tokyo Metropolitan University, Minami-Ohsawa 1-1, Hachioji, 192-0397*

[2] *Institute for Solid State Physics, The University of Tokyo, 106-1 Shirakata, Tokai, 319-1106*

[3] *Kyoto University, Kitashirakawa, Sakyo, Kyoto 606-8502*

[4] *High Energy Accelerator Research Organization, 1-1 Oho, Tsukuba 305-0801*

[5] *Hiroshima University, 1-7-1 Kagamiyama, Higashihiroshima 739-8521*

Amphiphiles in water and/or oil self-assemble to form various mesoscopic structures such as lamellar, micellar, hexagonal phaseses. In such an amphiphilic system, a phase transition is induced by temperature, pressure and so on. So far, we have focused on pressure- induced phase transitions of a microemulsion consisting of amphiphiles, water and oil (trinary system) by means of small angle neutron scattering (SANS) and neutron spin echo (NSE) [1]. On the other hand, in a binary system involving nonionic surfactant C_iE_j and water system, it has been reported that phase transition is induced by pressure [2]. In this study, we investigated pressure- induced phase transitions of $C_{16}E_7$/water systems by means of SANS and NSE.

The SANS experiments were carried out using the SANS-U spectrometer of JRR-3M, JAERI, Tokai. The momentum transfer q ranged over $0.03 \leq q \leq 0.14$ Å^{-1}. Pressure was changed from $1 \leq P \leq 1400$ bar with varing temperature from $T = 38$ to 70 °C. A surfactant concentration was 32 wt. % for $C_{16}E_7$/water system.

Figure 1 shows pressure dependencies of SANS profiles at $T = 38$ °C. At ambient pressure, a micellar phase is formed. With increasing pressure, the peak position of the micellar phases is slightly shifted to high-q, and we found a sharp bragg peak about $P = 1400$ bar.

Figure 2 shows the pressures where the sharp bragg peak appeared at $T = 15$, 38, 45 and 55 °C, with a melting curve of n-hexadecane ($C_{16}H_{34}$) whose carbon number is the same with $C_{16}E_7$. The melting curve of n-hexadecane is almost the same with the phase transition curves observed in SANS experiments. This result indicates that the pressure- induced phase transition might be due to melting or freezing hydrocarbon tails of $C_{16}E_7$.

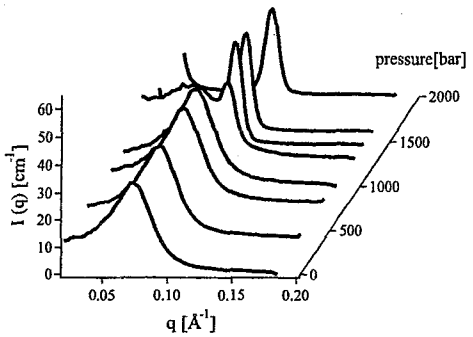

Fig. 1. Pressure dependencies of SANS profiles at $T = 38$ °C. At ambient pressure, a micellar phase is formed. A sharp bragg peak appears about $P = 1400$.

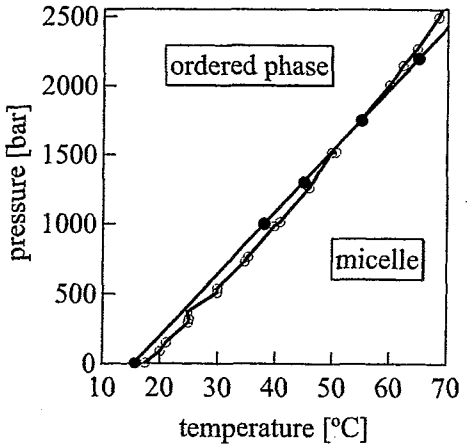

Fig. 2. T-P phase diagram at $T = 38$ °C in the $C_{16}E_7$/water system. The pressures where the sharp bragg peak appeared at $T = 15$, 38, 45 and 55 °C, with a melting curve of n-hexadecane ($C_{16}H_{34}$) are shown.

使用施設：JRR-3M，装置： C1-2 (SANS-U), C2-3-1 (iNSE)，分野： 6. Softmatter

In order to clarify the pressure effects, we performed NSE experiments by using the iNSE spectrometer at JAERI. The experiments were done in a micellar phase region under the pressure where the sharp bragg peak appears. We could not see the difference between the relaxation rate at high pressure ($P = 900$ bar) and that at ambient pressure. Dramatic changes of dynamic properties might appear near the phase transition temperature and pressure.

References

[1] Y. Kawabata *et al.*: Phys. Rev. Lett., **92**, (2004) 056103-1 - 056103-4 .

[2] Nishikido *et al.*: J. Colloid Interface Sci. **78**, (1980) 338-346.

研究テーマ：ポリビニルアルコール/アルギン酸ナトリウム水溶液の相互侵入網目の形成
表題：中性子小角散乱によるポリビニルアルコール/アルギン酸ナトリウムの IPN の研究

8) Small Angle Neutron Scattering Study on IPN from Poly(vinyl alcohol)/ Sodium Polyalginate Aqueous Solutions

Y. Takahashi, R. Ikematsu, T. Tsuji* and Y. Matsushita

*Department of Molecular and Material Sciences, Kyushu University, 6-1 Kasugakoen, Fukuoka 816-8580 Japan; * Department of Applied Chemistry, Nagoya University, Chikusa-ku, Nagoya 464-8603, Japan*

Blends of poly(vinyl alcohol) (PVA) and sodium polyalginate (ALG) is known as a miscible blend and both polymers posses gelation. The crosslink points for the former are micro-cristals and those for the latter are egg-box junctions which take in divalent cations such as calcium ions. Therefore, there is a possibility that interpenetrated network can be made from PVA/ALG blends in which two different crosslinps can be controlled independently. In this study, gelation behaviors of aqueous solutions of PVA, ALG, and their mixture with low ALG content (PVA: 21 g/dL; ALG: 0.55 g/dL) are examined by small angle neutron scattering (SANS) experiments to test the above idear.

The SANS measurements are performed by SANS-U spectrometer at the Neutron Scattering Laboratory of the ISSP, The University of Tokyo, established at C1-2 beam line of JRR3M in JAERI (Tokai), Ibaraki, Japan. The wavelength λ and beam size of incident neutrons was 0.7 nm and 3 mmϕ, respectively. The sample to detector distance was 4 m.

Figure 1 shows the time dependence of scattered profile for the homopolymer solutions. Time denotes the passed time after the samples are set in the cell. Each measurement was started at that time. It is clear that the gelation process is almost instantaneous for ALG solution after Ca^{2+} is added, while the scattered intensities for PVA solutions gradually but continuously increase with time after it was cooled to room temperature. After a long period, the intensities do not change any more and the gelation seems to be terminated for this system.

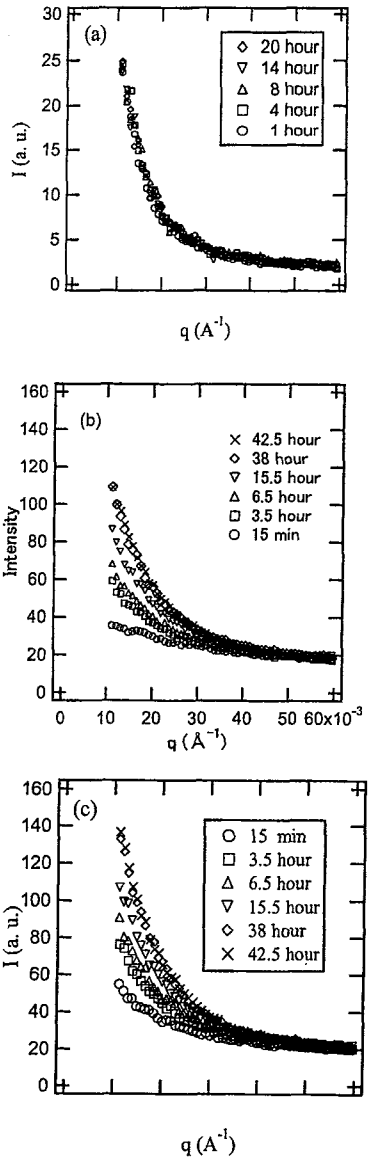

Fig. 1 Time dependence of I for (a) ALG, (b) PVA and (c) PVA/ALG solutions.

使用施設:JRR-3M, **装置**:SANS-U(C1-2), **分野** Softmatter

For PVA, it is reported[1] that this q region corresponds to length scale of network chain between crosslinks. Correlation length obtained from the above data was consistent with the reported data. Correlation length of ALG gel was also in the same order, implying that both polymers have similar network size.

Comparing the data in Figure 1, it can be point out that the data for PVA/ALG solution (c) at the beginning resembles to (a), while the data resembles to that for (b) at later time. For PVA/ALG solution, first Ca^{2+} is added then the solution was cooled to room temperature so that the time evolution may be controlled by gelation of PVA. Moreover, scattered intensities from two networks seems to be additive.

Figure 2 shows the data for the (PVA/ALG) mixed solutions after a long period. To test the above idear, the sum of scattered intensities for two homopolymer systems at long time end are shown by solid line. It is clear that the measured and calculated values coincide with each other, denoting that the scattering from two gels (networks) are additive.

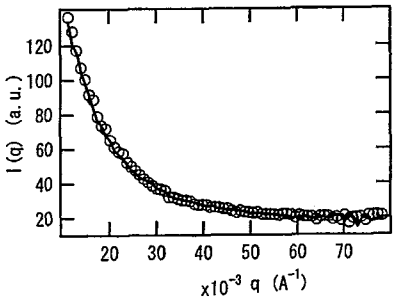

Figure 2. Plots of $I(q)$ vs q at long time end. Solid line denotes the sum of $I(q)$'s of two homopolymer gels at long time end.

The additivity of data was also confirmed for plateau modulus of the gels obtained by dynamic mechanical analysis, in which Ca^{2+} was added to PVA/ALG semi-IPN. Therefore, it can be concluded that the structure of PVA/ALG IPN does not depend on the order of the gelation of two polymers.

Refference

(1) H. Takeshita, T. Kanaya, K. Kaji, K. Nishida, Y. Nishikouji, M. Ohkura, *Koubunnshi Ronbunshu*, **55**, 595 (1998).

研究テーマ:中性子反射率測定に基づく(高分子誘電体/有機半導体)二層膜の構造評価
表題:中性子反射率測定に基づくハイブリッド高分子超薄膜の構造評価

9) Neutron Reflectivity Study on the Structure of Hybrid Polymer Ultrathin Films

K. Miyamoto, N. Hosaka, A. Takahara
Institute for Materials Chemistry and Engineering, Kyushu University, 6-10-1 Hakozaki, Higashi-ku, Fukuoka, 812-8581, Japan

Previous study showed that the addition of polyhedral oligomeric silsesquioxanes (POSS) to the polystyrene (PS) thin films led to an inhibition of dewetting [1]. This inhibition effect can be attributed to the changes of the energetics of the surface and interface of the film caused by the segregation of POSS. However, due to the extensive enrichment of POSS at the surface, the surface roughness appeared after annealing treatment. In order to reduce the surface heterogeneity, POSS was introduced as the chain end group of PS. In this study, neutron reflectivity (NR) technique is used to characterize the blend ultrathin film of deuterated PS (d-PS) and the PS with POSS end-group (PS-POSS: Figure 1).

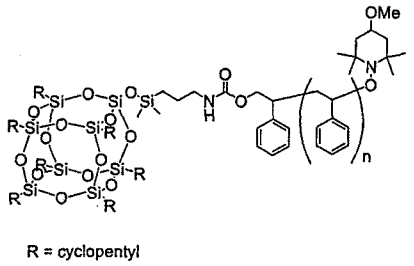

Figure 1: Chemical structure of PS-POSS.

NR measurements were performed on a thin d-PS (M_n=38.5k) films containing 25 wt% PS-POSS(M_n=38.6k) prepared on acid-cleaned Si wafer by spin-coating, and annealed at 393 K for 3 h. The measurements were conducted on C3-1-2 MINE at JRR3M in JAERI (Tokai) with 8.8 Å of incident neutron beam. NR curve of the (PS-POSS 38.6k/d-PS)(25/75w/w) thin film is shown in Figure 2. Morphological

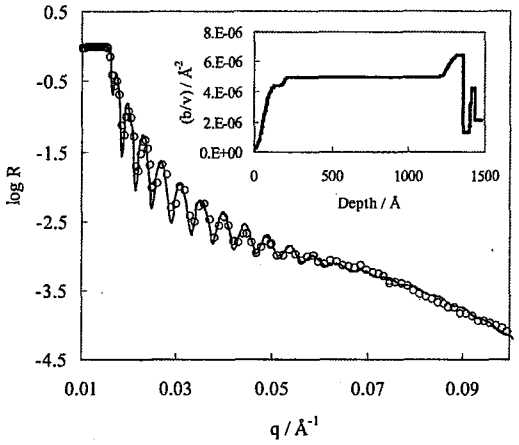

Figure 2. NR curve of (PS-POSS38.6k/d-PS) (25/75w/w) thin film. The inset shows the scattering length density profile of the film.

observation by scanning force microscopy and thermal behavior of bulk blend film did not show any phase separation. The solid line is model reflectivity data based on the scattering length density profile shown in the inset. As shown in the scattering length density profile, decrease in scattering length density was observed at the surface of the film, which can be attributed to the segregation of PS-POSS at the surface. The NR measurement was also performed on the d-PS film with 25 wt% PS-POSS(Mn=173.7k) after annealing at 393K for 3hours. . In this case, surface enrichment of low Mn and low surface tension dPS was observed.

References

[1] N. Hosaka, K. Tanaka, H. Otsuka, A. Takahara, *Composite Interfaces*, **11**, 297-306 (2004).

使用施設:JRR-3M, 装置:MINE(C3-1-2), 分野 Softmatter

研究テーマ：脂肪族ジカルボン酸ジエステルの運動性
表題：Dibutyleicosanedioateの固相相転移近傍での運動

10) Dynamics of Dibutyleicosanedioate near the Solid State Phase Transition

T. Kawaguchi, C. Akita, I. Kuwabara, and F. Kaneko
Department of Macromolecular Science, Graduate School of Science, Osaka University, 1-1 Machikaneyama-cho, Toyonaka, 560-0043

As the strategy to understand polymeric systems, small model compounds or oligomers are sometimes used to analyze the crystal structure and phase transition mechanism of polymers. This is because the model compounds can provide high resolution experimental data due to their simple structure. We investigate the structure and physical properties of dibutyleicosanedioate, which are worthwhile to have insight into the structure and physical properties of new biodegradable polyesters.

The DSC and powder-XRD data shows that the diester exhibits reversible solid phase transition near its melting temperature, which has not been reported.The XRD data suggest that the long period become short and lateral packing of methylene chains become looser at the transition.

The IR spectra of diester in both of the low and high temperature phase indicate that the methylene chain in diacid part forms all-trans conformation and have an inversion center. Further, the spectra show that the methylene chains form the Orthorhombic perpendicular subcell and the subcell rearrangement occurs at the transition. Raman spectra indicate that the butyl group has a rigid-all-trans conformation in low temperature phase and conformational defects are entered in high temperature phase.

We performed neutron quasielastic scattering measurements with AGNES of JRR3M in JAERI to know how the structure difference affects the dynamical properties of methylene chains.

Using Debye - Waller formula: $I_{el}(Q) = I_{el}(0)exp(-1/3 < u^2 > Q^2)$, we estimate mean-square-displacement $< u^2 >$. Figure 1 shows the temperature dependence of $< u^2 >$. In the low temperature phase, $< u^2 >$ increases steadily with increasing temperature. Stepwise increase indicates the high mobility in high temperature phase.

For the first step to analyze the quasielastic scattering, we tried curve fitting with two Lorentzian functions. Because the molecular motion in high temperature phase is thought not to be a simple diffusion, it is natural that the fitting results are not so good as in figure 2. We are now trying profile analysis of quasielastic scattering carefully to get the information of molecular motion in detail.

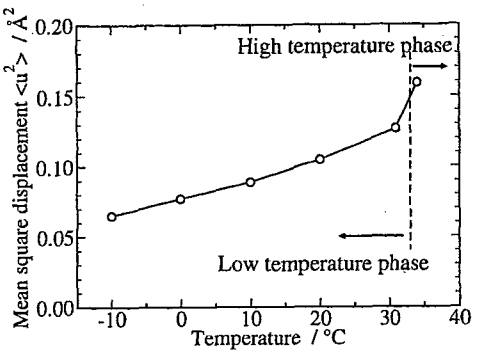

Fig. 1. Temperature dependence of the mean square displacement $<u^2>$.

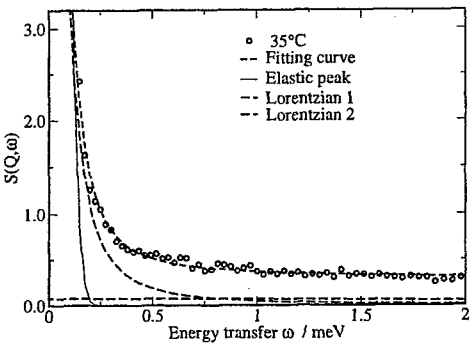

Fig. 2. An example of results of curve fit to the S(Q,ω) spectrum with the elastic component and two Lorentzian components.

使用施設：JRR-3M，装置：C3-1-1 (AGNES)，分野：6. Softmatter

研究テーマ:中性子反射率測定に基づく(有機高分子薄膜/水)界面における水の構造評価
表題:中性子反射率測定に基づく(有機単分子膜/水)界面における水の構造評価

11) Analysis of Water Structure at (Organic Monolayer/Water) Interface by Neutron Reflectivity

Nao Hosaka, Tomoyuki Koga, and Atsushi Takahara

Institute for Materials Chemistry and Engineering, Kyushu University, Hakozaki, Higashi-ku, Fukuoka 812-8581, JAPAN

Water at the solid interface plays an important role in the bio-applications of materials. The structure of water at the interface might influence the initial process of biological interaction[1]. However, since it is very difficult to apply X-ray reflectivity and spectroscopic method due to the optical non-transparency of water, a little study has been done on the structure analysis of water at the solid/water interface. Since a substrate such as silicon and quartz glass is highly transparent against neutron, a neutron reflectivity (NR) technique can be applied for the analysis of the water density profile near the solid interface. The purpose of this study is to apply NR experiment at (solid/water) interface and carry out preliminary experiment of NR.

Figure 1 shows the geometry of NR measurement at the (solid/water interface). The neutron beam was irradiated through the highly polished quartz glass. Octadecyltrichlorosilane (OTS; $CH_3(CH_2)_{17}SiCl_3$) and [2-(perfluorooctyl)ethyl]trichlorosilane] (FOETS; $CF_3(GF_2)_7CH_2CH_2SiCl_3$) were chemisorbed on to the quartz glass surface. The formation of monolayer was confirmed by several analytical technique[2]. The heavy water was used as an aqueous media. NR measurements were conducted on C3-1-2 MINE at JRR3M in JAERI (Tokai) with 8.8 Å of incident neutron beam.

As the quartz glass has a lower scattering length density ($4.22x10^{-6}Å^{-2}$) than D_2O($6.4x10^{-6}Å^{-2}$), this allows a critical angle to be measured at low q, which serves as a useful reference for the entire reflectivity profile. The NR profiles of the quartz glass/D_2O, OTS-quartz glass/ D_2O , and FOETS-quartz glass/ D_2O interfaces are shown

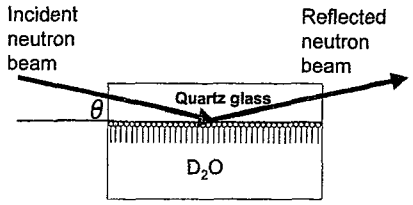

Figure 1 Schematic diagram of the sample cell used in this study.

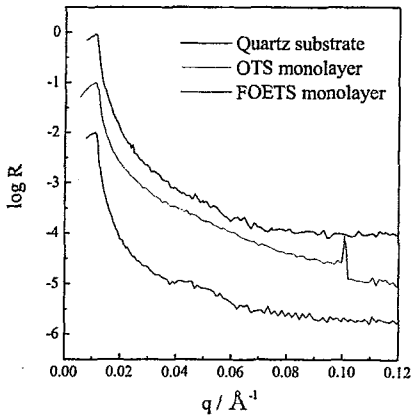

Figure 2 Neutron reflectivity profile of quartz glass substrate/D_2O, OTS-quartz glass/ D_2O , and FOETS-quartz glass/ D_2O interfaces.

in Figure 2. A critical angle was observed at q= 0.0113 $Å^{-1}$. The data seems to follow Fresnel's low at low q region. At present, since low S/N ratio of the detected reflection intensity, the density profile of heavy water near the surface was not evaluated from NR data..

References

[1] T. Tsuruta, *Adv. Polym. Sci.*, **126**,2(1996).
[2] A. Takahara, Molecular Assembly of Organosilanes, *Encyclopedia of Nanoscience and Nanotechnology*, Vol.3, 2031-2042, Dekker, NY(2004).

使用施設:JRR-3M, 装置:MINE(C3-1-2), 分野 Softmatter

研究テーマ：非イオン性界面活性剤系マイクロエマルションの圧力誘起構造相転移
表題：水、油、非イオン性界面活性剤系マイクロエマルションにおける膜弾性率の圧力依存性

12) Pressure-dependence of the bending modulus in a ternary microemulsion system composed of water, oil and non-ionic surfactant

M. Nagao, H. Seto[A], and Y. Kawabata[B]

Institute for Solid State Physics, The University of Tokyo, 106-1 Shirakata, Tokai, 319-1106
[A]Kyoto University, Kitashirakawa, Sakyo, Kyoto 606-8502
[B]Tokyo Metropolitan University, 1-1 Minamiosawa Hachioji 192-0397

We have reported the pressure effect on the phase transition as well as the membrane dynamics on a microemulsion system consisting of an ionic surfactant, AOT (dioctyl sulfosuccinate sodium salt), water and oil.[1, 2, 3, 4] These results are explained as follows: With increasing temperature, a counter-ion dissociation from a head group of AOT molecule is enhanced, and an electrostatic head-head repulsive force increases. On the other hand, at high pressure, an attractive interaction between hydrophobic tails of the AOT molecules increases. Both the effects decrease the spontaneous curvature of the surfactant monolayers, i.e., curved monolayers to surround water become more flat. Therefore, the phase transitions induced by temperature and pressure seem to be the same.

In order to clarify the universality of the pressure effects on the membrane dynamics, a microemulsion system consisting of non-ionic surfactant, $C_{12}E_5$ (pentaethyleneglycol dodecylether), water and octane was investigated by means of SANS and NSE. In this system, increasing pressure played the same role as decreasing temperature unlike the case of the microemulsion including the ionic surfactant AOT. Figure 1 shows a schematic $P-T$ phase diagram of the system. From the SANS results the origin of the pressure-induced phase transitions of this system was clarified as follows: [5] A hexagonal phase is induced at high pressure in the mixture with the volume fraction of water being 0.37, whose structure at ambient pressure is the lamellar structure. The mean curvature of surfactant monolayers in the lamellar phase is nealy zero, and it becomes finite negative value at high pressure. Thus the oil-in-water cylindrical structure is stabilized and they

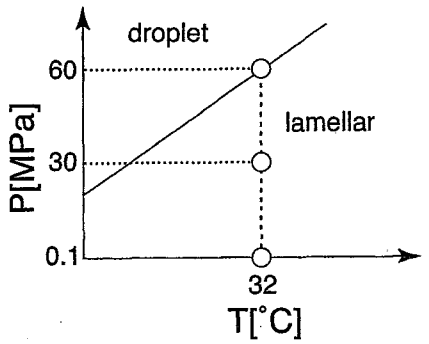

Fig. 1. Schematic phase diagram on pressure-temperature plane of the $C_{12}E_5$, water and octane microemulsion. The open circles indicate the conditions of the NSE experiment.

hexagonally packed. This tendency could be interpreted in terms of the compression of surfactant tails by pressure.

Pressure-variation of the intermediate structure factor $I(q,t)/I(q,0)$ was measured by NSE for the water volume fraction of 0.8. The observed $I(q,t)/I(q,0)$s' were analyzed with the model given by Zilman and Granek, [6]

$$I(q,t)/I(q,0) = \exp\left[-(\Gamma t)^{2/3}\right], \quad (1)$$

where Γ is proportional to q^3

$$\Gamma = Aq^3, \quad (2)$$

and the bending modulus is obtained by

$$\kappa = \left(A^{-1}0.025\gamma_\kappa (k_B T)^{3/2}\eta^{-1}\right)^2 \quad (3)$$

Here, parameters γ_κ could be assumed as 1. The viscosity η was assumed as the mean value of that of D_2O and that of C_8D_{18}. Using these equations, the pressure dependence of the bending modulus was obtained as shown in Fig. 2.

使用施設：JRR-3M，装置： C1-2 (SANS-U), C2-3-1 (iNSE)，分野： 106. Softmatter

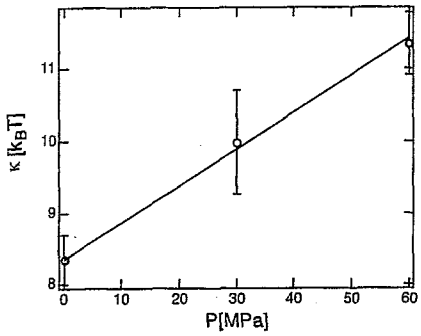

Fig. 2. Pressure dependence of κ at $T = 32$ °C. The solid line is a guide for eyes. It is clear that κ is an increasing function with respect to pressure.

It should be noted that the absolute values of the observed κ are not reasonable; too large comparing with the values in literature, i.e., the order of k_BT. This discrepancy might come from the effective viscosities, which should be used in the data analyses. The theoretical equations of the bending modulus include the viscosities as a parameter. (See Eq. (3)). In the present analyses, the viscosities were assumed as the values of bulk mediums. However, some modifications are necessary to take other interactions (for example, a steric repulsion from neighboring membranes) into account. [7, 8] Thus, if we use effective viscosities, which are several times larger than the bulk viscosities, reasonable values of the bending modulus will be obtained. At present, only the relative values are important and the unreasonable absolute values are not essential.

Figure 2 shows that the $C_{12}E_5$ monolayer becomes more rigid with increasing pressure, as the case of the AOT microemulsion. There, the attractive interaction between hydrocarbon chains of surfactant molecules increases with increasing pressure, and the free volume of hydrocarbon tail of a surfactant molecule decreases. [2] This picture is consistent with the pressure-dependence of the bending modulus of AOT monolayers. [4] It is reasonable to consider the increase of an attractive interaction between hydrocarbon tails of surfactant molecules is also responsible to the increase of the bending modulus of the $C_{12}E_5$ monolayer. [9]

The pressure effect on a polar head-group of a surfactant molecule is not yet clear. It should be complicated because the free volume of a head-group may be affected not only by the interactions among polar head-groups but also the hydration effect. This may be reasonable that the pressure effect on head-groups is not so significant comparing with that on the hydrocarbon tails. Under this consideration, the packing parameter, which is the ratio of the volume of a surfactant molecule and the product of the area of the polar head-group and the tail length, decreases with increasing pressure independent of kinds of head-group. In this context, we can conclude that the origin of the pressure-induced phase transitions of microemulsions and the increase of the bending modulus is the decrease of a free volume of a hydrocarbon tail of a surfactant molecule with increasing pressure. [9]

References

[1] M. Nagao and H. Seto: Phys. Rev. E. **59** (1999) 3169.
[2] H. Seto *et al.*: J. Chem. Phys. **112** (2000) 10608.
[3] M. Nagao *et al.*: J. Chem. Phys., **115** (2001) 10036.
[4] Y. Kawabata *et al.*: Phys. Rev. Lett. **92** (2004) 056103.
[5] M. Nagao *et al.*: J. Chem. Phys., in press.
[6] A. G. Zilman and R. Granek: Phys. Rev. Lett. **77** (1996) 4788.
[7] N. L. Yamada *et al.*: J. Phys. Soc. Jpn. **74** (2005) 875.
[8] N. Gov *et al.*: Phys. Rev. E 70 (2004) 011104.
[9] H. Seto *et al.*: submitted to Coll. Surf. A.

研究テーマ：
表題：(多分岐高分子/線状高分子) 混合膜における表面凝集構造解析

13) Surface and Interfacial Aggregation States in Blend Films of (Hyper Branched Polystyrene/Linear Polystyrene) by Neutron Reflectivity

F. Ariura, K. Tanaka, T. Nagamura, M. Schappacher†, A. Deffieux†, M. Hino‡, T. Kajiyama-

Department of Applied Chemistry, Faculty of Engineering, Kyushu University, Fukuoka 812-8581, Japan

†Laboratoire de Chimie des Polymères Organiques, UMR 5629 CNRS-ENSCPB, Université Bordeaux 1, 16 Avenue Pey Berland, 33607 Pessac Cedex, France

‡Research Reactor Institute, Kyoto University, Kumatori, Osaka 590-0494, Japan

-Kyushu University, Fukuoka 812-8581, Japan

Surface and interface of polymeric materials play an important role in many technological applications. In order to design highly functionalized polymeric materials, systematical understanding of aggregation states and physical properties in the vicinity of surface and interfacial layers, which are impossible to be deduced only by extrapolating the bulk ones, is of pivotal importance as the first benchmark. So far, we have studied surface composition in blend films of higher and lower molecular weight polystyrenes (PSs), and revealed that a smaller components is partitioned to the surface mainly due to a chain end effect and an entropic factor [1]. In this study, surface composition in blend films of chemically identical linear and hyper branched PSs is examined so that the effects should be more clearly seen.

Figure 1 shows the chemical structure of hyper branched PS (HB-PS) used, and the degrees of polymerization for backbone and branch, namely, *n* and *m*. Two monodisperse HB-PSs with longer and shorter branches, abbreviated as HLB-PS and HSB-PS, were used. The total molecular mass for the both was fixed to be 1M. Also, deuterated polystyrene (dPS) with molecular weight of 1M was used as a linear component. (HB-PS/dPS) (5/95 w/w) blend films were prepared on silicone wafers with a native oxide layer by a spin-coating method, and then, were annealed at 423 K for 48 h *in vacuo*.

Time-of-flight secondary ion mass spectroscopy (ToF-SIMS) revealed that HB-PS was preferentially segregated at the film surface. In general, deuterated species is enriched at the surface over protonated one due to the lower surface free energy. However, the opposite was observed here. In addition, HB-PS and dPS possess the same molecular mass. Thus, this surface segregation of HB-PS should be explained in terms of architectural difference between HB-PS and dPS. Although ToF-SIMS is one of the most surface sensitive spectroscopic techniques and the depth resolution should be within a few angstroms, it cannot be used to study depth profiling of components. Thus, neutron reflectivity (NR) was applied to the blend films of HB-PS and dPS.

NR measurement was performed using the multilayer interferometer for neutrons (C3-1-2, MINE) at JRR3M in JAERI (Tokai). The incident neutrons wavelength was 0.88 nm and a resolution of

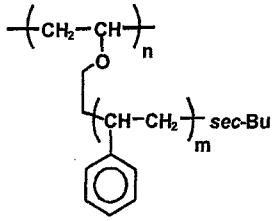

HSB-PS : n=740, m=13
HLB-PS : n=126, m=80

Figure 1 Chemical structure of HB-PS.

使用施設：JRR-3M，装置：MINE(C3-1-2)，分野 Softmatter

4.8 %. Figure 2(a) shows the scattering vector (q) dependence of reflectivity for the (HLB-PS/dPS) and (HSB-PS/dPS) films including 5 wt% HB-PS in bulk. Each film thickness was fixed to be ca. 50 nm. The data for the (HSB-PS/dPS) film is offset by 2 decades for the sake of clarity. Solid lines denote the best-fit calculated reflectivity, to the experimental data, on the basis of model scattering length density (b/V) profiles shown in Figure 2(b). Since the calculated curves are in good agreement with the experimental data, it can be claimed that the model (b/V) profiles well reflect the real composition variation through the blend films. The (b/V) values used for dPS and HB-PS were 6.46 x 10^{-4} and 1.5 x 10^{-4} nm^{-2}, respectively, meaning that a decrease in the (b/V) value corresponds to an increase in the HB-PS fraction. Based on the model (b/V) profiles, it is most likely that the blend films basically consist of three regions along the direction normal to the surface, as shown in the panel (b). In the surface region (I), the (b/V) value increased from zero with increasing depth, and became a constant of 2 x 10^{-4} nm^{-2}. This is originated from the surface roughness and the enrichment of HB-PS in this region. Such a HB-PS rich layer was also formed in the substrate interfacial region (III). The region with the (b/V) value of 4.2 x 10^{-4} nm^{-2} beneath it corresponds to the native oxide layer of the substrate. On the contrary, a higher (b/V) region of approximately 6 x 10^{-4} nm^{-2} was appeared in the middle (II), resulting from a bulk dPS rich layer. It is interesting to note that the (b/V) in the region (I) and the (b/V) value in the region (II) are dependent on the architecture of the HB-PS.

Surface and interfacial segregation of a branched component in its mixture with the corresponding linear one was also confirmed by self-consistent filed calculation. More conclusive work related to an effect of architecture on the segregation will be reported in the near future.

References

[1] K. Tanaka, T. Kajiyama, A. Takahara, S. Tasaki, *Macromolecules* **35** (2002) 4702.

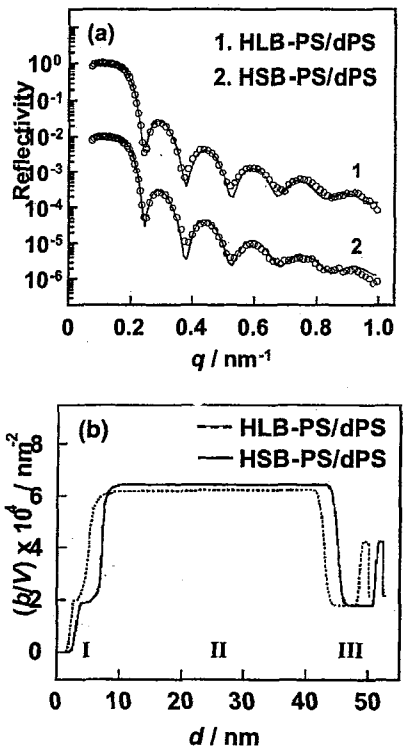

Figure 2 (a) Neutron reflectivity profiles for (HLB-PS/dPS) and (HSB-PS/dPS) (5/95 w/w) blend films. Circles are experimental data, and solid lines depict reflectivity calculated on the basis of model scattering length density profiles, shown in the panel (b). The data for the film including HSB-PS is offset by 2 decades for clarity. (b) Model scattering density profiles of (HB-PS/dPS) (5/95 w/w) blend films.

研究テーマ：ABCトリブロックコポリマーのナノ拘束空間における自己組織化過程に関する研究
表題：ポリスチレンとポリビニルメチルエーテルの相溶性に及ぼす化学結合の効果

14) Effect of Chemical Junction on the Miscibility of Polystyrene and Poly(vinyl methyl ether) : Comparison between PI-*b*-dPS-*b*-PVME Triblock Terpolymer and PI-*b*-dPS Diblock Copolymer/PVME Homopolymer Blend

K. Yamauchi, H. Mori, S. Akasaka, and H. Hasegawa

Department of Polymer Chemistry, Graduate School of Engineering, Kyoto University, Kyoto-Daigaku Katsura, Nishikyo-ku, Kyoto 615-8510, Japan

Recently, ABC triblock terpolymers consisting of three different polymer sequences collect researchers' interests because of their rich variety of microdomain morphologies, which may be utilized as the templates for functional nanotechnology materials.

We have been studying the phase behavior and self-assembling mechanisms of ABC triblock terpolymers consisting of polyisoprene (PI), deuterated polystyrene (dPS), and poly(vinyl methyl ether) (PVME). This system shows a complex phase behavior as follows. At room temperature, dPS and PVME blocks are mixed but microphase-separated from PI block in the toluene-cast film. As the temperature increases, segregation power between PI and dPS decreases and tends to mix, but repulsive interaction between PI and PVME is much stronger than that between PI and dPS resulting in suppression of the miscibility between PI and dPS and enhancement of the segregation power between dPS and PVME which show an LCST type phase behavior. The entropic effect that the chain ends are confined at the interfaces also suppresses the miscibility of the tethering diblocks. Thus, the miscibility between PI and dPS and that between dPS and PVME are both suppressed by the additional blocks in the terpolymer.

In this work, we examined the difference in the phase behavior between a PI-*b*-dPS-*b*-PVME triblock terpolymer and a polymer blend consisting of PI-*b*-dPS diblock copolymer and PVME homopolymer, which has the same molecular weight for each component and the same composition as the triblock terpolymer. Therefore, we can investigate the effect of chemical junction between dPS and PVME components on the phase behavior.

The triblock terpolymer was prepared by sequential living anionic polymerization followed by coupling of end-chlorinated PVME prepared by living cationic polymerization. PI-*b*-dPS diblock copolymer and PVME homopolymer used for the blend were the precursors used for the coupling reaction to make the terpolymer, thus having the same molecular weights and composition as those for the corresponding parts of the terpolymer. The molecular weights and compositions evaluated by GPC and ^{1}H-NMR are PI-*b*-dPS-*b*-PVME = 23.4k-*b*-13.8k-*b*-13.3k and PI:dPS:PVME = 46:27.5:26.5 for the terpolymer and PI-*b*-dPS/PVME = 23.4k-*b*-13.8k/13.3k and PI:dPS:PVME = 44.7:26.7:28.6 for the blend. The cast films were obtained by slow evaporation of the solvent from the 10% polymer solutions in toluene for 10 days.

SANS measurements were performed with SANS-U instrument of the University of Tokyo installed on JRR-3M research reactor at JAERI, Tokai, Japan. The incident neutron wavelength of 0.7 nm and the sample-to-detector distance of 4 m were used. The sample films were dried in a vacuum oven at 50°C for 3 d prior to the SANS measurement at 60°C under vacuum. The absolute intensity was obtained by

使用施設：JRR-3M，装置：SANS-U(C1-2)，分野 Softmatter

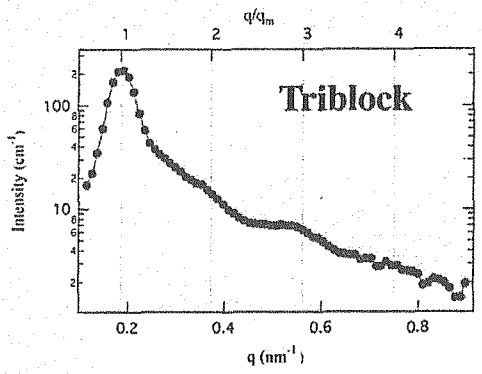

Figure 1: SANS profile from the dried cast film of PI-b-dPS-b-PVME triblock terpolymer.

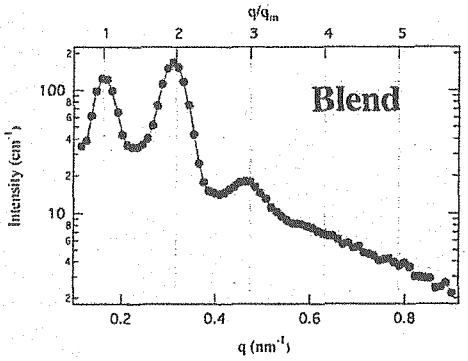

Figure 2: SANS profile from the dried cast film of PI-*b*- dPS diblock copolymer/PVME homopolymer blend.

using Luporen standard.

Figures 1 and 2 show the SANS profiles obtained for the terpolymer and the blend, respectively. Both profiles show distinct multiple scattering peaks with higher order peaks at the integer multiples of the first order peak indicating lamellar microdomain structures. However, the scattering profiles and the lamellar spacing evaluated from the first-order peaks for the two samples are very different from each other. The terpolymer shows the SANS profile where the second and fourth-order peaks are suppressed compared with the first and third-order peaks, suggesting a two-phase lamellae with almost symmetric volume fractions, i.e., dPS and PVME blocks are mixed and microphase-separated from PI.

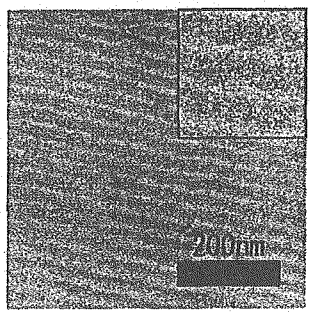

Figure 3: TEM image of the dried cast film of PI-b-dPS-b-PVME triblock terpolymer stained with RuO_4. The insertion shows a blow-up.

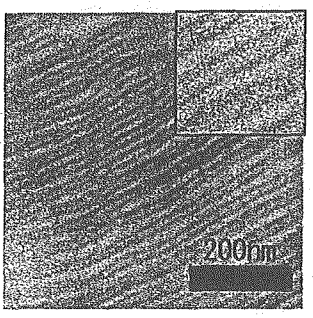

Figure 4: TEM image of the dried cast film of PI-*b*-dPS diblock copolymer/PVME homopolymer blend stained with RuO_4. The insertion shows a blow-up.

The two-phase lamellar morphology was confirmed with the TEM observation (Figure 3).

On the other hand, the blend shows a peculiar SANS profile. The second-order peak has higher intensity than the first-order peak. Such a profile is typical for the three-phase lamellar structure. Figure 4 showing the TEM image of the blend stained with RuO_4, which stains dPS component selectively, indicates the three-phase four-layer lamellar structure with the repeat units of PI, dPS, PVME and dPS in this order.

This result suggests that the terpolymer has a higher miscibility between dPS and PVME than the blend. This implies that the chemical junction between dPS and PVME blocks in the terpolymer increases the miscibility between dPS and PVME.

References

[1] K. Yamauchi et al., Polymer **43**, (2002) 3563.
[2] K. Yamauchi et al., J. Appl. Cryst., **36**, (2003) 708.

研究テーマ： リビング重合機構の中性子散乱による解明
表題：リビング重合機構の中性子散乱による解明

15) Small-angle Neutron Scattering Study of Living Polymerization Mechanism

H.Matsuoka, K.Matsumoto, P.Kaewsaiha, J.Nakashita, S.Matsubara

Department of Polymer Chemistry, Kyoto University, Kyoto 615-8510, Japan

Living polymerization is now a widely used technique to synthesize narrow molecular weight distribution polymers and block copolymers. However, the detailed mechanism of controlling the molecular weight is still not yet perfectly clear because of lack of direct information in molecular level during reaction. 3 years ago, we performed SANS experiments for living anionic polymerization process of styrene in benzene with *s*-butyllithium as an initiator,[1,2] and found an existence of large aggregate in the system. In this study, more precise (especially for sample preparation) experiments were performed,.

Three systems with different molecular weight (10K, 20K, and 40K) were prepared with deuterated benzene as a solvent, and measured by SANS just after living polymer preparation. All the samples showed dark orange color before and after SANS measurement, indicating that the system is perfectly living system. The "dead" polymer by addition of MeOH to the system was also measured. In addition, the "fainted" polymer, which showed no reddish color after treatment by oxygen in air was also measured as a reference.

Figure 1 shows an example of SANS curves for living, fainted, and dead polystyrene systems. SANS curve for dead PS(20K) was well reproduced by Debye function with radius of gyration (Rg) of 12.6Å. On the other hand, those for "living" and "fainted" PS, an upturn was observed in addition to Debye behavior at higher q, which certainly suggests an existence of large aggregates. The Rg of the aggregates were estimated to be 90Å for PS20 by Guinier analysis. This aggregate should be an association of active end group in non-polar solvent. Similar experiment and analysis were performed for other systems (Table 1). The formation of large cluster of active end group, which results in formation of "inverse micelle" is thought to be a "dormant" species, which controls the polymerization reaction process via unimer/micelle dynamic equilibrium.

The living radical polymerization process was also investigated by SANS for the polymerization of styrene in bulk at 120°C with DEPN as a mediator and AIBN as an initiator. No large aggregate was found, indicating that the living nature was controlled by association/dissociation equilibrium at the active end group. This is the first evidence for living radical systems.

Table 1 SANS data for living, fainted, and dead PS

Sample	Rg(Guinier) [Å]	Rg(Debye) [Å]
LvPS10	80	10.5
LvPS20	90	17.3
LvPS40	98	18.1
DePS10	---	7.7
DePS20	---	12.6
DePS40	---	11.8
FaPS	81	12.6

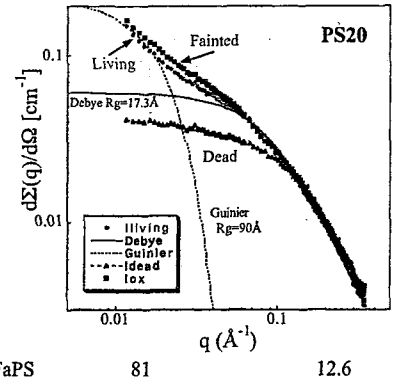

Figure 1 SANS profiles for "living", "fainted", and "dead" polystyrene by living anionic polymerization in d-benzene with s-BuLi as an initiator.

References

[1] H.Matsuoka and K.Matsumoto, *Meeting Abs. Jpn. Soc. Neutron Sci.*, **2**, 90 (2002).
[2] H.Matsuoka and K.Matsumoto, *Polymer Preprints, Japan*, **52**, 307 (2003).

使用施設：JRR-3M，装置：SANS-U(C1-2)，分野 Softmatter

研究テーマ：界面膜ダイナミクスの droplet 濃度依存性
表題：中性子小角散乱による三元系マイクロエマルションの静的構造の droplet 密度依存性

16) Microdomain structure in Model Bio-membranes Reveal by a Small Angle Neutron Scattering Technique

T. Masui, and M. Imai*

Department of Physics, Ochanomizu University
Otsuka, Bunkyo, Tokyo 112-8610, Japan

In recent years, lateral lipid segregation in biological membranes so-called microdomain (or lipid raft) gathers much attention because it is closely related to biological functions. Lipid rafts are liquid domains rich in cholesterol, sphingolipid, and in some cases particular proteins. Similar domains are observed in Giant Unilamellar Vesicles, which consist of ternary mixtures of cholesterol, saturated lipid (DPPC), and unsaturated lipid (DOPC) using fluorescence microscopy. Below the miscibility temperature, liquid domains appear spontaneously from homogeneous membrane and they grow up by repeating collision and coalescence. Various experimental results have been reported, while equilibrium domain structure has been unclear. In this context, we have investigated equilibrium structure using small unilamellar vesicles (SUV) by means of a contrast variation small angle neutron scattering technique, where we adjusted scattering length densities of solvent and mean lipid membrane using heavy water and deuterated lipid (DPPC-d62).

In Figure 1, we show fluorescence micrographs of GUVs having radius of ~ 5μm. By decreasing temperature, vesicles showed a homogeneous (Fig.1a) to multi-domain (Fig.1b) transition. The domains showed Brownian motion on the vesicle membranes and the size of domains were ~1μm. We followed the ordering process of the microdomains on SUV by the contrast match SANS techniqueas shown in Fig.2. Above the miscibility temperature (T=31°C), lipids are mixed with a molecular level, thus we cannot observe the scattering intensity. Below the miscibility temperature, however, the lateral segregation between unsaturated lipid (protonated) matrix and cholesterol-rich (deuterated DPPC-rich) domains gives a characteristic scattering profile having clear scattering maximum at ~0.03Å^{-1}. Temperature dependence of this excess scattering agrees with the homogeneous to multi-domains transition observed in the microscopy experiments. At T =22 °C we observed clear scattering maximum at ~0.03Å^{-1}. From the analysis of scattering profiles, we get equilibrium domain structure and the composition of domains and matrix as a function of the temperature.

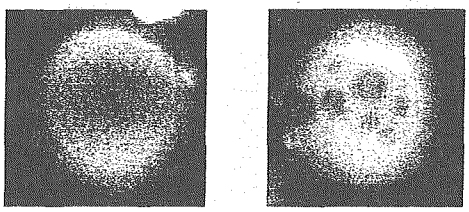

Figure 1: Fluorescence micrographs of Giant Vesicles. (a) T=40°C, (b) T=23°C.

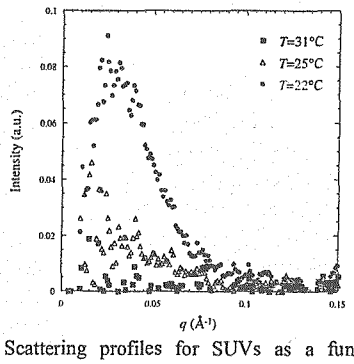

FIG.2: Scattering profiles for SUVs as a function of temperature.

使用施設：JRR-3M，装置：SANS-U(C1-2)，分野 Softmatter

研究テーマ：中性子散乱によるソフトマターの構造と機能の研究
表　題：デンドリマーを鋳型として活用したパラジウムナノ粒子組織体の合成

17) Synthesis of Self-Assembly of Palladium Nanoparticles Utilizing Dendrimers As Templates

H. Tanaka[1,2], T. Hashimoto[1,2], H. Ito[1], K. Naka[1], Y. Chujo[1], and S. Koizumi[2]

[1]*Department of Polymer Chemistry, Kyoto University, Kyoto 615-8510*
[2]*Advanced Science Research Center, JAERI, Tokai, Ibaraki 319-1195*

Metal nanoparticles show quantum mechanical properties, and are expected to be useful materials in nanotechnology. The patterning of the metal nanoparticles into organized structures is essential to achieve superior properties for various kinds of devices. One of the popular methods for controlling the organized structures involves formation of templates composed of metal ions and organic ligands and solvents. Recently, Chujo et al. have found that by using a polyamidoamine (PAMAM) dendrimer as such ligands, one can easily organize palladium nanoparticles into spherical aggregates *via* reduction of palladium ions in methanol solutions.

In this report, we focus on the structural analysis of palladium nanoparticles synthesized by alcoholic reduction of the mixture of palladium acetate in *N, N*-dimethylformamide and PAMAM dendrimer with three different generations in methanol at 50 ℃, by means of SANS and SAXS measurements. SANS measurements were performed with SANS-J at the guide hall of the reactor JRR-3 in JAERI.

Figure 1 shows SANS and SAXS profiles for the obtained colloidal solutions of palladium nanoparticles. The scattered intensity $I(q)$ is plotted as a function of scattering vector q defined by $q = (4\pi/\lambda)\sin(\theta/2)$, with θ and λ being the scattering angle and the wavelength of incident beam, respectively. It should be noted that SANS measurements cover relatively lower q region, $q < 0.2$ nm^{-1}, on the other hand, SAXS cover higher q region, $q > 0.2$ nm^{-1}. The scattering vector q can be related to characteristic length ξ, $q = 2\pi/\xi$, therefore, SANS profiles can provide information on the structure with relatively larger size, $\xi > 30$ nm, while SAXS profiles provide rather smaller structure, $\xi < 30$ nm.

SANS and SAXS profiles show quite different features: The SANS profiles seem to shift toward higher q-regions as the generation of dendrimers increase, indicating that the size of aggregated structures become smaller as the generation increase. As for q-regions covered by SAXS, as the generation increase, the scattered intensity seem to become stronger, though the profiles themselves are almost same. This indicates that the size of palladium nanoparticles are almost identical, though the number density of nanoparticles become larger as the generation increase. With these three profiles, we can estimate the size distribution function of the aggregated structures of palladium nanoparticles, as shown in Figure 2.

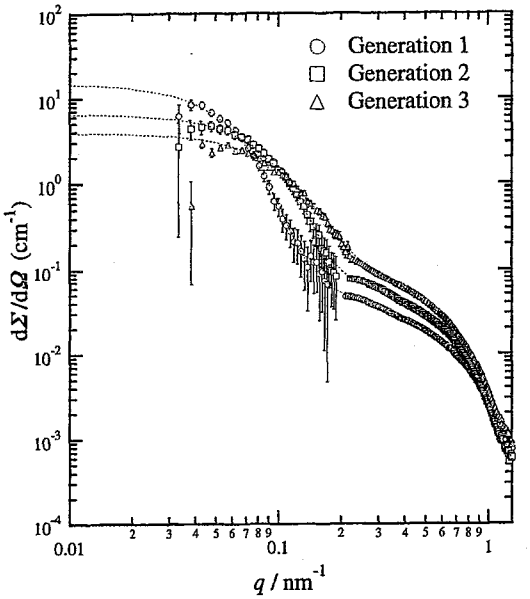

Figure 1: SANS and SAXS profiles for the obtained colloidal solutions of palladium nanoparticles.

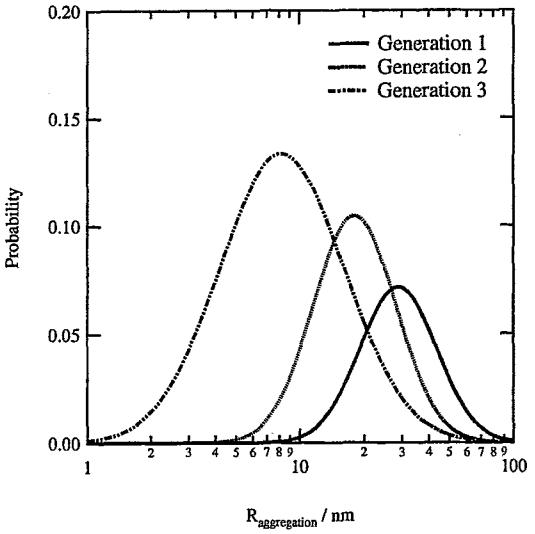

Figure 2: Size distribution of the aggregated structures of palladium nanoparticles as estimated by SANS and SAXS results.

原子炉：JRR-3　　装置：SANS-J(C3-2)　　分野：中性子散乱（高分子）

研究テーマ：ポリオレフィン/有機溶媒ゲル中の束縛溶媒の凝集構造

表題：ゲル中の自由溶媒と束縛溶媒の凝固点以下での凍結構造の相違

18) Investigation on Crystal Structure of o-Dichlorobenzene in Isotactic Polypropylene Gel by Wide Angle Neutron Scattering

T. Nakaoki, Y. Tanimura, M. Ishibashi, K. Saito, K. Inoue, and Y. Yamaguchi*

Faculty of Science and Technology, Ryukoku University, Seta Otsu 520-2194, Japan;

**Neutron Science Research Center, JAERI, Tokai 319-1195, Japan*

Most of investigations on gel have been focused in network structure including cross-linking point. However there are few reports on the solvent coagulated in the network structure below T_m of solvent. In general it has been well-known that there exist three types of solvent in the gel; free, bound, and non-freezable solvents. These solvents are predicted to coagulate in different structure. The purpose of this investigation is to elucidate the crystal structure of o-dichlorobenzene in isotactic polypropylene (iPP) gel below and above Tm of o-dichlorobenzene by wide angle neutron scattering (WANS).

Fig. 1 shows the temperature dependence of WANS (HERMES) for iPP/o-dichlorobenzene-d_8 30 wt% gel. Below and above the T_m of o-dichlorobenzene (around -15 °C), the scattering pattern changed drastically, corresponding to the melt of o-dichlorobenzene. Above T_m, only the diffraction peaks due to the crystalline iPP formed at cross linking point were observed.

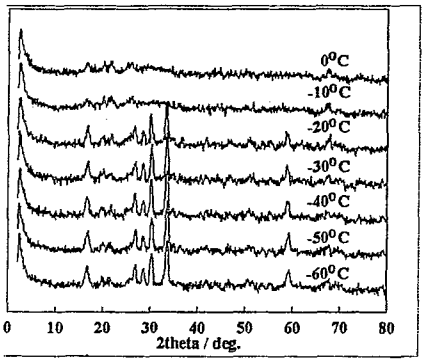

Fig. 1. Wide angle neutron scattering pattern of iPP/oDB(D) gel various temperature from -60 °C to 0 °C.

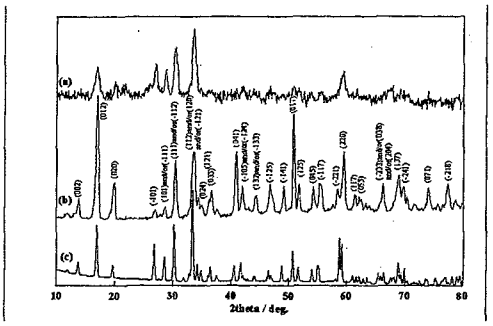

Fig. 2.Wide angle neutron scattering patterns of deuterated *o*-dichlorobenzene at -60 °C (a) 30 wt% iPP gel, (b) pure solvent, and (c) simulation by Rietbelt method.

In order to compare the crystal structure of o-dichlorobenzene in iPP gel with that of pure pure o-dichlorobenzene, WANS patterns were represented in Fig. 2. Rietbelt analysis of pure o-dichlorobenzene was also shown in the Figure. There is few differences between the observed and calculated diffraction patterns of pure o-dichlorobenzene. The diffraction pattern of o-dichlorobenzene in iPP gel is simpler than that of pure solvent. Perhaps this result can be explained by different space group. The entanglement of polymer chain made the solvent to coagulate in incomplete state.

In conclusion, since the crystal structure of o-dichlorobenzene coagulated in iPP gel at low temperature was different from that of pure o-dichlorobenzene, the solvent is more or less bound in polymer network so that there is no free state of o-dichlorobenzene in 30 wt% iPP gel.

使用施設：JRR-3M，装置：HERMES，分野　高分子

研究テーマ：反応系ブロックコポリマーに関する研究
表　題：中性子小角散乱によるリビングアニオン重合過程のその場観察

19) *In-situ* SANS Observation of Living Anionic Polymerization Process

K. Yamauchi[1], H. Hasegawa[1], H. Tanaka[1,2], R. Motokawa[2], S. Koizumi[2], and T. Hashimoto[1,2]

[1]*Department of Polymer Chemistry, Kyoto University, Kyoto 615-8510*
[2]*Advanced Science Research Center, JAERI, Tokai, Ibaraki 319-1195*

Polystyrene-*block*-polyisoprene were synthesized *via* simultaneous living anionic polymerizations of the two monomers with two kinds of solvent systems: (i) pure benzene and (ii) benzene with a trace amount of THF. In this study, we aim to elucidate the influence of the solvent polarity on the primary structures of block copolymers and also on their self-assembled structures. To accomplish this purpose, the living anionic polymerization processes were pursuited by *in situ* and *real time* SANS observations.

SANS measurements were carried out with the SANS-J spectrometer installed at JRR-3 research reactor in JAERI, Tokai, Japan. Cold neutrons were monochromatized with a velocity selector to have the mean wavelength λ of 0.65 nm. The scattered neutrons were detected by a two-dimensional detector. Sample to detector distance was set to be 6.0 m so as to cover q-regions of $0.05 < q < 0.5$ nm^{-1}. The obtained two dimensional data were circularly averaged and corrected for detector efficiency, transmission, and background scattering for further analysis. Figure 1 and 2 show the time evolution of SANS profiles during the polymerization process in benzene solution and benzene solution with a trace amount of THF, respectively.

It is well known from early studies concerning living anionic polymerization in 1960's that in both cases (non-polar systems and polar systems) isoprene monomers are preferentially polymerized first, and then styrene monomers are polymerized. Here, from *in-situ* SANS observations, we have found that in benzene solution, polymerization of styrene monomers after the completion of polymerization of isoprene monomers causes disorder to order phase transition (ODT) and further polymerization of styrene monomers leads to an order to order transition (OOT) from cylindrical to lamellar microdomain structures. In the case of the solution with a trace amount of THF, on the other hand, no such distinct ODT and OOT can be observed, and only a broad peak of block copolymers in the disordered state was observed during the whole polymerization process of styrene monomers. These different behavior may be explained in the viewpoints of the difference in the composition distribution along the polymer chains, resulting from the solvent polarity. The composition distribution along the polymers synthesized in non-polar solvent system is expected to have nearly square-wave-type function. On the other hand, the composition distribution of the polymers synthesized in polar solvent system may be rather smooth shaped distribution function, like a so called tapered block copolymer.

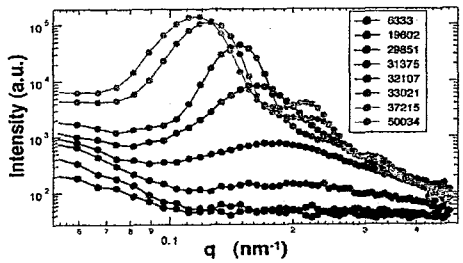

Figure 1: Time dependence of SANS profiles in the anionic polymerization process of styrene and isoprene monomers in benzene-d_6.

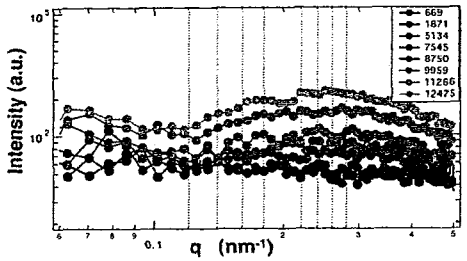

Figure 2: Time dependence of SANS profiles in the anionic polymerization process of styrene and isoprene monomers in benzene-d_6 with a trace amount of THF.

原子炉：JRR-3　　装置：SANS-J(C3-2)　　分野：中性子散乱（高分子）

研究テーマ：弱電解質PNIPA-アクリル酸高分子ゲルおよび溶液の相挙動
表題：中性子小角散乱による三元系マイクロエマルションの静的構造のdroplet密度依存性

20) Small-angle Neutron Scattering Investigation of Pressure Influence on the Structure of Weakly Charged Poly(N-isopropyl acrylamide) Solutions and Gels

I. Nasimova[1,2], T. Karino[1,3], S. Okabe[2], M. Nagao[2], and M. Shibayama[2,3]
[1] *Physics Department, Moscow State University, Moscow 119992, Russia*
[2] *Institute for Solid State Physics, The University of Tokyo, 106-1 Shirakata, Tokai, 319-1106*
[3] *CREST, 4-1-8 Honcho Kawaguchi, Saitama 332-0012, Japan*

Effects of pressure on the phase separation and structure of weakly charged poly(*N*-isopropyl acrylamide-*co*-acrylic acid) (PNIPA-AAc) solutions and gels were investigated by small-angle neutron scattering (SANS). The phase diagrams were determined in the pressure-temperature ($P-T$) plane respectively for the solution and gel with a light scattering method, which were parabolic functions, having maxima at ($P =$ 38.1 MPa, $T = 37.1$ °C; for the solution) and (100.2 MPa, 54.7 °C; for the gel). SANS experiments were carried out according to the $P-T$ phase diagrams.

At low temperature and pressure region, where the systems were in one phase, the scattering intensity functions, $I(q)$s, were well described with an Ornstein-Zernike functions. However, a scattering maximum appeared in $I(q)$s at elevated temperatures and pressures. This scattering maximum is due to microphase separation as a result of antagonism between the electrostatic and hydrophobic interactions.[1] In the case of the solution, an upturn in $I(q)$ at low q region was observed, indicating occurrence of macrophase separation in addition to microphase separation. For the polymer gels, such upturn in $I(q)$ was strongly suppressed by a pinning effect of cross-links.[2]

Fig. 1 shows the variations of $I(q)$s with increase of pressure at $T = 45$ °C. It can be noted that a clear scattering maximum q_{max} responsible for microphase separation, was observed in $I(q)$ at $P = 0.1$ MPa. With increasing P, however, the maximum diminished, similar to the case of the polymer solution, and completely disappeared at $P =$ 70 MPa. Further increase in P (> 200 MPa) led to re-appearance of scattering maximum but at a lower q value.

A comparison of the scattering profiles elucidated the essential roles of cross-links. In the case of polymer solution, macrophase separation takes place together with microphase separation at the low P region. However, an increase of P higher than 70 MPa led to suppression of microphase separation due to lowering a gain of the free energy originated from a negative volume change and destruction of iceberg-like structure of water molecules. The phase behavior and critical phenomena of PNIPA-AAc gels and solutions were discussed from the viewpoint of pressure effects on hydrophobic interaction.[3, 4]

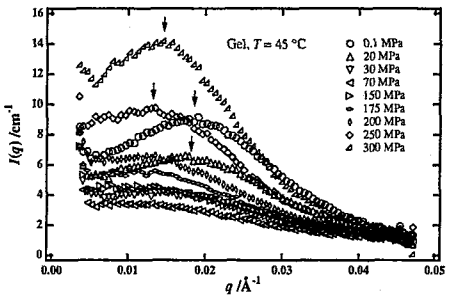

Fig. 1. Variation of $I(q)$s for PNIPA-AAc gel with pressure at $T = 45$ °C. The arrows indicate the positions of the scattering maxima. Note that peak disappears by increasing P and re-appears by further increasing P.

References

[1] M. Shibayama, *et al.*: J. Chem. Phys. **97** (1992) 6842.
[2] F. Ikkai, *et al.*: J. Polym. Sci. Part B, Polym. Phys. **43** (2005) 617.
[3] I. Nasimova, *et al.*: Macromolecules **37** (2004) 8721.
[4] I. Nasimova, *et al.*:J. Chem. Phys. **121** (2004) 9708.

使用施設：JRR-3M，装置： C1-2 (SANS-U)，分野： 6. Softmatter

研究テーマ：有機組織体の磁場誘起構造
表　題：磁場によって誘起される有機分子集合体構造

21) Magnetic-Field-Induced Structures of Organic Assemblies

I. Otsuka[1], T. Takahashi[1], T. Iiyama[1], H. Iwase[2], S. Koizumi[2] and S. Ozeki[1]

[1]*Department of Chemistry, Faculty of Science, Shinshu University, Matsumoto, Nagano 390-8621*
[2]*Advanced Science Research Center, JAERI, Tokai, Ibaraki 319-1195*

We showed that structure of organic molecular assembles such as micelles and vesicles may be controlled by steady magnetic fields. Under magnetic fields, vesicles composed of lipid bilayers changed the size and shape, but the mechanism is still an open question. Moreover, it was found that magnetic fields induced poly(*N*-isopropylacrylamide) (NIPA) gels to swell about 20% in size. These findings were attributed to magnetic orientation of domains comprising hydrocarbons and polymer chains. In this work, structural changes of membrane and polymer chain network induced by magnetic field was investigated by in-situ small angle neutron scattering (SANS) measurements.

SANS-J instrument at Japan Atomic Energy Research Institute (JAERI) JRR-3 research reactor was used with neutron wavelength of 0.65nm. Dipalmitoylphosphatidylcholine (DPPC) vesicles were prepared by the Bangham method. NIPA gels were obtained from aqueous solutions of 700mM *N*-isopropylacrylamide (NIPA) and 8.6mM *N*, *N*'-methylenebisacrylamide. The vesicles and gels in heavy water were put into a cell (1mm thickness) and set in a bore of a superconducting magnet at 298 and 318 K, respectively. SANS measurements were carried out at zero field and 9T which was applied in parallel to the cell.

SANS patterns of DPPC vesicle are shown in Fig. 1. The ring originated from lamellar structure was observed at zero-field. The ring became vague along besides x direction (the direction perpendiculat to a 9T magnetic field, suggesting that vesicles should be deformed from sphere to ellipsoid by magneto-orientation of lipid molecules. The radius of gyration R_G of vesicles (Table 1), estimated from the Guinier plot, changed from 66nm (sperical) to 55 (perpendicular) and 78nm (parallel) by a 9T magnetic field. The results are consistent with the formation of prolate ellipsoid under magnetic field, suggested by static light scattering technique.

The radius of gyration of NIPA gels estimated from the SANS intensity is summarized in Table 2. Under a 9T magnetic field, the radius of gyration changed associated with deformation of gel domains. This deformation again may arise from magneto-orientation of polymer chains which tend to orient in perpendicular to a magnetic field. In a swollen gel, the distance between chains would be large and thus it seems that no chains can orient cooperatively to magnetic field against thermal energy. Therefore, one may expect that hydrated water assists cooperative orientation of chains. Thermal analysis of the gels indicated that hydrated layer around polymer chains became thick under magnetic fields.

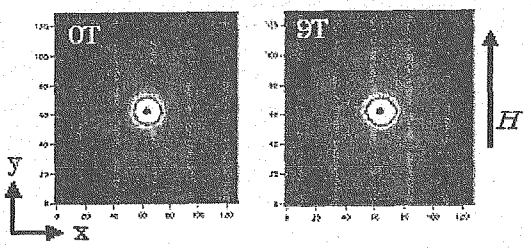

Figure 1: SANS patterns of DPPC vesicles.

Table 1: Radius of gyration of DPPC

Magnetic field	Radius of gyration
H / T	R_G / nm
0	66
9	55($H_\perp$)　78($H_{//}$)

Table 2: Radius of gyration of NIPA gels

Magnetic field	Radius of gyration
H / T	R_G / nm
0	6.6
9	7.2($H_\perp$)　6.2($H_{//}$)

原子炉：JRR-3　　装置：SANS-J(C3-2)　　分野：中性子散乱（高分子）

研究テーマ：高機能性ナノコンポジット型ハイドロゲルの機能発現メカニズムの解明
表題：PNIPA-クレイナノコンポジットゲルの構造とダイナミクス

22) Structure and Dynamics of Poly(N-isopropyl acrylamide)-Clay Nanocomposite Gels

M. Shibayama[1,2], J. Suda[1], T. Karino[1,2], S. Okabe[1], T. Takehisa[3], and K. Haraguchi[3]
[1] *Institute for Solid State Physics, The University of Tokyo, 106-1 Shirakata, Tokai, 319-1106*
[2] *CREST, JST, 4-1-8 Honcho Kawaguchi, Saitama 332-0012, Japan*
[3] *Kawamura Institute of Chemical Research, 631 Sakada, Sakura-shi, Chiba 285-0078, Japan*

Recently, clay-polymer nanocomposites have been gathering much attention because of their excellent physical properties. Haraguchi et al. reported a novel clay-polymer nanocomposite gels (NC gels) consisting of synthetic hectorite and poly(*N*-isopropyl acrylamide) (PNIPA). This NC gel has excellent physical properties, such as tough mechanical properties, large deformability, large swelling ratio, rapid shrinking capability, and high transparency.[1] We carried out structure investigation of the NC gels by small-angle neutron scattering (SANS) in order to account for their high strength and high deformability.[2]

NC gels were prepared by polymerizing a mixture of NIPA and an inorganic clay, synthetic hectorite (Laponite), $[Mg_{5.34}Li_{0.66}Si_8O_{20}(OH)_4]Na_{0.66}$ aqueous solutions with initiator and accelerator. The details of sample preparation are described elsewhere.[1, 2] SANS experiments were carried out at SANS-U, ISSP. The wavelength of the neutron was 7.0 Å. The structure of clay dispersions in water was found to be an assembly of clay platelets with 300 Å in diameter and 10 Å thick. The structure factors, $I(q)$, of the clay dispersions were reduced to a master curve by normalizing with the clay concentration, C_{clay}. On the other hand, the structure factors of the NC gels could not be represented with a simple addition of the structure factors of the components, i.e., the structure factors of PNIPA network and that of clay solution, but with a sum of Lorentz (L) and squared-Lorentz (SL) functions given by

$$I(q) = \frac{I_L(0)}{1+q^2\xi^2} + \frac{I_{SL}(0)}{(1+q^2\Xi^2)^2} \qquad (1)$$

where ξ and Ξ are the correlation length and the characteristic length of inhomogeneities, respectively.

It was found that the SL term, indicating the gel-inhomogeneities, becomes dominant by increasing C_{clay}. In Fig. 1 is shown the correlation length, ξ, for the NC gels is very close to that of PNIPA gel (the horizontal dotted line). This fact is quite reasonable since the PNIPA concentration is the same for all of the samples studied here. It is quite interesting to note that Ξ decreases with $C_{clay}^{-1/3}$ as shown by the dashed line. This indicates that the clay platelets are randomly dispersed in the three-dimensional space and the inter-platelet distance decreases with increasing the platelet concentration, C_{clay}.

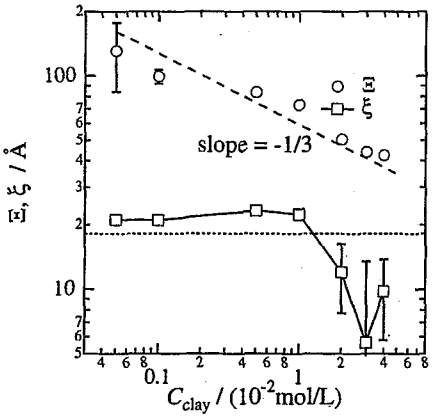

Fig. 1. C_{clay} dependence of the characteristic length of inhomoegneities, Ξ, and the correlation lenght, ξ. The dotted line indicates the value of ξ for the PNIPA solution shown for comparison.

References

[1] K. Haraguchi, *et al.* : Adv. Mater., **14** (2002) 1121.
[2] M. Shibayama, *et al.* : Macromolecules, **37** (2004) 9606.

使用施設：JRR-3M，装置： C1-2 (SANS-U)，分野： 6. Softmatter

研究テーマ：中性子散乱によるソフトマターの構造と機能の研究
表　題：中性子小角散乱によるリビングアニオン重合過程の検討

23) Small-Angle Neutron Scattering Study on the Process of Living Anionic Polymerization

N. Miyamoto,[1] S. Koizumi,[1] T. Hashimoto,[1] K. Yamauchi,[2] H. Hasegawa[2]

[1] *Advanced Science Research Center, JAERI, Tokai, Ibaraki 319-1195, Japan*
[2] *Department of Polymer Chemistry, Graduate School of Engineering, Kyoto University, Kyoto 606-8510, Japan*

Introduction Living anionic polymerization is known as an important technique to synthesize polymers with very narrow molecular weight distributions and/or with specific molecular structures such as block copolymers. It is generally accepted that anionic living ends and their counter cations are associated via electrostatic force to form aggregates in non-polar solvents. Szwarc *et al.*[1)] have been insisting that the effective concentration of living ends [P*] is lowered due to the presence of inert ionic aggregates, so that the reaction rate of living polymerization is governed according to $[P^*]^{\alpha}$ ($\alpha \leq 1$). By using small-angle neutron scattering (SANS), Fetters *et al.*[2)] reported that giant aggregates may exist and influence the living polymerization. Utilization of structural inhomogeneity in the system such as the aggregation of the living ends during the reaction will open up the way to rationally designing novel polymerization systems, where polymerization rate, stereoregularity, etc. are controllable; however, there is no systematic investigation and no investigation on the propagation process so far. Here we employ *in-situ* SANS and gel permeation chromatography to observe the process of the polymerization of isoprene on real time.

Experimental *Sec*-BuLi (5 wt % in cyclohexane), the initiator of the reaction, was purchased from Kanto Kagaku and was used as received. Since the living anionic reaction require strict elimination of water from the system, we conducted the experiments with a special care. For the SANS measurements, a glass tube with a branch was used as the vessel; the quartz cell was attached to the branch by using Teflon-coated o-ring as a connector. The tube was capped with a three-way stopcock, evacuated to vacuum, and purged with argon gas. This set up was enough to carry out the reaction without any unexpected termination of the living ends even with several times of pulling out samples for GPC measurements by using a dried syringe and needle. SANS measurements were performed on SANS-J located at JRR-3 atomic reactor, JAERI, Tokai-mura, Japan. GPC measurements were performed on Tosoh GPC-8020 equipped with a refractive index detector.

Results and Discussion The GPC measurement revealed that the average molecular weight at the final state is 5300 g mol^{-1} and the molecular weight distribution is very narrow, Mw / Mn = 1.03. The observed narrow molecular weight distribution is typical to living aninoic polymerization. Figure 1 show SANS q-profiles obtained at different time in the course of the living anionic polymerization of the polyisoprene. All the profiles shown are obtained by subtracting the data measured before the initiation step (before adding monomer to the solution of *sec*-BuLi in benzene-d_6) from the raw data. After the initiation step, the overall scattering began to increase. The change in the scattering profile indicates the increasing concentration and molecular weight of the polymer and even of the change in aggregation state.

Upon termination of the living polymerization by adding ethanol, SANS profile greatly changed (open circles in Figure 1). We clearly recognize two obvious changes as follows. First. strong upturn in the low-q region appeared ($q \leq 0.1$ nm^{-1}). This change is attributed to the generation of colloidal LiOH or $LiO(C_2H_5)$, which are insoluble in benzene. Second, the scattering intensity in the intermediate q-region ($0.2 \leq q \leq 1.0$ nm^{-1}) decreased, indicating decrease in the apparent molecular weight by the termination reaction. We attribute this observation that the living ends are associated to polymer aggregates in the lliving state, whereas the aggregated polymer disassemble to single polymers after the termination step.

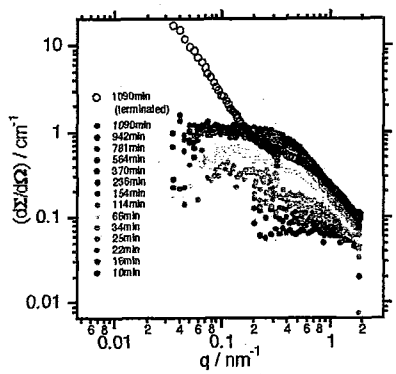

Figure 1: Time-dependent SANS profiles during living anionic polymerization of polyisoprene in benzene-d_6. The open circles represent the data measured after terminating the reaction.

References

1) M. V. Beylen, S. Bywater, G. Smets, M. Szwarc, and D. J. Worsfold: Adv. Polymer Sci. **86** (1988) 87.
2) L. J. Fetters, N. P. Balsara, J. S. Huang, H. S. Jeon, K. Almdal, and M. Y. Lin, Macromolecules **28** (1995) 4996.

原子炉：JRR-3　　装置：SANS-J(C3-2)　　分野：中性子散乱（高分子）

研究テーマ： トポロジカルゲルの滑車効果と不均一性解析
表題： トポロジカルゲルの滑車効果と不均一性解析

24) Pulley effect and spatial inhomogeneities of slide-ring gel

T. Karino[1,3], M. Shibayama[1,3], T. Kataoka[2], Y. Okumura[2,3], and K. Ito[2,3]
[1] *Institute for Solid State Physics, University of Tokyo, 106-1 Shirakata, Tokai, 319-1106*
[2] *Grad. School of Fronter Sciences, University of Tokyo, 5-1-5 Kashiwanoha, Kashiwa, 277-8561*
[3] *CREST, JST*

The spatial inhomogeneities of slide-ring (SR) gels were investigated with small angle neutron scattering (SANS). The SR gel was synthesized by coupling α-cyclodextrin (CD) molecules on polyrotaxane chains consisting of CD-threaded poly(ethylene glycol) (PEG)[?]. The cross-links of a SR gel can slide freely along the PEG chain. This implies that the network structure of SR gel might be able to rearrange homogeneously. We reported the static structure factor of a SR gel in previous works[?]. The purpose of this experiment was to observe sliding motion of CD molecules by uniaxial deformation.

Fig.1 shows the cross-link concentration, C_x, dependence of scattering intensity, $I(q)$. $I(q)$s decreased with increasing the cross-link density up to C_x=2wt% (CX20). In conventional chemical gels, $I(q)$ increases with increasing the cross-link density due to increase of cross-links inhomogeneities. On the other hand, the spatial inhomogeneities of the SR gels decreased by sliding the cross-links. At C_x=3wt% (CX30), however, $I(q)$ re-increased. This suggests that the sliding effect is suppressed by the large cross-link densities.

Fig.2 shows the two-dimentional scattering intensity patterns of C_x=1wt% (CX10) and C_x=2wt% (CX20). The stretching direction is horizontal. The scattering patterns of CX10 shows a "normal" butterfly pattern, which is a prolate isointensity pattern in the direction perpendicular to the stretching direction. This indicates that the spatial inhomogeneities hardly change by uniaxial stretching. On the other hand, CX20 shows an "abnormal" butterfly pattern, i.e., prolate patterns parallel to the stretching direction. Such "abnormal" butterfly patterns are generally observed in conventional chemical gel because the spacial inhomogeneities increased in the stretching direction. Hence, these results indicate that in high C_x, the mobile cross-links do not move effectively to reduce the spatial inhomogeneities[?].

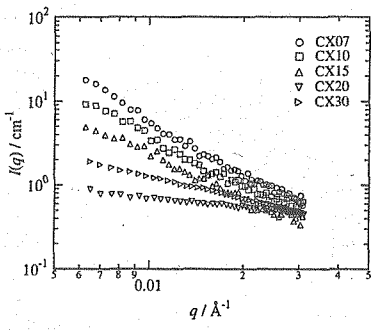

Fig. 1. The cross-link concentration dependence of the scattering intensity, $I(q)$.

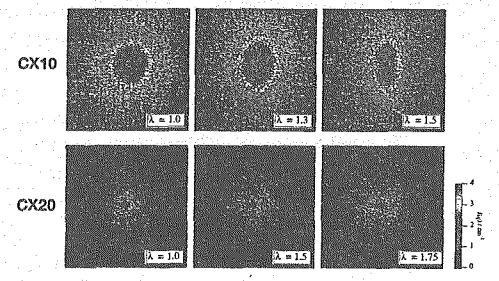

Fig. 2. SANS intensity patterns of the SR gel with CX10 (Cx = 1.0 %) and CX20 (Cx = 2.0 %). The stretching direction is horizontal.

References

[1] Okumura, Y. ; Ito, K. *Adv. Mater.* **2001**, *13*, 485.
[2] Karino, T. ; Shibayama, M. ; Okumura, Y. ; Ito, K. *Macromolecules* **2004**, *37*, 6177.
[3] Karino, T. ; Shibayama, M. ; Zhao, C. ; T. Kataoka, : Okumura, Y. ; Ito, K. *Macromolecules* in press.

使用施設：JRR-3M，装置： C1-2 (SANS-U)，分野： 6. Softmatter

研究テーマ：中性子散乱によるソフトマターの構造と機能の研究
表　題：水溶液中のニオブ酸ナノシートの構造観察と解析

25) Observation and Analysis of the Structure of Niobates Nanocheets in Aqueous Solutions

D. Yamaguchi[1], N. Miyamoto[1], S. Koizumi[1], T. Nakato[2] and T. Hashimoto[1,3]

[1] *Advanced Science Research Center, JAERI, Tokai, Ibaraki 319-1195*
[2] *Graduate School of Bio-Applications and Systems Engineering (BASE), Tokyo University of Agriculture and Technology, 2-24-16 Naka-cho, Koganei-shi, Tokyo 184-8588*
[3] *Department of Polymer Chemistry, Graduate School of Engineering, Kyoto University, Katsura, Bldg. A3/B1/010, Kyoto 615-8510*

Structure of exfoliated $K_4Nb_6O_{17}$ nanosheets in aqueous solutions were observed and analyzed by small-angle (SANS) and ultra-small-angle neutron scattering (USANS) spectrometers of JAERI (SANS-J and PNO) as well as ultra-small-angle X-ray scattering (USAXS) apparatus at Kyoto University. A comprehensive measurement revealed the structure of nanosheets in wide range of wave number, q, from 3 $\times$ 10^{-4} nm^{-1} to 1 nm^{-1}. In principle, structure of nanosheet depends on the concentration and the particle size of the nanosheet, and here we consider the particle size dependence at constant volume fraction of nanosheet $\phi \sim 3.6$ vol.%. In Figure 1 the whole scattering behavior of the two kinds of nanosheets, which have the same thickness of 1.8 nm but different lateral dimensions of 8μm and 0.2μm are presented. These scattering profiles can be featured as follows.

(i) In the smaller q region ($q < 1.3 \times 10^{-2}$ nm^{-1}) designated as region (a), the scattering profiles are independent of the nanosheet particle size and presented a power law behavior of which index is estimated as -2.5. This power low behavior is considered to indicate the mass fractal dimension of the assembled structure of nanosheets and interpreted as follows; in this scale, the assembly of the nanosheets takes similar three dimensionally crumpled conformation regardless of the lateral dimension of nanosheet.

(ii) In the intermediate q region (1.3×10^{-2} nm^{-1} $< q < 1.6 \times 10^{-1}$ nm^{-1}) designated as region (b), the scattering profiles deviate from power law of -2.5 and present different behaviors depending on the nanosheet particle sizes. In the case of nanosheets having lateral dimension of 8μm, the power law directly changed from -2.5 to -2 at $q \sim 0.01$ nm^{-1}. This slope change can be considered to occur due to the conformation change of the nanosheet from crumpled plate to flat plate and q the position where the slope changes is regarded as to be corresponding to the persistent length of the nanosheet. Namely, within the persistent length the nanosheet persists the rigidity and flat, while out of persistent length the nanosheet becomes bent and folded. While in the case of nanosheets having lateral dimension of 0.2μm the scattering intensity decreased abruptly at around $q = 0.02$ nm^{-1}, then plateau appears, persists up to q ~ 0.1 nm^{-1} and finally turns to power law of -2. This behavior is not clearly specified but can be speculated as due to the remarkable excluded volume effect and extent of q independent regime before the beginning of Guinier law. Both of these effect occurs due to the fact that the lateral dimension of the nanosheet is as small as the persistent length.

(iii) In the higher q region (c), ($q > 1.6 \times 10^{-1}$ nm^{-1}), several scattering maxima originated from the liquid crystalline order (or stacking) of nanosheets appear. In this region, the nanosheets whose lateral dimension is 0.2 μm shows higher degree of crystalline order. This fact is consistent with the drop of the intensity observed on region (b). The smaller nanosheets, which can be regarded as rigid flat plate, exhibit distinct excluded volume effects and consequently the distance between the nanosheet becomes rather uniform. While in the case of larger nanosheets, the lateral dimension of the nanoshhets is larger than the persistent length, and the individual nanosheet particle should be bent, resulting in irregularity in the distance between the sheet, which brings about the breadth of the scattering maxima. We can find that the exfoliated $K_4Nb_6O_{17}$ nanosheets have some similarity to an amorphous polymer chain which is a rigid rod within the persistent length but to be a flexible random coil in the scale out of persistent length. In other words, the exfoliated $K_4Nb_6O_{17}$ nanosheets can be regarded as a two-dimensional version of an amorphous polymer chain.

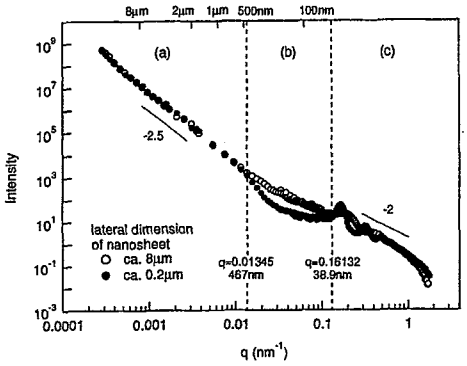

Figure 1: USANS, USAXS and SANS Combined Data for Nanosheet Solutions.

原子炉：JRR-3　　装置：SANS-J(C3-2)　　分野：中性子散乱（高分子）

研究テーマ： 有機ゲルのネットワーク構造
表題： 小角中性子散乱による有機ゲルのネットワーク構造の研究

27) Small-Angle Neutron Scattering Study on Network Structure of Organogels

S. Okabe and M. Shibayama
Institute for Solid State Physics, The University of Tokyo, 106-1 Shirakata, Tokai, 319-1106

Gelators are known to self-assemble in organic or aqueous solvents in terms of noncovalent interactions to form network structure. When the gelator concentration, C, is higher than the minimum gelation concentration, C_g, the system becomes self-supporting state, i.e., a gel, where the network covers the whole system. Recently, Dastidar et al. prepared a series of novel organic gelators with a combinatorial method.[?] Small-angle neutron scattering was carried out on one of the organogel systems containing a cholic acid derivative coded as 1a7b in order to investigate the structure of the gel network. A mixture of deuterated dimethyl sulfoxide (d-DMSO) and deuterated water (D_2O) (vol:vol=1:1) was used as the solvent since a transparent gel is obtained at the composition.

Fig. 1 shows the variation of SANS intensity function, $I(q)$, for 1a7b gels with C = 1.0 wt% during cooling process. Note that eht seven curves of I(q) wre classified to two states, i.e., sol and gel states. At high temperatures (sol state), there are only incoherent scattering arising mainly from hydrogen in the system, where the state is assign to be molecular dispersion. With decreasing temperature,a gel was formed, At these temperatures, $I(q)$ suddenly increased at low q regions and was scaled as $I(q) \sim q^{-4}$. This clearly indicates that the scattering objects consist of a two-phase structure with a sharp boundary (Porod's law) and there is no characteristic size in the observation window. By taking account of AFM observation (not shown here) and other studies on related gelator systems, we conclude that the state at lower temperatures contains rodlike objects with a broad distribution of the radius. Similar behavior was observed in the systems with different C's.

Fig. 2 shows reduced $I(q)$'s with respect to C =0.50, 1.0, and 5.0 wt% at 15 °C. Here, the incoherent scattering intensity is subtracted. Interestingly, the q^{-4} relationship is clearly observed for all of the systems and all the scattering functions are superimposed to each other by scaling with C. This indicates that the structures of gels are self-similar irrespective of the gelator concentration at least for $C \geq 0.50$ wt%. This also supports the AFM observation, i.e., an assembly of fibrous clusters having a wide range of thickness randomly oriented in the space.

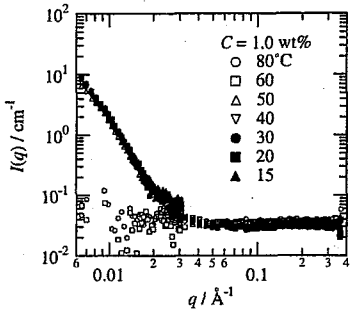

Fig. 1. $I(q)$s for 1a7b in (d-DMSO/D_2O) system with C =1.0 wt% during cooling process.

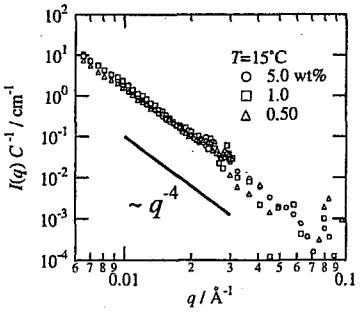

Fig. 2. SANS intensity functions for C =0.50, 1.0, and 5.0 wt% systems divided by C.

References

[1] P. Dastidar *et al.*: Chem. Mater. **17** (2005)741.

使用施設：JRR-3M, 装置： C1-2 (SANS-U) , 分野： 6. Softmatter

研究テーマ：中性子散乱によるソフトマターの構造と機能の研究
表　題：ヘテロジェミニ型界面活性剤の凝集構造

27) Aggregation Properties of Novel Heterogemini Surfactants with Nonidentical Headgroups

H. Iwase[1], S. Koizumi[1], T. Hashimoto[1,2], K. Nyuta[3], T. Yoshimura[3] and K. Esumi[3]

[1] *Advanced Science Research Center, JAERI, Tokai, Ibaraki 319-1195*
[2] *Department of Polymer Chemistry, Graduate School of Engineering, Kyoto University, Katsura, Kyoto 615-8510*
[3] *Department of Applied Chemistry and Institute of Colloid and Interface Science, Tokyo University of Science, Kagurazaka, Shinjuku-ku, Tokyo 162-8601*

Gemini or heterogemini surfactants, which consist of two hydrocarbon chains and two hydrophilic moieties connected by spacer, have been designed and synthesized by many researchers. Their surfactants have attracted an increasing amount of interest in recent years due to their essential properties, such as higher efficiency in reducing the surface tension at low concentration than the corresponding monomeric surfactants. In addition, unique structural properties are also reported. Thus, for synthesize of a novel surfactant, it is important to study not only physicochemical properties but also structural properties such as particle shape or size, membrane thickness, and so on.

In this study, in order to determine the phase diagram and to clarify the relationship between physicochemical and structural properties, we have investigated an aggregates behavior of recent synthesized heterogemini surfactants in aqueous solution by small-angle neutron scattering (SANS) experiments.

Surfactants used for the present experiments were zwitterionic heterogemini surfactants, N, N-dimethyl-N-[2-(N'-alkyl-N'-b-carboxypropanoylamino)ethyl]-1-alkylammonium bromides with nonidentical headgroups containing ammonium and carboxylate ($2C_nAmCa$, where n is the hydrocarbon chain lengths). Details of the procedure of sample synthesis were described elsewhere. [1] Their surfactants was solubilized in D_2O at pD=11 adjusted by adding NaOD.

The SANS experiments were performed on the SANS-J spectrometer at the JRR-3 of Japan Atomic Energy Research Institute (JAERI), Tokai, Japan. The neutron wavelength was 6.5 Å with $\Delta\lambda/\lambda = 0.12$. The sample-to-detector distances were 2 m and 10 m, and the total covered Q range is 0.003 - 0.15 $Å^{-1}$. The exposure time for one measurement was varied from 2 to 10 h, depending on a solute concentration and on the sample-to-detector distance. All SANS measurements were performed at room temperature. To obtain scattering data of low concentration samples with high-statistical accuracy, we employed the focusing geometry SANS (FSANS) experiments using a neutron-focusing lens of biconcave-shaped MgF_2 single crystal.

Figure 1 shows the phase diagram of zwitterionic heterogemini surfactants ($2C_nAmCa$) in aqueous solution. We have obtained the following results in the present SANS experiments. With increasing number of hydrocarbon chain n, the aggregated formation change showed the following tendency; spherical micelles→rod-like micelles→vesicles. Such a behavior is agreement with that of typical monomeric surfactants, and the theoretical prediction. [2] On the other hand, $2C_{12}AmCa$, whose critical micelle concentration (CMC) is the lowest in the $2C_nAmCa$ (n=8~14), showed the coexistence of rod-like micelles and vesicles above 300 times of CMC. By using a model fitting analysis of scattering dates, we suggested that the membrane bilayer forms an interdigitated structure in the vesicles. The coexistence of two different formations at wide concentration range and the interdigitated bilayer are extremely peculiar properties of the present heterogemini surfactant system.

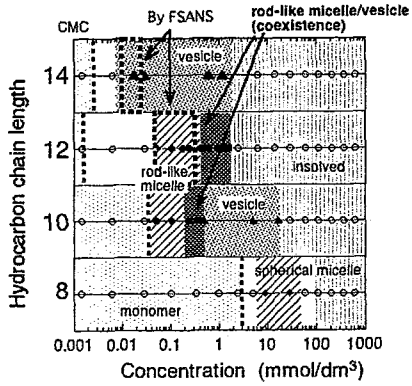

Figure 1: Structural phase diagram of zwitterionic heterogemini surfactants ($2C_nAmCa$) in aqueous solution.

References

1) T. Yoshimura, K. Nyuta, K. Esumi : Langmuir **21** (2005) 2682.
2) J. N. Israelachvili, D.J. Mitchell, B. W. Ninham : J. Chem. Soc. Faraday Trans. II. **72** (1976) 1525.

原子炉：JRR-3　　装置：SANS-J(C3-2)　　分野：中性子散乱（高分子）

研究テーマ：ゲル中に構造凍結された球状マイクロエマルションの構造解析
表題：中性子小角散乱による高分子ネットワーク中に混入されたマイクロエマルションの構造

28) Small-Angle Neutron Scattering Study on a structure of microemulsion mixed with polymer networks

M. Nagao, S. Okabe, and M. Shibayama
Institute for Solid State Physics, The University of Tokyo, 106-1 Shirakata, Tokai, 319-1106

The structure of a microemulsion mixed with polymer networks was investigated by means of small-angle neutron scattering (SANS). The system consists of nonionic surfactant, polymer network, oil, and water. As a nonionic surfactant, pentaethyleneglycol dodecylether ($C_{12}E_5$) was used, and a mixture of $C_{12}E_5$, water and octane was mixed with an *N*-isopropylacrylamide (NIPA) monomer solution. After the mixing these materials, NIPA monomer was polymerized by a redox polymerization with and without cross-linker. In the present measurement, native microemulsion, native PNIPA aqueous solution and gel, mixture of NIPA monomer and microemulsion (monomer-emulsion), mixture of PNIPA aqueous solution and microemulsion (polymer-emulsion), and mixture of PNIPA gel and microemulsion (gemulsion) were irradiated by neutron. Polymer solutions and gels were made by polymerizing monomer solutions in the presence of microemulsion droplets.

Figure 1 is shown the SANS result obtained from the native microemulsion and monomer-emulsion for the film contrast case. A scattering peak at $q \sim 0.06\text{Å}^{-1}$ for the native microemulsion shifted toward higher-q when NIPA monomer is added to the system. This result indicated the size reduction of the microemulsion droplets. Therefore, it is concluded that NIPA monomer behave as a co-surfactant.

Figure 2 shows the SANS profiles from the polymer-emulsion and gemulsion. Strong scattering intensity at low-q region indicates a phase separation to polymer-rich and -poor phases. Interestingly, however, SANS results indicated that a well-developed ordered structure of oil domains was formed in polymer network. Furthermore, the system underwent two different types of structural transitions with respect to temperature. One

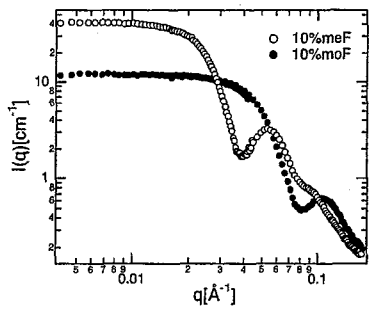

Fig. 1. SANS profiles obtained from the native microemulsion (10%meF) and monomer-emulsion (10%moF) at $T = 20\,^\circ$C.

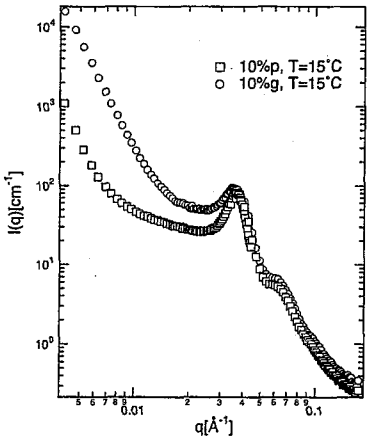

Fig. 2. SANS profiles obtained from the polymer-emulsion (10%p) and gemulsion (10%g) at $T = 15\,^\circ$C.

was originated from the structural transition of microemulsion due to the change of the spontaneous curvature and the other from the volume phase transition of NIPA gel. The detail of the present result is described in the submitted paper.[1]

References

[1] M. Nagao, S. Okabe, M. Shibayama: submitted to J. Chem. Phys.

使用施設：JRR-3M，装置：C1-2 (SANS-U)，分野：6. Softmatter

研究テーマ：中性子イメージングプレートを利用した合成高分子一溶媒複合システムの構造解析と溶媒効果の解明
表　題：中性子イメージングプレートによる全重水素化合成高分子の結晶構造解析

29) Structural Analysis of Fully-deuterated Crystalline Polymers on the Basis of 2-Dimensional Neutron Diffraction Data taken with an Imaging Plate System

K. Tashiro, I. Tanaka[1], T. Oohara[2], K. Kurihara[2], N. Niimura[1], S. Fujiwara[2], T. Tamada[2], and R. Kuroki[2]

Department of Future Industry-oriented Basic Science and Materials, Graudate School of Engineering, Toyota technological Institute, Tempaku, Nagoya 468-8511

[1]*Department of Engineering, Ibaraki University, Hitachi, Ibaraki 316-8511*

[2]*Neutron Science Research Center, Japan Atomic Energy Institute, Tokai-mura, Ibaraki 319-1195*

In order to solve the structure-property relationship of polymer crystals in a quantitative manner, we need to establish the atomic positions in the crystal lattices, in particular the positions of hydrogen atoms because most of the important intermolecular interactions, which govern the anisotropy of physical properties, are due to the H···H pairs of the adjacent polymer chains. In the previous paper[1)] we reported the detailed structural analysis of orthorhombic polyethylene crystal on the basis of 2-dimensional neutron fiber diffraction patterns taken for both the fully-deuterated and fully-hydrogeneous samples using a BIX-3 system installed in Japan Atomic Energy Institute. The successful extraction of hydrogen atomic positions was made, giving a stereochemically reasonable structural information with relatively small errors.

We applied this technique to the other crystalline polymers such as isotactic polypropylene, atactic poly(vinyl alcohol), poly(ethylene oxide), etc. For example, Figure 1 shows the 2D neutron diffraction patterns measured for (a) fully-deuterated and (b) hydrogeneous species of uniaxially oriented isotactic polypropylene samples. The difference in relative intensity of the observed reflections between these two species can be simulated quite well by using a software Cerius[2] (Accelrys) as shown in Figure 2. We are now trying to extract hydrogen atomic positions.

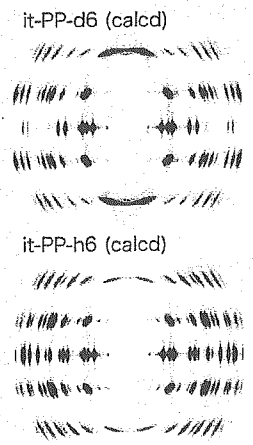

Figure 2: Simulated neutron diffraction patterns of it-PP-d6 and h6 samples.

References

1) K. Tashiro, I. Tanaka, Y. Oohara, N. Niimura, S. Fujiwara, and T. Kamae: Macromolecules **37** (2004) 4109.

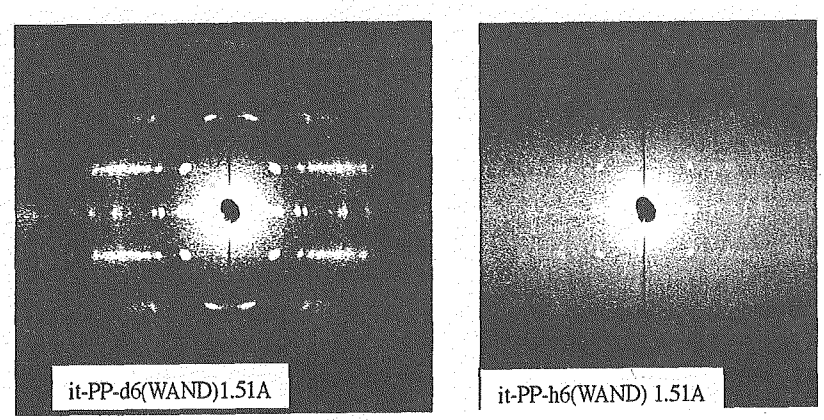

Figure 1: Neutron fiber diffraction patterns observed for (a) deuterated and (b) hydrogeneous isotactic polypropylenes.

原子炉：JRR-3　　装置：BIX-3(1G-A)　　分野：中性子散乱（高分子）

研究テーマ :中性子小角散乱を用いたシシカバブ構造解析
表題 :中性子小角散乱を用いたシシカバブ精密構造解析

30) Detailed Analysis for Shish-Kebab Structure with Small Angle Neutron Scattering

G. Matsuba, Y. Ogino, K. Nishida, T. Kanaya

Institute for Chemical Research, Kyoto University, Gokasho, Uji, Kyoto-fu, 611-0011 Japan

When semi-crystalline polymers crystallize under shear flow or drawing, crystallization rate is enhanced and the so-called "Shish-kebab structure can be observed with some scattering method and electron micrographs. The "Shish-kebab structure" consists of the long central fiber core (shish-structure) and an assembly of crystal lamella surrounded along the shish-structure (kebab-structure). It is considered that shish-structure is formed by stretched polymer chains. The kebab structure consists of the folded chain lamella crystals and grows to the direction normal to the shish-structure. The shish-kebab structure has been studied for a long time because it is structural origin of ultra-high modulus fiber.

In this study, the detailed analysis for the shish-kebab structure was carried out with small-angle neutron scattering (SANS) profiles in range of nanometer- and micron-scale. Samples are polymer blends consisting of ultra-high molecular weight protonated polyethylene (h-PE) with weight average molecular weight (M_w) of 2000000 and deuterated polyethylene (d-PE) with M_w of 200000. The blend including 1 wt % h-PE was prepared with the co-precipitation method. SANS measurements were performed with SANS-U spectrometer (C1-2) at JRR-3M reactor in Japan Atomic Energy Research Institute, Tokai, Japan. The wavelength of neutron was 7 Å and the sample to detector distance was 4000 and 8000 mm.

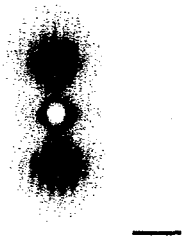

Figure 1: 2D SANS scattering images in DR =10. The drawing direction is longitudinal. The scale bar is q = 0.02 $Å^{-1}$.

Figure 1 shows SANS image of drawing h-PE and d-PE blends with drawing ratio (DR) = 10. The drawing direction is longitudinal, which is the same as the fiber direction. The two spots parallel to the drawing direction are assigned to long spacing period between oriented lamellae (kebab-structure). The equatorial streak -like scattering is observed normal to the drawing direction. This streak-like scattering must be due to the orientated shish-structure or the micro-fibrils along the drawing (fiber) direction. We analyzed the SANS data using the core-shell model mentioned below.

We assumed that the shish-kebab structure consists of a bi-layered cylinder [1], core-shell model with the radii of small cylinder, R_s, and of the overall large cylinder (shell), R_L. Figure 2 shows the cylinder with length 2H and radius R oriented in the direction (α,Ω) with respect to the reference angle z'. The incident beam propagates along x' axis and is scattered in the direction **s'**. μ is the azimuthal angle of observation and is the angle between the two planes, O-x'z' and O-$\mathbf{s}_0$**s'**, 2θ is the scattering angle and, $\mathbf{s}_0$ and **s'** are unit vectors parallel to the propagation direction of incident and scattered beams, respectively. The form factor of core-shell model of a cylinder would be written as follows;

使用施設 :JRR-3M, 装置 :SANS-U(C1-2), 分野 Softmatter

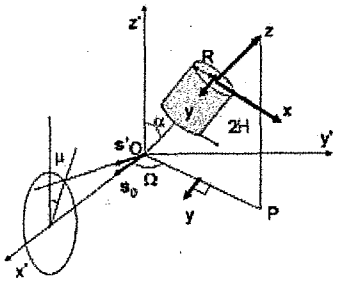

Figure 2: Schematic drawing of a cylinder with radius R and height 2H.

$$P_{shish}(q) = \{(\rho_s - \rho_L)V_s A(q, R_s, H_s) + (\rho_L - \rho_0)V_L A(q, R_L, H_L)\} \quad (1)$$

where ρ_s, ρ_L and ρ_0 are the scattering length density of the small cylinder, large one and the matrix. V_s and V_L are volumes of small and large cylinders with the radii of R_s and R_L, the height of $2H_s$ and $2H_L$, respectively. The form factor of a cylinder A(q, R, H) depends on both (α,Ω) and the azimuthal angle μ. In this the equatorial scattering case, the form factor of the cylinder A_{eq}(q,R,H) is given by [2];

$$A_{eq}(q,R,H) \sim \frac{\sin(qH\sin\Omega\sin\alpha)}{qH\sin\Omega\sin\alpha} \frac{2J_1(\sqrt{\sin^2\Omega\cos^2\alpha+\cos^2\Omega}qR)}{\sqrt{\sin^2\Omega\cos^2\alpha+\cos^2\Omega}qR} \quad (2)$$

where $J_1(x)$ is the first Bessel function of order 1.

Before fitting the theoretical function to the data, we should calculate the scattering length density in the model. For calculation of ρ_s, ρ_L and ρ_0, we assumed the component of each regions as follows. The small cylinder (core) and the matrix consist of crystalline pure h-PE and amorphous pure d-PE. The large cylinder (shell) is a mixture of crystalline 65 wt% d-PE and amorphous 35 wt% d-PE because calculated thickness of lamella and inter-lamella region of the kebab structure

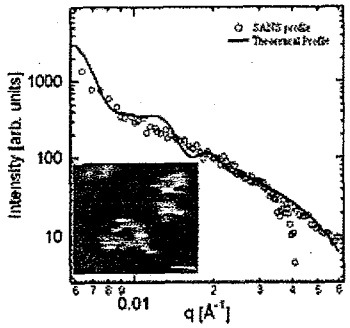

Figure 3: The scattering profile of SANS (open circle) and theoretical profile calculated from eq(2). The inset shows the scanning electron micrograph. The scale bar is 0.1 μm.

were 200 Å and 110 Å, respectively. Then ρ_s, ρ_L and ρ_0 are -3.57 x 10^9, 8.1 x 10^{10} and 7.28 x 10^{10} cm^{-2}, respectively. Figure 3 shows the SANS profile normal to the drawing direction in DR = 10 and the theoretical curve calculated from eq (2). The agreement is good. The obtained values are R_L = 950 Å, R_s = 50 Å and H = 15000 Å (1.5 μm). It is very difficult to evaluate the accurate value of H in the fit because it is too large compared with the pq-range of SANS measurement. However, the scanning electron micrograph (inset Figure 3) supports the value of 2H (several μm).

From the fits, the fraction of shish core (all h-PE crystal) in overall cylinder is about 0.25 %. The results suggests that h-PE chains exist not only in the shish core but in overall cylinder (kebab-structure). The h-PE chains in kebab structure should be taken into account in the structural analysis of kebab-structure.

References

[1] M. Nakano et al., Macromolecules, **32** (1999) 697.
[2] M. Shibayama et al., J. Appl. Phys. **66** (1989) 4188.

研究テーマ：ヒトヘモグロビンの高次構造と酸素挙動の中性子構造生物学研究
表題：中性子回折によるヒトヘモグロビンの構造研究

31) Neutron Structural Study on Human Hemoglobin

Y. Morimoto, S. Y. Park[1], N. Shibayama[2], K. Kurihara[3], I. Tanaka[4], N. Niimura[5], T. Tamada[3] and R. Kuroki[3]

Research Reactor Institute, Kyoto University, Kumatori, Osaka 590-0494
[1]Yokoharma City University, Turumi, Yokohama 230-0045
[2]Department of Physiology, Jichi Medical School, Minamikawachi, Tochigi 329-0498
[4]Neutron Science Research Center, Japan Atomic Energy Research Institute, Tokai, Ibaraki 319-1195
[4]Faculty of Engineering, Ibaraki University, Hitachi, Ibaraki, 316-8511
[5]Graduate School of Science and Engineering, Ibaraki University, Hitachi, Ibaraki, 316-8511

The most popular protein in a protein crystallography is a hemoglobin which plays an important role of oxygen molecules in the living organisms by highly controlled quaternary structural changes. The precise structure of the hemoglobin has been obtained by X-ray or synchrotron radiation at atomic resolution, and the result depicts how a residue near heme group does a function and a salt bridge at the terminal of the molecule stabilize a quaternary structure. Since, there are so many mechanisms are presented how hydrogens or protons near the heme groups to control an oxygen concentration in human blood, we are starting a structural study oh the hemoglobin by the neutron diffraction method. Here we report results of the neutron experiment and interpretative nuclear distribution maps for the hydrogens.

The hemoglobin was isolated and purified from human blood, and crystallized by a batch method under the anaerobic conditions. A protein concentration was 10 mg/ml and a protein solution was prepared to be 4.3M NH_4, 1.94M SO_4, 0.242M PO_4, by D_2O. A deoxy-form hemoglobin crystal was obtained during one month and the size was about 3 × 3 × 4 mm, and packed for a neutron experiment in a special quartz capillary with a small amount of a mother liquor and chemicals for oxygen eater. Neutron diffraction data were collected by the BIX-3 diffracotmeter installed at JRR-3 reactor, JAERI Tokai. The expected cell dimensions of the crystal are 80 Å, still photographic method was applied. In order to collect a higher resolution data an exposure period was set to 110 minutes a frame. This crystal obtained from ammonium sulfate solution was space group $P2_1$, data acquisition was required for a hemi-sphere in the reciprocal space. We collected and merged diffraction spots from 1,209 frames.

Table 1: Data statistics

Crystallographic Data	
Cell dimensions	
a=63.792, *b*=84.445, *c*=54.347Å, b=99.33°	
a=63.105, *b*=82.914, *c*=53.650Å, b=99.29°	X-ray data
Space group = P2₁	
Z = 2	
Resolution	= 62.95 - 2.1Å
No. of refs.	= 56,073
unique	= 21,841

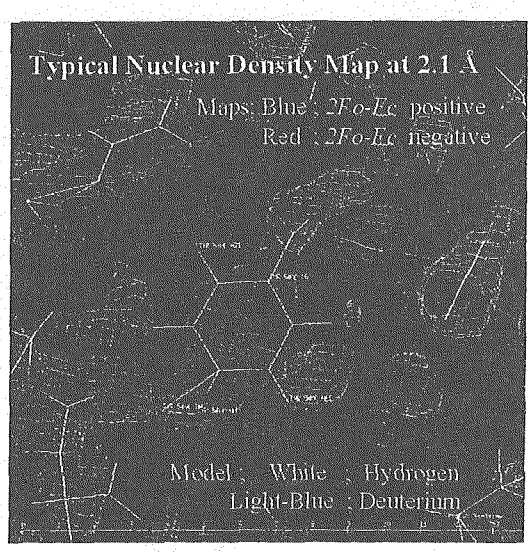

Figure 1: Typical nuclear density map.

原子炉：JRR-3　　装置：BIX-3（1G-A）　　分野：中性子散乱（高分子）

研究テーマ：高分子鎖を内包した膜の形態転移
表題：高分子の拘束が誘起する球状マイクロエマルションのネマチック転移

32) Polymer-Confinement-Induced Nematic Transition of Microemulsion Droplets

K. Nakaya and M. Imai

Department of Physics, Faculty of Science, Ochanomizu University, 2-1-1, Otsuka, Bunkyo-ku, Tokyo, 112-8610, Japan

The effects of the polymer confinement become more pronounced when polymer chains are confined inside of a spherically closed membrane. Such confinement reduces the conformational entropy of polymer chains considerably, which may induce new membrane morphologies. In this study we show a series of morphology transitions of microemulsion droplets induced by changing the degree of polymer confinement [1].

Since in microemulsion systems the oil and water regions are separated by surfactant monolayers, the microemulsion droplets can confine the polymer chains inside of the closed nano-space by selecting the solubility of the polymer to the solvent. As a typical example, we studied a water-in-oil microemulsion droplet system consisting of water, isooctane, surfactant AOT (sodium bis (2-ethylhexyl) sulfosuccinate), to which system a gelatin is added as a water-soluble polymer. A gelatin is a linear random-coil molecule and has high solubility to the nano - scale water pool. The gelatin is purchased from Sigma Co. Ltd. It has Bloom strength of 300 and the z-averaged molecular weight of 96,000 with a rather large polydispersity. The degree of confinement of the gelatin is characterized by two parameters, i.e., the ratio of the end-to-end distance of a gelatin chain in the bulk state to the diameter of a spherical water pool $R_F/2R_S$, and the average polymer weight concentration W in the water pool. The radius of gyration of a gelatin molecule R_g obtained by SANS measurements is R_g = 89 Å, and we assumed that $R_F = \sqrt{6}R_g = 218$ Å for simplicity. We controlled the radius of the water pool, R_S, with keeping the total volume fraction of droplets $\phi = \phi_{sur} + \phi_{dis}$ constant, where ϕ_{sur} and ϕ_{dis} are the volume fractions of surfactant and dispersed water phase. In the SANS measurements, we employed the film contrast condition, i.e., we used deuterated oil, water, hydrogenated surfactant and gelatin. SANS measurements were carried out with the SANS-U (C1-2) instrument of ISSP at the JRR3M in JAERI (Tokai).

We first show the change in the scattering profiles induced by the confinement of the gelatin chains in the spherical microemulsion droplets in Fig. 1. This experiment was performed at a dilute solution of droplets, i.e. ϕ = 0.07. The scattering profile of the microemulsion droplets without gelatin has a characteristic maximum at q_{max}=0.06 Å^{-1} (q is the magnitude of scattering vector) and well fitted by the following expression

$$I(q) = nP(q)S(q) \qquad (1)$$

where n is the number density of droplets, $P(q)$ is the form factor for a spherical core-shell structured particle [2], and $S(q)$ is the structure factor of the Percus-Yevick model [3]. The fitting result using this model is shown by the solid line with the values of the fitting parameters $n = 5.4\times10^{16}$ /cm^3 , the length of a surfactant molecule δ = 8 Å, and $2R_s$ = 119.6 Å. By introducing the gelatin chains inside the droplets, the characteristic maximum shifted to a larger value of q_{max}= 0.08 Å^{-1}, and the scattering

使用施設：JRR-3M，装置：SANS-U(C1-2)，分野 106(Softmatter)

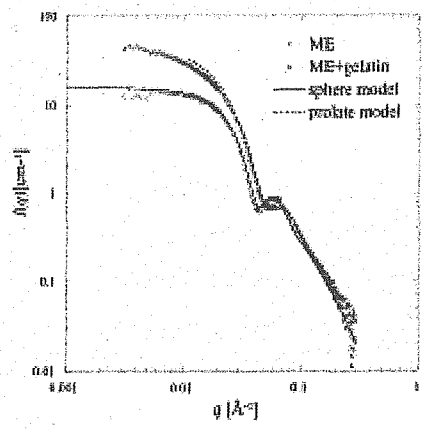

Fig.1:SANS profiles for water-in-oil micro-emulsion droplet consisting of AOT-isooctane-water at ϕ=0.07 without (circle) and with (triangle) gelatin of W=9% at 30°C. The solid and dashed lines are fitting results with the sphere core shell and the prolate core shell model, respectively. The quantitative $S(q)$ of the prolate model is obtained from our Monte Carlo simulation.

intensity in the low q region increased considerably. In this case, the degree of confinement is $R_P/2R_S$ = 1.82 and the gelatin concentration in the water pool is W = 9.1wt%. In contrast to the pure droplet microemulsion, the scattering profile of the micro-emulsion containing the gelatin cannot be explained by the scattering function of the spherical model. Instead we can fit the observed profile using a prolate core-shell model [4]. The structure factor $S(q)$ for the prolate model was obtained by the Monte Carlo simulation of hard spherocylinders with corresponding rod size and volume fraction. The fitted curve using this model is given in Fig.1 by the dashed line that agrees well with the observed profile. The obtained fit parameters are R_c=41.3Å, the mean axis ratio $a_m \sim 4$ and n = 4.0×10^{16} /cm^3. This means that the averaged number of gelatin chains per droplet is roughly 0.8. Thus, the microemulsion droplet deforms from the spherical shape to the rod-like one by confining gelatin chains.

Based on the above experimental results, we expect that the rod-like droplets exhibit an isotropic - nematic transition when droplets are concentrated. Fig. 2 shows the evolution of the 2D scattering patterns of a concentrated solution of droplets (ϕ = 0.4) as a function of the polymer concentration W at 33°C. Here we fixed $R_P/2R_S$ = 1.43. Without gelatin, the scattering pattern shows an isotropic ring arising from the characteristic form factor peak, which is pronounced by the suppression of the scattering intensity in the low q region due to the structure factor. At W = 26%, the scattering pattern begins to show a highly oriented rod-like droplet phase. These results clearly demonstrate that the isotropic - nematic transition of the rod-like droplets is induced by the gelatin confinement. The interesting point here is the fact that combining a spherical droplet and a spherical polymer coil spontaneously forms an anisotropic structure.

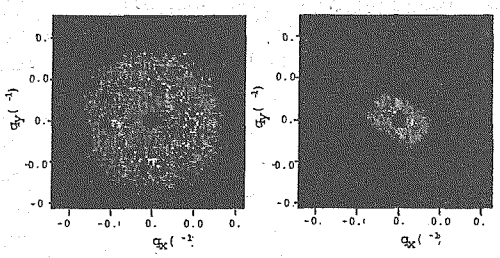

(a) W =0 *wt.%* (b) *W*=26 *wt.%*

Fig.2: The two-dimensional SANS patterns of the microemulsion confining polymer chains at 33°C. Concentrations of added polymer are (a)W=0 and (b)26 wt%.

References

[1] K. Nakaya and M. Imai et al, *Europhys. Lett.* in press
[2]A. Guinier and G. Fournet, *Small-Angle Scattering of X-rays* (Wiley, New York, 1995).
[3]J.K. Percus and G. J. Yevic, *Phys. Rev.* **110** (1958) 1.
[4] M. Kotlarchyk and S-H. Chen, *J. Chem. Phys.* **79** (1983) 2461.

研究テーマ：中性子散乱によるソフトマターの構造と機能の研究
表　題：中性子小角散乱による準リビング重合の観察

33) Small-angle Neutron Scattering Study on *In-situ* Observation of Poly(*N*-isopropylacrylamide) - *block* - Poly(ethylene glycol) Quasi-living Polymerization

R. Motokawa, S. Koizumi, T. Hashimoto, and M. Annaka[1]

Research Group of Neutron-Scattering Soft Matter, Advanced Science Research Center, JAERI, Tokai, Ibaraki 319-1195, Japan

[1]*Department of Chemistry, Kyushu University, Fukuoka 812-8581, Japan*

To synthesize an amphiphilic block copolymer of poly(*N*-isopropylacrylamide) - *block* - poly(ethylene glycol) (NE), a soap-free emulsion polymerization method was employed in an aqueous medium, where Poly(*N*-isopropylacrylamide) (PNIPA) was polymerized from the radically activated chain ends of poly(ethylene glycol) (PEG). As the polymerization proceeds, PNIPA block chains form micelle cores stabilized by PEG brush chains emanating therefrom. When this polymerization was carried out at temperatures equal to or higher than 34°C, narrowly-dispersed NE, which cannot be obtained by solution polymerization, was successfully obtained. Time-resolved gel permeation chromatography (GPC), enabling us to observe time-dependent monomer conversion and molecular weight of NE, revealed that radical polymerization proceeds living-likely. To elucidate origins of the quasi-living nature, we employed time-resolved ultra-small- and small-angle neutron scattering (USANS and SANS), which are advantageous to explore micelle formation during polymerization.

SANS-J spectrometer was installed at JRR-3 of JAERI at Tokai and covers a q-range of $0.03 \leq q \leq 1$ nm^{-1}and the incident neutron of $\lambda = 0.65nm(\Delta\lambda/\lambda = 13\%)$. The scattered neutrons were detected by a 2-dimensional ^{3}He position-sensitive detector of 0.58 m diameter. The 2-dimensional data were first corrected for counting efficiency, instrumental background and air scattering. After circular-averaging, we converted scattering intensity to absolute unit of cm^{-1} using a secondary standard of irradiated Al. Incoherent scattering from hydrogen was subtracted as the background by using a higher q-region where the scattering profile becomes q-independent. The double crystal spectrometer PNO is able to cover a q-region of ultra small-angle neutron scattering (USANS) of $10^{-4} \leq q \leq 10^{-2}$nm^{-1}, λ=0.2 nm. NIPA monomer and PEG were dissolved in D_2O, then $Ce(NO_3)_6(NH_4)_2$ was added to the solution as a redox initiator. The polymerization solutions were filled in a quartz cell of 2 mm thickness, which gives transmittance of 70%. The sample temperature was controlled for polymerization temperature at 25, 34, 40, 50, and 60°C. Then, the NE block copolymers were polymerized under the neutron beam.

Figure 1 shows the q-profiles for end of polymerization products with different polymerization temperatures. In the temperature range above 34°C, we observed the asymptotic q-behavior, $I(q) \sim q^{-4}$, originating from the interfacial structure of aggregated emulsion. We can estimate micelle core size, R, by form factor with a spherical shape, taking into account a log-Gaussian distribution for R. As the temperature increase from 34°C, the values of R become smaller. The solidity of micelles core were evaluated by R and M_n of block chain composed of micelle core.

On the basis of these *in-situ* and real-time SANS observations, it was revealed that (i) from 25 to 60°C, polymerized NE forms micelle in the solution when molecular weight reaches to a critical molecular weight for micelle formation, $M_{n,c}$, and (ii) as the temperature increases from 34°C, a water content in the micelle core becomes less because PNIPA block chains have a lower critical solution temperature around 34°C. These results obtained by GPC, USANS, and SANS strongly support our scenarios and low diffusivity of chain end radicals compartmentalized in the micelle core, effectively supressing the terminatiion reactions, leads to the quasi-living behavior of the polymerization.

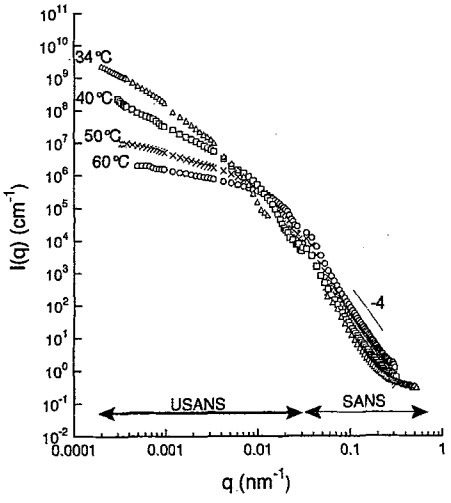

Figure 1: SANS profiles were obtained for end polymerization mixture at different polymerization temperature, 34 (triangles), 40 (squares), 50 (crosses), and 60°C (circles).

原子炉：JRR-3　　装置：PNO(3G)　　分野：中性子散乱（高分子）

研究テーマ：ずり流動場により誘起される界面活性剤ラメラ相の局所的相分離と膜のダイナミックス
表題：非イオン界面活性剤 ($C_{16}E_7$) /水２成分系におけるずり流動場誘起構造転移

34) Shear-Induced Structural Transition in a Binary System of Nonionic Surfactant ($C_{16}E_7$) /Water

K. Miyazaki, Y. Kosaka, Y. Kawabata, and T. Kato

Department of Chemistry, Tokyo Metropolitan University, Hachioji, Tokyo 192-0397, Japan

In the past 10 years, much attention has been paid to the effects of shear flow on the structure of a lamellar phase owing to the development of the apparatus which enables us to determine their structures directly under shear flow. In the previous studies, we have measured small-angle neutron scattering (SANS) on the lamellar phases of a nonionic surfactant $C_{16}H_{33}(OC_2H_4)_7OH$ ($C_{16}E_7$) in D_2O at 40, 48, and 55 wt% at 70°C under shear flow for the shear rates 10^{-3}–10 s^{-1} which is much lower than those for other studies reported so far. We have found anomalous decrease in the lamellar spacing for the shear rate of 0.1-1 s^{-1} suggesting local phase separation into concentrated lamellar and water-rich regions. In the present study, we have measured shear-strain dependence of SANS patterns under a constant shear rate to investigate the mechanism of the transition and to check whether the previous results depend on the shear history or not.

Measurements of SANS were carried out at the instrument SANS-U of Institute for Solid State Physics of University of Tokyo in JRR-3M at Tokai with a Couette shear cell [1]. Under a constant shear rate (0.3, 1, 3, 10, and 30 s^{-1}), time-resolved 2-D SANS patterns have been collected for about 6 hours for the sample containing 48 wt% of $C_{16}E_7$ at 70°C. Measurements have also been made for about 2 hours after stopping shear.

Figure 1 shows time evolution of 2-D SANS patterns after applying shear flow at 1 s^{-1} for the sample containing 48 wt% of $C_{16}E_7$ at 70°C. About 100 min after applying shear, a new diffraction peak appears at higher q and coexists with initial diffraction peak, suggesting some sort of transition. After 200 min, the peak at lower q disappears. These results indicate that the repeat distance decreases discontinuously. The decrease in the repeat distance has also been observed for the shear rates 3 - 30s^{-1}. It has been found that the repeat distance in the steady state takes a minimum around 1 s^{-1}, which is in good agreement with our previous results where the shear rate increases from lower to higher [2].

References

[1] Y. Takahashi et al., J. Soc. Rheol. Jpn. **28** (2000) 187.
[2] T. Kato et al. Langmuir **20** (2004) 3504.

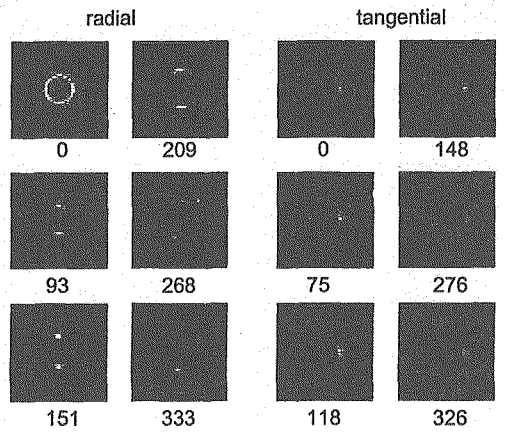

Fig. 1 Time evolution of 2-D SANS patterns after applying shear flow at 1 s^{-1} for the sample containing 48 wt% of $C_{16}E_7$ at 70°C for the radial (left) and tangential (right) configurations. The numerals indicate the time in minutes after applying shear flow.

使用施設：JRR-3M, 装置：SANS-U(C1-2), 分野 Soft matter

This is a blank page.

1. 中性子散乱 6) 生物学

1. Neutron Scattering 6) Biology

This is a blank page.

研究テーマ：細胞における蛋白質の高次構造化不全と細胞の異常死に関する研究（II）

表　題：中性子溶液散乱によるタウ蛋白質の構造研究

1) Mono-dispersed Structure of Tau in Water by Neutron Scattering

S. Naito[1,2], H. Mochizuki[2], T. Yasuda[2], Y. Mizuno[2], M. Furusaka[3], S. Ikeda[1], T. Adachi[4], M. H. Shimizu[4], J. Suzuki[5], and S. Fujiwara[5]

[1]KEK, Tsukuba, Ibaraki 305-0801, [2]Dept. of Neurol., Juntendo Univ. Sch. of Med., [3]Dept. of Mech. Intell. Eng., Grad. School of Eng., Hokkaido Univ., Kita 13, Nishi 8, Kita-ku, Sapporo 060-8628, [4]RIKEN, 2-1 Hirosawa, Wako, Saitama 351-0198, [5]Japan Atomic Energy Research Institute, Ibaraki 319-1195

Tauopacy is the abnormal aggregation of tau which is one of the microtubule-associated proteins often observed in Alzheimer's disease and Parkinson's disease brain. Such an abnormal protein aggregation in cells causes cellular degeneration and death, and finally end up with grave disorders. In order to understand the origin of the disease it is important to understand the abnormal state of these proteins (resulting from proteolysis, phosphorylation, or other modifications including disulfide bond (SS) formation) and the subsequent aggregation.

Last year, we have preliminarily observed the *de novo* synthesized human recombinant human tau by small-angle neutron scattering (SANS-J and SWAN). SANS showed tau (46KDa, consisting of 448a.a.) behaved in water as if it were originally and highly polymerized rod-like fibers (Ø= 18 Å in Figure.2) although the SDS-page showed tau was refined to a single molecule[1].

This result suggested lots of tau molecules were tightly cross-linked with intermolecular covalent bind, such as a disulfide bond, or aggregated by intermolecular hydrophobic interaction. We examined the variation of the tau structure in water at below C* at before and after treating with urea or heating with 10 mM reducing agent (dithiothreitol, DTT) by dynamic light scattering (DLS). Figure 1 shows the variation of the characteristic decay time distribution corresponding to R_H (hydrodynamic radius) by reducing cystine bonds (SS bond) with heating. The polymerized tau was observed at 37°C but the single dispersion profile became observed at 60°C and the size distribution gradually spread with the increase of temperature. Thus, tau was polymerized and formed fibrous structure by the intermolecular SS bond. SANS were conducted at SANS-J+40 lens [neutron wavelength (λ=6.4 Å), sample distance (L=9.6 m)] situated at the end of a cold-neutron guide tube from the JRR-3 reactor and at the WINK, small and wide angle diffractometer at the KENS (Pulsed Neutron Scattering Facility in KEK). Figure 2 shows the SANS profile of the single dispersed tau (after 60°C heating) at low concentration (~100 mg/ml) in the buffer (50 mM Tris-HCl buffer, pH 7.0 containing 10mM DTT). Tau formed multimers without intermolecular disulfide bonds by self-assembly. The radius of

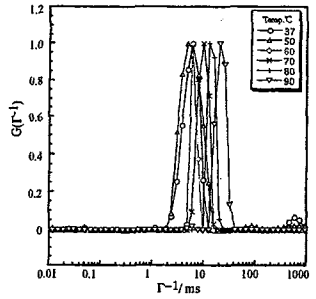

Figure 1: The variation of characteristic decay time distribution function, $G(\Gamma^{-1})$, for tau solution.

gyration of the tau cluster was estimated to be 272 Å from the Gunier analysis on the SANS profile in the lower q ranges. This size was very huge, meaning at least several thousand tau molecules were gathered by unknown self-assembly system. Furthermore, the SANS profile in the wider q ranges suggested the cluster might have an ambiguous but somewhat definit internal structure, like a micell of core-shell type. Such a formation of cluster having internal structure has been known to the other the amorphous proteins, i,e., crystalline. Tau may recognize each other in a special way and aggregate easily if there are not other proteins, such as microtubles. The reason tau having less crystalline structure, such as α-helix and β-sheet, forms rod structure has been unknown, especially in neurocyte of Alzheimer's disease and Parkinson's disease. Here, we could demonstrate the abnormal fibrillation of tau caused by intermolecular SS bonds under oxidative stress.

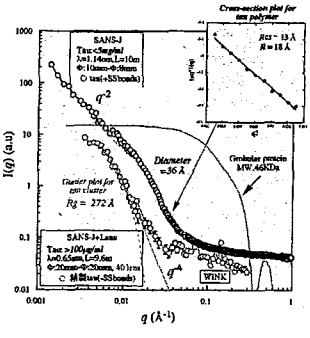

Figure 2: SANS profiles of fibrous tau by cross-linked SS bonds and the single dispersed tau in water.

Reference

1) S. Naito *et al.*, JAERI-Review 2005-013 (2005) 39.

原子炉：JRR-3　　装置：SANS-J (C3-2)　　分野：中性子散乱（生物）

研究テーマ：IgA分子のコンフォメーションと糖鎖との関係について
表　題：IgA溶液に関する中性子小角散乱測定

2) Small Angle Neutron Scattering Study for IgA Solutions

K. Onuma[1], S. Fujiwara[2], T. Kubota[1], Y. Narimatsu[1] and H. Narimatsu[1]

[1] *National Institute of Advanced Industrial Science and Technology, Tsukuba, Ibaraki 305-8566 Japan*
[2] *Neutron Science Research Center, JAERI, Tokai-mura, Naka-gun, Ibaraki 319-1195 Japan*

Every year, in Japan, about 100,000 people receive dialysis treatment for chronic renal failure. Once this condition has advanced, there are no effective recovery methods, and because the treatment period is extremely long, lasting more than 10 years, there is an extremely large economic burden on patients. There are two main factors that result in chronic renal failure: deterioration of renal functions due to diabetes, and an illness called IgA nephropathy. A glycoprotein called IgA (immunoglobulin A) exists within human blood, and performs a variety of functions. IgA nephropathy is a condition in which this IgA accumulates abnormally for some reason, and forms deposits within the glomeruli (filters) in the kidneys, causing inflammation.

There is no clear explanation of why aggregates of IgA, which normally is distributed in individual monomers, are formed in the blood. One broadly accepted theory is that the sugar chains in the IgA molecules of a healthy person are partially cut for some reason, and that as a result the interactions among IgA molecules change, causing the deposits to form. In fact, on an examination of the IgA aggregates sampled from the kidney tissue of patients afflicted with IgA nephropathy, the sugar chains are found to be deficient. This in itself, however, is not proof of an abnormality in the IgA molecules (sugar chain deficiency) in the patient's blood. In order to reach the conclusion that a deficiency in sugar chains that should normally be attached to the molecules is a factor in IgA nephropathy, we must examine and compare the IgA molecules in the blood of healthy persons and IgA nephropathy patients. To pursue this question further, we observed IgA molecules using Small Angle Neutron Scattering (SANS).

This year, we observed IgA refined from blood samples from healthy persons. Taking into consideration human biological conditions, we dissolved the IgA in a tris buffered 50mM solution, and adjusted to a pH of 7.4. For the measurement, we replaced the water in the solvent medium with heavy water having a different concentration, and then derived and analyzed the scattering curve for the heavy water concentrations. Figure 1 shows the scattering curve measured. The five curves, starting from the top, represent heavy water concentrations of 96.9, 77.0, 63.6, 0, and 18.2%. We analyzed the resulting scattering curves using a Guinier plot, and calculated the I(0)/c and radius of gyration for IgA in each heavy water. We found that the radius of gyration fell between 21.2nm and 24.0nm. Based on this information, we did a Stuhrmann plot, and attempted to derive information on the internal structure of the scatterer. Figure 2 shows the results of the Stuhrmann plot. We approximated the plot data with a 2-D curve, and determined the parameters. The results suggest that the region with a high concentration of scattering length (believed to be equivalent to the sugar chain region) is near the center of the scatterer.

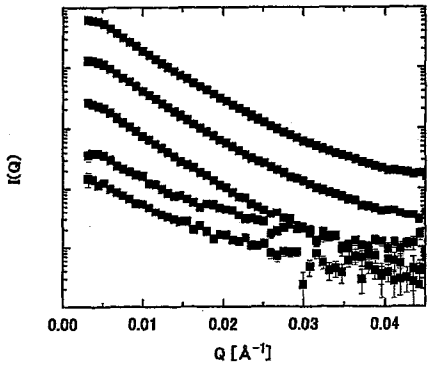

Figure 1: SANS scattering curves depending on the concentration of heavy water.

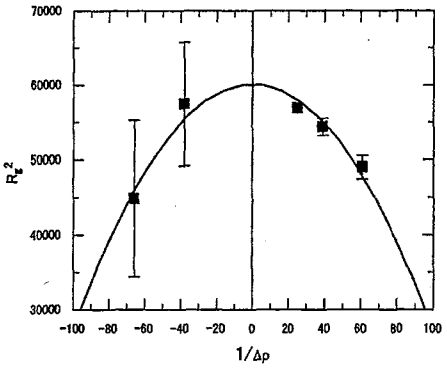

Figure 2 : The Stuhrmann plot for IgA solution.

原子炉：JRR-3　　装置：SANS-J（C3-2）　　分野：中性子散乱（生物）

研究テーマ：シャペロニン GroEL-標的ペプチド-GroES 複合体の中性子散乱法による構造解析
表　題：シャペロニン GroEL-標的ペプチド-GroES 複合体の構造解析 1

3) Neutron Scattering Study on Chaperonin GroEL-Target Protein- GroES Complex1

K. Ichimura, S. Fujiwara[1], Y. Kawata[2], and H. Kihara[3]

Department of Biochemistry, Dokkyo University Medical School, Mibu, Tochigi 321-0293
[1]*Neutron Science Research Center, JAERI, Tokai, Ibaraki 319-1195*
[2]*Department of Biotechonology, Tottori University, Tottori 680-8552*
[3]*Department of Physics, Kansai Medical University, Hirakata 573-1136*

The aim of the present study is to elucidate structure of target proteins when they are bound to chaperon protein, GroEL-GroES complex, and to observe the structure of GroEL at the ternary complex.

When proteins are synthesized *in vivo*, they are apt to fold with the aid of chaperon proteins. GroEL, a chaperon protein from *E. coli*, forms hydrophobic bonds with the newly synthesized target protein, assisting the folding of the target protein. We have performed structural analysis of GroEL by X-ray and neutron scattering.

One of the most interesting subjects is to elucidate the conformation of the target protein bound to GroEL. It is a difficult task, as (1) the target protein binds to GroEL only as a kinetically stable intermediate, and (2) the target protein is usually small compared to GroEL. By using contrast variation method, it is possible to observe only the target protein in the "transparent" GroEL. It can be realized either with the use of the deuterated target protein or with the use of the deuterated GroEL. However, it is a difficult problem to observe kinetically stable intermediate, as we need several hours to obtain a scattering profile. Recently, one of us, Y.K., has succeeded in preparing a mutated GroEL [1)], which takes stable complex with the target protein. In addition, the mutated GroEL binds GroES at its complex with the target protein.

In the present study, we used rhodanase as the target protein. GroEL was cultivated in 98% D_2O media. Both proteins were mixed with 1:1 stoichiometry. By changing D_2O/H_2O ratio (0 %, 21%, 80% and 9%) the scattering measurements were performed. With all these four experiments, we obtained radius of gyrations as 80.2, 91.4, 77.2 and 74.8 Å, respectively. The matching point is estimated as 40.9%. As the next step, we will observe the scattering profile of the rhodanase in the "transparent" GroEL with the use of this D_2O/H_2O ratio.

References

1) Y. Kawata, M. Kawagoe, K. Hongo, T. Miyazaki, T. Higurashi, T. Mizobata and J. Nagai: Biochemistry **38** (1999) 15731.

原子炉：JRR-3　　装置：SANS-J(C3-2)　　分野：中性子散乱（生物）

研究テーマ：中性子を用いた生体物質の構造に関する研究
表　題：細いフィラメント中のトロポニンＩの中性子小角散乱測定

4) Small-Angle Neutron Scattering Measurements of TroponinI within the Thin Filaments

F. Matsumoto[1,2], S. Deshimaru[1,2], K. Maeda[2], Y. Maeda[2], and S. Fujiwara[1]

[1]Neutron Science Research Center, Japan Atomic Energy Research Institute, Tokai, Ibaraki 319-1195
[2]Laboratory for Structural Biochemistry, RIKEN Harima Institute, Kouto, Hyogo 679-5148

Muscle contracts by mutual sliding of its two main filamentous components; actin-based "thin" filaments and myosin-based "thick" filaments. The molecular mechanism of the muscle contraction and its regulation is one of the most important problems in biophysics, as it is a typical example of energy transduction mechanisms in living organisms. In vertebrate skeletal and cardiac muscles, muscle contraction is regulated via the interactions between the thin filament proteins, troponin (Tn) C, TnI, TnT, tropomyosin, and actin, which are triggered by binding of Ca^{2+} to TnC. As a first step toward understanding the regulation mechanism of the muscle contraction, we investigated the structure of TnC within the thin filament with and without Ca^{2+} by small angle neutron scattering (SANS), and found that TnC assumes an extended dumbbell shape and that TnC moves closer to the filament axis by binding of Ca^{2+} [1]. Here, in order to investigate the structure of TnI within the thin filaments, we performed SANS measurements of the thin filaments containing deuterated (d-) TnI.

We prepared d-TnI by expressing the protein in *E. coli* in D_2O medium containing deuterated algal peptone. Tn-complexes were then reconstituted from this purified d-TnI, and protonated TnC and TnT purified from bovine heart, The Tn-complex containing d-TnI was exchanged into the native thin filaments. These reconstituted thin filaments containing d-TnI were then exposed to neutrons under the condition where the contrast of the other components of the thin filaments were matched out with 40% D_2O. Measurements were done with the Small-Angle Neutron Scattering Instrument (SANS-J) at the guide hall of the reactor JRR-3M in Japan Atomic Energy Research Institute. Experimental setting had been as follows: neutrons with the wavelength of 6.5 Å ($\Delta\lambda/\lambda$=12.98%) were employed, and the sample-to-detector distance was 4 m.

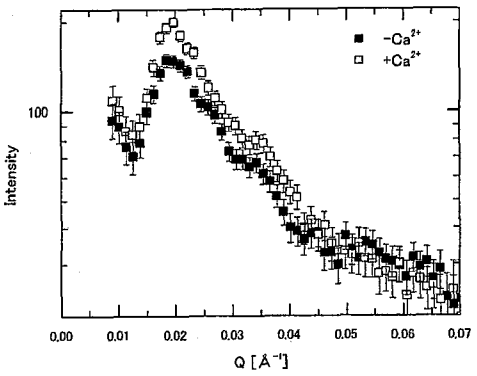

Figure 1: Neutron scattering curves of d-TnI within the thin filaments with and without Ca^{2+}.

Figure 1 shows the scattering curves of d-TnI within the thin filaments with and without Ca^{2+}. Clear differences in the scattering curves are observed, indicating large structural changes in TnI within the thin filaments occur by binding of Ca^{2+} to TnC. Assuming that spatial arrangement of TnI within the thin filament does not change with and without Ca^{2+}, this difference in the scattering curves implies qualitatively that by binding of Ca^{2+} to TnC, TnI becomes more compact. To interpret this change quantitatively, analysis of these scattering curves by model calculation is now underway.

Supported by Special Coordination Funds for Promoting Science and Technology from the Ministry of Education, Culture, Sports, Science and Technology, the Japanese Government.

References

1) F. Matsumoto *et al.*: J. Mol. Biol. 342 (2004) 1209.

原子炉：JRR-3　　装置：SANS-J（C3-2）　　分野：中性子散乱（生物）

研究テーマ：中性子を用いた生体物質の構造に関する研究
表　題：Ca^{2+}存在下及び非存在下における細いフィラメントの中性子繊維回折

5) Neutron Fiber Diffraction of Muscle Thin Filaments with and without Ca^{2+}

S. Fujiwara[1], F. Matsumoto[1,2], and S. Deshimaru[1,2]

[1]*Neutron Science Research Center, Japan Atomic Energy Research Institute, Tokai, Ibaraki 319-1195*
[2]*Laboratory for Structural Biochemistry, RIKEN Harima Institute, Kouto, Hyogo 679-5148*

Muscle contracts *via* sliding of the "thin" filaments and the "thick" filaments in muscle cells. Regulation of this contraction in skeletal and cardiac muscles is conducted through the interactions of the thin filament based proteins, troponin (Tn) C, TnI, TnT, tropomyosin, and actin. To understand the regulatory mechanism of the muscle contraction, it is important to obtain information of the structure of these proteins within the thin filaments.

We have been studying the structures of TnC within the thin filament by neutron scattering[1], and found that TnC assumes a dumbbell-like structure. To obtain more detailed information such as orientation of TnC within the thin filaments, neutron fiber diffraction method were employed. Native thin filaments (NTF) were purified from bovine heart, and the thin filaments containing deuterated TnC (dTnC-RTF) were prepared by the CDTA treatment of NTF followed by incubation with dTnC. These samples were sealed in quartz capillaries of a diameter of 3 mm, and then oriented in magnetic field of 18 Tesla. To detect possible orientational change of TnC by binding of Ca^{2+}, the oriented samples with and without Ca^{2+} were prepared. Neutron fiber diffraction patterns of these oriented samples were measured with the Small-Angle Neutron Scattering Instrument (SANS-J) at the guide hall of the reactor JRR-3 in Japan Atomic Energy Research Institute.

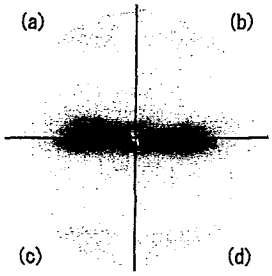

Figure 1: Neutron diffraction patterns of the oriented samples of (a) NTF without Ca^{2+}, (b) dTnC-RTF without Ca^{2+}, (c) NTF with Ca^{2+}, and (d) dTnC-RTF with Ca^{2+}.

Figure 1 shows neutron fiber diffraction patterns of the oriented thin filaments under various conditions. The background-subtracted patterns folded to quadrant are shown. The meridional reflections from Tn are clearly observed, as well as the strong equatorial intensity due to the thin filaments and the layer lined due to actin.

Figure 2 shows extracted intensity distributions of Tn reflections under various conditions. The intensity distributions are different between NTF and dTnC-RTF as well as between with and without Ca^{2+}, indicating that it is possible to extract the intensity distribution of TnC. Analysis of these reflections using one dimensional density distribution projected to the filament axis is currently underway.

Supported in part by Special Coordination Funds for Promoting Science and Technology from the Ministry of Education, Culture, Sports, Science and Technology, the Japanese Government, and also supported by the Ministry of Education, Science, Sports and Culture, Grant-in-Aid for Exploratory Research, 16657032, 2004.

References

1) F. Matsumoto *et al.*: J. Mol. Biol. 342 (2004) 1209.

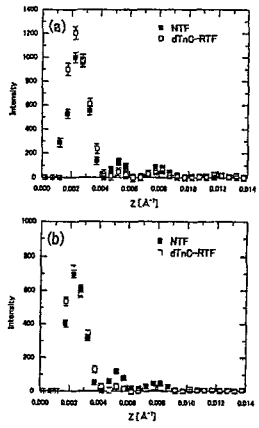

Figure 2: Meridional intensity distributions of Tn reflections (a) without Ca^{2+}, and (b) with Ca^{2+}.

原子炉：JRR-3　　装置：SANS-J（C3-2）　　分野：中性子散乱（生物）

研究テーマ：Stereum purpureum 由来Endopolygalacturonase I の中性子結晶構造解析
表　題：リンゴ銀葉病菌 Stereum purpureum 由来エンドポリガラクツロナーゼの
高分解能中性子結晶構造解析

6) Neutron Crystallographic Analysis of Endopolygalacturonase I from Stereum purpureum at Atomic Resolution

M. Sato, T. Shimizu[1], T. Nakatsu[1], H. Kato[1]

Graduate School of Integrated Science, Yokohama City University
[1]Graduate School of Pharmaceutical Sciences, Kyoto University

Endopolygalacturonases (endoPGs, EC 3.2.1.15) are α-inverting glycosidases and catalyze the hydrolysis of the α-1,4-glycosidic linkages between adjacent α-D-galacturonic acid residues within the pectin main chain. Reaction catalyzed by the inverting glycosidase proceeds by a general acid base catalysis, in which a general acid catalyst donates a proton to the glycosidic oxygen and a catalytic base guides the nucleophilic attack of water molecule on the anomeric carbon of the galacturonate. The X-ray crystal structure analyses of endoPG I from *Stereum purpureum* in complex with GalpA (β-D-galactopyranuroic acid) and GalfA (β-D-galactofuranuroic acid) have identified catalytic residues and puroposed for general acid-base catalysis of the enzyme[1]. It was however impossible to specify experimentally which catalytic residue is a general base or acid because no significant electron density for hydrogen atom is observed around the catalytic residues.

To identify the general base and acid experimentally, we carried out the neutron crystallographic analysis of endoPG I in complex with GalpA. The single crystals of endoPG I were prepared at pH 5.0 with hanging-drop vapor diffusion method using PEG4000 as the precipitant. Obtained crystals were then grown for high resolution neutron analysis by macroseeding for 100 days in a sitting-drop (drop: 0.5 ml/1% protein, reservoir: 4 ml) vapor diffusion. Typical size of the crystals grown was 2.2 x 2.0 x 1.0 mm. The crystals were soaked for 30 days in a D_2O-prepared reservoir solution, containing 2% GalpA, 25 % PEG-4000 and 10% MPD, and then subjected to neutron experiment.

Neutron diffraction data were collected at room temperature using a single-crystal diffractometer (BIX-4) at JRR-3 in JAERI, Tokai, and processed using Denzo-Scalepack program. In order to increase the yield of the diffraction data, neutrons were irradiated from three different directions to the crystal. The initial structure was obtained from X-ray analysis[1] and refined using the program SHELXS. Structural analysis of the complex is now in progress. Crystallographic data and data collection statistics are given in Table 1.

Table 1: Crystallographic data and data collection statistics

Space Group	P1
Cell Dimensions	
a / *b* / *c*	47.1 Å / 52.6 Å / 37.7 Å
α / β / γ	107.6°/ 109.9°/ 70.9°
Z	1
Resolution	48.8 Å -1.5 Å (1.55 Å – 1.5 Å)
No. of reflections	
Observed	123,314 (5,589)
Independent	44,331 (3,404)
Redundancy	2.4 (1.6)
Completeness	89.1% (68.5%)
Mean I/σ(I)	7.5 (3.2)
R_{sym}	11.7 (24.8)

Reference

1) T. Shimizu, T. Nakatsu, K. Miyairi, T. Okuno & H. Kato: *Biochemistry* 41 (2002) 6651-6659.

原子炉：JRR-3　　装置：BIX-4 (1G-B)　　分野：中性子散乱（生物）

研究テーマ：カルモデュリン/NAP-22 複合体の溶液構造
表題：コントラスト変化法を用いたカルモデュリン/NAP-22 複合体の小角中性子散乱研究

7) Small-Angle Neutron Scattering Study of Ca^{2+}-saturated Calmodulin Complexed with N^{α}-myristoylated NAP-22 by Contrast Variation

Y. Izumi, Y.Jinbo, N.Hayashi*, T.Matsufuji, and N. Matsushima **

*Graduate School of Science and Engineering, Yamagata University, Yonezawa, Yamagata 992-8510, Japan; *Fujita Health University, Toyoake, Aichi 470-1192, Japan; **Sapporo Medical University, Sapporo, Hokkaido 060-8556, Japan*

Solution structures of Ca^{2+}-saturated calmodulin (CaM) complexed with N^{α}-myristoylated NAP-22 (mNAP22) have been studied by small-angle neutron scattering (SANS-U) in H_2O/D_2O mixtures. CaM binds mNAP-22 with a 1 to 2 stoichiometry [1]. Samples The solutions with this molar ratio were prepared at a CaM concentration of 5.0 mg/ml. CaM, in both deuterated (dCaM) and nondeuterated (hCaM) forms, was prepared and used.

In the Stuhrmann plots for the complex, the data points were fitted by a parabola: $R_g^2=R_c^2+\alpha/\Delta\rho-\beta/(\Delta\rho)^2$, in which R_c=169 A, α=1,233, and β=29,350 for hCaM/mNAP22 [2] and R_c=170 A, α=-38,157, and β=49,475 for dCaM/mNAP22. Both the positive α and finite β value for hCaM/mNAP22 and the negative α and finite β value for dCaM/mNAP22 are conclusive evidence that CaM is more toward the inside of the complex as compared with mNAP22.

Figure 1 shows the Kratky plots for dCaM/mNAP22(1/2) in 0%D_2O (Top) and dCaM/mNAP22(1/2) in 80%D_2O (Bottom). Assuming internal scattering density fluctuations are negligible, the total scattering from a complex of a deuterated and nendeuterated protein can be written as

$$P(k, \Delta\rho_C, \Delta\rho_N) = \Delta\rho_C^2 P_C(k) + \Delta\rho_C\Delta\rho_N P_{CN}(k) + \Delta\rho_N^2 P_N(k),$$

where the subscripts C and N refer to dCaM and mNAP22, respectively. As a first step, however, the data points were fitted by a scattering curve without the cross-term $I_{CN}(k)$. As seen from Figure 1, the fitting is

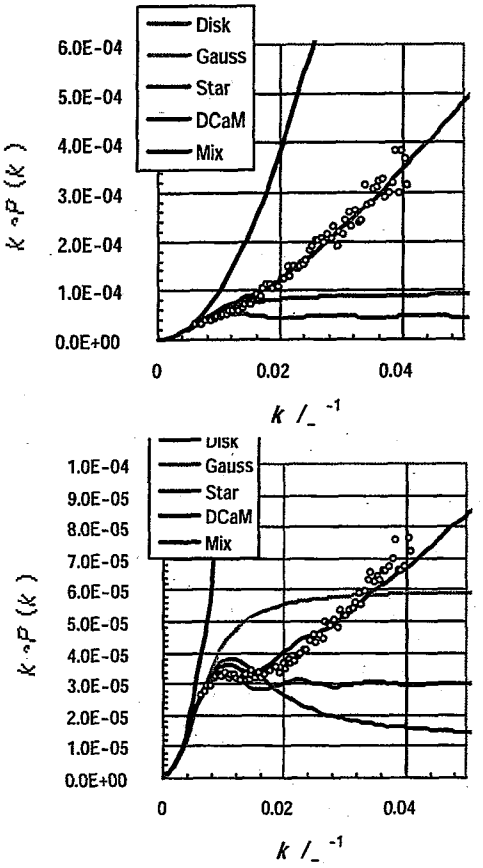

Figure 1: The Kratky plots for dCaM/mNAP22(1/2) in 0%D_2O (Top) and dCaM/mNAP22(1/2) in 80%D_2O (Bottom).

apparently satisfactory. Here, the experimental data for dCaM/mNAP22(1/2) in 28%D_2O was used to the $P_C(k)$ and the scattering function of a disk was used to the $P_N(k)$. At present, the evaluation of the cross-term is in progress.

References

[1] N.Hayashi, et al., Protein Sci. **9** (2000) 1905.
[2] Y.Izumi et al., This Report, **11** (2004)171.

使用施設：JRR-3M, 装置：SANS-U(C1-2), 分野 Biology

This is a blank page.

1. 中性子散乱 7) 基礎物理学・中性子光学

1. Neutron Scattering 7) Fundamental Physics Neutron Optics

This is a blank page.

研究テーマ：構造用材料の残留応力および負荷荷重下での材料特性評価
表　題：形状記憶合金のき裂先端における相変態の測定（第２報）

1) Phase Transformation at Crack Tip of Shape Memory Alloy TiNi (2nd Report)

Y. Akiniwa, H. Kimura, K. Tanaka and A. Moriai[1]

Department of Mechanical Science and Engineering, Nagoya University, Nagoya 464-8603
[1]Neutron Science Research Center, JAERI, Tokai, Ibaraki 319-1195

1. Intruduction

Shape memory alloy TiNi possesses excellent corrosion resistance, superelasticity and shape memory effect with large recovery strain. Owing to the unique properties, it's been utilized as pipe couplings, the frames of glasses and so on. In addition to the conventional use, TiNi is expected to be the most practical candidates as the actuator of "intelligent materials and structures", which are capable of sensoring a defect and repairing themselves. The TiNi actuators attached on CFRP laminates have been proven to increase the fracture toughness and decrease the crack propagation rate in mode I and II loading [1]. In spite of the potentiality, the actual application is limited because the fracture mechanism of TiNi has not been fully clarified. It is necessary to understand the martensitic transformation at a crack tip because the stress-induced martensitic phase plays an important roll in the fracture mechanism. The distribution of the martensite at a crack tip is believed to be different depending on the constraint condition. This implies that the stress condition, as well as the stress intensity factor, must be considered for the fracture design of TiNi. Neutron diffraction measurement is the most suitable method to measure the martensitic transformation in plane strain condition.

In this study, stress-induced martensitic transformation at a crack tip was investigated in shape memory TiNi. In the first report last year, stress-induced martensitic transformation at lower stress level was investigated. For the quantitative analysis, it is necessary to conduct the investigation for different stress levels because the difference in the stress level yield the difference in the transformation of the ligament of the specimen. In this report, the resolution of the neutron diffraction measurement was also improved from 0.5 to 0.3 mm in the beam width.

2. Material and measurement

TiNi specimen used for this measurement possesses shape memory effect at room temperature. It is mainly austenitic at room temperature without loading. A specimen in the dimension of 10 × 70 × 6 mm^3 were prepared with a fatigue crack introduced from a notch in the middle of the specimen. RESA was used for the neutron diffraction measurement. The width of the incident beam was 0.3 mm with the preset time of 1200 sec. The wave length of the beam was 0.2072 nm. The diffraction plane of (102) was employed for the 19-point measurement along the crack.

3. Experimental results

The results of the neutron diffraction at x = -600, -300, 0, 200, 400, 600, 900, 1200, 1500, 1800, 2100, 2500, 3000, 3900, 4400, 4500, 5000, 5500, 6000 micrometer, where crack tip is at x = 0 and crack propagation direction is along x axis, show that the diffraction intensity drops at around x = 2500. However, even beyond this point, the diffraction was obtained, indicating that the stress level and the transformation in the ligament have effect on the distribution of stress-induced martensitic transformation at crack tip. The precise distribution is to be calculated considering the scattering volume and intensity change of martensitic phase.

4. Conclusion

The distribution of martensitic phase at a crack tip was measured in plane strain condition by neutron diffraction measurement. Combined with the results from the surface measurement by EBSD, SEM, Nano-Indenter and X-ray diffraction, the results by neutron diffraction will be the base for the establishment of the prediction of fracture toughness and fatigue life in shape memory alloy TiNi.

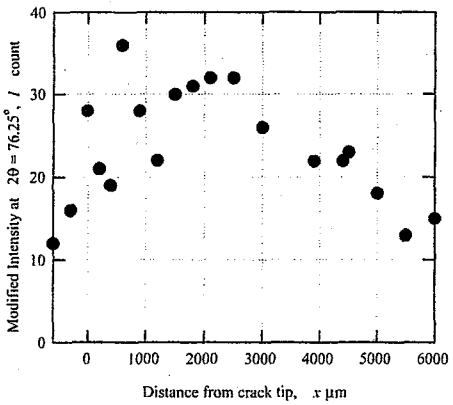

Figure 1: Change of Intensity of Martensite 102 Diffraction with Position along Crack.

References

1) H. Kimura: Int. J. of Fatigue (2005) to be published.

原子炉：JRR-3　　装置：RESA(T2-1)　　分野：中性子散乱（基礎物理）

研究テーマ：中性子散乱によるウラン化合物の物性研究
中性子散乱実験による $NpRhGa_5$ の磁気構造と二段の磁気転移

2) Neutron Scattering Study of the Magnetic Structure and the Transition of $5f$ Eletronic State in $NpRhGa_5$

Shintaro Jonen[1], Naoto Metoki[1,2], Fuminori Honda[1], Koji Kaneko[1], Etsuji Yamamoto[1], Yoshinori Haga[1], Dai Aoki[3], Yoshiya Homma[3], Yoshinobu Shiokawa[1,3], Yoshichika Ōnuki[1,4]

[1] *Advanced Science Research Center, Japan Atomic Energy Research Institute, Tokai, Naka, Ibaraki, 319-1195, Japan*
[2] *Department of Physics, Tohoku University, Sendai 980-8578, Japan*
[3] *Institute for Masterials Research, Tohoku University, Oarai, Ibaraki 311-1313, Japan*
[4] *Graduate School of Science, Osaka University, Toyonaka, Osaka 560-0043, Japan*

The actinide-based 115 compounds, $ATGa_5$, where A = (U, Np and Pu), and T = Transition metal, have been attracted much attention since the discovery of superconductivity in $PuCoGa_5$ [1]. The existence of wide variety of isostructural compounds and the availability of high quality single crystals open the possibility to perform a systematic study of strongly correlated f electron system. In order to study the magnetic structure and the $5f$ electron state, elastic neutron scattering measurements have been carried out on $NpRhGa_5$ single crystal.

High quality single crystal sample of $NpRhGa_5$ was grown by the Ga-flux method [2]. Neutron scattering experiments have been carried out at thermal and cold triple-axis spectrometers TAS-1, TAS-2 and LTAS installed at the research reactor JRR-3 in JAERI. The neutron beam was monochromatized and analyzed by PG crystal. Higher order contamination was removed via PG filter or Be filter cooled down to 20 K. High field up to 9 T was applied to obtain a single domain state with use of liquid ^{4}He free superconducting magnet, developed by JAERI.

$NpRhGa_5$ exhibits two successive antiferromagnetic transition at $T_{N1} = 36$ K and $T_{N2} = 33$ K. A-type antiferromagnetic structure with the propagation vector $\vec{q}$ = (0 0 1/2) has been revealed below T_{N1}. This structure can be described with a ferromagnetic layer on a basal plane, stacked along the tetragonal c-axis in an antiferromagnetic sequence. This A-type antiferromagnetic structure is the same as that for $NpCoGa_5$ [3], $UPdGa_5$ [4] and $UPtGa_5$ [5]. The identical magnetic structure is reasonably understood from the electronic structure; these iso-electronic compounds have very similar cylindrical fermi surfaces. The remarkable change of magnetic moment direction has been observed: for $T_{N2} < T < T_{N1}$, the Np moments are parallel to the c-axis; for $T < T_{N2}$ the moments are parallel to the ⟨1 1 0⟩ direction in the basal plane. The Np magnetic moments are $\mu = 0.44(16)\ \mu_B$ for $T = 35$ K and $\mu = 0.96(11)\ \mu_B$ at $T = 3$ K. Temperature dependence of the magnetic moment is shown in Fig. 1. The most remarkable point is the presence of a discontinuous change of magnetic moment observed at T_{N2}, indicative of change of $5f$ electronic state. We discussed this successive transition based on a localized picture for simplicity. The J-multiplet of Np^{3+} ion with $J = 4$ splits into doublet and singlet states under crystalline electric field (CEF) with tetragonal point symmetry. The doublet state has only diagonal component of J_z, thus an off-diagonal order involving singlet and doublet states is necessary for in-plane component J_x and J_y. Therefore the competing magnetic and quadrupolar interaction in the multi $5f$ orbital would be the origin of the successive magnetic transition. The observed magnetic form factor indicates the dominant contribution of orbital moment: $|\mu_L/\mu_S| = 1.44$, where μ_s and μ_L are the spin and orbital component of magnetic moment. However the orbital contribution is reduced from Np^{3+} free ion state ($|\mu_L/\mu_S| = 1.75$). This is consistent with the itinerant character of $5f$ electrons in $NpRhGa_5$, which is revealed by the dHvA experiments and the band calculation [6].

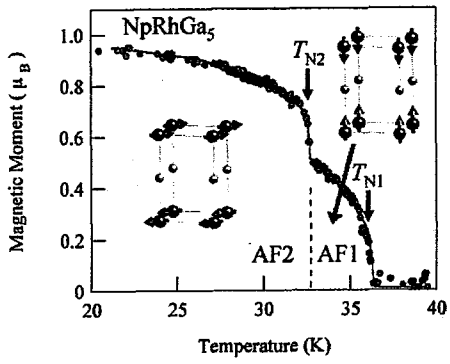

Figure 1: Temperature dependence of Np magnetic moments and the magnetic structure of $NpRhGa_5$. T_{N1} represents a antiferromagnetic order temperature. At T_{N2} the magnetic moments exhibit a sharp jump accompanied by a reorientation of moments.

References

1) J. L. Sarrao *et al.* Nature **420** (2002) 297.
2) D. Aoki *et al.* J. Phys. Soc. Japan *in press.*
3) N. Metoki *et al.* Phys. Rev. B *in press.*
4) S. Ikeda *et al.* J. Phys. Soc. Japan **72** (2003) 2677.
5) K. Kaneko *et al.* Phys. Rev B **68** (2003) 214419.
6) D. Aoki *et al.* J. Phys.: Condens. Matter **17** (2005) L169.

原子炉：JRR-3　　装置：TAS-1(2G)　　分野：中性子散乱（基礎物理）

研究テーマ： マッハ=ツェンダー型多層膜冷中性子干渉計の開発
表題： 冷中性子干渉光学のための「コヒーレントビームステアリング技術」の開発

3) "Coherent beam steering technique" for cold-neutron interferometry

Y.Seki[1], K.Taketani[1], H.Funahashi[1],
M.Kitaguchi[2], M.Hino[2], Y.Otaké[3], and H.M.Shimizu[3]

[1] *Department of Physics, Kyoto University, Kyoto 606-8502, Japan*
[2] *Research Reactor Institute, Kyoto University, Kumatori 590-0494, Japan*
[3] *RIKEN (The Institute for Physical and Chemical Research), Wako 350-0198, Japan*

We are preparing for precision measurements of small interactions, for example, the gravitational interaction of neutron matter wave by means of large-dimensional cold-neutron interferometers. For this purpose, we developed a Mach-Zehnder-type cold-neutron interferometer. The contrast of its interference fringes were not clear, less than 5%, without any adjustments. There must be remaining finite misalignments between the two beams superposed via the analyzer mirror of interferometer.

In order to correct the superposition of the two beams within the coherence volume and restore high contrast interference fringes, we are investigating utilization of magnetic devices, quadrupole electro magnets and prism coils (triangular solenoid coils) as "coherent beam steering technique"(Fig.1). Magnetic field gradient of quadrupole magnets or birefringence of prism coils deflect neutron beams according to the polarization.

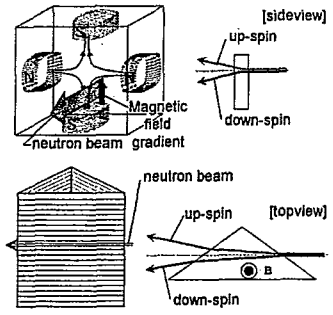

Fig. 1. Quadrupole electro magnet(top) and prism coil(bottom).

The experiments were performed at cold-neutron beam line MINE2 at the JRR-3M reactor in JAERI. The beam had a wave length of 0.88nm and a bandwidth of 2.4% in FWHM. Optical devices of MINE2 were arranged in neutron spin echo(NSE) setup with the divergence angles of beams of 16mrad in the vertical direction and 1.0mrad in the horizontal direction. The corresponding transverse coherence lengths of beams were evaluated $L_v^c \simeq 60$nm and $L_h^c \simeq 1\mu$m respectively. We have succeeded in observing clear and bright images of the Moiré fringes on neutron imaging plates, which corresponds to the crossing angles of beams of about 120nrad in the vertical direction with a quadrupole magnet(Fig.2). We have also observed Moiré fringes owing to the crossing angle about 600nrad in the horizontal direction with a prism coils. Applying the present technique, we can realize the adjustment of superposition accurately enough to achieve clear interference fringes. Moreover, this result suggests a way to spin dependent phase-sensitive neutron imaging.

We are also doing further researches on precision beam steering through developing a new type of cold-neutron interferometer using four quadrapole magnets. Incident beams are divided to spin up- and down-component with a pair of forward magnets and the two components are superposed with the backward pair as in Fig.3.

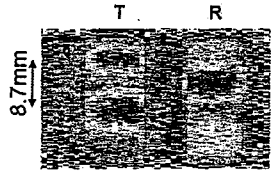

Fig. 2. Typical IP image of Moiré fringe with quadrupole magnets. R and T means reflected beam off the spin analyzer mirror of NSE and transmitted beam respectively.

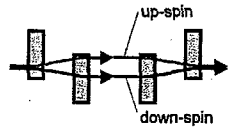

Fig. 3. Interferometer using four quadrupole magnets.

使用施設：JRR-3M，装置： C3-1-2-2(MINE2)，分野： 108.Fundamental Physics and Neutron Optics

研究テーマ：高Q平面および曲面多層膜スーパーミラーの冷中性子反射特性評価
表題：放物面型熱および冷中性子収束光学素子の開発

4) Development of Paraboloic and Paraboloidal Focusing Mirrors for Thermal and Cold Neutrons

K. Ikeda, T. Adachi, T. Shinohara, and K. Hirota
Image Information Reseach Unit, RIKEN, 2-1 Hirosawa, Wako, 351-0198

Neutron supermirrors (SM) with a parabolic surface or a paraboloidal one can work effectively as focusing devices for thermal and cold neutron beam transported through some guide tubes, because the guide tubes screen out neutrons with the divergence of more than the critical reflection angle of mirrors coated inside of them.

As shown in Fig.1, two kinds of neutron focusing mirrors were proposed and the fabrication of their prototypes has been going on. One was a one-dimensional focusing type with multiple parabolic planes. The prototype was designed for thermal neutron beam with the wavelength of 1.8Å and the width of 20 mm. It consisted of three channels by four parabolic planes and the total length and the focal distance from the tail of mirror to the focal point was 1200 mm and 300 mm respectively. In a preliminary experiment using 3Qc Ni/Ti SM by Xenocs Inc., neutron beam focusing and intensity gain were observed. A full-dress investigation will be carried out in near future. The other was a two-dimensional focusing type with a paraboloidal plane. The prototype was designed for cold neutron beam with the wavelength of 8.8Å and the size of 20 mm in diameter. The total length and the focal distance was 165 mm and 54 mm respectively.[1] Although the 3Qc Ni/Ti SM on the curved surface was peeled off the substrate because of a distortion in the deposited layers and the surface roughness of the substrate, the imperfect 3Qc SM on a quarter piece of the paraboloidal surface had neutron beam focusing and a little intensity gain. The distortion in the layers and the surface roughness of substrates should be much suppressed for a practical use of this paraboloidal mirror.

The reactively sputtering method [2] was introduced in our sputtering system and the reflectivity of a 3Qc Ni/Ti SM with 532 layers was improved up to 89% at the critical angle of m = 2.9 (Fig.2). It is desirable to realize this performance of SM on curved surfaces.

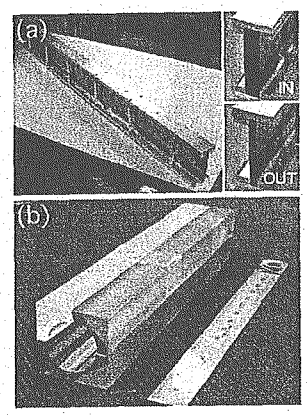

Fig. 1. Neutron focusing mirrors : (a) A one-dimensional focusing type with multiple parabolic planes and (b) a two-dimensional focusing type with a paraboloidal plane.

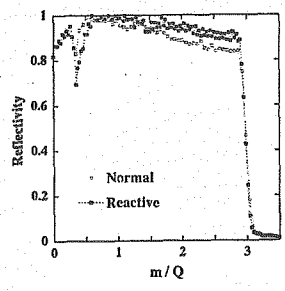

Fig. 2. Reflectivity vs. m-value for 3Qc Ni/Ti supermirrors fabricated at RIKEN. The reactively sputtering method improved the reflectivity at the critical angle of m = 2.9 from 84% to 89%.

References

[1] K. Ikeda *et al.*: Nucl. Instr. Meth. **A 529** (2004) 78.
[2] M.S. Kumar *et al.*: Physica B **276-278** (2000) 142.

使用施設：JRR-3M，装置： C3122 (MINE2)，分野： 108. Fundamental Physics and Neutron Optics

研究テーマ： Jamin型冷中性子干渉計を用いたアハラノフ＝キャッシャー効果の精密測定
表題： Jamin型冷中性子干渉計の位相安定性

5) Stability of interference fringes of Jamin-type cold neutron interferometer

M. Kitaguchi[1], H. Funahashi[2], K.Taketani[2], Y. Seki[2],
M. Hino[1], Y. Otaké[3] and, H. M. Shimizu[3]

[1] *Research Reactor Institute, Kyoto University, Kumatori 590-0494, Japan*
[2] *Department of physics, Kyoto University, Kyoto 606-8502, Japan*
[3] *RIKEN (The Institute for Physical and Chemical Research), Wako 350-0198, Japan*

A large dimensional interferometer for long wavelength neutrons has the advantage to increase the sensitivity to small interactions. Multilayer mirror is suitable for Bragg reflection of cold neutrons. We demonstrated Jamin-type interferometer for cold neutrons using 'beam splitting etalons (BSEs),' which enables us to align the four independent multilayer mirrors in the interferometer within required precision [1]. We are preparing for high-precision measurement of the topological Aharanov-Casher effect [2] with this type of interferometer. The interferometer for the AC measurements must have separated two paths enclosing an electrode. The separation between the two paths in the interferometer depends on the spacing between two mirrors in a BSE, which was 9.75μm in the above demonstration. We have developed BSEs with the spacing of 189μm in order to separate the two paths perfectly.

The phase difference between the two paths is written as

$$\Delta\phi = 2D(\sin\theta_1 - \sin\theta_2), \qquad (1)$$

where D is the spacing of the BSEs, θ_1 and θ_2 are incident angles for the first and the second BSE respectively. The large spacing of BSEs increases the fluctuation of the phase difference by the alignment of BSEs.

When the two BSEs with the spacing of 9.75μm were set on two automatic stages individually, irregular drift of phase about 0.01rad/min was found in continuous scans without any changing of the setup (Fig. 1). The relative angle between the BSEs was not stable because of, for example, vibration of the system, deformation by thermal fluctuation. Surface plane which can hold two BSEs rigidly has been prepared for check the drift reduction (Fig. 2). Although the long-term drift was still remaining, jumping of the phase of interferograms was remarkably reduced by introducing the rigid base as shown in Fig.1(B). We are doing further researches on the stability of the whole of the system.

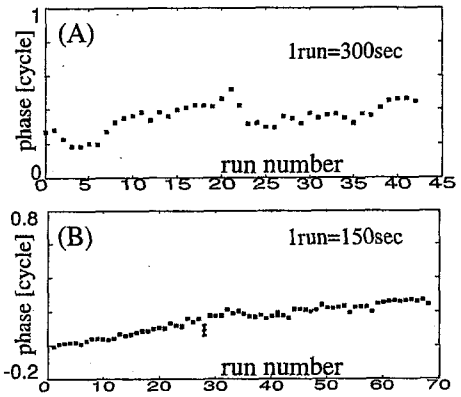

Fig. 1. (A) Drift of phase by the original interferometer with two independent BSEs. (B) Drift of phase by interferometer with two BSEs on a rigid base.

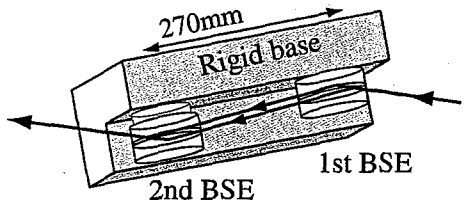

Fig. 2. Rigid base setup. BSEs are pushed onto the surface plane.

References

[1] M. Kitaguchi *et al.*: Phys. Rev A **67** (2003)033609
[2] A. Cimmino *et al.*: Nucl. Instrum. Methods Phys. Res. A **440** (2000)579

使用施設：JRR-3M, 装置： C3122: MINE2 , 分野： 108: Fundamental Physics and Neutron Optics

This is a blank page.

1. 中性子散乱 8)装　置

1. Neutron Scattering　8) Instrument

This is a blank page.

研究テーマ：圧電性結晶による中性子制御の実験的研究
表　題：圧電性単結晶を用いた中性子光学素子の原理検証実験

1) Possibilites of Using Piezoelectric Single-crystal as Neutron Electric Optical Dvices

S. Kawamura[1], J. H. Kaneko[1], K. Aizawa[2], D. Yamaguchi[2], Y. Otake[3], H. Fujimoto[4], F. Fujita[1], M. Furusaka[1]

[1] *Hokkaido University, N13 W8, Kita-ku, Sapporo, 060-8628, Japan*
[2] *JAERI, Tokai, Naka, Ibaraki 319-1195 ,Japan*
[3] *Riken, 2-1 Hirosawa, Wako, Saitama 351-0198, Japan*
[4] *AIST, Umezono 1-1-1, Tsukuba 305-8563, Japan*

D-spacing of a piezoelectric-crystal varies with applying electric field. We have been trying to develop novel neutron-optical-devices using the piezoelectricity. A principle-verification experiment has been conducted using α-quartz single-crystals whose piezoelectricity is low but properties are well known. This experiment was carried out using the PNO instrument equipped at the JRR-3 reactor of the Japan Atomic Energy Research Institute.

As shown in Fig. 1 using X-cut α-quartz single-crystals in the double crystal arrengement, rocking curves were measured with 2.3 Å neutrons. Aluminum electordes were attached to two sides of the 2nd crysta and DC bias voltage of 5kV/cm was applied to the 2nd crystal. The (110) peak was used whose diffraction angle was approximately 28 degrees. A very preliminary result is shown in Fig. 2. We could not obtain further meaningful results because of a trouble in the monochrometer-set of PNO.

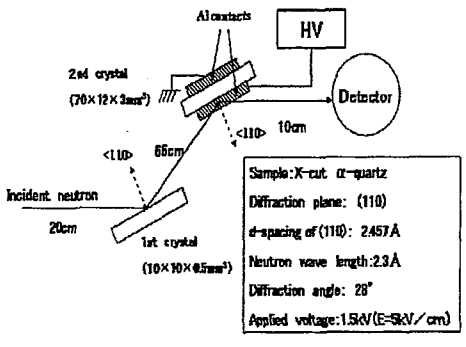

Figure 1: Experimental set up.

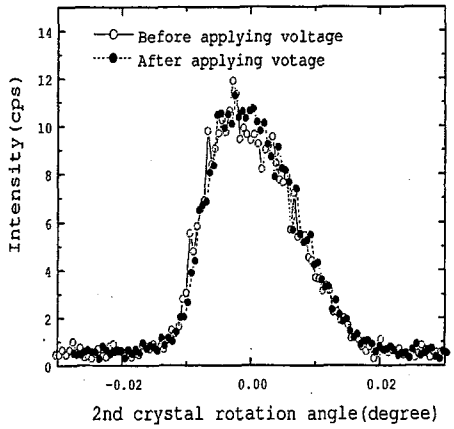

Figure 2: Rocking curves of α-quartz single-crystal.

原子炉：JRR-3　　装置：PNO(3G)　　分野：中性子散乱（装置）

研究テーマ：冷中性子屈折光学系と評価用検出器の基礎研究
表　題：抵抗分割型中性子検出器の開発と評価

2) Development of a Neutron Detector Based on a Position Sensitive Photomultiplier

Katsuya Hirota, Takenao Shinohara, Kazuaki Ikeda, Tomohiro Adachi, Hirohiko M. Shimizu, Setsuo Satoh[1], Takayuki Oku[2], Hajime Sasao[2] and Jun-ichi Suzuki[2]

RIKEN, Wako, Saitama 351-0198
[1]*KEK, Tsukuba, Ibaraki 305-0801*
[2]*Advanced Science Research Center, JAERI, Tokai, Ibaraki 319-1195*

Neutron optical devices such as a neutron magnetic lens and material lens for a cold neutron beam have been developed [1] recently. These devices need good spatial resolution of less than 1mm^2 for the detector. We are therefore developing scintillation detectors [2], which is called RPMT, with good spatial resolution, high signal-to-noise ratio and user friendliness.

The RPMT has three major components; the neutron sensor, DAQ system and monitoring system (see Fig.1). The neutron sensor consists of a scintillator and a position-sensitive PMT (PSPMT). A ZnS(Ag)/^{6}LiF plate is used for a neutron scintillator. This scintillator has a large light yield, more than ten thousand photons, for a cold and thermal neutron detection. The PSPMT has a 12-stage coarse-mesh dynode structure and multiple anode wires crossing one another in the X and Y directions. Output signals from each anode wire are divided in two by registers. The detection position is calculated by the ratio of these two signals for each coordinate. In total, only five lines, four signal lines and a high-voltage line, are used.

There are two types of detection area in the PSPMT. The effective area of the larger detector is ϕ 90 mm (5 inch PMT), and smaller one is ϕ50 mm (3 inch PMT). Both types of detectors have image distortion. To reduce the image distortion, we create a distortion correction table and use it to transform the image.

Detection efficiency for cold neutron and gamma ray is measured. Neutron detection efficiency is measured using a cold neutron beam with a wavelength of 9.5 Å. The beam flux is calibrated with a ^{3}He gas detector of known efficiency. The result of detection efficiency is 30 %. Gamma ray detection efficiency was measured by using a ^{60}Co gamma-ray source, which produces gamma rays of 1.173 and 1.333 MeV. The result is about 10^{-9}. The neutron and gamma-ray detection efficiency is lower than that of the usual scintillation detector because of using the thin scintillator and high threshold value.

The spatial resolution was measured using a cadmium collimator with a diameter of 0.5 mm. The neutron beam wavelength was 9.5 Å. The Fig.2 presents a typical X-axis projection of a 2D image. The spatial resolution consisting of a collimator and the detector, was about 0.8 mm FWHM in the central region of the RPMT detector. In the peripheral region, the spatial resolution was worse than in the central region because of the image distortion.

We wish to thank Prof. Keiichi Kuroda of IHEP, Protvino for useful discussion. The origin of this detector was developed in 1980's [3]. This work is conducted under the NOP project with support by the Special Coordination Funds for Promoting from the Ministry of Education, Culture, Sports, Science and Technology.

References

1) H. M. Shimizu *et al.*: Physica B **311** (2002) 23.
2) Katsuya Hirota *et al.*: Phys. Chem. Chem. Phys. **7** (2005) 1836.
3) K. Kuroda : Nucl. Instr. Meth. Phys. Res. A **277** (1989) 242.

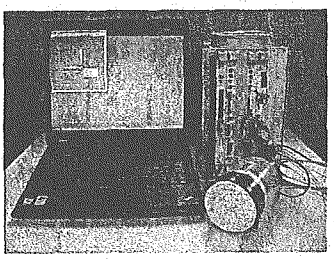

Figure 1: Apparatus of position sensitive neutron detector.

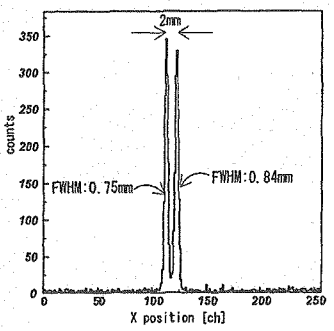

Figure 2: Measurement of spatial resolution. Cadmium collimator is 0.5 mm in diameter and 2 mm separation.

原子炉：JRR-3　　装置：NOP(C3-1-2-1)　　分野：中性子散乱（装置）

研究テーマ：研究炉の高度化の技術開発
表　題：ガラス状カーボンを基板としたNiミラーの中性子反射率

3) Neutron Reflectivity of Nickel Mirror on Glassy Carbon

K. Yamamoto, I. Tamura, K. Soyama[1], M. Hino[2], Y. Kawabata[2] and Y. Murayama

Department of Research Reactor, JAERI, Tokai, Ibaraki 319-1195
[1] *Neutron Science Research Center, JAERI, Tokai, Ibaraki 319-1195*
[2] *Department of Material Science, Kyoto University Research Reactor Institute, Kumatori, Osaka 590-0494*

In order to increase the intensity of cold neutron beam in JRR-3, it is important to gain cold neutrons from liquid hydrogen moderator and to increase the performance of transportation in neutron guides. The cold neutron guides have been installed with nickel monolayer neutron mirrors. The substrates of these mirrors are sodium silicate glasses at highly dose rate area and boron silicate glasses for area from shutter to beam port. In order to enhance transportation performance of long wave neutrons especially, we have an idea that the neutron guides are to be closing to neutron source. However resistance ability of the Ni monolayer neutron guide to the radiation was unknown, we have tried to find neutron guides with new substrates. The substrate of grassy carbon (AC-140S, Nisshinbo Industries, Inc.) had been applied for the radiation-resistant mirror. The carbon is well known to resist to gamma and neutron radiation as nuclear reactor material. In this study, we report the neutron reflectivity of mirrors with grassy carbon substrate.

Two kinds of samples were measured the neutron reflectivity. One is a polished grassy carbon mirror. Another is Ni mirror deposited on a polished grassy carbon using ion beam sputtering instrument. The size of the samples is 105 mm in diameter and 1.5 mm in thickness. We measured surface roughness of grassy carbon by Zygo (Maxim GP200, Zygo corp.) optical interferometer. The roughness of carbon mirror was Ra=0.6 ± 0.1nm. The measurement of the neutron reflectivity of carbon mirror and Ni mirror was performed using LTAS at JRR-3.

The critical angle of the carbon mirror was greater than that previously measured, because density of grassy carbon mirror is higher than that previously measured[1)]. Neutron reflectivity of Ni mirror is shown in Figure 1. The solid line is the calculated reflectivity of a layer with the thickness of 59 nm and including effect of roughness (rms) of 3.5 nm. Open circle shows the measurement neutron reflectivity of Ni mirror on grassy carbon. We have already confirmed that the performance of Ni mirror on the grassy carbon is greater than that of polished carbon mirror.

References

1) Y. Kawabata, M. Hino, H. Unesaki, S. Tasaki, M. Suzuki, A. Wakata: *Proc. ASR-2000, International Symposium on Advanced Science Research, JAERI, Tokai, Oct31th-Nov.2. 2000*, ed. S. Katano, N. Metoki, Y. Morii, Y. Ishii (JAERI) p. 492-494.

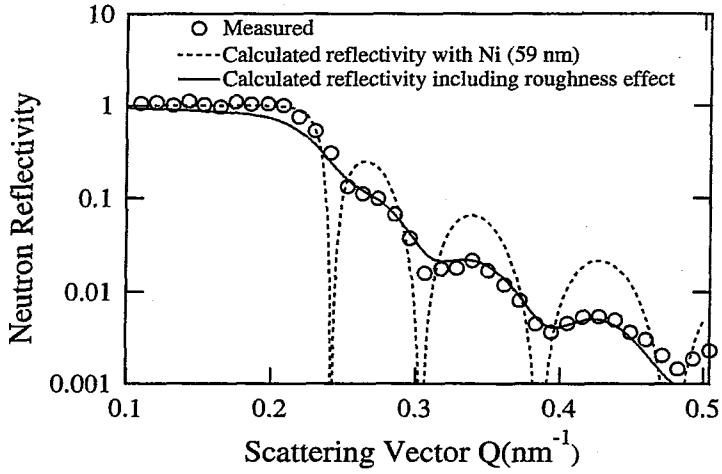

Figure 1: Neutron reflectivity with nickel monolayer mirror on the grassy carbon measured by using LTAS at JRR-3.

原子炉：JRR-3　　装置：LTAS(C2-1)　　分野：中性子散乱（装置）

研究テーマ：中性子の制御及び検出に関する開発研究
表　題：個別読み出し型二次元中性子検出器の開発

4) Development of a two-dimensional neutron gas detector with individual readouts

H. Yamagishi, T. Nakamura , H.Tanaka ,K. Soyama and K. Aizawa
Neutron Science Research Center, JAERI, Tokai, Ibaraki 319-1195

Next generation neutron detectors for neutron scattering experiments using intense pulsed neutron source have been developed. The requirements for detector performance are a high spatial resolution, a fast temporal response, a large sensitive area, a low neutron and gamma-ray ratio and a high detection efficiency. Because there is no detector, which suits with all above characteristics, each spectrometer selects the detector performance. We have been developed the two-dimensional neutron detector with individual readouts [1,2], which can flexibly suits to the requirements with changing the detection heads. To examine the two-dimensional detection system performance, the multi-wire (MW) detection head was used.

In this report, we present the spatial resolution and temporal response as the detection system performance.

[Individual readouts system]

Our detection system is comprised of a MW detection head, a gas vessel withstanding up to 10 atm, 541 channel signal feedthroughs, four amplifier-shaper-discriminator (ASD) amplifier boards, an encoder for detecting the incident neutron position, and two-dimensional data display. Secondary particles emitted from nuclear reaction in ^{3}He(n,p)T ionize gas molecules along the path. Ionized electrons drift toward anodes extended in parallel with the gap of 1 mm. After gas multiplication occurred at neighborhood of the thin anode wires, induced signals of cathode wires formed below anode wires with the distance of 1 mm are treated as x-direction information. Furthermore, induced charge signals of backstrip formed on polyimide insulator and orthogonally lied cathode wires treated as y-direction information. The currents in both of cathodes and backstrips are feed to ASD amplifier with the time constant of 80 ns, and the pulse signals over the setting discrimination level become the trigger of the low voltage differential signaling output. The encoder detects the incident neutron position with centroid determination of the "Hit" channel produced along the range of secondary particles. This data acquisition process ensures the fast temporal response.

[Experiments and results]

To examine the two-dimensional detection system with the individual readouts under the gas condition of 3.5 atm ^{4}He(^{3}He partial pressure of 0.26 atm) with 1.5 atm C_2H_6, the penciled beam collimated in the size of 1.3 × 1.3 mm was used. Figure 1 shows the beam profile at the center position of sensitive area. The measured spatial resolution of cathodes(x) and backstrips(y)-direction were 1.7 and 1.9 mm in full width at half maximum (FWHM) . Considering the beam size, the spatial resolution is less than 1.4 and 1.6 mm (FWHM).

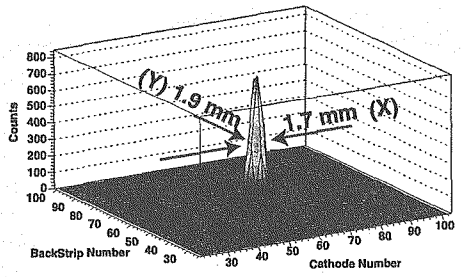

Figure 1: Beam profile at the center of sensitive area.

A detection efficiency of about 70% at 1.8 Å is expected by substituting all of the ^{4}He with ^{3}He. The deviations of the detection efficiency at the whole sensitive area was ± 8% without the sensitivity correction.

The image distortion at the both sides of sensitive area was caused by the lack of uniform electronic field and the gas gain fluctuation. However, the establishment of the more uniform wire pitch can solve this problem.

[Summary]

We confirmed the two dimensional neutron detection system using MW detection head and a well collimated neutron beam. The characteristics of developed detector system with the MW was showed in Table 1.

Table 1: Characteristics of developed two-dimensional MW detector system

Spatial(X) resolution (mm)	Spatial(Y) resolution (mm)	Efficiency (%)	Uniformity (%)
1.7 ~ 2.6	1.7 ~ 2.3	70 (1.8Å)	± 8

References

1) H.Yamaghishi, *et al.*: Nucl. Instru. And Meth. **A529** (2004) 365.
2) T.Nakamura, *et al.*: Nucl. Instru. And Meth. **A529** (2004) 336.

原子炉：JRR-3　　装置：CHOP(C2-3-3-2)　　分野：中性子散乱（装置）

研究テーマ：中性子光学素子の開発と中性子分光法の研究
表　題：窒素添加効果によるオーステナイト系ステンレス鋼の微細構造解析

5) Effect of Nitrogen Addition on Microstructure of Austenitic Stainless Steel

Keita Ikeda[1] , Jun-ichi Suzuki[2] and Yo Tomota[3]

[1] *Graduate student of Ibaraki University, Hitachi, Ibaraki 316-8511*
[2] *Advanced Science Research Center, JAERI, Tokai, Ibaraki 319-1195*
[3] *Graduate School of Science and Engineering, Ibaraki University, Hitachi, Ibaraki 316-8511*

1. Introduction

Recently, nickel bearing austenitic steels have various problems such as a human body allergens and depletion of resources. So nitrogen attracts attention as a substitute element of nickel. It is known that nitrogen addition to austenitic stainless steels improves various mechanical properties[1]. Especialy, nitrogen addition increases yield strength and work hardening[2]. Recent researches have revealed that nitrogen addition increases thermal stress component as well as athermal stress[3]. By an atom probe analysis, a pair of nitrogen and molybdenum atoms was found[4]. However, the strengthening mechanism and microstructure like nano-sized cluster has not been found. And it is considered that dislocation structure changed because of nano-sized cluster as shown in Fig. 1. We studied this topic by using a small angle neutron scattering method.

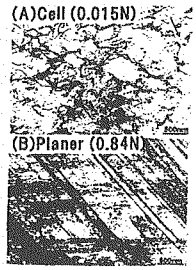

Figure 1: TEM micrographs of deformation specimens ; (A) low N and (B) high N.

2. Experimental procedures

The chemical compositions of materials used are shown in Table 1. The specimens were quenched into water after solution treatment to obtain single austenite structure. Change in nano-structure was examined by using SANS-J.

Table 1: Chemical compositions of materials used (mass%)

	C	Si	Mn	P	S	Cr	Ni	N
N1	0.048	0.33	0.80	0.002	0.001	25.1	19.8	0.023
N3	0.048	0.31	0.84	0.002	0.001	25.0	20.1	0.325

3. Result and Discussion

The result of the small angle neutron scattering is shown in Fig. 2. In a low-q region, the scattering cross section of N1 steel is larger than that of N3 steel, because of finer grains. The scattering cross section of N3 becomes larger than N1 at around q=0.1nm^{-1}. This q region is corresponding to the nano size structure in a real scale. It is hence suggested that nano-sized clusters are generated with nitrogen addition. However, the size, shape and amount of the clusters were not concretely able to be determined quantitatively, yet.

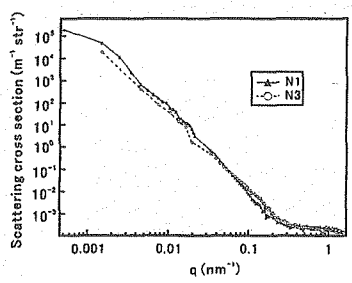

Figure 2: Relation between scattering cross section and q.

References

1) Y. Tomota, Tetsu-to-Hagane **80**(1994) N538 ; Netsushori **36** (1996) 218 ; Ferrum **7** (2002) 846, **7** (2002) 86.
2) Y. Tomota and S. Endo : ISIJ Int.**30** (1990) 656.
3) M. Kanda and Y. Tomota : CAMP ISIJ **15** (2002) 434.
4) M. Murayama, K. Hono, H. Hirukawa, T. Ohmura, and S. Matsuoka : Scripta Materialia **41, 5** (1999) 467.

原子炉：JRR-3　　装置：SANS-J(C3-2)　　分野：中性子散乱（装置）

研究テーマ：中性子光学素子の開発と中性子分光法の研究
表　題：中性子磁気レンズを用いた集光型小角散乱装置の性能評価

6) A demonstration study of focusing geometry SANS using a magnetic lens

T. Oku[1], J. Suzuki[1], H. Sasao[1], S. Yamada[1], T. Adachi[2], T. Shinohara[2], K. Ikeda[2], M. Furusaka[3], H.M. Shimizu[1,2]

[1]*Advanced Science Research Center, JAERI, Tokai, Ibaraki 319-1195*
[2]*RIKEN, 2-1 Hirosawa, Wako, Saitama 351-0198*
[3]*KEK, 1-1 Oho, Tsukuba 305-0801*

We have developed magnetic neutron lens based on a sextupole magnet for application in focusing geometry SANS (FSANS) experiments [1,2]. In small-angle neutron scattering (SANS) experiment, we can improve q-resolution and/or measurement efficiency by focusing a neutron beam on a detector [3,4]. The magnetic lens is a suitable focusing device for the FSANS experiments because its neutron beam focusing mechanism is completely free of small-angle neutron scattering and absorption. However, the magnetic lens has a spin-dependent neutron focusing property: when neutrons enter the magnetic lens, neutrons polarized parallel (positive) and anti-parallel (negative) to the local field are focused and defocused by the lens, respectively. The defocused neutrons spread out on the detector and raise the background level. Therefore, the incident neutrons should be well-polarized for a good signal-to-noise ratio in the FSANS experiment using the magnetic lens. In this study, we performed a demonstration study of the FSANS experiment using the magnetic lens, which is a superconducting sextuple magnet (SSM) [2], with a polarized neutron beam. The performance of the instrument was evaluated by measuring SANS intensity of the monodispersed SiO_2 spherical particles.

The experiment was performed at the beam line of C3-1-2-1 (NOP) of JRR-3 in Japan Atomic Energy Research Institute (JAERI). The experimental setup is shown in Fig.1. Monochromatic neutrons with $\lambda = 9.16 \pm 0.3$ Å are produced by a double NiC/Ti multilayer monochromator. The polarizer is a FeSi magnetic supermirror. Since we used the polarizer in transmission geometry, the neutron beam after the polarizer has negative polarization. A radio-frequency gradient spin flipper (SF) [5] was employed to flip the spin of the neutrons incident to the SSM so that the neutrons would satisfy the focusing conditions. The SSM is a 2 m-long magnetic sextupole composed of six saddle-shape superconducting NbTi coils [2,6]. The detector is a neutron imaging plate (IP) (FUJI BAS-ND) with position resolution of 0.2 mm. We measured SANS intensity of the SiO_2 spherical particles whose mean radius $R_m = 250$ nm and standard deviation of radius $\sigma_R = 6.5$ nm. Figure 2 shows the measured SANS intensities as a function of q. The scattering form factor $F(q)$ for a spherical particle is given by

$$F(q) = (4/3)\pi\rho R^3 g(qR), \quad (1)$$
$$g(x) = 3(\sin x - x\cos x)/x^3, \quad (2)$$

where ρ is the nuclear scattering length density of the particle and R the particle radius. According to Eqs. (1) and (2), an oscillation with a period $q_p \sim \pi/R$ ap-

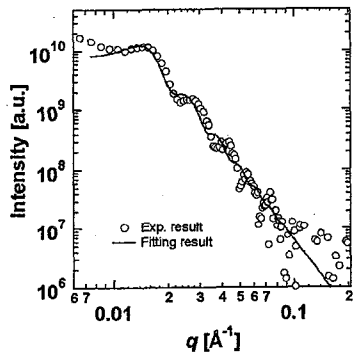

Figure 2: Measured SANS intensity as a function of q.

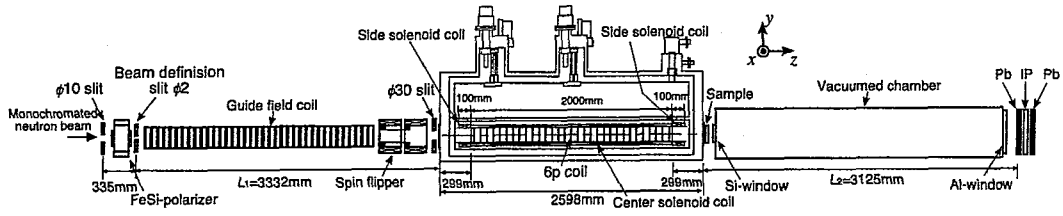

Figure 1: The experimental setup for the FSANS experiment. The neutron imaging plate detector (IP) is sandwiched between 2.5mm-thick Pb plates for γ-ray shielding.

原子炉：JRR-3　　装置：NOP(C3-1-2-1)　　分野：中性子散乱（装置）

pear in the SANS intensity curve if the q-resolution of the instrument, Δq, is sufficiently smaller than $q_p/2$. The oscillation was observed in the SANS intensity curve (Fig. 2). This must suggest that Δq is sufficiently smaller than $q_p/2 \sim 6.3 \times 10^{-4}$ Å^{-1}. The q-resolution of the instrument is described by

$$(\Delta q/q)^2 = (\Delta\lambda/\lambda)^2 + (\Delta\theta/\theta)^2, \quad (3)$$

where θ is the scattering angle. The monochromator produces the neutron beam with $\Delta\lambda/\lambda = 0.036$. The angular resolution results from the positional resolution of the detector and the beam divergence. In our FSANS setup, the beam divergence can be estimated by dividing the peak width of the direct beam intensity distribution on the detector by the distance from the exit of the SSM to the detector. The positional resolution of the detector is 0.2 mm. On the other hand, the peak width of the intensity distribution of the direct beam on the detector is 2.48 mm in FWHM. Thus, the angular resolution is dominated by the latter in this case and is estimated to be $\Delta\theta = 0.34$ mrad. According to Eq. (3), Δq is dominated by the angular resolution around $q = 0.001$ Å^{-1} and is determined to be $\Delta q = 2.3 \times 10^{-4}$ Å^{-1}. The obtained SANS intensity curve was analyzed based on the spherical particle model, taking into account the effects of the particle size distribution, the particle spatial distribution and the q-resolution of the instrument. The scattering function is given by

$$I(q) \propto \int \exp\left[-(q-q')^2/(2\Delta q^2)\right] \times S(q') \int \exp\left[-(R-R_m)^2/(2\sigma_R^2)\right] F(q')^2 \mathrm{d}R\mathrm{d}q', \quad (4)$$

where,

$$\begin{aligned} S(q) &= 1/[1+24\eta G(R_{HS}\, q)/(R_{HS}\, q)], && (5)\\ G(x) &= \alpha(\sin x - x\cos x)/x^2 \\ &\quad +\beta[2x\sin x + (2-x^2)\cos x - 2]/x^3 \\ &\quad +\gamma\{-x^4\cos x + 4[(3x^2-6)\cos x \\ &\quad +(x^3-6x)\sin x + 6]\}/x^5, && (6)\\ \alpha &= (1+2\eta)^2/(1-\eta)^4, && (7)\\ \beta &= -6\eta(1+\eta/2)^2/(1-\eta)^4, && (8)\\ \gamma &= \eta\alpha/2. && (9) \end{aligned}$$

Here, $S(q)$ is a structure factor given for randomly packed monodispersed spherical particle system. R_{HS} the interaction radius and η the volume fraction of the particles [7]. The experimental data were fitted using Eq. (4) by fixing the values of the known parameters, Δq, λ, $\Delta\lambda$, R_m and σ_R. As the result of the least-square fitting, we obtained $R_{HS} = 440$ nm and $\eta = 0.52$. The fitted curves are plotted in Fig. 2. As we discussed above, the q-resolution in the low-q region of the instrument is limited by the angular resolution. The angular resolution is determined by the focusing geometry and is limited by the fairly short path length L_2 of ~3 m in this study. By increasing L_2 to tens of meters as for a typical SANS instrument, the q-resolution sufficient for analyzing structure with a length scale over 1 μm may be achieved.

In conclusion, the FSANS experiment was performed using the polarized cold neutron beam and the superconducting sextupole magnet as a neutron focusing device. The q-resolution sufficient for 500 nm scale structure analysis was obtained with path length $L_1 \approx L_2 \sim 3$m and $\lambda = 9.15 \pm 0.30$ Å. The obtained SANS intensity curves were well represented by the spherical particle model, taking into account the effects of the particle size distribution, the particle spatial distribution and the q-resolution of the instrument.

References

1) T. Oku *et al.*: Proc. of the ICANS-XVI, 1 355. Düseldorf, May, 2003.
2) J. Suzuki *et al.*: J. Appl. Cryst. **36** (2003) 795.
3) B. Alefeld *et al.*: Physica B **234-236** (1997) 1052.
4) S.-M. Choi *et al.*: J. Appl. Cryst **36** (2003) 795.
5) T. Oku *et al.*: Physica B **335** (2003) 226.
6) M. Furusaka *et al.*: Nucl. Instrum. Methods A **529** (2004) 223.
7) N. W. Ashcroft and J. Lekner: Phys. Rev. **83** (1966) 145.

研究テーマ：中性子光学素子の開発と中性子分光法の研究
表　題：熱中性子ビーム集光導管の開発と中性子ベータ崩壊実験

7) Development of Focusing Guides of Thermal Neutron Beam and Neutron Beta Decay Measurement

S. Yamada, T. Shinohara[1], K. Mishima[1], H. Sasao, T. Oku, J. Suzuki, K. Hirota[1], H. Sato[1], H. Matsue[2] and H.M. Shimizu[1]

Advanced Science Research Center, JAERI, Tokai, Ibaraki 319-1195
[1]RIKEN, Wako, Saitama 351-0198
[2]Neutron Science Research Center, JAERI, Tokai, Ibaraki 319-1195

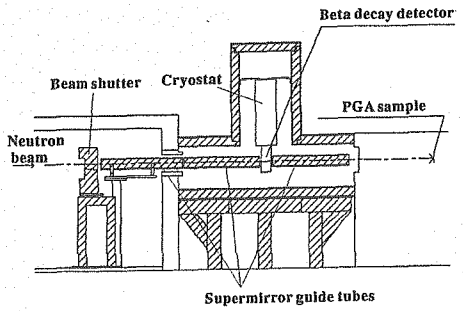

Figure 1: Schematic view of NBD (Apparatus for Neutron Beta Decay Measurement).

We have installed supermirror guide tubes in the thermal neutron beamline at JRR-3 to increase the neutron flux at the prompt gamma-ray analysis (PGA) system. PGA is one of the methods of the element analysis. In a PGA experiment, the energy of neutron-induced gamma rays from the sample irradiated by the neutron beam is measured with a Ge detector. From the energy spectrum of the gamma rays, the content of the element concerned in the sample can be obtained.

We have replaced a vacuum tube by two types of supermirror guide tubes; one is a straight guide with flat mirrors and the other is a focusing guide with parabolic mirrors. The straight guides increase the intensity of neutron beam whose distribution of the intensity is homogeneous. On the other hand, focusing guides collect the neutron beam to the focal point, where the PGA's sample is set. Therefore, when the size of the sample is small, the focusing guides improves the performance of PGA system greatly. There are more advantages of using the focusing mirrors in the PGA experiment. One is that the divergence of the focusing beam does not affect precision of a measurement. In addition to that, reflective optics does not have chromatic aberration, which suits to the focusing of the white neutron beam that is used in the PGA experiment.

For the installation of the guides and the neutron beta decay experiment which is described later, we have constructed the new beam port called NBD (Apparatus for Neutron Beta Decay Measurement) at T1-beamline of JRR-3. The schematic view is shown in Fig.1. Inside the external shield, there are a neutron beta decay detector, neutron guides and an exchange system of the guides driven by electrical motors. Using this system, one can choose the appropriate types of beams during the PGA experiment.

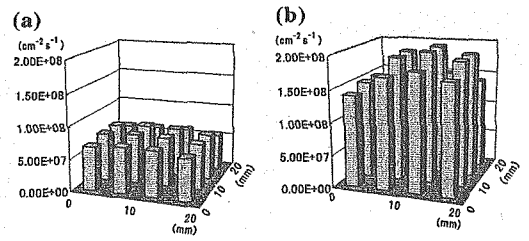

Figure 2: Results of the neutron flux measurement with (a) a vacuum tube and (b) straight m=3 supermirror guide tubes. The averaged flux in 2cm square increased by 2.3 times.

The straight guides consist of three separated parts. The length of one guide is 966mm and that of the other is 900mm. The critical angle of the mirrors is 3 times (m=3) as large as that of natural nickel. For the test of the performance of the guides, we have measured the neutron beam flux before and after the installation using the gold-foil activation method. The result is shown in Fig.2. The intensity of neutron beam is increased by about 2.3 times.

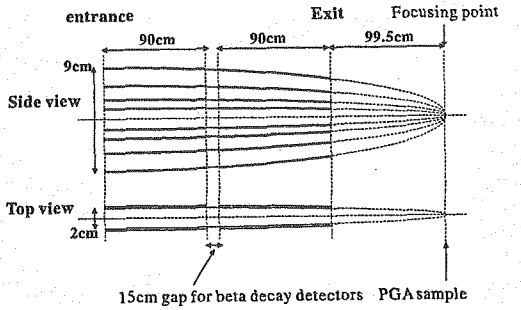

Figure 3: Schematic view of parabolic multichannel guides. Each mirror has a parabolic shape with the same focal point.

原子炉：JRR-3　　装置：NBD(T1-4-5)　　分野：中性子散乱（装置）

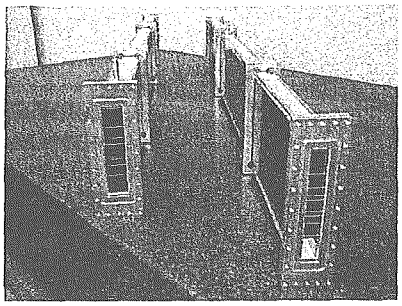

Figure 4: Picture of the parabolic multichannel guides manufactured by SwissNeutronics. In the ends of the guides, Al flanges are attached and ^{4}He gas are filled inside the guides.

The focusing guides have multichannel structure, seven channels in this case, to focus a neutron beam of wide area effectively. The schematic view is shown in Fig.3. The seven channel structure consisits of eight parabolically bent m=3.6 supermirrors of 0.55 mm thick. The area size of the guide is 90x20 mm^2 at the entrance and 52x12 mm^2 at the exit. The guide consists of two parts whose length is 900 mm and the focal length is 995 mm from the exit of the guide. Their picture is shown in Fig.4. They have been already installed at a thermal neutron beamline and their performance of the neutron beam focusing will be tested.

Besides the installation of the neutron optics, the experiment of fundamental physics is progressing in the NBD port. That is a neutron beta decay measurement, which aims at the test of the unitarity of the Cabbibo-Kobayashi-Maskawa(CKM) matrix[1,2] in the Standard Model of particle physics.

CKM matrix transforms the mass eigenstates (d, s, b) to the weak eigenstates (d', s', b'),

$$\begin{pmatrix} d' \\ s' \\ b' \end{pmatrix} = \begin{pmatrix} V_{ud} & V_{us} & V_{ub} \\ V_{cd} & V_{cs} & V_{cb} \\ V_{td} & V_{ts} & V_{tb} \end{pmatrix} \begin{pmatrix} d \\ s \\ b \end{pmatrix}. \quad (1)$$

For the conservation of the probability, this matrix satisfies the unitarity condition as is shown in Eq.2.

$$|V_{ud}|^2 + |V_{us}|^2 + |V_{ub}|^2 = 1. \quad (2)$$

While $|V_{us}|$ and $|V_{ub}|$ are measured in accelerator experiments, the value of $|V_{ud}|$ can be determined by the lifetime of the neutron and the correlation coefficient in a neutron beta decay spectrum, whose expression is shown in Eq.3[3].

$$W dE_e d\Omega_e d\Omega_\nu = p_e E_e (E_e^{\max} - E_e)^2 dE_e d\Omega_e d\Omega_{\bar{\nu}} \times \left[1 + a\frac{\vec{p}_e \cdot \vec{p}_{\bar{\nu}}}{E_e E_{\bar{\nu}}} + \vec{J}\left(A\frac{\vec{p}_e}{E_e} + B\frac{\vec{p}_{\bar{\nu}}}{E_{\bar{\nu}}} + D\frac{\vec{p}_e \times \vec{p}_{\bar{\nu}}}{E_e E_{\bar{\nu}}}\right)\right], \quad (3)$$

where e and $\bar{\nu}$ indicate the emitted electron and anti-neutrino, respectively, E is a kinetic energy, p is a momentum, and J is a spin of the neutron.

The main aim of the experiment is determining the value of the little a in Eq.3, which is obtained from an energy spectrum of an emitted proton. The kinetic energy of proton is very low (below 1keV) and it is difficult to detect by a normal detector without acceleration. In our scheme, the energy of proton is directly measured by superconducting devices, not using a spectrometer as in the previous experiments. The superconducting detectors suit to measuring the energy of the emitted proton because they have no dead layers as semiconductor detectors. We are now developing two types of the superconductive detectors; STJ (Superconductive Transition Junction) and TES (Transition Edge Sensor). At the same time, a preliminary experiment is under way in the NBD port. The main aim of the preliminary experiment is the detection of the beta decay events from the neutron beam. The setup is shown in Fig.5. We use a channel electron multiplier(CEM) as a proton detector, and plastic scintillator with a photomultiplier(PMT) as a electron detector. The background events can be eliminated by measuring the arrival time difference between PMT and CEM signals. We also use an energy spectrum of the signal from the plastic scintillator to determine the neutron beta decay events. After the detection of the beta decay events, we will install the superconducting detector in the beamline.

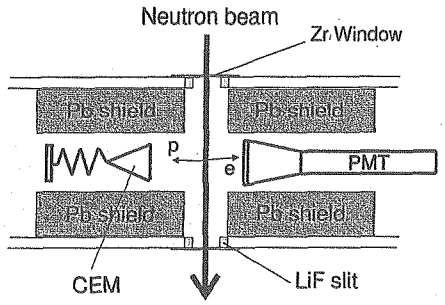

Figure 5: Top view of the setup of the preliminary beta decay experiment.

References

1) M. Kobayashi and T. Maskawa : Prog. Theor. Phys. 49 (1973) 652.
2) N. Cabibbo : Phys. Rev. Lett. 10 (1963) 531.
3) J.D. Jackson, S.B. Treiman, H.W. Wyld : Nucl. Phys. 4 (1957) 206.

研究テーマ：中性子光学素子の開発と中性子分光法の研究
表　題：物質レンズの集光性能の冷却効果評価

8) The Experimental Evaluation of the Neutron Transmission of MgF_2 Biconcave Lens under Cooling Atmosphere

H. Sasao[1], Y. Iwase[1], K. Ikeda[1], S. Yamada[1], T. Oku[1], J. Suzuki[1], S. Koizumi[1], H. Tanaka[1], T. Hashimoto[1], T. Shinohara[2], T. Adachi[2] and H. M. Shimizu[2]

[1] *Advanced Science Research Center, JAERI, Tokai, Ibaraki 319-1195*
[2] *RIKEN, 2-1 Hirosawa, Wako, Saitama 352-0198*

Biconcave lenses have been utilized for small angle neutron scattering (SANS) since Eskildesen *et al.* applied them to a focusing neutrons experiment [1]. We have also tried to apply biconcave lenses to the SANS-J-II [2] instrument.

We could find that biconcave lenses have good performance for condensing neutrons. However, the shape of the lens increases the effective thickness of the lens and then the effective transmissivity decreases with enlarging the diameter of the neutron beam. Furthermore, the problem gets more remarkable as more numbers of lenses are needed to focus short-wave length neutrons. Therefore, in order to improve the situation, we carried out the experiments for studying the neutrons transmissivity of MgF_2 lenses under the cooling atmosphere below the liquid nitrogen (LN_2) temperature 77K. It has started from the suggestion that the neutrons transmissivity of MgF_2 seems to be improved under the low temperature circumstance [3]. We show the result of a MgF_2 plate at first and move to the result of the MgF_2 lens.

Figure 1 shows the temperature dependence of the neutrons transmissivity. The sample is a plate of MgF_2 with 10 mm in thickness. Here, the triangles show the transmissivity evaluated from the integrated intensity over all channels of a 2D ^{3}He detector. The circles show the transmissivity evaluated from the integrated intensity over central 9 channels. The dotted line is the transmissivity theoretically evaluated with the absorption cross section of MgF_2. The transmissivity of both cases increases with decreasing the temperature and the improvement of the transmissivity about 4% is achieved. We have applied the result to practical biconcave lenses.

The MgF_2 lens is composed of 27 biconcave lenses, and set in a box filled with ^{4}He gas in a cryostat. Here, the diameter, the curvature of the surface, and the center thickness of each lens are 30mm, 25mm, 1mm, respectively. The neutron beam is collimated within about 4mrad in angular divergence. The averaged thickness of each biconcave lens is about 3mm. The total averaged thickness of the lens corresponds to 81 mm (=3mm×27). Applying the improvement ratio 3% which comes from the transmissivity at 200K in Fig.1, we can expect the improvement of 27%(=$(1.03)^{81/10}$).

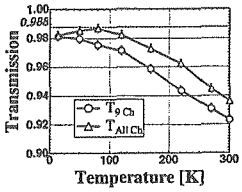

Figure 1: The temperature dependence of the neutrons transmissivity of a MgF_2 plate.

Figure 2 shows the temperature dependence of the neutrons transmissivity of the lens. Here, the neutrons transmissivity is defined as the ratio of the neutrons beam intensity with the lens against that without the lens, where both of intensities are integrated over the detector. Three different wave lengths λ of 0.65nm , 0.85nm, and 1.06nm, are used to find the difference of the temperature dependence. At first, in the case of λ = 0.65nm, the transmissivity is constant from 40K to 60K and decreases with increasing the temperature. In the case of λ = 0.85nm, the transmissivity is constant from 40K to 200K and decreases above 200K. In the case of λ = 1.06nm, the local maximum is found at 150K. And the transmissivity decreases with increasing the temperature above 200K.

We find a common behavior that every transmissivity monotonously decreases with increasing the temperature above 200K. The transmissivity increases from 300K to 200K are +21%, +24%, +19%, respectively. The results show that about 20% transmissivity increase is expected by cooling the lens from the room temperature to about 100K. The evaluated improvement of the MgF_2 biconcave lens is almost consistent with the result of the MgF_2 plate.

In summary, the neutron transmissivity of the MgF_2 is improved by cooling. The rate of the increase is evaluated to be about 20%.

References

1) M. R. Eskildsen *et al.* : Nature **391** (1998) 563.
2) S. Koizumi *et al.* : Hamon **14** (2004) 266.
3) S. Koizumi, and C. J. Glinka (NIST), private discussion.

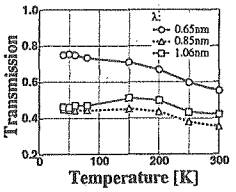

Figure 2: The temperature dependence of the neutrons transmissivity of the MgF_2 lens.

原子炉：JRR-3　　装置：SANS-J(C3-2)　　分野：中性子散乱（装置）

研究テーマ：中性子散乱によるウラン化合物の物性研究
原研三軸分光器 TAS-1 における新しいダブルベント PG モノクロメータの開発

9) New Improvement of Triple-Axis Spectrometer at JAERI: Simulation of High Flux Double Bent PG Monocromator with Wide Dynamic Range

Shintaro Jonen, Naoto Metoki, Koji Kaneko and Masayasu Takeda

Advanced Science Research Center, Japan Atomic Energy Research Institute, Tokai, Naka, Ibaraki, 319-1195, Japan

The Advanced Science Research Center (ASRC) in JAERI has installed three triple-axis spectrometers, TAS-1, TAS-2 and LTAS in the research reactor JRR-3. TAS-1, installed at reactor room, provides a high flux thermal neutron beam with spin polarization / polarimetry option. The low background and high resolution are the advantage of TAS-2 installed at guide hall, whereas cold source neutron spectrometer LTAS has a high energy resolution. These three spectrometers with distinct characteristics have been used for the study of strongly correlated systems such as actinide compounds and/or high T_c superconductors.

To improve the neutron flux of TAS-1 spectrometer at high neutron energies 30 $\sim$ 60 meV, a new double bent PG monochromator has been designed with *Monte Carlo* simulation using the software *McStas* (Risϕ National Laboratory / Institute Laue-Langevin). At present the TAS-1 use two type of monochromator: (i) vertical bent PG monochromator, and (ii) Heusler vertical / horizontal bents monochromator. We have designed a new type of bent curvature effective for neutron energy with wide dynamic range $13 < E < 60$ meV. The designed monochromator with the size 280 $\times$ 100 mm^2, is twice larger than the present vertical PG monochromator. Therefore we can obtain high flux, especially for high energy region, where the incident neutron beam will be used more efficiently. The vertical / horizontal bents have projected by using a 7 columns $\times$ 5 rows = 35 PG crystals (Fig. 1). This beam focusing system can condense the neutron beam in 20×20 mm^2 section area at sample position (Fig. 2). From this new double PG monochromator we are expecting a gain of neutron flux around 4 times as larger as the currently used vertical bent PG monochromator. This double bent monochromator will be checked soon after the installation.

We have constructed a new drum for three different type of monochromators: i) The double bent PG monochromator described above; ii) The double bent Cu monochromator for high energy; and iii) a flat Cu monochromator for magnetic form factor measurements up to high-Q range.

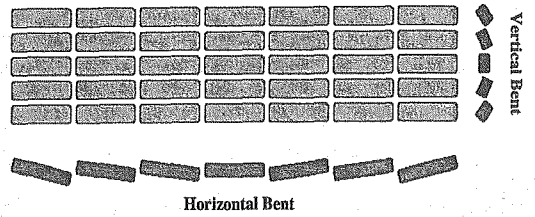

Figure 1: The double bent monochromator with 7x5 PG crystals designed by using a *Monte Carlo* simulation.

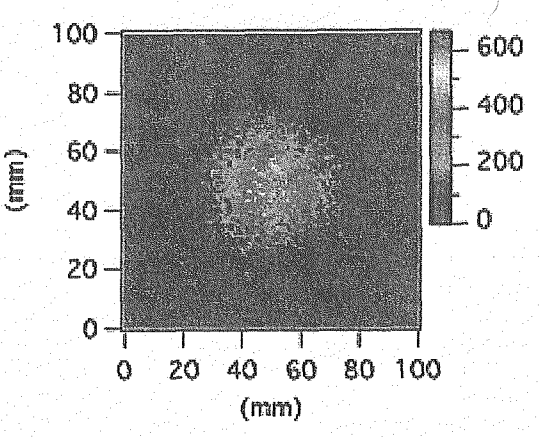

Figure 2: Neutron beam image at sample position. The designed double bent PG monochromator can condense the neutron beam to 20×20 mm^2 at sample position.

原子炉：JRR-3　　装置：TAS-1(2G)　　分野：中性子散乱（装置）

研究テーマ：高効率・高分解能マイクロストリップガス計数管の開発
表　題：高効率・高分解能マイクロストリップガス計数管の開発

10) Development of a High-resolution Microstrip Gas Chamber

H. Takahashi, P. Siritiprussamee, K. Fujita, T. Oku[1], and J. Suzuki[1]

Department of Nuclear Engineering and Management, Graduate School of Engineering, The University of Tokyo 113-8656

[1]*Advanced Science Research Center, JAERI, Tokai, Ibaraki 319-1195*

Nowadays, neutron detectors draw many attentions since new intense spallation neutron sources and new neutron optics are being developed. Conventional neutron detectors suffer from their low count rate, poor position resolutions, and low energy resolutions, etc. Since those properties are depending on the detector types, new innovative neutron detectors are demanded. In particular, high-resolution and low-gamma-background detectors will be major instruments in the next generation neutron scattering facilities. This study concentrates on the development of a new He-3 gas counter based on the recent new technology. New multi-grid-type He-3 MSGCs (MicroStrip Gas Chamber) are designed [1], fabricated, and tested in this research. Here we describe the recent results in this type of the detector.

Multi-grid-type MSGCs are designed for stabilizing electric field by placing many intermediate electrodes between the anode and the cathode. This detector enables fast signals and can operate in a very high pressure gas under a high concentration of the stopping gas such as CF_4. Figure 1 shows a typical gas gain characteristics of our detector operated at more than 4 bars. We could achieve the gas gain of more than 100 for this gas[2]. It is notable that such a high gain is not achieved in other types of micropattern gas detectors. In order to measure signals from backside. floating pads are placed in the vicinity of the cathode. These pads successfully transmit induced charge signals to the backside. Although the amount of induced charge becomes slightly smaller than the front signals, we could almost collect more than 80 % of the total charge if 300 μm thick substrate is used with an anode pitch of 400 μm to 800 μm. This detector is tested at the JRR-3 NOP beam line. Figure 2 shows an obtained backside resolution for two-dimensional M-MSGC. The measured resolution was about 600 μm (FWHM). However, the diameter of the collimator was 500 μm, Therefore, our detector resolution corresponds to the intrinsic position resolution of 400μm (FWHM). This is close to the best value obtained with the gaseous neutron detector.

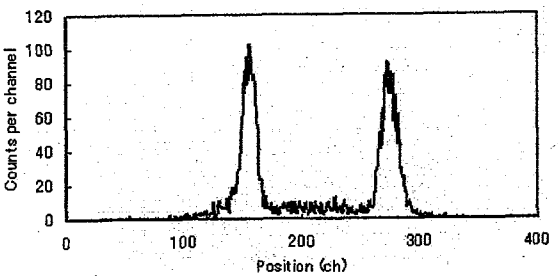

Figure 2: Energy resolution of He-3 M-MSGC.

References

1) H. Takahashi, P. Siritiprussamee, M. Kai, M. Nakazawa, T. Ino, M. Furusaka, S. Kishimoto, M. Taniguchi, S. Ito, M. Kanazawa, "Development of a two-dimensional multi-grid-type microstrip gas chamber for spallation neutron source": Nuclear Instruments and Methods in physics research A **529** (2004) 348.

2) P. Siritiprussamee, H. Takahashi, J.Y. Yeom, T. Ishitsu, M. Kai, M. Nakazawa, S. Kishimoto, T. Ino, M. Furusaka, "A new M-MSGC readout method and front-end ASIC development": Nuclear Instruments and Methods in physics research A **525** 1-2, **225-228** (2004) 225.

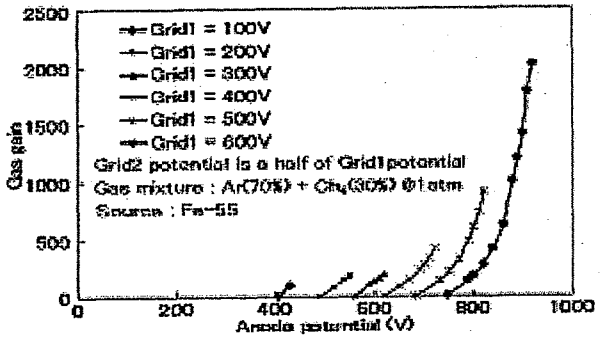

Figure 1: Gas gain characteristics of M-MSGC.

原子炉：JRR-3　　装置：NOP(C3-1-2-1)　　分野：中性子散乱（装置）

1. 中性子散乱 9) 残留応力

1. Neutron Scattering 9) Residual Stress

This is a blank page.

研究テーマ：中性子散乱による産業用物質材料の構造解析の開発研究
表　題：格子定数の不要な中性子応力測定法を用いた突合せ溶接材の残留応力評価

1) Residual Stress Measurement of Butt Weld Sample Using Neutron Stress Measurement Method without Strain-Free Lattice Constant

H. Suzuki, A. Moriai, N. Minakawa[1] and Y. Morii

Neutron Science Research Center, JAERI, Tokai, Ibaraki 319-1195
[1]Advanced Machine Factory Ltd., Hitach, Ibaraki 319-1231

We have developed new stress measurement method which can determine the residual stresses without using measured lattice spacing d_0 in strain-free condition. This method is explained as follow. Relation between lattice spacing, say d_{ii}, and each stress components, say σ_{ii}, is expressed by the following equations in cubic crystal structure.

$$
\begin{aligned}
d_{11}\sqrt{h_n^2+k_n^2+l_n^2} &= \frac{\sigma_{11}-\nu\sigma_{22}-\nu\sigma_{33}}{E_{h_nk_nl_n}} + a, \\
d_{22}\sqrt{h_n^2+k_n^2+l_n^2} &= \frac{-\nu\sigma_{11}+\sigma_{22}-\nu\sigma_{33}}{E_{h_nk_nl_n}} + a, \quad (1) \\
d_{33}\sqrt{h_n^2+k_n^2+l_n^2} &= \frac{-\nu\sigma_{11}-\nu\sigma_{22}+\sigma_{33}}{E_{h_nk_nl_n}} + a,
\end{aligned}
$$

where a is the lattice constant in strain-free condition. If all variables, which are indicated by diffraction elastic constants in Eq. (1), can be regarded as independent variables, the lattice constant a and the residual stress states σ_{ii} can be determined by making the multiple regression analysis after measuring the lattice spacings d_{ii} of two or more kinds of diffraction families in three orthogonal directions.

If correlation between each independent variable in Eq. (1) is higher, reliability of stresses evaluated by regression analysis is becoming lower. Especially, the correlation coefficient will be 1.0 in the case of using theoretical elastic constants in assumption of homogeneous, so that it is better to utilize measured elastic constants depending on crystallographic texture. These measured elastic constants may not be the same as theoretical values, so it will make this correlation lower. Likewise, intergranular strain generated by plastic deformation affects the lattice constant in Eq. (1) so as to make it variable value. Therefore, it is difficult to apply this proposed method to the plastic deformation sample.

This proposed method was applied to evaluate the residual stress distributions in butt weld sample of high tensile strength steel exhibiting the bcc crystal structure. Lattice spacings of 110 and 200 were measured in normal direction and those of 200 and 211 were measured in transverse and longitudinal directions. In order to compare the conventional method with proposed method, the distribution of lattice constant of welded sample was experimentally measured by using the coupon samples which were cut from the companion welded sample. The elastic constants of all three diffractions were measured by uniaxial tensile test, and following results were obtained; E_{110}=255±19GPa, ν_{110}=0.18±0.1, E_{200}=163±4GPa, ν_{200}=0.25±0.02, E_{211}=215±8GPa, ν_{211}=0.27±0.05, If these elastic constants are utilized in proposed method, the correlation coefficient is very close to 1.0. In order to reduce this coefficient, the values of Poisson ' s ratio were optimized within error band so as to be minimum coefficient. As a result of optimization of Poisson ' s ratio, 0.28 in ν_{110}, 0.23 in ν_{200} and 0.32 in ν_{211} were obtained to make the coefficient lowest. These optimized elastic constants were utilized in proposed method and intact measured elastic constants were utilized in conventional method.

Figure 1 shows the lattice cosntant and residual stress distributions in 2mm depth of butt weld sample evaluated by the proposed and the conventional methods. The lattice cosntant evaluated by proposed method agreed well with that measured using coupons. Furthermore, The residual stress distributions obtained by our proposed method agreed well with those measured by conventional method within the experimental uncertainty of about ±50MPa. This result indicated that the optimization of elastic constants did not reduce the reliability of stress evaluation using proposed method, and this proposed method can be applied to determine residual stresses in the samples with the complex residual stresses. If we apply this method to plastic deformed sample, *hkl* diffractions, which are not affected by intergranular strain, will allow us to use this method.

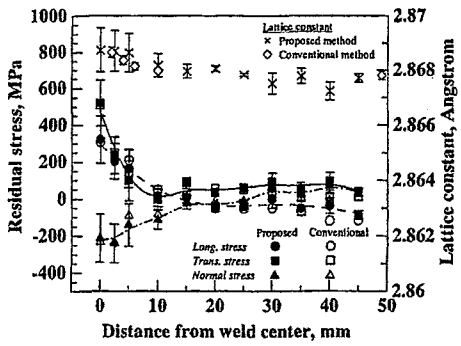

Figure 1: Distributions of lattice cosntant and residual stress.

原子炉：JRR-3　　装置：RESA(T2-1)　　分野：中性子散乱（残留応力）

研究テーマ：中性子散乱による産業用物質材料の構造解析の開発研究
表　題：円筒状２次元炭素複合材料の製造工程における残留歪みの測定

2) Measurements of Residual Strain for the Cylindrical 2-dimensional Carbon-carbon Composite at Manufacturing Process

S. Baba, A. Moriai[1], N. Minakawa[1], M. Yamaji and K. Sawa

Department of Advanced Nuclear Heat Technology, JAERI, Oarai, Ibaraki 311-1394
[1]Neutron Science Research Center, JAERI, Tokai, Ibaraki 319-1195

1. INTRODUCTION

Owing to excellent characteristics such as high strength and high thermal shock resistance, carbon-carbon composite materials (C/C composite) have been thought as promising materials to the high temperature components in nuclear facilities, e.g. elements of control rod for the use in HTGR (High Temperature Gas-cooled Reactor). The C/C composite is study as the powerful candidate material for the elements of control rod of the HTGR in the future; however, the delamination occurred in 2-dimensional cylindrical C/C composites during manufactured process.

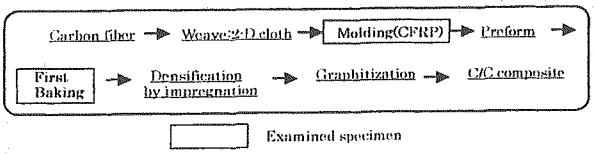

Figure 1: Manufacturing process of 2-d C/C composite (CX-270G).

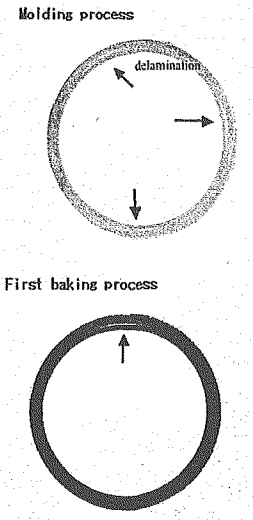

Figure 2: Neutron radiography of the cylindrical C/C composite.

2. EXPERIMENTAL PROCEDURES

Manufacturing process of 2-dimensional C/C composites is shown in Fig.1. It was observed to confirm the delamination occurred during manufactured process in the molding process and in the first baking process by non-destructive testing such as Neutron Radiography by Imaging Plate (NRIP) and X-ray Radiography (XR) method. These radiography images are shown in Fig.2 and Fig.3, respectivily.

In the present study, the change of residual strain in 3-axes direction (radial, hoop and axial) of the 2-d C/C composites were measured for clear the causes of the delamination. Two kinds of specimen were examined which are molding process and first baking process, these heat treatment temperature (HTT) were 433K and 1273K, respectively. The residual strain was measured by neutron diffraction method using the RESA (REsidual Stress Analyzer, Fig.3) in the JRR-3M (Japan Research Reactor-No.3 Modified) of the Tokai Establishment of JAERI. The strain measurement by the neutrons method is based on the Bragg diffraction of neutrons by crystals. For the test, a single wavelength is selected by the monochromator made of pyrolytic graphite. When a monochromatic

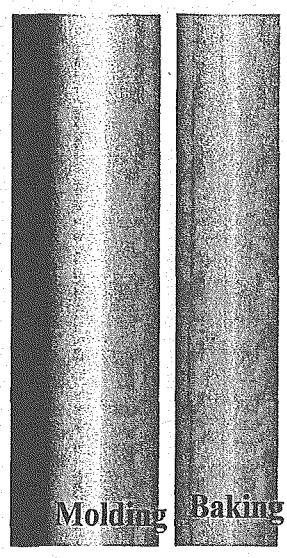

Figure 3: X-ray radiography of the cylindrical C/C composite.

原子炉：JRR-3　　装置：RESA(T2-1)　　分野：中性子散乱（残留応力）

ray (002 plane) of the wavelength is irradiated on the crystal, the diffraction takes place at the angle θ which satisfies the following equation:

$$\lambda = 2d \sin\theta \quad \text{----------(1)}$$

Where d is the spacing of diffracting planes. When the lattice spacing changes from d_0 to d due to stresses, the strain ε is defined by

$$\varepsilon = (d - d_0) / d_0 \quad \text{----------(2)}$$

The measurement procedures were as follows.
(1)The precise wavelength of neutron diffraction was determined using the Ni(111), (200) and (220) diffractions.
(2)The most suitable line for lattice spacing of strain-free samples was determined by C/C composite powder, which are made by filing for each one of samples on the molding and the first baking process.
(3)The change of residual strain in 3-axes direction (radial, hoop and axial) of the 2-d cylindrical C/C composites samples were measured.
(4)The measured (002) diffraction intensity of the each C/C composite samples showed the peak with the shoulder in the low angle site, and the intensity of the peak appears respectively at higher position with narrow width for well-graphitized parts and at lower position with wide width for not well-graphitized parts. The both parts means the matrix region and the carbon fiber region in the C/C composite material, respectively.
(5)The intensity vs. ($2\sin\theta / \lambda$) of (002) diffraction profile were plot in Fig.4. The narrow peak position takes to layer spacing of the matrix region, and also the wide peak position takes the carbon fiber region. The strain ε of 3-axes directions of 2-dimensional cylindrical C/C composite samples were calculated from these layer spacing data d and d_0 by equation (2).
The calculated values are showed in Table 1: the minus values mean compressive strain and the no marked values mean tensile strain.

3. RESULTS and DISCUSSIONS

There are the residual strains in the molding process, tensile mode are showed from 20000 to 50000$\mu\varepsilon$ at the fiber parts and the compression mode are showed from 1000 to 2000$\mu\varepsilon$ at the matrix parts as shown in Table 1. The other hand, the residual strains in the first baking process are changed from tensile mode to compression mode at the direction of radial and hoop in the fiber parts, but the matrix parts are changed reverse from compression mode to tensile mode . Also the residual strains are eased on the process of the molding to first baking in the 3-axis directions. This reason is evaluated that the strain release takes place by the heat treatment temperature of the molding to first baking process. Therefore, the delaminations decreased in the step of molding process to the first baking process.

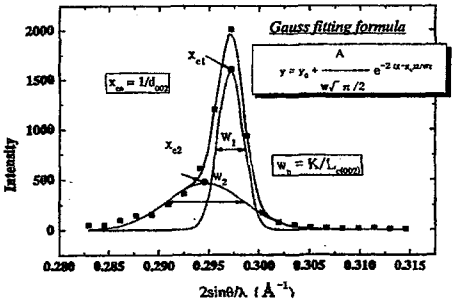

Figure 4: Gauss fitting fomula of 002 layer spacing and crstallite,Lc for C/C composie.

Table 1: Residual strain of molding and baking sample

Molding	Axial	Radial	Hoop
matrix($\mu\varepsilon$)	-1240	-930	-2130
fiber($\mu\varepsilon$)	18090	20500	48170
Baking	Axial	Radial	Hoop
matrix($\mu\varepsilon$)	-690	410	760
fiber($\mu\varepsilon$)	3140	-11930	-2010

研究テーマ：放電プラズマ焼結法で作製した SiC-C 複合材の残留応力測定
表　題：放電プラズマ焼結法で作製した SiC-C 複合材の残留応力測定

3) Residual Stress in SiC-C Composite Materials made by Spark Plasma Sintering

K. Inoue, H. Suzuki[1], A. Moriai[1], M. Ohyanagi, T. Yamamoto and T. Nakayama

Faculty of Science and Technology, Ryukoku University, Otsu 520-2194
[1]Neutron Science Research Center, JAERI, Tokai, Ibaraki 319-1195

A silicon carbide, SiC (β-phase), has excellent properties of oxidation-proof and radiation-proof. Meanwhile, a graphite, C (2H-graphite), has high heat-conductivity, though it is oxidized. It is expected to be very useful, if we succeed in connecting the two materials strongly to make a new high quality functional material. For instance, it can be used for a nose-head or a plasma-proof wall of a space shuttle, where the high heat conductivity is necessary in addition to the oxidation-proof and radiation-proof properties.

So far it has been difficult to obtain a high density material made of these two materials because of their high melting point. However, some of the authors [1,2] have succeeded in making a connected material with high density, by designing the special procedures of the milling of source powders and by using the spark plasma sintering method. The three layered material, SiC-C(10mass%B)-SiC, made by the spark plasma sintering, is shown in Figure 1. It is 30 mm in diameter and each layer has a thickness of 3 mm. From the crack made with an intension of seeing the internal part of the material, we recognize that the material is very dense and the connection of two materials is very tight.

We have estimated the residual stress in the SiC layer of this three layered material. Three directional residual strains were measured at each position on the radius of the plane with a depth of 1.5 mm from the surface of SiC layer. RESA at JRR-3 was used. As the thickness of the SiC layer was only 3 mm, the slit for the incident neutron beam was 2 mm × 2 mm and the slit for scattered beam was 2 mm × 10 mm. Much time was necessary to adjust the beam center at the depth of 1.5 mm from the surface. The (111) scattering was used for axial direction and the (311) scattering was used for hoop and radial directions. For the measurement of the strain-less lattice spacing, d_0, the block of the SiC (β-phase) with a size of 3 mm × 3 mm × 5 mm was used. For the calculation of the stress, Kröner model was used. The Young's modulus, E, was 456 GPa for (111) plane and was 386 GPa for (311) plane. The Poisson ' s ratio was 0.139 for (111) plane and was 0.194 for (311) plane.

The estimated stress at each position is shown in Figure 2. We see that the stress at each position was compressive for all direction. This experimental result is consistent with the fact that this three layered material is very hard and is not destroyed easily.

This compressive force is desirable, because we have a plan to make a functionally gradient material to connect β-SiC and 2H graphite, where many interval layers of composite material are inserted. In each layer the ratio of the 2H-graphite versus β-SiC are changed gradually.

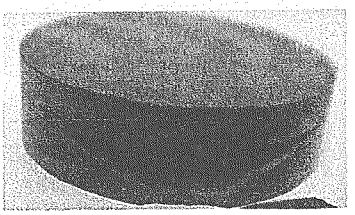

Figure 1: Phtograph of the sample.

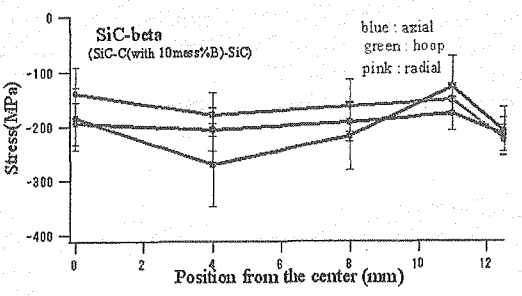

Figure 2: Residual stress at each position of SiC layer.

References

1) T. Yamamoto, T. Ishii, Y. Kodera, H. Kitaura, M. Ohyanagi and Z. Munir : J. Ceramic Society Jpn. **112** (2004) S940.
2) T. Yamamoto, H. Kitaura, Y. Kodera, T. Ishii, M. Ohyanagi and Z. Munir : J. Am. Cerum. Soc. **87** (2004) 1436.

原子炉：JRR-3　　装置：RESA(T2-1)　　分野：中性子散乱（残留応力）

研究テーマ：鉄鋼材料の塑性加工あるいは加工熱処理に伴うミクロ組織形成と残留応力発生の中性子回折その場測定
表　題：SUS304 鋼機械部品の中性子残留応力測定

4) Residual Stress Measurement by Neutron Diffraction for a SUS 304 Mechanical Component

S. Jin, Y. Shiota[1], Y. Tomota[2], S. Matsushima[3], H. Suzuki and A. Moriai[4]

Graduate student of Ibaraki University, Hitachi, Ibaraki 316-8511
[1] *Graduate student of Ibaraki University, Hitachi, Ibaraki 316-8511*
[2] *Graduate School of Science and Engineering, Ibaraki University, Hitachi, Ibaraki 316-8511*
[3] *NIDAK Co. Ltd., Takahagi, Ibaraki 318-0004*
[4] *Neutron Science Research Center, JAERI, Tokai, Ibaraki 319-1195*

1. Introduction

The residual stress in a rotating mechanical component induces stress-corrosion cracking or fatigue fracture, frequently. Because thermal conductivity of austenitic stainless steel is very low, large residual stress generates during cooling after solution treatment. Such residual stress is usually relaxed by annealing but higher annealing temperature cannot be employed because it brings microstructural change leading to embrittlement. In addition, machining like drilling to make holes etc. is performed after solution treatment sometimes, so that measurement of the stress condition in an interior region of the component is very important. Therefore, neutron diffraction technique was used to measure such residual stresses after solution treatment and after the stress-relief annealing.

2. Experimental Procedures

A rotating mechanical component was machined from a forged SUS 304 stainless steel rod. The component was solution-treated at 1353 K for 3 hs to make microstructure austenite, followed by quenching into water. Then the component was annealed at 823 K for 24 hs to relax the residual stress. These residual stresses were measured by neutron diffraction using a diffractometer, RESA, at JAERI. The gauge volume adopted was 10 x 10 x 10 mm where 111 peak position was chosen. Coupons with 3x3x3 mm were prepared by spark cutting to determine stress-free spacing d0. Then, elastic strain was determined by using the measured (111) spacing d by (d - d0)/d0. As shown in Fig. 1, hoop, radial and axial strains were measured at 6 points. Then the obtained strains were input into the general Hooke's law to calculate stresses, where the elastic constants, i.e., Young modulus E and Poisson ratio ν were taken as 220GPa and 0.30, respectively. The axial strain at the position 4 could not be measured within the permitted machine time, so that the stresses there were not calculated.

3. Results and Discussion

In an as-quenched condition after solutionized, the residual stresses determined were measured. The residual hoop stress near the surface at 6 is compressive which was lowered at 5. These are typical thermal stresses for a simple round bar specimen. It is found that high tensile hydrostatic stresses exist in the interior part like the position 3. This must be attributed to the cooling condition for complicated geometry in Fig. 1. These residual stresses are however not relaxed by the annealing treatment as shown in Fig. 2. Hence, more appropriate stress relief treatment should be employed.

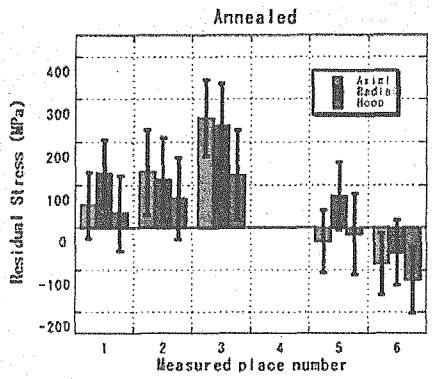

Figure 1: Geometry of a component and positions measured.

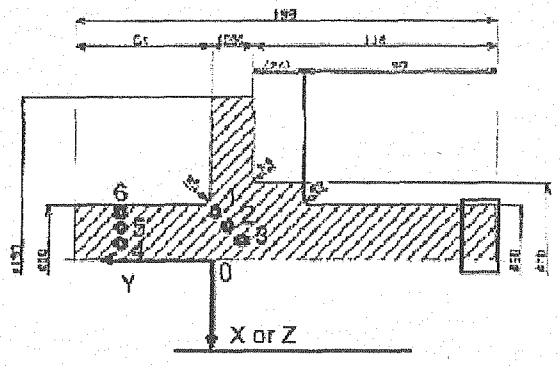

Figure 2: Residual stresses after stress-relief annealing.

原子炉：JRR-3　　装置：RESA(T2-1)　　分野：中性子散乱（残留応力）

研究テーマ：組織傾斜材料の内部応力測定
表　題：中性子による SPS 焼結材料の評価

5) **Neutron Evaluation of SPS Sintered Materials**

Y. Kawasaki[1], I. Shimizu[1], M. Hataya[1], T. Matsubara[2], A. Moriai[3], K. Kusaka[1] and T. Hanabusa[1]
[1] *Tokushima University,* [2] *TPITC,* [3] *JAERI*

1 Introduction

Spark Plasma Sintering (SPS) is a technology that easily makes high density materials from powder samples in a short time. Therefore, SPS is paid to attention as a method of making new materials such as composite materials and the functionally gradient materials. In this experiment, residual stresses and particle size in the sintered materials made by SPS were measured by neutron diffraction.

2 Experimental Method

In this experiment, the powder of α-Fe and α-Al_2O_3 were chosen as a general material. α-Al_2O_3 was sintered at the temperature between 1273K and 1673K by every100K and α-Fe was between 873K and 1273K. Table 1 shows the sintering conditions and Fig.1 shows the positions of measurement. Residual stresses in the specimens were measured by RESA of JAERI. Triaxial stress measurement was made at every measurement position. Table 2 shows the measurement conditions for neutron diffraction.

Table 1: Sintering conditions

Sintering time (min)	10
Load (MPa)	35
Atmosphere pressure (Pa)	3~4

Table 2: Measurement conditions for neutron diffraction method

	α-Fe (110)	α-Al_2O_3 (113)
λ (nm)	0.207238	0.207236
d_0 (nm)	0.202672	0.208561

3 Results and Discussions

Figure 2 shows the relationship of the sintering temperature and FWHM at each position in the sintered α-Al_2O_3. A similar tendency was observed for the sintered α-Fe. Residual stresses were almost the same regardless of the sintering temperature. The FWHM decreased with increasing the sintering temperature followed by the constant of 0.40 deg for α-Al_2O_3 and 0.38 deg for α-Fe. No change in the size of α-Fe particles was observed whereas a remarkable grain growth was observed in α-Al_2O_3 above 1473K. Residual stresses in α-Al_2O_3 and α-Fe were almost constant independent of the sintering temperature as well as the position, valuing 20 and 70MPa, respectively. Furthermore, microscopic stresses are seemed to decrease with increasing the sintering the temperature.

4 Conclusions

In this experiment, the characteristics of sintered α-Fe and α-Al_2O_3 by SPS were examined by measureing stresses and FWHM using neutron diffraction. Although further systematic investigations are necessary, the present experiment showed the possibility that the best sintering temperature can be decided from the diffraction data on the relationship between sintering temperature and FWHM of α-Fe and α-Al_2O_3.

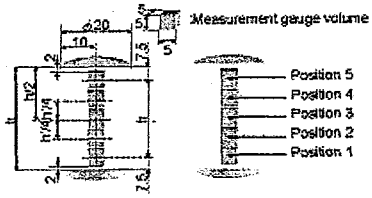

Figure 1: Definition of measurement positions.

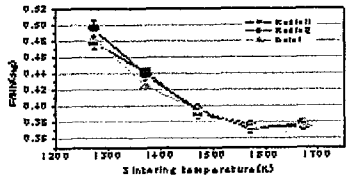

Figure 2: Relationship between sintering temperature and FWHM of α-Al_2O_3 diffraction.

原子炉：JRR-3　　装置：RESA(T2-1)　　分野：中性子散乱（残留応力）

研究テーマ：鉄鋼材料の塑性加工あるいは加工熱処理に伴うミクロ組織形成と残留応力発生の中性子回折その場測定
表　題：高窒素オーステナイト鋼の加工による組織変化と残留応力

6) Microstructure, Deformation and Residual Stress in Plastically Deformed High Nitrogen Austenitic Steels

K. Ikeda[1], M. Ojima[1], Y. Tomota[2], A. Moriai[3], B. S. Seong[4]

[1] *Gradurate student of Ibaraki University, Hitachi, Ibaraki 316-8511*
[2] *Ibaraki Univ. Graduate school, Hitachi, Ibaraki 316-8511*
[3] *Neutron Science Reseach Center, JAERI, Ibaraki 319-1195*
[4] *HANARO, KAERI, Yuseong, Daejeon , Korea 305-600*

1 introduction

Recentry, nickel bearing austenitic steels have brought various problems such as human body allergy and depletion of resources. So nitrogen attracts much attention as a substitute element of nickel. It is known that nitrogen addition to austenitic stainless steels improves various mechanical properties[1]; nitrogen addition increases yield strength and work hardening[2]; recent reseaches have revealed that nitrogen addition increases thermal stress component as well as athermal stress[3]. By an atom probe analysis, a pair of nitrogen and molybdenum atoms was found[4]. However, the strengthening mechanism and microstructure like nano-sized cluster.

2 Experimental procedures

Materials used in this investigation were two austenitic steels which contained different nitrogen concentrations, whose chemical compositions were listed in Table 1. The steels were made at Naoetsu Lab. of Sumitomo Metal Industries Co. Ltd. N1 steel was melted by a conventional vacuum furnace while N2 steel was melted by using a pressure furnace in a nitrogen gas atmosphere. The steels were swaged to rods with 3.0 mm in diameter after the solution treatment at 1523K for 1800s to obtain single austenite structure. The deformation behavior was studied by RESA at JAERI using an AD technique to measure residual stress and FCD at KAERI to measure texture.

Table 1: Chemical compositions of material used (mass%)

steels	C	Cr	Ni	Mo	N
N1	0.014	16.98	12.25	2.36	0.015
N2	0.050	16.94	12.90	2.35	0.556

3 Result and Disccusion

The results of the residual stress is shown in Figure 1. While textures are shown in Figures 2. It is found that lattice plane spacing becomes larger and that $< 111 >$ fiber texture decomes stronger in high nitrogen steel. The reasons of larger residual intergranular stresses and stronger $< 111 >$ fiber textures are speculated to be caused by dislocation motion, i.e., cross slip occures easily in low nitrogen steel but hardly occures and Lomer-Cottrell reaction takes place in higher nitrogen steels as was reported by Tomota *et al.*[5]

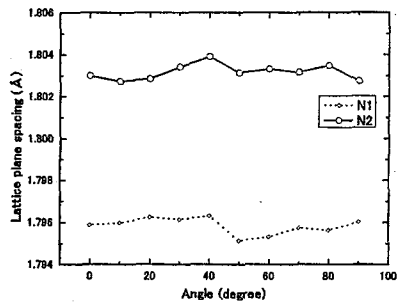

Figure 1: Lattice plane spacing on (200) as a function of angle from the swaging diretion.

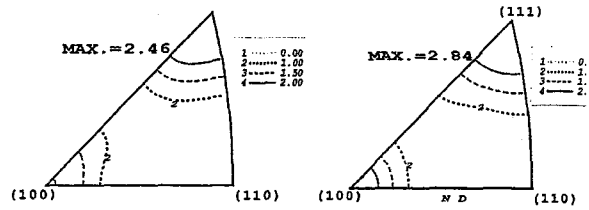

Figure 2: Inverse pole figures : (a) N1 and (b) N2.

References

1) Y. Tomota: Tetsu-to-Hagane **80**(1994) N538; Netsushori **36**(1996) 218; Ferrum **7**(2002)846, **7**(2002) 86.
2) Y. Tomota and S. Endo : ISIJ Int. **30**(1990) 656.
3) M. Kanda and Y. Tomota : CAMP ISIJ **15**(2002) 434.
4) M. Murayama, K. Hono, H. Hirukawa, T. Ohmura and S. Matsuoka : Scripta Materialia **41, 5**(1999) 467.
5) S. Kubota, Y. Xia and Y. Tomota: ISIJ Int. **38**(1998) 474-481.

原子炉：JRR-3　　装置：RESA(T2-1)　　分野：中性子散乱（残留応力）

研究テーマ：原子炉炉内構造物の溶接継手部における残留応力評価
表　題：中性子回折による NCF600-SQV2A の異材溶接継手部の残留応力評価

7) Evaluation of welding residual stress by neutron diffraction for NCF600-SQV2A dissimilar metal weld joint

R. Mizuno, A. Moriai[1], H. Suzuki[1] and Y. Morii[1]

NDE Center, Japan Power Engineering and Inspection Corporation, Yokohama 230-0044
[1]Neutron Science Research Center, JAERI, Tokai, Ibaraki 319-1195

1.Introduction

Stress corrosion cracking (SCC) has occurred at weld joints with Ni-based alloy. It is important to determine the residual stress distribution inside the weld joints in order to evaluate the crack propagation of SCC. Usually, the residual stress distribution of real weld structures is evaluated by FE analysis, but it is difficult to estimate the residual stress with high accuracy. To improve weld residual stress estimations by FE analysis it is available that the calculated results are compared with the measured data. It is possible to measure the stress distributions inside bulk by neutron diffraction. Using conventional weld joint the inside residual stress is measured by this method.

2.Experimental procedures

Tables 1 and 2 show chemical compositions of NCF600 and SQV2A that is Mn-Mo-Ni low alloy steel for pressure vessel, respectively. Butt weld joint with a double V groove is prepared by gas tungsten arc welding using their plates as shown Figure 1. Ni-based alloy(JIS Z 3334 YNiCr-3) is used as filler metal. The base metals are annealed for stress relief before welding. Figure 1 shows the measured points and three directions for residual stress measurement. The slit sizes used are $3\times15mm^2$ for normal and transversal direction and $3\times3mm^2$ for longitudinal direction. Measured diffraction plane is Ni(111).

3.Results

Figure 2 shows the measured results of the residual stress distribution. The large tensile stress over the yield stress(≈400MPa at 20°C) is measured at 3mm depth, 12mm from weld center. This data will be available to make progress in estimations of residual stress distribution by FE analysis.

Table 1: Chemical composition of NCF600(JIS G 4902).(wt%)

	C	Si	Mn	P
NCF600	≤0.15	≤0.50	≤1.00	≤0.030
S	Cr	Fe	Cu	Ni
≤0.015	14.00-17.00	6.00-10.00	≤0.50	Bal.

Table 2: Chemical composition of SQV2A(JIS G 3120) used.(wt%)

	C	Si	Mn	P
SQV2A	0.18	0.28	1.43	0.006
	S	Mo	Ni	Fe
	0.002	0.51	0.69	Bal.

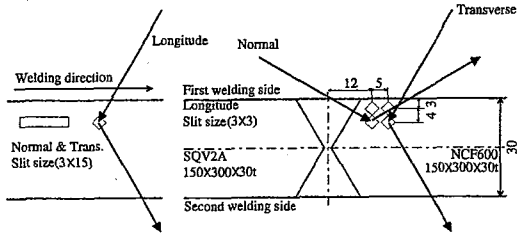

Figure 1: Measured points and directions for residual stress.

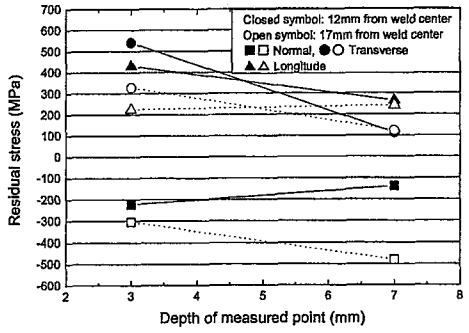

Figure 2: Results of residual stress measurement.

原子炉：JRR-3　　装置：RESA(T2-1)　　分野：中性子散乱（残留応力）

研究テーマ：鉄鋼材料の塑性加工あるいは加工熱処理に伴うミクロ組織形成と残留応力発生の中性子回折その場測定
表　題：強伸線フェライト鋼およびパーライト鋼の残留粒応力分布の測定

8) The Residual Grain Stress Distribution Measurement in Heavily Drawn Ferrite and Pearlite Wire

T. Shiratori, T. Masubuchi, Y. Shiota, Y. Tomota[1] and A. Moriai[2]

Graduate student of Ibaraki University, Hitachi, Ibaraki 316-8511
[1]Graduate School of Science and Engineering, Ibaraki University, Hitachi, Ibaraki 316-8511
[2]Neutron Science Research Center, JAERI, Tokai, Ibaraki 319-1195

1. Introduction

Macroscopic inhomogeneous plastic deformation occurs in the cross section of heavily drawn steel wire, leading to the generation of macroscopic residual stress. Beside of this stress, the grain (intergranular) stresses are generated due to the heterogeneous plastic flow in individual [hkl] oriented family grains [1,2]. In this study, residual grain stress distribution between the inside and the outside parts of the wire were investigated by using neutron diffraction.

2. Experimental Procedures

Drawn ferrite (true strain 5.3) and pearlite (2.5) wires were used and the surface layer of some sample were removed by electrolytic polishing. The residual grain stresses were determined from (110) and (200) diffraction profiles obtained by the AD method changing direction with respect to the drawing direction.

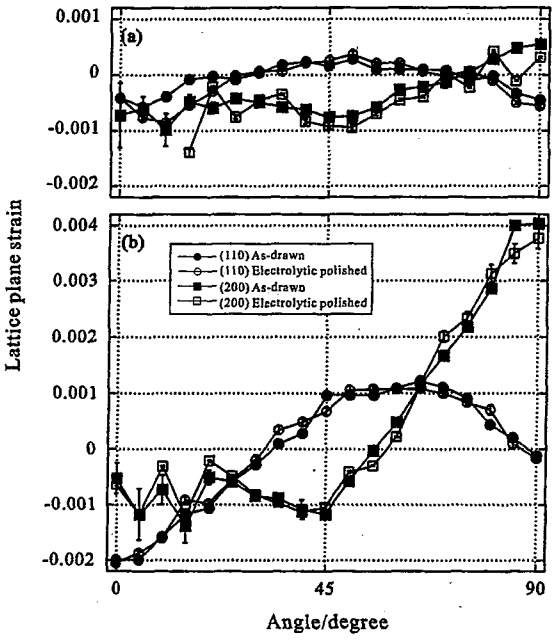

Figure 1: Residual grain strains as a function of the angle between the measuring and the drawing direction for ferrite (a) and pearlite (b) wire determined by the AD method with RESA at JAERI.

3. Results and Discussion

A typical example is shown in Fig. 1. Microscopic inhomogeneous plastic deformation related to intergranular stress is almost similar between the inside and the outside parts of a wire. Because of the strong (110) fiber texture (shown Fig. 2), the (200) diffraction at 0 degree with respect to the drawing direction is extremely weak to evaluate the elastic strain. The residual (110) grain stress changes from compression to tension and again toward compression with increasing of the angle from the drawing direction. It implies that the plastic misfit strains between different [hkl] family grains are yielded during the drawing resulting in the heterogeneous residual stresses. The magnitude of the residual grain strains becomes larger but the overall trend is hardly changed with carbon concentration. Hence, the [hkl] grain strains are caused by plastic heterogeneity in the ferrite matrix; individual ferrite grains for a ferrite steel or ferrite blocks in case of pearlite steel.

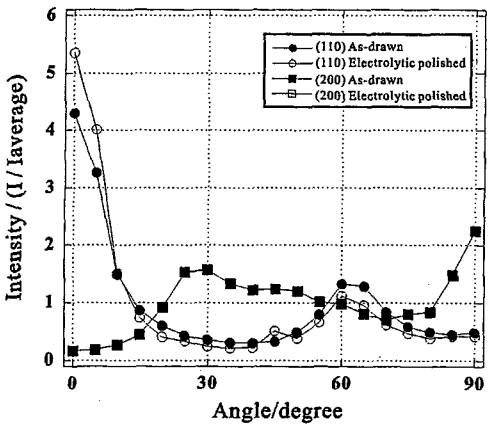

Figure 2: (110) fiber texture measured by neutron diffraction for pearlite wire.

References

1) T. Suzuki, Y. Tomota, M. Isaka, A. Moriai, N. Minakawa and Y. Mori: ISIJ Int 44 (2004) 1426.
2) Y. Tomota, T. Suzuki, A. Kanie, Y. Shiota, M. Uno, A. Moriai, N. Minakawa, Y. Morii: Acta Mater 53 (2005) 463.

原子炉：JRR-3　　装置：RESA(T2-1)　　分野：中性子散乱（残留応力）

This is a blank page.

1. 中性子散乱　１０）その他

1. Neutron Scattering　10) Others

This is a blank page.

1) Development of high pressure micro-cell for sequential measurements between magnetization and neutron scattering under high pressure

Tetsuya Fujiwara[1], Naofumi Aso[2], Masakazu Nishi[2], Yoshiya Uwatoko[1], Toru Shigeoka[3] and Kazuma Hirota[2]

[1] *ISSP, Univ. of Tokyo, Kawahiwa, Chiba 277-8581*
[2] *Neutron Sci. Lab., ISSP, Univ. of Tokyo, Tokai, Ibaraki 319-1106*
[3] *Yamaguchi Univ., Yamaguchi 753-8521*

Over the past few decades, a considerable number of studies have been conducted on the physical properties of Ce-, Yb- and U-based intermetallics, the so-called strongly correlated electron systems. In these systems, an external pressure is often a key to bring about a new type of ground state accompanied with exotic physical phenomena, such as a heavy fermion superconductivity [1] or valence transition [2] and so on. Accordingly, nowadays, the concern with an application of high pressure generation techniques to various sorts of experimental measurements has been growing remarkably. To neutron scattering experiments are no exception too. In the circumstances, we have designed a high pressure micro-cell for magnetization and specific heat measurements under $P = 2.0$ GPa, recently. (see Fig.1) [3] This micro-cell is amazingly so small as the design of the cell is subject to measure the magnetization by a commercial SQUID magnetometer, MPMS (Quantum Design Co. Ltd.) As is shown in Fig.1, an outer diameter and a length of the cylinder are 8.8 mm and 21 mm, respectively. A volume of an effective sample space under $P \sim 2.0$ GPa is $\sim \phi 2.7 \times 3$ (mm^3).

In this time, we attempt to apply this micro-cell to the neutron scattering experiments. In other words, we seek a posibility of sequential measurements without any re-adjustments of pressure condition between magnetization and neutron diffraction. $TbNi_2Si_2$ was adopted as a test case sample. According to Shigeoka et al. [4], the tetragonal $TbNi_2Si_2$ compound undergoes successive two magnetic phase transitions; below $T_N = 15$ K an amplitude modulated anti-

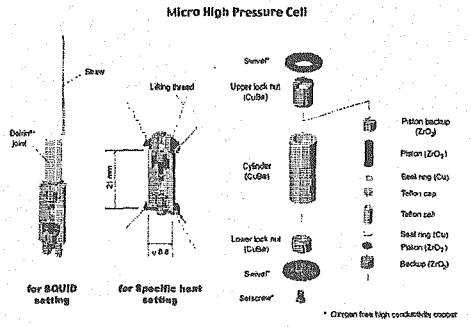

Fig. 1. A schematic drawing o the high pressure micro-cell.

ferromagnetic structure (phase I) with $Q_1 = (1/2 \pm \tau, 1/2 \mp \tau, 0)$, $\tau = 0.075$, and then below 9 K a simple antiferromagnetic structure (phase II) with a propagation vector $Q_2 = (1/2, 1/2, 0)$, having a magnetic moment ($M = 8.8\ \mu_B$) close to the maximum value for a Tb^{3+} ion and parellel to the c-axis. Furthermore, Kawano et al. [5] revealed that any changes of magnetic structures are not induced by pressure without external magnetic field.

In the experiment, a small single crystal of $TbNi_2Ge_2$ with sample volume $1 \times 1 \times 3$ (mm^3) was mounted into the micro-cell together with a small piece of Sn. linear scans were mainly performed on the ($hk0$) reciprocal lattice plane at $1.5 \leq T \leq 15$ K using a tripl-axis spectrometer (PONTA) at JRR-3M of reactor of JAERI. Generated pressure was calibrated on the basis of pressure dependence of superconducting transition temperature of Sn using the SQUID magnetometer (MPMS).

Fig.2 shows linear scan along (h 1 $-h$ 0) direction at $T = 9$ K under $P = 1.02$ GPa in $TbNi_2Si_2$. As is recognizable from the figure,

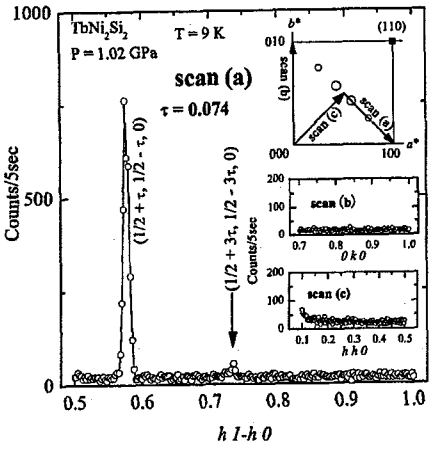

Fig. 2. A linear scan along (h 1 − h 0) direction at T = 9 K under P = 1.02 GPa in $TbNi_2Si_2$. The insets show a reciprocal lattice map and linear scans along (0 k 0) and (h h 0) directions from above, respectively.

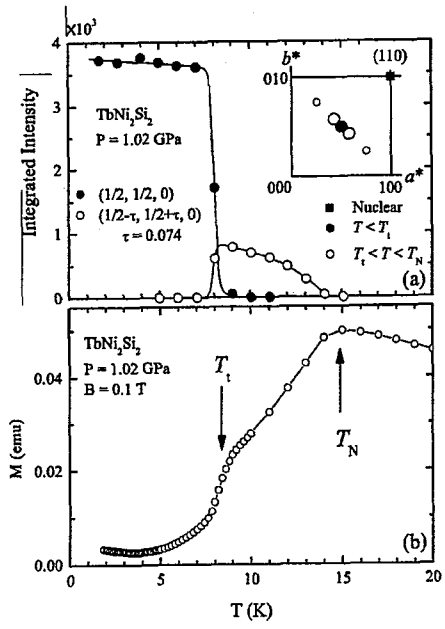

Fig. 3. (a) Peak intensities of the (1/2, 1/2, 0) and (1/2 - τ, 1/2 + τ, 0) (τ = 0.074) antiferromagnetic reflections as a function of temperature under P = 1.02 GPa. (b) Temperature dependence of magnetization at B = 0.1 T applied along c-axis under P = 1.02 GPa in $TbNi_2Si_2$.

it was succeeded to detect clearly a third harmonics of antiferromagnetic bragg reflection from the small single crystal in the micro-cell in spite of monitoring for 5 seconds. In addition, This micro-cell does not contribute to make back ground at $2\theta \leq$ 35-degree. Subsequently, magnetization measurements were performed by appling magnetic field parallel to the c-axis of $TbNi_2Si_2$ under the same pressure condition. Fig.3 (a) and (b) give a peak intensities of the (1/2, 1/2, 0) and (1/2 - τ, 1/2 + τ, 0) (τ = 0.074) antiferromagnetic reflections under P = 1.02 GPa as a function of temperature and temperature dependence of magnetization at B = 0.1 T under P = 1.02 GPa in $TbNi_2Si_2$, respectively. Both results are in good agreement with those observed by Shigeoka et al. [4] As just described, we succeeded to measure sequentially both neutron diffraction and magnetization in Tb compound without any readjustments of pressure condition.

References

[1] N. D. mathur *et al.*: Nature (London), **394** (1998) 39.
[2] I. Felner *et al.*: Phys. Rev. B, **33** (1986) 617.
[3] Y. Uwatoko *et al.*: J. Phys: Cond Mater, **17** (2005) S1011.
[4] T. Shigeoka *et al.*: J. Phys. Soc. Jpn, **61** (1992) 4559.
[5] S. Kawano *et al.*: Physica B, **241-243** (1998) 657.

研究テーマ：中性子イメージングプレートによる中性子応力測定
表題：中性子イメージングプレートによる中性子応力測定に関する基礎的研究

2) A Fundamental Study on Neutron Stress Measurement Using an Image Plate

T. Sasaki, Y. Morii* and N. Miyakawa *

*Dept. of Materials Science and Engineering, Kanazawa University, Kakuma-machi, Kanazawa 921-1192, Japan; *The Japan Atomic Energy Research Institute, Tokai, Ibaraki-ken 319-1195, Japan*

Residual stresses can play an important role in fracture processes in many engineering components. The X-ray diffraction method can be applied to measure residual stresses non-destructively. However, the measuring depth (X-ray penetration depth) is limited to less than about 0.1 mm. So the measurement for inside material needs to remove the surface layer using, for example, the electro-polishing, which will disturb the stresses that exist in the material initially. Stress measurement using the neutron diffraction technique is a useful tool for evaluating the stress state inside materials.

A use of an area detector (two dimensional detector) such as, for example, a neutron image plate (NIP) enables us to use huge amount of diffraction data at a stretch, compared to the ordinary method. Such feature of sampling a lot of diffraction data expects us to perform more precise and detailed stress analysis. The present study was made to find such possibility of the neutron image plate for the stress measurement.

The neutron experiment was conducted using the research reactor named JRR-3 at the Japan Atomic Energy Research Institute (JAERI). Thermal neutrons derived from the reactor passed through the guide tube and were monochromated to the wave length of 0.20888 nm. A slit made from cadmium of the diameter of 3 mm was put at the exit. The NIP was put into the cassette which was covered with both an aluminum plate (1 mm thickness) and a lead plate (1 mm thickness). The cassette, placed normal to the incoming beams, had a hole at its center so the neutron beam can pass through. The specimen was put after the NIP with an incident angle of 20 degree against incoming beams. The distance between the NIP and the specimen was 65 mm. Figure.1 shows the apparatus used in the experiment set at the beam line called RESA (Residual Stress Analyzer).

The material used was steel, JIS S50C. The specimen was processed to have the geometry of 150mm length, 15 mm width and 2 mm thickness. It was then heat-treated for stress release under the condition of 650 degree C for 30 minutes.

The results obtained in this study were reported in refs[1,2]. The summary is as follows. The peak locations of the neutron diffraction ring show a curved pattern even if the stress in the material is released, which is caused by the distortion of the diffraction intensity profile due to the superposition of diffractions emerged from entire depth in the material that the neutron beams penetrate.

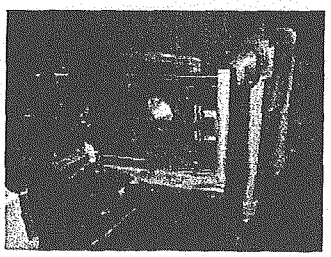

Figure 1 : *Experimental setup for stress measurement with neutron image plate (NIP).*

References

[1] T.Sasaki, N.Minakawa, Y.Morii, N.Niimura and Y. Hirose, Transactions of the Japan Society of Mechanical Engineers, vo.69, No.688, p.1711 (2003)..

[2] T.Sasaki and Y. Hirose, Transactions of the Japan Society of Mechanical Engineers, vo.71, No.704, p.670(2005).

使用施設：JRR-3M，装置：RESA，分野 Industrial Application

研究テーマ： IRT 課題
表題： 低温中性子回折実験用小型 CuBe 製ピストンシリンダー型圧力セルの開発とその性能

3) The development and the properties of a small copper-beryllium-based piston-cylinder-type clamp cell for low temperature neutron diffraction measurements

Naofumi Aso, Tetsuya Fujiwara[1] and Yoshiya Uwatoko[1]
Neutron Sci. Lab., ISSP, Univ. of Tokyo, Tokai, Ibaraki 319-1106,
[1]*ISSP, Univ. of Tokyo, Kashiwa 277-8581*

During the last two decades, many investigations of strongly correlated electrons systems such as Ce-, Yb- and U- based intermetallic compounds have been performed extensively. Recently, these studies have been actively attempted under high pressures since such strongly correlated electrons systems have ground states which are quite sensitive to external pressure. Therefore, advances of high pressure generation techniques for these measurements not only yield enormous amount of information to understand the physical properties of systems but also occasionally lead to discover of much more interesting new physical phenomena, for example, exotic superconducting states induced upon pressurization in $CePd_2Si_2$ [1], $YbInCu_4$ [2] and UGe_2 [3].

The McWhan-type High Pressure Cell [4, 5] has been long used for a lot of neutron scattering experiments under pressure in the reactor JRR-3M in JAERI, Japan. But this pressure cell is so big and heavy that it cannot be used for the low temperature measurements using the cryostat such as a dilution refrigerator due to the limitation of the space. Thus, there is an urgent need to develop more small and convenient pressure cell for low-temperature neutron scattering measurements. In this report, the development and the properties of a small copper-beryllium-based piston-cylinder-type clamp cell is introduced. It is attributed to the studies for the low temperature neutron diffraction measurements.

The pressure cell was planned for the existing ISSP dilution refrigerator with the sample space (height: $\sim$ 65 mm, diameter: $\sim$ 30mm). Figure 1 shows the schematic drawing of a piston-cylinder-type clamp cell.

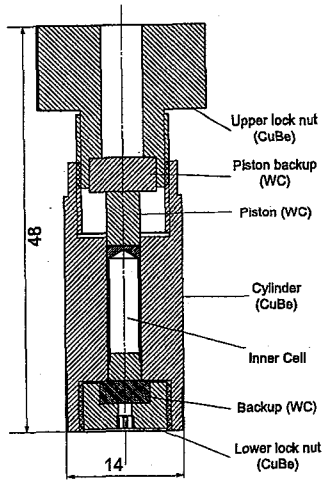

Fig. 1. A schematic drawing of the pressure cell.

Hardened copper-beryllium (CuBe) alloy was chosen as the most parts of the cell to obtain the maximum pressure of 2 GPa. Tungsten carbide (WC) is used as a piston and a backup. We are testing the various inner cells made of teflon, copper and aluminum. Fluorinert FC75 or the mixture of Fluorinert FC70 : FC77 = 1 : 1 or Daphne 7373 was used as a pressure transmitting medium. The outer diameter of the cylinder is 14 mm and the diameter of the inner cell is 4 mm. We can attach almost all the cryostats in JRR-3M.

Pressurizing tests have been performed on the triple-axis spectrometers HER (C1-1), HQR (T1-1) and PONTA (5G). Figure 2 illustrates one example of the pressurizing test for NaCl obtained on the HER by using the fluorinert FC75. Pressure was estimated by determining the change in lattice parameter of the NaCl itself. The pressurinzing curve shows roughly linear behaviour and it can be pressurized up to 1.72 GPa at room temper-

使用施設：JRR-3M, 装置： 5G (PONTA), C1-1 (HER), T1-1 (HQR) , 分野： 107: Instrumentations

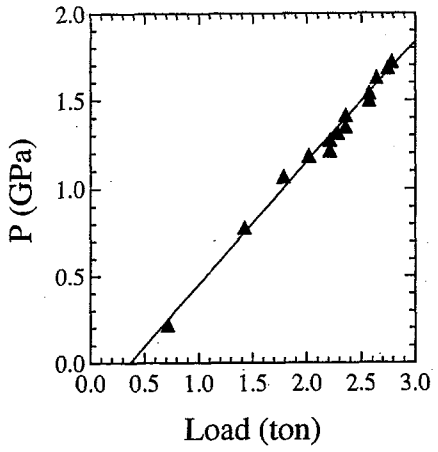

Fig. 2. Pressures vs. applied forces at room temperature.

ature for this test.

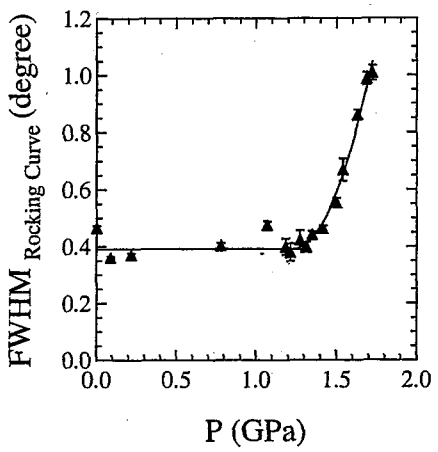

Fig. 3. Rocking curve linewidth of Q = (2,0,0) Bragg reflections in NaCl as a function of pressure. Fluorinert FC75 was used as a pressure transmitting media.

Figure 3 shows a rockin curve linewidth of Q = (2,0,0) Bragg reflections in NaCl as a function of pressure, using the fluorinert FC75 as a pressure transmitting media. The linewidth becomes constant up to around P = 1.4 GPa, where it start increasing. The fluorinert FC75 seem to have the critical pressure that shows the limit of hydrostatic pressure at around P = 1.4 GPa.

The cell introduced here is still under development but it was also used for the neutron diffraction measurements for UGe_2 [6] and $YbMn_2Ge_2$ [7]

References

[1] N.D. Mathur et al., Nature (London) **394** (1998) 39.
[2] Y. Uwatoko et al., Physica B **329-333** (2003) 1658.
[3] S.S. Saxena et al, Nature (London) **406** (2000) 587.
[4] D.B. McWhan et al., Phys. Rev. **20** (1979) 4612.
[5] A. Onodera et al., Jpn. J. Appl. Phys. **26** (1987) 152.
[6] N. Aso et al., submitted.
[7] T. Fujiwara et al., in these activity reports.

4) Inspection of neutron scattering and transmitting performances of pressure transmitting mediums for neutron scattering experiments under high pressures

Tetsuya Fujiwara, Naofumi Aso[1], Masakazu Nishi[1], Yoshiya Uwatoko and Kazuma Hirota[1]
ISSP, Univ. of Tokyo, Kashiwa, Chiba 277 – 8581,
[1] *Neutron Sci. Lab., ISSP, Univ. of Tokyo, Tokai, Ibaraki* 319 – 1106

Over the past few decades, a considerable number of studies have been conducted on the physical properties of Ce-, Yb- and U-based intermetallics, the so-called strongly correlated electron systems. In these systems, an external pressure is often a key to bring about a new type of ground state accompanied with exotic physical phenomena, such as a heavy fermion superconductivity [1] or valence transition [2] and so on. Accordingly, nowadays, the concern with an application of high pressure generation techniques to various sorts of experimental measurements has been growing remarkably. To neutron scattering experiments are no exception too. Thus, we got to work on a development of high pressure apparatuses for neutron scattering experiments. In this paper, we will report the results of inspection about which kind of pressure transmitting medium is suitable for neutron experiments. Firstly, neutron scattering examinations are carried out on several kinds of typical pressure transmitting mediums. To evaluate accurately, each medium is filled with an isometric Al cell ($\phi 5 \times 20$ mm^3). Scattering intensities per 30 seconds are plotted as a function of scattering angle in Fig.1. Scattering intensities of a mixture of methanol : ethanol = 4 : 1 (Metha & Etha), a silicon oil and Daphne7373 are higher than those of other mediums over the investigated 2θ regions. This is attributed to an incoherent scattering by hydrogen due to that these mediums contain much amount of proton. In particular, the Metha & Etha and Silicon oil show a remarkable enhancement of scattering intensity below 50-degree, so that it is advisable to avoid using these mediums for neutron scattering experiments. On the other hand, although Daphne7373 makes relatively higher B.G, not only the scattering intensity is approximately uniformity over the extensive scattering angle but also any peak structure is not observed. A mixture of Fluorinert FC70 : FC77 = 1 : 1 (Fluorinert FC70+77) and Fomblin YH-VAC140/13 (Fomblin 140/13) does not contribute to make B.G. However, it is recognizable that additional scatterings occur at $20 \leq 2\theta \leq 30$ in these mediums, which are contributed to their molecular structures. Compared to these two mediums, Deuterized Metha & Etha (D-Metha & Etha) scatters neutrons additionally at significantly high scattering angle regions ($30 \leq 2\theta \leq 50$) and makes a relatively high B.G.

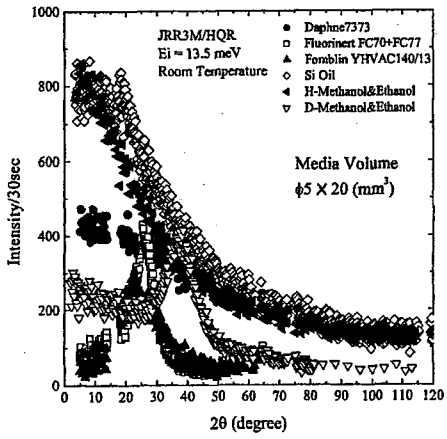

Fig. 1. Scattering intensities per 30 seconds as a function of scattering angle in various kinds of pressure mediums.

And then, to estimate a neutron transmission coefficients, neutron transmissivities were investigated in respective mediums except Metha & Etha and Si oil. Fig.2 shows neutron transmission coefficient as a function of incident neutron energy in various kinds of pressure mediums. Fluorinert FC70+77

and Fomblin 140/13 have the most excellent neutron transmissivity among all. Predictably, Daphne7373 containing a lot of proton is inferior to any other kinds of mediums as concerning with neutron transmissivity. Estimating the neutron transmission coefficients, that of Daphne7373 is by one order larger than those of Fluorinert FC70+77 and Fomblin 140/13.

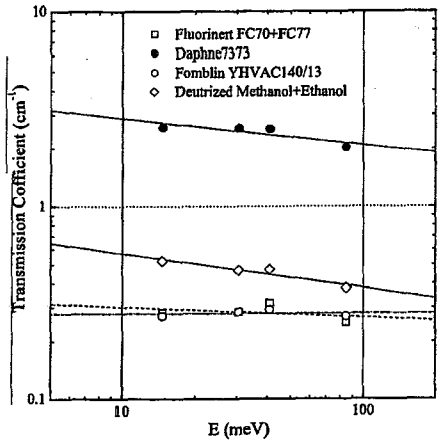

Fig. 2. Neutron transmission coefficient as a function of incident neutron energy in various kinds of pressure transmitting mediums.

To sum up above results, in the case of that there does not exist any significant scatterings from sample near 25-degree, Fluorinert FC70+77 and Fomblin 140/13 must be of use for neutron scattering experiment. When a sample scatters neutron elastically and sufficiently, Daphne7373 would measure up to our expectations. To put it differently, this is not suitable for an identification of pressure induced incommensurate magnetic structure. But, we must not forget the fact that Daphne7373 has .superior hydrostaticity to both Fluorinert FC70+77 and Fomblin 140/13 and its pressure reduction by cooling is several times as small as that of Fluorinert FC70+77 [3].

Neutron scattering and transmissivity examinations were performed on the triple-axis spectrometers HQR(T1-1) and PONTA (5G), respectively.

References

[1] N.D. Mathur et al., Nature (London) **394** (1998) 39.
[2] I. Nowik et al., Phys. Rev. B **33** (1986) 617.
[3] K. Murata et al, Rev. Sci. Instrum **69** (1997) 2490.

研究テーマ:中性子反射率法によるトライボロジー(摩擦、潤滑、摩耗)の研究
表題:中性子反射率法による固体一固体界面の面粗さ測定

5) Observation of the Surface Roughness at Solid-Solid Interface by Neutron Reflectometry

K. Inoue, T. Hirayama, S. Tasaki [*], T. Ebisawa [**] and M. Hino [***]

Faculty of Science and Technology, Ryukoku University, Otsu 520-2194, Japan; [*] Graduate School of Engineering, Kyoto University, Sakyo-ku, Kyoto 606-8501, Japan; [**] Neutron Science Research Center, JAERI, Tokai 319-1195, Japan; [***] Research Reactor Institute, Kyoto University, Kumatori 590-0494, Japan

In the field of tribology which treats the phenomena of friction and wear, there has been no effective technique for the observation of the change of surface roughness at solid-solid interface, because the phenomena occur at the internal surface area of the material. However, neutron beam is able to penetrate far into the material and to reach the interface. Thus, an experiment to detect the neutron beam reflected from the solid-solid interface was tried. When the reflection is observed successfully, it is expected to obtain the information concerning the surface roughness.

When the surface of the material has a roughness as shown schematically in Figure 1, an irregular reflection of the beam will occur even if the incident angle of the beam is lower than the critical angle corresponding to a flat surface. Two dimensional image of the reflected beam observed by the imaging plate (IP) is expected to show the surface roughness of the material. In this experiment it was tried to observe the image of reflected beam on IP. Firstly, to observe the reflection form the surface in the air was tried. Next, to observe the reflection from the solid-solid interface was tried.

Iron blocks which have various types of surface roughness were prepared. The surface area of the iron blocks was 50 mm × 50 mm and the thickness was 20 mm. Each surface was polished by the following three ways. Sample 1 was polished to make a mechanical mirror surface with Rmax=0.1 μ m. Sample 2 was ground systematically using a grinding machine to have a parallel abrasive trace. The roughness, Rmax, was intended to be 1.0 μ m. Sample 3 was lapped randomly by planetary drive, aimed to make Rmax = 1.0 μ m. Each roughness of the surface was measured by a contact-type roughness gauge and the result is shown in Figure 2.

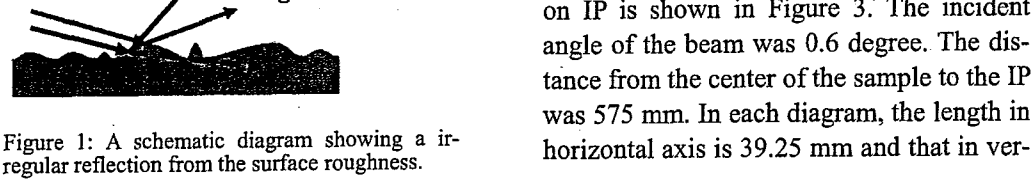

Figure 1: A schematic diagram showing a irregular reflection from the surface roughness.

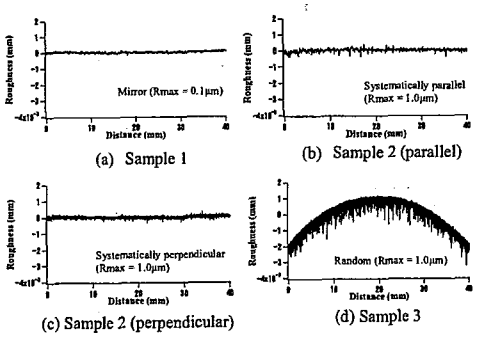

(a) Sample 1 (b) Sample 2 (parallel)
(c) Sample 2 (perpendicular) (d) Sample 3

Figure 2: Roughness of each sample along the center line of the surface, parallel to incident beam. (a) for Sample 1, (b) for Sample 2 where the grinding direction is along the center line, (c) for Sample 2 where the grinding direction is perpendicular to the center line and (d) for Sample 3.

The whole view of each reflected image on IP is shown in Figure 3. The incident angle of the beam was 0.6 degree. The distance from the center of the sample to the IP was 575 mm. In each diagram, the length in horizontal axis is 39.25 mm and that in ver-

使用施設:JRR-3M, 装置:MINE-2(C3-1-2-2), 分野 Others

tical axis is 78.5 mm. The intensity of the reflected beam is classified by the colors. Figure 3 (a) shows the image of direct beam. The other images from (b) to (e) show those reflected from the surface in the air. The image (f) is that from the interface between Sample 2 and the Si-block, where the ground trace of Sample 2 is perpendicular to the incident beam direction.

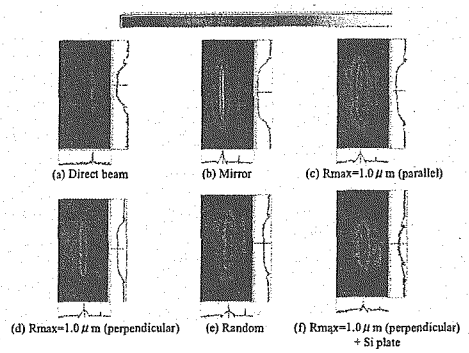

Figure 3: (a) Image of direct beam, (b) Image from Sample 1 in the air, (c) Image from Sample 2 in the air where the ground trace is parallel to the beam direction, (d) Images from Sample 2 in the air where the ground trace is perpendicular to the beam direction, (e) Image from Sample 3 in the air and (f) Image from the interface between Sample 2 (perpendicular case) and the Si-block. The color bar at the top of the figure indicates the order of the strength of beam counts

In Figure 4, the intensity at the center of each image in Figure 3 is magnified and a half on the right-hand side of each image is shown. In Figure 4 the disorder of the color is remarkable, especially in Figures (e) and (f). The distribution of the color is thought to be influenced by the two dimensional distribution of the roughness in real space. The notable disorder of the intensity in the figure (e) is consistent with the remarkable distribution of the roughness shown in Figure 2 (d). The reason of the large disorder in Figure (f) is possibly due to the air space made between Fe-sample and Si-block.

The intensity distribution on the horizontal cursor of the image, which is shown at the bottom of each diagram in Figures 3 and 4, is magnified and shown in Figure 5.

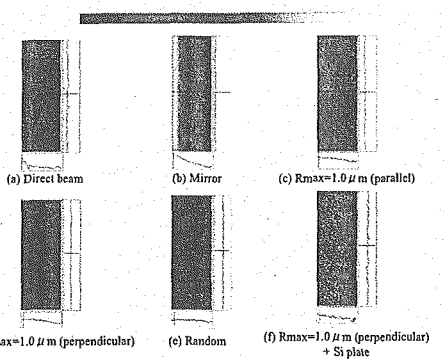

Figure 4; Images on IP, which are a half on the right–hand side, magnified at the center of each image in Figure 3.

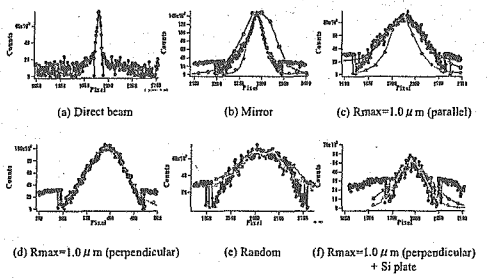

Figure 5; Intensity distribution on the horizontal cursor on IP image. Each figure corresponds to each daigram in Figsures 3 and 4. Intensity distribution of the reflected beam calculated from the measured roughness in Figure 2 is shown by the gray lines.

Each figure corresponds to each image in Figures 3 and 4. Intensity distribution of the reflected beam calculated from the measured roughness in Figure 2 is also shown by the gray lines in Figure 5. By comparing the calculated intensity distribution with the observed distribution of the image on IP, we conclude that the roughness in real space can be estimated by the intensity distribution of the reflected beam on IP.

It was also found that the color distribution of the image on IP projects very well the local irregularity of the surface in real space. Therefore, it becomes possible to know the surface roughness visually.

研究テーマ：ピエゾ結晶の電気的な変形制御による新しい中性子光学素子の開発研究
表題：中性子光学素子を目指した圧電性単結晶の変形測定

6) Deformation measurements of piezoelectric single-crystals for neutron optical devices

S. Kawamura[a], J. H. Kaneko[a], Y. Otake[b], H. Fujimoto[c], F. Fujita[a],
T. Sawamura[a], P. Mikula[d], M. Furusaka[a]

[a] Hokkaido University, N13 W8, Kita-ku, Sapporo, 060-8628, Japan,
[b] Riken, 2-1 Hirosawa, Wako, Saitama 351-0198, Japan,
[c] AIST, Umezono 1-1-1, Tsukuba 305-8563, Japan,
[d] Nuclear Physics Institute, 250 68 Rez near Prague, Czech Republic,

We can change the d-spacing of the piezoelectric crystals by applying an electric field results in change of the Bragg diffraction angle [1-4]. A deformation measurement for neutron optical devices using piezoelectric single crystals was carried out. Although α-quartz has a small piezoelectricity, α-quartz was used in this experiment because characteristics of α-quartz are well known and it is easy to obtain high quality and large size single crystals. As shown in Fig. 1, double crystal diffraction measurement using 4.7 Å cold neutrons was carried out to investigate the relation between diffraction angle variation and thickness of crystals. This experiment was carried out using the Ultra Small angle scattering instrument (ULS) of the institute for Solid State Physics (ISSP), University of Tokyo, equipped at the JRR-3 reactor of the Japan Atomic Energy Research Institute. For these experiments, DC bias voltage was applied to the crystals. As shown in Fig. 2, it was observed that diffraction angle variation do not depend on crystal thickness. These values were approximately one order larger than the theoretical values. Macroscopic distortion and change of thickness caused by an applied electric field were observed by laser interferometers [5]. Therefore, these results were influenced by macroscopic bending of the crystal. The inhomogeneous electric field distribution caused by misalignment of electrodes attached to two sides of crystal is considered as the reasons of bending.

References
[1] A. Paturle et al.: Phys. Rev. B**43** (1991) 14683.
[2] H.Graafsma et al.: Acta Cryst.(1997).B**53**,565.
[3] R.Guillot et al.: Acta Cryst.(2002).A**58**(Supplement),C327.
[4] U.Pietsch et al.:J. Physics and Chemistry of Solid **62**(2001)2129.
[5] J.H. Kaneko et al.:Nucl. Instr. Meth A **529** (2004) 166–168

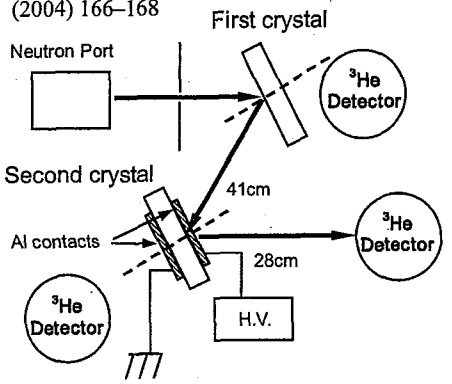

Figure 1 Experimental set-up of double crystal diffraction measurement using 4.7 Å neutrons. Neutrons were diffracted by the (110) surface of the α-quartz single crystal.

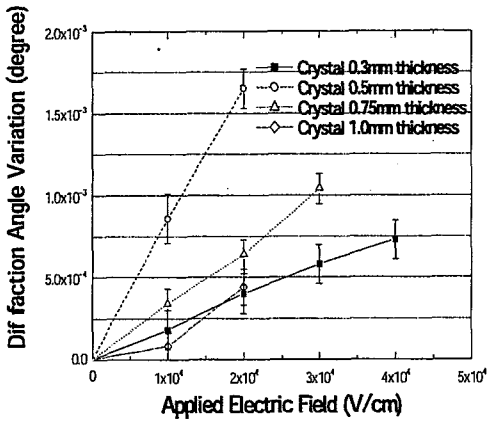

Figure 2 Diffraction angle variations by applying electric fields

使用施設：JRR-3M, 装置：ULS(C1-3), 分野 Instrumentations

研究テーマ：超流動反応場の原子・分子研究
表　題：1.6K 液体ヘリウム－３の中性子照射下における偏極と偏極溶液中での H, T の再結合反応の可能性

7) Possibilities of Polarization of Liquid ^{3}He and of Chemical Reaction in Polarized Medium under Neutron Irradiation at 1.6K

Y. Aratono*1 and K. Iguchi2

[1]*Advanced Science Research Center, JAERI, Tokai, Ibaraki 319-1195*
[2]*Department of Environmental Sciences, JAERI, Tokai, Ibaraki 319-1195*
*1E-mail:aratono@popsvr.tokai.jaeri.go.jp

Liquid helium has very unique properties such as the lowest polarizability, the high compressibility as well as superfluidity and these properties have been opening very unique inter-disciplinary areas between low temperature physics and chemistry. During the course of investigation on the low temperature chemistry in the quantum media such as liquid helium, the authors found the different reactivity in superfluid and normal fluid media for the recombination reactions between thermalized hydrogen (H) and tritium (T) atoms, H+H→H_2, H+T → HT and T+T → T_2, and proposed the tunneling recombination mechanism between two isotopes in the bubble state[1]. Presented here is the experimental work on the same reactions in the liquid ^{3}He focusing on the exceptionally high compressibility.

Two experimental works, the observation of the recombination reactions and the neutron transmission experiment, were performed between saturated vapor pressure and 1.3MPa at 1.6K. The former was carried out at the T1 thermal neutron beam port of JRR-3 and the latter at the C2 cold neutron beam port at the same beam guide room.

The experimental mol % yield of T_2, $(YT_2)_{exp}$ = [{(radioactivity of T_2)/2} / {(radioactivity of HT) + (radioactivity of T_2)/2}] x 100, is presented in Fig. 1a) as a function of the pressure. Fig. 1b) shows the relative transmitted neutron intensity at various pressures(●). The data presented are a compilation of two independent runs. The theoretical values for the neutron transmission are also shown in Fig. 1b)(○). Note that in spite of the completely different phenomena, i.e., Fig. 1a) is based on the chemical phenomenon and Fig. 1b) physical one, the turning pressures in a) and b) are almost same each other. This similarity suggests that the recombination reactions are essentially controlled by the factor that causes the unusual neutron transmission seen in Fig. 1b). The neutron transmission is a function of atomic density of liquid ^{3}He and absorption cross section for ^{3}He(n, p)T. First, the abnormality of the former due to radiation chemical processes induced during neutron irradiation was considered based on the electron bubble model and track model but the effect was not responsible to the unusual transmission in Fig. 1b).

It has been well known that the cross section of ^{3}He(n, p)T reaction is nuclear spin-dependent due to the broad resonance ($J^\pi = 0^+$) in the intermediate ^{4}He* state (n+^{3}He →^{4}He*→p+T). Therefore if ^{3}He is polarized during the irradiation, the cross section will decrease and the transmission will increase. At present, no decisive evidence for the polarization is obtained. However the process similar to the metastability exchange in the polarization of ^{3}He gas[2] might occur under the hyperfine interaction between electron in bubble state and ^{3}He during compression since the metastable species such as 2^3S_1 and 2^3P_0 and electron bubbles are reported to be produced during the thermalization of the recoil H and T atoms. Recently, the physical properties such as viscosity, thermal conductivity, specific heat and vapor pressure have been reported to depend on the degree of the polarization. If the unusual transmission over about 0.3 MPa is due to the polarization of the medium induced by the nuclear reaction, the chemical reactions will be influenced in a similar manner as the transmission because the chemical reaction is sensitive to the properties of the medium.

The authors are grateful to Dr. K. Kakurai, Dr. M. Takeda, Dr. M. Nakamura and Mr. Y. Shimojo for their cooperation in TAS-1 experiment at JRR-3. Thanks are also due to Dr. M. Katagir and Mr. F. Sasajima for their technical advices and discussions. The authors would like to thank to Prof. K. Okuno for his cooperation.

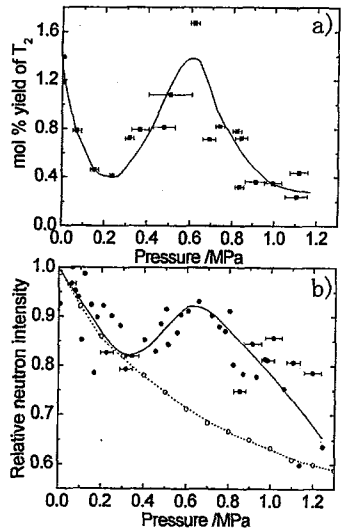

Figure1: Comparison of mol % yield of T_2 and neutron transmission.

References

1) Y. Aratono *et al.*: J. Phys. Chem. A 107 (2003) 3741.
2) F. D. Colegrove *et al.*: 132 (1963) 2561.

原子炉：JRR-3　装置：LCE (T1-4-1A)　分野：放射化学（低温化学）

研究テーマ： 中性子スピンエコー分光器 ISSP-NSE
表題： iNSE のダイナミックレンジの拡大 ～ 50ns へ ～

8) Extension of the dynamic range of iNSE ～ up to 50 ns ～

M. Nagao, H. Seto[A], N. L. Yamada[B] and T. Takeda[C]
Institute for Solid State Physics, The University of Tokyo, 106-1 Shirakata, Tokai, 319-1106
[A]Kyoto University, Kitashirakawa, Sakyo, Kyoto 606-8502
[B]High Energy Accelerator Research Organization, 1-1 Oho, Tsukuba 305-0801
[C]Hiroshima University, 1-7-1 Kagamiyama, Higashihiroshima 739-8521

The neutron spin echo (NSE) spectrometer, iNSE, was relocated from the C2-2 port to C2-3-1 port. Due to the relocation, the applicable wavelength, λ, range increased by using a neutron velocity selector. In order to upgrade the performance in Fourier time, t, we changed the incident neutron beam of $\lambda = 10.7$ Å from 7.1 Å, and fit all the conditions. Because t is proportional to the field integral, $D(= \int Bdl)$, and the third power of λ ($t \propto D\lambda^3$), the increase of λ is quite effective to increase the time resolution of NSE. The key factor to work with longer wavelength is tuning of the spiral coils with respect to the current of the coils and the spatial positioning for compensation of inhomogenieties of the field integral of the neutron beam path.

A ternary microemulsion system consisting of an ionic surfactant, AOT, water and decane as oil is known to form a water-in-oil droplet structure at wide concentration and temperature range. [1] The composition of the system is the same volume fraction of water and decane and the AOT concentration was about 20%. The dynamical behavior of this system was investigated by Nagao *et al.* [2]

The equation proposed by Zilman and Granek [3] has the following form,

$$I(q,t) = I(q,0)\exp\left[-(\Gamma t)^{2/3}\right], \quad (1)$$

where the decay rate Γ is expressed as,

$$\Gamma = 0.025\gamma(k_BT)^{3/2}\kappa^{-1/2}\eta^{-1}q^3, \quad (2)$$

within an assumption of a deformation motion of an isolated membrane in two dimensions, such as lamellar structure. Therefore, from an intermediate structure factor, $I(q,t)/I(q,0)$ observed by NSE, a product of the bending modulus, κ, and the viscosity of the system, η, can be evaluated.

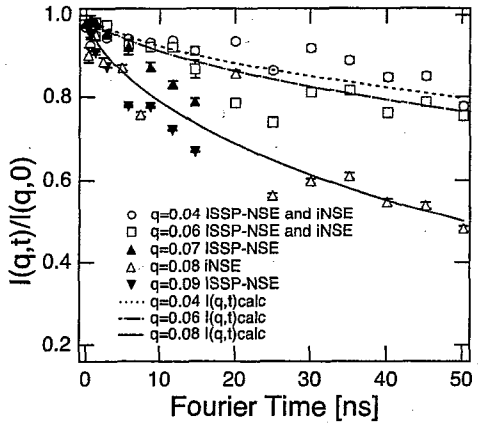

Fig. 1. Observed $I(q,t)/I(q,0)$ at ISSP-NSE (below 15 ns) and iNSE (above 15 ns). The longest Fourier time was extended up to 50 ns.

In Fig. 1, the observed $I(q,t)/I(q,0)$ is shown with respect to t. The data below $t = 15$ ns was observed at ISSP-NSE [2] and above $t = 15$ ns at iNSE. The solid lines are the simulated results by using the fit parameters obtained at $t \leq 15$ ns, and the new result follows the curve well. Although the neutron intensity is one order of magnitude less than that at 7 Å and the statistics is not enough, it could be mentioned that the present result is consistent with that at ISSP-NSE. This result shows a feasibility of iNSE in the time window up to 50 ns.

References

[1] M. Nagao *et al.*: J. Appl. Cryst. **36** (2003) 602.
[2] M. Nagao *et al.*: J. Chem. Phys. **115** (2001) 10036.
[3] A.G. Zilman and R. Granek, Phys. Rev. Lett. **77** (1996) 4788.

使用施設：JRR-3M, 装置： C2-3-1 (iNSE), 分野： 107. Instrumentations

研究テーマ：レーザーピーニングした配管内面における残留応力分布測定
表　題：レーザーピーニングした鉄鋼における内部残留応力の非破壊測定

9) Non-destructive Measurement of Residual Stress beneath the Surface of Laser Peened Steel

K. Akita, H. Tanaka, Y. Sano[1], S. Ohya, H. Suzuki[2] and A. Moriai[2]

Department of Mechanical Systems Engineering, Musashi Institute of Technology, Tokyo 158-8557
[1] *Power and Industrial Systems Research and Development Center, Toshiba Corporation, Yokohama 235-8523*
[2] *Neutron Science Research Center, JAERI, Tokai, Ibaraki 319-1195*

Laser peening process is one kind of surface treatment technology using a mechanical interaction between the surface of a metallic material and the plasma induced by the irradiation of a nanoseconds-order laser pulse. The laser peening introduces compressive residual stress in surface layer, and it is effective for the improvements of fatigue strength and the corrosion resistance[1)] and the prevention of stress corrosion cracking (SCC)[2)]. The laser peening, therefore, has been applied to reactor core shrouds of nuclear power plants to prevent SCC.
In this study, non-destructive measurements of depth profiles of residual stress near the laser peened surface of flat steel plates were performed using neutron diffraction to understand the generation mechanism of the residual stress on laser peening.

The material used for this study was a high tensile strength steel, HT1000. The size of the specimen was 40 ×40 mm^2 with the thickness of 15 mm. The specimens were annealed by furnace cooling after keeping at 973 K for 3 hours for removing residual stress caused by machining. The fundamental wave of a Q-switched Nd: YAG laser is frequency-doubled to a water penetrable wave (wavelength = 532 nm) by a second harmonic generator with a nonlinear optical crystal. The specimen was driven to x- and y-directions in a water jacket during laser irradiation. The treatment was applied in the area of 31×31 mm^2 of the specimen surface. The coverage C_v is defined as: $C_v = (\pi D^2/4) \times N_d$, where D is the diameter of laser spot (≃1mm), N_d is the irradiation density which is the average number of laser pulses irradiated in unit area. C_v for the specimens were 800 % and 5000 %. Our laser peening process in this study did not use any coating materials such as black paint. Table 1 shows the conditions of laser peening.
The neutron diffractometer, RESA, in JRR-3 was used to measure the residual stresses. The measured diffraction planes were α-Fe 110 for the strain measurements in the surface normal direction and α-Fe 211 for the strain measurements in the in-plane direction. The diffraction angle 2θ for each diffraction plane was 62 and 126 deg, respectively. The gage volume was 1.0×1.0×10 mm^3. The wavelength of neutron beam was measured using a Ni powder and it was 2.072 Å. 27 small coupons(2×2×2 mm^3) cut from the material by a wire electric discharge machining were reassembled into a cubic specimen (6×6×6 mm^3) and it was used to measure the stress free lattice spacing d_0.[3)]

Figure 1 shows the measured depth distributions of residual stress beneath the laser peened surfaces. The direction of the residual stresses is Y-direction. Results within 20 μm from surface in the figure were measured using synchrotron diffraction at the SPring8[4)].

Table 1: Conditions of laser peening

Specimen	TP1	TP2
Coverage, %	800	5000
Pulse energy, mJ	215	200
Spot diameter, mm	1.0	0.8
Irradiation density, pulse/cm^2	1019	10000

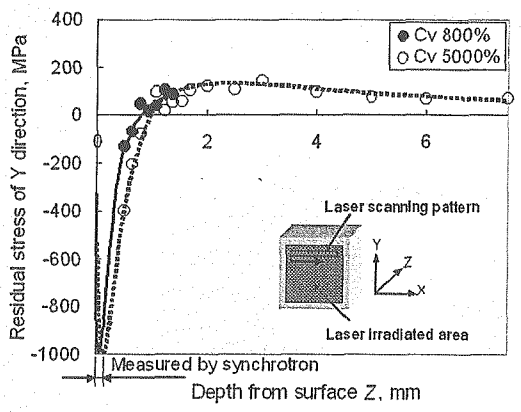

Figure 1: Depth profiles of residual stress on laser peened specimen (HT1000).

Compressive residual stress increased towards interior portion and reached the maximum value at a depth within 100 μm. The depth of compressive residual stress increased with increasing coverage. The compressive residual stress was gradually decreased and it reached about 1 mm depth from the specimen surface. Then the residual stress changed to tension and it decreased to almost zero. Measured depth profiles of residual stress are useful to optimize the condition of laser peening.

References

1) R. Fabbro, *et al.*: J. Laser Applications **10** (1988) 265.
2) Y. Sano, *et al.* : *Proc. 8th Int. Conf. on Nuclear Engineering (ICONE-8), Baltimore, 2000*, Paper No. 8441.
3) D. G. Carr, *et al.*: Acta Materialia **52** (2004) 4083.
4) H. Tanaka, K. Akita, Y. Sano, S. Ohya, A. Moriai, K. Kajiwara, and M. Sato: *Proc of the 54th JSMS Annual Meeting, Sendai, 2005*, pp. 155.

原子炉：JRR-3　　装置：RESA(T2-1)　　分野：中性子散乱（その他）

研究テーマ：cis-不飽和脂質のダイナミックス

表題：エルカ酸の凝集構造の分子運動性に与える影響

10) The influence of the aggregations state of erucic acid on the dynamical property

C. Akita, T. Kawaguchi and F. Kaneko

Graduate School of Science, Osaka University, Toyanaka 560 – 0043, Japan

A major part of natural fats and lipids contain *cis*-unsaturated acyl chains. It is well known that large steric hindrance arising from *cis*-unsaturated bond disturbs the closed packing of hydrocarbon segments and promotes their mobility. In a previous study on solid states of *cis*-unsaturated fatty acids using ^{13}C solid-state NMR spectroscopy [1], we clarified that the lateral packing manner of acyl chains affects their dynamics properties remarkably.

In order to obtain more detailed relationship between the lateral packing and dynamical properties of acyl chains, we followed the $\gamma \rightarrow \alpha$ phase transition of erucic acid [*cis*-$CH_3(CH_2)_7CH{=}CH(CH_2)_{11}CO_2H$] by quasielasic neutron scattering in this study. Our previous X-ray study showed that both methyl-sided and carboxyl-sided chains formed an O'// subcell in the γ phase and that the methyl-sided chain changed its subcell structure to an O$\perp$ like one in the α phase, which portion takes loose packing and conformational disordering [2].

The difference in mobility originating from the lateral packing modes was reflected in the quasielastic neutron scattering spectra measured with AGNES of JRR3M in JAERI. The mean square displacement $<U^2>$ was obtained from the Q ($= 4\pi\sin\theta/\lambda$) dependence of the elastic scattering intensity. Fig.1 shows the temperature dependence of $<U^2>$. The value of $<U^2>$ increased very slowly with temperature up to about 260K, just below the $\gamma \rightarrow \alpha$ phase transition point of 272K, and then it increased with temperature rapidly. In the temperature range of 260-300K, the value of $<U^2>$ nearly tripled. This $<U^2>$ behavior is similar to that of the α phase of tristearin [3] whose acyl chains' motions can be modeled as uniaxial rotational diffusion in a one-fold cosine potential [4]. Hence, the steep increase of $<U^2>$ means that a diffusive molecular motion, that is, rotational fluctuation about the chain axis starts around 260K.

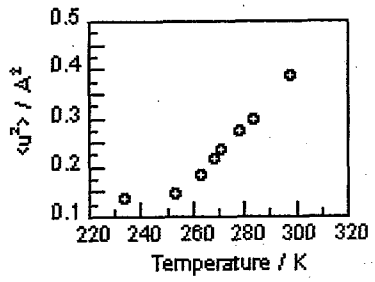

Fig.1 Temperature dependence of $<U^2>$

We infer that this temperature dependence of $<U^2>$ is closely related to the subcell structure change, as discussed below. In the γ phase where both the methyl-sided and carboxyl-sided chains form the dense O'// subcell, only molecular motions having a character of harmonic oscillators are allowed, leading to an increase of $<U^2>$ nearly proportional to temperature. However, on the $\gamma \rightarrow \alpha$ transition, the subcell of the methyl-sided chain is reconstructed into a loose O$\perp$ like subcell with conformational disordering, which results in the onset of large diffusive motions around the chain axis.

Reference

[1] C. Akita et al. *J Phys. Chem.B*, **108 (15)**, 4862, (2004)

[2] F. Kaneko et al. *J. Phys. Chem.*, **100**, 9138 (1996)

[3] C. Akita et al. *J. Crys. Growth*, **275**, e2187 (2005)

[4] F. Guillaume, C. Sourisseau, A.J. Dianoux, *J. Chim. Phys.*, **88**,1721 (1991)

使用施設：JRR-3M, 装置：AGNES, 分野 その他

研究テーマ：中性子利用実験装置の開発研究
表　題：Zn-Mg-Sc 準結晶および Zn-Sc 近似結晶の格子振動

11) Phonon Dynamics in the $Zn_{17}Sc_3$ 1/1 Cubic Approximant

K. Shibata, S. Francoual[1,2], T. J. Sato[3] and M. de Boissieu[2]

Neutron Science Research Center, JAERI, Tokai, Ibaraki 319-1195
[1]*Institut Laue-Langevin (ILL), BP 156, F-38042 Grenoble Cedex 9, France*
[2]*LTPCM/ENSEEG, UMR CNRS 5614, INPG, BP 75, 38402 St Martin d'Heres Cedex, France*
[3]*Institute for Solid State Physics, University of Tokyo, Tokai, Ibaraki 319-1106*

Experimental details: We have investigated the dispersion of TA modes on the JAERI TAS-1 three-axis spectrometer on a 0.5 cm^3 Brigmann-grown single-grain sample. We worked in a constant-k_F mode with k_F=2.662 $Å^{-1}$. The energy of incoming (outgoing) neutrons was selected using a PG002 monochromator (analyzer). We used a sapphire filter after the monochromator and a graphite filter after the sample in order to reduce fast neutron background and contamination by higher order harmonics, respectively. We used 60'×40'×40'×80' apertures for the collimations. With such a set-up, we could probe low energy acoustic excitations from 2 to 5 meV with a $\Delta E fwhm$ = 0.93 meV energy resolution and a $\Delta Q/Q = 0.65\times10^{-2}$ spatial accuracy. For higher energy transfers, counting rates increasing, we opened to 80'×80' the collimations before and after the sample so that we increase by 2.2 the intensity at the expense of less resolution : $\Delta E fwhm$ = 1.25 meV and $\Delta Q/Q = 1.3\times10^{-2}$. The sample was placed in an Al-vacuum box and orientated so that the (1,0,0) and (0,1,0) reflections define the scattering plane. The sample quality was checked performing large elastic A3 scans in and outside the scattering plane. Within constant-k_F, constant-Q, E-scans, we measured TA modes originating from the (10,0,0) and (3,5,0) strong Bragg peaks, with a q wave vector lying along the (0,-1,0) and (1,-1,0) directions, dispersing up to 8 and 4 meV, respectively.

Experimental Results: The most important result is the measured anisotropy of the sound velocity with the direction of the q wave vector. The transverse sound velocity for modes propagating along (0,-1,0) is 2705±30 $m.s^{-1}$ along (0,-1,0) whereas it is 2870±50 $m.s^{-1}$ along (1,-1,0). We can estimate A, the anisotropy factor, from the relation A = ($\nu_{TA,110}/\nu_{TA,100}$)^2. It gives A = 1.125 ± 0.06. This value will have certainly to be revisited using most precise techniques. If it can be confirmed, this anisotropy factor would be the strongest ever measured for a 1/1 cubic approximant of a QC phase. It would mark, moreover, a new difference with the $Cd_{5.7}Yb$ approximant which one exhibits lowest TA sound velocities due to the larger atomic mass of Cd atoms and for which no elastic anisotropy could be measured. Other noticeable results concern excitations propagating along (0,-1,0). As shown in Fig.1, the dispersion relation is almost linear up to the 1st Brillouin Zone (ZB). Almost no curvature is observed when approaching the BZ and no low-lying flat optic branch is observed up to 9 meV. Moreover, TA modes are found resolution limited up to q=0.3 $Å^{-1}$ as this is usually observed in QCs. For higher q values, a broadening seems to occur but the exact way it takes place must be estimated from a fitting procedure taking into account the convolution of the phonon response function with the 4D instrumental resolution. Such data treatment is underway.

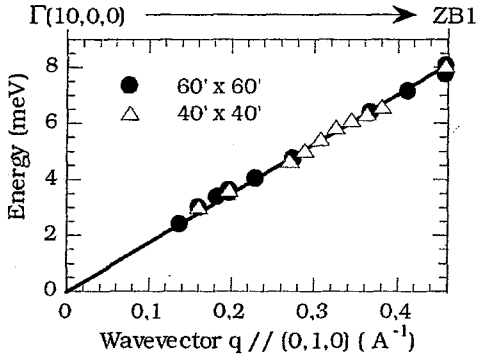

Figure 1: Dispersion curve for the Transverse Acoustic mode propagating along the (0,1,0) direction. Different symbols indicate measurements with different configurations of the collimations. Slope is found at 17.80 meV·Å.

原子炉：JRR-3　　装置：TAS-1(2G)　　分野：中性子散乱（その他）

研究テーマ：トリアシルグリセロールにおけるアシル鎖の分子構造と運動性の相関
表題：トリアシルグリセロールにおけるアシル鎖の分子構造と運動性に関する中性子準弾性散乱法による研究

12) **Quasielastic Neutron Scattering Study on the Relationship between Molecular Structures and Dynamic Properties in Triacylglycerols**

A. Chikayo, F. Kaneko, and T. Kawaguchi

Graduate School of Science, Osaka University, Toyonaka, Osaka 560-0043, Japan

Introduction

Triglycerides are the major constituents of natural fats and oils that form a large group of lipids. TAGs consist of a glycerol backbone and three esterified fatty acids. In particular, cis-unsaturated acyl chains are abundant in natural occurring TAGs.

One of the important features of TAGs is polymorphism. A variety of solid states of TAGs is generated depending crystallization conditions and thermal history. It has been clarified that cis-unsaturation of acyl chains has the following influence on the polymorphism of TAGs. First, the melting point of each polymorphic phase is greatly reduced. Second, the metastable α phase forms a relatively loose lateral packing of acyl chains. However, few studies have been done on the dynamic aspect of cis-unsaturated TAGs.

In this study we investigated the dynamical property of the stable phase α and the metastable phase β of cis-unsaturated TAGs by quasielastic neutron scattering. The results are presented here in comparison with those obtained for saturated TAGs [1] and trans-unsaturated TAGs.

Experimental

In order to reduce the contribution of the glycerol portion to neutron scattering spectra, the following partially deuterated TAGs were synthesized: trierucin, C_3D_5(cis-$OCOC_{11}H_{22}CH{=}CHC_7H_{14}CH_3$), tristearin C_3D_5(n-$OCOC_{16}H_3CH_3$), and trielaidin C_3D_5(trans-$OCOC_7H_{14}CH{=}CHC_7H_{14}CH_3$). The synthesized products were characterized by means of elemental, mass spectrometric and NMR analyses.

Quasielastic neutron scattering measurements were carried out with a direct geometry chopper-type spectrometer AGNES. The energy resolution was 0.12 meV and the scattering vector Q range was 0.23-0.27 $Å^{-1}$.

Results

The mean-square displacement of hydrogen atom $\langle U^2 \rangle$ was obtained as a slope of the plot of the measured elastic scattering intensity $I_{el}(Q)$ as a function of Q^2. Fig. 1 shows the temperature dependence of $\langle U^2 \rangle$ for tristearin, trielaidin and trierucin.

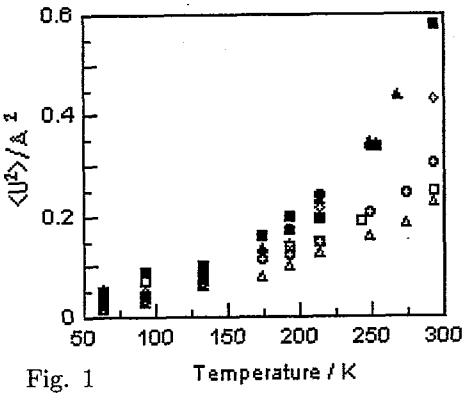

Fig. 1 Open squares, triangles and circles: the β phase of tristearin trielaidin and trierucin. Open diamonds: the β' phase of tristearin. Closed squares, triangles and circles: the α phase of tristearin trielaidin and trierucin.

The three kinds of TAGs show the same tendency. First of all, the $\langle U^2 \rangle$ for the metastable phase α is larger than that for the stable phase β. Second, the $\langle U^2 \rangle$ for the β phase of tristearin increases in proportion

使用施設：JRR-3M，装置：ANGES，分野 その他

to temperature up to 300K. Third, the $<U^2>$ for the α phase (and the β' phase of tristearin) also increases in proportion to temperature up to 190K, but above this temperature, the $<U^2>$ increases nonlinearly and steeply.

According to the previous study[1], the large difference between the α and β phases as to the $<U^2>$ value of high temperature region can be ascribed to the difference in the packing density of hydrocarbons. The α phase forms a loose subcell structure compared with the T// subcell of the β phase, and therefore, librational motions around the long axis of hydrocarbon chains are highly activated, in particular above 190K.

Recent our X-ray study has clarified that cis-unsaturation has a significant influence on the cross-sectional area of hydrocarbon chain in the α phase. For example, the cross-sectional area at 200 K is 20.8 $Å^2$ for trierucin α, whereas it is 19.3 $Å^2$ for tristearin α. However, such a large difference in the cross sectional area is not clearly reflected in the value of $<U^2>$, as shown in Fig. 1. It seems that cis-unsaturation has not so large influence on the librational motions of hydrocarbon chains. Indeed, any clear difference was not observed at the central peak that consists of two components, a sharp elastic peak and a broadened quasielastic peak.

We found that cis-unsaturation was reflected rather in the temperature dependence of the scattering intensity in the 2-5 meV range far away from the central peak. As shown in Figure 2, tristearin α did not show any clear intensity increase of this region at low temperatures, whereas trierucin α showed a gradual intensity increase from the lowest temperature. Such a gradual intensity increase of this region was not observed in the β phase of both tristearin and trierucin.

This temperature change suggests that local fast modes start from a very low temperature only in the α phase of trierucin. According to a previous polymorphic study on erucic acid [2], two C-C bonds bound to cis-C=C bond has a very shallow potential well as to internal rotation. Furthermore, cis-unsaturated chains are loosely packed in trierucin α. Therefore, it is reasonable to infer that the portion around cis-C=C bond starts to carry out fast local fluctuations from the lowest temperature stage, which results in the gradual increase of a very broad background.

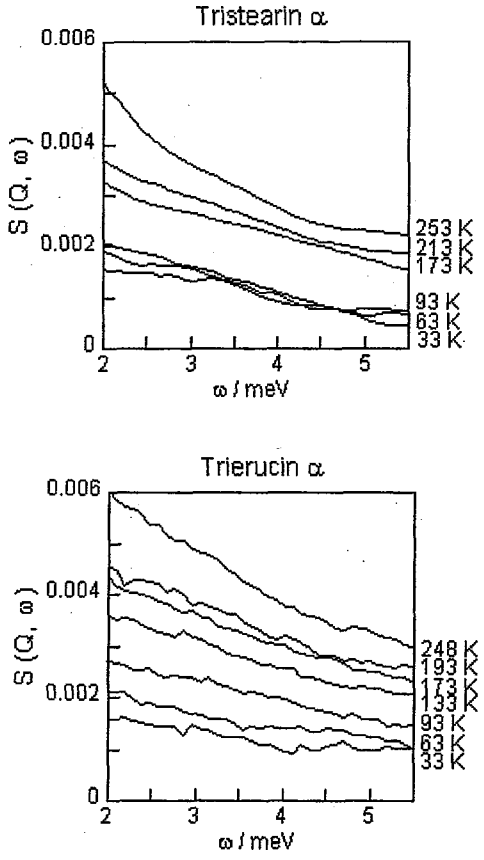

Figure 2. Temperature dependence of the scattering intensity in the 2-5meV range.

References

[1] C. Akita et al. *J. Crystal Growth* **275** (2005) e2187

[2] F. Kaneko et a, *J. Phys. Chem.*, **100**, 9138 (1996)

研究テーマ：中性子散乱装置の改良に関する研究
表　題：Geモノクロメータの非対称反射を用いたHRPDのビーム増強に関する研究

13) Beam Enhancement by the Asymmetric Reflection of the Ge Monochromator in HRPD

H. Yamauchi, N. Igawa and Y. Ishii

Neutron Science Research Center, JAERI, Tokai, Ibaraki 319-1195

The high resolution neutron powder diffractometer, HRPD, installed at JRR-3 has features such as a fine horizontal collimation system, high take-off angle of monochromator and 64 of 3rd-collimator and detector systems. These situation produce very high resolution diffraction data sets which are satisfactory to many users. However, we otherwhile feel the deficiency in the neutron beam intensities. We are therefore trying to enhance the neutron flux using asymmetric reflection of monochromator, where there is a condensation of the incident beam of the width W to the diffracted beam of the width w ($w < W$) as shown in Figure 1. Therefore, it is expected that the diffracted neutron density is increased.

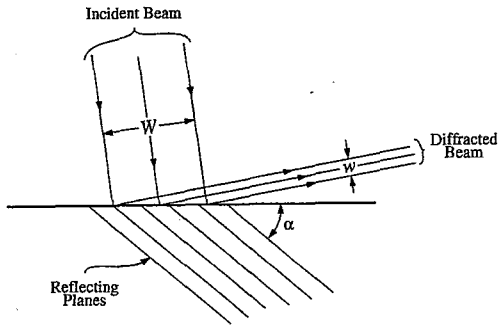

Figure 1: Schematic geometry of asymmetric reflection of Ge monochromator.

Because HRPD usually has been utilized with the neutron wavelength of about 1.83 Å produced by the Ge(3 3 1) reflection (and take-off angle of 89°), we prepared and tested the three types of Ge single crystals cut at angles α ($\alpha = 20°$, 30° and 40°) relative to the reflecting planes of (3 3 1). The test pieces were $w3 \times h2 \times t1$ cm^3 in size and made by hot-press to increase the crystal mosaic spread. The conditions for hot-press were referred to Ref. [1].

Table 1: Results of several test pieces

	α (°)	Peak intensity (counts/30 sec)	FWHM (′)
Perfect	20	3293	2.52
Imperfect	20	12636	5.52
	30	8807	4.62
	40	9460	7.92

First, in order to check whether the conditions and procedures for hot-press are proper or not, we measured the rocking curves on the triple-axis spectrometer TAS-2 installed at the JRR-3 reactor. We used the well collimated initial beam with the wavelength of 1.823 Å obtained by Si(3 1 1) monochromator and the horizontal collimation of (guide)-20′-(test pieces)-10′-80′ to measure the resolution of test pieces more precisely. Table 1 shows the results obtained from the rocking curves of several test pieces. The result of the perfect crystal with $\alpha = 20°$ is also shown for comparison. All the rocking curves were well fitted to the Gaussian shape function. Each peak intensity of hot-pressed imperfect crystals was 3–4 times higher than that of the perfect crystal. The imperfect crystals showed good resolution (FWHM) compared to the monochromator presently installed at HRPD (20′).

In addition, we also tested the aspects of the beam condensation using neutron imaging plates. The results taken just near samples showed that the imperfect crystal with $\alpha = 40°$ showed the highest beam condensation of the initial beam width of about 30 mm to the diffracted beam width of about 10 mm. Therefore, from overall viewpoint of the neutron intensity, resolution and neutron condensing, we assessed the imperfect crystal with $\alpha = 40°$ was the best choice as the monochromator among the test pieces.

Next, in order to check the beam divergence of the diffracted beam from the imperfect crystal with $\alpha = 40°$, we took diffracted images at the positions of 50 mm and 1000 mm from the sample using neutron imaging plates. The initial beam with the wavelength of 1.651 Å obtained by PG(0 0 2) monochromator was used. The horizontal collimation was set to (guide)-20′-(sample)-∞-∞. The diffracted images showed that the beam widths at 50 mm and 1000 mm were about 18 mm and 24 mm. It is thought that this divergence is large enough to compensate for the beam condensation by asymmetric reflection because in HRPD the current distance between the monochromator and sample position is about 2500 mm. The reason for the above result may be supposed to use the PG monochromator when we checked the beam divergence. We are therefore considering the measures against the above result and the recheck using the Si(3 1 1) monochromator if necessary.

References

1) T. Kanouchi: Master Thesis (Tohoku University, 1996).

原子炉：JRR-3　　装置：TAS-2(T2-4)　　分野：中性子散乱（その他）

研究テーマ：研究テーマ：極薄面間隔の多層膜中性子反射ミラーの開発
表題：面間隔 d の薄い多層膜モノクロメーターの開発

14) Development of a very small d-spacing multilayer monochromator

M. Hino, Y. Yoshimura[1], H. Yoshino, R. Maruyama[1], S. Tasaki[1], M.Kitaguchi, Y. Kawabata, T. Krist[2] and P. Schubert[2]

Research Reactor Institute, Kyoto University, Kumatori, Osaka 590-0494, Japan
[1]Department of Nuclear Engineering, Kyoto University, Sakyo, Kyoto 606-8501, Japan
[2]Hahn Meitner Institute, 14109 Berlin, Germany

We have succeeded in fabricating d<3nm NiC/Ti multilayer monochroimator using ion beam sputtering technique. In this report, we show the neutron reflectivity and Transmission Electron Microscope(TEM) picture of the monochromator.

Multilayer was deposited on a polished silicon wafer using ion beam sputtering instrument installed at KURRI. The dimension of silicon substrate is 3 inches diameter and 3 mm in thickness. The ordinary deposition rate of nickel-carbon(NiC), titanium(Ti), are 0.031 and 0.035 nm/sec, respectively. The substrate holder rotated with 10 rpm during deposition. The measurement of reflectivity of multilayer mirrors was carried out at C3-1-2 port of the JRR-3M reactor in the Japan Atomic Energy Research Institute (JAERI). The incident wavelength is 0.88 nm and the resolution is 2.7 % in full width half maximum. The divergent angle is smaller than 1 mrad.

Figure 1 shows comparison between reflectivity of NiC/Ti multilayer. monochromator in which number of layer is 10000, and which d-spacing is less than 3 nm. The d-spacings are gradually increased in order to reflect all component of the incident neutron beam at MINE2, and the resolution of d-spacing was about 5%. The reflectivity is 0.24 and 0.0022 at first and second Bragg angles, respectively. The surface roughness was also estimated to be 0.55nm using neutron reflectometry.

Figure 2 shows TEM picture of the NiC/Ti multilayer monochromator In Fig.2, the black and white lines indicate NiC and Ti layer, respectively. Though the average layer thickness is smaller than 1.4nm, it shows beautiful layer structure.

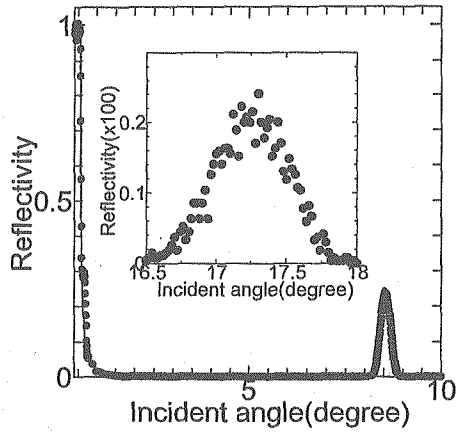

Figure 1: Measured reflectivities of d=2.97nm NiC/Ti multilayer monochromator in which number of layers is 10000. The solid lines is calculated from one-dimensional Schrödinger equation.The inserted figure shows reflectivity at second order of Bragg angle.

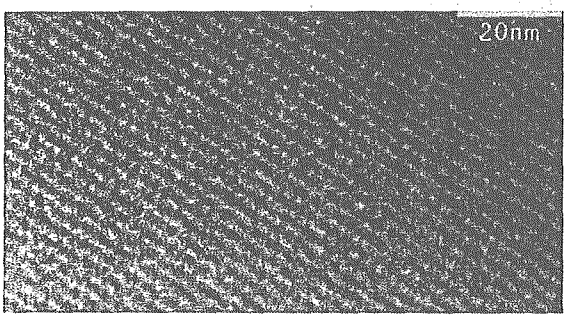

Figure 2: TEM picture of NiC/Ti multilayer in which number of layer is 10000. The black and white lines indicate NiC and Ti layer, respectively.

[1] M.Hino, H. Sunohara, Y. Yoshimura, R. Maruyama, S. Tasaki, Y.Kawabata, Nucl. Inst. Meth. Phys. Res. A (2004), 529(2004) 54.

使用施設：JRR-3M, MINE2(C3-1-2-3), 7. Instrumentation

研究テーマ：エリアディテクタによる材料内部の残留応力分布測定法の開発
表題：中性子イメージングプレートによる中性子応力測定に関する基礎的研究

15) A Fundamental Study on Neutron Stress Measurement Using an Image Plate

T. Sasaki, Y. Morii[1] and N. Minakawa[1]

Dept. of Materials Science and Engineering, Kanazawa University, Kakuma-machi, Kanazawa 921-1192, Japan

[1]The Japan Atomic Energy Research Institute, Tokai, Ibaraki-ken 319-1195, Japan

Residual stresses can play an important role in fracture processes in many engineering components. The X-ray diffraction method can be applied to measure residual stresses non-destructively. However, the measuring depth (X-ray penetration depth) is limited to less than about 0.1 mm. So the measurement for inside material needs to remove the surface layer using, for example, the electro-polishing, which will disturb the stresses that exist in the material initially. Stress measurement using the neutron diffraction technique is a useful tool for evaluating the stress state inside materials.

A use of an area detector (two dimensional detector) such as, for example, a neutron image plate (NIP) enables us to use huge amount of diffraction data at a stretch, compared to the ordinary method. Such feature of sampling a lot of diffraction data expects us to perform more precise and detailed stress analysis. The present study was made to find such possibility of the neutron image plate for the stress measurement.

The neutron experiment was conducted using the research reactor named JRR-3 at the Japan Atomic Energy Research Institute (JAERI). Thermal neutrons derived from the reactor passed through the guide tube and were monochromated to the wave length of 0.20888 nm. A slit made from cadmium of the diameter of 3 mm was put at the exit. The NIP was put into the cassette which was covered with both an aluminum plate (1 mm thickness) and a lead plate (1 mm thickness). The cassette, placed normal to the incoming beams, had a hole at its center so the neutron beam can pass through. The specimen was put after the NIP with an incident angle of 20 degree against incoming beams. The distance between the NIP and the specimen was 65 mm. Figure.1 shows the apparatus used in the experiment set at the beam line called RESA (Residual Stress Analyzer).

The material used was steel, JIS S50C. The specimen was processed to have the geometry of 150mm length, 15 mm width and 2 mm thickness. It was then heat-treated for stress release under the condition of 650 degree C for 30 minutes.

The results obtained in this study were reported[1,2]. The summary is as follows. The peak locations of the neutron diffraction ring show a curved pattern even if the stress in the material is released, which is caused by the distortion of the diffraction intensity profile due to the superposition of diffractions emerged from entire depth in the material that the neutron beams penetrate.

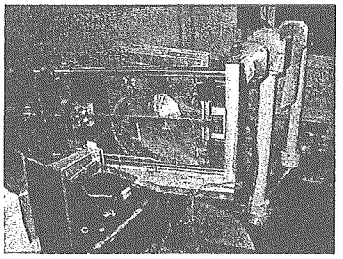

Figure 1: Experimental setup for stress measurement with neutron image plate (NIP).

References

1) T. Sasaki, N. Minakawa, Y. Morii, N. Niimura and Y. Hirose: Transactions of the Japan Society of Mechanical Engineers 69 No.688 (2003) 1711.
2) T. Sasaki and Y. Hirose: Transactions of the Japan Society of Mechanical Engineers 71 No.704 (2005) 670.

原子炉：JRR-3　　装置：RESA（T2-1）　　分野：中性子散乱（その他）

研究テーマ： 中性子スピンエコー分光器 ISSP-NSE
表題： 中性子スピンエコー分光器 iNSE の移設

16) The relocation of the neutron spin echo spectrometer, iNSE

M. Nagao, N. L. Yamada[A], Y. Kawabata[B], H. Seto[C], T. Takeda[D], Y. Kawamura, S. Watanabe, T. Asami and H. Yoshizawa

Institute for Solid State Physics, The University of Tokyo, 106-1 Shirakata, Tokai, 319-1106
[A]High Energy Accelerator Research Organization, 1-1 Oho, Tsukuba 305-0801
[B]Tokyo Metropolitan University, 1-1 Minamiosawa Hachioji 192-0397
[C]Kyoto University, Kitashirakawa, Sakyo, Kyoto 606-8502
[D]Hiroshima University, 1-7-1 Kagamiyama, Higashihiroshima 739-8521

The neutron spin echo (NSE) spectrometer, ISSP-NSE, located at the C2-2 port [1] was relocated to the C2-3-1 port from Dec. 2003 and renamed "iNSE". In this report, the re-construction of the spectrometer is summarized. In Fig. 1, the dynamic range of ISSP-NSE and iNSE is shown. ISSP-NSE had very narrow dynamic range and measurable scientific theme has been limited. Due to the relocation of the spectrometer, the dynamic range can be enhanced to the range presented in Fig. 1 as a bold line.

1 Spatial dynamic range

The scattering angle, 2θ, of ISSP-NSE was limited at $2\theta \sim 15^\circ$ by the next beam line. ISSP-NSE used a supermirror bender as a monochrometer and the available wavelength, λ, was not easy to change from 7.14 Å with the wavelength resolution, $\Delta\lambda/\lambda$, of 18%. Therefore, the highest momentum transfer, q, was about 0.2 $Å^{-1}$.

On the other hand, iNSE has a neutron velocity selector and λ is easy to tune in the range from 4 to 15 Å with $10 \leq \Delta\lambda/\lambda \leq 20\%$. In order to achieve the large scattering angle, a dancing floor for a counter arm was newly equipped. A new type of epoxy resin was introduced from the power plant technology. The viscosity of the epoxy resin gradually increased, and finally the surface becomes very hard and flat. In Fig. 2 the measured surface roughness is shown. The flatness is within 100 μm for the whole surface area of $42m^2$. [2] Thus the counter arm moves smoothly up to 98°. The maximum q is possible to cover up to 2.8 $Å^{-1}$ with $2\theta = 98^\circ$ and $\lambda = 4Å$.

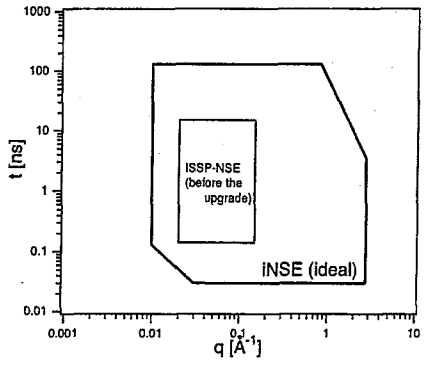

Fig. 1. Dynamic range of ISSP-NSE and iNSE.

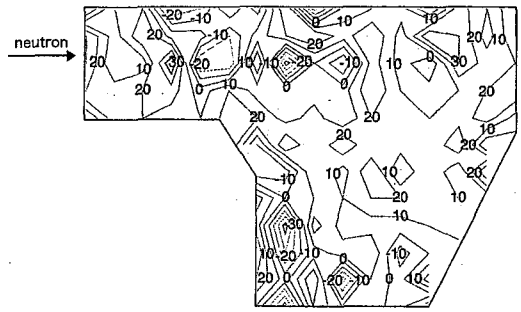

Fig. 2. Final surface level of the dancing floor of iNSE. The unit of the number is in μm.

2 Temporal dynamic range

Because the Fourier time, t, is proportional to the field integral, $D(= \int Bdl)$, and the third power of λ ($t \propto D\lambda^3$) for the Mezei NSE, the increase of λ is the most effective choice to increase the time resolution of NSE. Where B and l are the magnetic field and the length of the precession field, respectively. In this upgrade, the maximum D did not change because the precession coils were the same as before. Therefore, the maximum t can be estimated from the maximum λ of the spectrometer. By using $\lambda = 15Å$, the maximum

使用施設：JRR-3M, 装置： C2-3-1 (iNSE), 分野： 107. Instrumentations

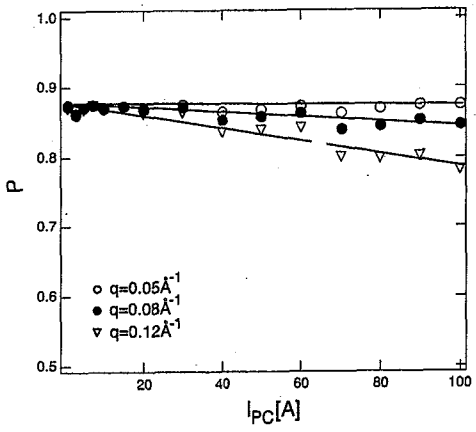

Fig. 3. Observed neutron polarization with respect to the precession coil current and q. The measured sample was grafoil, which is an elastic scattering standard sample. The solid lines are guides for eyes.

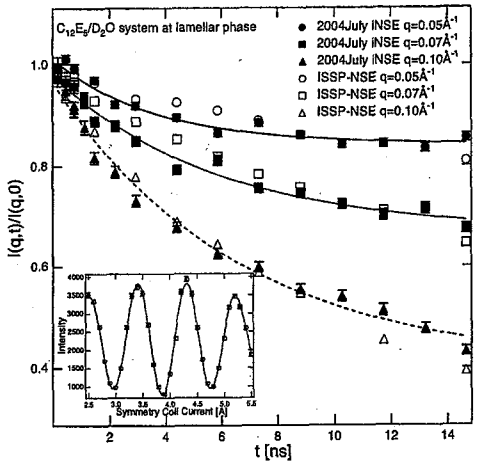

Fig. 4. Comparison between the data observed at ISSP-NSE and iNSE. The inset figure shows a typical NSE signal at iNSE at $q = 0.05$Å^{-1} and the precession coil current of 100A.

t is expected to be 130ns.

The maximum t also depends on the incident neutron intensity in order to get reliable data. The incident neutron flux for $\lambda = 7$ Å was estimated from the measurement of the irradiation to the gold leaf. The result indicated that the neutron flux at sample position is about 3×10^5 n/cm^2/s and it is several times higher than that at ISSP-NSE.

3 Reliability of NSE signals

Spin polarizer and analyzer were changed and the overall polarization slightly decreased from 0.9 at ISSP-NSE to 0.88 at iNSE. ISSP-NSE used polarizer and analyzer as a reflection geometry with high magnetic field, and it was necessary to align the supermirrors depending on λ. On the other hand, iNSE uses a remanent supermirror bender guides for both the polarizer and analyzer. The advantages of these mirrors are weak magnetic field and the realignment free geometry against the change of λ. In Fig. 3 the precession coil current, I_{PC}, dependence of the polarization, P, is shown. Almost a constant value of P was obtained at low-q, while at high-q, it is a decreasing function with I_{PC}.

Finally, a comparison of the intermediate scattering functions, $I(q,t)/I(q,0)$, between the data at ISSP-NSE and at iNSE is shown in Fig. 4. The inset figure shows the typical NSE signal at iNSE. The measured sample was a binary $C_{12}E_5$ / water system with the surfactant volume fraction of 0.1. Open symbols show the data obtained by ISSP-NSE [3] and full symbols by iNSE [4] with the fit result according to the Zilman and Granek theory. [5] It is clearly indicated that the quality of the data is almost the same between ISSP-NSE and iNSE, while the exposure time at iNSE is much shorter than that at ISSP-NSE. This result indicated the reliability of iNSE and completion of the relocation. Further upgrades are now progressed.

References

[1] T. Takeda *et al.*: Nucl. Inst. Meth. Phys. Res. Sec. A **364** (1995) 186.

[2] Y. Kawamura *et al.*: Jpn. J. Neutron. Sci. **14** (2004) 209. [in Japanese]

[3] M. Imai *et al.*: Euro. Phys. J. E **13** (2004) 391.

[4] N. L. Yamada *et al.*: J. Phys. Soc. Jpn. **74** (2005) 875.

[5] A.G. Zilman and R. Granek, Phys. Rev. Lett. **77** (1996) 4788.

2. 中性子ラジオグラフィ

2. Neutron Radiography

This is a blank page.

研究テーマ：高時間分解能中性子ラジオグラフィ技術の開発と応用
表　題：液体金属二相流における瞬時速度場計測

1) Measurements of Instantaneous Velocity Fields in a Liquid-Metal Two-Phase Flow

K. Mishima[1], Y. Saito[1], and M. Matsubayashi[2]
[1] *Research Reactor Institute, Kyoto University, Osaka 590-0494*
[2] *Neutron Science Research Center, JAERI, Tokai, Ibaraki 319-1195*

Introduction

Liquid-metal two-phase has a larger liquid-to-gas density ratio and higher surface tension in comparison with those of ordinary two-phase flows such as air-water flow. In order to predict the flow behavior of a gas-molten metal mixture in a pool precisely, it is essential to examine the applicability of the existing model to the gas-molten metal mixture pool, and to propose suitable constitutive relations in the momentum exchange between phases.

From this point of view, present authors [1,2] performed study on the flow characteristics of N_2-molten lead bismuth (Pb-Bi) mixture in a rectangular pool, and measured the void fraction distribution and time averaged liquid velocity field using neutron radiography (NR) and particle image velocimetry (PIV) techniques [3]. In this study, particle tracking velocimetry (PTV) was applied by using high-spatial resolution system to obtain an instantaneous velocity fields in a liquid-metal two-phase flow.

Experimental

The test section was a rectangular tank made of stainless steel wall of 5 mm thickness (300 mm high, 100 mm wide, 10 mm thick). A gas injector consisting of seven stainless steel tubes arranged along a straight line was mounted at the bottom of the tank. Experiments were performed by using the JRR-3 at the Japan Atomic Energy Research Institute. A high-speed video cameras (RedLake HG-100K) was tested to achieve high spatial resolution. A high-gain, fast gated image intensifier by HAMAMATSU was employed to amplify the light intensity of phosphorescent images on a fluorescent converter (^{6}LiF/ZnS:Ag).

As for the visualization and measurement of liquid velocity field, particles made of gold-cadmium ($AuCd_3$) inter-metallic alloy were employed as the tracer [4]. The sizes of the tracer particles were around 1.0mm. The liquid velocity field could be measured by analyzing movement of the tracer particles [5].

Results

Example of original instantaneous vector map calculated by PTV at the superficial gas velocity j_g of 1.7cm/s is shown in Fig.1. The counter clockwise vortex can be clearly seen. Bubble coalescence, breakup and velocity fluctuation caused by bubble motion can be clearly observed from the successive velocity fields.

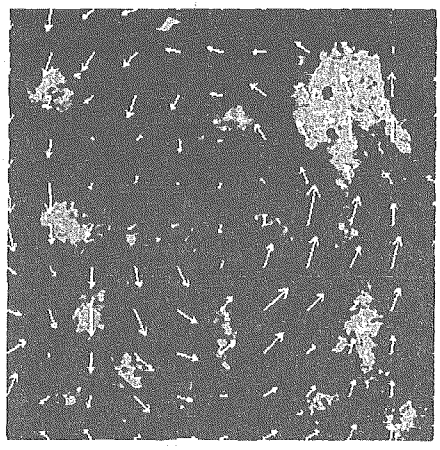

Figure 1: Instantaneous velocity field by PTV (j_g = 1.7cm/s).

Conclusions

As part of basic research on the flow characteristics of liquid-metal two-phase flow, visualization and measurement of N_2-molten Pb/Bi two-phase flow were performed by using the neutron radiography. The results are summarized as follows.

1) Instantaneous liquid velocity vector fields were calculated from tracer images using particle tracking velocimetry (PTV).

2) From the successive instantaneous velocity vector, velocity fluctuation and the effect of rising bubble can be observed.

References

1) K. Mishima, T. Hibiki, Y. Saito, Y. Tobita, K. Konishi and M. Matsubayashi: Nucl. Instrum. Methods Phys. Res. A **424** (1999) 229.
2) T. Hibiki, Y. Saito, K. Mishima, Y. Tobita, K. Konishi, and M. Matsubayashi: Nucl. Eng. Des. **196** (2000) 233.
3) Y. Saito, K. Mishima, Y. Tobita, T. Suzuki and M. Matsubayashi: Applied Radiation and Isotopes **61** (2004) 683.
4) N. Takenaka, T. Fujii, A. Ono, K. Sonoda, S. Tazawa, and N. Nakanii:*Neutron Radiography Vol.4 (ed. Barton J.P.)* (Gordon and Breach, 1993) 355.
5) Y. Saito, K. Mishima, Y. Tobita, T. Suzuki, M. Matsubayashi, I. C. Lim, J. E. Cha, C. H. Sim: Nucl. Instrum. Methods Phys. Res. A **542** (2005) 168.

原子炉：JRR-3　　装置：NRG(7R, C2-3-3-1)　　分野：中性子ラジオグラフィー（熱水力）

研究テーマ：中性子産業利用技術の開発研究
表　題：中性子ラジオグラフィによる水素吸蔵合金中の水素分布の観察

2) Observation of Hydrogen Distribution in Hydrogen-absorbing-alloys by Using Neutron-radiography Technique

M. Matsubayashi, T. Ebisawa[1], K. Kubo[2], H. Arashima[2], and H. Itoh[2]

Neutron Science Research Center, JAERI, Tokai, Ibaraki 319-1195
[1]Machinery Research Laboratory Yokohama branch, The Japan Steel Works, Ltd., Yokohama, Kanagawa 236-0004
[2]Muroran Research Laboratory, The Japan Steel Works, Ltd., Muroran, Hokkaido 051-8505

1. Introduction

It is considered that hydrogen storage alloys are remarkable for supply source of hydrogen gas to fuel cells, which are regarded as clean energy source in next generation. However, it is important to optimize the structure of a hydrogen tank, a filling-up method of the alloys into the tank, and filling-up density of the alloys, because the hydrogen storage alloys expand the volume due to storing the hydrogen. In order to investigate hydrogen concentration distribution in the alloys and tank, we applied neutron radiography method to the investigation.

2. Observation of the hydrogen storage materials

Ti-Cr-V alloys were prepared and heated for a solid solution process, being hydrided with concentrations, 0, 30, and 100 cc/g after the process. In the results, the number of transmitting neutrons was decreased with increasing the amount of storaged hydrogen into alloys as shown in Fig.1. In case of the alloys with 100cc/g hydrogen, no neutron transmitted it. On the other hand, reaction products cannot store hydrogen were found in the vicinity of the sample surface due to the heat treatment. In the results of chemical analyses, the reaction products were α-Ti containing rich oxygen. Therefore, it is necessary to reduce the oxygen to minimum level in atmosphere when heat treatment is performed for the Ti-Cr-V alloys.

3. Observation of small type hydrogen-storage-alloy tank

Distribution of the alloys inside the tank after performing the release and storage process with 100 and 140 cycles was observed as shown in Fig.2. In the projection images (Fig.2-a), the rich hydrogen region is observed near a gas injection port for the hydrogen release in both tanks. Tomographs in Fig.2-b show that there are many alloy-particles with rich hydrogen in the region.

The particles with rich hydrogen did not release the hydrogen because size of the particles was relatively larger than that of the other region without being the small size particles just like "powder" even after many cycles of storing and releasing process. Therefore, those large particles move and gather to bottom of the tank. In addition, it is considered that rib structure of the tank has an effect to gather the particles to the gas injection port.

Those results show that movement behavior of alloy particles under hydrogen release should be investigated to design new tank with stable performance.

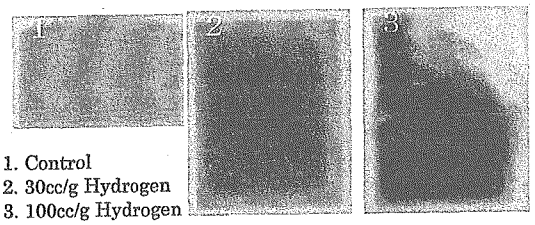

Figure 1: Projection images of the hydrogen storage alloys with various hydrogen concentrations.

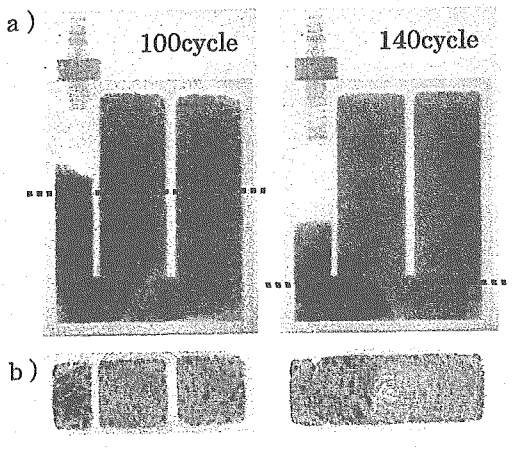

Figure 2 : Distribution of the alloys inside the tank after.
a) : Projection images of the tanks.
b) : Tomographs at the dotted line in the projection images.

原子炉：JRR-3　　装置：NRG(7R, C2-3-3-1)　　分野：中性子ラジオグラフィー（新素材）

研究テーマ：植物試料における水動態解析
表　題：植物試料における水動態解析

3) Water Movement Analysis in a Plant Sample by Neutron Radiography

T. M. Nakanishi, K. Tanoi, Y. Ichimaru[1], H.Iikura[2] and M. Matsubayashi[2]

Graduate School of Agricultural and Life Science, the University of Tokyo, Bunkyo-ku, Tokyo 113-8657
[1]Nagasaki Agricultural and Forestry Experiment Station, Kaizu-cho, Isahaya-shi, Nagasaki 854-0063
[2]Neutron Science Research Center, JAERI, Tokai, Ibaraki 319-1195

1. Introduction

Water plays an important role for plant physiology. Since many biological process take place through water, it is important to study water movement within an intact plant. However little has been known for the role or kinetics of water in plants, mainly due to lacking the tools for the research.

In this research, we tried to analyze the change of water amount or distribution in fruit plants or flowers while agricultural treatment or during delivery process by neutron radiography (NRG) method. It has been known that water deficiency enhances the sugar content in fruits. But, at the same time, water deficiency induces water stress phenomenon in plant. As representative samples for water treatment, we targeted a melon and an orange plant to analyze water distribution in leaves before and after water deficient treatment.

In the case of roses, so called, 'bent neck' phenomenon is a serious problem to ruin the commercial value of the cut flowers. Only flower part bents down during long delivery process. Though this phenomenon is estimated to be induced by the inhibition of water translocation to the flower part, the mechanism has not been known yet.

2. Materials and Methods

Water deficient treatment was performed to orange and melon plants. Water supply was restricted to once in three days and every other day for an orange and a melon plant, respectively. After the treatments, the samples were delivered from Isayaha-City, in Nakagsaki Prefecture, to Tokai establishment of JAERI. To measure water content in the melon plant, a leaf very closes to the fruit was chosen for NRG sample.

In the case of roses, roses grown in Nagasaki Prefecture were cut and transported to JAERI by a truck with two methods, packed in a paper box and given water in a bucket at low temperature. When they arrived at JAERI, the flowers were irradiated to get NRG images.

All the samples were set vertically to neutron beams from a research reactor, JRR-3, installed at JAERI. The irradiation was performed for 1 second and neutrons, converted to light through fluorescent converter (Kasei Optonix, Co.), were taken by a cooled charge coupled devices (CCD) camera (Hamamatsu Photonics, Co.) to get the image.

3. Results end Discussion

Neutron radiograph of the samples were shown in Figures 1 and 2. Since there is a correlation between darkness in the neutron image and water amount[1], the relative darkness in the figure were analyzed.

In the case of roses, some roses packed in a paper box showed bent neck phenomena, and water content in bent neck plant was decreased (Fig. 1). Especially at the bent stem, water content was found to be about 85 to 90% compared to that of control sample (indicated by circles). In addition, water decrease in the pith part of a stem was remarkable (indicated by arrows). It was suggested that the decrease of water pressure in each cells, induced by water-less stress, at the stem caused bent neck phenomenon.

In the case of fruit leaves, the difference of water content in both melons and oranges between with and without treatments of water stress was not able to detect (Fig. 2). Since statistical analysis is needed for this kind of experiment, the authors continue the similar experiment and analyze water content to calculate errors, especially for orange and melon sample.

原子炉：JRR-3　　装置：NRF（7R, C2-3-3-1）　　分野：中性子ラジオグラフィ（農学）

We were able to find out the difference in bent neck sample of roses. Therefore, we will try to get the successive image during bent neck induction by water stress treatment. We are also planning to supply water to roses to visualize the recovering process from bent neck. We will try to get CT image besides 2 dimensional images to analyze spatial water distribution for the further step.

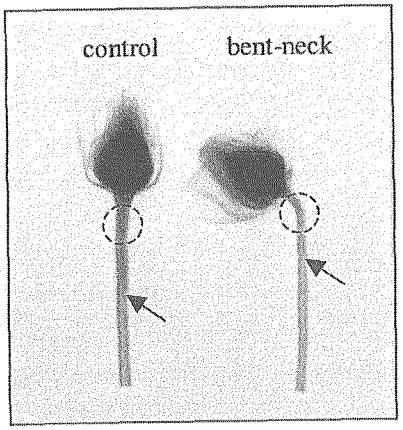

Figure 1: The neutron image of rose. The rose transported long distance caused 'bent neck' phenomenon (right).

References

1) Nakanishi. T. M, Okuni. Y, Hayashi. Y and Nishiyama. H, "Water Gradient Profiles at Bean Plant Roots Determined by Neutron Beam Analysis" : *Journal of Radioanalytical and Nuclear Chemistry* 264 Issue 2 (2005) 313-317.

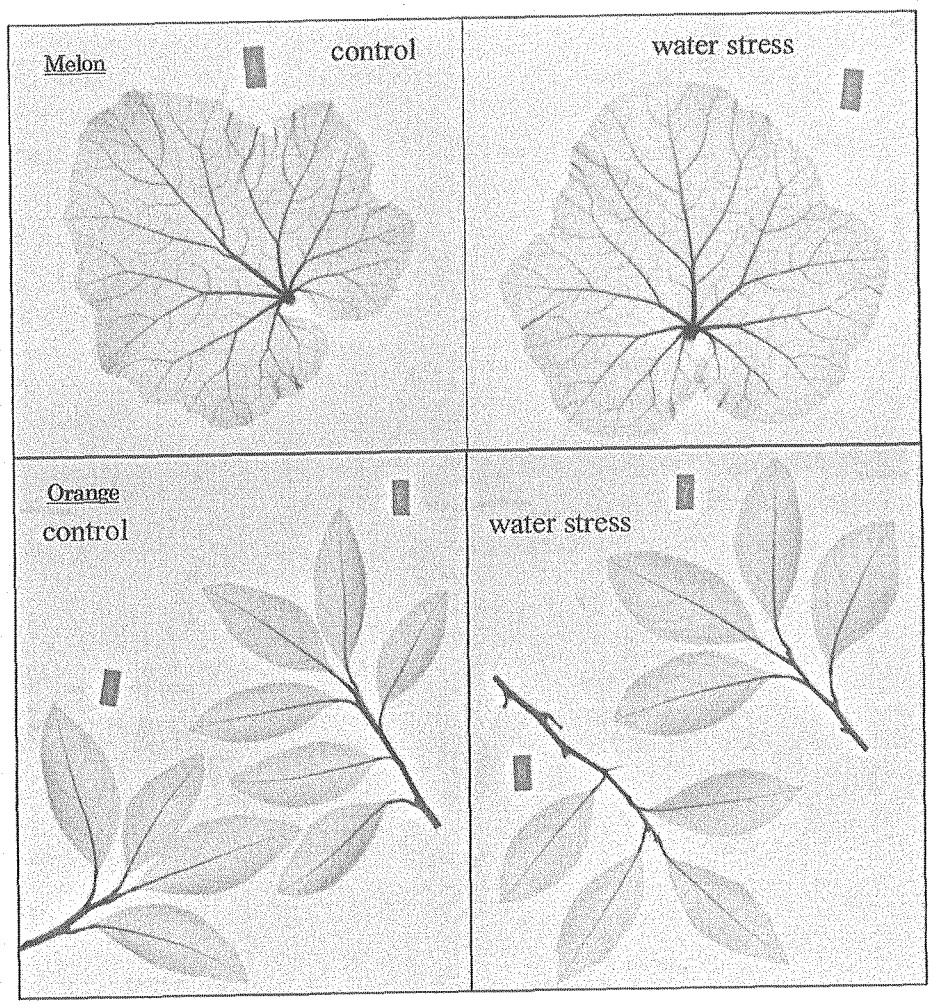

Figure 2 : The neutron images of melon (upper) and orange (lower) leaves. Water supply was restricted to once in three days and every other day for an orange and a melon plant, respectively (right) .

「中性子ラジオグラフィによる固気二相流の定量評価」

4) Quantitative Measurement of Solid-Gas Two-Phase Flow by Neutron Radiography

関西大学工学部　梅川　尚嗣，小澤　守，古井　秀治
大倉　正詞，池田　秀紀，辻 陽平

緒　論

伝熱，燃焼，化学反応などに対して優れた特性を有する流動層は多岐の分野で注目され化学反応装置やボイラーなどで利用されている．本研究で対象とする流動層は，固気二相流で形成されておりその流動特性を把握することが先の諸特性を理解する上で非常に重要となる．しかし，固相である層材粒子は内部流動構造を観察するに当っては障害となるため，定量評価を行うためには何らかの工夫が必要となる．

今回実施した共同研究ではこの定量評価に中性子ラジオグラフィを用い，主として流動層内部に設置した垂直管周りの流動・伝熱特性ならびに流動層内部で発生する偏析挙動(セグレゲーション)特性把握を目的とした実験を実施した．ここではこれらの結果から，セグレゲーション特性に関する実験の内容を簡単に報告する

セグレゲーションは流動層内に存在する特性の異なる粒子が分離偏析する現象であり，粒子径，粒子密度，粒子形状，空気流束など多岐の要因に影響される．セグレゲーションに関する実験的研究としてはセグレゲーションを発生させた後流動層を静止させ層上部から順にサンプリングして評価するという手法が多く取られているが，この場合動的な情報は得ることが出来ない．また，X線を使用した可視化手法の適用も試みられているが，X線はその特性上減衰の大きな物質は密度が大きくなるため先のセグレゲーションの発生要因に影響し任意の層材組み合わせに対しての適用は出来ない．これに対し中性子ラジオグラフィを用いた本研究では硝酸ガトリニウム水溶液に層材を浸漬させた後乾燥させることで中性子に対して着色する手法を用いた．このガドリニウムは層材の主成分である珪素と比べて非常に大きな質量減衰係数を有しており，層材のみかけ密度に影響しない程度の少量の付着で十分中性子に対して色付けが可能となる．また，本手法は動画として画像取得できることから従来情報のなかったセグレゲーション挙動の動的な情報が詳細に取得出来ることとなる．

実験概略

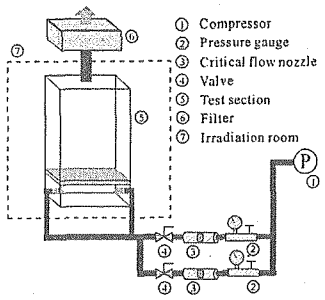

Fig.1 Experimental setup.

図1に本研究で使用した実験装置の系統図を示す．テストセクションは中性子に対して透過性の高いアルミ製の矩形容器(H350mm W100mm D65mm)で沈降粒子(以下 J 粒子;粒径 404, 610 μm 静止層高 100, 150mm)と浮遊粒子(以下 F 粒子;粒径 143, 176 μm J 粒子に対する混合割合は 20wt%)を層内に充填する．これらの粒子は何れも実際に流動層ボイラで層材として使用されているけい砂をふるい分けたものであり物性的にはJ粒子とF粒子は同一のものである．なお，前述した硝酸ガドリニウムによる色づけはF粒子に対して行った．

これらの装置をまずコンプレッサから供給する十分な流束の流動化ガス(空気)で混合した後に，バルブの切替で瞬時に所定の値まで流動化ガス流束を減少させる．この時に発生したセグレゲーション挙動の一例が図 2 に示すものであり，これらの画像はSIT管カメラを用いてビデオレートで撮影した．

図中黒く見える部分が着色された F 粒子であり，時間の経過とともに上部に偏析していく様相が観察できる．

次にこのようにして得られた可視化画像から定量評価を行うことを考える．図 2 で撮影された画像の輝度値は次式で示すことが出来る．

$$S(x,y,t)=G(x,y)\exp[-\rho_{w}\mu_{mw}\delta_{w} -\delta_{s}(1-\varepsilon(x,y,t))\{X_{f}(x,y,t)\rho_{sf}\mu_{msf} +(1-X_{f}(x,y,t))\rho_{sj}\mu_{msj}\}]+O(x,y)$$

JRR-3M7R　中性子ラジオグラフィ装置　熱工学

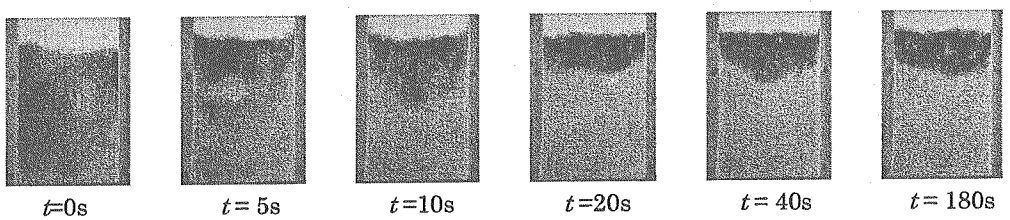

Fig.2 Visualization image of neutron radiography
(D_{PJ}=610μm D_{PF}=176μm H_J=100mm J_G=0.73m/s=>>0.329m/s)

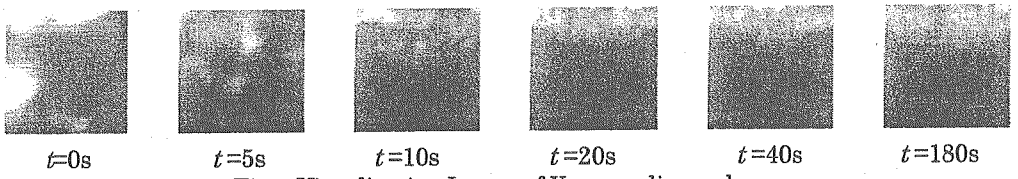

Fig.3 Visualization Image of X-ray radiography
(D_{PJ}=610μm D_{PF}=176μm H_J=100mm J_G=0.73m/s=>>0.329m/s)

ここで，Gはゲインρは密度，μ_mは質量減衰係数δは透過厚さ，εは空隙率，XはF粒子の体積分率，Oはオフセット値を示し，下付文字のWはテストセクション，sは層材粒子，f,jはそれぞれF粒子，J粒子を示す．

式から判るように通常二相流等に対してラジオグラフィ手法を適用した場合と比較すると，本手法では体積分率Xが空隙率εに加わるために未知数が二つとなる．このため，この画像情報から体積分率を求めるためには何らかの手法で空隙率を決定する必要が出てくる．

これに対して本手法では図3に可視化結果を示すX線ラジオグラフィを併用することを考えた．X線ラジオグラフィでは図に見られるように中性子に対して色付けした程度のガドリニウムの付着では減衰率の差としては感知できないために，取得画像上では単一の層材として評価され，先の式の未知数の内体積分率は現れず空隙率だけとなる．なお，X線と中性子線を同時に照射可視化することは出来ないため，個別に可視化画像を得ることになり，評価においては実験の再現性が重要となる．無論気泡個々の挙動まで含めた再現性を確保することは出来ないが，セグレゲーション挙動は図2にも見られるようにテストセクション長手方向に発生し水平方向には変化がないとみなせることから，水平方向へ空間積分平均することで個々の気泡の影響を軽減した．この結果，図3に一例を示すように時間ならびに垂直方向位置に対して高い再現性が得られた．これによりX線ラジオグラフィにより空隙率を評価しその空隙率と中性子ラジオグラフィの可視化画像により体積分率が求まることとなる．

なお，定量評価を行うに際して検討を要した要素に図4に示す散乱線の影響がある．図はJ粒子のみの場合とF粒子をJ粒子の上に積層した場合の映像を示しているが，吸収体として働くF粒子が加わることで散乱線の分布が変化することがわかる．通常流動層では散乱線の影響は水などに比べて小さく空隙率の定量評価ではそれほど大きな問題とはならないが，本研究の場合のように混合率を測定することを目的とした場合，F粒子とJ粒子の混合によって変化する散乱線強度は無視できない影響を与えることになる．ここでは，この影響に対して任意の混合率で予め作製したファントム試験体を用いて校正を行い定量評価を行った．なお，継続研究では測定精度を向上することを目的にテストセクション前に炭

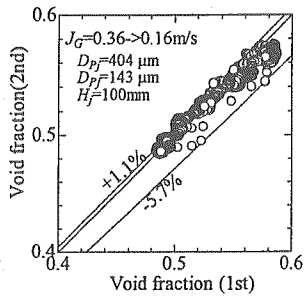

Fig 3 Reproducibility of the experiment

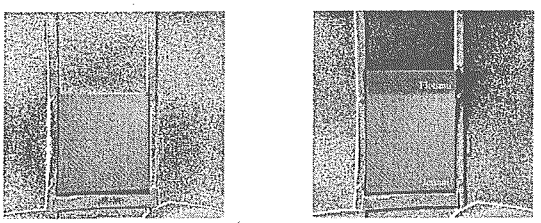

Fig.4 Distribution of neutron scattering around the particle bed.

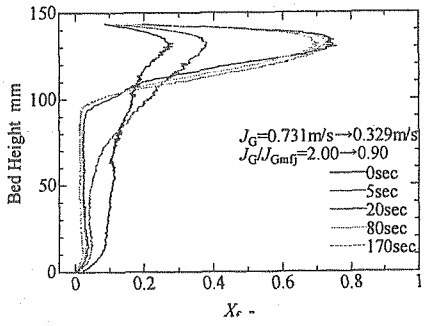

Fig.5 Distribution of flotsam fraction, (d_{pf}=143μm, d_{pj}=610μm, H_j=100mm)

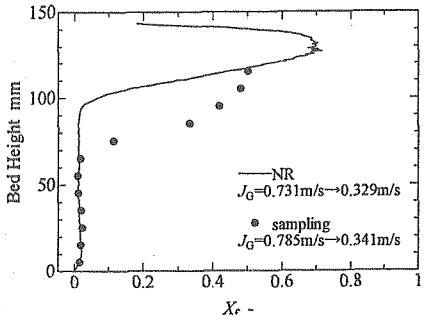

Fig.6 Comparison of X_f between NR and sampling method.

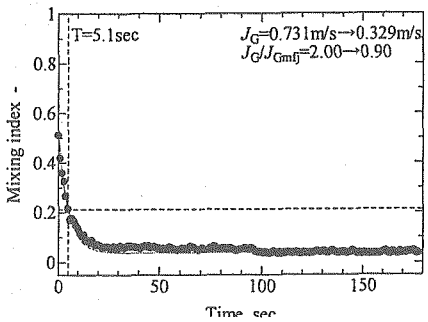

Fig.7 Mixing index.

化ホウ素で作製した格子を設置しアンブレラ法にて散乱補正することを試みている．

これらの手法によって得られた層内の混合率の時間変化が図5でありサンプリング法で得られた値との比較を行ったのが図6である．サンプリング法では層を静止させた状態でしか測定が行なえないため流動化状態で測定した本手法とは若干の差は生じているが両手法の測定結果は良く一致していることがわかる．また，図7は混合率の時間変化を示したグラフであるが，ここで示した情報は本手法以外では取得が困難であり今後偏析挙動を詳細に検討していく上で重要な情報であると考えている．

まとめ

中性子ラジオグラフィは流動層の可視化に際して他の手法に対して種々の優位性を有していることは，これまでの本一連の研究でも報告してきたとおりであるが，特にセグレゲーション研究での優位性は圧倒的であり，これまで取得できなかった多くの有益な情報が取得できることが示せた．今後は測定精度を上げるために手法を若干変更してさらにデータ取得範囲を広げる予定である

Publications

S.Furui, H.Umekawa, K.Hayashi, M.Ozawa and N.Takenaka; Bubble Behavior in Vertical Tube Banks Installed in a Fluidized-bed, Heat Transfer Asian Research, 32-8(2003), 727-739.

M.Ozawa, H.Umekawa, S.Furui, K.Hayashi and N.Takenaka; Quantitative Flow Visualization of Fluidized-bed Heat Exchanger by Neutron Radiography, Applied Radiation and Isotopes 61(2004), 715-724.

S.Furui, H.Umekawa, Y.Oshima, M.Okura, M.Ozawa and N.Takenaka; Segregation Process of Binary Mixture in a Gas-Solid Fluidized-bed, Proc. of 5th ICMF (2004) Paper No.590.

S.Furui, H.Umekawa, M.Tsuzuki, M.Okura, M.Ozawa and N.Takenaka; Visualization of Fluidized-bed Heat Exchanger in Upward/Downward Flow Condition by Neutron Radiography; Nuclear Instruments and Methods in Physics Research A, 542 (2005) 161-167.

S.Furui, H.Umekawa, K.Hayashi, M.Ozawa and N.Takenaka; Flow Visualization of Segregation Process in a Fluidized-bed by Neutron Radiography, IEEE Transactions on Nuclear Science, 52-1(2005), 295-298.

H.Umekawa, S.Furui, Y.Oshima, M.Okura, M.Ozawa and N.Takenaka; Quantitative Measurement of Segregation Phenomena in a Binary Mixture Fluidized-bed by neutron radiography, Nuclear Instruments and Methods in Physics Research A, 542 (2005), 219-225.

中性子ラジオグラフィによる樹木病変部の特性解明

5) Analysis of Properties of Tree Xylem Lesion by Neutron Radiography

東京大学大学院農学生命科学研究科 山田利博、青木葉子、小松雅史、楠本　大、大和万里子、中西友子

Graduate School of Agricultural and Life Sciences, the University of Tokyo

T. Yamada, Y. Aoki, M. Komatsu, D. Kusumoto, M. Yamato and T.M. Nakanishi

I. 研究の目的と意義

中性子線は水素中での減衰率が大きいことから、中性子ラジオグラフィ法は樹木の材内をはじめとする植物体内の水の分布を非破壊的に知る有用な手法である。樹木では材の病変部で健全部と異なる水分分布を示すことから、本法の樹木病理学への応用を考えた。

非破壊的に水分分布の変化を捉えることができれば、樹木の診断や病態生理等さまざまな応用が考えられる。例えば、野外における樹木の倒壊の危険度診断にストレス波伝達速度やγ線の透過率測定が用いられようとしている。これは腐朽部、空洞部を捉えるための手法であるが、腐朽部の水分分布が樹種によって異なることが推測され、診断の確度を低くする要因となる。この水分分布の変動の検出、さらにその原因となる樹木の生理的な反応の追跡に中性子ラジオグラフィが利用できると考えられる。

最初に、いくつかの樹種の成木を使って傷害による水分分布の変化を調べた。次に、樹木の萎凋枯死を引き起こす病害としてナラ類萎凋病を材料に、萎凋機構解明の一環として、苗木に病原菌を接種した後の病変部の検出を試みた。さらに、材質劣化や枯死を引き起こす胴枯・枝枯病としてスギ暗色枝枯病を材料に、病原菌の病原力やストレスの影響を明らかにすることを試みた。なお、以下の実験はすべて JRR-3M を利用して行い、熱中性子のフラックスは 1.5×10^8 n/cm^2/s、冷中性子のフラックスは 2.3×10^8 n/cm^2/s である。

II. 傷害による材中の水分分布の変化

1. 緒言

樹木は木部に達する傷害や感染を受けると材変色を生じ、ひいては腐朽につながる。材変色・腐朽部の特性を知ることは、樹木の健全性・危険度診断にとって必要な情報であることから、中性子ラジオグラフィを用いて水分の分布を調べた。

2. 実験

1998 年に樹幹に人為的な傷害を与えたウラジロモミ、ケヤキ、サクラ、コナラから 2002 年に円板を採取した。傷上 5cm（材変色部あり）と対照として傷上 1m から厚さ約 1cm の円板を切り出し、円板における水の分布を組織が生きている状態で熱中性子を 19 秒間照射し、ガドリニウム製 n/γ コンバータ（厚さ 25μm）を使用して X 線フィルムで撮影した。さらに絶乾後に再び熱中性子を照射し、状態と比較することで、材変色部、腐朽部における水の分布と樹種による違いを明らかにした。

3. 結果とまとめ

辺材部の水分量と心材部の水分量の差が殆どない樹種（ケヤキ、コナラ）と辺材部の水分量の方が多い樹種（ウラジロモミ、ヤマザクラ）があった（図 II-1）。材変色部はどの樹種でも肉眼で認められたが、広葉樹の場合は中性子ラジオグラフィ像では識別が困難で、両者の含水率に大きな差がないことが示された。しかし、ウラジロモミでは健全部と材変色部との境界は明瞭で含水率が低いことが示された。コナラとヤマザクラに見られた腐朽部は水分量が少なかった。

このように樹種や部位毎の水分分布の特性を明らかにすることができた。

III. ナラ類萎凋病における病変部の検出と萎凋機構

1. 緒言

1980 年代末から日本海側で蔓延しているナラ類の萎凋病では、病原菌 *Raffaelea quercivora* の感染による通水阻害が萎凋枯死機構に深く関わっているとされる。通水阻害機構を明らかにするために、病原菌接種苗木で接種部付近の水分状態の変化を中性子ラジオグラフィを用いて観察した。

2. 実験

2002 年 6 月初旬、6 本の鉢植え 4 年生ミズナラの幹に有傷接種を行った。接種源には、PDB 培地をしみこませた爪楊枝に *R. quercivora* を 23℃で 1 週間培養したものを用いた。地上 20cm の樹幹に錐で深さ 2mm、直径 1mm 程度の穴を 1 個あけ、接種源を差し込み、パラフィルムで巻いた。対照とし

JRR-3M 7R　中性子ラジオグラフィ装置　樹木医学

て滅菌した爪楊枝を6本の苗木に接種した。

接種の4、6日目に接種苗と対照苗3本ずつ、接種後14、19日目に残りの苗に熱中性子を照射して撮像した（X線フィルム）。

撮像後、地上部を地際から切り取り、染色液として0.5%酸性フクシン水溶液を吸収させ通水域を調べた。

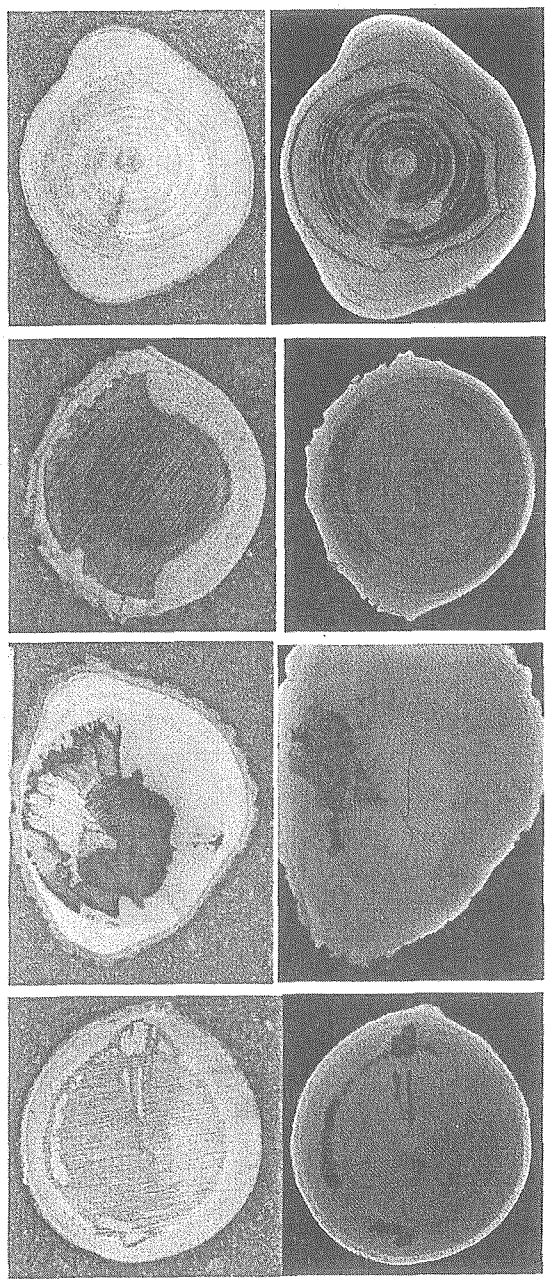

図 II-1 上から、ウラジロモミ、ケヤキ、コナラ、ヤマザクラ傷害部の断面写真（左）と中性子ラジオグラフィ像（右）

3. 結果

接種部の周りには水分量が少ない部位がみられた。乾燥域の長さは同一個体では時間経過に伴ってやや増加した。しかし、菌接種苗と対照苗とで乾燥域の長さに差はなかった。

染色液を吸収させて調べた通水阻害域は、菌接種苗で対照苗より大きかった。通水阻害域は乾燥域よりも接種苗で4～16倍、対照苗で1.5～4倍大きく、菌接種苗で通水阻害が著しく拡大した。

4. まとめ

マツ材線虫病では急激なキャビテーションが引き起こされて通水が停止して、萎凋枯死すると考えられている。それに対して、今回の試験では菌接種苗で対照苗よりも広範囲の通水阻害が起こったにもかかわらず、乾燥域の長さに差がみられなかったことから、本病における通水阻害では急激なキャビテーションは発生していないと考えられた。

IV. スギ暗色枝枯病における病変部の検出

IV-1. 熱中性子線による検出

1. 緒言

スギ暗色枝枯病をはじめとする胴枯、枝枯病は材変色を引き起こし、林業上大きな問題である。暗色枝枯病は気象条件による乾燥ストレスによって大発生し、日本の主要林業樹種であるスギ、ヒノキの集団枯死を起こすことがある。そこで、この問題への対応としてスギ－暗色枝枯病菌－環境ストレスとの相互作用の研究を進めている。

針葉樹では一般に材内に病原菌が侵入して生じた材変色部およびその周囲の乾燥帯（移行帯）では、通水が阻害され含水率が低下している。スギでも暗色枝枯病菌などの菌類が材内に侵入すると早い時期に乾燥した組織が形成される。こうした針葉樹における乾燥帯形成は、宿主樹木の防御反応に伴うものとされている。そこで、スギと病原菌との相互作用に関する研究に応用することを目的として、本法を用いて暗色枝枯病菌を接種したスギ苗木における材内病変部の進展過程の非破壊的な追跡を試みた。

なお、スギ材への菌感染の初期段階では材変色部の色は薄く肉眼ではほとんど識別できないが、その周囲に乾燥帯が形成される。今回検出した範囲は乾燥帯の範囲と一致すると考えられることから、以下ではこの範囲を病変部とする。

2. 実験

2-1. 菌の成長に及ぼす中性子線の影響

プラスティックシャーレ内のジャガイモ寒天培

地（PDA）平板培地上で培養した暗色枝枯病菌（強病原力菌株 MA14 および弱病原力菌株 MA21）に対し熱中性子線を 19 あるいは 38 秒間照射した。照射後は 12、20 あるいは 25℃暗黒下で培養し、菌糸の成長速度を測定した。

2-2. 菌の接種

2002 年 6 月、東京大学演習林田無試験地の苗畑において鉢植えの 3 年生スギ実生苗木に暗色枝枯病菌（MA14 と MA21 の 2 菌株）を接種した。接種菌は長さ 2cm に切断した爪楊枝を載せた PDA 培地上で 25℃で 7 日間培養し、錐で約 3mm の深さにあけた穴に爪楊枝を差し込んだ。対照には湿らせた滅菌爪楊枝を用いた。

2-3. 中性子照射と病変部の検出

接種の 3, 7, 13, 22 日後に苗木に熱中性子線を照射して撮像した（X 線フィルム）。接種の 3 日後と 7 日後、13 日後と 22 日後の照射には同じ個体を用いた。苗木は照射実験開始後は炉室内に置いた。

3. 結果

3-1. 菌の成長に及ぼす中性子線の影響

シャーレおよび PDA 培地は中性子線をほとんど透過した。しかし、用いた菌株、照射時間、温度条件で、シャーレの蓋を閉めて照射した場合、開けて照射した場合とも菌の成長を阻害する影響はみられなかった（図 IV-1）。今回の苗木への照射では苗木内部の中性子線の強度はこれらシャーレでの培養に照射した条件下より小さいと考えられることから、今回の接種試験では中性子照射は苗木内の菌の伸長には影響を与えないものと考えられた。

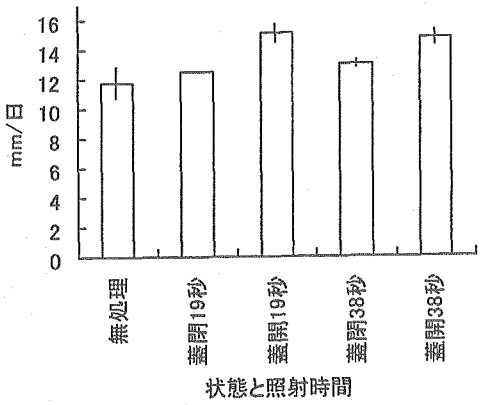

図 IV-1. 暗色枝枯病菌の成長速度に対する中性子線の影響. PDA 培地上、25℃

3-2. 木部病変部の検出

接種苗木内部の病変部は X 線フィルム上で暗い部分として認められ（図 IV-2）、接種の 3 日後には明瞭に検出された。

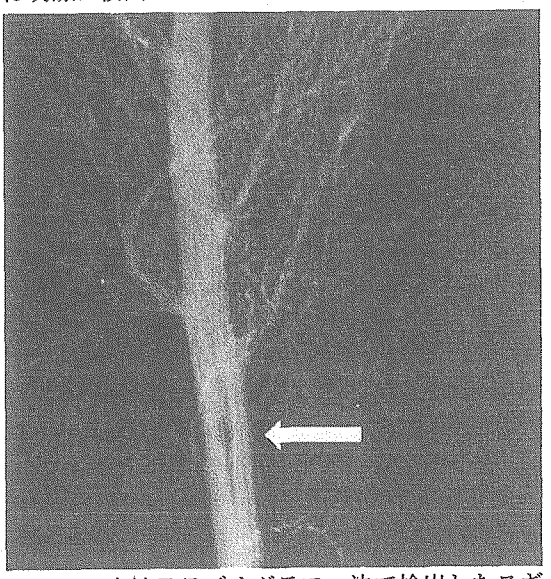

図 IV-2. 中性子ラジオグラフィ法で検出したスギ苗木材内の病変部. MA14 接種 22 日後

傷害のみと菌接種、また接種菌の病原力の違いによる病変部の大きさの差異が観察された。病変部の範囲は時間の経過と共に広がる傾向を示した。病変部の幅は接種菌株の違いなど処理間で大きな差異はなかったが、長さは初期段階から大幅に異なった（図 IV-3）。この違いは菌株の違いによる生立木材内部での菌糸伸長速度の違いを反映していると考えられる。

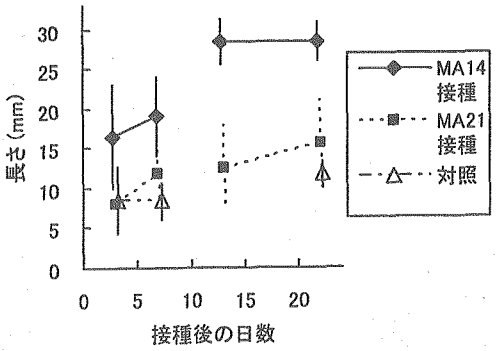

図 IV-3. 暗色枝枯病菌を接種したスギ苗木の材内の病変部の長さ

3-3. 含水率低下の評価

含水率がどの程度低下しているかを評価するため、像の黒化度をスタンダードと比較して計算し

た。接種孔の近くではほとんどの水分が失われていた。この極端に乾燥した組織は傷害／接種の 3 日後には観察された。開口部の影響と思われる。

4. まとめ

以上の結果から、中性子ラジオグラフィは、スギの木部病変部の進展を乾燥帯の範囲として非破壊的に追跡することができることから、病理学的な研究手法として有用であると考えられた。

IV-2. 冷中性子線による暗色枝枯病菌接種スギ苗木の材内病変部の検出

1. 緒言

スギ苗木の木部病変部検出に熱中性子線を用いたラジオグラフィの有効性が明らかになったため、次に均質でコントラストの高い冷中性子線を用いたラジオグラフィを試みた。

2. 実験

2002 年 9 月 5 日、東京大学演習林田無試験地の苗畑に植栽された 1 年生スギ実生苗木に暗色枝枯病菌（強病原力の MA7 と弱病原力の MA21 の 2 菌株）を接種した。接種菌は長さ 1cm に切断した爪楊枝を載せた PDA 培地上で 25℃で 7 日間培養し、錐で約 2mm の深さにあけた穴に爪楊枝を差し込んだ。対照には湿らせた滅菌爪楊枝を用いた。接種の 6 日後に運搬のために鉢植えにした。接種の 1 および 2 週間後に苗木に冷中性子線を照射し、イメージングプレートで撮影した。イメージングプレートは解像度 50μm で読みとった。照射実験開始後、苗木は室内に置いた。

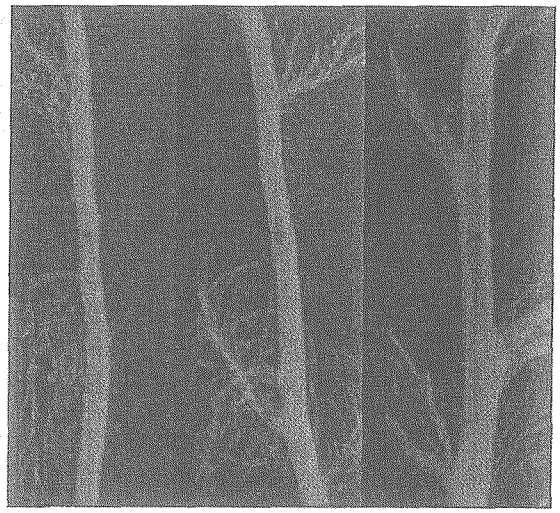

傷対照　　弱病原力菌株接種　　強病原力菌株接種

図 IV-1. 接種 2 週間後の冷中性子ラジオグラフィ像

3. 結果とまとめ

病変部は接種の 1 週間後には明瞭に検出され、その範囲は処理によって異なった（図 IV-1）。病変部の大きさはその後広がる傾向を示した。このように、冷中性子を用いたラジオグラフィは、熱中性子を用いたラジオグラフィと同様、スギの材内病変部の進展を乾燥帯の範囲として非破壊的に追跡することができた。

V. スギ暗色枝枯病の進展に対する水ストレスの影響

V-1. 水ストレスの影響

1. 緒言

材変色・腐朽は林業、林産業において大きな問題であるが、材変色の大きさを規定する要因はまだ十分に解明されていない。動的、静的な防御反応や tension のような物理的な要因が指摘されている。この中で何が重要な要因なのかを明らかにする必要がある。

暗色枝枯病は水ストレス下では病原菌や病変部の拡大速度が速いことが予想される。そこで、水ストレスをかけた場合とかけない場合とで、本病菌を接種したスギ苗木における材内病変部の拡大を中性子ラジオグラフィ法で追跡して、病変部の拡大に対する水ストレスの影響を明らかにするとともに、tension と宿主反応の重要性について検討をおこなった。

2. 実験

(1) 菌の接種

2003 年 5 月、東京大学演習林田無試験地苗畑において育成した 2 年生スギ実生苗木（苗高 60～70cm）を鉢植えにして、土壌水分を調節し、暗色枝枯病菌（強病原力菌株 MA7 と弱病原力菌株 MA21 の 2 菌株）を接種した。苗木の成長による重量の誤差を避けるため、鉢に移植後すぐに処理を開始した。接種菌は長さ 2cm に切断した爪楊枝を載せた PDA 培地上で 25℃ 暗黒下で 10 日間培養した。錐で主軸を突き抜ける穴を開けて爪楊枝を差し込み、パラフィルムで封じた。対照には湿らせて高圧滅菌した爪楊枝を用いた。

(2) 土壌水分の調整

プラスチック鉢を用い、バーミキュライト-パーライト（1:1, w/w）に苗木を植栽し、田無試験地温室内に置いた。植栽時に十分灌水し、乾燥区はそのまま 10 日間放置した後に菌を接種した。菌接種後は土壌含水率（w/w）150%を維持するよう灌水を行った。湿潤区は植栽 4 日後に十分灌水し、その後は土壌含水率 300%を維持するように灌水し

た（接種までは毎日、接種後は1回目の観察後）。

菌接種を行ったのは曇天日の夕方で、接種後直ちにプレッシャーチャンバを用いて苗木の水ポテンシャルを測定した。

(3) 中性子線の照射と材内病変部の検出

接種1および7日後に熱中性子線を3秒間照射し、イメージングプレートを使用して、材内部の病変部の像を得た。イメージングプレートは解像度 50 μm で読みとった。苗木は照射実験開始後は炉室内に置いた。

3. 結果

(1) 土壌水分と苗木の水分生理状態

土壌含水率 300%以上を維持した湿潤区に対し、乾燥区では菌接種時に含水率は約 150%に低下した。このときの接種時の苗木の水ポテンシャルは、乾燥区は平均-1.47MPa、湿潤区は平均-0.71MPa と両者で大幅に異なった（図 V-1）。

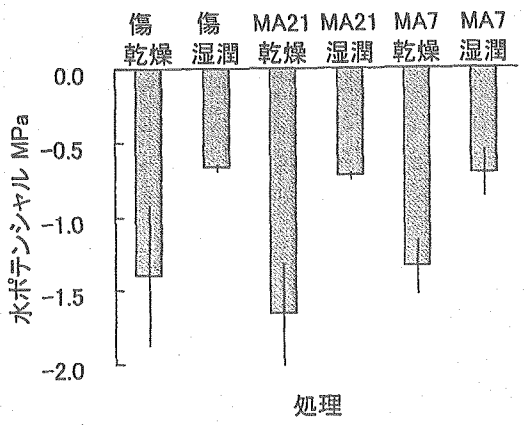

図 V-1. 接種時の苗木の水ポテンシャル

MA21 接種 乾燥区　MA7 接種 湿潤区　MA7 接種 乾燥区

図 V-2. スギ苗木材内の病変部. 接種 7 日後

(2) 材内病変部の拡大

病変部は接種孔を中心に紡錘形に認められた。病変部は乾燥区では時間の経過と共に広がる傾向を示したが、湿潤区では強病原力菌株 MA7 接種を含めほとんど拡大しなかった（図 V-2, 3）。接種の 1 日後では乾燥区と湿潤区との間で病変部の大きさに差異がなかったが、接種の 7 日後になると顕著な差異が認められた（図 V-2, 3）。このように水ストレス下で病変部の拡大が大きくなることが示された。

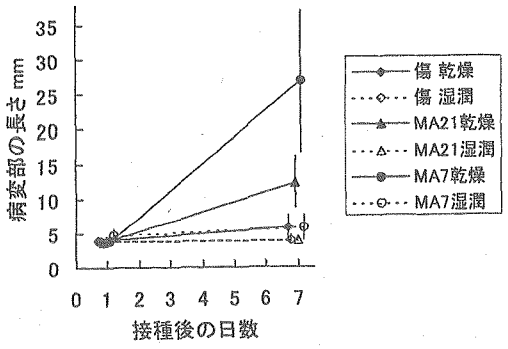

図 V-3. 暗色枝枯病菌を接種したスギ苗木の材内の病変部の長さ（接種孔を含む）

4. まとめ

MA7 接種では湿潤区でも病変部がやや拡大したが、MA21 接種乾燥区の方が病変部が大きく、今回の条件では菌の病原力の違いよりも水ストレスの方が病変部の拡大に及ぼす影響が大きいと考えられた。

接種 1 日後では乾燥区と湿潤区とで菌接種、傷対照の場合とも病変部の大きさに差異がみられなかったことから、水ストレス下で病変部（乾燥帯）が大きくなるのは、蒸散に伴って接種孔から空気が侵入する物理的な力よりも、菌と宿主との相互作用のためであると考えられた。

以上の結果から、水ストレスを加えたときの方が材変色の進展が促進されることが分かった。水ストレスは、傷害直後に起こる負圧による通水阻害部の形成・拡大にではなく、病原菌との相互作用による材変色の進展に関与することが示唆された。

V-2. 傷口の乾湿の影響

1. 緒言

水ストレスを誘因として大発生する暗色枝枯病は、水ストレス下では病原菌や病変部の拡大速度が速い。水ストレス下ではテンションが大きいために材変色（針葉樹の材変色部は乾燥する）の拡

大が速いという説がある。しかし、V-1では有傷接種1日後には水ストレスの程度によって乾燥部の拡大には差異がみられず、宿主と病原菌との相互作用（加害と防御）が材変色の拡大を決める主要因であることを示した。今回は、傷口の湿り具合（傷口からの空気の入り易さ）が木部病変部の大きさに影響するかどうかを調べた。傷口の湿り具合と水ストレスの程度を変え、暗色枝枯病菌を接種したスギ苗木における木部病変部の拡大を、中性子ラジオグラフィ法で追跡した。

2. 実験

2004年5月、東京大学演習林田無試験地苗畑において育成した2年生スギ実生苗木を鉢植えにして、土壌水分を調節し、暗色枝枯病菌（強病原力菌株MA7）を接種した。

バーミキュライトーパーライト（1:1, w/w）を入れたプラスチック鉢に苗木を植栽し、田無試験地温室内に置いた。十分灌水後、土壌乾燥区はそのまま8日間放置した後（土壌含水率（w/w）206%）に菌を接種し、実験終了時（同163%）まで灌水を行わなかった。土壌湿潤区は十分灌水し土壌含水率300%以上を維持するようにした。菌接種後直ちにプレッシャーチャンバを用いて苗木の水ポテンシャルを測定した。

接種菌は長さ2cmに切断した爪楊枝を載せたPDA培地上で25℃7日間培養した。錐で主軸を突き抜ける穴を開けて爪楊枝を差し込んだ。対照には湿らせた滅菌爪楊枝を用いた。傷乾燥区は傷口と爪楊枝をそのままパラフィルムで封じた。傷湿潤区は水で濡らしながら穿孔、接種を行い、濡らした脱脂綿で覆って、パラフィルムで封じた。接種3日後までは脱脂綿に適時水を補給した。

熱中性子線を3秒間照射し、イメージングプレートを使用して、材内部の病変部の像を得た（接種1、3、15日後）。苗木は照射実験開始後は炉室内に置いた。

3. 結果とまとめ

接種時の苗木の水ポテンシャルは、土壌乾燥区は平均-1.20MPa、土壌湿潤区は平均-0.99MPaと有意に異なった。

病変部は土壌乾燥区では時間の経過と共に広がる傾向を示したが、土壌湿潤区ではほとんど拡大しなかった。接種の1日後では乾燥区と湿潤区との間で病変部の大きさにほとんど差異がなかったが、接種の3日後になると差異が認められた。このように水ストレス下で病変部の拡大が大きくなることが示された。傷乾燥区と傷湿潤区とでは、病変部の大きさに差異は認められなかった。傷口の乾燥つまり傷口からの空気の侵入によって病変部の拡大が促進されることはないと考えられる。逆に、接種1日後は傷湿潤区で菌を接種した場合に病変部がやや大きかった。傷湿潤区の方が菌の初期成長に適していたと考えられる。

VI. 今後の課題

CTを用い3次元的に病変部を捉えることが課題として残された。また、樹種による病変部あるいは防御反応発現部位の特性の違いと木部の組織構造あるいは防御反応のタイプとの関連を明らかにすることが今後必要である。

VII. 成果の公表

青木葉子・山田利博・鈴木和夫 (2002) 中性子ラジオグラフィによる材中の水分分布. 第7回樹木医学会大会講演要旨集:45

大和万里子・山田利博・鈴木和夫・中西友子 (2003) *Raffaelea quercivora* 接種苗の水分通道—中性子ラジオグラフィによる非破壊的観察. 日本林学会学術講演集 114:108

山田利博・小松雅史・楠本　大・中西友子 (2003) 中性子ラジオグラフィを用いた暗色枝枯病菌接種

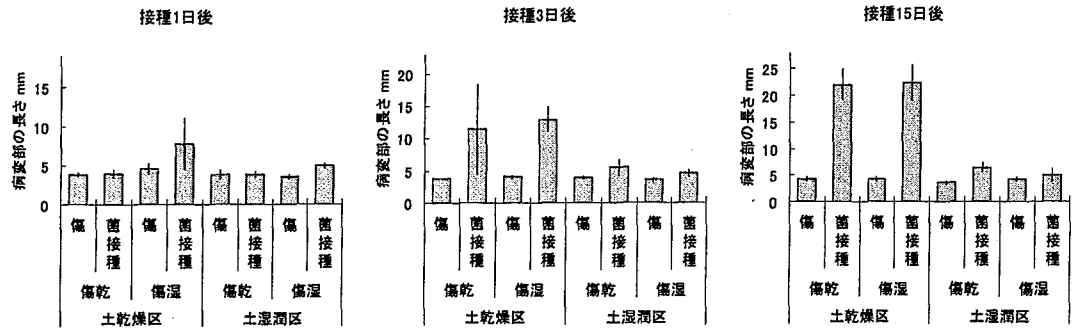

図V-4. 暗色枝枯病菌接種スギ苗木の病変部の大きさと処理

スギ苗木の材内病変部の検出. 日本林学会学術講演集 114:560

Yamada, T., Aoki, Y., Yamato, M., Komatsu, M., Kusumoto, D., Suzuki, K. & Nakanishi, T.M. (2003) Detection of wood discoloration in a canker fungus-inoculated Japanese cedar by neutron radiography. Final Program and Abstracts. 6th International Conference Methods and Applications of Radioanalytical Chemistry - MARCVI. Kailua-Kona, Hawaii, USA, Apr. 7-11m 2003:179-180

山田利博・小松雅史・鈴木和夫・中西友子 (2003) 冷中性子線による暗色枝枯病菌接種スギ苗木の材内病変部の検出. 第8回樹木医学会大会講演要旨集:43

山田利博 (2004) 中性子ラジオグラフィを用いた樹木病理の研究. 「中性子ラジオグラフィ」専門研究会報告書（平成15年度）:65-78

山田利博・大和万里子・林　芳武・中西友子 (2004) 暗色枝枯病菌を接種したスギ苗木の木部病変部の拡大に及ぼす水ストレスの影響. 日本林学会学術講演集 115:748

山田利博 (2005) 傷害時の傷口の乾湿はスギ材変色の大きさを決める要因となるか？ 第116回日本森林学会要旨:PA156

Yamada, T., Aoki, Y., Yamato, M., Komatsu, M., Kusumoto, D., Suzuki, K. & Nakanishi, T.M. (2005) Detection of wood discoloration in a canker fungus-inoculated Japanese cedar by neutron radiography. Journal of Radioanalytical and Nuclear Chemistry 264(2):329-332

6) パルス中性子デジタルラジオグラフィ技術の開発研究

Development of Digital Neutron Radiography Using Pulse Neutron Beam

名古屋大学大学院　工学研究科　原子核工学専攻
玉置　昌義、飯田　一寛、岡田　誠、甲賀　健、森　典章、蘆田　高規

1．本研究の目的

JRR－3M 高強度中性子ビームを利用したラジオグラフィ基礎技術開発の経験経験を基に、定量性確立を進めてきたイメージングプレート・冷却型 CCD を利用する広ダイナミックレンジ・デジタルラジオグラフィ画像取得・処理・解析システムの開発研究をさらに高度化するとともに、大強度パルス中性子源建設進捗に合わせて，パルス中性子ラジオグラフィ対応基本技術を創製して，熱外・熱・冷中性子と物質の相互作用の特性を生かした科学研究用解析手段となる中性子画像分光学と呼べる新たな学問分野確立に必要な技術的支援を進める。

（1）先端的中性子画像撮像システム構築にむけて CNRF・TNRF を用いて実験的に抽出した課題を解決するための要素技術開発の研究を進める。具体的には、冷却型 CCD 中性子カメラ，中性子用およびX線用イメージングプレートの併用による定量的画像情報の取得・処理・解析方法の高度化を図っていく。

（2）物質と冷中性子の相互作用の中性子スペクトルによる変化を高中性子束およびパルスＮＲの開発によって新しい分光学的利用法開発に関する基礎研究を CNRF で進める。

(3) 熱外・熱・冷中性子と物質の相互作用の特性を生かした科学研究用解析手段となる中性子画像分光学の確立にはＴＯＦ式中性子ラジオグラフィ装置の開発が欠かせない．今まで開発してきた検出システムをパルス中性子・ＴＯＦ対応のラジオグラフィ式画像計測装置化することを目指す概念的および実験的研究を進める．

2．研究の概要

単色中性子ラジオグラフィ法の概念的および実験的検討，Ｄｙ－ＩＰの開発を進めた．ＣＮＲＦ利用実験に関しては，改造・運転の不具合などで 2003・2004 年度には有効な利用実験ができず，成果が初歩的に終った．結果の概要を以下にまとめる．

2－1．中性子画像分光学の概念と将来展望

NRT は理工学研究手段としてより高度化するためには、NRT 手法の高度化と施設の高性能化もまた不可欠である。21 世紀に入って、わが国において NRT にかかわる新設が近い将来利用できるようになることが明らかになった。スポレーション(核破砕)という核反応に基づくもので、高エネルギー陽子(水素原子核) と重い原子核(たとえばタングステン・鉛・水銀)の間の核反応によって発生する大強度の中性子を利用する方法で、大強度陽子加速器計画(J－PARC)プロジェクトとして既に建設が進んでいる。

原研と高エネルギー加速器研究機構(KEK)は、2001 年から大強度陽子加速器とそれを用いる多様な実験研究施設群からなる大強度陽子加速器計画を確定し、その建設に着手した。本計画は 2007 年度完成・2008 年度施設稼動開始の予定である。

この計画の中で、物質・生命科学（中性子散乱）実験施設の核破砕中性子源は、1 MW の陽子パルスビームによりパルス状中性子(25Hz)を発生させる。線源から 10m の被写体位置でパルスあたり $5x10^8 n/cm^2$ の中性子束強度が得られる予定である。

JRR-3M7R・C2、熱・冷中性子ラジオグラフィ装置、中性子画像分光学

このパルス中性子源でおこなうNRTには、従来の被写体撮像法やCT法はもちろん、連続パルスを利用するストロボ撮像法による高速度撮影が可能となる。さらにパルスの時分割法とタイム-オブ-フライト(TOF)法を開発する事によって、物体の3次元内部構造の原子レベルからマクロ構造までのサイズスケール的階層構造の可視化・解析を、空間的・時間的に目指す全く新しいNRT手法(中性子画像分光法)が提案されている。この手法が切り開く学問領域は、中性子ラジオグラフィから中性子画像分光学(Neutron Radiographic Spectroscopy)への展開となろう。非破壊検査としてNRTの飛躍的高度化が期待できる。

一般に非破壊検査で可視化したい被写体はcmのスケールであり、その中に含まれるmm－μmスケールの微細構造の検出が目指される。さらに微視的に見るとμm以下のスケールの欠陥・析出物、nmスケールの原子分子・結晶構造・格子欠陥、そしてfmスケールの原子核の存在があり、それらのスケール間の協同現象として巨視的構造物の諸性質がある。一般材料における変形、変態、相変化、流動、反応などにおいては、上に述べた複数のスケールの協同現象が伴うとみなされる。近い将来、この視点は生命体の協同現象にまで拡張されて、これらの協同現象を空間的、時間的そしてスケール的に同時計測・可視化することで構造と運動の多層的な理解が望まれる事になろう。たとえば、髪の毛のスケールによる階層構造は多くの実用材料においても多かれ少なかれ見うけられる階層構造である。この構造解析には、パルス中性子による時分割・TOFを組み合わせたNRT(中性子画像分光法)が期待に応えてくれ、新しい次元の非破壊検査・構造解析になるだろう。

スポレーションで発生した高エネルギー中性子パルスは、減速体内で高速中性子から冷中性子までの幅広いエネルギー群をもった中性子のパルスに変わる。これは、原子核のスケールの波長(fm、keV)から巨大分子・析出物のスケールの波長(μm-nm、meV-μeV)間の波長(エネルギー)をもった中性子で構成される。このパルス状中性子が、コリメータを通して中性子ラジオグラフィ実験装置内に引き出される。

被写体を透過するにつれて構造スケールに応じた様々な波長の中性子が相互作用をし、その変化を受けたパルス中性子は、それぞれのエネルギーに対応する速度で並進運動を続け、空間移動とともに、その進行方向にパルス幅が広がり、いわば、空間的・時間的に波長(エネルギー)弁別された分布になる。その中性子波長スペクトル分布は、被写体を透過する瞬間におこったスケールに応じた波長の中性子と物質との相互作用の特性とその強度に関する情報を含んでいる。

これらの情報を含む中性子スペクトルは、適切な検出器により、時間・空間およびスケール(波長)に関わる情報として同時的に計測され、検査物体のスケールを含む時空間挙動が同時的に可視化され、構造解析可能な情報とすることができる。これは原子・分子の格子振動、格子欠陥、結晶構造、析出物、結晶ひずみなどの空間的、時間的情報が同時的に得られるということで、中性子を利用する非破壊検査法の新しいステップになると期待される。

2－2．ジスプロシウム入りイメージングプレート応用のための予備実験

2-2-1. はじめに

スポレーション中性子源からのパルスビームによる次世代デジタル中性子ラジオグラフィ技術は、10年後を目途に、ストロボ撮像法とTOF撮像法の開発を必要とし、その基礎手法確立のためにJRR-3Mビームの改造が着手された。本研究は、性能を向上させたジスプロシウム入りイメージングプレート(Dy-IP)を応用して、パルス中性子ラジオグラフィでの定量的画像の取得・解析のための予備実験として、基礎的な中性子ビーム特性と画像特性の評価とともに、被写体の局所的な検査等を展望した模擬小角散乱実験やIPのダイナミックレンジの拡張評価を試みた。また、パルス中性子によるストロボ撮像模擬実験として同一IP上に時間依存の画像データを得る撮像手法を試みた。

2-2-2. 実験および解析

実験は、日本原子力研究所JRR-3M熱・冷中性子ラジオグラフィ装置TNRF・CNRF及び、スイスPaul Scherrer Instituteのスポレーション中性子源SINQの中性子ラジオグラフィ装置NEUTRAを用いて行った。

1) CdおよびGdナイフエッジの中性子IP画像から求めた線広がり関数等の基礎的な評価を行い、スポレーション中性子源によるビームに必要な特性評価のための予備的なデータを取得した。

2) ストロボ撮像模擬実験として、砂時計を一定時間ごとに撮像した画像データを用い、ビームのみの画像データとの比をとることによりビームむらの補正を行い、模擬ストロボ画像を取得した。

3) 1mmφの中性子ビームを用いた模擬小角散乱実験として、被写体Si, Fe, Pb, C, プラスティック

等を透過後の減衰したビーム画像を用いて散乱中性子成分分布の可視化を行った。
4）微弱な散乱中性子画像のS/N比向上を目指すIPのダイナミックレンジ拡張の模擬実験として、小型ガンマ線源による照射で読み取りダイナミックレンジを越えさせたIPを、多数回繰り返し読むことによって得られたデータセットを再構成し、IPが潜在的に持つダイナミックレンジのデータの抽出、復元を試みた。

2-2-3. 結果と考察
1）PSIでの実験結果から（L/D）比550における画像のぼけを評価できた。これはJRR-3Mの（L/D）比100に比べてより鮮鋭度の高い画像が得られることを示した。しかし、目指すTOFラジオグラフィや単色中性子ラジオグラフィの装置開発等には、（L/D）比1,000を超えるビームが得られるような配置の装置作りが必要である。
2）パルス中性子を模擬したストロボ撮影による粉体の堆積の時間的変化を1枚のIP上に画像化し、画像間処理による空間的シェーディング補正で、砂の堆積の様子を示す規格化された連続画像を得ることができた。この模擬手法結果は、パルスビームを用いる場合の時間的画像データから定量的なエネルギー画像情報を得る場合に有用である。
3）ほとんど相互作用は見られないSi像を基準として、Fe像との比をとった結果を図1に示す。中性子との相互作用において比較的大きな散乱断面積を有するFeは興味深い散乱線広がりを示した。この結果はフィルターにより単色化した中性子によるラジオグラフィを用いる局所的な構造検査の可能性を示したと言える。
4）IPを繰り返し読む操作によって、IP読み取り器の読み取り限界を取り払うことができ、IPに本来備わるダイナミックレンジを定性的に評価することができた。これを図2に示す。また、この操作により、これまでの実験データでは埋もれてしまっていた微弱な小角散乱成分を抽出し評価するといったような手法への応用の可能性を示せた。

2-2-4. 今後の課題
以上の予備的な実験結果を元にして、以下のような具体的装置作りへの必要な検討を加えていきたい。
・被写体の小角散乱については、平行性の高い単色中性子ビーム装置を作成して、ビームの局所的照射による構造体の検査への発展の可能性を模索する。
・IPの読み取りを繰り返す手法は有用ではあるが、IPのダイナミックレンジを活かすためには、撮像からIP読み取りまでの再現性のある手法の開発が必要である。

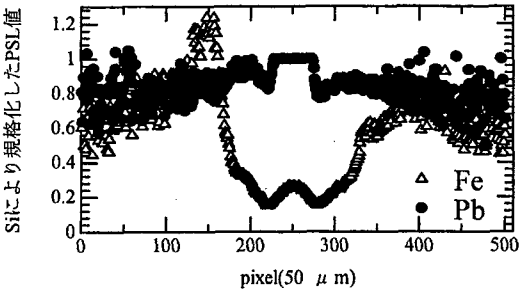

図－1 Siで規格化したPb、Feによる散乱成分評価

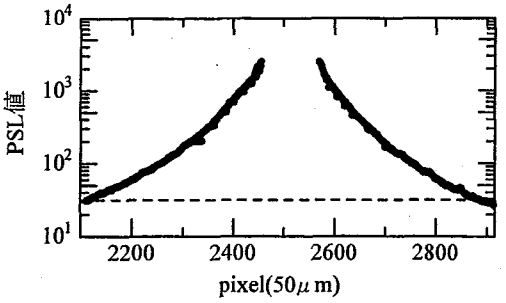

図-2 IPのダイナミックレンジ評価

2－3．単色中性子ラジオグラフィ技術のための井戸型フィルターの開発

大強度陽子加速器（J-PARC）計画による大強度なパルス中性子源の完成までに、単色中性子ラジオグラフィ技術の可能性や課題を探る必要がある。本研究では、従来の白色中性子に対して試作した井戸型フィルターを用い、実験的に単色中性子ラジオグラフィ画像を取得する手法を構築する第一歩を試みた。

2-3-1. 緒言
中性子ラジオグラフィ技術のさらなる発展応用のため、単色中性子ラジオグラフィ技術が現在注目されている。現在進行中の大強度陽子加速器計画によるパルス中性子源の利用を念頭においた予備的実験や、単色中性子ラジオグラフィの可能性や課題を探る必要がある。本研究では、連続スペクトル中性子ビームに、井戸型フィルターを用いてブラッグ反射によって特定の波長を除去した中性子ビームを作り、それによってラジオグラフィ撮像を行ない、特定波長欠損画像を得て、連続スペクトルによって得た画像

からそれを差し引くことによって特定波長中性子ラジオグラフィ画像を取得することを原理とする。これを実験的に検証し、解析することによって単色中性子ラジオグラフィの可能性を探り、課題を明らかにすることが本研究の目的である。

2-3-2. 研究概要

実験は日本原子力研究所 JRR-3M 熱中性子ラジオグラフィ装置で行なった。井戸型フィルターに、Pyrolytic graphite (以下 Pg) を用いた。ここで、特定波長欠損画像用フィルターは、公称モザイク度 1° であり、熱中性子全波長画像用フィルターは、公称モザイク度 0.1° とした。また撮像系に本研究室で開発されたジスプロシウム入りイメージングプレートと CCD カメラを用いた。被写体に熱中性子領域でエネルギー依存性に特徴のある Ti、Pb を用い、中性子入射方向に 13.5° 井戸型フィルターを傾けて中性子波長 1.57A を回折させ、特定波長欠損有無のスペクトルを持つ中性子ビームで画像をそれぞれ取得した。得た画像データから差分画像を作成し全断面積を評価した。チタンを被写体とした熱中性子全波長 (A) 画像、特定波長欠損 (B) 画像、特定波長 (C) 画像をそれぞれ図 3 に示した。

2-3-3. 研究結果

撮像で得た画像データから、Ti、Pb それぞれの透過率を求めた (図 4)。各々の結果から全断面積を評価すると、表 1 のような結果となった。これは特定波長から中性子エネルギー33.3meV に対応しているはずである。文献値とほぼ合致した値を得ることができた。この結果から単色中性子ラジオグラフィ技術の応用によって、物質固有のエネルギー依存全断面積を評価することが可能であることを示した。

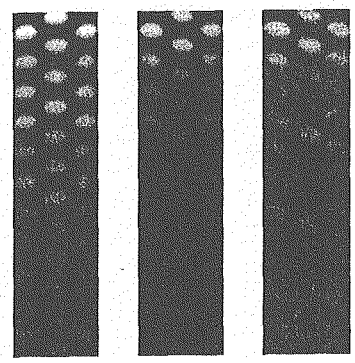

図 3:撮像画像 (左より A、B、C)

2-3-4. 結言

原理的な単色中性子ラジオグラフィ画像を取得する手法を構築した。これは、単色中性子を用いて物質を判別することができる可能性があることを示しており、中性子を用いた非破壊検査法のさらなる応用の可能性を広げたと言える。今後の課題として井戸型フィルターのモザイク度の測定をする必要がある。また様々な物質についても試行すべきである。より中性子エネルギーの低い冷中性子領域で、中性子入射角度を変えて行なうことによって、ブラックカットオフをも計測することが可能であろう。今後単色中性子ラジオグラフィ技術によって、中性子の応用分野が広がっていくことになることを期待している。

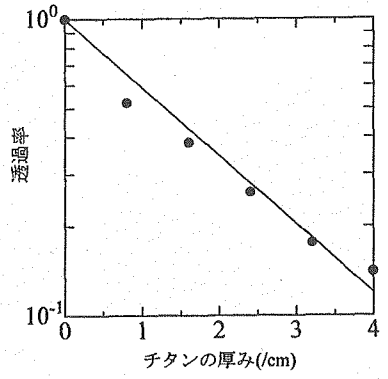

図 4： Ti の特定中性子透過率

表 1　各金属の全断面積比較(±0.05)

金属名	チタン	鉛
実験値 (33.3meV)	0.51	0.24
文献値 (BNL325)	0.54	0.29
実験値(連続スペクトル	0.47	0.3

3．本研究の成果

(1)玉置　昌義、“解説　中性子ラジオグラフィ (NRT) の将来展望”、非破壊検査　第 53 巻、2 号　、84-87 ページ (2004).

(2) Masayoshi Tamaki, " Conceptual monochromatic digital neutron radiography using continuous cold neutron", Nuclear Instruments and Methods in Physics Research A32-37(2005).

(3) Masayosgi Tamaki, Kazuhiro Iida, Noriaki Mori, Eberhard H. Lehmann, Peter Vontobel, Mirko Estermann, "Dy-IP characterization and its application for experimental neutron radiography test under realistic conditions", Nuclear Instruments and Methods in Physics Research A320-323(2005).

(4)飯田一寛、玉置昌義、"JRR-3M TNRF・CNRF における IP・NR 技術の開発と応用研究"、原総センターシンポ(2002.10).

(5)岡田誠、玉置昌義、"RR-3M TNRF・CNRF における C-CCD・NR 技術の開発"、原総センターシンポ(2002.10).

(6)玉置昌義、森典章、岡田誠、E.H.Lehmann、"照射後燃料透視検査への Dy-IP 中性子ラジオグラフィの応用"、日本原子力学会秋の年会 (2004.9)

(7)芦田高規、森典章、玉置昌義、"中性子ラジオグラフィ用ジスプロシウム入りイメージングプレートの特性の最適化"、第 42 回アイソトープ・放射線研究発表会(2005・7).

(8)森典章、芦田高規、玉置昌義、E.H.Lehmann、"Dy-IP を応用した NR による照射後スポレーションターゲットの可視化"、第 42 回アイソトープ・放射線研究発表会(2005・7).

JRR-3M 熱中性子を利用した混相流の動態計測法の高度化

7) Development of Measurements for Multiphase Flow Dynamics by Using Neutron Beam of JRR-3M

京都大学原子炉実験所 三島 嘉一郎

研究目的

沸騰や凝縮を伴う混相流は、多くの動力プラント、化学プラントおよび空調・冷凍装置に関係し、これらの機器の最適設計を行う上で極めて重要である。近年、気液二相流や固液二相流に関して様々な数値解析手法が発達し、解析対象によっては極めて精度の高い予測が可能となってきているが、非定常性の強い過渡的な現象については必ずしも理解は十分ではなく、さらに実験事実を積み重ねる必要がある。

中性子ラジオグラフィはX線（あるいはγ線）ラジオグラフィと相補的な性質を有し、混相流計測に貴重な情報を提供する有力なツールの一つである。しかし、時間平均ボイド率や定常状態を仮定したCT解析の技術はほぼ確立しているものの、混相流の動態計測法に至っては数多くの課題が残っている。課題の一つは、高速度で中性子画像を得た場合の画質の劣化である。これは、中性子の計数誤差に起因した統計誤差と撮像系のノイズによるが、中性子束の増大が望めないとすれば撮像系を改良することにより、画質を向上させることが必要である。また、もう一つの課題としては、得られた画像から混相流の理解に対して有益な情報を抽出する計測処理手法を開発することである。本研究では、これまでに開発してきた撮像系を高度化するとともに、それを混相流計測に適用することを目的とする。

対象とする混相流としては、液体金属二相流を取り上げた。液体金属流は、鉄鋼精錬プロセス等に対して重要であるばかりでなく、液体金属炉や加速器駆動未臨界炉のような液体重金属を利用した新しいエネルギーシステムに関連して、その流動伝熱特性を理解することが極めて重要である。しかし、液体金属流に対して可視光の適用は不可能であるため、ここでは中性子ラジオグラフィを用いた。本研究では、混相流の動態計測法の確立と応用を主目的とし、特に加速器駆動未臨界炉などのような液体重金属を利用したエネルギーシステムに関連して注目されている液体重金属二相流の動態計測を行った。

高速度撮像システム

Fig.1 に中性子ラジオグラフィによる高速度撮像系の概要を示す。高速度撮像法では、高感度の画像増幅器（以下 I.I.)を備えた高速度カメラと蛍光コンバータが必要であるが、高い画質を得るためには、蛍光コンバータと I.I.との最適の組み合わせを工夫する必要がある。高速度撮像法に用いられる蛍光コンバータには、強い発光量、高い空間解像度、そしてさらに、優れた残光特性が要求される。このような要求を満たすのは、現時点では、^{6}LiF/ZnS:Ag コンバータ（化成オプトニクス NR コンバータ）のみである。また、I.I.の光電面材質としては、一般にはマルチアルカリ光電面（S20)が用いられることが多いが、本研究では、蛍光コンバータの蛍光スペクトルと光電面の量子効率とのマッチングを考慮し、第三世代の I.I.として半導体光電面（GaAsP)を用いた I.I.を採用した。Fig.2,3 に蛍光コンバータの蛍光スペクトルと光電面の量子効率の波長依存性を示す。この図からわかるように蛍光スペクトルのピーク付近では、従来の S20 と比較して、GaAsP は数倍高い量子効率を示している。また、空間分解能を高くするために、マイクロチャンネルプレート（MCP)は 1 枚とした。

高速度ビデオカメラは、感度と空間分解能の高い Phantom V7.0（800×600 ピクセル）および RedLake HG-100K（1,512×756 ピクセル）の２機種を用いた。

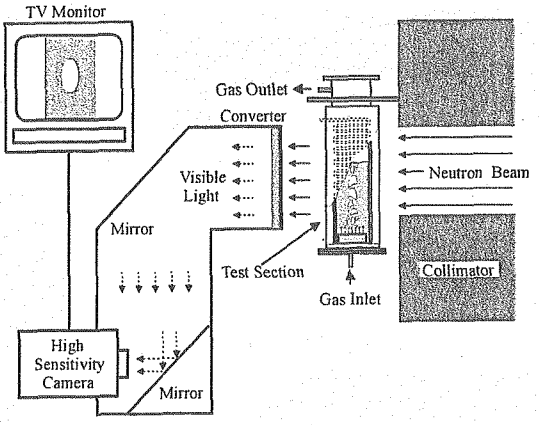

Fig.1 Schematic of High frame rate NR.

JRR-3M, TNRF-2,中性子ラジオグラフィを用いた構造解析

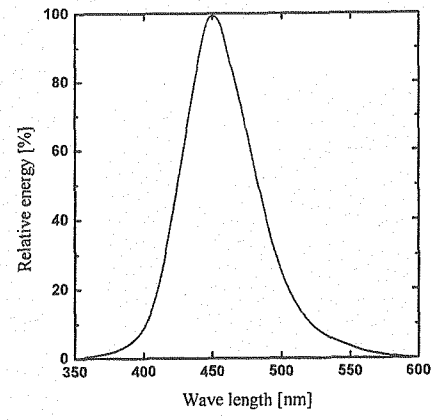

Fig.2 Emission spectra of NE426Eq.

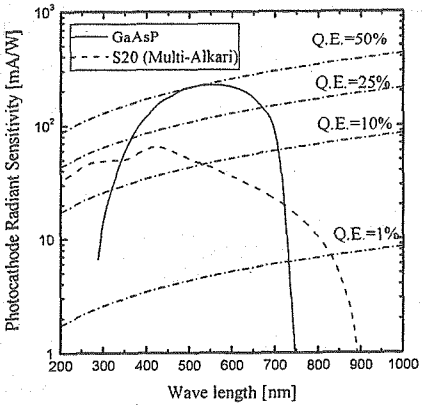

Fig.3 Photocathode radiant sensitivity.

実験装置及び実験方法

Fig.4 に実験装置の概略を示す。試験部はアルミニウム製矩形容器（高さ 530 mm、幅 100 mm、奥行き 20 mm）であり、試験部底部にはステンレス製ノズル（内径 0.5 mm）7 本からなるガス噴出部が設けられている。矩形容器両側には加熱用電気ヒータが取り付けてあり、試験部全体は絶縁材および断熱材で覆われている。作動流体としては、プール内高密度比二相流現象を模擬するため、作動流体として窒素ガス、液体鉛ビスマス（融点 124 ℃）を用いた。溶融金属の温度計測は、アルメル･クロメル熱電対により試験部底部から 2.5cm, 7.5cm, 10cm の 3 個所の位置で行った。ガス温度はガス流量計入口とガス噴出ノズルのプレナム内の 2 個所で計測した。

実験は容器内温度を 200℃に保ち、溶融金属プールの初期液高を 14 cm として、窒素ガス流速を 0 cm/s ～30 cm/s に変化させて行った。さらに、液相速度分布を計測するために金カドミウム・トレーサーを用いて PTV 法を用いて速度分布の計測を行った。

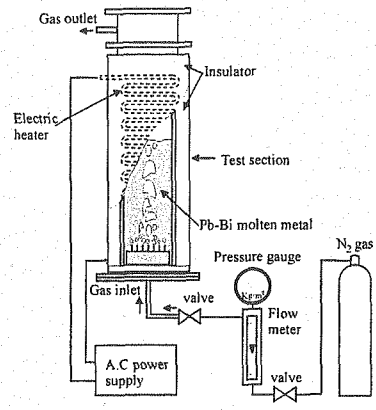

Fig.4 Schematic of a flat bubble column.

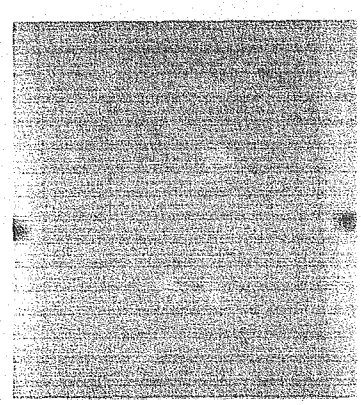

Fig.5 Original image (FastCam Ultima, S20)

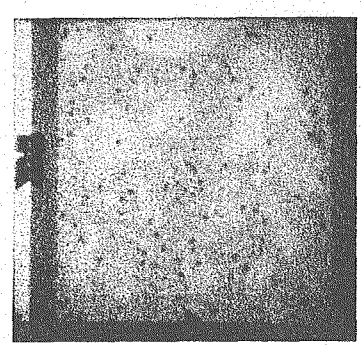

Fig.6 Original image (Phantom V7.0 + GaAsP)

実験結果及び考察

Fig.5,6 に従来のシステム（FastCam Ultima＋S20）と今回開発した撮像システムにより得られた画像をそれぞれ示す。画像の中の灰色の部分が液相である鉛ビスマスを表し、明るい部分が気相を表す。また、Fig.5 では確認しにくいが黒い点が金カドミウム・トレーサを表す。

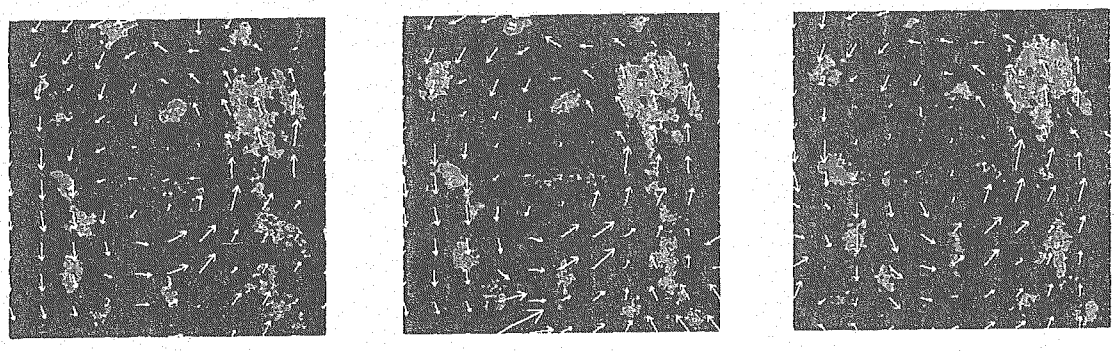

a) t=0ms　　b) t=8ms　　c) t=16ms

Fig.7 Instantaneous velocity field calculated by particle tracking velocimetry (j_g = 1.7cm/s).

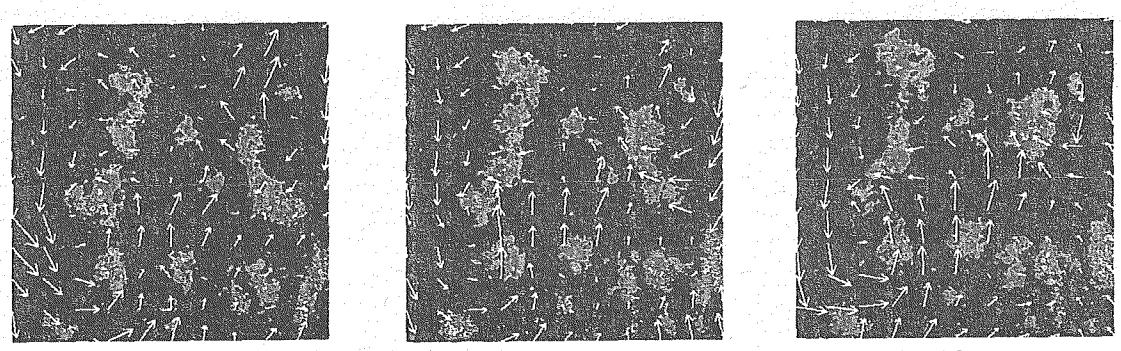

a) t=0ms　　b) t=8ms　　c) t=16ms

Fig.8 Instantaneous velocity field calculated by particle tracking velocimetry (j_g = 13.3cm/s).

図から、撮像系により全く異なる画質が得られ、開発した撮像系を用いれば、気相と液相の界面や、トレーサが鮮明に捕らえられることがわかる。

また、今回得られた画像から、ボイド率計測法とPTV法を併用して、ボイド率と液相内速度分布の同時計測を行った。Fig.7は、ガスの見かけ速度j_g=1.7cm/sにおける短時間平均ボイド率と速度ベクトルを表す。図からわかるように反時計回りの流れが起きている。この流れの向きは、周期的に変化していたが、これは、矩形容器内における気泡プリュームの不安定性によって引き起こされているものと考えられる。Fig.8は、j_g=13.3cm/sにおけるボイド率と速度ベクトルを表す。図から、ガス流束が大きくなると、装置全体に広がる大きな循環流は消え、小規模の不安定な循環流が支配的になることがわかる。

結論

中性子ラジオグラフィを用いてより詳細な混相流観察を行うために、第三世代のイメージインテンシファイア（GaAsP光電面）と高解像度高速度ビデオカメラを用いた撮像系を開発し、液体金属二相流のボイド率・速度場計測の同時計測に適用し、良好な結果を得た。

今後の方針

これまで、混相流の動態計測法の開発を相変化のない場合について進めてきたが、凝縮や沸騰など相変化がある場合の解析法は未だ確立されていない。現在、当研究グループでは、共同利用研究の課題として、「JRR-3M熱中性子を利用した混相流の動態計測法の高度化-II」を、平成17年度から3年計画で継続している。この一環として、今後、急激な相変化を伴う混相流の計測技術の開発を行いたい。

参考文献

[1] Y. Saito et al., "Application of High Frame-Rate Neutron Radiography to Liquid-Metal Two-Phase Flow Research," Nucl. Instrum. Methods Phys. Res. A, vol.424, pp.229-234, 2005.

[2] Y. Saito et al., " Development of High Resolution High Frame-Rate Neutron Radiography," Nucl. Instrum. Methods Phys. Res. A, vol.424, pp.229-234, 2005.

[3] T. Hibiki, Y. Saito, K. Mishima, Y. Tobita, K. Konishi, and M. Matsubayashi, Nucl. Eng. Des., vol.196, pp.233-245, 2000.

[4] Y. Saito, K. Mishima, Y. Tobita, T. Suzuki, and M. Matsubayashi, Proc. 9th Int. Symposium on Flow Visualization, Edinburgh, U.K. 2000.

[5] K. Mishima, T. Hibiki, Nuclear Science and Engineering, Vol.124, pp.327-338, 1996.

[6] Takenaka N., Fujii T., Ono A., Sonoda K., Tazawa S., and Nakanii N., Neutron Radiography. Vol.4. (ed. Barton J.P.), Gordon and Breach, 1993pp.355-362

3. 即発ガンマ線分析

3. Prompt Gamma-ray Analysis

This is a blank page.

研究テーマ：即発γ線ドップラー広がり法のホウ素の状態分析への応用
表　題：即発γ線ドップラー広がり法のシリカゲル細孔のキャラクタリゼーションへの応用

1) Application of Doppler Broadening of Prompt γ-Ray to Characterization of Silica-gel Pores

Y. Sakai, M. K. Kubo[1], H. Matsue[2] and C. Yonezawa[2]

Daido Institute of Technology, Nagoya 457-8530, Japan
[1]*International Christian University, Tokyo 181-8585, Japan*
[2]*Japan Atomic Energy Research Institute, Ibaraki 319-1195, Japan*

In our previous reports [1,2],it has been revealed that the prompt γ-ray analysis (PGA) can be applied to characterization of materials containing boron species by probing the Doppler broadened line shape of 478-keV γ-ray emitted from ^{7*}Li produced in the ^{10}B(n, α)^{7*}Li reaction. The energetic ^{7*}Li ion loses the kinetic energy through the interaction with atoms which the moving ion encounters in medium. It was proved that the velocity *v(t)* decreases with time *t*; $v(t) = v_0 \exp(-Dt)$, where v_0 is the initial velocity and *D* is called " degradation constant ",that is, a reciprocal of time constant of the degradation of ^{7*}Li ions in material. *D* is expected to reflect the elemental composition and the average density of a material where ^{7*}Li ions move and lose their kinetic energy.

In the present article, we report on an application of the Doppler broadening method to characterization of silica-gel pores. Three types of silica gels investigated here were presented by Fuji-Davison Chemical Ltd., with the specific surface areas, specific pore volume and mean pore diameters as shown in Table 1.

The pore volumes of silica gel (A, B, and ID type) were just filled with an aqueous solution of boric acid (H_3BO_3) with a concentration of 1.9 w%, which were called " AQUA " sample. The AQUA samples were dried in air at 95℃ for 2.5 hours, resulting in the dried silica-gel samples named "DRIED". The DRIED and AQUA silica-gel samples containing boric acid were submitted to the prompt γ-ray measurement using the PGA apparatus installed at the neutron-beam guide in JRR-3 [3]. Measurement time was about one hour for a sample. The Doppler broadened line-shapes of 478-keV prompt γ-ray for the DRIED samples of the A, B, and ID type are shown in Figure 1, where the abscissa refers to an energy shift from 478 keV. The spectral data was analyzed by our own fitting program [4], evaluating a degradation constant *D*. The obtained *D* values are listed as D_{exp} in Table 1. The *D* values were also calculated according to the LSS model, which are shown as D_{LSS} in Table 1. The calculation procedure for D_{LSS} was reported in our previous articles [1,2]. As seen in the table, the D_{exp} and D_{LSS} are close each other for the DRIED sample of ID type, while not so close for A and B types. Since the D_{LSS} was calculated assuming that water should be completely removed from the pores in drying, these findings imply that water could be sufficiently removed for the ID silica-gel but not completely for the A and B silica-gels, which might be consistent with the fact that mean pore size is much larger in the ID silica-gel than in the A and B silica-gels.

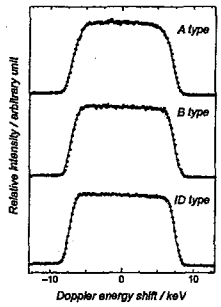

Figure 1: Spectral line-shapes of prompt γ-ray of 478 keV of ^{7*}Li for the DRIED silica-gels of A, B, and ID type.

References

1) Y. Sakai, C. Yonezawa, M. Magara, H. Sawahata, Y. Ito, E. Tachikawa : Nuclear Instrum. Methods, Phys. Res. **A353** (1994) 699.
2) Y. Sakai, M. K. Kubo, H. Matsue, C. Yonezawa : J. Radioanal. Nucl. Chem. **265** (2005) 287.
3) C. Yonezawa, A. K. Haji Wood, M. Hoshi, Y. Ito : Nuclear Instrum. Methods, Phys. Res. **A329** (1993) 207.
4) M. K. Kubo, Y. Sakai : J. Nucl. Radiochem. Sci. **1** (2000) 83.

Table 1: Degradation constants (*D*) in silicagels of A, B, and ID type

Type of silica gel	Spesific surface area m^2/g	Spesific pore volume cm^3/g	Mean pore diameter nm	*D* for DRIED samples D_{exp}/D_{LSS} $10^{12}s^{-1}$	*D* for AQUA samples D_{exp}/D_{LSS} $10^{12}s^{-1}$
A	650	0.36	2.2	1.08(2) / 0.91	1.35(2) / 1.39
B	450	0.80	7.0	0.69(2) / 0.58	1.24(2) / 1.28
ID	310	1.20	15.5	0.48(1) / 0.47	1.03(2) / 1.24

原子炉：JRR-3　　装置：PGA(T1-4-1,C2-3-2-2)　　分野：即発γ線分析実験（工業材料）

研究テーマ：中性子インビームメスバウアー分光装置の開発
表　題：中性子インビームメスバウアー分光装置の開発

2) Development of Neutron In-beam Mössbauer Spectrometer

M. K. Kubo, Y. Kobayashi[1], Y. Yamada[2], Y. Sakai[3], H. Shoji[4], H. Matsue[5]

Department of Chemistry, International Christian University, Tokyo 181-8585
[1]Applied Nuclear Physics Laboratory, RIKEN, Saitama 351-1098
[2]NDepartment of Chemistry, Tokyo University of Science, Tokyo 162-8061
[3]Daido Institute of Technology, Nagoya 457-8530
[4]Graduate School of Science, Tokyo Metropolitan University, Tokyo 192-0039
[5]Japan Atomic Energy Research Institute, Ibaraki 319-1195

Study of chemical and physical processes prompted by neutron capture reactions attracted much interest in the previous century and has practical importance in investigating the deterioration of nuclear reactor and fusion plant materials. But there are few *in situ* experimental techniques available for examining the initial processes occurring in materials under neutron irradiation. In-beam Mössbauer spectroscopy is a useful tool to investigate trace amount of chemical species produced by nuclear events, such as radioactive decay and nuclear reactions, and it has a great advantage of the ability to study solid materials non-destructively. But there have been limited number of research works of in-beam neutron Mossbauer spectroscopy[1]. We have started a new ^{57}Fe in-beam Mössbauer spectroscopic study aiming at the detailed *in situ* investigation on the chemical and physical behaviors of the trace species formed after neutron capture reactions using a parallel plate avalanche counter (PPAC)[2].

Iron disulfide (FeS_2, pyrite), a binary semiconductor compound, has the rock salt type crystal structure composed of Fe^{2+} cation and S_2^{2-} anion. The simple structure and composition of FeS_2 was promising to be the first sample of our research and used in this work. Iron disulfide was purchased from Kishida Kagaku Co., and used without further purification. Finely ground powder was pressed to form a thin disk of 20 x 20 cm^2 and about 100mg cm^{-2} in thickness. The sample was placed at the target position of the prompt γ-ray analysis setup[3] at the beam hall of the JRR-3 reactor of the Tokai Establishment of the Japan Atomic Energy Research Institute. The sample disk was oriented both to the beam and the PPAC detector at an angle of 45 degrees. The thermal neutron flux was about 1.0 x 10^8 cm^{-2}s^{-1}. The PPAC was stably operated in a continuous gas flow mode with perfluoropropane (C_3F_8) as the counter gas. The measurement took 70 hours at room temperature. The absorption spectrum of FeS_2 obtained by the usual transmission mode showed one doublet of IS = 0.303 mms^{-1} and QS = 0.618 mms^{-1}, indicating that the Fe^{2+} is in the low spin state. The in-beam spectrum was composed of two Lorentzian doublets (Figure 1). The minor species, component II, having area intensity of 1/3, showed Mössbauer parameters similar to the parent FeS_2 (Table I, the sign of IS is inverted for easy comparison with the absorption spectrum). The slight larger IS and QS of component II compared with pyrite could indicate that the ^{57}Fe atom formed by the neutron capture reaction experienced a small recoil and disturbed its environment moderately. On the other hand, component I consisting of 66% of the ^{57}Fe atoms produced by the nuclear reaction considerably changed their states. This component has not been clearly identified, but fairly large amount of recoil energy up to 547 eV could result in oxidation and/or lattice dislocation in FeS_2. Further measurements at low temperatures will be conducted in the near future.

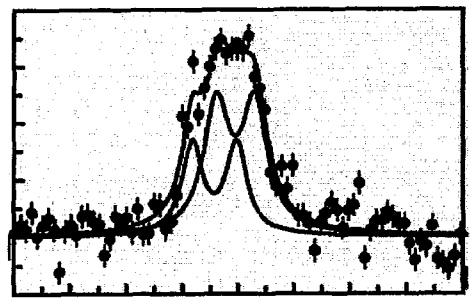

Figure 1: Example of a halfwidth figure.

References

1) W. G. Berger, J. Fink and F. E. Obenshain: Phys. Lett. **24A** (1967) 466.
W. G. Berger: Z. Phys. **225** (1969) 139.
G. Czjzek and W. G. Berger: Phys. Rev. **B1** (1970) 957.
2) T. Saito, Y. Kobayashi, M. K. Kubo, Y. Yamada: J. Radioanal. Nucl. Chem. **255** (2003) 519.
3) C. Yonezawa, A. K. H. Wood, M. Hoshi, Y. Ito and E. Tachikawa: Nucl. Instr. Meth. in Phys. Res.**A329** (1993) 207.

原子炉：JRR-3　　装置：PGA(T1-4-1,C2-3-2-2)　　分野：即発γ線分析実験（その他）

研究テーマ：中性子ガイドビームを用いた月探査用ガンマ線分光計の校正実験
表　題：惑星ガンマ線分光計測のための中性子捕獲ガンマ線生成率の校正実験

3) Calibration Experiments on Production Rates of Neutron-Capture Gamma Rays for Planetary Gamma-Ray Spectroscopy

M.-N. Kobayashi, N. Yamashita, N. Hasebe and H. Matsue[1]

Advanced Research Institute for Science and Engineering, Waseda University, Shinjuku, Tokyo 169-8555
[1]*Neutron Science Research Center, JAERI, Tokai, Ibaraki 319-1195*

Gamma rays are emitted from the surface of planets, their satellites and celestial bodies with little or no atmosphere, due to the decay of radioactive isotopes and excitation by energetic galactic cosmic ray (GCR) particles. Energy spectra of these γ rays have line peaks whose energies correspond to excited levels of nuclei of the surface materials and the intensities show the concentrations of the materials.

Some planetary missions sent or are carrying γ-ray spectrometers to the moon, Mars, an asteroid and Mercury to measure energy spectra of γ rays from them in their orbits. The γ-ray spectrometer onboard SELENE, the first Japanese lunar explorer orbiting the moon to be launched in 2007, employs a germanium detector and will measure energy spectra which will be much more precise than ones by past missions using scintillators [1].

The production of γ rays by cosmic rays is a complicated process as one needs to start with the high-energy (GeV) particles in GCR and follow the cascade of particles made in the planet until one of these particles produces a γ ray. The counts from spectrometers need to be converted to γ-ray intensities. Then elemental abundances are determined from them. For most elements, the γ rays used for planetary spectroscopy are made by inelastic-scattering reactions of neutrons with a few MeV of energy or by capture of neurons near thermal ($\sim$ eV) energies.

In the spectroscopy analysis of γ rays emitted from various elements, capture γ rays are preferred because they are likely to have relatively high energy, $>$ 6 MeV, and continuum background γ rays are decreased at such high energy region. To determine elemental abundance from the count rate measured by the γ-ray spectrometer, the comparison between the observations and numerical simulation results is mandatory. Physical processes computed in the simulation are preferred to be unified to be in one code from γ-ray production (nuclear process) through γ-ray detection (electromagnetic process). We adopt Geant 4 package [2] for this simulation. To simulate gamma ray production precisely, accurate nuclear data are necessary especially for cross section of neutron interaction and neutron capture cross sections for some elements have been verified in PGA (Prompt Gamma-ray Analysis) system in JRR-3 at JAERI.

The PGA utilizes thermal neutron beam whose fluence is very high and stable ($\sim 10^8$ n/cm^2 sec), introduced from the reactor to the target for chemical analysis. In this year, we measured the energy spectra of standard materials, Fe, Al, Na, Ca, Mg and Ti by a γ-ray spectrometer of the PGA to compare computational simulation, raising the reliability of the simulation code and nuclear data.

Under the present circumstances, the simulation cannot be executed in a unified way. γ-ray production rates are not reproduced properly in the calculations. The code and/or nuclear data needs to be improved. To avoid this problem, the production rates were calculated outside the simulation. Then γ rays were put back into the simulation. Accordingly, Geant 4 is used only for γ-ray transportation and γ-ray detection in the PGA spectrometer. In that "outside simulation", we adopt neutron-capture cross sections from a database of prompt γ rays [3] and verified the accuracy of them for line peaks that will be used for SELENE γ ray spectroscopy .

The calculation results agree with experiments within errors of $\sim$ 8 % at a maximum for the major peaks of Fe, Al, and Na, and $\sim$ 20 % for Ca, Mg, and Ti [4]. Figure 1 shows an example of comparisons bewteen calculations and experiments for Fe and Al. For the large differences, neutron-capture cross section can have some errors and/or there can be uncertainty other than that. We will check out the differences and improve the simulation for the further study.

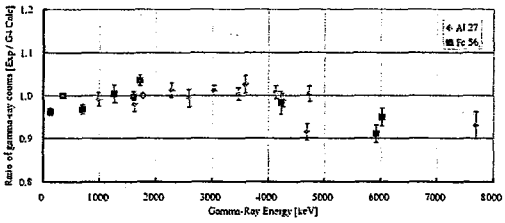

Figure 1: Comparison between calculations and experimentals. Fe normalized at 352 keV, Al normalized at 1779 keV.

References

1) M. Kobayashi, *et al.*: Nucl. Intr. Meth. 2005 in press.
2) http://wwwasd.web.cern.ch/wwwasd/geant4/.
3) Prompt Gamma Rays from Slow Neutron Capture for Elemental Analysis, IAEA.
4) N. Yamashita, *et al.*, *The 40th Vernadsky/Brown Microsymposium on Comparative Planetology, October, 2004, Moscow Russia*, Abstract #79.

原子炉：JRR-3　装置：PGA(T1-4-1,C2-3-2-2)　分野：即発γ線分析実験（地球科学・宇宙科学）

研究テーマ：リアルタイム非破壊超微量元素分析法の開発
表　　題：多重即発ガンマ線の測定とデータ解析

4)　多重即発ガンマ線の測定とデータ解析

藤　暢輔、大島真澄、小泉光生、長　明彦、木村　敦
日本原子力研究開発機構　原子力基礎工学部門　核変換用核データ測定研究グループ

多重即発ガンマ線分析法では、即発ガンマ線のエネルギー情報とその時間間隔であるタイミング情報がセットになったリストデータとしてテープ装置もしくはハードディスクにイベント毎に記録される。そのため、リストデータをソーティングしてノイズとなる信号を除去する事により検出限界や精度などを向上させる事が可能である。そのアルゴリズムとしてアッドバックモードとアンチコインモードと呼ぶモードでのソーティングを行うソフトウェアを開発した。クローバGe一検出器は４つの四角柱状のGe結晶を密に配置した構造であるため、あるGe結晶でコンプトン散乱されたガンマ線が他の結晶に入って検出される事象の確率が非常に大きい。この事象は一般的にシグナル/ノイズ比(S/N 比)を悪化させるため、ソーティングでこの事象の処理を行うことにより検出装置の性能が改善すると予測された。ソーティングモードとしては２つのモードにより解析を行った。１つはアッドバックモードであり、隣接するGe結晶の信号ペアを足すモードである。もう一方はアンチコインモードであり、隣接するGe結晶の信号が存在した場合には、そのイベントを取り除くというモードである。どちらのモードもGe結晶の組み合わせの数などが多い為、様々なバリエーションが存在するが、今回はシンプルな組み合わせでソーティングを行った。

図１にアンチコインモードでのソーティングの結果、得られた２次元スペクトルを示す。図１にはオンラインで得られた２次元スペクトルも同時に示す。オンラインのスペクトルは全てのイベントをそのまま加算しているため全体的にバックグラウンドが高い。斜めに現れる線はガンマ線のエネルギーの一部が欠落した事象であり、バックグラウンドの一つである。アンチコインモードによるソーティングを行ったスペクトルではバックグラウンドが減少している。そのためS/N比が良く、検出限界が高いと考えられる。しかし、実際のピークカウントも減少しているため、短い測定時間で分析を行いたい場合にはアッドバックモードが有利な場合もあると考えられる。

アッドバックモードの評価を正確に行うためには特定の検出器間に存在しているクロストークを無くす必要があるため、検出器のプリアンプ配線を改良する予定である。

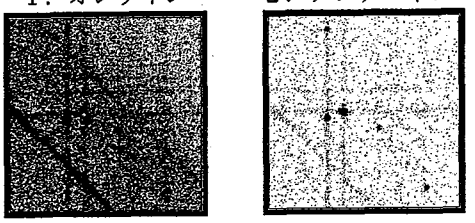

図１リストデータ解析によるバックグラウンド低減効果（左図：オンライン、右図：アンチコインモードによる解析）

原子炉：JRR-3　　装置：多重即発ガンマ線分析装置　　分野：即発γ線放射化分析（その他）

4. 放射化分析

4. Neutron Activition Analysis

This is a blank page.

研究テーマ：中性子放射化分析法の環境影響元素・物質研究に対する新利用法と高度化技法の開発
表　　題：金属元素類（重金属元素等）の同位対比測定法の開発による土壌中の挙動解明

1) 放射化分析法によるイネへの^{114}Cd吸収濃度の測定

櫻井泰弘、木方展治
独立行政法人 農業環境技術研究所

環境中の無機元素（Cd, Se, Zn, 等）の動態解明や影響評価に資するために、野外での使用が可能である安定同位体(SI)による環境物質の標識化法と中性子放射化分析による安定同位体の高精度測定法を開発する。今年度はCdのイネへの吸収量を測定するのに必要な放射化分析の実験条件を、水耕栽培したイネを用いて明らかにする。

1）イネの水耕栽培実験

内容積5Lの容器に培養液を調製し、イネ（コシヒカリ、アキタコマチ）を1容器あたり4株づつ約3ヶ月間栽培した。収穫10日前から培養液中に所定の濃度（表1）になるように$^{114}Cd^{2+}$ または^{114}Cd標識化フルボ酸を添加しイネへ吸収させた。

2）イネ試料中^{114}Cdの放射化分析による定量実験

部位別（根、茎、葉）に粉砕したイネ乾燥試料は各300mgづつポリエチレン袋に密閉し、標準試料(各濃度の^{114}Cd 溶液を300mg添加したロ紙）と共に日本原子力研究所研究炉JRR-4で熱中性子を照射し、2時間～5日間冷却後、生成した放射性核種のγ線スペクトルを計測した。^{114}CdはISOFLEX社製、メタル型99.01%を濃硝酸に溶解して使用した。

Cd安定同位体を吸収したイネの放射化分析条件を検討した結果、イネ乾燥試料300mgへ10分間の$3\times10^{17}(m^{-2}s^{-1})$の熱中性子束を照射し、1日冷却後300秒のγ線計測で^{115}Cdの定量が可能であり、標準試料による検量線から5.32×10^{-3}～2.66×10^{-1} μMの領域で計測できた。水耕栽培でCd安定同位体またはCd安定同位体で標識化したフルボ酸のイネへのCd吸収濃度を放射化分析で測定した結果（コシヒカリの結果だけを図1に示す）、培養液中Cd濃度の増加により植物体中Cd濃度も増加し、植物体各部位の^{115}Cdの濃度は全ての試験区で根＞茎＞葉の順であった。フルボ酸Cdは根への吸収は少ないが茎、葉への吸収は　Cd添加区よりも多い。根への吸収濃度は両品種で同等であったが、葉への吸収濃度はコシヒカリ＞アキタコマチであった。

表1．イネ水耕栽培試験区

試験区	Cd添加試薬	Cd濃度(μM)
BLK	なし	0
I	$^{114}Cd(NO_3)_2$	1.37
II	〃	2.92
III	〃	3.97
IV	〃	4.97
F-I	フルボ酸^{114}Cd	4.16

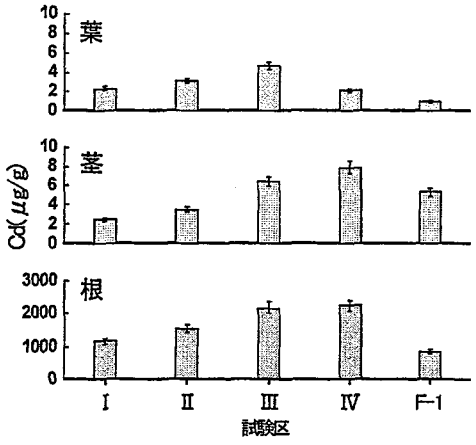

図1 イネ(コシヒカリ)各部位の^{115}Cd濃度

原子炉：JRR-3M,4　　装置：水送管　　分野：放射化分析（農・水産物）

研究テーマ：中性子放射化分析法の環境影響元素・物質研究に対する新利用法と高度化技法の開発
表題：臭素同位体比(Br-81/Br-79 比)測定法の開発による土壌浸透水の野外・長期間追跡への利用

2) 土壌水を追跡するための臭素同位体比測定法の野外適用—重水との比較および水田への適用

木方展治、藤原英司
農業環境技術研究所

1．はじめに

土壌浸透水のより改善された追跡手法として、自然存在比（^{81}Br と ^{79}Br）が大きく異なる臭素安定同位体試薬溶液をトレーサとして利用する方法を開発する。本年度は野外における臭素の動態を重水と比較した。また稲の生育している水田に臭素同位体試薬を散布し、土壌浸透水の追跡可能性について検討した。

2．実験方法

②方法

1）重水の散布

裸地畑圃場に 45cm×45cm の木製の枠を設置し、90 atom%^{79}Br 試薬添加液と 90 atom%^{81}Br 試薬添加液を 99atom%重水に溶存させ、散布した。先端にセラミック製ポーラスカップを装着した土壌水採取管を深さ 12.5cm から 25 cm 間隔で 112.5cm まで 1 本ずつ埋設し、真空ポンプによる吸引で土壌水の採取を行った。

2）水田への同位体試薬の散布

5 月上旬に水稲（品種名；コシヒカリ）の移植を行った水田に 60cm×35cm で高さ 15.5cm の無底枠を 6cm 深さに埋め込んだ。枠内には水稲 3 株が入るようにした。中干し後、たん水状態で 90 atom%^{79}Br を含む 4000mg/L NH_4Br 溶液 10mL を添加し、枠内の田面水と混じた。枠の側面にシリコンゴム栓をしており、田面水の供給が必要なときはこれを開栓して、枠外から補うこととした。土壌水の採取は 1）と同様に行った。

3）分析法

土壌土壌水は、ろ紙に 100μL 吸わせ、ポリエチレン製袋に 2 重封入し、カプセルに入れた後、原研東海研の JRR-4 炉（水力 T パイプ）および JRR-3M 炉（気送管）（ともに熱中性子束、約 $5\times10^{17}m^{-2}s^{-1}$）で 2 分～20 分照射した。実験室搬入後、外側の袋を包み替えて、γ線スペクトロメトリにより、臭素の定量を行った。

水の重水素（$^{2}H,D$）存在比は、水蒸気を温度平衡状態にした後に質量分析計に導入し分析した。

3．結果および考察

1）重水の散布試験

第 1 図には深さ 35cm の土壌水における臭素および重水素の同位体比変化を示した。縦軸には図内で定義されるδ値を用いた。同位体変動試薬添加区の臭素同位体比変化は、重水素の同位体比変化と矛盾せず、臭素同位体比の変化が水移動の状況を大まかに表すものと考えられた。ただし臭素同位体比のピークからの降下速度は、水素同位対比よりも低い傾向があった。これは黒ボク土壌に特徴的な高い陰イオン交換容量(AEC)を考慮する必要があることを示唆しているものと考えられる。

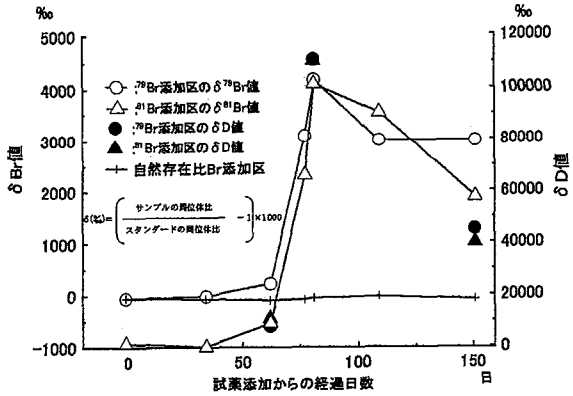

第 1 図　臭素と重水素の同位体比変化

2）水田への散布試験

第 2 図に水田土壌水各深さにおける臭素同位体存在比の経日変化を示した。臭素同位体のピークは深さ 12.5cm から 37.5cm,62.5cm と順次現れた。深さ 37.5cm 位置での臭素同位体比のピークは試薬添加後約 23 日、深さ 62.5cm では約 37 日で現れた。これは、1 日 16～17mm 程度の速度で水の浸透があることを示している。また枠内のイネに生育の以上は認められなかった。

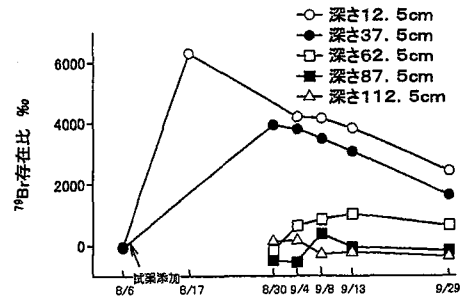

第 2 図　水田土壌水中における臭素同位体存在比の経日変化

参考文献

1)日本土壌肥料学会学会講演要旨集(2005),p.272

原子炉：JRR-3M、JRR-4　装置：気送管、水力 T パイプ　　分野：放射化分析（環境、農・水産物）

研究テーマ：フィッショントラック法による環境試料中の核物質検出
表　　題：フィッショントラック法の保障措置環境試料パーティクル分析への応用

3)　フィッショントラック法の保障措置環境試料パーティクル分析への応用
井口一成，李致圭，伊奈川潤，鈴木大輔[1]，福山裕康，桜井聡，
臼田重和，江坂木の実，小野寺貴史，江坂文孝[1]，渡部和男[1]，間柄正明

日本原子力研究所　環境科学研究部　環境技術開発研究グループ
[1]日本原子力研究所　環境科学研究部　分析科学研究グループ

[はじめに]　未申告原子力活動の検知を目的とする保障措置環境試料のパーティクル分析について、サブミクロン粒子の分析もできるフィッショントラック(FT)法を応用したパーティクル分析技術の開発を進めている。これまでに、本法が環境試料中の核物質含有粒子の検出および同位体比測定に有効な分析法であることを示した。今回は FT 法による核物質の検出の際に重要になる FT 検出器のエッチング挙動について調べたので、その結果について報告する。

[FT 検出器の作製]　原子力関連施設内から拭き取りにより採取した試料(スワイプ試料)から、吸引法[1]により、ポリカーボネートメンブランフィルター(直径 25 mm, 細孔径 0.1 μm, Advantec)に核物質含有粒子を捕集した。そのフィルムを 1,2 ジクロロエタンとジクロロメタン混合液に溶解した。良く撹拌した後、ガラス板上に伸ばして再固化させ、粒子を含んだフィルム(検出器)を作製した。JRR-4 にて熱中性子(フルエンス: 8×10^{14} ncm^{-2})を検出器に照射した後、NaOH 溶液(55℃, 6 M)で化学エッチングを行うことでFTを可視化した。

[FT 検出器のエッチング挙動]　本法では粒子は FT の中心に存在するので、デジタル顕微鏡(VHX100, Keyence)により、FT を観察することで核物質含有粒子が検出できるのが特徴の一つである(図 1a)。エッチングによる FT の変化を調べたところ、図 1b に示されるようにエッチングの進行により粒子の脱落が起こることがわかった。このことからエッチングは適度な条件で行う必要があることがわかる。更にエッチングにより粒子が検出されるまでの時間(粒子検出開始時間)および粒子の脱落が始まるまでの時間(粒子脱落開始時間)について整理したところ、それらの時間は濃縮度により異なることがわかった。天然ウランでは 4 分のエッチング後に粒子の検出が始まり、6 分以後では粒子の脱落が始まった。濃縮度が高くなる程、それらの時間は短くなり、85%濃縮ウランでは、検出開始時間 0.17 分、脱落開始時間 1.7 分だった。これは、高濃縮度ほど核分裂をする ^{235}U の量が増えるので、同じフルエンスの熱中性子を照射した場合、核分裂の数が増え、それに伴い粒子周辺の損傷が大きくなるためである。濃縮度により、粒子検出及び脱落開始時間が変化したことは、エッチング時間を制御することで、ウラン粒子の濃縮度別の分離ができる可能性を示している。

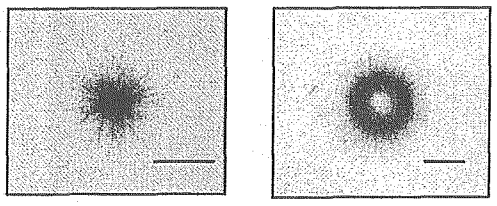

図1　FTデジタル顕微鏡写真
(a) 粒子検出
(b) 粒子脱落

[まとめ]　ウランの濃縮度が高くなるほど、粒子検出開始および粒子脱落開始時間が短くなることから、エッチング時間の制御により、ウラン粒子の濃縮度別検出の可能性が示された。また、エッチング条件を改善することにより脱落粒子の抑制が可能と考えられる。

参考文献

1) K. T. Esaka *et al.*, Jpn. J. Appl. Phys., 43(2004) 915.

研究テーマ :中性子放射化分析法による環境試料の分析
表　　題 :大気エアロゾル粒子のキャラクタリゼーション

4) 大阪で観測した大陸性土壌粒子の影響

伊藤憲男　溝畑　明
大阪府立大学先端科学イノベーションセンタ

研究目的　日本では主に春季に黄砂現象で見られるように、中国大陸からの土壌粒子の影響を受けている。大陸からの土壌粒子の影響が大きいときにどの程度大気エアロゾル粒子の濃度が増加して、土壌粒子の影響が大きい粗大粒子の組成がどのように変化するかを明らかにする。

実験方法　長期間連続して大阪府堺市の大阪府立大学で大気エアロゾル粒子を粒径を分けて捕集して、その濃度及び組成を分析する。元素組成の分析法として中性子放射化分析法を使用する。中性子放射化分析法は、日本原子力開発機構の研究炉 JRR-3 PN-3(30秒照射)と JRR-4 TA(30分間照射)を使用した。

結果

粒径別塵濃度　2000年に粒径別に6期間に分けて捕集したエアロゾル粒子の濃度をFig.2に示す。粒径の範囲を、>4.7μm,2.1-4.7μm, <2.1μmに分けた。2.1μm以上の範囲を、大陸性土壌粒子の影響が大きいと思われる2.1-4.7μmと局地的影響が大きいと思われる　>4.7μmの範囲に分けた。4月11日-25日に観測した期間の粒径範囲 >4.7μm,2.1-4.7μmで濃度が、他の観測期間と比べて、>4.7μmで3.7倍、2.1-4.7μmで5.4倍の増加があった。土壌粒子の影響が大きい粒径範囲で濃度の増加が認められ、大陸性土壌粒子の影響を大きく受けたと推定される。特に2.1-4.7μmの粒径範囲の影響が>4.7μmの粒径範囲の影響に比べて大きく、長距離輸送されてくる粒径の小さい土壌粒子の影響が大きくなったことを示している。

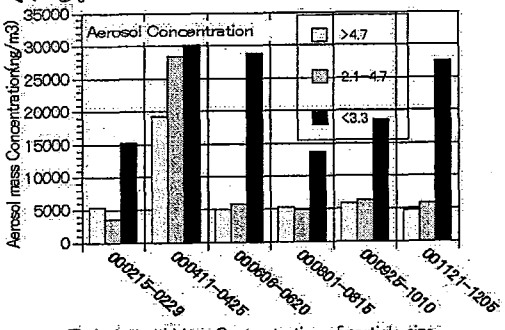

Fig.1 Aerosol Mass Concentration of particle size range for each sampling period

Al,Caの濃度変化　上記で示した試料について中性子放射化分析法により、AlとCaの分析を行った。>4.7μm,2.1-4.7μmの粒径範囲の分析結果をFig.3に示す。塵濃度と同様に、4月11日-25日に観測した期間に他の観測期間と比べて濃度の増加が認められ、大陸性土壌粒子の影響により土壌の主成分であるAlとCaの濃度の増加が確認できた。Alの濃度増加は、>4.7μmで4.4倍、2.1-4.7μmで10倍であった。Caの濃度増加は、>4.7μmで3.5倍、2.1-4.7μmで6.6倍であった。濃度増加は、CaよりAlが大きく、粒径範囲についてはAlとCaそれぞれ>4.7μmより2.1-4.7μmが大きかった。この結果は、大陸性土壌粒子は観測地点付近の土壌粒子と元素組成(AlとCaの濃度)が異なり、4.7μm以下の粒径の小さい粒子で主に構成されていることをしめしている。

Ca/Al >4.7μm,2.1-4.7μmの粒径範囲の各観測期間でのCaとAlの濃度比Ca/Alを、Tab11に示す。4月11日-25日に観測した期間で、Ca/Alが低下することが認められた。2.1-4.7μm粒径の範囲で>4.7μmと比べて低下の割合が大きかった。

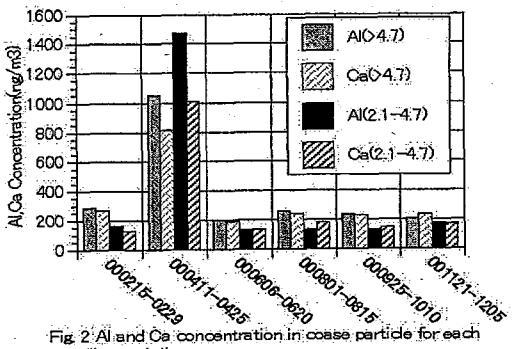

Fig.2 Al and Ca concentration in coase particle for each sampling period

Table1 Ca/Al for coarse particle in each sampling period

Sampling period in 2000	*Ca/Al in particle diameter range (μm)*	
000215-0229	0.95	0.79
000411-0425	0.78	0.68
000606-0620	0.95	1
000801-0815	0.92	1.39
000925-1010	0.98	1.06
001121-1205	1.14	0.99

原子炉：JRR-3　装置：放射化分析用照射設備　分野：放射化分析(環境)
原子炉：JRR-4　装置：Tパイプ　分野：放射化分析(環境)

5) アーバスキュラー菌根を形成した植物の微量元素分析と植物保護技術としてのアーバスキュラー菌根菌の利用可能性の検討

Determination of trace elements in arbuscular mycorrhizal plant by INAA and application of arbuscular mycorrhizal fungi in pytoremediation of polluted soil

千葉大学：鈴木弘行・村松雅子・鈴木悠一・荻山慎一・熊谷 宏・坂本一憲
東京大学：野川憲夫

(1) 研究の目的、意義、計画について

平成 11 年ー13 年度に行った原研施設利用共同研究において、鈴木ら（2003）はアーバスキュラー菌根の発達状態を一般的な格子交点法で評価した感染率（菌根形成率）を基にして、マリーゴールドにおけるアーバスキュラー菌根の形成が Zn や Mn などの微量元素の吸収に影響を及ぼすことを明らかにした。しかし、アーバスキュラー菌根の発達状態を感染率（菌根形成率）のみで評価しただけでは、菌根の吸収機構の解明には不十分である。アーバスキュラー菌根内には外生菌糸と植物との物質交換に関係があるとされる樹枝状体のような共生器官が形成されるので、共生器官の発達状態などを共生強度として評価し微量元素吸収との関係を調査することがアーバスキュラー菌根による微量元素の吸収機構を解明するために重要である。

そこで本研究では、アーバスキュラー菌根を形成した植物の微量元素分析を行い、アーバスキュラー菌根内の共生器官の発達状態と微量元素吸収との関係について調査した。まず、アーバスキュラー菌根の形成が宿主植物の種類だけでなくアーバスキュラー菌根菌の菌種によっても変化することから、接種菌株の違いが宿主植物の微量元素吸収に及ぼす影響を共生器官の発達状態などの共生強度の点から調査した。次に、アーバスキュラー菌根菌との共生系が強化あるいは抑制されたモデルとして研究されているダイズの菌根変異体を用いて、共生器官の発達状態などの共生強度が異なる条件下での微量元素の吸収について調査した。

さらに本研究ではアーバスキュラー菌根を形成した植物では希土類元素による植物毒性が軽減された報告（鈴木ら 2001）を踏まえ、植物保護技術としてのアーバスキュラー菌根菌の利用可能性について検討することを計画していた。当初の計画では、重金属等に汚染された土壌を用いてアーバスキュラー菌根菌を接種した植物と非接種の植物を栽培し、生育や元素吸収について調査する予定であった。しかし、実験に用いる汚染土壌の調査に難航したため計画を達成するには至らなかった。計画の未達成部分は平成 17 年度以降の原研施設利用共同研究において継続する予定である。このため、植物保護技術としてのアーバスキュラー菌根菌の利用可能性の検討については、今後の実験に用いる予定の土壌に関して得られた成果を報告する。

(2) 試料および方法

実験Ⅰ：接種菌株の違いが宿主植物の微量元素吸収に及ぼす影響

実験Ⅰでは実験Ⅱにおいてダイズの変異体を用いることを踏まえて、宿主植物としてダイズ（*Glycine Max* (L.) Mirr, 品種名 エンレイ）を用いた。宿主植物に接種したアーバスキュラー菌根菌は *Glomus etunicatum* Becker and Gerdemann、*Gigaspora rosea* Nicolson and Schenk C1 (MAF520062)、*Acaulospora longula* Spain and Schenk F-1 (MAFF520060) の 3 種類とした。試験区は *Glomus etunicatum* 接種区（G.e.区）、*Gigaspora rosea* 接種区（Gi.r.区）、*Acaulospora longula* 接種区（A.l.区）の 3 区と対照区として非接種区を設定し、各試験区とも 3 連制とした。

培土にはオートクレーブ滅菌した川砂と鉢底石を用いた。栽培には 1/10000a のワグネルポットを使用し、ポット底に鉢底石 100g を敷いた上に川砂 1kg を充填した。このポットにダイズ種子を 3 粒ずつ播種した。播種後、3 つの接種区には各菌株の胞子をそれぞれ 200 胞子接種した。栽培はバイオトロン内（気温 25℃、明期 14 時間、湿度 50%、照度 35000Lx）で 71 日間行った。各ポットのダイズは本葉が展開した後に 1 個体に間引きした。施肥は PETERS 液肥を用いて行い、栽培期間中に 1 ポットあたり 164mg の N、3.1mg の P、176mg の K を与えた。

採取したダイズは地上部と根部に分けた後、付着した培土を除くために蒸留水で洗浄した。根部の一部は菌根の形成を観察するために凍結保存し、残る根部と地上部は80℃で48時間乾燥した。乾燥した地上部と根部は粉砕し放射化分析用の試料とした。菌根の観察はPhillips and Hayman (1970) の方法に従って染色し、菌根形成頻度、菌根形成強度、樹枝状体形成率をTrouvelot法 (Trouvelot et al. 1986) で測定した。

放射化分析は日本原子力研究所の原子炉JRR-4を利用して行った。短寿命核種の測定は気送管で20秒照射し、3分間冷却後Ge半導体検出器で測定した。中長期寿命核種の測定はTパイプA系統で10分間照射し、1週間程度冷却後Ge半導体検出器で測定した。放射化分析のための標準試料にはNBS Peach Leaves (SRM1547) とNCS Stream Sediment (DC73317) を用いた。

実験Ⅱ：アーバスキュラー菌根の共生強度と微量元素の吸収との関係

宿主植物としてダイズ (*Glycine Max* (L.) Mirr, 品種名 エンレイ) を用いた。ダイズは実験Iで用いたエンレイ (WT) の他、樹枝状体を形成しやすいエンレイの変異体 (En6500)、樹枝状体を形成しにくいエンレイの変異体 (En1282) の計3種類を用いた。アーバスキュラー菌根菌の接種には *Glomus etunicatum* Becker and Gerdemann と *Gigaspora rosea* Nicolson and Schenk C1 (MAF520062) を用いた。試験区は対照区として3つの非接種区 (WT－C区、En6500－C区、En1282－C区)、*Glomus etunicatum* を接種した3区 (WT－G.e.区、En6500－G.e.区、En1282－G.e.区)、*Gigaspora rosea* を接種した3区 (WT－Gi.r.区、En6500－Gi.r.区、En1282－Gi.r.区) を設定し、各試験区とも3連制とした。

培土にはオートクレーブ滅菌した川砂と鉢底石を用いた。栽培には1/10000aのワグネルポットを使用し、ポット底に鉢底石100gを敷いた上に川砂1.2kgを充填した。このポットに芽出ししたダイズを2個体移植した。移植後、G.e.とGi.r.の接種区には各菌の胞子をそれぞれ200胞子接種した。栽培はバイオトロン内(明期14時間、気温28℃、湿度50%、照度35000Lx:暗期10時間、気温23℃、湿度50%、照度0Lx) で73日間行った。各ポットのダイズは本葉が展開した後に1個体に間引きした。施肥はPETERS液肥を用いて行い、栽培期間中に1ポットあたり164mgのN、3.1mgのP、176mgのKを与えた。

採取した植物体は茎葉部、子実部、根部に分け、付着した培土を除くために蒸留水で洗浄した。根部の一部は菌根の形成を観察するために凍結保存し、残る根部、茎葉部、子実部は80℃で48時間乾燥した。菌根形成頻度、菌根形成強度、樹枝状体形成率の測定と放射化分析については実験Iと同様に行った。

実験Ⅲ：植物保護技術としてのアーバスキュラー菌根菌の利用可能性の検討 (実験に用いる土壌の微量元素分析)

循環型社会の構築を目指して様々な有機性未利用資源の土壌への還元が行われるようになったことを踏まえて、下水汚泥を資材として投入した土壌における微量元素の蓄積性について調査した。調査は千葉大学園芸学部内の圃場において下水汚泥コンポストを3年間施用した褐色森林土について行った。

【調査土壌の履歴】千葉県暖地園芸研究所内の畑より採取した褐色森林土を千葉大学園芸学部内の圃場に1998年8月に搬入した。試験区はオガクズ汚泥コンポスト区とモミガラ汚泥コンポスト区、対照区として化学肥料区の計3区を設置した。

化学肥料区はA社製の化学肥料 (N：P_2O_5：K_2O=8:8:5) を1作あたり1.25 t ha^{-1}または1.88t ha^{-1}施用した。オガクズ汚泥コンポスト区にはB市においてオガクズと下水汚泥を混合し堆肥化したオガクズ汚泥コンポストと化学肥料区と同量の化学肥料を施用した。モミガラ汚泥コンポスト区には，C市においてモミガラと下水汚泥を混合し堆肥化したモミガラ汚泥コンポストと化学肥料区と同量の化学肥料を施用した。オガクズ汚泥コンポストとモミガラ汚泥コンポストはそれぞれ乾物として初回のみ12 t ha^{-1}，以降は各作ごとに10t ha^{-1}施用した。これらの試験区には冬作としてエンバク (*Avena sativa* L.)，夏作として大豆 (*Glycine max* L.) またはニンジン (*Daucus carota* L.) を栽培した。

試験は1998年10月に開始し2001年5月までに化学肥料とコンポストを合計5回施用した。

土壌試料は2001年5月に化学肥料、オガクズ汚泥コンポスト、モミガラ汚泥コンポストの6回目の施用前に各試験区からランダムに3箇所を選び、それぞれの表層土 (0－15cm) を採取した。採取した土壌は乾燥後粉砕し0.5mmの篩を通過させて分析に供試した。

【放射化分析】放射化分析は日本原子力研究所の原子炉JRR－4を利用して行った。短寿命核種の測定は気送管で10秒照射し、1－3分間冷却後Ge半導体検出器で測定した。中長期寿命核種の測定はTパ

イプA系統で10分間照射し、1週間程度冷却後Ge半導体検出器で測定した。放射化分析のための標準試料にはNBS Peach Leaves (SRM1547) とNCS Stream Sediment (DC73317) を用いた。またオガクズ汚泥コンポスト、モミガラ汚泥コンポスト、化学肥料についても土壌と同様に放射化分析を行った。

(3) 結果および考察

実験Ⅰ

放射化分析の結果、ダイズからはSc、Cr、Mn、Fe、Co、Zn、Br、Rb、Sr、Cs、Ba、La、Ce、Sm、Eu、Yb、Lu、Th、Uの微量元素が検出された。各試験区における根部の元素含有率を表1に、地上部の元素含有率を表2に示した。根部の元素含有率ではZnにのみ試験区間で有意差が認められ、Zn含有率はGi.r.区において非接種区よりも有意に高くなった。しかし、Gi.r.区のZn含有率はG.e.区とA.l. 区とほぼ同じであった。地上部の元素含有率はCrとZnに試験区間で有意差が認められた。Cr含有率はG.e.区において非接種区よりも有意に低くなった。Zn含有率はGi.r.区において他の3試験区よりも有意に高くなった。本実験において、地上部の乾物重には試験区間で違いが認められなかったので (表2)、アーバスキュラー菌根の形成はダイズの植物生育にほとんど影響を及ぼしていないと考えられた。このため、植物生育量はG.e.区におけるCr含有率の低下やGi.r.区におけるZn含有率の増加には影響を及ぼしていないと思われる。菌根形成頻度、菌根形成強度、樹枝状体形成率にはG.e区、Gi.r区、A.l. 区の3試験区間で有意差は認められなかった (表1)。しかし、Gi.r区ではG.e.区よりも菌根形成強度が2倍、樹枝状体形成率が3倍高くなる傾向があり、このような傾向はダイズの地上部と根部のZn含有率がGi.r区において最も高くなったことと関連があるのかもしれない。一方、菌根形成頻度、菌根形成強度、樹枝状体形成率がG.e.区、Gi.r.区、A.l. 区の試験区間では最も低い傾向を示したG.e.区において地上部のCr含有率が非接種区よりも低下したことは、G.e.の接種と関係があると考えられ、菌根形成頻度、菌根形成強度、樹枝状体形成率は地上部のCr含有率の低下とはあまり関係がないと思われる。

実験Ⅰの結果をまとめると、Gi.r.にはG.e.やA.l.よりもZn吸収を高める性質があり、そのような性質は菌根形成強度や樹枝状体形成率と関係している可能性がある。またG.e.には他の2菌種よりもダイズのCr吸収を低下させる性質があり、そのような性質は菌根形成強度や樹枝状体形成率とはあまり関係がないと考えられた。

実験Ⅱ

放射化分析の結果、実験Ⅱのダイズからは実験Ⅰと同様の元素が検出された。アーバスキュラー菌根菌非接種の場合、根部のCoとRb、茎葉部のCr、Mn、Zn、Sr、Ba、La、Sm、Eu、子実部のBaの含有率に試験区間で違いが認められた (表3)。各試験のダイズの根部新鮮重、茎葉部乾物重、子実体乾物重を非接種の3試験区間、G.e.接種下の3試験区間、Gi.r.接種下の3試験区間で比較した結果、いずれの3試験区間でも有意差は認められなかったので (表3ー5)、3タイプのダイズにおける各部位の元素含有率の違いに対しダイズの生育量の違いはほとんど影響を及ぼしていないと考えられた。非接種の3試験区間でダイズの生育量に違いが認められなかったにもかかわらず、元素含有率に違いが認められたことは、特定の元素に対してダイズの変異体ごとに固有の吸収特性があることを示唆していると思われた。

G.e.を接種した場合では、根部のMn、茎葉部のMnとSrの含有率に試験区間で違いが認められた (表4)。茎葉部のMnとSrの含有率については表3に示した非接種の場合と同様な傾向が認められたことから、G.e.接種下の茎葉部のMnとSrの含有率は変異体に固有の元素吸収特性による影響を受けていると考えられた。根部のMn含有率についてはEn6500- G.e.区でEn1282- G.e.区よりも有意に高くなった。G.e.接種下における菌根形成は菌根形成頻度、菌根形成強度、樹枝状体形成率とも3試験区間で有意差は認められなかったが、En6500- G.e.区の樹枝状体形成率はEn1282- G.e.区の約2倍であった (表4)。このため、En6500- G.e.区において根部のMn含有率がEn1282- G.e.区よりも有意に高くなったことは、En6500- G.e.区の樹枝状体形成率が高かったことと関連があるのかも知れない。

Gi.r.を接種した場合では、根部のLa、Ce、Eu、Yb、Lu、茎葉部のMn、子実部のFeとCoの含有率に試験区間で違いが認められた (表5)。茎葉部のMn含有率については表3に示した非接種の場合と同様な傾向が認められたことから、変異体に固有の元素吸収特性が影響を及ぼしていると考えられた。Gi.r.接種下における菌根形成は菌根形成頻度、菌根形成強度、樹枝状体形成率とも3試験区間で有意差は認められなかったが、En6500- Gi.r.区の樹枝状体形成率はEn1282- Gi.r.区よりも約4倍高くなった (表5)。Gi.r.接種下の根部のLa、Ce、Eu、Yb、Lu、子実部のFeとCoの含有率の増加については、元素含有率が樹枝状体形成率と同様にEn6500-

Gi.r.区で最も高くなっていることと、変異体に固有の元素吸収特性の影響を受けていないことから、樹枝状体形成率の増加と関連性があるのかもしれない。

実験Ⅲ

オガクズ汚泥コンポスト,モミガラ汚泥コンポストおよび化学肥料の分析結果を表6に示した。オガクズ汚泥コンポストとモミガラ汚泥コンポスト中の元素含有率が化学肥料を上回った元素は、オガクズ汚泥コンポストでは Sc、Cr、Mn、Fe、Co、Zn、Sr、Ag、Sb、Ba、La、Ce、Sm、Eu、Ta、Th であり、モミガラ汚泥コンポストでは Sc、Cr、Mn、Fe、Co、Zn、As、Ag、Sb、Ba、Ta であった。これらの元素の中では Zn について、土壌に蓄積しやすい重金属として規制値が示されており、平成 13 年に改正された肥料取締法においては 900mg kg^{-1} 以上含む場合に表示の義務付けがなされている。オガクズ汚泥コンポストとモミガラ汚泥コンポストの Zn 含有率は規制値以下の約 500mg kg^{-1} であったが、化学肥料よりも約7倍高い値を示した。化学肥料と比べて7倍以上高い含有率を示した元素には Zn の他にも、オガクズ汚泥コンポストにおいて Mn、Fe、Ag、Ba、La、Ce が、モミガラ汚泥コンポストにおいて Mn、Ag、Ba があった。これらの元素については、Zn 同様に土壌への蓄積性を検討する必要があると思われる。

本実験では、オガクズ汚泥コンポスト区あるいはモミガラ汚泥コンポスト区の土壌から検出された元素の中では Ag の含有率のみが化学肥料区よりも有意に高くなった。

Ag は、オガクズ汚泥コンポストやモミガラ汚泥コンポストの Ag 含有率が化学肥料の Ag 含有率に対する比が最も高くなるため、土壌への蓄積が最も早く現れたと思われる。しかし、モミガラ汚泥コンポストの Ag 含有率はオガクズ汚泥コンポストと比べて約6倍（1回のコンポストの投入に伴う量としては約5倍）の差があったがオガクズコンポスト区とモミガラコンポスト区の土壌の Ag 含有率には有意差が認められなかった。土壌に投入された Ag の総量の違いが土壌の Ag 含有率に影響を及ぼさなかった点については不明であるため、土壌中における Ag の動態を把握するためにさらに調査が必要であると思われる。

Ag は一般的に毒性が低い元素であると考えられているが、微生物や植物に対して毒性を示すことが知られている（浅見 2001, Leep et al. 1995)。また、抗菌商品として用いられた Ag による環境汚染や公衆衛生的な問題も指摘されている（浅見 1995)。重金属による土壌汚染を浄化する方法の一つとしてファイトレメディエーションが注目されているので、今後、Ag 汚染土壌におけるファイトレメディエーションの有効性やファイトレメディエーションを行う場合に Ag の植物毒性を緩和する保護技術としてアーバスキュラー菌根菌の利用可能性を検討することが重要であると思われる。

(4) 今後の方針

本研究においてアーバスキュラー菌根の微量元素吸収機構を樹枝状体形成率のような菌根の植物−菌根菌側での共生強度を基に解析した結果、Zn などいくつかの微量元素の含有率の増加が樹枝状体形成率の増加と関連があることが示唆された。今後は、アーバスキュラー菌根の微量元素吸収機構を外生菌糸量のような菌根菌− 土壌側の共生強度からも解析する予定である。

また、微量元素の土壌汚染に対して植物保護技術としてアーバスキュラー菌根菌を利用する予備検討で土壌調査を行った結果、下水汚泥を含むコンポストコンポストを3年間施用した土壌において Ag の蓄積が明らかになった。今後、Ag 等の汚染土壌においてファイトレメディエーションや植物毒性を緩和する保護技術としてアーバスキュラー菌根菌の利用可能性を検討する予定である。また、放射化分析を利用した土壌調査を継続し、元素の分析に抽出操作を要する機器分析では見落とされていた微量元素の土壌汚染等について調査する予定である。

(5) 引用文献

浅見輝男：抗菌商品と銀，金属，65，1061−1064 (1995)

浅見輝男：日本土壌の有害金属汚染，p.249−255，アグネ技術センター，東京 (2001)

Leep, N.W., Edwards, R. and Jones, K.C.: Silver; in Heavy Metals in Soils, ed. B.J. Alloway, p.324-330, Blackie Academic & Professional, London (1986)

Phillips, J.M. and Hayman, D.S.: Improved procedures for clearing roots and staining parasitic and vesicular arbuscular fungi for rapid assessment of infection., Trans Br. Mycol. Soc., 55, 158-161 (1970)

鈴木弘行・森 史子・熊谷 宏・坂本一憲・犬伏和之：希土類元素の添加とアーバスキュラー菌根の形成がマリーゴールドの生育に及ぼす影響，日本土壌肥料学雑誌，72, 627-632 (2001)

鈴木弘行・熊谷 宏・野川憲夫・澤幡浩之・川手 稔・

大橋國雄：アーバスキュラー菌根の形成が宿主植物の各種元素の吸収に及ぼす影響., 原研施設利用共同研究成果報告書, 41, 94-103 (2003)

Trouvelot, A., Kough, J.L. and Gianinazzi-Pearson, V.: Mesure du taux de Mycorhization VA d'un systeme radiculaire. Recherche de methodes d'estimation ayant une signification fonctionnelle.; in Physiological and genetical aspects of mycorrhizae, ed. Gianinazzi-Pearson, V. and Gianinazzi, S. , p.217-221, INRA, Paris (1986)

(6) 成果の公表

(学会発表)

Suzuki, H., Kumagai, H., Nogawa, N., Kawate, M., Sawahata, H., Sakamoto, K., Inubushi, K., Enomoto, S. and Oohashi, K.: The uptake mechanism of trace elements by arbuscular mycorrhizal plant., 16th International symposium on environmental biogeochemistry, Abstracts (II), p.114 (2003)

荻山慎一・坂本一憲・鈴木悠一・鈴木弘行・野川憲夫・犬伏和之：家畜ふんコンポストおよび下水汚泥コンポストの施用が畑土壌の各種微量元素含量に及ぼす影響, 日本土壌肥料学会講演要旨集第 50 集, p.180 (2004)

鈴木弘行・村松雅子・熊谷 宏・野川憲夫・坂本一憲・犬伏和之：アーバスキュラー菌根の共生強度とダイズの各種元素吸収との関連性, 第 22 回根研究集会要旨集, p.20 (2005)

表1　各試験区のダイズ根部の元素含有率と菌根形成[1)]

	非接種区	G..e.区	Gi.r.区	A.l.区
Sc	0.68 a	0.81 a	0.60 a	0.61 a
Cr	5.75 a	18.8 a	19.8 a	21.8 a
Mn	65.0 a	63.3 a	56.6 a	54.6 a
Fe	849 a	1.31×10^{3} a	898 a	1.05×10^{3} a
Co	0.65 a	0.85 a	0.81 a	0.77 a
Zn	8.54 a	12.1 ab	15.7 b	11.4 ab
Br	1.41 a	1.21 a	1.56 a	1.18 a
Rb	4.26 a	4.68 a	5.02 a	4.71 a
Sr	50.1 a	52.1 a	55.2 a	46.7 a
Cs	0.33 a	0.39 a	0.35 a	0.43 a
Ba	33.6 a	35.1 a	28.2 a	33.6 a
La	2.37 a	2.79 a	2.38 a	2.50 a
Ce	4.14 a	5.07 a	4.05 a	4.40 a
Sm	0.54 a	0.64 a	0.52 a	0.58 a
Eu	0.11 a	0.13 a	0.11 a	0.11 a
Yb	0.26 a	0.28 a	0.24 a	0.23 a
Lu	0.04 a	0.04 a	0.03 a	0.05 a
Th	0.13 a	0.15 a	0.14 a	0.13 a
U	0.08 a	0.08 a	0.12 a	0.08 a
菌根形成頻度（%	0	88.9 a	97.8 a	98.9 a
菌根形成強度（%	0	20.3 a	44.1 a	35 a
樹枝状体形成率	0	11.5 a	35.6 a	20.9 a

1）表中の同一英文字は元素含有率では4試験区間で、菌根形成は非接種区を除く3試験区間で有意差がないことを示す（ボンフェローニ法，$p<0.05$，　表中の値は3連の平均値）．

表2　各試験区のダイズ地上部の元素含有率と地上部乾物重[1)]

	非接種区	G..e.区	Gi.r.区	A.l.区
Sc	< 0.01	< 0.01	< 0.01	< 0.01
Cr	0.89 b	0.31 a	0.45 ab	0.66 ab
Mn	120 a	119 a	97.7 a	91.8 a
Fe	48.4 a	56.7 a	42.3 a	55.4 a
Co	0.06 a	0.07 a	0.07 a	0.06 a
Zn	14.8 a	16.3 a	27.4 b	11.8 a
Br	1.54 a	1.39 a	1.68 a	1.69 a
Rb	19.5 a	17.4 a	19.2 a	9.09 a
Sr	85.7 a	91.7 a	81.6 a	103 a
Cs	0.36 a	0.50 a	0.45 a	0.49 a
Ba	9.80 a	8.81 a	8.50 a	10.1 a
La	0.12 a	0.15 a	0.09 a	0.17 a
Ce	< 0.01	< 0.01	< 0.01	< 0.01 a
Sm	0.02 a	0.02 a	0.01 a	0.03 a
Eu	< 0.01	< 0.01	< 0.01	< 0.01
Yb	< 0.01	< 0.01	< 0.01	< 0.01
Lu	< 0.01	< 0.01	< 0.01	< 0.01
Th	< 0.01	< 0.01	< 0.01	< 0.01
U	< 0.01	< 0.01	< 0.01	< 0.01
地上部乾物重（g）	3.96 a	5.37 a	4.82 a	6.30 a

1）表中の同一英文字は試験区間で有意差がないことを示す（ボンフェローニ法，$p<0.05$，表中の値は3連の平均値）．

表３： 非接種の3試験区におけるダイズの根部、茎葉部、子実部における各種元素含有率 (mg kg^{-1})
各部位の生育量、菌根形成

測定部位	根部			測定部位	茎葉部			測定部位	子実部		
試験区	WT-C区	En1282-C区	En6500-C区	試験区	WT-C区	En1282-C区	En6500-C区	試験区	WT-C区	En1282-C区	En6500-C区
Sc	1.55 a	1.60 a	2.14 a	Sc	< 0.01	< 0.01	< 0.01	Sc	< 0.01	< 0.01	< 0.01
Cr	23.5 a	62.3 a	58.4 a	Cr	6.09 b	0.207 a	3.06 ab	Cr	0.25 a	0.14 a	0.10 a
Mn	153 a	184 a	238 a	Mn	289 ab	201 a	314 b	Mn	143 a	164 a	180 a
Fe	1.75×10^3 a	2.43×10^3 a	2.16×10^3 a	Fe	105 a	81.5 a	113 a	Fe	49.0 a	55.3 a	65.5 a
Co	3.39 a	4.74 b	5.81 c	Co	0.183 a	0.160 a	0.215 a	Co	0.141 a	0.155 a	0.209 a
Zn	21.6 a	17.1 a	20.3 a	Zn	31.1 b	23.3 a	35.2 b	Zn	32.6 a	32.0 a	37.0 a
Br	0.90 a	1.03 a	1.07 a	Br	2.24 a	2.15 a	1.83 a	Br	0.65 a	0.58 a	0.62 a
Rb	31.7 a	49.9 b	45.3 ab	Rb	16.5 a	15.1 a	45.3 a	Rb	30.1 a	31.7 a	35.4 a
Sr	44.6 a	42.5 a	50.4 a	Sr	82.9 a	75.1 a	107 b	Sr	46.3 a	57.8 a	60.3 a
Cs	1.38 a	2.49 a	2.29 a	Cs	0.40 a	0.39 a	0.38 a	Cs	0.40 a	0.45 a	0.44 a
Ba	49.2 a	59.6 a	49.4 a	Ba	37.1 b	24.8 a	39.2 b	Ba	17.8 a	16.7 a	22.5 b
La	6.42 a	5.67 a	7.06 a	La	0.59 ab	0.47 a	0.70 b	La	0.07 a	0.07 a	0.10 a
Ce	12.0 a	10.7 a	14.0 a	Ce	0.85 a	0.74 a	1.12 a	Ce	< 0.01	< 0.01	< 0.01
Sm	1.99 a	1.64 a	2.18 a	Sm	0.10 b	0.08 a	0.14 c	Sm	0.01 a	0.01 a	0.01 a
Eu	0.42 a	0.34 a	0.47 a	Eu	0.02 a	0.02 a	0.03 b	Eu	< 0.01	< 0.01	< 0.01
Yb	0.88 a	0.75 a	0.96 a	Yb	< 0.01	< 0.01	< 0.01	Yb	< 0.01	< 0.01	< 0.01
Lu	0.15 a	0.12 a	0.16 a	Lu	< 0.01	< 0.01	< 0.01	Lu	< 0.01	< 0.01	< 0.01
Th	0.17 a	0.36 a	0.26 a	Th	< 0.01	< 0.01	< 0.01	Th	< 0.01	< 0.01	< 0.01
U	0.31 a	0.27 a	0.27 a	U	< 0.01	< 0.01	< 0.01	U	< 0.01	< 0.01	< 0.01
新鮮重 (g)	21.6 a	21.4 a	22.3 a	乾物重 (g)	3.43 a	2.88 a	3.17 a	乾物重 (g)	1.18 a	1.16 a	1.55 a
菌根形成頻度(%)	0	0	0								
菌根形成強度(%)	0	0	0								
樹枝状体形成率(%)	0	0	0								

表中の同一英文字は各部位において試験区間で元素含有率に有意差がないことを示す(ボンフェローニ法, $p<0.05$)， 表中の値は3連の平均値.

表４： G.e.接種下の3試験区におけるダイズの根部、茎葉部、子実部における各種元素含有率 (mg kg^{-1})
各部位の生育量、菌根形成

測定部位	根部			測定部位	茎葉部			測定部位	子実部		
試験区	WT-G.e.区	En1282-G.e.区	En6500-G.e.区	試験区	WT-G.e.区	En1282-G.e.区	En6500-G.e.区	試験区	WT-G.e.区	En1282-G.e.区	En6500-G.e.区
Sc	1.88 a	1.68 a	1.71 a	Sc	< 0.01	< 0.01	< 0.01	Sc	< 0.01	< 0.01	< 0.01
Cr	50.5 a	22.6 a	29.9 a	Cr	1.08 a	1.27 a	1.38 a	Cr	1.93 a	2.1 a	0.41 a
Mn	111 ab	91.4 a	134 b	Mn	233 ab	169 a	275 b	Mn	148 a	148 a	161 a
Fe	2.12×10^3 a	1.63×10^3 a	1.56×10^3 a	Fe	71.1 a	64.7 a	102 a	Fe	66.2 a	64.2 a	76.6 a
Co	3.96 a	3.50 a	4.26 a	Co	0.15 a	0.15 a	0.19 a	Co	0.19 a	0.21 a	0.21 a
Zn	15.0 a	14.2 a	14.2 a	Zn	31.8 a	31.1 a	34.4 a	Zn	37.4 a	32.0 a	37.9 a
Br	0.60 a	0.56 a	0.60 a	Br	1.85 a	1.97 a	2.03 a	Br	0.49 a	0.45 a	0.47 a
Rb	49.3 a	51.6 a	43.8 a	Rb	17.9 a	19.3 a	16.0 a	Rb	39.5 a	38.3 a	37.2 a
Sr	50.1 a	40.4 a	41.3 a	Sr	67.0 a	74.8 ab	103 b	Sr	55.2 a	66.6 a	68.2 a
Cs	2.90 a	3.08 a	2.48 a	Cs	0.47 a	0.57 a	0.43 a	Cs	0.71 a	0.67 a	0.60 a
Ba	54.8 a	37.3 a	41.2 a	Ba	24.1 a	22.3 a	31.7 a	Ba	18.8 a	17.2 a	22.5 a
La	7.02 a	6.15 a	6.72 a	La	0.48 a	0.53 a	0.61 a	La	0.07 a	0.08 a	0.07 a
Ce	13.3 a	11.9 a	13.3 a	Ce	0.72 a	0.88 a	0.89 a	Ce	< 0.01	< 0.01	< 0.01
Sm	2.25 a	1.92 a	2.06 a	Sm	0.08 a	0.10 a	0.10 a	Sm	0.01 a	0.01 a	0.01 a
Eu	0.47 a	0.42 a	0.45 a	Eu	0.02 a	0.02 a	0.02 a	Eu	< 0.01	< 0.01	< 0.01
Yb	0.96 a	0.84 a	0.94 a	Yb	< 0.01	< 0.01	< 0.01	Yb	< 0.01	< 0.01	< 0.01
Lu	0.16 a	0.14 a	0.16 a	Lu	< 0.01	< 0.01	< 0.01	Lu	< 0.01	< 0.01	< 0.01
Th	0.35 b	0.18 a	0.21 a	Th	< 0.01	< 0.01	< 0.01	Th	< 0.01	< 0.01	< 0.01
U	0.38 a	0.22 a	0.23 a	U	< 0.01	< 0.01	< 0.01	U	< 0.01	< 0.01	< 0.01
新鮮重 (g)	24.9 a	18.8 a	21.8 a	乾物重 (g)	5.85 a	5.75 a	4.85 a	乾物重 (g)	0.95 a	1.60 a	1.57 a
菌根形成頻度(%)	93.3 a	85.6 a	95.6 a								
菌根形成強度(%)	22.4 a	20.8 a	31.8 a								
樹枝状体形成率(%)	13.5 a	12.4 a	20.2 a								

表中の同一英文字は各部位において試験区間で元素含有率に有意差がないことを示す(ボンフェローニ法, $p<0.05$)， 表中の値は3連の平均値.

表５： Gi.r.接種下の3試験区におけるダイズの根部、茎葉部、子実部における各種元素含有率 (mg kg^{-1})
各部位の生育量、菌根形成

測定部位	根部			測定部位	茎葉部			測定部位	子実部		
試験区	WT-Gi.r.区	En1282-Gi.r.	En6500-Gi.r.区	試験区	WT-Gi.r.区	En1282-Gi.r.	En6500-Gi.r.区	試験区	WT-Gi.r.区	En1282-Gi.r.	En6500-Gi.r.区
Sc	1.24 a	1.33 a	1.50 a	Sc	< 0.01	< 0.01	< 0.01	Sc	< 0.01	< 0.01	< 0.01
Cr	32.0 a	42.3 a	63.8 a	Cr	1.26 a	13.0 a	1.58 a	Cr	0.99 a	0.28 a	0.50 a
Mn	121 a	101 a	130 a	Mn	201 b	161 a	244 c	Mn	123 a	102 a	136 a
Fe	1.17×10^3 a	1.50×10^3 a	1.57×10^3 a	Fe	66.8 a	87.4 a	83.7 a	Fe	55.9 ab	51.4 a	65.0 b
Co	3.45 a	2.93 a	4.30 a	Co	0.16 a	0.38 a	0.29 a	Co	0.16 ab	0.15 a	0.20 b
Zn	19.2 a	25.8 a	21.4 a	Zn	48.1 a	59.2 a	54.3 a	Zn	38.9 a	39.3 a	47.0 a
Br	0.73 a	0.80 a	0.59 a	Br	2.12 a	2.89 a	2.70 a	Br	0.56 a	0.61 a	0.56 a
Rb	38.4 a	38.0 a	37.6 a	Rb	14.9 a	18.6 a	17.5 a	Rb	31.1 a	32.0 a	35.6 a
Sr	44.8 a	49.5 a	52.0 a	Sr	75.0 a	101 a	109.0 a	Sr	56.7 a	71.4 a	68.1 a
Cs	2.18 a	2.12 a	2.07 a	Cs	0.39 a	0.46 a	0.42 a	Cs	0.50 a	0.50 a	0.59 a
Ba	42.5 a	45.1 a	39.0 a	Ba	31.9 a	22.9 a	32.6 a	Ba	21.4 a	21.8 a	21.8 a
La	6.03 ab	5.80 a	6.45 b	La	0.50 a	0.63 a	0.59 a	La	0.06 a	0.07 a	0.07 a
Ce	10.7 ab	10.6 a	11.8 b	Ce	0.70 a	0.63 a	0.60 a	Ce	< 0.01	< 0.01	< 0.01
Sm	1.78 a	1.69 a	1.89 a	Sm	0.08 a	0.10 a	0.09 a	Sm	0.01 a	0.01 a	0.01 a
Eu	0.38 ab	0.36 a	0.43 b	Eu	0.02 a	0.02 a	0.02 a	Eu	< 0.01	< 0.01	< 0.01
Yb	0.80 a	0.76 a	0.95 b	Yb	< 0.01	< 0.01	< 0.01	Yb	< 0.01	< 0.01	< 0.01
Lu	0.13 a	0.13 a	0.16 b	Lu	< 0.01	< 0.01	< 0.01	Lu	< 0.01	< 0.01	< 0.01
Th	0.15 a	0.22 a	0.16 a	Th	< 0.01	< 0.01	< 0.01	Th	< 0.01	< 0.01	< 0.01
U	0.25 a	0.23 a	0.25 a	U	< 0.01	< 0.01	< 0.01	U	< 0.01	< 0.01	< 0.01
新鮮重 (g)	19.5 a	17.9 a	19.0 a	乾物重 (g)	4.70 a	4.99 a	4.79 a	乾物重 (g)	1.33 a	1.38 a	1.09 a
菌根形成頻度(%)	95.6 a	92.2 a	95.6 a								
菌根形成強度(%)	27.3 a	19.3 a	35.4 a								
樹枝状体形成率(%)	12.6 a	5.0 a	22.4 a								

表中の同一英文字は各部位において試験区間で元素含有率に有意差がないことを示す(ボンフェローニ法, $p<0.05$)， 表中の値は3連の平均値.

表6. 下水汚泥コンポスト、化学肥料、各試験区の土壌試料中の元素含有率

元素	下水汚泥コンポストおよび化学肥料 (mg kg^{-1} D.W.)			土壌試料[b] (mg kg^{-1} D.W.)		
	オガクズ汚泥コンポスト	モミガラ汚泥コンポスト	化学肥料	オガクズ汚泥コンポスト区	モミガラ汚泥コンポスト区	化学肥料区
Sc	1.18	1.86	0.85	33.9 a	33.5 a	34.1 a
Cr	28.0	16.1	9.1	48.5 a	55.6 a	56.1 a
Mn	1.63×10^3	1.46×10^3	232	1.12×10^3 a	1.15×10^3 a	1.10×10^3 a
Fe	11.7×10^3	31.6×10^3	3.06×10^3	65.7×10^3 a	64.5×10^3 a	66.4×10^3 a
Co	4.98	3.14	1.20	22.1 a	20.5 a	24.0 a
Zn	516	527	74	177 a	169 a	155 a
As	6.21	15.1	7.04	5.26 a	5.39 a	5.13 a
Br	32.7	22.4	86.6	9.22 a	8.97 a	9.25 a
Rb	4.50	6.67	10.6	59.9 b	30.0 a	34.5 ab
Sr	183	92.7	148	139 a	128 a	121 a
Zr	29.2	< 0.01	53.6	99.3 a	104 a	112 a
Ag	6.4	36.1	< 0.01	3.12 b	3.13 b	< 0.01 a
Sb	1.29	1.50	1.06	0.34 a	0.37 a	0.30 a
Cs	0.48	0.49	0.55	3.58 a	3.65 a	3.72 a
Ba	1.25×10^3	754	107	386 a	377 a	335 a
La	183	3.3	18.4	19.9 a	16.2 a	14.9 a
Ce	228	4.0	18.2	31.3 a	24.1 a	24.2 a
Sm	4.25	0.51	3.13	3.78 a	3.53 a	3.66 a
Eu	0.62	0.10	0.60	1.08 a	1.07 a	1.08 a
Yb	0.38	0.29	0.91	2.31 a	2.23 a	2.38 a
Lu	0.05	0.06	0.16	0.44 a	0.45 a	0.42 a
Ta	0.23	0.10	0.07	0.29 a	0.31 a	0.30 a
Th	1.39	0.64	0.98	4.68 a	4.24 a	4.42 a
U	< 0.01	< 0.01	3.69	1.18 a	1.06 a	1.13 a

a) 下水汚泥コンポストおよび化学肥料は3連の平均値、土壌試料は3採取地点の平均値.
b) 表中の同一英文字は試験区間で元素含有率に有意差がないことを示す（ボンフェローニ法, $p<0.05$）.

「植物の大気汚染粒子集積性についての検討」
6) Study on the Accumulation of Air Pollutants in plant

川西幸子（武蔵野学院大）、野川憲夫（東大ＲＩ総合センター）、
澤幡浩之（東大原研共同利用管理本部）、野村貴美（東大工学部放射線管理室）
Sachiko Kawanishi, Norio Nogawa, Hiroyuki Sawahata, Takami Nomura

１．目的・意義

植物の元素集積性は生育環境によって差があり、集積植物と集積元素には特定の組み合わせがあることが、明らかになってきている[1]。

著者らは大気汚染地域および比較的非汚染地域における樹木葉の汚染元素を分析し、大気汚染環境の指標になる植物および浄化を目的に使用できる植物を探してきた。その結果、いくつかの候補が得られた。

その後、大気を経由して土壌を汚染し、土壌汚染から健康被害をもたらす事例に対処するために植物を利用することへの検討を進めた。

後者は土壌汚染防止法施行に伴い、安価な浄化方法として検討する必要性が高まってきている。汚染元素をSbおよびZnの２種にしぼり、ある程度の成果を得た。

現在、Sbは生活の中に難燃剤などの目的で日常の布、紙製品に知られざる添加物として入り込んでおり、石油燃焼、廃棄物償却、自動車排気ガス等に含まれ、Sb精錬工場や電池工場近傍の土壌汚染が確認されているが、[2) 3) 4) 5)]一般に植物は含有量が低く研究されていない。現在Sbの浄化法はよい方法がない[6)]とされている。

ある電池工場跡地[7)]は浄化処理せずに、マンションが建ち、公園が出来ていたが、跡地近傍の土壌を入手することが出来た。具体例として、この土壌を中心に汚染元素浄化法の検討を進めることにした。

２．実験概要

2.1.植物葉採集地

大気汚染の進んだ地域の街路樹同種の何本かについて、平均的に葉を数枚採集した（①②）。また、比較的清浄地で、同種の樹木を探して同様に採集した（③④⑤）。

① 川崎：首都高速神奈川１号(川崎市、池上新町交差点付近)
② 砧：東名高速（東京都世田谷区砧付近）（A，Bは同一樹木の特徴ある葉を区別した）
③森林：武蔵丘森林公園（埼玉県滑川町）
④狭山：武蔵野学院大学校庭（埼玉県狭山市）
⑤日吉：(神奈川県横浜市港北区)

2.2 採集および栽培植物試料の処理

採集葉は、ビーカーに入れ、イオン交換精製水を加え、超音波洗浄機を用い、拭き取紙に肉眼的に汚れがつかなくなる迄、洗浄を繰り返した。乾燥機内６０℃で乾燥後、セラミック臼を用いて粉末化した。水耕栽培実験では、洗浄後、根、茎、葉の３部あるいは根、茎および葉の２部にセラミック鋏で切り分けて乾燥し、重量を測定後、粉末化した。

2.3 水耕栽培実験

キズタなどの幼苗をポットで入手し、根を出来るだけ傷つけないように株ごとに分離して洗浄し、各条件の培養液で水耕法を行い、直射日光の差し込まない室内植物栽培用ガラス戸棚で１～４週間栽培した。

１）培地：0.7mM KNO_3, 2.0mM $Ca(NO_3)_2$, 0.1mM KH_2PO_4, 0.5mM$MgSO_4$, 0.1mM KCl, 1~10 μM H_3BO_3, 0.5 μM $MnSO_4$, 0.5 μM $ZnSO_4$, 0.2 μM $CuSO_4$, 0.01 μM $(NH_4)_6Mo_7O_{24}$, 10 μM $FeC_6H_5O_7$ (ferric citrate)

２）EDTA（キレート試薬）：0.1mM Ethylenediaminetetraacetic acid3K Salt

３）pH 調整：各条件の培養液について、苗を植える前に、NaOH,HClでpH6.5に調整した。

2..4 土壌栽培実験

市販園芸用土あるいは汚染土壌＊で培養液を用いず、水を十分加えた状態で、同時に各種条件における比較実験をおこなった。試薬SbおよびZn溶液を添加した実験においてはNaOH,HClで中和後、植物を生育させた。＊電池工場跡地近傍土壌[7)]

2.5 中性子放射化分析条件

各試料は60℃で乾燥固体とし、厚さ0.05mmポリ袋に入れてシールし、東洋ろ紙51Aを挟み、さらに同ポリ袋に入れシールして試料とした。日本原子力研究所東海研究所ＪＲＲ－３原子炉、照射孔：ＰＮ－１＆２，照射位置：下段、5.2& 4.7×10^{17}／cm^2・sec, 20分間照射、また、ＪＲＲ－４原子炉、簡易照射筒Ｔパイプ、5.3&4.3×10^{17}／cm^2・sec, 20分間照射,10日後より測定を開始した。測定は東京大学アイソトープ総合センターで、MODEL SC100L放射能測定用遮蔽体付オートサンプルチェンジャー(東

研究施設と装置名： JRR-3, JRR-4　研究分野：　環境科学

洋メディック)を用いて, 10,000secで測定した。

3．結果と考察

3.1 地域差のある植物葉成分と樹種

大気汚染地点の街路樹として｛表１｝に示す17種の植物を選び、比較的汚染の低い地点の同樹木葉と共にSb,Co,Sc,Zn,Fe,Crの６元素を分析して比較した。

蓄積量がある程度あり且つ非汚染地区との差が大きい樹種を元素ごとに見てみると、〔Sb〕オオムラサキ、マテバシイ、キョウチクトウ、キヅタ、ツバキ、クス、〔Co〕キョウチクトウ、クス、アオキ、スズカケ、アラカシ、〔Sc〕サンゴジュ、オオムラサキ、〔Zn〕キョウチクトウ、ケヤキ、マテバシイ、〔Fe〕ツバキ(40倍)、オオムラサキ（21倍)、〔Cr〕アオキ、オオムラサキであった。

いずれも広い地域で街路樹に選ばれており、環境汚染の低減に役立つと思われるが、そのままでは落葉後、土壌汚染や水・大気環境に戻ると考えられる。汚染指標植物として意味がある樹種である。

3.2 土壌汚染浄化に役立つ植物の条件検討

3.1の樹種の中で、水耕栽培が出来る利点から、キズタに注目した。キズタはウコギ科Hedera属で、多くの種類がある。在来品種Hedera rhombea Bean.（フエヅタ）はヨーロッパ原産のivyと呼ばれるHedera helix(セイヨウキズタ)より、成長が遅いので、今広く栽培されているHedera helixで検討することにした。ivyは他にH.helix subsp.canariensis Wild, H. colchica K.Koch., H. tobleri, H .taurica Carr.などがある。[8)]

まず、葉、茎、根の３部分に分けてSbおよびZnの吸収蓄積能力を水耕栽培で調べた。

｛表２｝に数回の実験の平均値を示した。苗を植えてから、1〜2週間で主に根に蓄積する。EDTAを加えると、地上部にSb,Znとも多少移行し、根には少なくなることが分かった。

次に、土壌での挙動を調べたところ、水耕栽培と同レベル(0.5μg)では吸収蓄積が1/10以下に低下し、添加量を高める(2.5μg)と吸収蓄積濃度も高まる。

さらに種々検討した結果、土壌を耕作すると同時に、磁石で吸着する物質を除いてから、キヅタを植えることにより、水耕栽培以上の倍率をあげることが出来た。

作業としては、①土壌を耕作する.②磁石で吸着する物質を集める。③水を十分に撒く。④Hedera helixの苗木を植え 1〜２週間栽培する。⑤地上部を刈り取る（挿し木にして、半年位で苗木としてリサイクルする)。⑥根部を掘り起こして集める。これら一連の作業が農業機械で可能なことは能率上利点があると思われる。必要に応じて繰り返すことにより、浄化の目的を達する。

磁石を利用することは、浄化のために土壌に出来るだけ化学薬品類を加えない方針に合致し、機器を考案することにより、能率的に目的を果たす方法であると考える。また、補助として、Sbには活性炭シートも有効であったが、活性炭シートはZnが含まれる素材であったため、Znには不適当であった。

植物各部分の濃度の格差は同条件で数%以下であるが、植物１株当たりの能率を土壌中汚染元素残留値でみると、ポット毎にばらつきが大きく、Sbで１〜７割、Znで３〜４割という実験値が得られた。

植物の個々の根の大きさ、活性度等が影響すると思われる。

今後、実際の小スケールで実験を行い、含有濃度による効率の検討、および１m^2当たりの植物の適正株数を求め、さらに土壌および植物の科学的な解明を進める予定である。

参考文献

1）高田實弥「放射化分析による植物葉中の元素の特異集積について」放射化分析５，　29−41(1997)

2）高田實弥「植物の放射化分析について」(植物葉中の微量元素の分布と特異集積の研究 **11**, 50−51(2000)

3）久保田正亜「忍び寄る日本のレアメタル汚染」化学と生物、**35**,　12(1997)

4）堀内将人「大気—水—土壌—植物系でのアンチモンの動態把握と健康リスク評価」放射化分析 **18**,　32−39(2005)

5）新名惇彦・吉田和哉監修「植物代謝工学ハンドブック」ＮＴＳ　p 680-688(2002)

6）森田真史「精錬工場周辺におけるアンチモンの動態と制御に関する研究」環境工学研究論文集 **35**, (1998)

7）浅見輝男「データで示す一日本土壌の有害金属汚染」アグネ技術センター　p 269 -274(2001)

8）川西幸子、野川憲夫、澤幡浩之、野村貴美「環境に関わるヘデラ属植物について（その１)」武蔵野短期大学研究概要　第17輯　11−19 (2003)

表1　地域差のある植物葉成分の検討

試料内容			Sb		Co		Sc		Zn		Fe		Cr	
	科	種名	濃度(ppm)	比率	濃度(ppm)	比率	濃度(ppm)	比率	濃度(ppm)	比率	濃度(ppm)	比率	濃度(ppm)	比率
常緑	ぶな	うばめがし 川崎/狭山	0.0006 / 0.12	0.005	0.26 / 0.21	1.2	0.02 / 0.01	2.0	48 / 29	1.7	396 / 125	3.2	11.7 / 3.4	3.4
		あらかし 砧／森林	0.00 / 0.00	0.0	0.15 / 0.02	7.5	0.01 / 0.01	1.0	15 / 15	1.0	126 / 77	1.6	5.9 / 8.2	0.7
		まてばしい 砧/森林	0.28 / 0.03	9.3	0.49 / 0.27	1.8	0.01 / 0.01	1.0	71 / 12	5.9	0 / 148	0.0	5.3 / 0.8	6.6
	くすのき	くす 川崎/狭山	0.51 / 0.09	5.7	0.44 / 0.03	14.7	0.004 / 0.04	0.1	53 / 16	3.3	255 / 176	1.4	5.5 / 0.7	7.9
	つばき	もっこく 砧/狭山	0.21 / 0.00	(>20)	0.02 / 0.07	0.3	0.02 / 0.01	4.0	13 / 9	1.4	25 / 122	0.2	1.5 / 3.6	0.4
		つばき 砧/森林	0.29 / 0.04	7.3	0.05 / 0.08	0.6	0.12 / 0.16	0.8	15 / 7	2.2	120 / 3	40.0	0.2 / 1.7	0.1
	ばら	あかめもち 川崎／狭山	0.00 / 0.07	0.0	0.21 / 0.24	0.9	0.02 / 0.02	1.0	43 / 20	2.2	89 / 252	0.4	1.6 / 1.3	1.2
	ゆずりは	ゆずりは 川崎/森林	0.29 / 0.07	4.1	0.09 / 0.02	4.5	0.04 / 0.02	2.0	36 / 22	1.6	430 / 74	5.8	3.9 / 0.4	9.8
	みずき	あおきB 砧B/砧A	0.05 / 0.02	2.5	0.29 / 0.05	5.8	0.01 / 0.01	1.0	37 / 51	0.7	163 / 73	2.2	4.0 / 0.2	20.0
		あおき 砧B/森林	0.05 / 0.09	0.6	0.29 / 0.02	14.5	0.01 / 0.00	—	37 / 30	1.2	163 / 23	7.1	4.0 / 0.6	6.7
	うこぎ	きづた 砧/日吉	0.29 / 0.04	7.3	0.08 / 0.10	0.8	0.01 / 0.04	0.3	169 / 38	4.5	244 / 302	0.8	1.2 / 1.2	1.0
	つつじ	おおむらさき 川崎/森林	0.77 / 0.00	(>70)	0.77 / 0.62	1.2	0.18 / 0.03	6.0	147 / 44	3.3	2545 / 122	20.9	75.9 / 9.3	8.2
	きょうちくとう	きょうちくとう 川崎/日吉	0.57 / 0.07	8.1	0.19 / 0.00	(>200)	0.03 / 0.01	3.0	39 / 2	19.7	480 / 129	3.7	12.8 / 5.1	2.5
	すいかずら	さんごじゅ 川崎/狭山	0.07 / #REF!		0.41 / 0.50	0.8	0.13 / 0.01	13.0	61 / 33	1.9	246 / 66	3.7	3.5 / 0.9	3.9
落葉	いちょう	いちょう 砧／狭山	0.12 / 0.31	0.4	0.03 / 0.08	0.4	0.02 / 0.04	0.5	5 / 4	1.3	168 / 216	0.8	1.3 / 3.4	0.4
	にれ	けやき 川崎/狭山	0.43 / 0.22	2.0	0.18 / 0.13	1.4	0.02 / 0.03	0.7	47 / 4	11.7	426 / 271	1.6	12.7 / 2.8	4.5
	すずかけのき	すずかけ 川崎/日吉	0.57 / 0.20	2.9	0.31 / 0.04	7.8	0.05 / 0.01	5.0	45 / 9	5.0	545 / 95	5.7	16.2 / 3.3	4.9

表2　Hedera helix 栽培分析表

Ⅰ．水耕栽培

〔Sb〕	part	con.(ppm)
Blank	Leaf	0
	Stem	0
	Root	0
Sb 10ppm(0.5μg)	Leaf	3
	Stem	36
	Root	571
EDTA*/Sb10(0.5μg)	Leaf	6
	Stem	41
	Root	304

〔Zn〕	part	con.(ppm)
Blank	Leaf	30
	Stem	38
	Root	80
Zn200ppm(10μg)	Leaf	62
	Stem	740
	Root	7,709
EDTA*/Zn200(10μg)	Leaf	362
	Stem	636
	Root	2,866

Ⅱ．土壌栽培

〔Sb〕	part	con.(ppm)
Gardening Soil Blank	L&S	0
	Root	0
Gardening Soil Sb 10ppm(0.5μg)	L&S	1
	Root	50
〔Contaminated Soil〕		50
Contaminated Soil Blank	L&S	0
	Root	4
Contaminated Soil Sb+Zn(each2.5μg)	L&S	3
	Root	355
C.Soil Pretreat.Magnet** Sb+Zn(each2.5μg)	L&S	6
	Root	578

〔Zn〕	part	con.(ppm)
Gardening Soil Blank	L&S	16
	Root	18
Gardening Soil Sb 10ppm(0.5μg)	L&S	46
	Root	29
〔Contaminated Soil〕		1,245
Contaminated Soil Blank	L&S	50
	Root	130
Contaminated Soil Sb+Zn(each2.5μg)	L&S	306
	Root	1,777
C.Soil Pretreat.Magnet** Sb+Zn(each2.5μg)	L&S	145
	Root	1,649

**Soil pretreated with Magnet

The Rate of Efficiency in Soil

	Sb
L&S	0～1%
Root	26～86%
Magnet fraction	1%
Residue in Soil	9～73%

	Zn
L&S	7～14%
Root	41～45%
Magnet fraction	5%
Residue in Soil	33～37%

九州産黒曜石に関するＦＴ年代測定とＩＮＡＡ

7) Fission-track dating and INAA for obsidians from Kyushu, Japan

鹿児島大学教育学部

鈴木達郎

Tatsuo Suzuki

Faculty of Education, Kagoshima University

1. 緒言

九州には多くの黒曜石産地が知られている。それらの黒曜石については考古学的観点から坂田（1982）などの記載があり，産地についても詳しく紹介されている。またその古代における石器としての交易・流通といった観点から，蛍光 X 線分析や放射化分析による元素組成を用いた産地同定のための多くの研究がある。

黒曜石は珪長質火山岩の急冷相としての産状が直接野外でも露頭で観察できる場合もあるが，海岸や畑地の転石としてのみ知られることも少なくなく，母岩としての流紋岩・熔結凝灰岩などが近くにみられないこともある。これは黒曜石部分が堅牢なため侵食に耐えて残存したものかあるいは運搬に耐えて再堆積したものと考えられる。黒曜石はガラス部分が変質せず新鮮であればフィッション・トラック年代測定にとっても適した試料となり数百万年から数万年の間で年代測定が得られるが，その年代測定値を地質学的に適用するためには，その母岩としての火山岩体あるいは熔結・非熔結の火砕流堆積物あるいは降下火砕堆積物などの地質学的位置が明らかでなければならない。その場合にもどの地質体に由来するものかを比定するための産地同定が必要になる。しかし小規模に存在する黒曜石の詳細な地質学的位置づけについての研究は従来不充分であった。このような場合黒曜石の詳細な化学的性質を検討することがそのような問題解決にも有効であると考えられる。

一方機器中性子放射化分析（INAA）によれば、多数の試料について多元素同時分析が可能であるので、多様な黒曜石のキャラクタリゼーションが容易にできると期待できる。またフィッション・トラック（FT）年代測定によれば、ガラス試料ではウラン濃度が特別高くなくとも広い検鏡面積が比較的容易にとれるため，新第三紀～第四紀においても年代値が得られるだけでなく、トラック長などの計測値からその地域の熱史についてのデータも得られると期待できる。

これらの観点から九州地域に知られる黒曜石について蛍光X線分析，放射化分析による元素定量およびアイソサーマル・プラトー法によるフィッション・トラック年代測定による検討を行ってきている。現在まだ進行中の部分も多いが、今までに得られた結果をここに報告する。なお黒曜石は岩石名としては黒曜岩と呼ぶのが適当であるとすることもあるが，ここではより一般的な呼称を踏襲している。

JRR-3M PN1, JRR-4 Tパイプ, 地球科学試料放射化分析

2. 分析試料

九州各地に良く知られた黒曜石産地のうち，佐賀県の腰岳，長崎県の大崎，淀姫，古里，針尾、牟田免、鹿児島県の五女木，日東，上牛鼻，鹿児島市三船，から黒曜石を採取した（Table 1)。また大口市日東，同　五女木から得た黒曜石についてフィッション・トラック年代測定を試みた。

Table 1.　Sampling Locality

Sp. Code	採取地
Kd	佐賀県伊万里市腰岳
Fs	長崎県松浦市星鹿町牟田免
Os	長崎県東彼杵郡川棚町大崎
Os	長崎県東彼杵郡川棚町大崎
Yd	長崎県佐世保市天神町淀姫神社付近
Fs	長崎県佐世保市古里海岸
Fs	長崎県佐世保市針尾中
Gm	鹿児島県大口市五女木
Nt	鹿児島県大口市日東
Us	鹿児島県薩摩郡樋脇町上牛鼻
Mf	鹿児島県鹿児島市吉野町三船
Ng	鹿児島県大根占町長谷松崎の浜

3. 中性子放射化分析

中性子放射化分析法による元素定量のための試料作成は以下のようにおこなった。採取した黒曜石試料には数ｇ程度のものもあるので，原岩試料をマイクロカッターでスライスにした破片をアセトンで洗浄したのち乾燥させて分析試料としたものもある。多量の試料が得られた場合には粉砕し，メノウ製ボールミルで粉末試料とする。これらをポリエチレン製の薄手の袋に 100mg 程度を秤量して照射試料とする。目的試料 10 個から 30 個に USGS（アメリカ合衆国地質調査所）の標準岩石試料 G-2・AGV-1 および GSJ（通産省工業技術院地質調査所，現 産業技術総合研究所）の標準岩石試料 JR-1・JB1a を加えて順序をチェックして照射用キャプセルに詰める。これを日本原子力研究所東海研究所の研究用原子炉 JRR-4 の T パイプ 350ｋW 出力時で 90 分、あるいは JRR-3M　PN1 で 10 分間の照射をおこなった。照射後 1 週間程度冷却して中寿命核種定量を，また 2 週間ないし 1ヶ月後に長寿命核種定量のための測定をおこなった。ガンマ線スペクトル測定は鹿児島大学共同利用 RI 実験室において実施した。

ガンマ線スペクトロメトリーは，フロッピーディスクに保存したスペクトルデータを用いて，ネットカウント計算（GSPAN：鈴木，2001b），ついで放射能計算（ACTCLQ80：鈴木，未公表），元素定量計算（CONTDET9：鈴木，未公表）の計算プログラムを使用しておこなった。定量計算では SiO_2 成分として試料の岩質の比較的近い USGS（アメリカ合衆国地質調査所）の G2，AGV1，GSP1 のデータ（Potts et al., 1992）を標準値とし GSJ（旧工業技術院地質調査所，現 産業技術総合研究所）の JR1・JB1a を位置補正のためのワーキングスタンダードとして使用している。

今回得られた分析結果についての詳細は、蛍光Ｘ線分析による主成分・副成分のデータと併せて別途報告の予定である。USGS（アメリカ合衆国地質調査所）の標準岩石試料の GSP1 や AGV1 などについての分析結果は、現在知られるデータ（Potts ほか，1992）と良く一致している。九州産の黒曜石のデータは、従来報告値のあるものについてはそれらとおおよそ似た元素組成であり、産地分析としてグルーピング可能であるといえるが，どの地質体に由来したものでありそれが地質学的にあるいは岩石学的に特徴づけられるかを検討するためには，まだそれらの母岩となりうる地質体の分析値が充分とはいえない。従って今後さらに広域に火山岩・火砕岩試料を収集し、それらの微量元素組成なども詳細に検討する必要があると思われる。

4. フィッション・トラック年代測定

フィッション・トラック年代測定は試料そのものを検出器とする放射能測定(radiometry)であり測定計器の較正に相当するプロセスが本質的に必要である。原子炉中性子に関わるそれらの問題を避けるため他の年代測定法により“充分検討され確立”した“年代の標準試料”と比較して，未知試料の年代を決定しようとするゼータ値による標準化(Hurford and Green, 1986)が提案され，推奨されてきた(Hurford, 1990)。しかしこれは測定可能な試料が“年代の標準試料”のあるジルコン・アパタイト・スフェンに事実上限られることになる。現在確立された“年代の標準試料”のない黒曜石などガラスのフィッション・トラック年代測定は困難ということになる。このような事情から，モニターガラスを用いた正確な核分裂反応率の絶対値算出を試みてきた。核分裂反応率を直接求める係数を天然比のウランを含むモニターガラスについて定める目的で B_0 値 (Suzuki, 2000) を導入した。B_0 値を次式のように定義する。

$$B_0 = [\sigma \phi]_{total} / \rho_d \qquad [1]$$

このとき σ： U-235 の核分裂反応断面積，ϕ：中性子束密度，$[\sigma \phi]_{total}$：$[\sigma \phi]$ の全エネルギーでの積分値 (U-235 の誘導核分裂反応率)，ρ_d: U-235 の誘導核分裂トラック密度。

またゼータ法の“年代の標準試料”を用いない年代算出係数 Z_0 は次式で与えられる。

$$Z_0 = B_0 I / \lambda_f \qquad [2]$$

ここで I: U-235/U-238 同位体比，λ_f: U-238 の自発核分裂による壊変定数。

このように B_0 値を確立し，トラックの検出効率と壊変定数の問題を解決すれば熱中性子の卓越した照射場と天然比のウランを含むモニターガラスを用いることによりフィッション・トラック年代測定値の絶対評価は充分可能になる。

この観点からガラスの年代標準試料候補のモルダヴァイトについて Isothermal Plateau アニーリング法を用いて，フィッション・トラック年代測定を試み Table 2 に示すような結果を得た。このとき得られた 150℃における等温プラトー曲線を Fig. 1 に示す (Suzuki, 2002)。このとき用いたパラメターを Table 3 に示した。

Table 2 Analytical Data for Fission Track Dating of Moldavite

ρs	$= 9.59 \times 10^3 /cm^2$
$\rho s + \rho i$	$= 6.87 \times 10^4 /cm^2$
Uncorrected $\rho s/\rho i$:	0.162 (±4.8%)
Plateau $\rho s/\rho i$:	0.190
ρi (CN5) mica	$= 2.35 \times 10^5 /cm^2$
Thermally Corrected Age:	15.6±0.8 Ma
	($\lambda f = 8.46 \times 10^{-17}$ /yr)

Table 3 Parameters for B0 Calibration

B(0) [CN5]	$= 4.039 \times 10^{-12}$
λf	$= 7.03 \times 10^{-17}$ /yr (Roberts et al., 1968)
Z(0) [CN5]	=419
λf	$= 8.46 \times 10^{-17}$ /yr (Galliker et al., 1970)
Z(0) [CN5]	=349

またメキシコ Durango 産のアパタイトについて自発トラックの検出効率をマイカの外部ディテクターに対して評価する方法をこの B0 値と併せ用いて妥当な結果を得た (Suzuki, 2005)。

これらの結果に基づき適用可能性が明らかになった B0 値を用いて鹿児島県大口市日東，五女木産の黒曜石を南米産 Macsanite 黒曜石とともにフィッション・トラック年代の測定を試みた。中性子照射は JRR-3M PN1 で 60 秒間おこなった。また外部ディテクターとして使用した白雲母は 46%HF 20℃ 15 分間、黒曜石は 46%HF 20℃ 15 秒分でエッチングして、適正なトラックを検出しえた。なお年代測定値の算出にあたっては、モニターガラスとして CN5 を使用した。

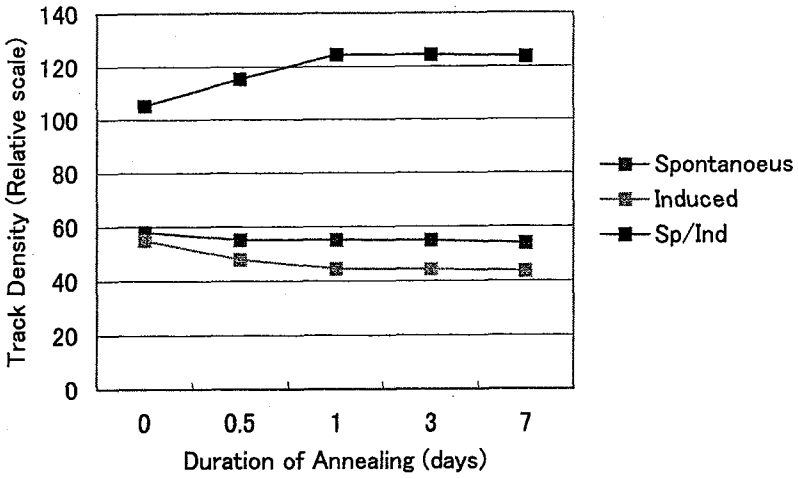

Fig. 1 Iso-thermal Plateau Curves for Moldavite

Table 4 Fission-track analytical data for obsidians from Kagoshima Prefecture, Japan, Macsanite and Moldavite

Sample Code	Annealing Duration at 150℃ (days)	Spontaneous tracks ρs (/cm^2)	Spontaneous and Induced Tracks $\rho s + \rho i$ (/cm^2)	$\rho s/\rho i$ $\times 10^{-2}$	CN5 monitor ρD (/cm^2)	Age (Ma)
Nt2-2	0	1.35×10^3 (184)*	1.677×10^5 (2620)	0.805	2.839×10^5	0.79 +/- 0.06
Nt2-2	3	1.28×10^3 (177)	8.860×10^4 (1380)	1.33	2.839×10^5	1.32 +/- 0.11
Nt2-2	14	1.20×10^3 (126)	8.261×10^4 (1383)	1.47	2.839x105	1.46 +/- 0.14
Nt2-2b	0	1.45×10^3 (266)	2.266×10^5 (5057)	0.644	3.893×10^5	0.88 +/- 0.06
Nt2-2b	14	1.20×10^3 (203)	1.264×10^5 (5096)	0.958	3.893×10^5	1.30 +/- 0.10
Nt2-1	0	1.71×10^3 (225)	1.691×10^5 (2853)	1.01	2.839×10^5	1.00 +/- 0.07
Nt2-1	14	1.48×10^3 (229)	9.506×10^4 (1604)	1.56	2.839×10^5	1.55 +/- 0.12
Gm3	14	1.49×10^3 (130)	1.471×10^5 (1368)	1.02	3.930x105	1.40 +/- 0.13
MCS	14	1.43×10^4 (258)	4.37×10^5 (2709)	3.38	4.002×10^5	4.72 +/- 0.32
Mld01	14	8.43×10^3 (184)	9.97×10^4 (865)	9.24	4.110×10^5	13.3 +/- 1.1

* Numbers counted

今回の測定では、日東（Nt），五女木（Gm）産の両試料とも、平均値として1.45Maを示している。これは同時に測定をおこなったMacsanite黒曜石（MCS），モルダヴァイト（Mld01）の測定結果から支持される。北九州の黒曜石の想定される年代値を考えるときこの測定結果は極めて興味深い。九州の他の地域の黒曜石の年代測定を同一の方法で実施すべく現在準備中である。

5. まとめと今後の課題

九州の主要な黒曜石産地から黒曜石試料を採取してその放射化分析による元素組成分析を試み、14点の分析値を検討し，この地域の火山岩類への比定のための基礎として化学的特徴を明らかにした。またこれらのうちから鹿児島県大口市日東，同　五女木から得た黒曜石についてアイソサーマルプラトー法とBO法によるフィッション・トラック年代測定を試み、それらの黒曜石の年代値を初めて明らかにした。今後これらの調査・研究をさらに継続して九州産黒曜石の地質学的位置を検討するとともに，それらをもたらした火山活動史とその後の熱史を明らかにすることが今後の課題である。

6. 謝辞

本研究に使用したモルダヴァイトはBiggazi博士（ピサ，イタリー）から，Macsanite黒曜石はNaeser博士（USGS）から，JR1黒曜石原岩試料は安藤　厚博士（元地質調査所）から恵与を受けた。また試料の中性子照射とそのガンマ線測定については、東京大学原子力研究総合センター東海分室大学開放研究室・鹿児島大学アイソトープセンターおよび郡元地区共同利用RI実験室にお世話になった。これら関係各位に深甚の謝意を表する。

7. 引用文献

Potts, P.J., Tindle, A.G. and Webb, P.C. (1992): *Geochemical reference material compositions*. Whittles Publishing. 313pp.

坂田邦洋（1982）：九州の黒曜石―黒曜石の産地推定に関する考古学的研究. 146pp.　広雅堂.

Suzuki, T. (2000): B_0 value of uranium doped glasses: a proposal for the standardization of fission track ages. *On Track*, Vol.10, No.2, p.9-10.

鈴木達郎（2001）：GSPAN：ガンマ線スペクトル解析プログラム.　鹿児島大学教育学部研究紀要（自然科学編），Vol.52, p.33-44.

Suzuki, T. (2002): Fission track dating of a moldavite using BO age calibration. Abst. 21st Internat. Conf. Nucl. Tracks in Solids, New Delhi, India, p.130.

Suzuki, T. (2005): Detection efficiency of fission tracks in apatite by the spike irradiation technique. *Radiation Measurements*, (in press).

8. 成果の発表

鈴木達郎（2002）：等温プラトー法およびBO法を用いたガラスのフィッション・トラック年代測定.　地球化学会2002年会講演要旨集，p.98.

鈴木達郎（2002）：中性子放射化分析. RIセンターニュース（鹿児島大学アイソトープ総合センター），No.2, p.2-3

鈴木達郎（2002）：中性子放射化分析による入戸火砕流堆積物の微量元素組成. 鹿児島大学教育学部研究紀要（自然科学編），Vol.53, p.29-44

Suzuki, T. (2002): Detection efficiency of fission-track in glasses estimated by spike irradiation technique. Abst. 21st Internat.

Conf. Nucl. Tracks in Solids, New Delhi, India, p. 22.

Suzuki, T. (2002): Neutron absorption in NIST SRM 963 glass estimated by fission-track analysis and gamma-ray spectrometry. Abst. 21st Internat. Conf. Nucl. Tracks in Solids, New Delhi, India, p. 26.

Suzuki, T. (2002): Fission track dating of a moldavite using BO age calibration. Abst. 21st Internat. Conf. Nucl. Tracks in Solids, New Delhi, India, p. 130.

Suzuki, T., Yuan, W. and Zhu, B. (2003): Fission track evidence for the age of ore minerlizaion of the Sarbulak gold deposit in the Altay Mountains, Xinjiang Uygur Autonomous Region, China. Abst. Intern. Field Symp. in Urumqi, Xinjian, China., p. A1-A4.

鈴木達郎 (2003)：鹿児島県薩摩半島地域の四万十帯堆積岩類に関する中性子放射化分析. 鹿児島大学教育学部研究紀要(自然科学編), Vol. 54, p. 29-36.

鈴木達郎 (2004)：フィッション・トラック年代測定値の絶対評価. 放射化分析研究会(東海村, 日本原子力研究所), p. 3.

Suzuki, T. (2004): Absolute determination of fission-track ages of obsidians from Kagoshima Prefecture, Japan. Abst. 22nd Internat. Conf. Nucl. Tracks in Solids, Barcelona, Spain, p. 74.

Suzuki, T. (2004): Detection efficiency of fission tracks in apatite revealed by spike irradiation technique. Abst. 22nd Internat. Conf. Nucl. Tracks in Solids, Barcelona, Spain, p. 181.

鈴木達郎 (2005)：フィッション・トラック年代測定値の絶対評価. 地質学会西日本支部 2004 年度総会ならびに第 150 回例会講演要旨集, p. 3.

Suzuki, T. (2005): Detection efficiency of fission tracks in apatite by the spike irradiation technique. *Radiation Measurements*, (in press).

草津白根山周辺温泉の微量元素溶存濃度の経年変化とその地球化学的解釈

8) Secular changes of minor elements in hot spring waters from Kusatsu-Shirane volcano area, Gunma, Japan

上智大学理工学部
Faculty of Science and Technology, Sophia University

木川田喜一・大井隆夫・川井智・長谷川潤・小坂美紀子・金田哲人・早津岳宏・
佐野淳子・久野吉郎・西野剛弘
Yoshikazu Kikawada, Takao Oi, Satoshi Kawai, Jun Hasegawa, Mikiko Kosaka,
Tetsuhito Kaneda, Takehiro Hayatsu, Junko Sano, Yoshiro Kuno, Takahiro Nishino

1. はじめに

湧水や温泉水は，その水質から地下の様子を捉えられるという点で，地球・環境化学分野における極めて重要な試料である．水温，pH，溶存成分濃度などで示される湧水や温泉水の水質は地下の環境に基づき形成され，その環境の変化に応じて変化する．

上智大学理工学部化学科では，1965年より群馬県草津白根火山地域の地球化学的調査を開始し，当該地域の源泉，河川水，湖沼水の採水調査を現在まで継続している．調査開始からすでに40年が経過し，我々が所有する過去40年分の採水データは，地域内の環境変化を知る上で極めて貴重なデータとなっている．これまで採水試料の水質変化から，当該地域の地下環境に関する多くの貴重な知見を報告しているが[1-4]，それらは主として主要溶存成分を対象としたものであった．そこで本研究では，微量元素を含む非主要成分を指標としてより多くの地下環境に関する情報を得ることを目指した．通常の水質分析では取り扱われない微量元素等の成分組成は，主要成分のみからでは捉えることの出来ない，より詳細でかつ確度の高い地下環境の推定を可能とすることが期待される．本研究では，上智大学理工学部化学科に採水後保存されている1965年からの草津白根火山地域の保存温泉水試料に対して中性子放射化分析法を適用し，従来，定常的には分析されていなかった成分の一斉定量を行い，その結果を基に当該地域の地下熱水環境を明らかにすることを目的とした．

2. 研究対象試料

本研究で分析対象とした試料は，現地調査において採取後，密栓して暗所保存されていた，草津白根火山東麓に湧出する主要3源泉(草津湯畑源泉，万代鉱源泉，香草3号泉)の温泉水である．これらは全て火山性の酸性源泉である．

草津湯畑源泉は草津白根山山頂から東方へ約6 km離れた草津町温泉街(草津温泉)の中心に，万代鉱源泉は温泉街と草津白根山山頂との間，草津湯畑源泉から山頂方面に約2 km上った位置に湧出しており，この2源泉により草津温泉で利用される温泉水のほとんどが占められる．草津湯畑源泉は1193年にはその存在が記録に残る歴史の古い源泉であるが[5]，一方の万代鉱源泉は1970年に硫黄鉱山掘削中の坑道内より突如湧出した新しい源泉である．

これらに対し，香草3号泉は草津白根山山頂から約2 km東方の，山頂に近い位置に湧出する源泉群(香草源泉群)のひとつであり，草津町温泉街周辺の源泉に比較して溶存成分濃度が極めて高いことで知られる未利用源泉である．

JRR-3 気送管，JRR-4 Tパイプ・S-パイプ・気送管，環境・地球化学試料放射化分析

3. 予備実験による分析条件の検討

3.1 予備実験の概要

まず，2002年に採水した万代鉱源泉の温泉水試料を用いて，中性子放射化分析法による分析方法の検討を行った．2002年採水の万代鉱源泉水の主要成分組成をTable 1に示す．

本研究では火山性温泉を対象としていることから，火山性揮発物質のひとつであり，火山周辺での熱水活動を反映することが期待されると同時に，環境問題にも直結するヒ素の定量を第一目標とした．この際，中性子放射化分析法はヒ素と始めとするいくつかの元素に対しては極めて高感度であり，かつ多元素同時分析が可能なことから，ヒ素以外の成分も同時定量されることが期待される．

3.2 照射条件ならびに試料調製方法の検討

過去40年近くの経年変化を複数の源泉について求めるには試料数が膨大な数に上ることから，照射試料の調製が簡便であると同時に，少ない照射回数で多量の試料を照射・測定することが望まれる．そこで照射試料の小型化を考慮し，マイクロピペットにて分取した試料水1 cm^3を約1.5 cm角のろ紙に染み込ませ，40℃の強制循環式恒温乾燥器にて乾燥させたものを用意した．これを日本原子力研究所のJRR-4において，気送管で5分間照射し，1日冷却後に600秒，2日冷却後に2000秒のγ線計測を行った．この照射時間ならびに冷却期間は主たる定量目的元素であるヒ素の核データ（$^{75}As(n, \gamma)^{76}As$，半減期 26.40 h）に基づき暫定的に定めた．得られたγ線スペクトルから照射条件ならびに定量可能核種について検討を行った．

Fig. 1に万代鉱源泉水試料の予備照射試料におけるγ線スペクトルを示す．ヒ素と臭素（$^{81}Br(n, \gamma)^{82}Br$，半減期 35.4 h）の極めて明瞭なピークが見られ，本法によって両元素の定量は十分可能である．また2日冷却後においてもピーク高さは十分であることから，ヒ素ならびに臭素を定量目的とする限り，照射試料量ならびに照射時間を減ずることも可能である．両元素以外の主だったピークは主要溶存成分のナトリウムとカリウムであり，これらはすでに分析値が得られていることから本研究における定量対象元素としては取り上げなかった．

上記以外の元素に関しては，2日冷却後のスペクトルには小さいながらもサマリウムのピークが認められた．したがって計測時間を伸ばすことでサマリウムの定量は可能であると考えられるが，半減期の比較的短い核種を対象とした場合，計測時間の延長は一回の照射における分析試料数の減少に大きく作用するため，今回は測定試料数を優先してヒ素ならびに臭素の定量に限定し，サマリウムの同時定量は見送ることとした．

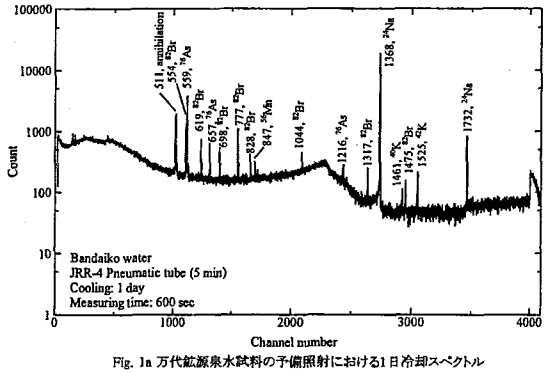

Fig. 1a 万代鉱源泉水試料の予備照射における1日冷却スペクトル

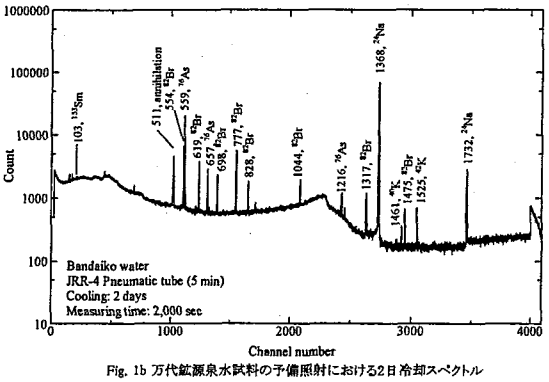

Fig. 1b 万代鉱源泉水試料の予備照射における2日冷却スペクトル

Table 1 2002年採水の万代鉱源泉水の水質

採水日	水温 /℃	pH	溶存成分濃度 / mg dm^{-3}									
			Na	K	Mg	Ca	Fe	Al	Mn	Si	Cl	SO_4
2002. 7. 27	91.8	1.73	138	80.4	65.4	115	9.33	64.9	2.97	128	945	1786

3.3 試料乾燥条件の検討

ヒ素，臭素は揮発性であるため，試料乾燥に際してその一部が散逸してしまう可能性がある．そこで，ヒ素，臭素を対象として試料の乾燥条件を検討した．

検討用試料として，和光純薬工業の原子吸光用ヒ素標準溶液(100 ppm)ならびに特級臭化アンモニウム試薬を蒸留水に溶解して調製した 1000 ppm 臭素標準溶液と，2000 年 5 月採水の万代鉱源泉水試料を用意した．標準溶液についてはヒ素，臭素それぞれが 1 μg となるようにマイクロピペットでろ紙上に滴下後乾燥させ，温泉水試料についてはその 0.5 cm^3 を同じくろ紙片上に滴下後乾燥させた．何れの試料も乾燥条件として室温において自然乾燥させたものと，40℃に設定した強制循環式乾燥器内で乾燥させたものとを各 5 個ずつ用意した．

用意した照射試料は JRR-4 の T パイプで 5 分間照射後，冷却時間 1 日でγ線計測を実施し，乾燥条件の違いによって生じる定量値の差異と再現性について検討した．計測時間はヒ素，臭素の標準試料については 2,000 秒，万代鉱源泉水試料については 1,200 秒とした．

Fig. 2 には，試料乾燥条件検討実験の結果を示した．ここでは便宜上，ヒ素，臭素の標準溶液を自然乾燥により調製したものの一つを比較標準試料（両元素をそれぞれ 1 μg 含む）として，その他の試料の濃度を求めている．標準試料 (Figs. 2a, b) について見てみると，ヒ素，臭素共に自然乾燥試料に比較して，40℃乾燥試料は小さい定量値を示すと共に，定量値のバラツキが大きい．一方，温泉水試料 (Figs. 2c, d) の場合，自然乾燥と 40℃乾燥とで平均定量値には有意差が認められないが，定量値のバラツキはやはり 40℃乾燥の方が大きい．以上から，試料の乾燥には自然乾燥を採用することとした．

3.4 実試料による定量精度の確認

照射条件ならびに試料調製方法の検討の結果に基づき，今回分析対象とした源泉の保存試料水の中からすでに従来法でヒ素，臭素の分析値が得られている幾つかの採水試料を選び，ヒ素ならびに臭素の定量値を求め，その結果の比較を行った．

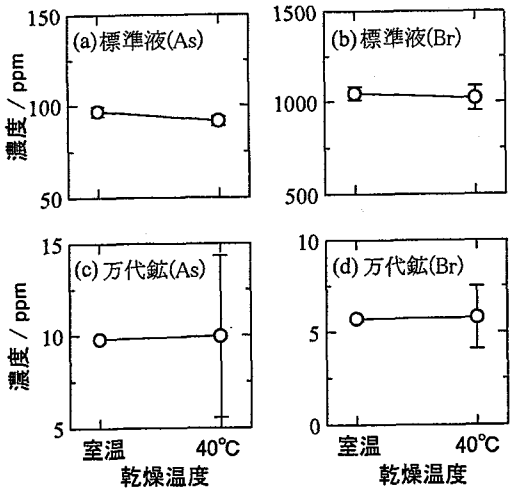

Fig. 2 試料乾燥条件の違いによる定量値の比較
(a)ヒ素標準試料のヒ素定量値，(b)臭素標準試料の臭素定量値，(c)万代鉱源泉水試料中のヒ素定量値，(d)万代鉱源泉水試料中の臭素定量値．エラーバーは90%信頼限界を示す．ヒ素の定量には559.1 keV，臭素の定量には554.4 keVのピークを使用した．

照射試料は源泉水 0.5 cm^3 をろ紙に染み込ませ自然乾燥したものとし，比較標準試料としては前項と同様にしてヒ素，臭素をそれぞれ 10 μg 含むものを調製した．試料は比較標準試料ならびに各年の万代鉱試料水の各 1 個を組として，これを 3 組用意してそれぞれ中性子照射を行った．照射は日本原子力研究所 JRR-3 の PN-1 気送管を用いて 3 分間照射とし，冷却期間 1 日でγ線計測を実施した．計測時間は全試料とも 3,000 秒とした．

Tables 2, 3 には，今回得られたヒ素，臭素定量結果を，過去の定量結果と共に示す．過去の定量結果は，ヒ素については水素化還元気化法による原子吸光光度法 [6]，臭素についてはイオンクロマトグラフ法により得られたものである [7]．今回の放射化分析法による定量値は，これら過去の定量値と良い一致を示し，精度として十分満足できるものである．

4. 草津白根山東麓主要 3 源泉のヒ素，臭素濃度経年変化

予備実験を踏まえ，中性子放射化分析法により，上智大学理工学部化学科に保管されている試料水を用いて草津白根山東麓の主要 3 源泉の溶存ヒ素なら

Table 2 本法によるヒ素濃度定量値と従来法分析値との比較 (ppm)

採水年	万代鉱源泉		草津湯畑源泉		香草源泉3号泉	
	NAA [a)]	HGAAS [b)]	NAA [a)]	HGAAS [b)]	NAA [a)]	HGAAS [b)]
1977	1.43 ± 0.12	1.32	0.55 ± 0.09	0.59		-
1978		-	0.68 ± 0.08	0.57	0.31 ± 0.05	0.35
1980	1.53 ± 0.28	1.73	0.50 ± 0.13	0.54	0.49 ± 0.06	0.58
1981	1.52 ± 0.22	1.17	0.37 ± 0.19	0.34	0.33 ± 0.02	0.34

a) Determined values by NAA (this work).
"±" shows the 90% confidence limit (n = 3).
b) Analytical data determined by hydride generation atomic absorption spectrometry.

Table 3 本法による臭素濃度定量値と従来法分析値との比較 (ppm)

採水年	万代鉱源泉	
	NAA [a)]	IC [b)]
1977	1.53 ± 0.13	1.55
1979	1.48 ± 0.08	1.36
1980	1.50 ± 0.11	1.38
1981	1.31 ± 0.22	1.23
1983	1.36 ± 0.12	1.27
1984	1.46 ± 0.11	1.39
1985	1.86 ± 0.08	1.65
1986	1.93 ± 0.06	1.75
1987	1.94 ± 0.03	1.86
1988	2.26 ± 0.14	2.06
1989	2.12 ± 0.09	2.08
1990	2.56 ± 0.38	2.36
1991	2.72 ± 0.23	2.46
1992	2.87 ± 0.42	2.69

a) Determined values by NAA (this work).
"±" shows the 90% confidence limit (n = 3).
b) Analytical data determined by ion chromatography.

びに臭化物イオン濃度の経年変化を求めた．照射条件はJRR-3 PN-1もしくはJRR-4 Tパイプで3分照射とし，3回の分析操作を行って90%信頼限界をもって誤差とした．得られた結果をFigs. 3a～3cに示す．これを見ると，ヒ素，臭化物イオン共に3源泉で異なる経年変化を示している．

草津湯畑源泉では，1980年代半ばより臭化物イオン濃度が急激に上昇しているが，ヒ素濃度は継続的な減少傾向を示している．これに対し万代鉱源泉ではヒ素，臭化物イオン共に1980年代半ばより急激に上昇し，特にヒ素濃度に関しては現在10 ppm前後と，極めて高濃度となっている．これら2源泉に対し，香草3号泉では継続的な上昇傾向も減少傾向も認められず，大きな上下動を繰り返している．

3源泉のヒ素，臭化物イオンの経年変化傾向を各源泉の主要溶存成分濃度の経年変化傾向（Figs. 4a～4c）と比較してみれば，香草3号泉のヒ素，臭化物イオン濃度は多くの主要溶存成分と同期した上下動[3)]を示しており，その経年変化には主要溶存成分と異なるような特徴的な挙動は認められない．すなわち火山活動の盛衰に連動した全体的な溶存成分濃度[3)]の変動として説明できる．

草津湯畑源泉においては，それまで継続的な減少傾向にあったナトリウム，カリウムならびに塩化物イオンが1984年頃より突如として上昇を始めた．これは1982年頃に同成分濃度の急激な上昇が始まった万代鉱源泉の源泉水が，地表下を通って標高のより低い草津湯畑源泉に約2年の時間差を持って混入しているためと解釈されている[2)]．これを踏まえれば，草津湯畑源泉における臭化物イオン濃度の上昇もやはり万代鉱源泉の混入によるものと言える．万代鉱源泉における臭化物イオン濃度の上昇開始時期は塩化物イオンのそれと完全に一致しており，ハロゲン化物イオンとして同時に供給量が増加したものと考えられる．一方，草津湯畑源泉のヒ素濃度はそれまで減少傾向であったものが1980年代半ばには下げ止まった．これも万代鉱源泉水の地下混入の影響の現れと考えられる．ヒ素は比較的土壌へ吸着され易いことから，他の成分に見られるような顕著な濃度上昇には至らなかったものと推察される．

5. 万代鉱源泉水のヒ素濃度上昇要因

万代鉱源泉の溶存ヒ素濃度は1980年代半ばからの約10年間に7～8倍となった．これと時期を同じくしてナトリウム，カリウム，塩化物，臭化物の各イオン濃度も上昇を始めるが，その挙動の詳細を比較すると，ヒ素濃度の上昇開始時期が1985年であ

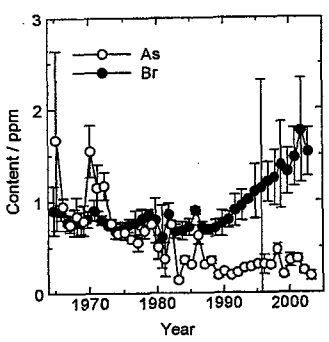

Fig. 3a 草津湯畑源泉の溶存ヒ素，臭素濃度経年変化

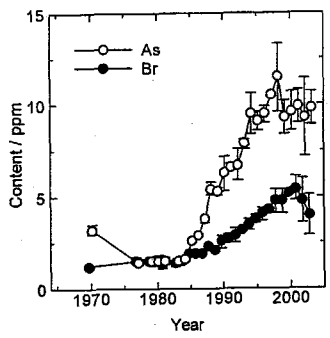

Fig. 3b 万代鉱源泉の溶存ヒ素，臭素濃度経年変化

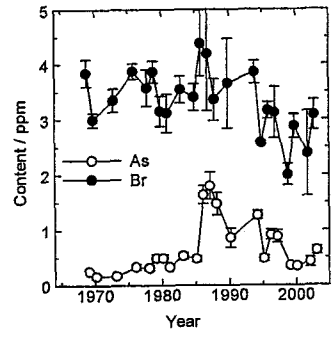

Fig. 3c 香草3号泉の溶存ヒ素，臭素濃度経年変化

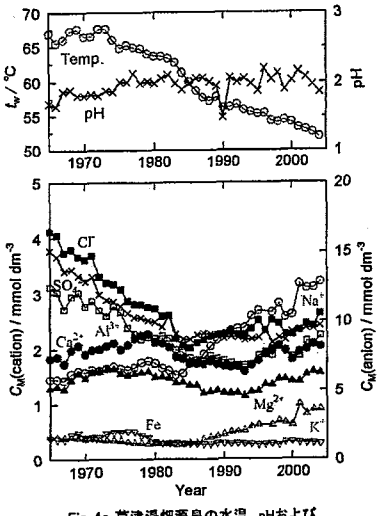

Fig. 4a 草津湯畑源泉の水温，pHおよび主要溶存成分経年変化

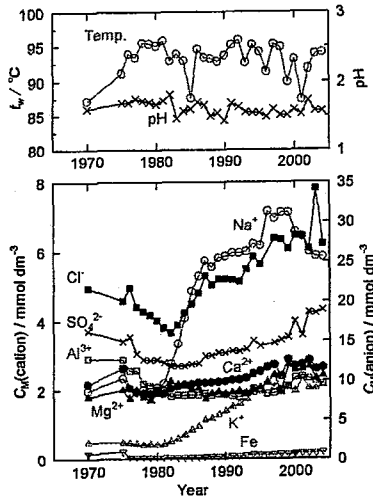

Fig. 4b 万代鉱源泉の水温，pHおよび主要溶存成分経年変化

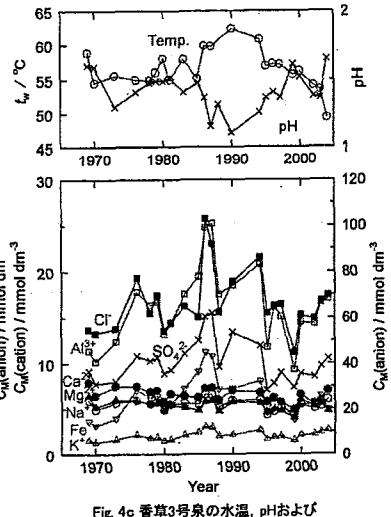

Fig. 4c 香草3号泉の水温，pHおよび主要溶存成分経年変化

るのに対し，ナトリウム，カリウム，塩化物，臭化物イオン濃度の上昇開始は 1982 年であって，ヒ素とその他の成分では数年の時間差がある．

一方，溶存鉄イオンに注目すると，万代鉱源泉はこの地域の酸性源泉としては特異的に鉄イオン濃度が低かったが，1980 年代半ばよりその上昇が始まり，かつその上昇開始時期はヒ素と同じ 1985 年であった（Fig. 5）．さらに両者はその経年変化挙動がほぼ完全に一致するばかりか，溶存濃度は等モルである．

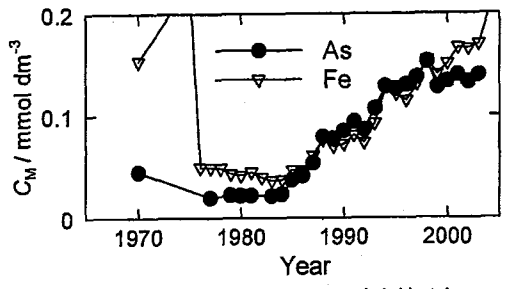

Fig. 5 万代鉱源泉におけるヒ素と鉄イオン濃度経年変化の比較

万代鉱源泉は先に触れたように硫黄鉱山の掘削中に湧出した源泉である．ヒ素は天然において硫黄と相伴って産出するが，万代鉱の坑道は草津白根山東方中腹に位置する殺生河原火山ガス噴気地帯に向いており，その噴気地帯周辺には硫化鉄に鉱染された硫気変質帯が存在することがボーリング調査により明らかにされている[8]．万代鉱源泉の源泉水がこのような変質帯を通って湧出しているとするならば，ヒ素の供給源はヒ素を豊富に含む硫化鉄層であると考えられる．そしてヒ素と鉄がほぼ等モル濃度を保ち変動する事実は，硫砒鉄鉱（FeAsS）の存在を強く示唆している．ヒ素の供給源が硫化鉄系鉱物であるならば，同時に溶解生成する硫酸イオンも類似の経年変化を示すはずである．ヒ素濃度の急上昇が最も顕著であった期間，1984 年から 1998 年までの万代鉱源泉におけるヒ素，鉄イオン，硫酸イオンの濃度相関性を見てみると（Fig. 6），この 3 成分は極め

て高い相関性を示している．したがってヒ素の供給源はヒ素含有硫化鉄鉱物であると見て間違いない．

万代鉱源泉はそれまで密閉されていた地下熱水帯水層から突如湧出し，その後も絶えることなく豊富な湧出量（9270 L/min）[9]を維持している．それは，それまできわめて還元的だった地下環境が，坑道掘削による空気の進入と，湧出した熱水を補うための新たな天水の供給を継続的に受ける状況へと変化したことを意味する．坑道からの空気と，天水に含まれる溶存酸素は万代鉱周辺の地下環境を徐々に酸化的にし，結果として地下に存在する硫化鉄鉱物の酸化溶解を促進しているものと考えられる．

6. 草津白根山東麓主要3源泉のヒ素供給量の見積

2004年の主要3源泉の溶存ヒ素濃度定量値と，報告されている各源泉湧出量[9]から，現在のヒ素供給量を見積もった結果をTable 4に示した．

万代鉱源泉はこの地域で最大の湧出量を誇っており，その溶存ヒ素濃度の高さと相まって，驚くべきことに年間50トン強のヒ素を供給していると見積もられた．草津湯畑源泉の湧出量は万代鉱源泉の約3分の1を有するが，溶存ヒ素濃度は万代鉱源泉の100分の1以下であるため，ヒ素供給量としては年間約0.1トンに過ぎない．香草源泉群の場合，溶存ヒ素濃度は比較的高いものの，その湧出量がきわめて小さいことからヒ素供給量としては微々たるものである．また，草津町温泉街に湧出する他の源泉を全て合わせても草津湯畑源泉と同程度の湧出量に過ぎず，その幾つかを分析した結果も，その溶存ヒ素濃度は草津湯畑源泉と同レベルであった．したがって当該地域における環境中へのヒ素負荷量のほとんどは万代鉱源泉起源のものであり，環境保全の観点から，同源泉における今後のヒ素供給量の推移を注意深く見守る必要がある．

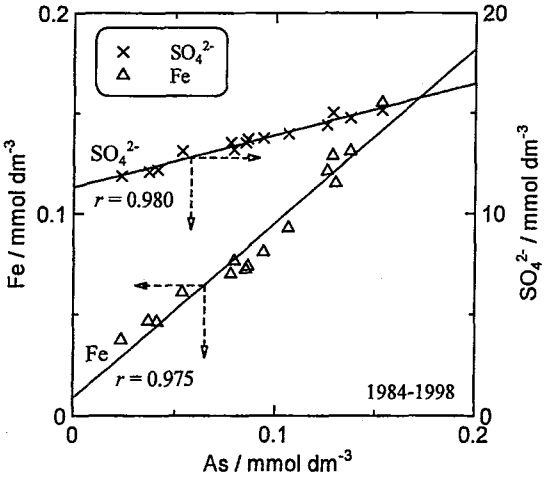

Fig. 6 万代鉱源泉における1984年から1998年にかけての溶存ヒ素，鉄，硫酸イオン濃度の相関性

Table 4 源泉からのヒ素供給量の見積

源泉名	採水日	ヒ素濃度 (mg /L)	湧出量* (L /min)	ヒ素供給量 (ton /year)
香草3号泉	2004.08.02	0.37	25	0.005
万代鉱源泉	2004.07.31	10.9	9270	53.1
草津湯畑源泉	2004.07.28	0.07	3111	0.11

* 湧出量は平林・水橋 (2004)による．

7. まとめ

中性子放射化分析法を用いて，群馬県草津白根火山東麓の主要3源泉の40年間にわたる溶存ヒ素，臭化物イオン濃度の経年変化を求めた．我々が今回最適化した分析条件では，JRR-4 Tパイプあるいは JRR-3 PN-1を利用しての3分照射で，1キャプセルあたり20試料以上の分析が可能であった．

分析結果からは，主要3源泉のヒ素，臭化物イオンの経年変化挙動は互いに異なることが示された．特に万代鉱源泉では1980年代半ばよりヒ素濃度が急上昇を示し，近年では約10 ppmというきわめて高い溶存ヒ素濃度となっている．その湧出量から万代鉱源泉の年間ヒ素供給量を見積もると，現在では年間50トンを越えており，当該地域の最大ヒ素供給源となっていることが明らかとなった．また，溶存ヒ素濃度の経年変化挙動を主要溶存成分のものと比較した結果，万代鉱における溶存ヒ素濃度急上昇の原因は，源泉周辺のヒ素含有硫化鉄鉱物の酸化溶解が促進された結果であると結論付けられた．

今回の研究成果により，温泉水における微量溶存成分の経年変化挙動が周辺地下環境の変化を捉えるための有効なツールであることが示された．

8. 今後の展望

草津白根山周辺の源泉は強酸性であり，湧出後の源泉水は酸性河川を形成して下流へと流れる．万代鉱源泉から供給される年間 50 トンのヒ素も，この酸性河川水に溶存した状態で流下しており，今後は下流域へのヒ素拡散の実態について評価する予定である．また，草津白根山東麓域では酸性河川中和事業が行われており，中和事業が河川水中のヒ素の挙動に与える影響を明らかにすることも求められる．

参考文献

1) 小坂丈予，小坂知子，平林順一，大井隆夫，大場武，野上健治，木川田喜一，山野眞由美，油井瑞明，福原英城 (1997) 群馬県草津白根山火口湖“湯釜”の水質変化と火山活動．*地球化学*，**31**，119-128.
2) 小坂丈予，小坂知子，平林順一，大井隆夫，大場武，野上健治，木川田喜一，飛田典子 (1998) 万代鉱源泉の湧出に伴う草津温泉源泉群の水質変化について．*温泉科学*，**47**，166-178.
3) 木川田喜一，小金井桂，大井隆夫，小坂丈予 (2000) 香草源泉において観察された成分変動と草津白根山の火山活動との関係．*温泉科学*，**50**，34-42.
4) 木川田喜一，大井隆夫，小坂丈予 (2002) 群馬県万座地域主要源泉の溶存成分濃度経年変化．*地球化学*，**36**，35-49.
5) 川合勇太郎 (1966) *草津温泉史話*，太平出版，15-26.
6) 上智大学理工学部化学科無機化学講座，未発表データ
7) 山野眞由美，小坂知子，大井隆夫，小坂丈予 (1995) 草津白根山地域温泉水中のハロゲン化物イオンの濃度，*日化誌*，656-659.
8) 安藤武 (1960) 草津殺生河原地熱地帯調査報告，*地質調査所月報*，**8**，131-137.
9) 平林順一，水橋正英 (2004) 草津白根山から放出される揮発性成分量，*第4回草津白根火山の集中総合観測報告書(2003 年 7 月～11 月)*，167-174.

成果の公表

(1)学術誌：

- Kikawada, Y., Kawai, S., Oi., T. (2004) Determination of arsenic and bromine in hot spring waters by neutron activation analysis. *J. Radioanal. Nucl. Chem.*, **261**, 381-386.

(2)学会発表：

- Kawai, S., Kikawada, Y., Oi, T. (2003) The primary cause for recent increase in iron concentration of Bandaiko hot spring, Gunma, Japan. 13th Annual V.M. Goldschmidt Conference, *Geochim. Cosmochim. Acta*, **67**, Suppl. 1, A206.
- 木川田喜一，川井智，大井隆夫 (2004) 草津温泉における溶存ヒ素濃度経年変化，2004 年度日本地球化学会年会
- 川井智，木川田喜一，大井隆夫 (2004) 草津温泉周辺の酸性河川水中のヒ素，2004 年度日本地球化学会年会

(3)紀要等：

- 木川田喜一，川井智，本多照幸，大井隆夫 (2003) 中性子放射化分析法による温泉水中のヒ素ならびに微量元素の定量，*武蔵工業大学原子力研究所研究所報*，**29**，18-24.
- 川井智，木川田喜一，本多照幸，大井隆夫 (2004) 中性子放射化分析法による温泉水中のヒ素ならびに微量元素の定量(2)，*武蔵工業大学原子力研究所研究所報*，**30**，28-33.
- 佐野淳子，川井智，木川田喜一，本多照幸，大井隆夫 (2005) 中性子放射化分析法による草津白根山西麓源泉(万座温泉)のヒ素，臭素の定量，*武蔵工業大学原子力研究所研究所報*，**31**，24-27.

海洋底堆積物、海洋底玄武岩、島弧火山岩の中性子放射化分析

9) Instrumental Neutron Activation Analyses of volcanic rocks from Island arcs, Mid-oceanic Ridge Basalts and Ocean Floor Sediments

長谷中利昭[1]・三好雅也[2]

[1]熊本大学理学部・[2]熊本大学大学院自然科学研究科

Toshiaki HASENAKA[1] and Masaya MIYOSHI[2]

[1]Faculty of Science, Kumamoto University, [2]Graduate School of Science and Technology, Kumamoto University

1. はじめに

島弧や大陸縁に産する火山岩マグマの生成には，海溝において地下深部に沈み込んでいった海洋底の堆積物，玄武岩溶岩などが何らかの形で関与してると信じられている．このことは様々な岩石の高温高圧下での溶融実験結果や，現在までに得られている火山岩類の微量元素組成などから予想されていることである．しかし，海洋プレートが島弧や大陸縁に沈み込む過程において，様々な微量元素がどのように循環していくかは，定量的に十分議論できる状況にないので，関与していると考えられる岩石の系統的な分析が必要である．鍵になる元素としてホウ素を選んで，現在，原研施設利用共同研究として即発ガンマ線分析装置で分析中である（課題番号：5161）．それに加えて希土類元素，トリウム，ハフニウム，タンタル等の元素を放射化分析で行い，モデルのクロスチェックをして，島弧や大陸縁の火山岩の特異性，多様性を説明しうるモデル構築を目指した．

本プロジェクトを完結するには起源物質である島弧直下のマントルかんらん岩(1)，沈み込み成分を代表する海洋底堆積物(2)，変質した海洋底玄武岩(3)，さらに生成物質である島弧火山岩(4)の試料を入手し，それらの化学分析を行った上で分析結果を検討することが不可欠である．しかし研究期間中に得られる中性子照射実験の割り当て，実験室の測定器のマシンタイム割り当てを考えると，検討できる分析試料数に限りがある．従って本研究期間中においてプロジェクトを(4)の島弧火山岩の分析，中でも中部九州の火山活動を代表する阿蘇の火山岩類に絞って行うこととした．

阿蘇火山はカルデラを形成する大規模な火砕流噴火を過去に４度起こしており，その中で最後の９万年前に起こった阿蘇４と呼ばれる火砕流が最も規模が大きい．阿蘇火山の活動はこれらのカルデラ形成期の活動とカルデラ後の活動の対照的な２つの活動に分けることができる（小野・渡辺，1983）．カルデラ形成期には大規模な火砕流と火山灰を伴う噴火が起こり，カルデラ後の活動ではカルデラ内外で小規模な火山活動が起こっている．後者の活動は溶岩流の流出，タフコーン，スコリア丘，小規模な成層火山の形成などで代表される．また阿蘇カルデラ形成以前に活動したと思われる火山岩体がカルデラ外部に部分的に露出しているのが確認される．

阿蘇を含め現在活動的な九州の火山のいくつかはフィリピン海プレートの沈み込みが起因していると考えられている．深発地震震源位置の断面図を見ると中部九州では阿蘇の直下で斜めに沈み込んできたプレートがほとんど垂直な方向に折れ曲がっているのが観察される．このフィリピン海プレートが沈み込みを始めたのは400万～600万年前で，現在は年間 4cm の速度で沈み込み続けている（鎌田，1992, Seno and Maruyama, 1984）．これに加えて阿蘇，雲仙を含む別府－島原地溝帯においては年間 1.5cm の速度で南北に地殻が開いており(多田，1985)，別府の近くの鬼蓑スコリア丘では非島弧的なマグマの組成が観察されている（太田ほか，1992）．

本報告では阿蘇における火山岩の組成，時間変化を調べ，プレートの沈み込みの進行状況と沈み込み成分の変化について調べた結果を報告する．

2. 試料と実験

分析試料として阿蘇の後カルデラ噴出物，カルデラ形成に伴う火砕流堆積物，先阿蘇火山岩類を選んだ．阿蘇の後カルデラ噴出物は構成斑晶鉱物，化学組成に基づいて７つのタイプに分類した（三好ほか，2005）．図１はそれらの７つの岩石タイプに基づいて溶岩流を分類して描いた地質図である．カルデラ形成に伴う火砕流堆積物については Hunter (1998) が報告した分析値を用いた．先阿

JRR-4 T パイプ　地球科学試料放射化分析

蘇火山岩試料は本研究において採集した．

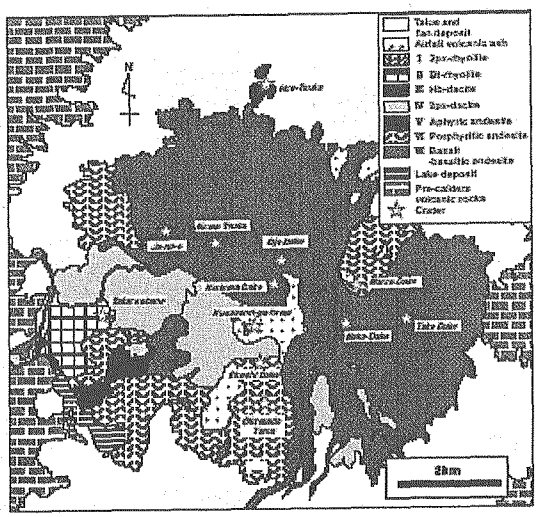

図１．阿蘇火山地質図（Miyoshi，1995）

分析は，それぞれ約 60mg の粉末試料をポリエチレンバイアルに詰めた後，ハンダゴテでバイアルの蓋を融封したものを，ポリエチレン袋に入れてポリシーラーで封入し，指定照射容器に詰め（試料 20 個），JRR4 原子炉 T パイプで 100kW 出力の下で 6 時間照射した．実験期間後半では粉末試料約 200mg，定格出力下で 20 分照射という条件に変えた．照射 1 週間後に試料カプセルを開封，ポリエチレン袋を交換し，大学開放研究室の JRR-3 実験利用棟 113，115 実験室のガンマ線検出器（ASC-20）を用いて短寿命核種（Nd, Sm, U, Lu, Th, Cr, Yb, La, Ba, As, Cs, Sc, Rb）のガンマ線測定を行った．照射 1 ヵ月後には試料を熊本大学に郵送してもらい，熊本大学生命資源研究・支援センター，黒髪地区アイソトープ施設にあるガンマ線検出器を用いて長寿命核種（Nd, Eu, Hf, Ce, Ta, Tb, Th, Cr, Ba, Zr, Cs, Ni, Sc, Rb, Co）のガンマ線測定を行った．長寿命核種の測定においては手動で試料交換をしなければならなかったので，実験期間後半では 113，115 実験室のガンマ線検出器（ASC-20）を用いた自動測定に切り替えた．各元素の含有量は同時に照射した地質調査所の標準試料 JB-1a の推奨値を用いて計算し，別の標準試料で分析値をチェックした．

3. 結果と考察

図２は阿蘇の後カルデラ噴出物，カルデラ形成に伴う火砕流堆積物，先阿蘇火山岩類の代表的な

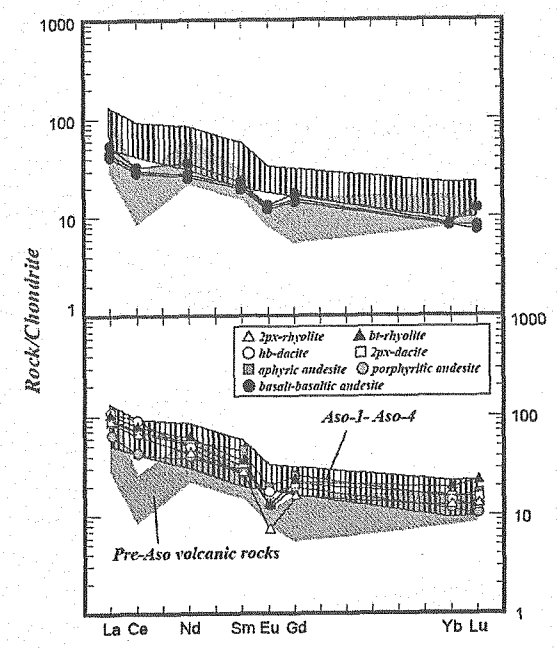

図２．阿蘇火山岩類の希土類元素パターン図

試料について希土類元素の濃度をコンドライトで規格化して図示したものである．火砕流堆積物については Hunter (1998)の分析値を使ったが，それ以外は本研究において分析したデータである．30 万年前から 9 万年前にかけて 4 回にわたって噴出した大規模火砕流堆積物と 5 万年未満の時期にかけて活動した後カルデラ噴出物は共に似通ったパターンを示し，30 万年間にわたって共通の起源物質からマグマが生成していることが推察される．すなわちフィリピン海プレートの沈み込みの影響はこの期間においては同じであることがわかる．これに対して 100 万年前あるいはそれ以前と考えられる先阿蘇火山岩類は明らかに異なるパターンを示している．セリウムの負異常が認められ，重希土がやや枯渇している点が，若い噴出物と異なっている．従って阿蘇カルデラ火山が出現する以前においては異なった起源物質からマグマが生成していたことが考えられる．

年間 4cm のプレート収束速度を考えると 100 万年前では 40km プレートが後退した位置にあったことになる．このことはフィリピン海プレートが阿蘇火山直下の位置に達していても起源マントル物質に影響を与えるまでには至っていなかったことを示唆している．原研施設利用共同研究の即発ガンマ線分析（課題番号：5161）の予察的分析結果においても，先阿蘇火山岩類ではフィリピン海プレートからのホウ素の寄与が少ないこ

とがわかっている．テクトニックなモデルとも整合的な結果が得られており，今後，九州を含む西南日本弧の発達モデルを考える上で貴重なデータを提供すると考える．

今後，より定量的な議論をするためには，はじめにの項で述べた島弧直下のマントルかんらん岩(1)，沈み込み成分を代表する海洋底堆積物(2)，変質した海洋底玄武岩(3)，特に西南日本および九州弧を代表する試料を得て，それらの分析をすることが大きな課題になると考えている．

謝辞

中性子放射化分析を行う上で共同利用実験計画，試料準備，測定器利用などにおいて澤幡浩之氏，川手稔氏をはじめとする大学開放研究室の皆様には実験の立ち上げにあたって多大のアドバイス，ご援助を受けました．皆様のサポートなくしては本研究の遂行は難しかったと思います．深く感謝いたします．また試料準備，測定条件に関して立正大学の福岡孝昭教授や学生の皆様，富士常葉大学の佐野貴司助教授にもご教示いただきました．合わせて感謝いたします．

引用文献

Hunter A., G. (1998) Intracrustal controls on the coexistence of tholeiitic and calc-alkaline magma series at Aso volcano, SW Japan J. Petrol., v.39, p.1255-1284.

鎌田浩毅（1992）中央構造線の西方延長としての大分－熊本構造線の右横ずれ運動とフィリピン海プレートの右斜め沈み込み．地質学論集．v. 40, p. 53-63.

Miyoshi, M. (1995) Origin of the compositional diversity in the post-caldera volcanism of Aso volcano: constraints from petrography, mineralogy and bulk rock chemistry, Master's thesis, Kumamoto University.

小野晃司・渡辺一徳（1985）阿蘇火山地質図，地質調査所.

太田 岳洋・長谷中 利昭・伴 雅雄・佐々木 実（1992）由布－鶴見地溝内、鬼箕単

成火山の非島弧的な地質学的、岩石学的特徴，火山，v. 37, p. 119-131.

Seno, T. and Maruyama, E. (1986) Paleogeographic reconstructions and origin of the Philippine Sea, Tectonophysics, v. 102, p. 53-84.

多田尭(1985)沖縄トラフの拡大と九州地方の地殻変動(2)，地震 2，v. 38, p. 1-12.

成果の公表

学会誌

1) Verma, S.P. and Hasenaka, T. Sr, Nd, and Pb isotopic and trace element geochem-ical constraints for a veined mantle source of magmas in the Michoacan-Guanajuato volcanic field, west-central Mexican Volcanic Belt. Geochem. J. v. 38, 43-65 (2004).

2) Sano, T., Naruse, H., Hasenaka,T. and Fukuoka, T., Boron content of Leg sediments. Proc. Ocean Drilling Prog., Scientific Results, 192 [Online] http://www-odp.tamuedu/publications/192_SR/ (2004).

3) 三好雅也・長谷中利昭・佐野貴司（2005）阿蘇カルデラ形成後に活動した多様なマグマとそれらの成因関係について，火山，v. 50, p. 269-283.

学会発表

1) 三好・長谷中・横瀬(2003)阿蘇火山西部の後カルデラ火山活動噴出物―層序と化学組成の特徴について―地球惑星科学関連学会 2003 年合同大会

2) 三好・長谷中・佐野（2003）阿蘇火山西部におけるカルデラ形成後の火山活動―微量元素化学組成と温度推定．日本火山学会 2003 年度秋季大会

3) 加藤・長谷中・三好・佐野・福岡（2003）九州北部火山岩類のホウ素含有量．日本火山学会 2003 年度秋季大会

4) Miyoshi, Hasenaka, Sano (2003) Magma evolution model for the post-caldera volcanism of Aso volcano: constraints from geochemistry and mineralogy. American Geophysical Union, 2003 fall meeting, San Francisco.

5) 三好・長谷中・佐野（2004）阿蘇火山マグマは地殻の溶融物質か？地球惑星科学関連学会 2004 年合同大会

6) Miyoshi, Hasenaka, Sano (2004) Magma evolution model for the post-caldera volcanism of Aso volcano: constraints from geochemistry and mineralogy. American Geophysical Union, 2003 fall meeting, San Francisco.

7) 三好・長谷中・佐野（2005）阿蘇カルデラ形成後の火山活動におけるマグマ供給系について．地球惑星科学関連学会 2005 年合同大会

10) 陶材粉末中のウランの定量
— LEPS測定時における鉛レンガからの特性X線の影響 —

森脇 一成、小幡 純[1]、古山 俊介[2]
澤幡 浩之[3]、川手 稔[3]、石本 光憲[3]
日本大学歯学部総合歯学研究所RI, 歯周病学[1], 松戸歯学部生理学[2]
原研共同利用大学開放研究室[3]

Determination of uranium content in dental porcelains by the activation analysis

K. Moriwaki, J.Obata[1] and S. Furuyama[2]
H.Sawahata[3], M.Kawate[3] and M.Ishimoto[3]
Division of Immunology and Pathobiology, RI Research, [1] Department of Periodontology, Nihon University School of Dentistry
[2] Department of Physiology, Nihon University School of Dentistry at Matsudo
[3] The Inter-University Laboratory of the Joint Use of JAERI Facilities

1 はじめに

歯科の臨床上その審美性と強度が優れている点から陶歯が多用されている。陶歯には既製の陶歯と各個焼成用陶材冠があるが、そのいずれにも天然歯様の色調と蛍光を付与する目的でウラン化合物を添加することが一般に行われている。1970年代半ばからウランからの放射線による被曝が問題とされるようになってきた[1-5]。我々は日本国内で市販されている内外の陶歯と陶材について核分裂飛跡法(Fission Track Method)と中性子放射化分析法(Thermal Neutron Activation Analysis)とを用いてウラン等の放射性元素の分布と定量、およびそれらを装着した際の口腔組織の被曝線量を算定して報告してきた。

従来、立教大学原子炉共同利用研究によりウランの定量を行ってきたが、その閉炉に伴い2001年から原研施設利用共同研究により継続して定量を行っている。その際、LEPSの測定器の近辺に鉛レンガがあると、それからの特性X線は^{239}Uのγ線エネルギーに近いため、その影響を検討した。

2 方法

試料：金属焼付用陶材 DEGSERAM GOLD- OD2, OD4を秤量してポリエチレン袋に二重に熔封し、照射試料とした。標準試料は酢酸ウラニル二水和物[Uranyl acetate dihydrate $(CH_3COO)_2UO_2 \cdot 2H_2O$]を用いた。秤取した標準試料を少量のエタノールで溶かし、水でAdjustして100ppmの標準液を得た。その20μlを濾紙に滴下して室温にて風乾した。照射：JRR-4の照射筒をCdシャッターで覆い、1分間低出力照射（100kW）を行った。

測定：LEPSの測定器を鉛レンガで覆った場合と覆わない場合のスペクトル(図1、2)と測定値を得た。測定器に密着して照射試料を置き、鉛レンガとの距離を各々 ①1cm ②7 cm ③10 cm ④15 cm ⑤20cm および ⑥鉛レンガで覆った場合について200秒間測定をした。(図3)

研究施設	研究分野
JRR−4	放射化分析

PD による測定：室内から試料を Chamber 内に移し、試料と PD との距離 10ｃｍで 20 分間隔で 60 分まで、以後 1 時間おきに 4 時間測定し、その後試料を取り出して測定した。
分析：日本原子力研究所（JAERI）の 4 号炉（JRR-4）で 1 分間、熱中性子照射（flux:4.5×1013n/cm2・sec）を行った後、γ-Spectrometry を行った。（Genie-2000, CANBERRA series 35 plus）

結果

図 1 の鉛レンガで覆った DEGSERAM GOLD-OD2 のスペクトルでは 72.8keV および 74.9keV に特性 X 線のピークが認められた。それに対して鉛レンガで覆わない DEGSERAM GOLD- OD4 のスペクトルでは特性 X 線の二つのピークは見られず、74.7 keV にウランのピークが認められた。すなわち前者の 74.9 keV のピークにはウランのピークが重層していることになる。図 2 の標準試料の場合も同様である。図 3 に示すように Cd シャッターを掛け、100kW の低出力照射した場合、鉛の特性 X 線は見られず、検出器を鉛レンガで覆った場合でもピークの位置および形は変わらなかった。

研究成果

E. Sairenji etc.: Determination of uranium content in dental porcelains by means of the fission track method and estimation of radiation dose to oral mucosa by radioactive elements. Health Physics, 38, 483-492 (1980)
K. Moriwaki etc.: Improvement of track counting accuracy and efficiency in the fission track method. Radioisotopes, 47, 611-616 (1998)

文献

1) M.C.O' Riordan and G. J. Hunt: National Radiological Protection Board, NRPB Report No.25 (1974)
2) W. T. Wozniak, B. K. Moor and E. Smith: Fluorescence spectra of dental porcelains. Comparisons with ultraviolet light. J. Dental Research, 55, B186 (1976)
3) W. T. Wozniak and B. K. Moor: Luminescence spectra of dental porcelains. J. Dental Research, 57, 971 (1978)
4) D. R. Peplinski, W. T. Wozniak and J. B. Moser: Spectral studies of new luminophors for dental porcelain. J. Dental Research, 58, 244 (1979)
5) G. Baran and W. J. O'Brien: Colored emission of rare earth ions in potassium feldspar glass. J. Dental Research 56, A 53 (1977)

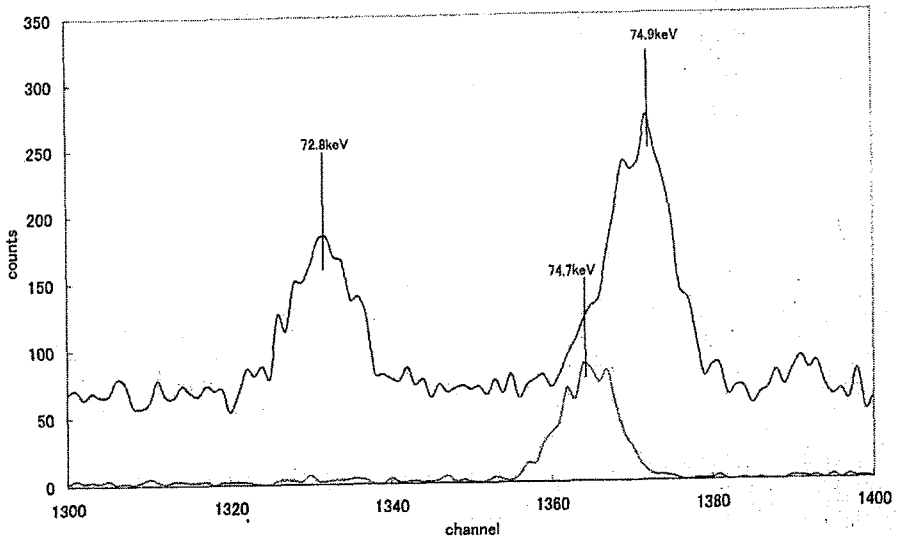

図1　鉛レンガの影響－1

——— LEPSを鉛ブロックで覆って測定したスペクトル(DEGSERAM GOLD-NO.220-OD2)

——— LEPSを鉛ブロックで覆わないで測定したスペクトル(standard 100ppm)

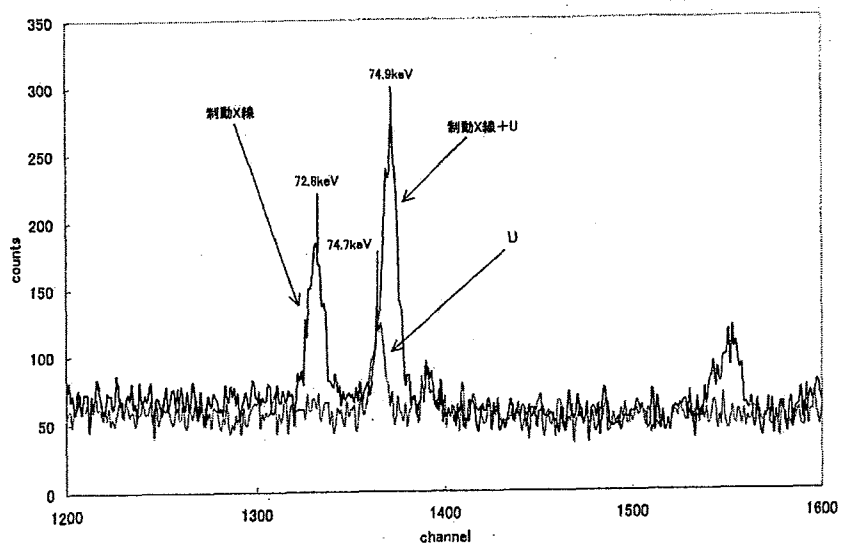

図2　鉛レンガの影響－2

——— LEPSを鉛ブロックで覆って測定したスペクトル(DEGSERAM GOLD-NO.220-OD2)

——— LEPSを鉛ブロックで覆わないで測定したスペクトル(DEGSERAM GOLD- NO.219-OC4)

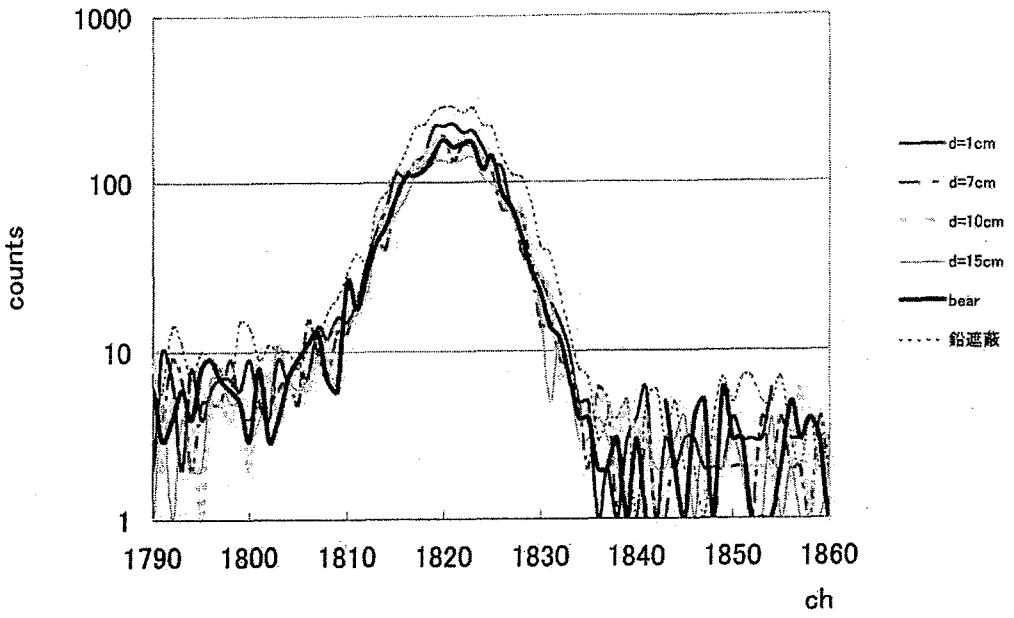
1000
100
10
1
counts
1790
1800
1810
1820
1830
1840
1850
1860
ch
d=1cm
d=7cm
d=10cm
d=15cm
bear
鉛遮蔽

図3　鉛レンガの影響－3

隕石試料の中性子放射化分析

11) Neutron activation analysis of the extraterrestrial materials

海老原充、大浦泰嗣、本橋健晴，唐牛譲，白井直樹，岡本千里，

M. Ebihara, Y. Oura, T. Motohashi, Y. Karouji, N. Shirai, C. Okamoto

東京都立大学大学院理学研究科

Graduate School od Science, Tokyo Metropolitan University

1 はじめに

平成14年度から16年度にかけて、標記課題で原研施設を利用した共同研究を行った。この間に行った研究は2つに分類できる。1つは宇宙物質の非破壊中性子放射化分析（機器中性子放射化分析）（INAA）であり、もう一つは目的元素を絞って高感度な分析を行う放射化学的中性子放射化分析（RNAA）である。どちらにおいても、いくつかの異なる種類の隕石について、その元素含有量を正確に求め、その元素存在度に基づいて、それらの隕石が形成された太陽系初期の物質の進化について考察することを目的として研究を行った。中性子放射化分析法は宇宙物質の元素分析法としてはもっとも有効な分析法であり、今後の宇宙探査計画で地球に持ち帰られる地球外試料の分析に最も威力を発揮する分析法であると考えられる．そのような観点から，中性子放射化分析法の有効性を確認するための実験も行った．

本報告では2つの研究成果について述べる．一つは中性子放射化分析を隕石試料に適用した例として，火星隕石の非破壊分析についてその成果を紹介する．もう一つは，将来の惑星探査計画による試料回収を想定して，微少の回収試料からどのような情報が引き出されるかを，未知試料を分析することにより評価したので，その成果に関して紹介する．どちらの分析も，非破壊中性子放射化法（INAA）によって行ったものである．

2 火星隕石の非破壊中性子放射化分析

南極大陸からは多くの隕石試料が回収されているが，その中にはこれまで余り発見されていなかったような稀少な隕石が少なくない．例えば月から飛来した月隕石は南極大陸で初めて発見されたし，火星からきたと考えられているSNC隕石（以下，火星隕石とする）も，少なからぬ数が南極大陸で発見され，回収されてきた．そのような火星隕石の一つとしてYamato (Y) 980459隕石があり，その化学組成を中性子放射化分析法で求めた．

Y980459は1997年から1999年に行われた南極探査によって発見された隕石である．南極隕石はこれまでシャーゴッタイト，ナクライト，シャシナイトの3種類が知られていた．そのうちシャーゴッタイトは従来，玄武岩質シャーゴッタイトとレーゾリティックシャーゴッタイトの2種類のサブグループに分類されてきたが，シャーゴッタイトには第3のサブグループがあることが明らかにされた．このサブグループは大きな橄欖石の結晶を含むことからオリビンフィリック・シャーゴッタイトとよばれる．Y 980459はこのオリビンフィリック・シャーゴッタイトに分類されることが鉱物学的観察から示唆されていた．このグループにはY 980459以外にもEETA 79001A, DaG 476, SaU 005, Dhofar 019等の隕石が属することが知られている．

本実験で用いた試料は2.585 gの塊状の試料

研究施設名と装置　JRR-3M, JRR-4　　研究分野　宇宙化学

を瑪瑙乳鉢で良く粉砕し，均一に調整したもので，この粉末試料の一部（0.0338 g）を正確に秤量し，清浄なポリエチレン製の袋に溶封した．試料をJRR-3の気送管照射装置（中性子束：1.5 x $10^{13}cm^{-2}s^{-1}$）によって10秒照射し，数分冷却後，γ線の測定を行った．測定終了後，同じ試料を4号炉で20分照射し，照射後試料を都立大学RI研究センターに持ち帰り，冷却時間を変えて数回γ線測定をおこなった．2度の照射のどちらにおいてもマグネシウムの試薬（MgO）を照射し，ナトリウムの定量に対して$^{24}Mg(n,p)^{24}Na$の反応による寄与分の補正を行った．比較標準試料として玄武岩試料JB-1（地質調査所）と隕石試料Allende（米国スミソニアン博物館）を同じ条件で照射し，定量値を求めた．これによって，Na, Mg, Al, K. Ca, Sc, Ti, V, Cr, Mn, Fe, Co, Ni, Zn, La, Sm, Eu, Yb, Luの各元素の定量値を求めることができた．

ここに述べたINAAの他に，放射化分析法として即発γ線分析（PGA）と，誘導結合プラズマ質量分析法（ICP-MS）を実施し，前者では主成分元素を，後者では希土類元素，トリウム，ウランの定量値をそれぞれ求め，INAAのデータとともに，Y 980459隕石の元素組成上の特徴を明らかにした．

得られたデータのうち，微量元素に関する値をTable 1に示す．この表ではPGAやICP-MSで得られたデータも一緒に示した．また，Y 980459に関する文献値や，Y 980459以外に，同じオリビンフィリック・シャーゴッタイトに属するいくつかの隕石について，その文献値も比較のために示した．本研究で得られた値は他のデータとおおむね良い一致を示すが，Laに関して無視できない不一致が認められる．K/La比は惑星物質の分類によく使われる値であり，火星隕石では635と言う値がこれまで知られていた．本研究で得られた値は778で，従来の値より明らかに大きな値である．これは南極大陸上での風化による汚染に原因があると考えている．

Mg/Si比とCa/Si比を両軸にとると，火星隕石をグループごとに分類することができる．この図にY 980459をプロットしたものがFig. 1である．この図で明らかなように，Y 980459は化学組成上においてもおりびんオリビンフィリック・シャーゴッタイトに分類されることが明らかである．

3　惑星探査による回収試料を想定した未知試料の非破壊中性子放射化分析

1960年代のソ連のルナ無人探査機と米国のアポロ有人探査機は人類が能動的に地球外試料（ともに月試料）を地球に回収した点で画期的なものであった．しかし，アポロ計画による6回の月探査の後，試料回収を目的とした宇宙探査計画は実施されてこなかった．21世紀に入って，世界の先進諸国は競って惑星探査，しかも試料回収宇宙探査を計画し，実施に移しており，新しい時代の到来を印象づける結果となっている．日本のMuses-C計画もその流れの一つとして位置づけられる．この計画は小惑星から試料を回収しようとするもので，2003年5月に当時の宇宙科学研究所から探査機が打ち上げられ，打ち上げ成功後，探査機はHayabusaと命名された．その後順調に飛行を続け，2005年秋から暮れにかけて小惑星Itokawaに近づき，その表面試料を採取して地球に持ち帰ることになっている．予定通り行けば2007年に試料が地球に回収される予定である．

このItokawaからの回収試料を分析するためのリハーサルをINAAを用いて実施した．分析試料はG1とG2と名付けられた粉末未知試料で，組成は知らされていない．配布された試料100 mgをまずPGAで分析し，その試料を2つに分割して，一方をINAAに，残りを機器光量子放射化分析（IPAA）に利用した．INAAではJRR-3Mで10秒照射し，Mg, Al, Ca, V, Mnを定量した．次いで同じJRR-3Mで1分照射し，Ga, Na, Kを定量した．さらに同じ試料をJRR-4で20分照射し，K, Ca, Sc, Cr, Fe, Co, Ni, Zn, As, Se, Br, La, Sm, Eu, Lu, Os, Ir, Au, Hgを定量した．PGAとIPAAのデータをあわせると，合計37元素について定量値を得ることができた．

定量値のうち，Al, S, Mnのデータを用いて，S/Mn比とAl/Mn比を縦軸と横軸にとって，得られた定量値をプロットした．その図をFig. 2に示す．この図から試料2GはCVグループに属す

る炭素質隕石であることが推定できた．しかし試料 1G は Fig. 2 上のどのグループにも属さない．IG の元素組成上の特徴は Ni や Ir 等の，いわゆる難揮発性親鉄元素の含有量がどのコンドライト隕石に比べても低いことである．恐らく，コンドライト隕石から金属相を分離した残りの試料であろうと推定された．そこで，もとのコンドライトグループを特定するために，Ni と Ir の値を縦軸と横軸にとって，1G の値を既存の隕石グループの値と比べたところ，どのコンドライト隕石よりも Ir, Ni の含有量が低いことが確認されるとともに，Ir/Ni 比が L コンドライトの値と等しいことがわかった．このことから，試料 1G は L コンドライトから鉄ニッケル合金相を分離した残りの試料であろうと推定された．

以上のことから，INAA を主体とする放射化分析は，微少試料に対しても正確な定量値を与え，その結果，未知試料に対してもかなりの確度でその特徴を記述することができることが証明された．この結果から，2007 年に地球に回収される予定である小惑星 Itokawa の表面物質の分析においても INAA を中心とする放射化分析法を駆使することによって，少量の試料でも十分信頼に値するデータを得られる見通しが得られた．以上用いた分析法は非破壊分析なので，分析終了後，十分冷却すれば他の分析に回すことも可能で，INAA を主体とする放射化分析法は，ごく限られた量の採取試料に対しても大変有効な分析手段であることが証明された．

研究成果（発表論文）

（共同研究の期間に JRR-3M、JRR-4 を用いて得られた成果報告）

1. A. Yamaguchi, R. N. Clayton, T. K. Mayeda, M. Ebihara, Y. Oura, Y. N. Miura, H. Haramura, K. Misawa, H. Kojima, K. Nagao (2002) A new source of basaltic meteorites inferred from Northwest Africa 011. Science 296, 334-336.
2. Y, Oura, M. Ebihara, S. Yoneda, N. Nakamura (2002) Chemical composition of the Kobe meteorite; Neutron-activation prompt gamma ray analysis study. Geochem. J. 36, 295-307.
3. X. L. Li, M. Ebihara (2003) Determination of all platinum-group elements in mantle-derived xenoliths by neutron activation analysis with NiS fire-assay preconcentration. J. Radioanal. Nucl. Chem. 255, 131-135.
4. J. Chai, Y. Oura, M. Ebihara (2003) Comparative study of RNAA and ICP-MS for the determination of ultra-trace Th and U in geological and cosmochemical samples. J. Radioanal. Nucl. Chem. 255, 471-475.
5. Y. Oura, N. Shirai and M. Ebihara (2003) Chemical composition of Yamato (Y) 000593 and Y 000749: Neutron-induced prompt gamma-ray analysis study. Antarctic Meteo. Res. 16, 80-93.
6. A. J. Jurewicz et al. (2003) The Genesis solar-wind collector material. Space Science Review 105, 533-560 (2003).
7. H. Minowa, M. Ebihara (2003) Separation of rare earth elements from scandium by extraction chromatography: Application to radiochemical neutron activation analysis for trace REE in geological samples. Anal. Chem. 489, 25-37 (2003).
8. Y. Arakawa, X. Li, M. Ebihara, E. Meriz, I. Tansel, S. Nargu, H. Koral, M. Matsunami (2003) Element profiles and Ir concentration of Cretaceous-Tertiary (K-T) oayers at Medetli, Golpazail, northwestern Terkey.
9. M. Ebihara, Y. Oura (2004) Chemical characterization of the extraterrestrial material returned by future space mission: An application of nuclear activation methods: Space Sci. Rev. 34, 2305-2310
10. P. C. Buchanan, T. Noguchi, D. D. Bogardd, M;. Ebihara, I Katayama (2005) Glass veins in unequilibrated eucrites Yamato 82202. Geochim. Cosmochim. Acta 69, 1883-1898.

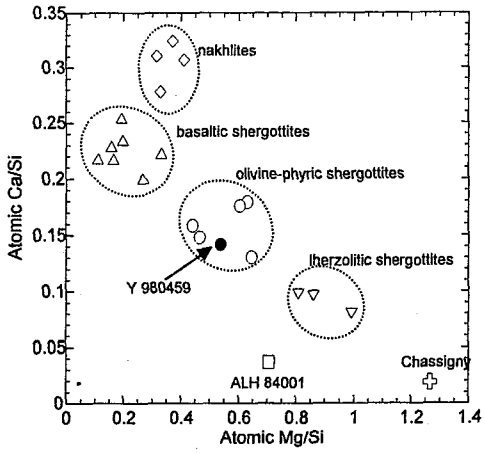

Fig. 1 Mg/Si vs. Ca/Si atomic ratios diagram for Martian meteorites.

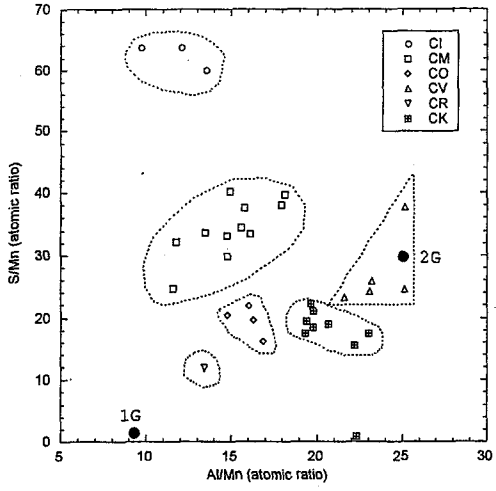

Fig. 2 S/Mn vs. Al/Mn diagram for carbonaceous chondrites.

Table 1. Trace element abundances of Y980459 compared with literature values (I~V) for other olivine-phyric shergottites (in ppm)

	Y980459			EETA79001A	DaG476	SaU005	Dho019	NWA1068
	This Work*	(I)	(II)	(III)	(II)	(II)	(IV)	(V)
B	1.00 ± 0.13							
S	1650 ± 320		1700	2100 ± 700	2700	1600		
Cl	64.4 ± 11.3		57	26	82	143		
Sc	34.9 ± 0.2		36.4	36 ± 2	29.9	29.9	31.2	37
V	188 ± 6			210 ± 15			175.1	280
Co	51.6 ± 1.1	70	56.2	48 ± 4	51.1	55	44.5	56.2
Ni	203 ± 30	270	240	180 ± 70	300	310	65.3	232
Zn	81.1 ± 7.0		76	73 ± 8	66	61	62	49
Ba	1.54 ± 0.02		<30	<10	73	<20	19.4	127
La	0.166 ± 0.002		0.12	0.4 ± 0.045	0.12	0.11	0.24	2.25
Ce	0.426 ± 0.006		<0.7	1.27 ± 0.23	0.354	0.35	1.45	5.38
Pr	0.0841 ± 0.0012						0.11	0.783
Nd	0.567 ± 0.012			1.35 ± 0.07	0.486	0.47	0.69	3.82
Sm	0.466 ± 0.003		0.498	0.74 ± 0.05	0.4	0.43	0.48	1.49
Eu	0.254 ± 0.003		0.25	0.37 ± 0.02	0.199	0.18	0.2	0.552
Gd	1.13 ± 0.01				0.845	0.86	0.99	2.14
Tb	0.244 ± 0.003		0.25	0.28 ± 0.04	0.181	0.19	0.2	0.414
Dy	1.70 ± 0.01		1.6	1.9 ± 0.3	1.32	1.35	1.3	2.8
Ho	0.379 ± 0.004		0.44	0.5	0.304	0.3	0.27	0.59
Er	1.09 ± 0.01						0.81	1.63
Tm	0.155 ± 0.001		0.17	0.18 ± 0.06			0.12	
Yb	0.971 ± 0.011		1.05	1.12 ± 0.08	0.81	0.79	0.81	1.37
Lu	0.150 ± 0.002		0.164	0.17 ± 0.02	0.125	0.12	0.12	0.198
Th	0.0213 ± 0.0007		<0.1	0.08	0.012	0.012	0.04	0.409
U	0.00596 ± 0.00009		<0.02	0.019	0.09	0.05	0.11	0.1

(I) Misawa (2003); (II) Dreibus et al. (2003); (III) Lodders (1998); (IV) Taylor et al. (2002); (V) Barrat et al. (2002).

* Errors are due to counting statistics (1 σ) in γ -ray counting for elements except for REEs, Th and U, for which values of standard deviations (n=5) in ICP-MS are quoted.

This is a blank page.

5. ＲＩの製造

5.Production of Radio Isotopes

This is a blank page.

研究テーマ：放射性同位元素の製造と利用法開発
表題：ガン治療用生薬中の微量元素の放射化分析

1) ガン治療用生薬中の微量元素の放射化分析

本木良蔵、立川　登、木暮広人、加藤岑生
日本原子力研究所、研究炉技術課

1．はじめに

ガン治療における補完代替医療の分野において、植物生薬は抗ガン剤として、また、この副作用の緩和や免疫療法に用いられている。

一般に植物中の微量元素はB, Mn, Mo, Zn, Cu等であるが、種類によっては、特定の元素を含み、濃縮している物がある。植物生薬は微量元素の含有量が、特異的に高いと考えられる。上記の効果に秀でる生薬中の微量元素の含有率を同定することは、ガン治療の補完代替医療の分野に、有益な知見を提供することになる。そこで、含まれる微量元素の分析に、多元素を同時分析できる放射化分析を用いた。

2. 試料の種類

分析対象とした生薬は日本癌学会総会や補完代替医療学会等において、その効果を示している物、または医薬品に登録されている物とし、紫イペ、タヒボ、ヒュウガトウキを選んだ。紫イペとタヒボは、いずれもブラジルに自生する樹木の樹皮と内部樹皮である。ヒュウガトウキは宮崎県等で民間薬として使用されてきた根茎である。いずれも市販品である。

3．試料処理と照射条件

生薬の粉末試料は原子炉内の照射孔で、安全に照射するため、予め300℃で加熱し、水分を除き試料とした。比較標準元素については、事前に生薬をJRR-3Mの気送管や水力ラビットで照射し、定性分析した結果を基に選択した。

定量のための放射化分析では、JRR-4は、R4-16-20サイクルにPN(照射時間100秒)を、JRR-3はR3-16-12サイクルにHR-1(照射3時間)を、R3-16-01サイクルにPN-1(照射15分)を使用した。試料包装には、照射時間に対応してポリエチレンフイルム、PEN、石英管を用いた。

4．測定と解析

測定には、JRR-4およびRI製造棟の Ge半導体検出器とキャンベラ社製のGenie2000を、解析には、東洋テクニカ製のPC/GAMMAを用いた。

5. 結果

ガン治療用生薬の放射化分析の結果をTable. 1に示す。

Table. 1 ガン治療用生薬中の微量元素と濃度

元素	紫イペ (μg/mg)	タヒボ (μg/mg)	ヒュウガトウキ (μg/mg)
Sc	0.005	0.003	0.1
Cr		1.8	
Mn	3.1	1.5	1.6
Fe	38	25	270
Co			0.17
Zn	5.4		
Rb		42	470
Sr	670	160	
Ba		6.2	25.0
La			0.11

紫イペはSrが、タヒボはRbとSrが、ヒュウガトウキは、FeとRbとBaの濃度が特異的に高い結果が得られた。この放射化分析により、植物生薬の特徴を明らかにできた。

この微量元素の存在が、各種生薬の薬効にどのように関与しているのか、不明な点が多い。生薬中に特異的に存在する元素を放射化し、標識化合物としてRIトレーサに製造できるなら、有効成分研究や薬理試験に利用できる可能性がある。

参考文献

1) 桜井 弘、田中秀彦編集、生体微量元素、平成6年3月15日 廣川書店発行

原子炉：ＪＲＲ－３　装置:気送管、水力ラビット　分野：RIの利用法開発
原子炉：ＪＲＲ－４　装置:気送管　分野：RIの利用法開発

This is a blank page.

6. その他

6. Others

This is a blank page.

研究テーマ：フィッション・トラック年代測定
表　　題：FT年代測定のためのディテクターの開発

1)　フィッション・トラック法に用いるＤＡＰプラスティックディテクターの改良

岩野英樹[1]・吉岡　哲[1,2]・檀原　徹[1]・鶴田隆雄[2]
[1]:(株)京都フィッション・トラック　[2]:近畿大学原子力研究所

最近、フィッション・トラック（FT）年代測定法の外部ディテクターとしてジアリルフタレート（diallyl phthalate：DAP）樹脂[1,2,3,4,5,6]が用いられている。従来天然の鉱物の白雲母が使われてきたが、原子炉での照射後 Sc-46(半減期 84 日)と Ta-182(半減期 115 日)が突出して放射化されることから、放射線障害防止の観点上、放射化の小さい DAP 樹脂への変更が進んでいる[7]。またDAP樹脂ではトラックの自動計測が可能で、FT法において重要な役割を果たしている[8]。

しかし DAP 樹脂の放射化分析の結果から、Br が不純物として含まれることが明らかになった[9]。Br-82 の半減期は 35 時間と比較的短いが、照射直後から数日間は比較的高い放射線量をもつ。

DAP 樹脂は、DAP モノマーに対し開始剤 IPP モノマーを 3%添加、重合させて作られるが、原料のメーカーが異なる新しい DAP 樹脂製品を入手した。そこで、従来の DAP 樹脂と新しい樹脂（どちらも山本光学㈱製）の特性を予察的に検討したので報告する。

まず、JRR-4 炉気送管(3.5MW)において熱中性子照射を 120 秒間行い、GM サーベイメータを用いて表面線量を測定した。照射から 6 日後、従来の DAP 樹脂の線量はバックグランドレベルの約 2 倍であったのに対し、新 DAP はバックグランドレベルとなり、より早く冷却した。放射化分析による Br の定量化は現在行っている。

次にフィッション・トラックのエッチング特性を調べた。標準ガラスに貼り付け、60 秒間照射した 2 種類の DAP 樹脂について、PEW-65 溶液（60℃）[6,8]を用いて 2 分間エッチングした。この条件は従来の DAP 樹脂の最適エッチング条件である[6,8]。その結果、次の 3 点が明らかになった:(1)新DAPのエッチング速度の方が大きく、同エッチング条件でトラック径に差が認められた（図 1）。(2)従来の樹脂にはリコイルトラック(ノイズ)が多く見られるが、新しい樹脂には少ない。(3)トラック密度にわずかに差が認められ、従来の樹脂を 1 とした時、新しい樹脂では 0.94 となった（表 1）。(1)の結果から、2 種類の樹脂の適正エッチング条件が異なることがわかった。また(3)の結果は、(1)と(2)が影響している可能性がある。

新 DAP 樹脂は従来のものより放射化しない点で優れているといえる。エッチング特性についてはさらに検討する必要がある

参考文献

1) Tsuruta, T. (1999) Radiat. Meas., 31, 99-102.
2) Tsuruta, T. (2000) Radiat. Meas., 32, 289-297.
3) Tsuruta, T. (2001a) Radiat. Meas., 34, 167-170.
4) Tsuruta, T. (2001b) American Society for Testing and Materials, 100, 789-796.
5) 小口・鶴田 (2001) 第 1 回先進放射線応用シンポジウム(大阪大学), 103-106.
6) 吉岡哲・鶴田隆雄・岩野英樹・檀原徹 (2002) FT　ニュースレター, 第 15 号, 1-8.
7) Danhara, T., Iwano, H., Yoshioka, T. and Tsuruta, T. (2003) Jour. Geol. Soc. Japan, 109, 665-668.
8) Yoshioka, T., Tsuruta, T., Iwano, H. and Danhara, T. (2003) Nucl. Instr. and Meth. B 207, 323-332.
9) Yoshioka, T., Tsuruta, T., Iwano, H. and Danhara, T. (in press) Radiat. Meas.

原子炉:JRR-4　　装　置:気送管　　分　野:その他(放射年代学)

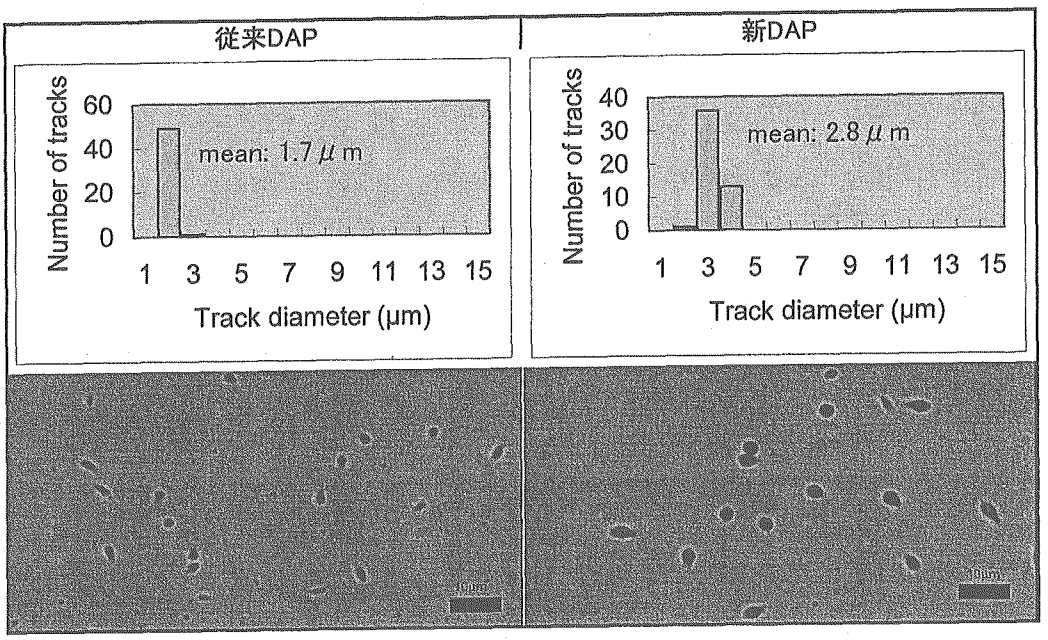

図 1. 2 種類の DAP 樹脂のトラックエッチング実験結果（上：トラック径、下：顕微鏡写真）.

	従来DAP	新DAP
測定システム	Nikon E1000顕微鏡 + Victor HV-M1500高品位モニタ	
標準ガラスコード1	NIST-SRM612(GL-45)	
FT計数(個)	3608	3397
測定面積(cm^2)	0.0112	0.0112
FT密度(cm^{-2})	3.221E+05	3.033E+05
FT密度の誤差(±1σ)	5.4E+03	5.2E+03
検出効率	1 とした時	0.942
標準ガラスコード2	NIST-SRM612(GL-46)	
FT計数(個)	3721	3484
測定面積(cm^2)	0.0112	0.0112
FT密度(cm^{-2})	3.322E+05	3.111E+05
FT密度の誤差(±1σ)	5.4E+03	5.3E+03
検出効率	1 とした時	0.936

表 1. 2 種類の DAP 樹脂のトラック検出効率実験結果.

原子炉:JRR-4　　装 置:気送管　　分 野:その他(放射年代学)

2) 中性子捕捉療法の難治性癌治療への適応拡大に関する基礎的・臨床的研究

Basic & Clinical Study of Application of Boron Neutron Capture Therapy for Cancer

柳衛宏宣、三井清加、緒方亜弥、江里口正純　東京大学先端科学技術研究センター
丸山一雄、桑田康宏　帝京大学薬学部生物薬剤学教室
山瀬利博　東京工業大学資源化学研究所
Hironobu Yanagie[1], Sayaka Mitsui[1], Aya Ogata[1], Yasuhiro Kuwata[2], Kazuo Maruyama[2],
Tosihiro Yamase[3], & Masazumi Eriguchi [1]
[1]Research Center for Advanced Science & Technology, The University of Tokyo,
[2]Dept. of Pharmaceutics, School of Pharmaceutical Sciences, Teikyo University,
[3]Chemical Resources Laboratory, Tokyo Institute of Technology

1　研究の目的と意義

中性子捕捉療法（Neutron Capture Therapy： NCT）は、中性子捕獲確率の高い核種を含む化合物に腫瘍集積性を持たせ、外部から照射される少量の熱中性子との核反応で生ずる放射線を用いて腫瘍細胞にダメージを与える新しいタイプの放射線治療法である。NCTでは主に^{10}B化合物が用いられボロン中性子捕捉療法（BNCT）と呼ばれており、世界各国の臨床試行で良好な治療成績を収めている。BNCTの特徴は^{10}B(n, α)^{7}Li反応で生じるα線及びLi反跳核の飛程（飛距離）が細胞１個分程度（～10μm）であり、放射線エネルギーの全てを細胞１個の範囲内に落とすため殺細胞性が極めて高いことである。またホウ素薬剤が腫瘍細胞のみに集積していれば、隣接する正常細胞を傷つけることなく腫瘍のみを選択的に撃退できるため、浸潤の激しい腫瘍（悪性脳腫瘍・悪性黒色腫等）を患部の機能を温存したまま根治できる画期的な治療法である。

我々は、Immunoliposome を用いたボロンの腫瘍選択的なデリバリーシステムを利用して熱中性子を照射すると腫瘍細胞に著しい細胞障害効果を確認した。さらに生体においてボロンを投与する場合、肝臓、脾臓などの細網内皮系による捕捉を回避する必要があるため、Polyethylene-glycol で ^{10}B 封入 liposome を被覆し、いわゆる Boronated Stealth Liposome を作製し、腫瘍へのボロンの集積性を増加させ、熱中性子照射後、著しい腫瘍増殖抑制効果を認めた。

臨床においては膵癌に対するβ線の術中照射を約30 例、乳癌の乳房温存手術後の放射線療法を約４０例経験しており、中性子捕捉療法による術前・術中照射を肺癌・消化器癌の臨床治験および炎症性乳癌に対する術前・術中照射に応用する準備は整いつつある。ボロン化合物の開発と投与法、原子炉の種々の照射の特性を検討していくことにより、さらに患者個人に適したオーダーメイドの中性子捕捉療法ができ、応用を拡大できると思われる。

今回、我々は、ボロン化合物が細胞内に取り込まれた際により核近傍にボロン原子が接近できるように化合物内にボロン原子を多く含有させる化合物を合成することに成功した。共同研究者の山瀬らにより^{10}Bを32個含有するボロノポリ酸を合成した。ポリ酸（ポリオキソメタレート）は金属と酸素原子との結合からなるナノからミクロサイズの陰イオンであり、多くは水溶液中で合成が可能である。現在までに山瀬らはポリ酸の構造化学、光化学、光電気化学を世界に先駆けて研究しており、多くの新しい構造、光触媒反応、ホトクロミック、エレクト ロクロミック、電場発光等の蛍光体及び抗腫瘍、抗ウイルス活性等を見出した。すなわち、タングステン金属からなるポリ酸は、インフルエンザウイルス、はしかウイルス、パラインフルエンザウイルス、さらにアシクロビル耐性のヘルペスウイルスサイトメガロウイルス、HIVに優れた抗ウイルス効果を認めている。さらに、モリブデンを核としたポリ酸において、乳癌細胞株、大腸癌細胞株、繊維肉腫細胞株を用いた担癌マウスにおいて腫瘍増殖抑制効果を見いだした。ポリ酸（ポリオキソメタレート）は金属と酸素原子との結合からなるナノからミクロサイズの陰イオンであり、結合する金属の種類、数によりその抗腫瘍効果や水溶液中の安定性が変化してくる。

JRR4　照射炉、回転細胞照射装置、即発ガンマ線測定装置
JRR3　中性子ラジオグラフィー装置　　医学

7個のモリブデン原子からなるポリ酸を膵臓癌細胞AsPC-1に投与しTUNEL染色によりアポトーシスを検出できた。このことよりポリ酸の作用メカニズムとして、ポリ酸の強力な還元作用があり癌細胞のミトコンドリアにおける電子伝達系の抑制効果を生じ、波及的にアポトーシスに至り、癌細胞死に導くものと考えている。最近の知見では、抗エイズウイルス作用を示すタングステンのポリ酸がメチシリンと併用して強いMRSA抗菌活性も示す事、バナジウムのポリ酸がPRSPに対し強い抗菌作用を示すという重要な発見があり、ポリ酸の構造と抗腫瘍活性部位の同定に多大なヒントを提供するものである。

このような背景をもとに、より有効な中性子捕捉療法を行うためには、より高濃度の^{10}B原子が腫瘍内に取り込まれる必要が有り、今回の研究ではポリ酸を用いた新規ボロン化合物を作成し、そのBNCT効果の検討を行った（図１　a、b)。

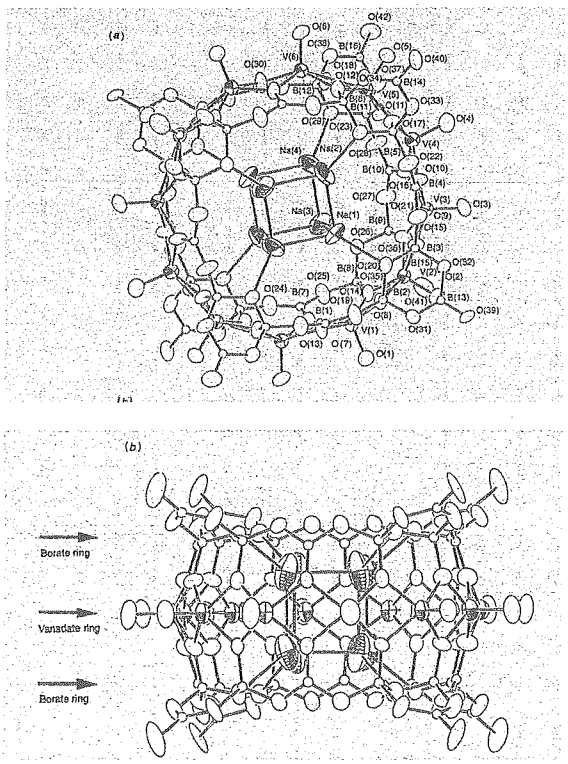

図１．$H_{15}[V_{12}{}^{10}B_{32}O_{84}Na_4]\cdot 13H_2O$ の構造式

２　方法

ポリ酸 ($H_{15}[V_{12}{}^{10}B_{32}O_{84}Na_4]\cdot 13H_2O$; ^{10}B32)の合成：10B で構成されたホウ酸ナトリウム(H3BO3)とバナジウム([NH3Bu]4[V4O12])を pH7.0～8.0 の条件化で MeOH を還元剤として加え 500W の高圧水銀灯を用いて光を当てることにより、Keggin 構造を持つ ^{10}B32 を沈澱させ、集積物に NaCl を加え塩を形成させ合成した。

癌細胞：ヒト膵臓癌細胞株 AsPC-1 を用いた。AsPC-1 は 10%FCS および 100μg のペニシリン／ストレプトミシン含有 RPMI1640 培養液にて 37℃で５% CO2 インキュベーター内で培養した。

Liposome の調整：腫瘍内局注において局所の Liposome の分散性を高めるため、Lipsome 膜表面の荷電が陰性である COTOSOME-EL を用いて、ボロン化合物封入 Liposome を調整した。Liposome 内封入ボロン濃度は順天堂大学の ICP-MAS および学習院大学の HPLC を用いて測定した。

中性子ラジオグラフィー用中性子照射：ヒト膵臓癌細胞株（AsPC-1）を用いた担癌マウスにおいて ^{10}B32 水溶液、^{10}B 封入 PEG-Liposome / TF-PEG-Liposome を静脈注射後、40μm の全身切片を作製し、切片を CR39 detector に貼り付け、JRR3 中性子ラジオグラフィー装置（熱中性子、冷中性子）において中性子ラジオグラフィーを行った (fluence : Imaging 用; 2 x 10^{12} n/cm^2 : thermal、2 x 10^{11} n/cm^2:cold、^{10}B 濃度測定用 ; 2 x 10^{10} n/cm^2) (図２a、b)。

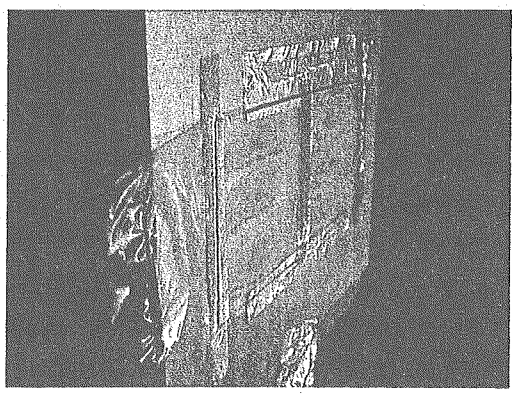

図２a. JRR3 における中性子ラジオグラフィー：CR39 track detector にマウス切片サンプルをはりつけ照射する

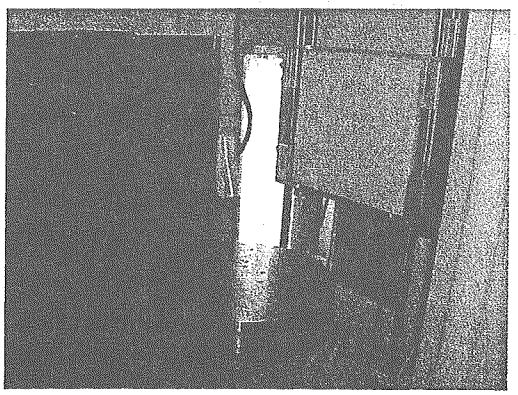

図２b. JRR3 ラジオグラフィー用熱中性子照射装置

エッチング：CR39 detector を 6.25 N NaOH 溶液あるいは KEW 溶液にて 70℃で 120 分処理し、α線の飛程を同定した。
抗腫瘍効果用照射：（1）$5x10^3$ 個の癌細胞を種々の濃度の 10B32 含有培養液に反応させつつテフロンチューブに入れ、JRR4 の細胞照射装置を用いて、fluence :2 x 10^{12} n/cm^2 の熱中性子を照射した。照射後、5 cm 径シャーレに 1x103 個の癌細胞を撒き、培養液を入れ、2週間 37℃で5% CO2 インキュベーター内で培養した。2週間後に、シャーレ内の培養液を洗浄し、増殖してきたコロニーを Cristal Violet 液にて染色し、コロニー数を計測し、細胞増殖抑制効果を検討した。
（2）AsPC-1 担癌マウス（n=20）に新規ホウ素化合物（^{10}B32）、BSH、それぞれの封入 Liposome を腫瘍内局所注射し、専用マウスホールダーに固定し熱中性子を照射し、BNCT の効果を検討する。2 x 10^{12} n/cm^2 の熱中性子を照射する。照射終了後は、JRR 4 の原子炉設備のマウス飼育施設において飼育する。経時的に腫瘍のサイズを測定し、腫瘍増殖抑制効果を確認する。

3 結果

（1）中性子ラジオグラフィー：今回は、preliminary な結果として、JRR3 の冷中性子照射装置において 2 x 10^{11} n/cm^2 の照射を行い ^{10}BSH 封入 PEG-Liposome のイメージを得ることができた。Liposome を PEG 化することにより腫瘍への集積性が増大することがわかった（図3a）。

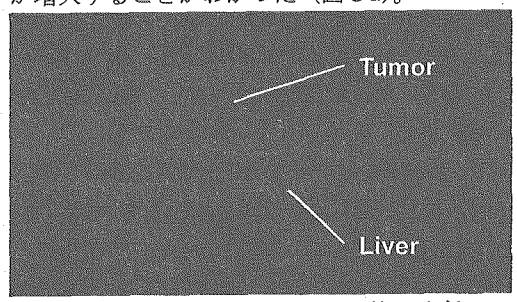

図3a. ^{10}BSH 封入 PEG-Liposome 静脈注射 48 時間後の担癌マウスイメージング

さらに、^{10}B32 水溶液(700 μg)を静脈注射2時間後のイメージにおいては、全身にボロン原子が分布しているのがわかった（図3b）。

（2）癌細胞障害効果

^{10}B32 水溶液の濃度および熱中性子依存性に BNCT により癌の増殖抑制効果があることがわかった。^{10}B32 水溶液の濃度が高くなる程細胞毒性も認められている（図4a、b）。

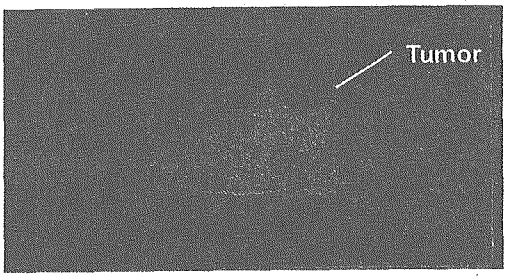

図3b. ^{10}B32 水溶液静脈注射2時間後の担癌マウスイメージング

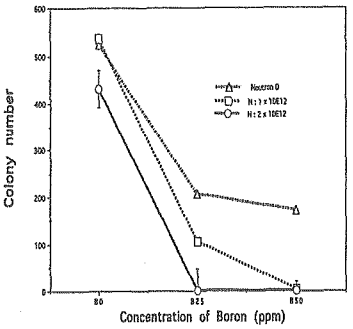

図4a. ^{10}B32 を用いた BNCT によるコロニー増殖抑制効果-1

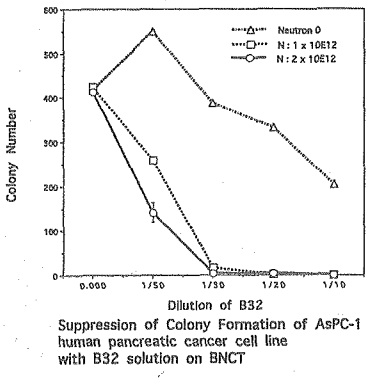

図4b. ^{10}B32 を用いた BNCT によるコロニー増殖抑制効果-2；1/10：70 ppm, 1/20：50 ppm, 1/30：30 ppm, 1/50：10 ppm ^{10}B32 相当

（3）腫瘍増殖抑制効果

^{10}B32 水溶液および ^{10}BSH 水溶液を封入した Cationic Liposome と Anionic Liposome を腫瘍内に局注し、熱中性子を照射すると、明らかに、腫瘍の増殖抑制効果を認めた。その効果は ^{10}BSH よりも ^{10}B32 を用

いた場合の方が強かった。ボロン封入 Liposome を局注群においても、担癌マウスの体重減少はみとめられず、顕著な毒性は認められなかった（図５a、b)。

4　考察

我々が、Drug Delivery System (DDS)として用いている Polyethylene Glycol(PEG)にて Liposome 表面を被覆した Stealth Liposome は、今回の中性子ラジオグラフィーの Imaging においても腫瘍への集積性を確認できた。癌細胞に多く発現している Transferrin Rreceptor に対して Transferrin を PEG に結合させればさらに集積性も増加するものと考えられる。今後も、これらの DDS を用いて腫瘍選択的なボロンデリバリーを考え、照射部位を限局できることにより、照射による副作用を細小限に軽減できると考えられる。

癌細胞内に DDS を用いてボロン化合物をデリバリーした際に化合物内のボロン原子数を増加させることにより、細胞質内にボロン原子がより多く分散することにより、熱および熱外中性子照射時に遺伝子の break が生じやすくなると考え、今回、ボロン原子を多く含むポリ酸を合成した。合成したボロンポリ酸は水溶性が 35mg/ml であった。In vitro および Invivo において著明な、中性子捕捉反応を示し抗腫瘍効果を示した。これからは、さらに安全性の確認および、投与後の各種臓器の組織学的変化、生化学的指標の変化などを検討していく。さらに、DDS に封入することにより選択的な腫瘍への送達も確認していきたい。

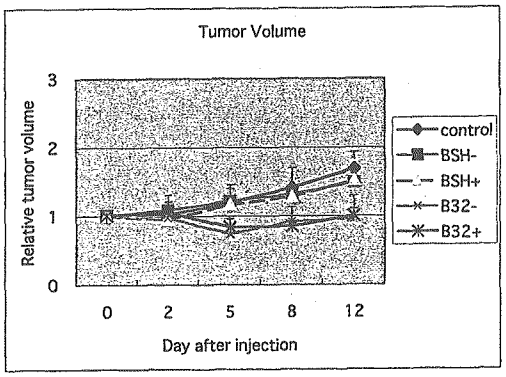

図５a. ^{10}B32 封入 Liposome の腫瘍内投与後の BNCT による腫瘍増殖抑制効果

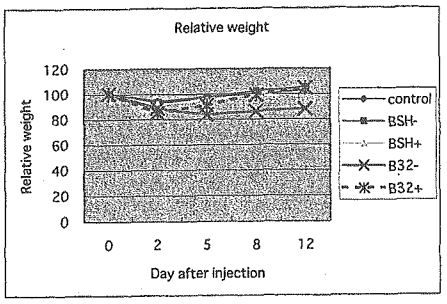

図５b. ^{10}B32 封入 Liposome を用いた BNCT 後のマウスの体重の推移

5　今後の展望及び方針

Liposome を PEG 化することにより、^{10}B 原子の腫瘍集積性を増強を認めた。現在は、BSH と BPA の２つのボロン化合物が臨床試験に使用されているが、さらに腫瘍選択性のあるボロン化合物が開発されれば、単体もしくは DDS キャリアーに封入し、この手法を用いて臓器集積性の検討が行え、化合物の開発に伴い中性子捕捉療法の適応拡大に寄与できると思われる。すなわち、JRR3 の中性子ラジオグラフィー装置を使用させて頂き、新規ボロン化合物の腫瘍集積性の確認を中性子ラジオグラフィーを用いて検討する（Imaging およびボロンの濃度の測定)。続いて、JRR4 の細胞照射装置において、In vitro での BNCT 効果を Colony formation assay で検討し、In vivo において、担癌マウスにボロン化合物キャリアーを投与後、中性子捕捉反応を行い、腫瘍増殖抑制効果を確認する。さらなる新規ボロン化合物の開発を続けていきたい。

我々は、消化器外科及び乳腺外科領域の癌に対しての BNCT の適応拡大を目指している。現在使用されているボロン化合物をキャリアーに封入し選択的に癌組織に送達後、BNCT を行う臨床試験を計画中である。JSCD での検討、倫理委員会申請などの準備を開始している。

Publications

1. H Yanagie, K Ogura, K Takagi, K Maruyama, T Matsumoto, Y Sakurai, J Skvarc, R Illic, G Kuhne, T Hisa, I Yoshizaki, K Kono, Y Furuya, H Sugiyama, H Kobayashi, K Ono, K Nakagawa, M Eriguchi：Accumulation of boron compound to tumor with polyethylene-glycolbinding liposome by using neutron capture autoradiography, Applied Radiation and Isotopes, 61,

639-646, 2004.
2. Maruyama K, Ishida O, Kasaoka S, Takizawa T, Utoguchi N, Shinohara A, Chiba M, Kobayashi H, Eriguchi M, Yanagie H. Intracellular targeting of sodium mercaptoundecahydrododecaborate (BSH) to solid tumors by transferrin-PEG liposomes, for boron neutron-capture therapy (BNCT). J Control Release. 2004 Aug 11;98(2):195-207
3. Ogura K, Yanagie H, Eriguchi M, Lehmann EH, Kuhne G, Bayon G, Kobayashi H. Neutron capture autoradiographic study of the biodistribution of 10B in tumor-bearing mice. Appl Radiat Isot. 2004 Oct;61(4):585-90.
4. 柳衛宏宣、江里口正純：新しい術中放射線治療ーボロン中性子捕捉療法の現状と将来展望、現代医療、36(1), 1111-1121, 2003.

低温核偏極による超微細相互作用の研究

3) Study of Hyperfine Interaction using Low-Temperature Nuclear Orientation

大矢　進，大坪　隆，政森洋平，泉川卓司[1]，西村克彦[2]，武藤　豪[3]
S. Ohya,T. Ohtsubo, Y. Masamori,T. Izumikawa, K. Nisimura, S. Muto

新潟大学自然科学研究科
Graduate School of Science and Technology, Niigata University
[1]新潟大学アイソトープ総合センター
[1]Radioisotope Center, Niigata University
[2]富山大学工学部
[2]Faculty of Engineering, Toyama University
[3]高エネルギー加速器研究機構中性子研究所
[3]Neutron Science Laboratory, KEK

1．はじめに

原子と原子核の間には超微細相互作用があり、これまで色々な方法で研究されてきた。我々は低温核偏極の方法で、放射性原子核をプローブにしてこれまで困難であった領域の超微細相互作用の研究を可能にしてきた。この研究目的は放射性原子核をプローブとして用いて、非磁性体あるいは磁性体での超微細相互作用を研究するものである。超微細相互作用の強さは原子核の磁気モーメントあるいは電気的四重極モーメントと磁場あるいは電場勾配との積となって現れる。その測定の方法とて ^{3}He/^{4}He 希釈冷凍機で～７mK に冷却して核スピンを偏極させる方法を用いる。偏極核からのガンマ線，ベータ線の角分布の異方性の測定，さらにこの偏極核に高周波をかけて，共鳴を起こさせ，この共鳴を異方性の崩れで測定する核磁気共鳴により，精度良い超微細相互作用の情報を得ることが出来る。この方法は NMR-ON (Nuclear Magnetic Resonance on Oriented Nuclei) といわれ大変精度と感度が良い。原子核の電磁モーメントの値が知れているときは，結晶場の内部磁場，ナイトシフトなどの情報を得る。また結晶場の情報が知られているときには，これを用いて原子核の電磁モーメントを決定できる。これらの方法で ^{185}W の基底状態の磁気モーメントの決定，及び ^{197}Pt のニッケル中の超微細相互作用の測定に成功したので報告する。

2．^{185}W の基底状態の磁気モーメントの測定

2．1　^{185}W 研究目的と意義

原子核の構造を調べるのに磁気モーメントの値は大変重要である。我々はこれまで ^{187}W 測定を NMR-ON の方法で行い $|\mu(^{187}W)| = 0.621(15)\ \mu_N$ [1]と決定した。この値はニールソンモデルによる 3/2$^-$[512]状態の理論値の予想と一致していた。^{185}W の基底状態も 3/2$^-$[512]状態と思われる。これらの系統性とモデルの正当性の検討のため ^{185}W の磁気モーメント測定を試みた。

JRR-3 水力照射設備　HR-1, 2　　原子核物理学，核物性物理学分野

2．2　^{185}W の測定方法，試料作成

^{185}W の崩壊は図１に示すように 99.9%の β 線のみを出す。

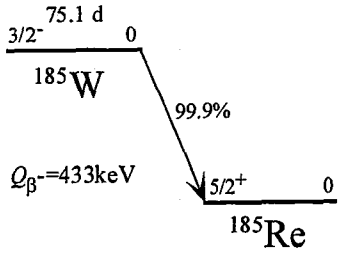

図１．^{185}W の崩壊様式

そのため測定はこのベータ線をプローブとした NMR-ON の実験を行った。試料は純鉄の中にタングステンを原子量で 0.15%入れたものをローラで伸ばして 2 ミクロンの厚さにして，これから 4mmϕ のものを打ち抜き製作した。この試料を原研の 3 号炉を用いて熱中性子を照射して，鉄の中に非常に希薄な ^{185}W を作った。　照射後は 800 度でこの試料を真空中で 1 時間熱処理をした。これを ^{3}He/^{4}He 希釈冷凍機で約 8mK に冷却した。β 線は 50 mm^2 面積の厚さ 0.5 mm の Si 検出器で測定した。外部磁場は箔に対して平行に超伝導マグネットを用いて印加された。

3．^{185}W の結果及び検討

図２に観測された共鳴線を示す。それぞれの外部磁場 0.1, 0.2, 0.4T に対しての典型的な共鳴線が観測された。縦軸はベータ線の 0 度と 180 度の非対称性（スケールは任意）を示す。　横軸は印加された高周波の周波数である。図２の共鳴の実線はガウス形と直線でフィットしたものである。

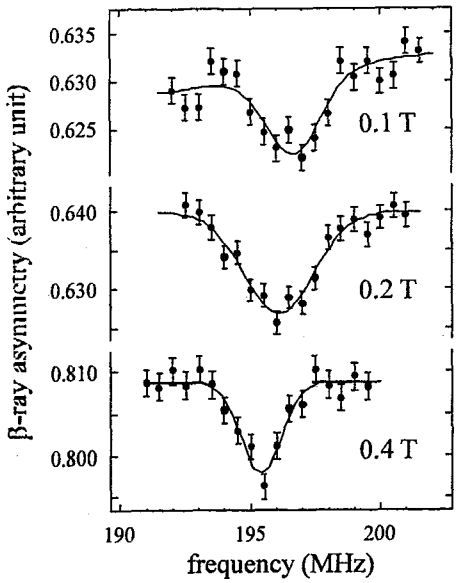

図２．^{185}W の NMR-ON 共鳴図

これらかの結果を表１に示す。

表 I.　^{185}W*Fe*.の実験結果

B_0 (T)	共鳴周波数 (MHz)
0.1	196.6(2)
0.2	196.1(2)
0.4	195.4(2)

純粋な磁気相互作用であると共鳴周波数は次のようになる

$$h\nu = | g \{ B_{hf} + (1+K)B_0 \} | \mu_N.$$

ここで B_{hf} は内部磁場，K はナイトシフトを表わす。鉄中の W の内部磁場は我々が前に測定して $B_{hf}(^{187}WFe) = -71.4(18)$ T [1]と得ている。ナイトシフトは非常に小さいので無視して，この内部磁場を用いると，磁気モーメントは次のようになる。

$\mu(^{185}W) = +0.543(14)\ \mu_N$.

符号はベータ線の非対称性から決定した。この値は Ekstroem *et al.*[2]が実効的なスピンの g-factor g_s を自由なものの 0.6 倍であるとした場合，理論値が$+0.57\mu_N$.となる値に良い一致を示している。

4．^{197}Pt のニッケル中の内部磁場の測定

4．1　^{197}Pt の内部磁場の研究目的と意義

超微細相互作用は原子核と束縛電子が作り出す磁場との相互作用によって生じる。束縛電子のフェルミコンタクトにより，磁場は原子核領域での分布は一様でなく原子核中心からの距離に依存する。そうすると原子核が作る磁気モーメントは原子核が有限の広がりを持つために，モーメントを作り出す位置により磁場が異なるために平均として同位元素による内部磁場が異なってくる。この同位体間での差を hyperfine anomaly(以後 HFA という)という。

本研究では、実験によって ^{197}Pt の共鳴周波数を求めることによって、^{197}Pt、^{191}Pt について強磁性体中 HFA の影響を受ける NMR-ON 法で求められた共鳴周波数と、強磁性体中での HFA の影響を受けない方法で求められた磁気モーメントの結果を用い、HFA を求め、理論値との比較を行った。

4．2　^{197}Pt の測定方法，試料作成

測定方法，試料作成は２．２に述べられているものとほとんど同じである。ホストは鉄でなくニッケルを用いて Pt は濃縮された ^{196}Pt を用いた。図３に ^{197}Pt の崩壊様式を示す。^{197}Pt の基底状態のスピンは 1/2-なので偏極してもガンマー線の異方性はない。そのためベータ線をプローブとして共鳴測定を行った。

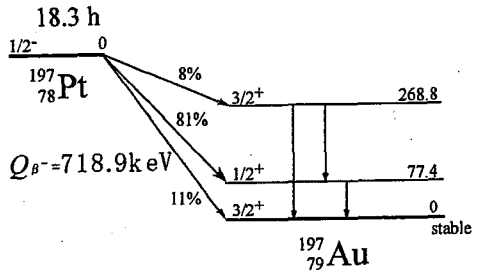

図３　^{197}Pt の崩壊様式

5．測定結果及び検討

今回の測定では、外部磁場を 0.2T、0.4T、0.6T としたときについて NMR-ON 測定を行った。その結果を得られた共鳴スペクトルを図４に示す。図４の共鳴の実線はガウス形でフィットしたものである。外部磁場依存性の関係式から 0T での共鳴周波数 230.7(1)[MHz]が得られた。ただし、ナイトシフト K は非常に小さいと仮定し $K = 0$ とした。

HFA $^{191Pt}\Delta^{197Pt}$ は以下のように定義される。

$$\frac{\nu(^{191}\mathrm{Pt}Ni)}{\nu(^{197}\mathrm{Pt}Ni)} = \frac{g(^{191}\mathrm{Pt})}{g(^{197}\mathrm{Pt})}(1 + {}^{191Pt}\Delta^{197Pt})$$

ν (^{191}Pt*Ni*)、g (^{191}Pt)は Zech らの NMR-ON 実験[3]によって得られており、g (^{197}Pt)の値は Atomic Beam 法を用いた実験[4]で得られている。ν (^{191}Pt*Ni*)に今回の実験で得られた値を用いると、

$$^{191Pt}\Delta^{197Pt} = 12(5)\%$$

となる。

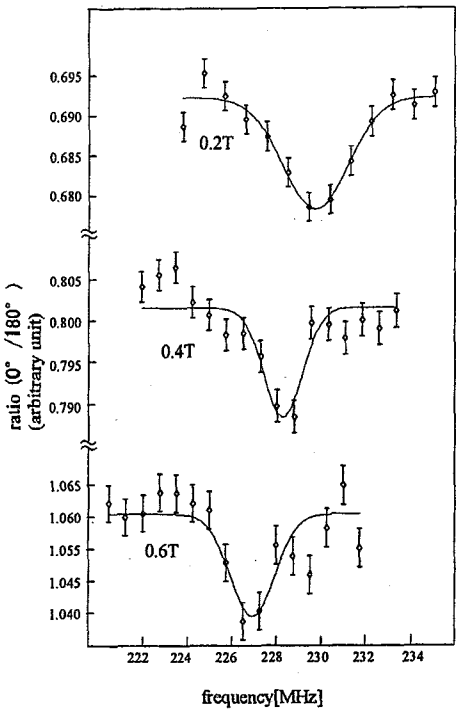

図4　^{197}Pt の NMR-ON 共鳴図

粒子模型によって計算される $^{191Pt}\Delta^{197Pt}$ は+0.2%であり、この実験値が非常に大きな値である事がわかる。これほど大きな HFA は通常考えられない。そこで、実験値同士の比較のために ^{197}Pt と同じスピンパリティ状態である ^{195}Pt を用いて, $^{195Pt}\Delta^{197Pt}$ を求め以下の様になった。^{195}Pt の g-factor、及び共鳴周波数についてはそれぞれ核磁気共鳴[5]、Spin-echo[6]で得られた値を用いた。その結果次のようになる。

$^{195Pt}\Delta^{197Pt}$=15(5)%

通常 HFA は核構造が異なるときに 大きな値を持つが、$^{195Pt}\Delta^{197Pt}$ はそれぞれ同じ スピンパリティ状態であるにもかかわらず、$^{191Pt}\Delta^{197Pt}$ と同様に非常に大きな値となった(理論値: +0.04%)。以上の点から Atomic Beam 法により得られた ^{197}Pt の g-factor　1.02(4) μ_N. について検討をするべきである。しかしながら報告されている値については、publish された論文はなく private communication[4]となっている。同一スピンパリティ状態での HFA は小さいことから内部磁場の値は ^{195}Pt によって求められたものを用いると ^{197}Pt の g-factor は g(^{197}Pt)=0.90(2) μ_N.と決定できる。別な方法でこの g-factor を精度よく決定できると HFA は求められる。今後の課題である。

参考文献

[1] S. Ohya, K. Nishimura and N. Mutsuro, Hyp. Int. 36 (1987) 219.

[2] C. Ekstroem and H. Rubinsztein, Phys. Scripta 14 (1976) 199.

[3]G. Seewald, *et.al,* Phys,Rev.B66174401 (2002)

[4] Y.W. Chan, *et.al,* Bull. Am. Phys. Soc. 13, No.6, 895 CE14(1968) ; Priv. Comm.(1968)

[5]M. Kontani and J. Itoh, J. Phys. Soc. Japan 22 345 (1967)

[6]W.G. Proctor and F.C. Yu Phys. Rev. 81 20(1951)

成果の公表

1．T. Ohtsubo, S. Ohya and S. Muto, Magnetic moment of the 3/2$^-$ ground state of ^{185}W, to be published in Hyperfine Interaction (in press)

2．T. Ohtsubo, S. Ohya, K. Nishimura, T. Izumikawa, J. Got, M. Tanigaki, A. Taniguchi, Y. Ohkubo, Y. Kawase, and S. Muto, Bohr Weisskopf effect measurements using NMR-ON, 2nd Joint Meeting of the Nuclear Physics Divisions of the American Physical Society and the Physical Society of Japan, Sep. 18-22, 2005, Hawaii.

謝　辞

本報告書の発刊にあたり、多くの皆様から多大なご協力を頂きました。編集に際し、ご協力頂いた、東京大学物性研究所吉沢英樹氏、東京大学大学院工学系研究科システム量子工学専攻中沢正治氏、研究炉部長桜井文雄氏、JRR-4管理課加島洋一　氏に深く感謝致します。

付　録

Appendix

This is a blank page.

付 録

原研研究炉の利用設備一覧

1．ＪＲＲ－３

1）実験設備

実 験 孔	実 験 装 置
１Ｇ	高分解能粉末中性子回折装置（ＨＲＰＤ）
１Ｇ－Ａ	生体高分子用中性子解析装置（ＢＩＸ－Ⅲ）
１Ｇ－Ｂ	生体高分子用中性子解析装置（ＢＩＸ—Ⅳ）
２Ｇ	三軸型中性子分光器（ＴＡＳ－１）
３Ｇ	中性子トポグラフィ及び精密光学実験装置（ＰＮＯ）
４Ｇ	汎用三軸型中性子分光器（ＧＰＴＡＳ）
５Ｇ	偏極中性子散乱装置（ＰＯＮＴＡ）
６Ｇ	東北大学中性子散乱分光器（ＴＯＰＡＮ）
７Ｒ	中性子ラジオグラフィ装置（ＴＮＲＦ）
Ｔ１－１	中性子偏極回折装置（ＨＱＲ）
Ｔ１－２	単結晶中性子回折装置（ＫＳＤ）
Ｔ１－３	粉末中性子回折装置（ＫＰＤ）
Ｔ１－４－１	即発ガンマ線分析装置（ＰＧＡ）
Ｔ１－４－１Ａ	化学反応実験装置（ＬＣＥ）
Ｔ１－４－２	多重即発ガンマ線分析装置（ＭＰＧＡ）
Ｔ１－４－３	ＴＯＦ型中性子反射率計（ＴＯＦ）
Ｔ１－４－４	中性子ラウエ回折装置（ＬＡＵＥ）
Ｔ１－４－５	中性子ベータ崩壊基礎測定装置
Ｔ２－１	残留応力測定中性子回折装置（ＲＥＳＡ）
Ｔ２－２	中性子４軸回折装置（ＦＯＮＤＥＲ）
Ｔ２－３	中性子ＩＰ付生体物質中性子回折計（ＢＩＸ－Ⅱ）
Ｔ２－４	高分解能三軸型中性子分光器（ＴＡＳ－２）
Ｃ１－１	高エネルギー分解能三軸型中性子分光器（ＨＥＲ）
Ｃ１－２	二次元位置測定小角散乱装置（ＳＡＮＳ－Ｕ）
Ｃ１－３	超高分解能後方散乱装置（ＵＬＳ）
Ｃ２－１	冷中性子散乱実験デバイス開発装置（ＬＴＡＳ）
Ｃ２－２	中性子反射率計
Ｃ２－３－１	中性子スピンエコー分光器（ＮＳＥ）
Ｃ２－３－２－１	多重即発ガンマ線分析装置（ＭＰＧＡ）
Ｃ２－３－２－２	即発ガンマ線分析装置（ＰＧＡ）
Ｃ２－３－３－１	冷中性子ラジオグラフィ（ＣＮＲＦ）
Ｃ２－３－３－２	パルス中性子機器開発装置（ＣＨＯＰ）
Ｃ２－３－３－３	ＴＯＦ型中性子反射率計（ＴＯＦ）
Ｃ２－３－３－４	中性子ラウエ回折装置(ＬＡＵＥ)
Ｃ３－１－１	高分解能パルス冷中性子分光器（ＡＧＮＥＳ）
Ｃ３－１－２－１	中性子光学システム評価装置（ＮＯＰ）
Ｃ３－１－２－２	多層膜中性子干渉計／反射率計（ＭＩＮＥ）
Ｃ３－２	中性子小角散乱装置（ＳＡＮＳ－Ｊ）

2）照射設備

水力照射設備	HR－1，2
気送照射設備	PN－1，2
放射化分析用照射設備	PN－3
均一照射設備	SI－1
回転照射設備	DR－1
垂直照射設備	VT－1，RG－1～4 BR－1～4，SH－1

2．JRR－4

1）実験設備

プール
中性子ビーム設備
散乱実験設備
冷却水循環ループ
医療照射設備（BNCT）
即発ガンマ線分析装置

2）照射設備

簡易照射筒	Tパイプ（水力）
	Sパイプ
	Dパイプ
	Nパイプ
気送管照射設備	PN